applied sciences

Applications of Medical Physics

Edited by
Salvatore Gallo and Ivan Veronese

Printed Edition of the Special Issue Published in *Applied Sciences*

www.mdpi.com/journal/appliedsci

MDPI

Applications of Medical Physics

Applications of Medical Physics

Editors

Salvatore Gallo
Ivan Veronese

MDPI • Basel • Beijing • Wuhan • Barcelona • Belgrade • Manchester • Tokyo • Cluj • Tianjin

Editors

Salvatore Gallo
University of Milan
Italy

Ivan Veronese
University of Milan
Italy

Editorial Office
MDPI
St. Alban-Anlage 66
4052 Basel, Switzerland

This is a reprint of articles from the Special Issue published online in the open access journal *Applied Sciences* (ISSN 2076-3417) (available at:
https://www.mdpi.com/journal/applsci/special_issues/Applications_of_Medical_Physics).

For citation purposes, cite each article independently as indicated on the article page online and as indicated below:

LastName, A.A.; LastName, B.B.; LastName, C.C. Article Title. *Journal Name* **Year**, *Volume Number*, Page Range.

ISBN 978-3-0365-3613-2 (Hbk)
ISBN 978-3-0365-3614-9 (PDF)

Contents

About the Editors

Salvatore Gallo (PhD) is a research scientist at the Department of Physics at the University of Milan (Italy). He received his Ph.D. in Applied Physics in 2016. He performs research in the field of dosimetry for various radiation beams (photons, electrons, neutrons, protons, and carbon ions) by means of electron spin resonance (ESR) and 3D gels.

Ivan Veronese (PhD) is an Associate Professor at the Department of Physics at the University of Milan (Italy) and a member of the National Institute of Nuclear Physics (INFN). He received his PhD in Physics in 2004 from the University of Milan after a Marie Curie Fellowship at the Helmholtz Zentrum München. His main research interests are in the field of applied physics, with a focus on ionizing radiation dosimetry and radiation protection.

applied sciences

MDPI

Editorial

Applications of Medical Physics

Salvatore Gallo [1,2] and Ivan Veronese [1,2,*]

[1] Dipartimento di Fisica "Aldo Pontremoli", Università degli Stud di Milano, Via Celoria 16, 20133 Milano, Italy; salvatore.gallo@unimi.it
[2] Istituto Nazionale di Fisica Nucleare (INFN), Sezione di Milano, Via Celoria 16, 20133 Milano, Italy
* Correspondence: ivan.veronese@unimi.it

1. Introduction

Since the discovery of X-rays, the use of the principles and methods of physics in medicine has contributed to the improvement of human health. Physics-based techniques have been progressively developed and optimized with the aim to support physicians to formulate prompt diagnoses and to set up the effective treatments of several diseases.

Together with the continuous advances in the clinical procedures making use of ionizing radiations and related instruments, several other emerging and powerful resources are becoming more and more important. Tools such as ultrasounds for oncological and neurological therapeutic practices, nanoparticles, nanotechnologies for theragnostic applications, and artificial intelligence for quantitative medical imaging are just a few examples of the rich panorama of instruments currently available to the Medical Physicists.

Today, medical physics is a mainstream discipline recognized worldwide, with applications covering numerous areas of medicine and whose impact and scientific results deserve to be disseminated among the community of the applied sciences.

With this mission in mind, the scope of this Special Issue of *Applied Sciences*, entitled "Applications of Medical Physics", is to collect original research manuscripts describing cutting-edge physics developments in medicine and their translational applications, as well as reviews providing update on the latest progresses in this field.

A total of 28 manuscripts have been submitted to the Special Issue, and 20 of them have been accepted for publication. The final collection includes 17 original research manuscripts and 3 reviews by authors from 9 different countries. The published papers cover several areas, spanning from radiation therapy, nuclear medicine, radiology, dosimetry, radiation protection, and radiobiology.

A quick overview and general classification of the manuscripts is given below.

2. Contributions

Various contributions of this Special Issue deal with the research toward physics-based innovative approaches for the treatment of oncological diseases or, more in general, propose the optimization of the methods currently employed in several clinical practices. External radiation therapy, brachytherapy, and theragnostic approaches are considered, the improvement of patient outcomes being the final and common aim of the studies. The attempt to reveal and understand the biological or radio-biological mechanisms governing such approaches is also often highlighted.

In this context, Crapanzano et al. propose in their review [1] an overview of the inorganic and hybrid nanoparticles of interest for X-ray-based oncological treatments. The authors point out how the physicochemical properties of the nanoparticles, together with the choice of surface functionalization and targeting strategies, affect the key parameters of external X-ray radiation therapy and X-ray activated photodynamic therapy in terms of energy deposition and total delivered dose in target tissues.

The optimization of radiotherapy procedures in the cohort of patients affected by esophageal cancer is considered in the manuscript by Tai et al. [2]. In fact, this study aims to

Citation: Gallo, S.; Veronese, I. Applications of Medical Physics. *Appl. Sci.* **2022**, *12*, 1852. https://doi.org/10.3390/app12041852

Received: 18 January 2022
Accepted: 5 February 2022
Published: 11 February 2022

evaluate the effect of radiation to the Epicardial Adipose Tissue (EAT) on survival outcomes in patients with esophageal cancer receiving neoadjuvant chemoradiotherapy followed by esophagectomy. The authors highlight the importance to consider EAT as an organ at risk (OAR) and propose the index of "EAT radiation exposure intensity" as a biomarker of survival outcomes in these patients.

Brachytherapy is the main field considered by Jo et al. [3]. In their manuscript, the authors highlight how potential applicator displacements can lead to significant changes in dose distribution during cervical brachytherapy treatments. To face this problem, a robust optimization scheme developed using a genetic algorithm combined with a median absolute deviation as a robustness evaluation function is proposed.

In the frame of eye proton therapy optimization for personalized treatments, Petringa et al. [4] compare Relative Biological Effectiveness (RBE) values obtained from in vitro experimental data with predictions made by the Local Effect Model, Monte Carlo approaches, and semi-empirical models based on Linear Energy Transfer (LET) experimental measurements. Their results evidence how a Treatment Planning System based on an RBE and LET prediction could improve the estimation of the radiobiological response of the treated neoplasia as well as the surrounding healthy tissues.

Finally, in the field of nuclear medicine, Urbano et al. [5] investigate the possible role of [^{99m}Tc]Tc-Sestamibi in the regulation of biological processes involved in breast cancer progression such as proliferation and apoptosis. Indeed, ex vivo and in vitro data about the correlation between sestamibi uptake and apoptosis suggest the possible role of sestamibi in the regulation of the pathophysiological processes involved in breast cancer. In conclusions, the authors suggest that the evidence of the accumulation of sestamibi in breast cancer cells and the subsequent mitochondrial damage can open new clinical perspectives on the use of this radiopharmaceutical in both the diagnosis and treatment of breast cancers.

Another subject that unites various contributions of this Special Issue is the research toward the optimization of the procedures employed in radiological imaging and the characterization of the related instruments and tools with the primary aim of patient dose reduction.

In this context, Albano et al. [6] compare radiation doses and imaging performances of an EOS imaging (Paris, France) system with those of conventional radiography and computed tomography (CT) in the case of the detection and measurement of enchondromas. The analysis suggests that low-dose EOS digital radiographic evaluation has the same capability as conventional radiography to detect and measure enchondroma-like inserts on a phantom. Thanks to its lower radiation dose, this imaging method could be particularly useful in the follow-up of patients affected by multiple enchondromas.

The study of Muhammad et al. [7] focuses on the possibility of reducing organ doses in pediatric CT chest-abdominal pelvis examination by optimizing the CT protocols. The effect of scan parameters such as tube voltage, tube current, slice collimation, pitch, and tube current modulation on image quality indices and organ doses are accordingly investigated. The results suggest that a significant potential reduction in the dose for such type of diagnostic examinations is achievable.

Dose optimization in CT scans is also considered in the manuscript by Barca et al. [8]. The authors highlight the need for an exhaustive characterization of noise properties in CT imaging with iterative reconstruction (IR) algorithms for assessing the actual dose-reduction potential of this technique, as well as its possible limitations for specific clinical applications. In their in-phantom study, the authors carry out a voxel-based assessment of noise properties in CT imaging with adaptive statistical iterative reconstruction (ASiR) and adaptive statistical iterative reconstruction-V (ASiR-V) for different blending levels of reconstruction and contrast objects. Their results confirm the potential of ASiR-V and ASiR in reducing noise as compared with conventional filtered back projection approaches, suggesting, however, that the use of pure ASiR-V or ASiR might be suboptimal for specific clinical applications. In conclusion, authors recommend a voxel-based characterization of noise

properties when dealing with a novel IR algorithm or when comparing the performances of different IR algorithms.

Quantitative imaging is another recurrent topic in various contributions of this Special Issue. Actually, the quantitative analysis of medical images proved to be a powerful approach for improving diagnostic and treatment strategies, as well as for developing predictive models.

Texture analysis is performed by Savini et al. [9] to characterize the impact of the acquisition angle on Digital Breast Tomosynthesis (DBT) images. The authors conclude that the DBT acquisition angle affects the textures extracted from DBT images, and this dependence should be considered when establishing baselines for classifiers of malignant tissue. Therefore, texture analysis in DBT has the potential to be an alternative to other quantitative techniques such as model observer methods for scoring and comparing DBT images.

Quantitative analyses are also increasingly used in nuclear medicine, both for diagnostic and therapeutic purposes. Di Martino et al. [10] highlight how the Partial Volume Effect (PVE) is the most important factor of loss of quantification in Nuclear Medicine. Therefore, in order to achieve an accurate quantification of the radioactivity concentration, PVE has to be considered and compensated, especially in small structures. In this context, the authors present a new approach for the correction of PVE, using a post-reconstruction process starting from a mathematical expression, which only requires the knowledge of the Full Width at Half Maximum of the Point Spread Function of the imaging system.

In the domain of low-field MR-guided radiotherapy for cervical cancer, Cusumano et al. [11] evaluate the performance of the radiobiological parameter Early Regression Index ERI_{TCP} in predicting pathological complete response. The results suggest that ERI_{TCP}, calculated by combining the tumor volume measured on the MR images acquired at simulation and during therapy, is a promising response biomarker for cervical cancer. If validated on a larger cohort of patients, the use of this index can represent a valuable tool to personalize the treatment strategy in the context of the cervical cancer, moving towards the anatomical and functional preservation of the irradiated tissues.

Mazzilli et al. [12] propose a semi-automatic segmentation method to characterize the lungs of COVID-19 patients with respiratory syndrome. The approach is based on a robust, operator-independent identification of threshold Hounsfield Unit (HU) values that distinguish three regions of the lungs with intuitively clear functional meaning. The next step toward a fully automatic segmentation is also considered by combining the implemented method with an atlas of CT images of COVID-19 patients. The quantitative analysis carried out on the HU histograms paves the way to the development of predictive models of early clinical outcome.

The fundamental role of CT images analysis in the COVID-19 pandemic scenario also emerges in the manuscript by Biondi et al. [13]. The authors propose a study about the classification performance for COVID-19-patient prognosis from automatic Artificial Intelligence (AI) segmentation. They highlight the possibility of obtaining a reliable automated segmentation of lungs and of Ground-Glass Opacities areas in CT scans using non-supervised approaches and using this segmentation in a prediction pipeline for patient prognosis. Semi-supervised segmentation, implemented using a combination of non-supervised segmentation and feature extraction, seems to be a viable approach for patient stratification and could be leveraged to train more complex models. This would be useful in a high-demand situation similar to the current pandemic to support gold-standard segmentation for AI training.

The growing demand and use of AI, not only for quantitative imaging, but in several other areas of medicine, is highlighted by Avanzo et al. [14]. In particular, in their review, the authors summarize the main applications of AI in medical physics and express their point of view on the role and the involvement of Medical Physicists (MPs) in this evolving scenario by defining the challenges of AI in healthcare for the MPs and by describing the skills the MPs can offer in this field.

Finally, the research toward the development or improvement of instruments and methods for accurate dose evaluation, both in external and internal dosimetry, confirmed to be very active, and various contributions of this Special Issue deal with this topic.

Arilli et al. [15] evaluate the combined use of the Integral Quality Monitor (IQM, iRT Systems GmbH, Koblenz, Germany) transmission detector and SoftDiso software (Best Medical Srl—Chianciano Terme, Italy) for in vivo dose monitoring for the simultaneous detection of delivery and patient setup errors in whole-breast irradiation. The authors show that the two devices provide complementary information and allow the fast detection of all types of errors. The proposed method represents a new strategy in Quality Assurance (QA) programs and would be an important step forward in the clinical routine to increase the quality of external breast irradiation.

The issue of in vivo dosimetry in charged particle radiation therapy is considered by Cirrone et al. [16]. The authors investigate the suitability of a new online, non-invasive, bias-less detector for relative dose monitoring. The detector, protected by both a national Italian and an International patent, exploits the idea that when a beam current is injected into the body of a patient undergoing a charged particle therapy, the current itself can be collected using a conductive electrode in contact with the skin of patient. After characterizing the system in vitro, preliminary in vivo tests highlight the capability of the device in acting as beam monitoring during a proton-therapy treatment and its ability in the verification of the correct dose delivered among the various fractions of the treatment.

A radiation detector with a relatively longer history is the GEMPix, a detector developed at CERN a few years ago. It couples two technologies, the Gas Electron Multiplier as an amplifier for electric charges and four highly pixelated Timepix ASICs as readout. Leidner et al. [17] propose a comprehensive review about the medical applications of GEMPix. The authors describe examples of the use of this device for relative dose measurements in X-ray radiation therapy and hadron therapy. Some preliminary measurements performed to check the capabilities of GEMPix in proton tomography are also illustrated, as well as the most recent application of the detector in the field of microdosimetry. A discussion about on-going and future developments concludes the review.

In the frame of internal dosimetry, the study by Milano et al. [18] aims at the validation of a platform, named MCID, based on patient-specific images and direct Monte Carlo (MC) simulations for internal dosimetry in the radioembolization of liver tumors with ^{90}Y-labeled microspheres. The validated platform allows the fast implementation of a personalized MC dosimetry, based on patient imaging data. Additionally, the authors investigate the impact of tissue inhomogeneities on the dosimetric evaluation for the radioembolization treatment and the potential improvement of a MC approach in this therapy.

The same treatment strategy for liver lesions, based on percutaneous ablation using ^{90}Y microspheres embedded into a sealant matrix, is considered by D'Arienzo et al. [19]. In this manuscript, the absorbed dose per unit administered activity is assessed in small lesions by MC calculations considering a simplified geometry. Furthermore, an analytical formula derived from MC calculations that incorporates the absorbed fractions for ^{90}Y is proposed. The authors conclude that in a scenario of the intra-tumoral injection of microspheres, the proposed equation can be usefully employed in the treatment planning of spherical lesions of small size (down to 0.5 cm diameter) providing dose estimates in close agreement with MC calculations.

Lastly, under the main topic of dosimetry, the Special Issue includes the study by Gonzales et al. [20] which contribute to the development of a practical protocol for fingernail electron spin resonance (ESR) dosimetry useful for the routine monitoring of the extremity exposures of medical workers handling radiation sources. The authors investigate the effects of chemical treatment using dithiothreitol (DTT) on the changes of the ESR spectra in irradiated and unirradiated fingernails after a long storage time. The results show that the treatment of fingernail samples with DTT lead to a significant reduction of the background signal. They also point out that freezer storage of the samples is more effective than vacuum storage. Furthermore, after the DTT treatment, the fingernail samples provided

good signal stability for both background and radiation-induced signals with less intra-individual variations.

3. Conclusions

In conclusion, we were very pleased to guest-edit this Special Issue that collects relevant contributions reflecting the increasingly widespread interest in medical physics and related applications.

We hope this Special Issue could reach the widest audience in the scientific community and contribute to boosting further scientific and technological advances into the intriguing world of medical physics and their multidisciplinary applications.

Finally, we wish this Special Issue may help the readers to conceive both new and improved ideas about the "Applications of Medical Physics" in their respective fields.

Author Contributions: Both Authors have contributed to the conceptualization, writing, review and editing of this manuscript. All authors have read and agreed to the published version of the manuscript.

Funding: This research received no external funding.

Acknowledgments: The Guest Editors would like to express their sincere thanks to all authors for their valuable contributions and to all peer-reviewers for their constructive comments and suggestions.

Conflicts of Interest: The authors declare no conflict of interest.

References

1. Crapanzano, R.; Secchi, V.; Villa, I. Co-Adjuvant Nanoparticles for Radiotherapy Treatments of Oncological Diseases. *Appl. Sci.* **2021**, *11*, 7073. [CrossRef]
2. Tai, H.-C.; Lee, J.; Huang, W.-C.; Liu, H.-C.; Chen, C.-H.; Huang, Y.-C.; Lee, C.-J.; Yun, C.-H.; Hsu, S.-M.; Chen, Y.-J. The Impact of Radiation to Epicardial Adipose Tissue on Prognosis of Esophageal Squamous Cell Carcinoma Receiving Neoadjuvant Chemoradiotherapy and Esophagectomy. *Appl. Sci.* **2021**, *11*, 4023. [CrossRef]
3. Jo, B.; Park, K.; Shin, D.; Lim, Y.K.; Jeong, J.H.; Lee, S.B.; Kim, H.-J.; Kim, H. Feasibility Study of Robust Optimization to Reduce Dose Delivery Uncertainty by Potential Applicator Displacements for a Cervix Brachytherapy. *Appl. Sci.* **2021**, *11*, 2592. [CrossRef]
4. Petringa, G.; Calvaruso, M.; Conte, V.; Bláha, P.; Bravatà, V.; Cammarata, F.P.; Cuttone, G.; Forte, G.I.; Keta, O.; Manti, L.; et al. Radiobiological Outcomes, Microdosimetric Evaluations and Monte Carlo Predictions in Eye Proton Therapy. *Appl. Sci.* **2021**, *11*, 8822. [CrossRef]
5. Urbano, N.; Scimeca, M.; Bonfiglio, R.; Mauriello, A.; Bonanno, E.; Schillaci, O. [99mTc]Tc-Sestamibi Bioaccumulation Can Induce Apoptosis in Breast Cancer Cells: Molecular and Clinical Perspectives. *Appl. Sci.* **2021**, *11*, 2733. [CrossRef]
6. Albano, D.; Loria, A.; Fanciullo, C.; Bruno, A.; Messina, C.; del Vecchio, A.; Sconfienza, L.M. Diagnostic Performance and Radiation Dose of the EOS System to Image Enchondromatosis: A Phantom Study. *Appl. Sci.* **2020**, *10*, 8941. [CrossRef]
7. Muhammad, N.A.; Kayun, Z.; Abu Hassan, H.; Wong, J.H.D.; Ng, K.H.; Karim, M.K.A. Evaluation of Organ Dose and Image Quality Metrics of Pediatric CT Chest-Abdomen-Pelvis (CAP) Examination: An Anthropomorphic Phantom Study. *Appl. Sci.* **2021**, *11*, 2047. [CrossRef]
8. Barca, P.; Marfisi, D.; Marzi, C.; Cozza, S.; Diciotti, S.; Traino, A.C.; Giannelli, M. A Voxel-Based Assessment of Noise Properties in Computed Tomography Imaging with the ASiR-V and ASiR Iterative Reconstruction Algorithms. *Appl. Sci.* **2021**, *11*, 6561. [CrossRef]
9. Savini, A.; Feliciani, G.; Amadori, M.; Rivetti, S.; Cremonesi, M.; Cesarini, F.; Licciardello, T.; Severi, D.; Ravaglia, V.; Vagheggini, A.; et al. The Role of Acquisition Angle in Digital Breast Tomosynthesis: A Texture Analysis Study. *Appl. Sci.* **2020**, *10*, 6047. [CrossRef]
10. Di Martino, F.; Barca, P.; Bortoli, E.; Giuliano, A.; Volterrani, D. Correction for the Partial Volume Effects (PVE) in Nuclear Medicine Imaging: A Post-Reconstruction Analytic Method. *Appl. Sci.* **2021**, *11*, 6460. [CrossRef]
11. Cusumano, D.; Catucci, F.; Romano, A.; Boldrini, L.; Piras, A.; Broggi, S.; Votta, C.; Placidi, L.; Nardini, M.; Chiloiro, G.; et al. Evaluation of an Early Regression Index (ERITCP) as Predictor of Pathological Complete Response in Cervical Cancer: A Pilot-Study. *Appl. Sci.* **2020**, *10*, 8001. [CrossRef]
12. Mazzilli, A.; Fiorino, C.; Loria, A.; Mori, M.; Esposito, P.G.; Palumbo, D.; de Cobelli, F.; del Vecchio, A. An Automatic Approach for Individual HU-Based Characterization of Lungs in COVID-19 Patients. *Appl. Sci.* **2021**, *11*, 1238. [CrossRef]
13. Biondi, R.; Curti, N.; Coppola, F.; Giampieri, E.; Vara, G.; Bartoletti, M.; Cattabriga, A.; Cocozza, M.A.; Ciccarese, F.; De Benedittis, C.; et al. Classification Performance for COVID Patient Prognosis from Automatic AI Segmentation—A Single-Center Study. *Appl. Sci.* **2021**, *11*, 5438. [CrossRef]

14. Avanzo, M.; Trianni, A.; Botta, F.; Talamonti, C.; Stasi, M.; Iori, M. Artificial Intelligence and the Medical Physicist: Welcome to the Machine. *Appl. Sci.* **2021**, *11*, 1691. [CrossRef]
15. Arilli, C.; Wandael, Y.; Galeotti, C.; Marrazzo, L.; Calusi, S.; Grusio, M.; Desideri, I.; Fusi, F.; Piermattei, A.; Pallotta, S.; et al. Combined Use of a Transmission Detector and an EPID-Based In Vivo Dose Monitoring System in External Beam Whole Breast Irradiation: A Study with an Anthropomorphic Female Phantom. *Appl. Sci.* **2020**, *10*, 7611. [CrossRef]
16. Cirrone, G.A.P.; Amato, N.; Catalano, R.; Di Domenico, A.; Cuttone, G.; Lojacono, P.; Mazzaglia, A.; Pace, F.; Pittà, G.; Raffaele, L.; et al. On the Possibility to Use the Charge Imbalance in Patients Undergoing Radiotherapy: A New Online, In Vivo, Noninvasive Dose Monitoring System. *Appl. Sci.* **2021**, *11*, 7005. [CrossRef]
17. Leidner, J.; Murtas, F.; Silari, M. Medical Applications of the GEMPix. *Appl. Sci.* **2021**, *11*, 440. [CrossRef]
18. Milano, A.; Gil, A.V.; Fabrizi, E.; Cremonesi, M.; Veronese, I.; Gallo, S.; Lanconelli, N.; Faccini, R.; Pacilio, M. In Silico Validation of MCID Platform for Monte Carlo-Based Voxel Dosimetry Applied to 90Y-Radioembolization of Liver Malignancies. *Appl. Sci.* **2021**, *11*, 1939. [CrossRef]
19. D'Arienzo, M.; Sarnelli, A.; Mezzenga, E.; Chiacchiararelli, L.; Amato, A.; Romanelli, M.; Cianni, R.; Cremonesi, M.; Paganelli, G. Dosimetric Issues Associated with Percutaneous Ablation of Small Liver Lesions with 90Y. *Appl. Sci.* **2020**, *10*, 6605. [CrossRef]
20. Gonzales, C.A.B.; Taño, J.E.; Yasuda, H. An Attempt to Reduce the Background Free Radicals in Fingernails for Monitoring Accidental Hand Exposure of Medical Workers. *Appl. Sci.* **2020**, *10*, 8949. [CrossRef]

applied sciences

MDPI

Review

Co-Adjuvant Nanoparticles for Radiotherapy Treatments of Oncological Diseases

Roberta Crapanzano [1], Valeria Secchi [1] and Irene Villa [2,*]

[1] Department of Materials Science, University of Milano-Bicocca, via R. Cozzi 55, I-20125 Milano, Italy; r.crapanzano2@campus.unimib.it (R.C.); Valeria.secchi@unimib.it (V.S.)
[2] Institute of Physics of the Czech Academy of Sciences (FZU), Cukrovarnická 10/112, 162 00 Prague, Czech Republic
* Correspondence: villa@fzu.cz

Abstract: Nanomedicine is emerging as promising approach for the implementation of oncological methods. In this review, we describe the most recent methods exploiting heavy nanoparticles and hybrid nanomaterials aiming at improving the traditional X-rays-based treatments. High-Z nanoparticles are proposed as radiosensitizers due to their ability to stop the ionizing radiation and to increase the locally delivered therapeutic dose. Other nanoparticles working as catalysts can generate reactive oxygen species upon X-rays exposure. Thanks to their high toxicity and reactivity, these species promote DNA cancer cells damage and apoptosis. Hybrid nanoparticles, composed by scintillators coupled to organic molecules, are suitable in X-rays activated photodynamic therapy. This work highlights the roles played by the diverse nanoparticles, upon ionizing radiation irradiation, according to their physico-chemical properties, surface functionalization, and targeting strategies. The description of nanoparticle qualities demanded by the oncological nanomedicine is presented in relation to the processes occurring in biological medium when X-ray radiation interacts with heavy nanoparticles, including the scintillation mechanisms, the stopping power amplification, and the disputed modeling of the effective deposit of energy within nanomaterials. The comprehension of these issues in nanomedicine drives the strategies of nanoparticles engineering and paves the way for the development of advanced medical therapies.

Keywords: nanoparticles; scintillation; ionizing energy deposition; radiotherapy; photodynamic therapy; singlet oxygen

Citation: Crapanzano, R.; Secchi, V.; Villa, I. Co-Adjuvant Nanoparticles for Radiotherapy Treatments of Oncological Diseases. *Appl. Sci.* **2021**, *11*, 7073. https://doi.org/10.3390/app11157073

Academic Editor: Salvatore Gallo

Received: 21 June 2021
Accepted: 28 July 2021
Published: 30 July 2021

1. Introduction

Today, cancer is still one of the greatest global causes of death. In 2018, there were 18.1 million new cases and 9.5 million cancer-related deaths worldwide. By 2040, the number of new cancer cases per year is expected to rise to 29.5 million with an estimation of cancer-related deaths close to 16.4 million [1,2]. Currently, regular screening and surveillance programs required for early diagnosis/intervention are the best ways to improve the outcome and survival. The diagnostic tools in use in healthcare rely on imaging methods, like optical imaging, radiography, magnetic resonance imaging (MRI), and computed tomography (CT), as well as nuclear imaging techniques [3,4]. More recently image-guided cancer treatments and molecular diagnostics have enabled to subcategorize each cancer type allowing efficient intervention with targeted therapeutics [5,6]. Over the last years, ceaseless efforts have been put by the scientific and medical communities in the cancer research with the aim of finding new diagnosis alternatives for the fabrication of simpler, broad use, and cost-effective imaging tools and scanners [7–9]. The most important goal is to surpass the typical drawbacks of conventional diagnostic procedures, which are, for instance, related to the choice among the available contrast agents presenting low accuracy and specificity, short half-life, low radiodensity, and rapid clearance [10,11]. These disadvantages result in the need of massive and prolonged exposure to high levels

of electromagnetic radiation of the patient for the collection of images with satisfactory resolution [12,13]. Conventional cancer treatments are chemotherapy, radiotherapy, and surgery. Despite, in the past years, these consolidate procedures have enabled an active fight against cancer ensuring long-term survival and quality of life for several malignancies in oncological patients, their broad use has been always associated to diverse drawbacks and side effects. One of the main problems of chemotherapy is the low specificity of chemotherapeutic drugs for cancer cells. Chemotherapy suffers from non-specific biodistribution and poor tumor accumulation of the therapeutic drugs, resulting in high toxicity, damages of the healthy cells, as well as systemic side effects [14,15]. Surgery can represent the only potentially curative therapy of high-risk patients. However, the high tumors recurrence rate associated with surgical resection as single oncological protocol is responsible for a significant morbidity and failure percentage in many malignancies [16]. Lastly, the radiation therapy is limited by the maximum cumulative radiation dose allowed without incurring significant injuries to the adjacent tissues or organs [17,18]. More recently, small molecules-based therapies and immuno-oncology have been demonstrated to be effective owing to some recent successes in the clinic [19,20]. Besides the monotherapies, the combination of the established and accessible therapeutic protocols with immunotherapy has been validated to be efficient in cancer patients [21,22]; however, the ability of the molecular agents used in immunological therapies to reduce immune suppression, or to enhance activation of cytotoxic processes in the tumor environment is associated to a severe toxicity, whose side effects results under debate [23,24].

Novel and targeted cancer therapeutic techniques have been recently developed to guarantee effective, efficient, affordable, and less invasive cancer cares to patients [25]. The search of developing tailored treatments for specific oncological demands has found its productive ground in the branch of nanomedicine; in order to visualize the timetable of the scientific efforts boosting the research on nanomedicine, we the proposed, for instance, works and reviews published in the recent twenty years [26–32]. The European Medicines Agency (EMA) defines nanomedicine as including all applications of nanotechnology and nanoparticles for tumor targeting, imaging, and therapy [27,33]. *Nanoparticles* (NPs) definition refers to those materials as large as 1- to 100-nm made from both inorganic and organic materials. NPs can be administered systemically (via injection inhalation, and oral intake) or locally (via intratumoral delivery and implantable devices such as implants loaded with NPs or anticancer agents) [34–37]. Organic based NPs used in biomedical applications include liposomes [38], polymer constructs [39], and micelles [40]. Inorganic NPs comprise mostly metal, semiconductor, and insulating systems (see [41] and within references to have an overview of the available NPs). Within the past few decades, inorganic NPs have been proposed in the biomedical fields for the implementation of the cancer therapies (chemotherapy, drug delivery [42,43], and hyperthermia [44,45], as well as radiotherapy, photodynamic therapy and X-ray activated photodynamic therapy [17,46]), or for the use as diagnostic agents for imaging techniques [12], as well as for the applications as theranostic tools for oncology and other fatal diseases [47]. The attractiveness of these NPs relies on the versatility and tunability of the physico-chemical qualities, which depend on their composition, morphology, size, and high surface-to-volume ratio. Specifically, NPs modifiable features, like shape, size, and surface charge [28], are key aspects for surface accommodation of functional groups or hydrophobic molecules. The functionalization of NPs surfaces results in enhanced solubility and biocompatibility, in improved stability and retention time in bodily fluids [48,49], and in the ability of the nanosystems to cross physiological barriers for their use in vivo [50]. Moreover, the engineering of the NPs surfaces by targeting ligands enables the specificity of their diagnostic and therapeutic activity towards the malignancy and illness sites in the patients' body and the release of the antitumoral drugs in a stable and controlled manner [51,52]. The adjustment of the physico-chemical properties of NPs by facile doping strategies as well as by the engineering of their size, crystallinity, and surface chemistry would also affect their luminescence behavior. Fluorescent NPs, such as lanthanide doped inorganic nanoparticles [53–55], quantum

dots [56], silica based nanosystems [57,58], as well as metal clusters and nanoparticles [59,60] have been proposed for in vitro and in vivo bioimaging, sensing, drug delivery, and light-triggered oncological therapies. The tuning of the luminescence is a crucial point to satisfy the performance requirements demanded to the nanomaterials for their exploitation in medicine [53,61,62]. Even though many NPs are composed by purely organic and inorganic materials, the development of organic/inorganic hybrid materials is eagerly hunted; hybrid NPs in form of core-shell structures, metal organic frameworks (MOFs), or of nanocomposites where hybrids NPs are dispersed into a polymeric matrix, enable to create a new class of functionalized theranostic NPs that possess unique advantages, exploiting synergistically the feature of their single components [63].

The world of nanomedicine and nanotheranostic is wide and covers many frontiers of medicine. The use of NPs of diverse composition can represent an alternative to the traditional oncology and, in parallel, a way to implement the established therapies and diagnostic tools. In this review, we focus our attention on the utilization of NPs in the X-rays based oncological treatments, with efforts in describing the multiplicity of the roles that the diverse NPs can play according to their compositions and surface functionalization from the radiosensitization in radiotherapy (RT), to the triggered activation of cancer killing agents in the photodynamic therapies (PDT) and in the X-ray activated photodynamic therapy (X-PDT). NPs suitable for X-rays can be divided in a simple way into passive and active nanoparticles. Passive nanomaterials include dense and high atomic number (Z) NPs (for instance, metal containing nanoparticles), able to efficiently stop the ionizing X-ray radiation enhancing the energy deposition within the tissue and thus increase the RT effects at lower doses. A group of active nanoparticles, such as inorganic photo (-and radio) catalysts, possess lower Z than the passive NPs but can sensitize the RT effects by generating an excess of reactive oxygen species (ROS) in cells upon X-rays and by causing ROS-dependent functional disorder/cell death/apoptosis. Another class of active NPs comprises inorganic/organic multicomponent systems allowing a dual effect because of the interaction with the ionizing beam: firstly, an improved response to the external stimuli due to the inorganic dense part; and then the triggered activation of cancer killing agents, such as singlet oxygen sensitizer, nearby the malignancy.

Specifically, in this review we present especially the use of inorganic NPs and hybrids that can efficiently interact with the ionizing irradiation in the RT. The use of organic NPs will be only briefly pictured for topic completeness, regarding especially the possibility to employ light molecular photosensitizers, like porphyrin molecules, with X-ray radiation. The exploitation of biomolecules and drugs in chemo-radiotherapy able, for instance, to increase the cells susceptibility to radiation [64] or inhibit the DNA repair after the treatment [65] are not included in this review.

2. Radiotherapy Mechanism

Radiotherapy is one of the most effective and widely used cancer therapeutic modalities. About 50% of cancer patients are treated with radiotherapy for curative and palliative purposes both as single therapeutic modality and in combination with other treatment methods [66,67]. Although RT cannot be applied to all types of cancer, it is established as a principal option for treatment of many malignancies, such as breast carcinoma, lung carcinoma, melanoma, gastrointestinal cancers, head and neck cancers, gynecological cancers, hematologic malignancies, prostate or cervix tumors, central nervous system neoplasms and thyroid carcinomas, as well as for an effective reduction of pain in the of case bone and brain metastases [68,69].

RT exploits ionizing beams—X-rays or radiation emitted by radionuclides—to stop the rapid proliferation of cancer cells and to achieve the therapeutic goals [70,71]. For the description of the RT mechanism, this review focuses mainly on RT applied by an external X-ray source. As summarized in Figure 1, the interaction of the high energy radiation within tissues induces the killing of tumor cells directly by the damage of the DNA and of the molecular structure leading to the termination of cell division and proliferation,

and even to cell necrosis or apoptosis; otherwise, cancer cells destruction can arise indirectly from the formation of cytotoxic ROS upon interaction with the cellular aqueous environment [72,73]. A detailed description of biochemical reactions occurring in cellular environment upon the interaction with the ionizing radiation is depicted by Clement and co-worker in Ref. [65]. Briefly, in cellular environment, water radiolysis by ionizing radiation results in the formation of several species, mainly: $e-aq$ (hydrated electrons), HO• (hydroxyl radicals), H• (hydrogen radicals), H_2 (radiolytic hydrogen), H_2O_2 (hydrogen peroxide), and $HO^{\bullet}_2$ (hydroperoxyl radical). Afterwards, these products can react and create further ROS, such as O^{-}_2 (superoxide), organic radicals (R•), hydroperoxides (ROOH), and singlet oxygen ($^1O_2$). Under physiological conditions cells generate a certain amount of ROS, whose concentration is regulated by the antioxidant system to maintain cellular homeostasis. Perturbing the cellular balance by radiation-induced ROS creation leads to oxidative stress that can trigger DNA damage and other cell death mechanisms, for instance by necrosis, apoptosis, autophagy, mutation, and senescence.

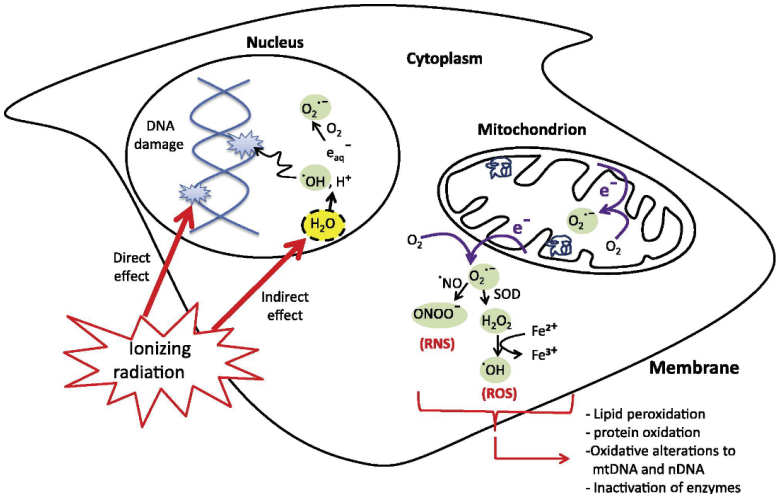

Figure 1. The direct and indirect cellular effects of ionizing radiation on macromolecules. Absorption of ionizing radiation by living cells directly disrupts atomic structures, producing chemical and biological changes and indirectly through radiolysis of cellular water and generation of reactive chemical species by stimulation of oxidases and nitric oxide synthases. Ionizing radiation may also disrupt mitochondrial functions significantly contributing to persistent alterations in lipids, proteins, nuclear DNA (nDNA) and mitochondrial DNA (mtDNA). Reproduced from *Cancer letters* **2012**, *327*, 48–60 [73]. Copyright Elsevier 2012.

Whatever the cancer cells killing mechanism, i.e., by physically direct ionization or using free radicals by water ionization, the goal of radiotherapy is to deliver the maximum dose to the target tumor tissue while safeguarding the surrounding normal tissue. Clinical radiotherapy uses high-energy external X-ray beam, from 6 MeV up to about 20 MeV, from linear accelerators. In typical launched protocols, patients are treated through fractionated regime with dose of 1.8–2 Gy over the course of 4–8 weeks to limit toxicity to normal tissues [74] but in advanced treatment planning the delivered dose to cancer can reach values close to 15–20 Gy [75]. Interactions of such X-rays with biological tissue can occur by (1) photoelectric effect, (2) Compton effect, and (3) pair production, according to the energy of the external X-ray source. In clinical RT the X-rays beams of few tens of MV are widely used for deep seated tumors, while low energy beams (up to 200 kV) have very few applications due to the lower penetration depth (<5 mm) [76]; at these working energies the Compton and the photoelectric effects are dominant (Figure 2), and the deposit of

their energy occurs through a cascade of secondary photoelectrons and Auger electrons, stimulating all the radiobiological effects above depicted.

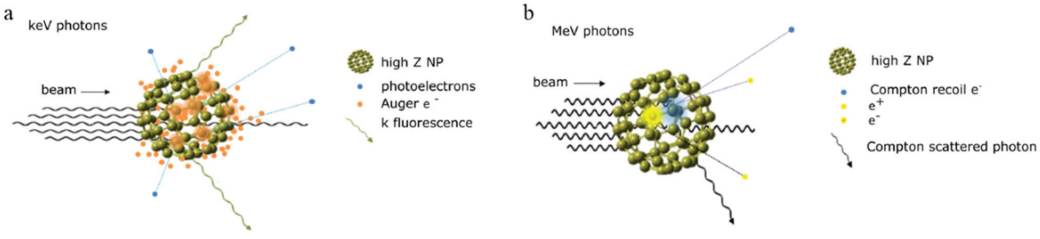

Figure 2. Schematic illustration of inelastic interactions with a high-Z nanoparticle for: (**a**) incident keV photons (orange clouds represent photoelectric events); (**b**) incident MeV photons (blue and yellow clouds represent Compton scatter and pair production events, respectively); Image reproduced with permission from Prof. Z. Kuncic and Dr. Y. Gholami from *Phys. Med. Biol.* 63 (2018) 02TR01 [77].

The radiobiological effects and efficacy in producing a permanent DNA damage in cells are related to the type and the energy of interacting radiation by the linear energy transfer (LET) physical factor i.e., energy deposited per unit distance along the ionization track. LET is higher for heavy ions than for photons (for example a 250 keV X-ray photon have an average LET of 2 keV/µm, whereas alpha particles LET is of hundreds of keV/µm) [78]. The main difference between high LET radiation and low LET radiation is due to a diverse induction of DNA damage that is the primary target required for cell killing: it has been proven that high LET radiation causes more extensive and less repairable cellular damage by very dense events of energy deposition along the track, without penetrating deeply into the human tissues; in turn low LET X-rays deposit energy in tissue in a highly dispersed manner and are thus able to reach deeper tissue penetrations [79]. In RT, the secondary products of the first ionizing event, especially of the photoelectric effect, include the Auger electrons. High LET makes the Auger electrons highly toxic to the cells inducing damage in macromolecular targets of a cancer cell and in the cell membrane, as detailed reviewed in [80] by A. Ku and co-authors, who display the use of Auger electrons in radiation dosimetry and for cancer treatments, such as targeted radiotherapy.

From the above picture, it is evidenced that the effective result of RT and the estimation of the dose deposited in the malignancy environment depend on the interactions in tissue involving a given particle and secondary particles. The modeling of the energy deposition by the ionizing radiation and the following radiobiological consequences are of fundamental importance towards the goal of surpassing the common drawback afflicting RT, like the lack of tissue selectivity, hindering the discrimination between the tumor and the healthy cells, and the need of high energy primary beam enabling the penetration of the radiation in deep tumors and the release of an amount of energy adequate to start the biochemical ROS production to destroy the proliferation of the malignant cells. The most advanced strategies exploit the use of NPs to enhance a localized therapeutic effect of RT, in order to reduce the local dose to be delivered and the toxicity towards normal surrounding tissue, and thus to improve the quality of life of the patience during and after the radiological treatments.

3. Nanoparticles in Radiotherapy

In the following sections, we aim at describing the most used and promising NPs that can be exploited in RT to overcome its limitations and to combine the common RT procedures with novel challenging strategies. Among these strategies, this review emphasizes the X-PDT. Nanomaterials are classified into passive (mostly inorganic containing heavy elements) and active (inorganic nanocatalysts and nanohybrids) NPs. For clarity, a summary of the properties and the application area of the NPs presented in the manuscript is provided at the end of this section, in Table 1. It is worth to notice that the boundaries

of the NPs classes are smooth. In particular, the categorization of the passive and single component inorganic active nanosystems is rather shaky. We have arbitrary chosen to consider as passive NPs all the dense and high Z systems that enable to enhance the energy depositions in the cancer environment; in turn, only nanometric catalysts with lower Z are sorted as active NPs enabling generation of ROS thanks to the high reactivity of their surface upon irradiation. Nevertheless, we are aware that (as discussed in Section 2) ionizing radiation, by interacting with passive heavy NPs, produces secondary charges that contribute at generating ROS localized in the neighborhoods of the ionizing event.

3.1. Passive Nanoparticles as Enhancers of Energy Deposition in RT

The scientific and medical communities strive to find X-ray based therapeutic solutions with the aim to improve the survival rate and life quality in oncological patients subjected to RT by reducing the illness recurrence, which is related mostly to the massive doses required for stopping the cancer cells division but delivered also towards the surrounding healthy tissue. High Z and dense inorganic nanomaterials represent the key to reduce RT parameters, such as external beam energy, delivered dose, and exposition time, while boosting all the toxic and fatal effects of the radiation [74,76]. The idea to exploit high Z materials comes from simple considerations. Indeed, the presence of heavy NPs in a regime of low energy ionizing radiation (<60 keV) maximizes the X-ray beams attenuation by photoelectric effects, whose cross section σ depends on $(Z/E)^{n}$, with $n \cong 3$–4 [77]. This dependency reveals that high Z materials turn out to be supportive in RT by enhancing the deposit of energy in the tumor and in the proximity of the malignant cells (thus, the dose delivered during radiotherapy) [81].

Since the early 1970s, the ability of diverse materials, like water/tissue equivalent materials, alloys of metals, and heavy metals, at stopping the ionizing radiation have been tested for applications in radiotherapy [82]. Later, it has been discovered that metal implants, composed by aluminum, tin, stainless steel, titanium, and lead, can alter the delivered doses in radiotherapy in patients affected by neck and mandibular cancers, due to the difference in Z value between the biological tissues and the metals [83,84]. In the last few decades, the scientific research has looked at the capacity of nanosized heavy metal particles in promoting the dose delivery in cancer tissue as a chance to improve the RT procedure and its therapeutic outcomes, due to the correlation between the enhanced energy dose and the increased cancer cell destruction [85].

Over the past few years, NP sensitizers have been proposed in combination with radiotherapy in order to improve tumor response and control the disease growth. For instance, there has been lot of interest in metallic—gold, gadolinium, silver, bismuth, and platinum—and bimetallic based NPs, as well as in nanometric metal oxides [86,87]. Thanks to the high atomic number, good biocompatibility, and relatively strong photoelectric absorption coefficient, gold nanoparticles (AuNPs, Z = 79) are largely studied for diagnostic and therapeutic applications in cancer therapy [88]. Especially, Au nanoparticles have been under investigation as possible agents for amplification of radiation dose in tumors, in the so called "gold nanoparticle-assisted radiation therapy". From the first decades of 2000's, AuNPs' action has been predicted to increase the fraction of the X-rays energy deposited close to gold NPs because of increased photoelectric interactions, thereby enhancing the local radiation dose also according to their shape, functionalization, concentration, and intracellular distribution [89]. In vivo studies performed by Hainfeld et al. [90] and Herold et al. [91] by injecting Au NPs and microspheres in tumor-bearing mice, have reported the occurrence of biologically effective dose enhancement by using kilovoltage photon beams; while the use of isotopes producing low-energy photons has been foreseen for significantly improving the clinical potential of interstitial brachytherapy. More recent works assess the Au actions considering the increment of dose together with the corollary activation of ROS within malignant cells [92] (see for example Figure 3 reproduced from Ref. [92]). Ongoing research promotes the optimization of nanoparticles targeting and functionalization

to reduce the total doses to be delivered, and to combine ionizing radiation with other therapeutic modalities [93–96]

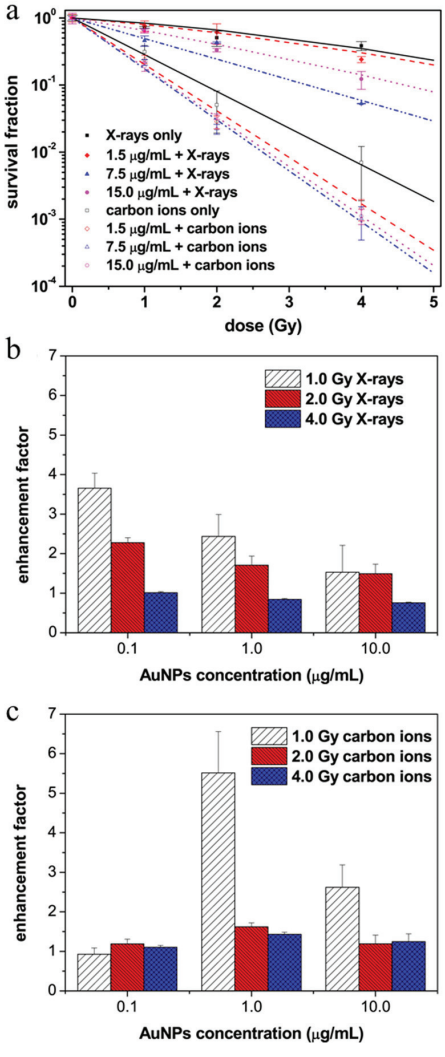

Figure 3. (**a**–**c**) Radiation enhancement effect of 14 nm citrate-capped gold nanoparticles (AuNPs). (**a**) AuNPs improve the cell-killing effects of X-rays and fast carbon ions. (**b**) AuNPs improve the hydroxyl radical production of X-rays (assessed by 3-CCA). (**c**) AuNPs improve the hydroxyl radical production of carbon ions (assessed by 3-CCA). Reproduced with permission from Ref. [92]. Copyright Elsevier 2015.

A valid candidate as sensitizers of RT is Gadolinium (Gd, Z = 64). In addition to its well-known application as contrast agent in MRI, recently the additional role of gadolinium nanostructures in RT has been modeled by computational analysis. Modeling results reveal the capability of Gd NPs at increasing the final delivered dose to the tumors site and the suitability in brachytherapy applications [97,98]. Moreover, studies on gadolinium-NPs, namely AGuIX, confirm the occurrence of sensitization under ionizing radiation in vitro assay on HeLa cells, revealing the attractiveness of gadolinium-based NPs as alternative to

the widely used gold NPs for improving the efficacy of radiation cancer treatments [99].The use of platinum (Pt, Z = 78) NPs (PtNPs) as promising radiation sensitizers in radiotherapy cancer treatment has come into light in a small number of works with respect to the Au and Gd NPs. For instance, in 2010, it has been examined the case of platinum nanoparticles upon irradiation by fast carbon ions (LET = 13.4 keV μm^{-1}). Their use enables the strong enhancement of the biological efficiency of ionizing radiations and the amplification of tumor cells DNA lethal damage (single strand breaks, and mostly double strand breaks) induced by irradiation; moreover, formation of radicals in PtNP proximity has been proved to further contribute to the DNA strand breaks [100]. More recently, porous Pt NPs have opened the way for novel therapeutic strategies. Indeed, while promoting radiation induced cell cycle arrest by an effective energy deposition within the cancer cells, porous Pt systems enable also to generate oxygens (O_2) from hydrogen peroxides (H_2O_2). The final outcomes of exploiting porous Pt NPs are the formation of DNA breaks with the generation of ROS and, at the same time, the hampering of the establishment of hypoxia condition in the tumor, being one of the major causes of cancer radioresistance [101].

Metal oxides nanoparticles are considered an alternative to full metallic systems. Hafnium oxide (hafnia, HfO_2) has been considered in RT as sensitizer to increase energy dose deposit within cancer cells, owing to its high atomic number, electron density, and chemical stability. Hafnium (Z = 72) oxide nanoparticles (NBTXR3) have been designed in terms of size, surface charge, and shape, to concentrate in tumor cells to achieve intracellular high-energy dose deposit with reduced health hazards. Monte Carlo simulation considering a high-energy source of a few MeV predicts an enhancement of local energy deposit, within and close to the tumors where NPs are located, almost 9 times larger with respect to RT alone. In vitro and in vivo studies on the HT1080 fibrosarcoma cell line with NBTXR3 nanoparticles with high-energy sources confirm the results of the simulation, denoting a higher radio-induced cancer cell destruction rate in presence of high Z NPs [102]. Another recently discovered effect of NBTXR3 marks their ability to impact on the activation of the antitumor immune-response, open the way for their use in radio-immunotherapy [103]. Other interesting high Z materials enabling strong absorption of X-rays, are tantalum pentoxide (Ta_2O_5) NPs and bismuth oxide nanoparticles—Bi_2Se_3, Bi_2S_3, and Bi_2O_3, the latter showing a multiplicity of characteristics for multimodal imaging, radiosensitization, as well as in radioprotection [81].

3.2. Active Nanoparticles and Catalysts Inducing ROS Generation

As extensively explained above, the augmented photoelectric effect cross section in presence of NPs with heavy Z enables the creations of secondary charges, mostly Auger electrons, and the productions of direct and indirect DNA cancer cells damages. However, as reviewed by Guerreiro et al. in Ref. [104], there are many evidences that also metal oxide NPs with lower atomic number (made up by Si, Al, Ti, Zn, Fe, Ce and Mn for instance) are responsible of radiosensitization phenomena within tumor cells. This output is imputed to the chemical and catalytic activities of the NPs surfaces contributing to the overall generation of radiation-induced radicals. From a general point of view, nanocatalysts are materials able to produce ROS under high energy light (photocatalysts) and ionizing radiation (radiocatalysts) to decompose unwanted chemical and biological agents. Despite the attempt to treat the radiocatalysis as similar to the well-known photocatalysis [65], it is worth to notice that the use of ionizing radiation guarantees diverse advantages, such as the increased rate of a catalytic reaction, the acceleration of degradation of pollutants, the overcoming of limited penetration of UV/Visible (Vis) light in solutions and biological tissue, as well as the possibility to use a wider range of catalyst also with wider band gap ($E_{g)}$ and greater redox capabilities [105–107]. If we consider the case of (nano) titanium oxide, TiO_2, as representative of photo-/radiocatalysis in semiconductors, catalysis phenomenon can be summarized in the following steps: (1) excitation by high energy ionizing radiation or light source with energy larger than the E_g of the material; (2) promotion of an electron (e^-) from the valence band to the conduction band, and the concomitant generation of

a hole (h^+) in the valence band; in an efficient nanocatalyst, where recombination of the generated e^-/h^+ is restrained, the last step (3) is the diffusion of e^-/h^+ charges towards the materials surface to rapidly (in sub-nanoseconds time range) initiate redox reactions among reactants adsorbed at the nanocatalyst surface, and to start the formation of ROS. In presence of aqueous environment, electrons reduce molecular oxygen forming superoxide radical anion; hydroxyl radicals and hydrogen peroxide molecules are induced by the holes oxidizing water molecules and hydroxide ions. In TiO_2, it has been also proven the occurrence of singlet oxygen creation ($^1O_2$) after oxidation of superoxide radical ion [108–110]. The reactive species, especially hydroxyl radicals, can be used to decompose a variety of pollutants in environmental applications [111]. More important for the goal of this review is the effective damage that the generated ROS can produce on DNA of cancer cells and biomolecules, thus contributing to the biological damage induced during radiotherapy, as well as to the lethal prolonged metabolic oxidative stress after irradiation [112]. Due to the large active surface area, it has been established the importance of morphological features (e.g., size, composition, specific surface ligands, surface charges) on the amount of ROS generated by NPs [113]. Numerous examples in the literature report chemistry strategies to fix up the NP surface properties also through functionalization/coating procedures [114,115].

In this review, we aim at providing straightforward examples illustrating the importance to conduct further research on lower Z radiocatalysts, whose effect in reducing cancer growth in RT is as effective as the one of high Z and dense NPs, thanks to the boosted ROS productions. We consider two well-known radio-photocatalyst NPs, specifically titanium and zinc oxide (TiO_2 and ZnO, respectively), which have been approved by Food and Drug Administration (FDA) [116]. In nanomedicine, the ability of ZnO and TiO_2 in producing ROS by themselves under UV/Vis excitation has been exploited for the photodynamic therapy [117]. Indeed, PDT is considered as a clinically deployed efficient and non-invasive alternative to the surgery and to the current oncological therapies. PDT is based on the cytotoxic effects originating when biocompatible photosensitizers (PSs) are photoexcited, producing ROS and singlet oxygen moieties that induce the cell death through oxidative damage of cellular membranes [118]. PSs can include organic dyes and aromatic hydrocarbons, porphyrins and related photosensitizers, transition metal complexes, and semiconductors [119]. Unfortunately, the PSs approved for routine PDT treatment require UV/Vis light to be activated. In this spectral region, the human tissue transparency is low, thus making PDT ineffective for tumors seated at depths larger than 1 cm [120]. Interestingly, TiO_2 and ZnO have been proved to create ROS also under ionizing radiation and to be suitable for X-ray based oncological treatments. For instance, a work of Youkhana, Esho Qasho, et al. reports the radiosensitization phenomenon in presence of anatase TiO_2 NPs under X-ray beam with energy set from keV to MeV [121]. Tests on cell viability assays have been performed on phantoms and in vitro to determine cells survival curves and the dose enhancement percentage. The obtained results evidence the occurrence of sensitization driven by two different mechanisms: in the keV range, the photoelectric effect coupled to the difference in the atomic numbers of the biological tissue and the TiO_2 NPs are responsible of the dose enhancement; when MeV energy is used, the cross section of the photoelectric effect decreases while the active catalytic surfaces of the NPs start to play the major role in the generation of cell killing ROS, leading to the final therapeutic sensitization of RT. The possibility to take advantage of the two mechanisms, i.e., photoelectric and Z-dependent radiosensitization, together with the generation of ROS capable of destroying tumor cells by nanocatalysts, is at the base of the development of novel composite materials, like Au nanoparticles supported on TiO_2 (Au@TiO_2), enabling the simultaneous and synergetic establishment of the two processes, which lead to superior performances over the single elements [122].

Nanoparticles of ZnO are attractive materials for biomedical applications due to noticeably low toxicity. ZnO NPs have been widely explored for anticancer, antidiabetic, antibacterial, antifungal, and anti-inflammatory activities, as well as for drug delivery applications. Especially, ZnO NPs anticancer action relies on their ability to trigger ROS

generation and apoptosis mechanisms under external excitations. Recently, the X-ray radiation-induced therapeutic behavior of ZnO NPs coated by a silica layer (ZnO/SiO_2) has been studied on prostate adenocarcinoma cell lines. The potentiality of ZnO/SiO_2 nanoparticles to increase radiation-induced killing of the cells has been validated by comparing cells survival after RT with and without NPs. Results display a 2-fold augmented killing rate in presence of ZnO based NPs; the findings show the active response to ionizing radiation of ZnO/SiO_2 by means of the radiocatalytic mechanisms occurring at its surface. The proven catalytic reactions induced by high energy radiation make ZnO/SiO_2 nanoparticles suitable for biomedical applications [123]. The combined use of ZnO with chemotherapeutics represents a step forward in the use of ZnO as anticancer. The loading of the anticancer drug, like doxorubicin as in ref [124], into the ZnO nanoparticles, results in an augmented cytotoxicity effects of the cancer therapy, due to the simultaneous combination of the anticancer action of the drug with the lethal ROS production by ZnO. Current research on nanocatalysts for RT focuses on other oxides, like superparamagnetic iron oxide nanoparticles (SPIONs) that, although the relatively low atomic number of iron (Fe, Z = 26), are used in combination with kV and MV X-rays beams and allow to enhance the impact of X-rays in tumor cells thanks to the production of ROS from catalysis reaction at the oxides surface [125]. Also, studies on cerium oxide NPs (CONPs) have demonstrated their capacity to enhance ROS production during RT in human pancreatic cancer cells and, at the same time, to play a protective role from toxic side effects of RT in normal tissues [126].

3.3. Multicomponent Nanoscintillators for X-PDT

The attempt of finding oncological cures alternative to surgery, chemotherapy and radiotherapy relies on the use of selective and non-invasive approaches with reduced side effects. In the previous paragraph, we mentioned at the advent of PDT as FDA approved oncological treatment, which has been proposed as alternative to the RT for the treatment of primary tumors of skin, esophagus and lung. Far from being an exhaustive explanation, in brief, PDT principle is based on photoexcitation of a PS (among which we can mention noble metal complexes, metal organic frameworks, metal oxides or carbon-based nanostructures, as well as polymeric PS and small organic moieties [127]) to locally generate ROS species and cause cancer cells death. After interaction with light, the PS is excited from ground state (S_0) to unstable singlet excited states. In particular, the first excited state (S_1) may undergo intersystem crossing (ISC) to form a more stable excited triplet state (T_1) with longer lifetime ($\approx\mu s$). Triplet state of PS can produce ROS by interacting with water and molecular oxygen. The first interaction generates free radicals (type I), while the second one produces singlet oxygen moieties (type II). However, the most common PSs can be excited by UV/Vis light; in this wavelengths range light is reflected and scattered by the human tissues, rendering the PDT ineffective for deep-tissue treatment [128]. Moreover, PDT painful side effects can appear immediately after treatment as well as after months. In the literature, many research studies have been reviewing in detail the PDT processes, the advantages and limitations, together with the PSs guideline, for instance see refs [129–133]. One possible solution relies on the so-called second-generation photosensitizers showing higher molar extinction coefficient in the near-infrared region where biological tissues present a transparency window [134,135]. Thanks to their high penetrability, X-rays offer another solution for adapting the PDT principle to deep tumors. From the first decades of the last century extensive studies have displayed the activation of the PS under ionizing radiation [136,137]. Recently, an extensive review by Larue et al. has offered an overview on the efficacy of X-rays in enhancing the toxic activity of some PSs, like hematoporphyrin derivatives, protoporphyrins, or metalloporphyrins They have listed the available photosensitizers used as radiosensitizers or as precursors of PDT effects in combination with radiation therapy [138].

A step forward in the progress of alternative therapies is provided by the so-called X-PDT. The strategy counts on the employment of scintillating nanoparticles (nanoscintillator;

NS), able to convert the ionizing radiations into ultraviolet or visible light through a three stage scintillation process consisting in-conversion, transport, and luminescence [139,140]. NS can be embedded in a biological surrounding, where both the absorption of X-rays by the NS and the deposition of energy by the exciting beam (or the following secondary particles) in its proximity can occur. Afterwards, NS can emit fluorescence (Figure 4a), alternatively, when NS is embedded in biological environment with other elements (organic dyes and therapeutics, for example), the energy can be transferred to the secondary moieties through multiple radiative emission/reabsorption process and/or through efficient energy transfer mechanisms (ET). The interaction can occur between the high-energy beam and the aqueous environment with the consequent excitation of the NS and then the activation of organics nearby (ET′); or the NS can directly absorb the X-rays and transfer the energy to the dye (ET″). Lastly, also the organic molecules can interact with the primary beam by themselves (ET‴) (Figure 4b). In X-PDT, high Z and dense NS are designed to be grafted by a PS therapeutic agent (Figure 4c). In order to employ energy transfer from the NS to the PS for triggering the ROS and $^1O_2$ production, the PS absorption spectrum should be resonant with the NS emission. Potentially, the exploitation of X-rays and heavy NS fulfills all the constraints for RT applications and for inducing radiosensitization (Section 3.1); at the same time, the use of PS, mostly $^1O_2$ producing PS, being attested to be more efficient in the killing of malignant biological tissues and cells [127], guarantees an additional cytotoxicity towards the cancer cells destruction, mimic the action of the traditional PDT. The outcome of the RT- and PDT coupling remains unclear: besides the concept that the final result is just a sum of the effects from the two individual therapies, it has been demonstrated that X-PDT can produce important synergetic effects resulting in an improved efficiency in killing the tumor cells and in the overall reduction of the total dose to the patient [18].

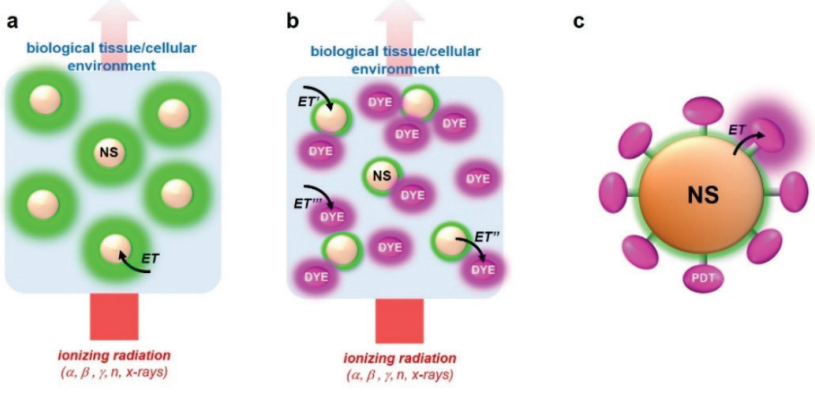

Figure 4. Sketch of the working principle of X-ray activated X-PDT. (**a**) Inorganic nanoscintillators (NS) can be easily embedded in a biological surrounding. (**b**) The NS scintillation luminescence can be exploited to excite a secondary photoactive moiety (dye) by energy transfer (ET). (**c**) Multicomponent hybrid nanosystems can be fabricated by decorating the NS surfaces with specific photoactive functionalities, for example PDT agents, whose action is sensitized by ET from the NS that mainly interacts with the ionizing radiation.

Many inorganic nanomaterials like oxides, fluorides, silica-based nanostructures and semiconductor nanocrystals have been combined with organic photosensitizers towards X-PDT applications [141–148]. We can consider, for instance the case of silica-based nanotubes coupled to PS, displaying noteworthy therapeutic effects thanks to the synergy between RT and PDT [149]. Previous studies have proved the low toxicity of stoichiometric chrysotile [$Mg_3(Si_2O_5)(OH)_4$] nanotubes featuring also the ability to pass the blood brain barrier, potentially important in cancer brain treatments [58]. Thanks to their density, chrysotile nanotubes have been proven to respond to X-ray irradiation by emitting light in the blue

wavelength range, suitable to excite meso-tetra(4-sulfonatophenyl) porphyrin (H_2TPPS^{4-}) as PS. Thus, the surface of chrysotile scintillating nanotubes has been functionalized by an ionic self-assembly strategy with this efficient PS, able to produce singlet oxygen toxic species upon photoexcitation (Figure 5a). The study of luminescence behavior under X-rays (RL) and light (PL) excitations discloses the occurrence of a fast energy transfer (in ps range) from the chrysotile to the PS, together with the sensitization of singlet oxygen production upon ionizing radiation (Figure 5b). As expected, also bare nanotubes enable a sensitization of the $^1O_2$ under ionizing radiation, due to the enhancement in energy deposition in presence of elements with higher Z than the surrounding biological medium. A further stabilization of the functionalized nanotubes has been obtained by covering their surface with polymeric shell. This ultimate composition boosts the ability of the NS to enhance the production of singlet oxygen in an aqueous environment by ET mechanism to PS under X-ray irradiation. Tests in vitro—mimic the radiotherapy dose depositions—show that stabilized chrysotile nanosystems functionalized with porphyrins enable to sensitize the singlet oxygen species at the lowest doses thanks to the contribution of a high-density material, and the effective toxic action of PSs activated by the nanoscintillators (Figure 5c,d). This opens the possibility of effectively reducing the high-energy radiation exposure of patients during oncological therapies.

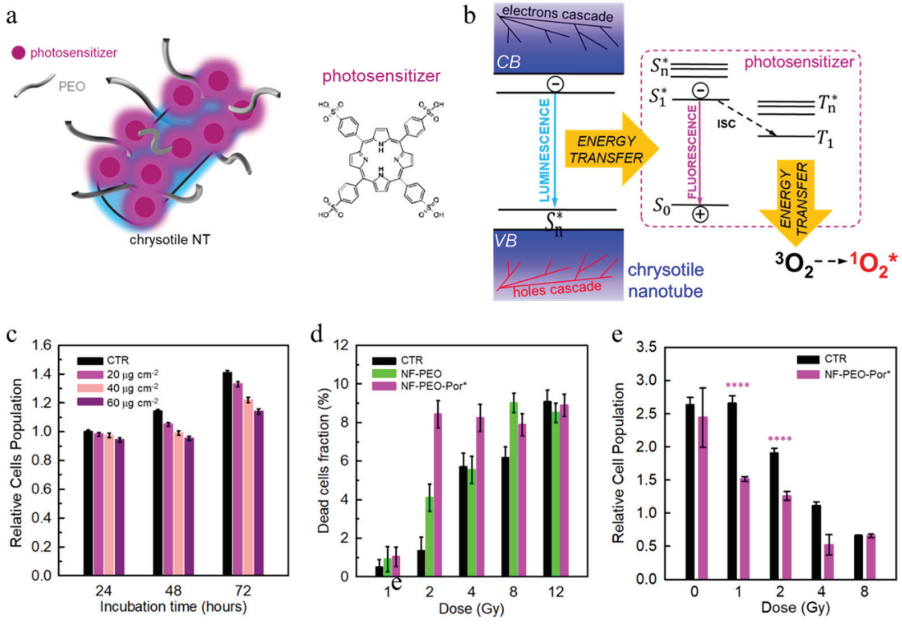

Figure 5. (**a**) Sketch of the hybrid nanoscintillator composed based on a chrysotile nanotube (NT) functionalized with and H_2TPPS^{4-} porphyrin (Por*) as singlet oxygen photosensitizer and PEO as stabilizer for colloidal dispersion (NT-PEO-Por*). (**b**) Outline of the photophysical process involved in the sensitization of singlet oxygen ($^1O_2$*) production upon irradiation with X-rays. Free electrons and holes generated by interaction with the ionizing radiation in the NT localize at an emissive state that transfers its energy to the photosensitizer molecules on the surface promoting their excited singlet state (S_1*). Upon intersystem crossing (ISC), the energy is transferred from the photosensitizer triplet to the dispersed molecular oxygen in triplet ground-state $^3O_2$, which is promoted to its excited singlet state. (**c**) Evaluation of cell metabolic activity by the MTT test on U-87 cells stained with 20, 40, and 60 μg cm^{-2} of NT-PEO-Por*. (**d**) Relative fraction of dead cells estimated by the Trypan blue cell exclusion assay on U-87cells stained with 20 μg cm^{-2} of NT-PEO-Por* as a function of the nominal dose delivered. (**e**) Evaluation of cell metabolic activity by the MTT test on U-87 cells stained with 20 μg cm^{-2} of NT-PEO-Por* as a function of the nominal dose delivered. MTT assays and Trypan blue cell counting were performed in triplicate. Statistical analysis: two-way ANOVA, $p < 0.0001$ ****. Error bars are the standard deviations of the mean values calculated for five independent experiments. Reproduced with permission from *ACS Appl. Mater. Interfaces* 2021, 13, 11 [149].

Metal-organic frameworks containing a heavy metal, such as Zr or Hf, have shown attractive scintillating performances; especially, MOF architecture can include high energy radiation interacting dense nodes linked through photosensitizer molecules for therapeutic and diagnosis applications [150–152]. A variation of the organic component allows for structural modifications useable to tailor the MOF properties quite easily, thus enabling the fabrication of molecular-size MOFs—based scintillators where organic dyes or therapeutics can be used as ligands interconnecting high Z NS. In this architecture, the proximity of NS and ligands enables the prompt activation of the ligands by energy transfer, after the interaction of ionizing radiation with the scintillators. The adaptability of these nanometric architectures has been exploited by Lu et al. in [152] to create cutting edge Hf based scintillating MOF (nMOF) for simultaneous X-PDT and immunotherapy (Figure 6). The synergetic combination of radiotherapy and immunotherapy represents a step forward towards the extension of the applications of radiotherapy for both local and systemic tumor rejection, by positively reducing the high-dose related RT toxicity.

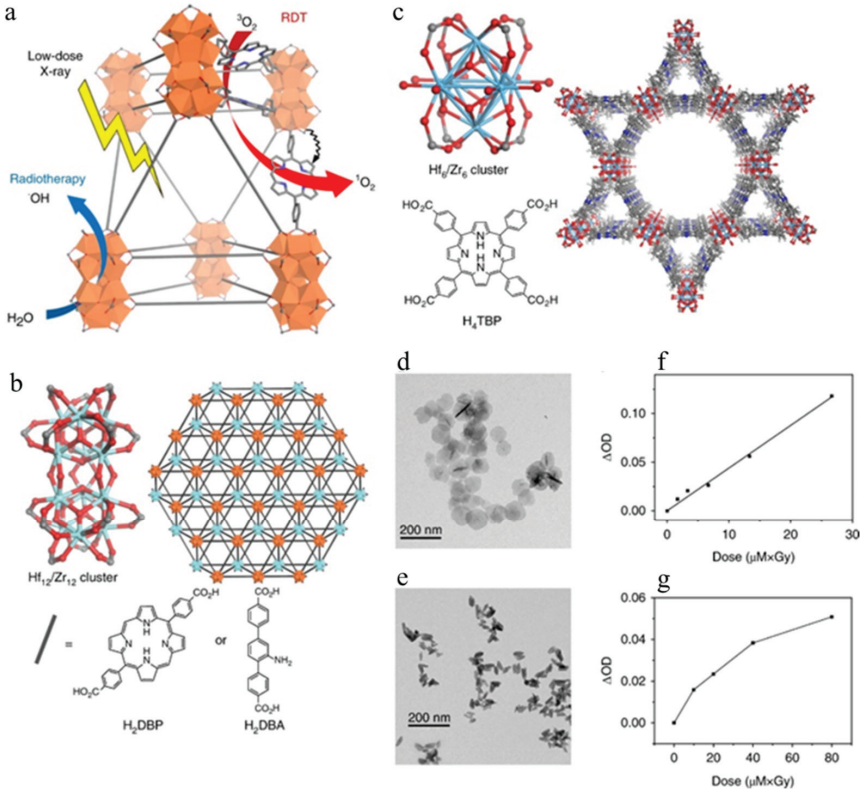

Figure 6. (**a**) Schematic illustration of the mechanisms of X-ray-induced RT–RDT by MOF nanocrystals. (**b**) Structure models of Hf_{12}/Zr_{12} secondary building units (SBUs), and 5,15-di(*p*-benzoato)porphyrin-Hf (DBP-Hf), 5,15-di(*p*-benzoato)porphyrin-Zr (DBP-Zr) and 2,5-di(*p*-benzoato)aniline- Hf (DBA-Hf) MOFs nanocrystals. (**c**) Structure models of Hf_6/Zr_6 SBUs, and TBP-Hf and TBP-Zr nMOFs. (**d**,**e**) Transmission electron microscopy images of DBP-Hf (**d**) and TBP-Hf (**e**). The nMOF syntheses were repeated more than 20 times in each case and the particle morphologies and sizes were similar. (**f**,**g**) $^1O_2$ generation of DBP-Hf (**f**) and TBP-Hf (**g**) upon X-ray irradiation (225 kVp, 13 mA), as determined by 4-nitroso-N,N-dimethylaniline assay. For DBP-Hf, the change in optical density (ΔOD) at 439 nm is linearly fitted against the product of MOFs concentration (μM) and X-ray dose (Gy). For DBP-Hf or TBP-Hf samples irradiated with 10 Gy at Hf concentrations of 10 μM, two independent experiments were performed, and similar results were obtained. Reprinted from *Nature Biomed. Eng.* 2, 600–610 (2018) [152] Copyright Springer Nature 2017.

In this work, hybrid nMOFs have been designed by linking Hf clusters and porphyrin-based photosensitizer ligands. The nMOFs exhibit the suitability to activate X-PDT mechanisms and the ability to stop the ionizing radiation and to trigger efficiently the $^1O_2$ species creation by PS (Figure 6f,g). In vitro experiments display that hybrid nMOF can induce cytotoxicity and DNA double-strand breaks for doses < 1 Gy, i.e., lower than the doses typically delivered in X-rays based oncological therapies. Cancer killing action by nMOF has been demonstrated in vivo by injection in subcutaneous tumor models of radioresistant head and neck squamous cell carcinoma (SQ20B), glioblastoma (U87M G) and prostate cancer (PC-3) xenografts, and into colorectal cancer (CT26) tumor-bearing mice. All tested cancer models disclose a rapid tumor regression at extremely low X-ray doses with minimal toxicity. Being a porous system, nMOF channels and pores have been loaded also with small-molecule IDO inhibitor (IDOi), which are able to reverse immunosuppression and control tumor growth, for the activation of immunotherapy modality. The synergy between IDO inhibition and X-PDT upon low-dose X-ray irradiation leads to the local regression and eradication of the tumors in in vivo models. Moreover, the blockade of inhibitory checkpoints by IDOi has been evaluated to reduce other systemic tumors placed far from the irradiation points. A comparison with no porous Hf based systems (NBTXR3; Nanobiotix), commonly used as sensitizer in RT, reveals the efficacy of the synergetic treatments with respect to the individual therapeutic modalities. The use of nanosystems with tunable properties, such as scintillating MOFs, enables to design materials with multiple therapeutic actions that can be simultaneously activated by X-rays at low doses resulting in a synergism among the treatments.

Table 1. Table summarizing the properties of the diverse nanoparticles, explored in the manuscript, together with the proposed application and the expected effects in RT, the type of radiations (with the final delivered dose), and the stage of the investigation (in vitro or in vivo studies).

Type of NP	Size	Surface Functionalization	Type of Radiation	Maximun Dose	Application	Type of Studies	Ref.
Gold NPs	15 nm	Capped with citrate	X-rays (50 kVp); Carbon ions (165 MeV/u);	4 Gy	Passive Radio-sensitization	In vitro	[92]
Gadolinium NPs	sub-5 nm	Coated with polysiloxane shell	X-rays (220 kVp); gamma rays (6 MV)	8 Gy	Passive Radio-sensitization	In vitro	[99]
Porous platinum NPs	116 nm	Conjugated with PEG	X-rays (250 kVp)	10 Gy	Passive Radio-sensitization	In vivo	[101]
Hafnium oxide NPs	50 nm	Coated with a biocompatible agent	Gamma rays (1.25 MeV and 0.38 MeV)	4 Gy	Passive Radio-sensitization	In vitro and in vivo	[102]
Anatase titanium oxide NPs	30 nm	Functionalized with amine or PEG	X-rays (80 kV and 6 MV)	8 Gy	Active ROS generation	Phantoms and in vitro	[121]
Zinc oxide NPs	8–100 nm	Coated with silica shell	X-rays (200 kVp)	10 Gy	Active ROS generation	In vitro	[123]
Cerium oxide NPs	5–8 nm	None	X-rays (160 kV)	5 Gy	Active ROS generation	In vitro	[126]
Chrysotile NTs	20 × 60 nm	Functionalized with PEO and porphyrin	X-rays (20 kV)	12 Gy	X-PDT	In vitro	[149]
DBP Hf nMOF	72 nm	None	X-rays (225 kVp)	1 Gy	X-PDT	Tumor models	[152]

4. The Effect of the Energy Release vs. X-PDT Efficacy

The perspective of discovering novel materials mostly shaped in form of organic and inorganic nanoparticle or hybrids demands a deeper comprehension of the processes occurring within the material after the interaction with the ionizing radiation. Indeed, the reduced material dimension is critical in presence of high energy ionizing radiation, as the migration distance of secondary charges generated in the NPs along the track from the point of the ionizing event (relaxation mechanisms) are significantly larger than the common nanometric radius of the NPs. Therefore, a fraction of energy escapes from the NPs, limiting the efficiency of activation of the RT and X-PDT mechanisms [18,153].

The effective energy deposition in RT, together with the activation of the scintillating NPs and the trigger of the PS therapeutic effects in X-PDT, are key open question in nanosystems. In nanomedicine, the debate can regard the comprehension of the increase of X-rays absorption cross section, the effective energy release within the nanomaterials embedded in the biological surrounding, and the radiation dose-enhancement in the vicinity of the malignancy due to the presence of high-Z elements. The main goal of exploiting the passive NPs or single component active NPs is to increase the RT effects at the lowest doses in the disease site, and to localize the radiation energy deposition and RT damages only in the cancer site, while preserving from the radiation lethal toxicity the healthy tissue and organ in the patient [154,155]. As discussed in Section 5, this point can be addressed by creating tumor-targeting NPs, such as NPs functionalized by folic acid, able to accumulate only in the cancer tissue and thus to locally increase the absorbed dose [93,156]. Moreover, the question on the X-PDT processes in hybrids is under debate: here, besides the mechanism due to the presence of high-Z nanoscintillator, the effect of the photo-toxicity of the PS grafted on their surface should be considered, together with the possible interaction of the high energy beam directly with the PS. If on the one hand, different publications in the literature have demonstrated the occurrence of a synergetic effect given by the simultaneous application of the RT and the PDT in presence of PS grafted on NS [18,152,157], on the other hand the X-PDT phenomenology lacks unique explanation—i.e., whether the dominant therapeutic effect is due to the presence of high Z elements allowing for an enhancement of radiation dose deposition close to the injured tissues, or to the establishment of a tradeoff between the RT and PDT enabling simultaneously the reduction of the total dose to the patient and the induction of additional cell death mechanisms by toxic singlet oxygen moieties.

In this context, Monte Carlo simulations are powerful tools enabling to properly connect the clinical beam simulations to the phenomena expected to occur at the NP level. Many Monte Carlo codes have been developed [158,159] to explore the dose enhancement in RT, especially with X-ray beams, electron beams, and proton beams; each of these simulations helps to quantify the spatial energy distribution resulting from the interaction between the X-ray photon at diverse energies and the NP/NS, which finally drives the sensitization efficiency in RT and the activation of molecular singlet oxygen sensitizers in PDT and X-PDT. In addition, these computational studies allow to model the release of secondary particles after the first ionization event in relation to the nanomaterials physical, chemical, and structural properties. For instance, interesting computational studies have explored the use of passive high Z agents, like iodine, gadolinium, and gold, to treat human brain tumors in synchrotron stereotactic radiotherapy (SSRT) with irradiation by monochromatic X-rays from a synchrotron source, tuned at an optimal energy [160]. Especially, Edouard et al. in [161] have developed theoretical dosimetric investigation, by using a Monte Carlo code developed for neutrons, photons, and electrons transport (MCNPX) on an idealized phantom representing a human head bearing a brain tumor volume. Simulations of irradiation have been conducted for diverse beams: monochromatic X-ray beams from a synchrotron source (30–120 keV); polychromatic X-ray beams have been used to simulate irradiations from a conventional X-ray tube (80, 120, and 180 kVp), and from a linear accelerator (6 MV). The results on the SSRT dose enhancement have been compared for the diverse ionizing radiation energy ranges and in the presence of iodine

elements. The enthusiastic data proves the major RT enhancement in presence of high Z agents for the medium energy beam by monochromatic source at 80 keV, despite the lower penetration of the keV X-rays with respect to the conventionally used higher energy X-rays. At keV energies, the maximum dose can be delivered to the tumor while preserving skull and healthy tissues from excessive radiations exposure. In particular, the simulation on X-ray penetration and dose deposition performed by Edouard and co-workers reveals that by using 6 MV irradiation, the doses delivered to the skull are similar to the value obtained for 80 keV from monochromatic source but, at the same time, the doses delivered to the healthy brain are hazardously higher if compared to low energy monochromatic and polychromatic beams. Moreover, the dose enhancement for 6 MV irradiation is almost negligible. This may be imputed to the different type of X-rays interaction with the biological medium, ruled by Compton and photoelectric effects working in the MeV and keV range, respectively. This work highlights the importance of computational modeling in order to find an optimized treatment in presence of radiosensitizers, able to significantly reduce the dose to the healthy tissue, hopefully avoiding the implication of megavoltage irradiation.

In another work, Bulin et al. in [162] have quantified, by Monte Carlo GEANT4 program, the amount of energy deposited in diverse scintillators such as gadolinium oxides (Gd_2O_3) nanoparticles, by varying the concentration of the NS in an aqueous medium, the NS dimension, and the energy of the first high energy beam, as well as the position of the first interaction event. In this work, the first estimation of the energy transfer from the primary interaction of an ionizing radiation beam with a sphere of water representing a volume of tumor, loaded with nanoscintillators, has been conducted by means of the mass energy absorption coefficient. The results reveal that the maximum energy transfer enhancement occurs for energies around 40–60 keV, confirming the importance of exploiting beams of ionizing radiation in the kiloelectronvolt energy range in presence of high-Z elements. However, Bulin and co-workers have highlighted that in such a composite compound, made by a large volume of water loaded with a small concentration of NS, the interaction between the first photon and the matter can occur either in the NS or in water. Especially, when the interaction occurs in the NS a fraction of the expected transferred energy can escape from the nanoparticle, typically due to the larger migration distance of the secondary particles generated after the first interaction with respect to the NS dimensions, and the deposited energy is shared between the water and the NS. In this context, the Monte Carlo GEANT4 calculation has helped to determine the spatial distribution of deposited energy in the volume surrounding the nanoparticle where the primary interaction occurs and to evaluate the fraction of energy loss during the energy relaxation and charge migration processes in the NS. The new parameter η has been introduced, which quantifies the percentage of energy that is deposited in the NS itself, as a function of both NS and external source parameters. The outcome of the computational investigation performed for three different NS diameters reveals that even for the nanoparticles of 100 nm of diameter, the deposited energy decreases very quickly when the incident beam energy increases, resulting in a large amount of energy loss outside the NS and deposited in the surrounding medium (see Figure 7). From this consideration, the estimation of η is crucial especially in the case of hybrid nanomaterials for X-PDT, where after the activation of the scintillating process in the nanoparticles by the external irradiation beam, the subsequent trigger of the singlet oxygen sensitizers is expected by energy transfer mechanisms (see Figure 4). The correct evaluation of the energy deposition is critical to optimize the singlet oxygen production in presence of NS for therapeutic purposes and to exploit the synergy among RT, radiosensitization and PDT.

The development of further theoretical studies devoted to the modeling of energy deposition in a biological medium and of scintillation phenomena in nanomaterials and hybrids is essential for the exploitation of NP/NS in nanomedicine. Computational simulations coupled with the experimental proofs would provide the guidelines for tuning the nanomaterial composition in order to optimize the interaction with X-rays and the activa-

tion of therapeutics or diagnostic agents, and thus to accomplish the different requirements according to the application target.

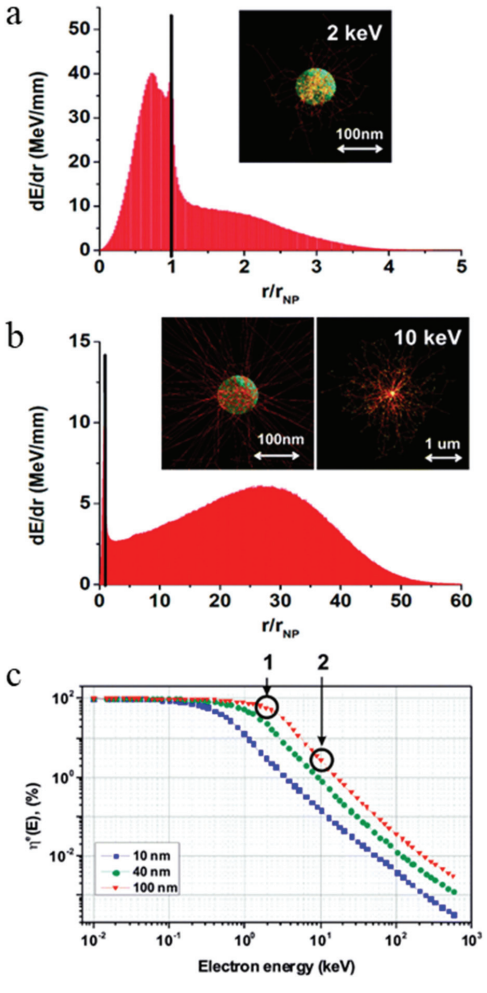

Figure 7. (**a**,**b**) Deposited energy per unit of normalized radial distance from the center of the NP (diameter of 100 nm of Gd_2O_3) for (1)—2 keV electrons and (2)—10 keV electrons. Visualization of the spatial distribution of the deposited energy is shown as insets. (**c**) Percentage of deposited energy per electron generated in a Gd_2O_3 nanoparticle for three different diameters, as a function of the primary electron energy. Reproduced from *Nanoscale* **2015**, *7*, 5744–5751 [162]. Copyright Royal Society of Chemistry 2015.

5. Targeting Strategies for Enhancing NPs Sensitizing Effects

Two important features are required to design effective nanotechnologies conceived for X-rays based oncological treatments: one is a selective tumor cell targeting and the other is a rapid clearance from human body after treatment [163,164]. These achievements are highly dependent on the size of the nanomaterials that can affect the efficacy of the treatment reducing its side effects (such as undesirable ROS generation, disruption of cellular compartments, immune reactions, inflammation, destruction of the host homeostasis) [165,166]: for instance, it has been reported that non-targeted heavy nanoparticles

with diameter ~50 nm have the highest cellular uptake and are able to increase the efficacy of RT treatment [164,167]. Thanks to their size, nanoparticles tend to accumulate more in tumor tissues with respect to the normal ones due to the enhanced permeability and retention (EPR) effect [168]. This passive targeting exploits the fact that tumors have a leaky vasculature, different pH, and different local temperature, and are devoid of an efficient lymphatic drainage system. Therefore, nanoparticles with suitable physicochemical characteristics and size can extravasate from leaky tumor vessels and accumulate in the tumors [169]. Passive targeting, however, may induce multi-drug resistance (MDR), a poor drug diffusion, and a-specific accumulation in liver and spleen [163,170]. One of the most promising approaches for improving the retention and accumulation of NPs in tumor cells relies on grafting the NPs surface with cancer cell-specific targeting ligands. Tumor accumulation of actively targeted nanoparticles has been found to be 5 times faster and approximately 2-fold higher than their passive counterparts, within the 60 nm diameter range [164]. Among the ligands used to target cancer cells we can mention antibodies, peptides, and aptamers to recognize and bind overexpressed cancer cell receptors (such as epidermal growth factor receptors), together with folate receptors and transferrin-receptors to enhance the cellular uptake of nanoparticles [171–173]. Some monoclonal antibodies have been exploited in strategies combining chemotherapeutic agents or immunotherapy with ionizing radiation; in vitro *and* in vivo results have proven that antibodies promote and potentiate apoptosis and cytotoxic effects, thus damaging DNA of the cancer cells. Successful medical outcomes have been obtained especially for the treatment of breast cancer [174–176]. In this context, the human epidermal receptor-2 (HER-2) is the most widely studied overexpressed targeting receptor for therapeutic applications [177]. The most commonly ligand targeted to HER-2, is the anti-HER-2 mAb [178]. The functionalization of gold nanoclusters (AuNCs) with anti-HER2-mAb and/or folic acid (FA) as a single and dual-targeted radiosensitizers has shown the increasing of cellular internalization and of the RT efficiency (Figure 8) [179].

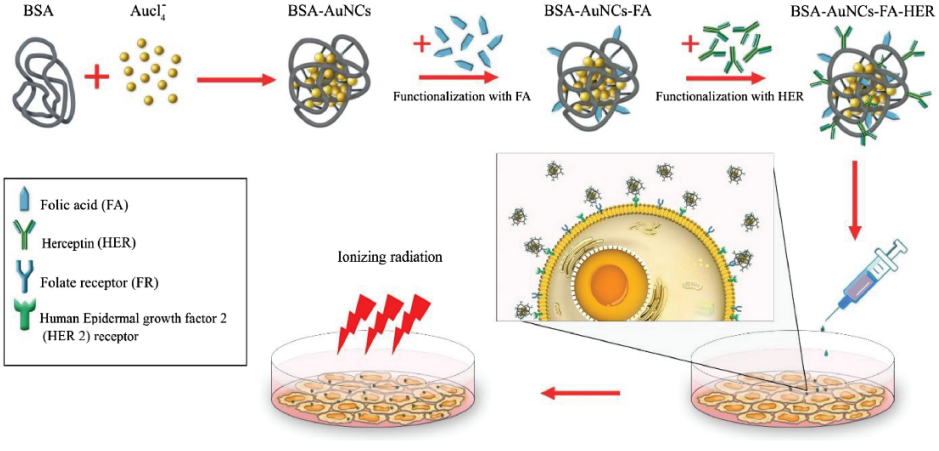

Figure 8. Schematic illustration of the functionalization process of bovine serum albumin (BSA) gold nanoclusters (AuNCs) with folic acid and Herceptin and the mechanism of cellular internalization by binding with folate and human epidermal growth factor 2 receptors on the surface of SK-BR3 cells. Reproduced from *European Journal of Pharmaceutical Sciences* **2020**, *153*, 105487. [179] Copyright Elsevier 2020.

Despite the fact that just an exceedingly small amount of antibody is needed to target a specific site, the expensive production and immunogenic properties may restrain their applications in clinical trials [180]. An alternative is represented by the aptamers that are attractive for in vivo visualization, as they can couple some diagnostic agents, such as fluorescent or radionuclide labels, bioconjugates and nanoparticles, for the delivery of

therapeutic agents and as sensitizers in RT, especially for brain tumors [181,182]. Aptamer functionalized metal oxides and metals containing nanostructures have been proposed for tumor-targeted delivery and efficient PDT treatment [183,184]. ZnO catalyst NPs have been studied for targeted PDT therapy in combination with chemotherapy by loading the NPs with anti-cancer drugs. The results presented in [184] show an enhanced cellular uptake of the NPs and they validate the successful therapeutic cytotoxic effect with a higher rate of death of cancer cells, if compared to the one of single photo—or chemotherapy.

In spite of the significant advancements made in targeting strategies of NPs, potential harmful effects may occur depending on the route of delivery. With the systemic intravenous delivery, only a small fraction of NPs has the possibility of reaching the target site, even in case of targeted NPs. Thus, a large number of NPs could remain in systemic circulation, leading to drug accumulation or systemic toxicity, and affecting the health of patients [37,185]. For this reason, other delivery routes, such as localized delivery via intratumoral injection have been studied. Localized delivery can be advantageous particularly in tumor sites where conventional systemic delivery routes fail, enabling the accumulation of the delivered NP at higher concentrations in the targeted tumor volume. Consequently, the use NPs localized delivery strategies helps to avoid repeated dosing, to decrease the final toxicity, and to increase patient compliance [186]. To improve the beneficial effect of localized delivery strategies, recently NP-loaded or drug-embedded implants have been obtained from biodegradable polymers. NP can degrade into biocompatible compounds that are easily absorbed in the body with virtually no side effects [187,188].

The final evaluation of the anticancer performances of each type of nanoparticles relies on many factors. The radiotherapeutic performance of nanoparticles is affected by their intrinsic parameters, mainly size, shape, surface charge/functionalization, and toxicity, as well as by external factors, such as the targeted type of tumor, the administration methodology, and the irradiation setup [76,189,190]. From this picture coupled to the description of the issue on the energy/dose deposition in heavy or hybrid materials at the nanoscale (Sections 3 and 4), it is clear that the comprehension of the physical phenomena occurring in NP exploited in X-rays-based oncotherapy, together with deeper studies for the engineering of nanoparticles performances and targeting, are mandatory. The research for a guideline towards the assessment of the relationship between the NPs key physico-chemical parameters and their therapeutic efficacy in RT is an open roundtable. However, it represents a challenging matter for the chance to design NPs with properties and performances that can be appropriate to address all the pending requests made by the clinical advanced therapies, to increase the survivor rate in oncology, and to improve the life quality of oncological patients.

6. Conclusions

The advanced nanomedicine is currently promoting the development of novel nanoparticles able to address the increasing demands for the fight against cancer. This paper proposes an overview of the inorganic and hybrid nanoparticles of interest for X-ray based oncological strategies. The aim is to highlight the characteristics that such nanoparticles should satisfy to be exploitable in oncology to promote the overcoming of the limitations of the traditional RT, with the following reduction of the collateral effects and improvement of the therapeutic efficacy. Indeed, this review points out that the physico-chemical properties of the nanoparticles, together with the choice on surface functionalization and the targeting strategies, affect the key parameters of RT and X-PDT, including energy deposition and total delivered dose in cancer tissues. Heavy nanoparticles or hybrids represent a successful chance in cancer fight as they can both assist the traditional RT as radiosensitizers and boost the therapeutic effects on malignant cells through the synergetic combination of radio and photodynamic therapies in X-PDT. The cutting-edge scientific research looks especially at the development of hybrid systems, whose properties are easily tunable with huge consequences for the therapeutic performances. However, the production of high-performing inorganic nanoparticles and nanohybrids for medical applications involving the use of

ionizing radiation must be accompanied by the advancement in the knowledge on scintillation at the nanoscale, in correlation with the physical-chemical features of nanomaterials. In this context, this review shows the importance of the theoretical studies on the ionizing radiation energy deposition in biological medium in the presence of heavy nanoparticles, as well as on the stimulation of anticancer activities in hybrid nanoscintillators coupled to toxic single oxygen agents. These studies aim at guiding the optimization of nanoparticles' qualities according to the specific medical applications. The future achievement of novel experimental knowledge and theoretical descriptions of the phenomena occurring in heavy and hybrids materials at nanoscale would represent a step beyond in the field of nanomedicine for the achievement of more and more efficient oncological X-rays based therapies.

Author Contributions: Conceptualization, I.V.; Supervision, I.V.; Writing—original draft, I.V., R.C., V.S.; Writing—review and editing, I.V., R.C., V.S., R.C. and V.S. have contributed equally. All authors have read and agreed to the published version of the manuscript.

Funding: This research was funded by Marie Skłodowska-Curie Actions Widening Fellowships (MSCA-WF): NUMBER 101003405—HANSOME.

Institutional Review Board Statement: Not applicable.

Informed Consent Statement: Not applicable.

Data Availability Statement: Not applicable.

Acknowledgments: This work was supported by (MSCA-WF)—HANSOME (101003405).

Conflicts of Interest: The authors declare no conflict of interest.

References

1. Siegel, R.L.; Miller, K.D.; Jemal, A. Cancer statistics, 2020. *CA A Cancer J. Clin.* **2020**, *70*, 7–30. [CrossRef] [PubMed]
2. Pucci, C.; Martinelli, C.; Ciofani, G. Innovative approaches for cancer treatment: Current perspectives and new challenges. *Ecancermedicalscience* **2019**, *13*, 961. [CrossRef] [PubMed]
3. Massoud, T.F.; Gambhir, S.S. Molecular imaging in living subjects: Seeing fundamental biological processes in a new light. *Genes Dev.* **2003**, *17*, 545–580. [CrossRef] [PubMed]
4. Lusic, H.; Grinstaff, M.W. X-ray-computed tomography contrast agents. *Chem. Rev.* **2013**, *113*, 1641–1666. [CrossRef]
5. Vogelstein, B.; Papadopoulos, N.; Velculescu, V.E.; Zhou, S.; Diaz, L.A.; Kinzler, K.W. Cancer genome landscapes. *Science* **2013**, *339*, 1546–1558. [CrossRef]
6. Braicu, C.; Buse, M.; Busuioc, C.; Drula, R.; Gulei, D.; Raduly, L.; Rusu, A.; Irimie, A.; Atanasov, A.G.; Slaby, O. A comprehensive review on MAPK: A promising therapeutic target in cancer. *Cancers* **2019**, *11*, 1618. [CrossRef]
7. Smith-Bindman, R.; Miglioretti, D.L.; Larson, E.B. Rising use of diagnostic medical imaging in a large integrated health system. *Health Aff.* **2008**, *27*, 1491–1502. [CrossRef]
8. Fazel, R.; Krumholz, H.M.; Wang, Y.; Ross, J.S.; Chen, J.; Ting, H.H.; Shah, N.D.; Nasir, K.; Einstein, A.J.; Nallamothu, B.K. Exposure to low-dose ionizing radiation from medical imaging procedures. *N. Engl. J. Med.* **2009**, *361*, 849–857. [CrossRef]
9. Wan, J.C.; Massie, C.; Garcia-Corbacho, J.; Mouliere, F.; Brenton, J.D.; Caldas, C.; Pacey, S.; Baird, R.; Rosenfeld, N. Liquid biopsies come of age: Towards implementation of circulating tumour DNA. *Nat. Rev. Cancer* **2017**, *17*, 223. [CrossRef]
10. Prasad, R.; Jain, N.; Conde, J.; Srivastava, R. Localized nanotheranostics. *Mater. Today Adv.* **2020**, *8*, 100087. [CrossRef]
11. Beckett, K.R.; Moriarity, A.K.; Langer, J.M. Safe use of contrast media: What the radiologist needs to know. *Radiographics* **2015**, *35*, 1738–1750. [CrossRef] [PubMed]
12. Wu, X.; Yang, H.; Yang, W.; Chen, X.; Gao, J.; Gong, X.; Wang, H.; Duan, Y.; Wei, D.; Chang, J. Nanoparticle-based diagnostic and therapeutic systems for brain tumors. *J. Mater. Chem. B* **2019**, *7*, 4734–4750. [CrossRef]
13. Frullano, L.; Meade, T.J. Multimodal MRI contrast agents. *JBIC J. Biol. Inorg. Chem.* **2007**, *12*, 939–949. [CrossRef] [PubMed]
14. Brigger, I.; Dubernet, C.; Couvreur, P. Nanoparticles in cancer therapy and diagnosis. *Adv. Drug Deliv. Rev.* **2012**, *64*, 24–36. [CrossRef]
15. Nurgali, K.; Jagoe, R.T.; Abalo, R. Editorial: Adverse Effects of Cancer Chemotherapy: Anything New to Improve Tolerance and Reduce Sequelae? *Front. Pharmacol.* **2018**, *9*, 245. [CrossRef] [PubMed]
16. Mahvi, D.A.; Liu, R.; Grinstaff, M.W.; Colson, Y.L.; Raut, C.P. Local cancer recurrence: The realities, challenges, and opportunities for new therapies. *CA A Cancer J. Clin.* **2018**, *68*, 488–505. [CrossRef]
17. Lucky, S.S.; Soo, K.C.; Zhang, Y. Nanoparticles in photodynamic therapy. *Chem. Rev.* **2015**, *115*, 1990–2042. [CrossRef] [PubMed]
18. Bulin, A.-L.; Broekgaarden, M.; Simeone, D.; Hasan, T. Low dose photodynamic therapy harmonizes with radiation therapy to induce beneficial effects on pancreatic heterocellular spheroids. *Oncotarget* **2019**, *10*, 2625–2643. [CrossRef] [PubMed]

19. Weinmann, H. Cancer immunotherapy: Selected targets and small-molecule modulators. *ChemMedChem* **2016**, *11*, 450–466. [CrossRef]
20. Finn, O. Immuno-oncology: Understanding the function and dysfunction of the immune system in cancer. *Ann. Oncol.* **2012**, *23*, viii6–viii9. [CrossRef]
21. Wang, J.; Shi, M.; Ling, R.; Xia, Y.; Luo, S.; Fu, X.; Xiao, F.; Li, J.; Long, X.; Wang, J. Adjuvant chemotherapy and radiotherapy in triple-negative breast carcinoma: A prospective randomized controlled multi-center trial. *Radiother. Oncol.* **2011**, *100*, 200–204. [CrossRef]
22. Ko, H.-J.; Kim, Y.-J.; Kim, Y.-S.; Chang, W.-S.; Ko, S.-Y.; Chang, S.-Y.; Sakaguchi, S.; Kang, C.-Y. A combination of chemoimmunotherapies can efficiently break self-tolerance and induce antitumor immunity in a tolerogenic murine tumor model. *Cancer Res.* **2007**, *67*, 7477–7486. [CrossRef] [PubMed]
23. Kerr, W.G.; Chisholm, J.D. The next generation of immunotherapy for cancer: Small molecules could make big waves. *J. Immunol.* **2019**, *202*, 11–19. [CrossRef]
24. Huck, B.R.; Kötzner, L.; Urbahns, K. Small molecules drive big improvements in immuno-oncology therapies. *Angew. Chem. Int. Ed.* **2018**, *57*, 4412–4428. [CrossRef]
25. ClinicalTrials. Database of Privately and Publicly Funded Clinical Studies Conducted Around the World. Available online: https://clinicaltrials.gov (accessed on 30 July 2021).
26. Whitesides, G.M. The 'right' size in nanobiotechnology. *Nat. Biotechnol.* **2003**, *21*, 1161–1165. [CrossRef]
27. Ferrari, M. Cancer nanotechnology: Opportunities and challenges. *Nat. Rev. Cancer* **2005**, *5*, 161–171. [CrossRef]
28. Doane, T.L.; Burda, C. The unique role of nanoparticles in nanomedicine: Imaging, drug delivery and therapy. *Chem. Soc. Rev.* **2012**, *41*, 2885–2911. [CrossRef] [PubMed]
29. Rizzo, L.Y.; Theek, B.; Storm, G.; Kiessling, F.; Lammers, T. Recent progress in nanomedicine: Therapeutic, diagnostic and theranostic applications. *Curr. Opin. Biotechnol.* **2013**, *24*, 1159–1166. [CrossRef] [PubMed]
30. Chen, H.; Zhang, W.; Zhu, G.; Xie, J.; Chen, X. Rethinking cancer nanotheranostics. *Nat. Rev. Mater.* **2017**, *2*, 1–18. [CrossRef] [PubMed]
31. Shi, J.; Kantoff, P.W.; Wooster, R.; Farokhzad, O.C. Cancer nanomedicine: Progress, challenges and opportunities. *Nat. Rev. Cancer* **2017**, *17*, 20. [CrossRef] [PubMed]
32. Dai Phung, C.; Tran, T.H.; Nguyen, H.T.; Jeong, J.-H.; Yong, C.S.; Kim, J.O. Current developments in nanotechnology for improved cancer treatment, focusing on tumor hypoxia. *J. Control. Release* **2020**, *324*, 413–429. [CrossRef]
33. Kim, B.Y.; Rutka, J.T.; Chan, W.C. Nanomedicine. *N. Engl. J. Med.* **2010**, *363*, 2434–2443. [CrossRef]
34. Furasova, A.D.; Fakhardo, A.F.; Milichko, V.A.; Tervoort, E.; Niederberger, M.; Vinogradov, V.V. Synthesis of a rare-earth doped hafnia hydrosol: Towards injectable luminescent nanocolloids. *Colloids Surf. B Biointerfaces* **2017**, *154*, 21–26. [CrossRef]
35. Hao, Y.; Altundal, Y.; Moreau, M.; Sajo, E.; Kumar, R.; Ngwa, W. Potential for enhancing external beam radiotherapy for lung cancer using high-Z nanoparticles administered via inhalation. *Phys. Med. Biol.* **2015**, *60*, 7035. [CrossRef]
36. Dong, Y.; Feng, S.-S. Poly (d, l-lactide-co-glycolide)/montmorillonite nanoparticles for oral delivery of anticancer drugs. *Biomaterials* **2005**, *26*, 6068–6076. [CrossRef]
37. Chenthamara, D.; Subramaniam, S.; Ramakrishnan, S.G.; Krishnaswamy, S.; Essa, M.M.; Lin, F.-H.; Qoronfleh, M.W. Therapeutic efficacy of nanoparticles and routes of administration. *Biomater. Res.* **2019**, *23*, 1–29. [CrossRef] [PubMed]
38. Bozzuto, G.; Molinari, A. Liposomes as nanomedical devices. *Int. J. Nanomed.* **2015**, *10*, 975. [CrossRef]
39. Prabhu, R.H.; Patravale, V.B.; Joshi, M.D. Polymeric nanoparticles for targeted treatment in oncology: Current insights. *Int. J. Nanomed.* **2015**, *10*, 1001.
40. Khalid, K.; Tan, X.; Mohd Zaid, H.F.; Tao, Y.; Lye Chew, C.; Chu, D.-T.; Lam, M.K.; Ho, Y.-C.; Lim, J.W.; Chin Wei, L. Advanced in developmental organic and inorganic nanomaterial: A review. *Bioengineered* **2020**, *11*, 328–355. [CrossRef] [PubMed]
41. Lohse, S.E.; Murphy, C.J. Applications of colloidal inorganic nanoparticles: From medicine to energy. *J. Am. Chem. Soc.* **2012**, *134*, 15607–15620. [CrossRef]
42. Zhao, C.-Y.; Cheng, R.; Yang, Z.; Tian, Z.-M. Nanotechnology for cancer therapy based on chemotherapy. *Molecules* **2018**, *23*, 826. [CrossRef] [PubMed]
43. Ghosh, P.; Han, G.; De, M.; Kim, C.K.; Rotello, V.M. Gold nanoparticles in delivery applications. *Adv. Drug Deliv. Rev.* **2008**, *60*, 1307–1315. [CrossRef]
44. Jaque, D.; Maestro, L.M.; Del Rosal, B.; Haro-Gonzalez, P.; Benayas, A.; Plaza, J.; Rodriguez, E.M.; Sole, J.G. Nanoparticles for photothermal therapies. *Nanoscale* **2014**, *6*, 9494–9530. [CrossRef]
45. Maestro, L.M.; Haro-González, P.; Del Rosal, B.; Ramiro, J.; Caamano, A.; Carrasco, E.; Juarranz, A.; Sanz-Rodríguez, F.; Solé, J.G.; Jaque, D. Heating efficiency of multi-walled carbon nanotubes in the first and second biological windows. *Nanoscale* **2013**, *5*, 7882–7889. [CrossRef]
46. Cline, B.; Delahunty, I.; Xie, J. Nanoparticles to mediate X-ray-induced photodynamic therapy and Cherenkov radiation photodynamic therapy. *Wiley Interdiscip. Rev. Nanomed. Nanobiotechnol.* **2019**, *11*, e1541. [CrossRef]
47. Wong, X.Y.; Sena-Torralba, A.; Alvarez-Diduk, R.; Muthoosamy, K.; Merkoci, A. Nanomaterials for nanotheranostics: Tuning their properties according to disease needs. *ACS Nano* **2020**, *14*, 2585–2627. [CrossRef]
48. Shang, L.; Nienhaus, K.; Nienhaus, G.U. Engineered nanoparticles interacting with cells: Size matters. *J. Nanobiotechnol.* **2014**, *12*, 1–11. [CrossRef] [PubMed]

49. Salata, O.V. Applications of nanoparticles in biology and medicine. *J. Nanobiotechnol.* **2004**, *2*, 1–6. [CrossRef]
50. Teleanu, D.M.; Chircov, C.; Grumezescu, A.M.; Volceanov, A.; Teleanu, R.I. Blood-brain delivery methods using nanotechnology. *Pharmaceutics* **2018**, *10*, 269. [CrossRef] [PubMed]
51. Nam, J.; Won, N.; Bang, J.; Jin, H.; Park, J.; Jung, S.; Jung, S.; Park, Y.; Kim, S. Surface engineering of inorganic nanoparticles for imaging and therapy. *Adv. Drug Deliv. Rev.* **2013**, *65*, 622–648. [CrossRef]
52. Sun, T.; Zhang, Y.S.; Pang, B.; Hyun, D.C.; Yang, M.; Xia, Y. Engineered nanoparticles for drug delivery in cancer therapy. *Angew. Chem. Int. Ed.* **2014**, *53*, 12320–12364. [CrossRef]
53. Liu, Y.; Tu, D.; Zhu, H.; Chen, X. Lanthanide-doped luminescent nanoprobes: Controlled synthesis, optical spectroscopy, and bioapplications. *Chem. Soc. Rev.* **2013**, *42*, 6924–6958. [CrossRef]
54. Labrador-Páez, L.; Pedroni, M.; Speghini, A.; García-Solé, J.; Haro-González, P.; Jaque, D. Reliability of rare-earth-doped infrared luminescent nanothermometers. *Nanoscale* **2018**, *10*, 22319–22328. [CrossRef]
55. Villa, I.; Villa, C.; Monguzzi, A.; Babin, V.; Tervoort, E.; Nikl, M.; Niederberger, M.; Torrente, Y.; Vedda, A.; Lauria, A. Demonstration of cellular imaging by using luminescent and anti-cytotoxic europium-doped hafnia nanocrystals. *Nanoscale* **2018**, *10*, 7933–7940. [CrossRef]
56. Gao, X.; Cui, Y.; Levenson, R.M.; Chung, L.W.; Nie, S. In vivo cancer targeting and imaging with semiconductor quantum dots. *Nat. Biotechnol.* **2004**, *22*, 969–976. [CrossRef]
57. Li, L.; Wang, W.; Tang, J.; Wang, Y.; Liu, J.; Huang, L.; Wang, Y.; Guo, F.; Wang, J.; Shen, W. Classification, synthesis, and application of luminescent silica nanoparticles: A review. *Nanoscale Res. Lett.* **2019**, *14*, 1–23. [CrossRef]
58. Villa, C.; Campione, M.; Santiago-González, B.; Alessandrini, F.; Erratico, S.; Zucca, I.; Bruzzone, M.G.; Forzenigo, L.; Malatesta, P.; Mauri, M. Self-assembled pH-sensitive fluoromagnetic nanotubes as archetype system for multimodal imaging of brain cancer. *Adv. Funct. Mater.* **2018**, *28*, 1707582. [CrossRef]
59. Santiago-González, B.; Monguzzi, A.; Pinchetti, V.; Casu, A.; Prato, M.; Lorenzi, R.; Campione, M.; Chiodini, N.; Santambrogio, C.; Meinardi, F. "Quantized" Doping of Individual Colloidal Nanocrystals Using Size-Focused Metal Quantum Clusters. *ACS Nano* **2017**, *11*, 6233–6242. [CrossRef] [PubMed]
60. Seferos, D.G.D.; Daniel, W.; Massich, M.; Patel, P.; Mirkin, C. Gold nanoparticles for biology and medicine. *Angewchem. Int. Ed* **2010**, *49*, 3280–3294.
61. del Rosal, B.; Jia, B.; Jaque, D. Beyond phototherapy: Recent advances in multifunctional fluorescent nanoparticles for light-triggered tumor theranostics. *Adv. Funct. Mater.* **2018**, *28*, 1803733. [CrossRef]
62. Yao, J.; Yang, M.; Duan, Y. Chemistry, biology, and medicine of fluorescent nanomaterials and related systems: New insights into biosensing, bioimaging, genomics, diagnostics, and therapy. *Chem. Rev.* **2014**, *114*, 6130–6178. [CrossRef]
63. Taylor-Pashow, K.M.; Della Rocca, J.; Huxford, R.C.; Lin, W. Hybrid nanomaterials for biomedical applications. *Chem. Commun.* **2010**, *46*, 5832–5849. [CrossRef] [PubMed]
64. Kwatra, D.; Venugopal, A.; Anant, S. Nanoparticles in radiation therapy: A summary of various approaches to enhance radiosensitization in cancer. *Transl. Cancer Res.* **2013**, *2*, 330–342.
65. Clement, S.; Campbell, J.M.; Deng, W.; Guller, A.; Nisar, S.; Liu, G.; Wilson, B.C.; Goldys, E.M. Mechanisms for Tuning Engineered Nanomaterials to Enhance Radiation Therapy of Cancer. *Adv. Sci.* **2020**, *7*, 2003584. [CrossRef] [PubMed]
66. Chen, H.H.; Kuo, M.T. Improving radiotherapy in cancer treatment: Promises and challenges. *Oncotarget* **2017**, *8*, 62742. [CrossRef] [PubMed]
67. Baskar, R.; Lee, K.A.; Yeo, R.; Yeoh, K.-W. Cancer and radiation therapy: Current advances and future directions. *Int. J. Med. Sci.* **2012**, *9*, 193. [CrossRef]
68. Delaney, G.; Jacob, S.; Featherstone, C.; Barton, M. The role of radiotherapy in cancer treatment: Estimating optimal utilization from a review of evidence-based clinical guidelines. *Cancer: Interdiscip. Int. J. Am. Cancer Soc.* **2005**, *104*, 1129–1137. [CrossRef] [PubMed]
69. Gutt, R.; Dawson, G.; Cheuk, A.V.; Fosmire, H.; Moghanaki, D.; Kelly, M.; Jolly, S. Palliative radiotherapy for the management of metastatic cancer: Bone metastases, spinal cord compression, and brain metastases. *Fed. Pract.* **2015**, *32*, 12S.
70. Behr, T.M.; Béhé, M.; Löhr, M.; Sgouros, G.; Angerstein, C.; Wehrmann, E.; Nebendahl, K.; Becker, W. Therapeutic advantages of Auger electron-over β-emitting radiometals or radioiodine when conjugated to internalizing antibodies. *Eur. J. Nucl. Med.* **2000**, *27*, 753–765. [CrossRef] [PubMed]
71. Lutz, W.; Winston, K.R.; Maleki, N. A system for stereotactic radiosurgery with a linear accelerator. *Int. J. Radiat. Oncol. Biol. Phys.* **1988**, *14*, 373–381. [CrossRef]
72. Hall, E.J.; Giaccia, A.J. *Radiobiology for the Radiologist*; Lippincott Williams & Wilkins: Philadelphia, PA, USA, 2006; Volume 6.
73. Azzam, E.I.; Jay-Gerin, J.-P.; Pain, D. Ionizing radiation-induced metabolic oxidative stress and prolonged cell injury. *Cancer Lett.* **2012**, *327*, 48–60. [CrossRef]
74. Voyant, C.; Julian, D.; Roustit, R.; Biffi, K.; Lantieri, C. Biological effects and equivalent doses in radiotherapy: A software solution. *Rep. Pract. Oncol. Radiother.* **2014**, *19*, 47–55. [CrossRef] [PubMed]
75. Moding, E.J.; Kastan, M.B.; Kirsch, D.G. Strategies for optimizing the response of cancer and normal tissues to radiation. *Nat. Rev. Drug Discov.* **2013**, *12*, 526–542. [CrossRef] [PubMed]
76. Retif, P.; Pinel, S.; Toussaint, M.; Frochot, C.; Chouikrat, R.; Bastogne, T.; Barberi-Heyob, M. Nanoparticles for Radiation Therapy Enhancement: The Key Parameters. *Theranostics* **2015**, *5*, 1030–1044. [CrossRef]

77. Kuncic, Z.; Lacombe, S. Nanoparticle radio-enhancement: Principles, progress and application to cancer treatment. *Phys. Med. Biol.* **2018**, *63*, 02TR01. [CrossRef] [PubMed]
78. Knoll, G.F. *Radiation Detection and Measurement*; John Wiley & Sons: Hoboken, NJ, USA, 2010.
79. Niemantsverdriet, M.; van Goethem, M.-J.; Bron, R.; Hogewerf, W.; Brandenburg, S.; Langendijk, J.A.; van Luijk, P.; Coppes, R.P. High and low LET radiation differentially induce normal tissue damage signals. *Int. J. Radiat. Oncol. Biol. Phys.* **2012**, *83*, 1291–1297. [CrossRef] [PubMed]
80. Ku, A.; Facca, V.J.; Cai, Z.; Reilly, R.M. Auger electrons for cancer therapy—A review. *EJNMMI Radiopharm. Chem.* **2019**, *4*, 1–36. [CrossRef] [PubMed]
81. Choi, J.; Kim, G.; Cho, S.B.; Im, H.-J. Radiosensitizing high-Z metal nanoparticles for enhanced radiotherapy of glioblastoma multiforme. *J. Nanobiotechnol.* **2020**, *18*, 1–23. [CrossRef] [PubMed]
82. Thoraeus, R. Attenuation of Gamma Radiation from 60Co, 137Cs, 192Ir, and 226Ra in Various Materials Used in Radiotherapy. *Acta Radiol. Ther. Phys. Biol.* **1965**, *3*, 81–86. [CrossRef]
83. Allal, A.S.; Michel Richter, M.; Russo, M.; Rouzaud, M.; Dulguerov, P.; Kurtz, J.M. Dose variation at bone/titanium interfaces using titanium hollow screw osseointegrating reconstruction plates. *Int. J. Radiat. Oncol. Biol. Phys.* **1998**, *40*, 215–219. [CrossRef]
84. Melian, E.; Fatyga, M.; Lam, P.; Steinberg, M.; Reddy, S.P.; Petruzzelli, G.J.; Glasgow, G.P. Effect of metal reconstruction plates on cobalt-60 dose distribution: A predictive formula and clinical implications. *Int. J. Radiat. Oncol. Biol. Phys.* **1999**, *44*, 725–730. [CrossRef]
85. Pottier, A.; Borghi, E.; Levy, L. New use of metals as nanosized radioenhancers. *Anticancer Res.* **2014**, *34*, 443–453. [PubMed]
86. Ahmed, S.; Rao, A.G.; Sankarshan, B.; Vicas, C.; Namratha, K.; Umesh, T.; Somashekar, R.; Byrappa, K. Evaluation of Gold, Silver and Silver–Gold (bimetallic) nanoparticles as radiosensitizers for radiation therapy in cancer treatment. *Cancer Oncol. Res* **2016**, *4*, 42–51. [CrossRef]
87. Liu, Y.; Zhang, P.; Li, F.; Jin, X.; Li, J.; Chen, W.; Li, Q. Metal-based nanoenhancers for future radiotherapy: Radiosensitizing and synergistic effects on tumor cells. *Theranostics* **2018**, *8*, 1824. [CrossRef]
88. Singh, P.; Pandit, S.; Mokkapati, V.; Garg, A.; Ravikumar, V.; Mijakovic, I. Gold nanoparticles in diagnostics and therapeutics for human cancer. *Int. J. Mol. Sci.* **2018**, *19*, 1979. [CrossRef]
89. Carter, J.D.; Cheng, N.N.; Qu, Y.; Suarez, G.D.; Guo, T. Nanoscale energy deposition by X-ray absorbing nanostructures. *J. Phys. Chem. B* **2007**, *111*, 11622–11625. [CrossRef] [PubMed]
90. Hainfeld, J.F.; Dilmanian, F.A.; Slatkin, D.N.; Smilowitz, H.M. Radiotherapy enhancement with gold nanoparticles. *J. Pharm. Pharmacol.* **2008**, *60*, 977–985. [CrossRef] [PubMed]
91. Herold, D.M.; Das, I.J.; Stobbe, C.C.; Iyer, R.V.; Chapman, J.D. Gold microspheres: A selective technique for producing biologically effective dose enhancement. *Int. J. Radiat. Biol.* **2000**, *76*, 1357–1364.
92. Liu, Y.; Liu, X.; Jin, X.; He, P.; Zheng, X.; Dai, Z.; Ye, F.; Zhao, T.; Chen, W.; Li, Q. The dependence of radiation enhancement effect on the concentration of gold nanoparticles exposed to low-and high-LET radiations. *Phys. Med.* **2015**, *31*, 210–218. [CrossRef]
93. Babaei, M.; Ganjalikhani, M. The potential effectiveness of nanoparticles as radio sensitizers for radiotherapy. *BioImpacts BI* **2014**, *4*, 15.
94. Cooper, D.R.; Bekah, D.; Nadeau, J.L. Gold nanoparticles and their alternatives for radiation therapy enhancement. *Front. Chem.* **2014**, *2*, 86. [CrossRef]
95. Liu, X.; Liu, Y.; Zhang, P.; Jin, X.; Zheng, X.; Ye, F.; Chen, W.; Li, Q. The synergistic radiosensitizing effect of tirapazamine-conjugated gold nanoparticles on human hepatoma HepG2 cells under X-ray irradiation. *Int. J. Nanomed.* **2016**, *11*, 3517. [CrossRef] [PubMed]
96. Cui, L.; Her, S.; Borst, G.R.; Bristow, R.G.; Jaffray, D.A.; Allen, C. Radiosensitization by gold nanoparticles: Will they ever make it to the clinic? *Radiother. Oncol.* **2017**, *124*, 344–356. [CrossRef] [PubMed]
97. Toossi, M.T.B.; Ghorbani, M.; Mehrpouyan, M.; Akbari, F.; Sabet, L.S.; Meigooni, A.S. A Monte Carlo study on tissue dose enhancement in brachytherapy: A comparison between gadolinium and gold nanoparticles. *Australas. Phys. Eng. Sci. Med.* **2012**, *35*, 177–185. [CrossRef] [PubMed]
98. Delorme, R.; Taupin, F.; Flaender, M.; Ravanat, J.L.; Champion, C.; Agelou, M.; Elleaume, H. Comparison of gadolinium nanoparticles and molecular contrast agents for radiation therapy-enhancement. *Med. Phys.* **2017**, *44*, 5949–5960. [CrossRef] [PubMed]
99. Luchette, M.; Korideck, H.; Makrigiorgos, M.; Tillement, O.; Berbeco, R. Radiation dose enhancement of gadolinium-based AGuIX nanoparticles on HeLa cells. *Nanomed. Nanotechnol. Biol. Med.* **2014**, *10*, 1751–1755. [CrossRef] [PubMed]
100. Porcel, E.; Liehn, S.; Remita, H.; Usami, N.; Kobayashi, K.; Furusawa, Y.; Le Sech, C.; Lacombe, S. Platinum nanoparticles: A promising material for future cancer therapy? *Nanotechnology* **2010**, *21*, 085103. [CrossRef] [PubMed]
101. Li, Y.; Yun, K.-H.; Lee, H.; Goh, S.-H.; Suh, Y.-G.; Choi, Y. Porous platinum nanoparticles as a high-Z and oxygen generating nanozyme for enhanced radiotherapy in vivo. *Biomaterials* **2019**, *197*, 12–19. [CrossRef]
102. Maggiorella, L.; Barouch, G.; Devaux, C.; Pottier, A.; Deutsch, E.; Bourhis, J.; Borghi, E.; Levy, L. Nanoscale radiotherapy with hafnium oxide nanoparticles. *Future Oncol.* **2012**, *8*, 1167–1181. [CrossRef] [PubMed]
103. Zhang, P.; Darmon, A.; Marill, J.; Anesary, N.M.; Paris, S. Radiotherapy-activated hafnium oxide nanoparticles produce abscopal effect in a mouse colorectal cancer model. *Int. J. Nanomed.* **2020**, *15*, 3843. [CrossRef] [PubMed]

104. Guerreiro, A.; Chatterton, N.; Crabb, E.M.; Golding, J.P. A comparison of the radiosensitisation ability of 22 different element metal oxide nanoparticles using clinical megavoltage X-rays. *Cancer Nanotechnol.* **2019**, *10*, 1–20. [CrossRef]
105. Welsher, K.; Sherlock, S.P.; Dai, H. Deep-tissue anatomical imaging of mice using carbon nanotube fluorophores in the second near-infrared window. *Proc. Natl. Acad. Sci. USA* **2011**, *108*, 8943–8948. [CrossRef]
106. Kamkaew, A.; Chen, F.; Zhan, Y.; Majewski, R.L.; Cai, W. Scintillating nanoparticles as energy mediators for enhanced photodynamic therapy. *ACS Nano* **2016**, *10*, 3918–3935. [CrossRef]
107. Hoertz, P.G.; Magnus-Aryitey, D.; Gupta, V.; Norton, C.; Doorn, S.; Ennis, T. Photocatalytic and radiocatalytic nanomaterials for the degradation of organicspecies. *Radiat. Phys. Chem.* **2013**, *84*, 51–58. [CrossRef]
108. Nosaka, Y.; Daimon, T.; Nosaka, A.Y.; Murakami, Y. Singlet oxygen formation in photocatalytic TiO_2 aqueous suspension. *Phys. Chem. Chem. Phys.* **2004**, *6*, 2917–2918. [CrossRef]
109. Fujishima, A.; Zhang, X.; Tryk, D.A. TiO_2 photocatalysis and related surface phenomena. *Surf. Sci. Rep.* **2008**, *63*, 515–582. [CrossRef]
110. Linsebigler, A.L.; Lu, G.; Yates, J.T., Jr. Photocatalysis on TiO_2 surfaces: Principles, mechanisms, and selected results. *Chem. Rev.* **1995**, *95*, 735–758. [CrossRef]
111. Higgins, M.M.; Banu, A.; Pendleton, S.; Rojas, J. Radiocatalytic performance of oxide-based nanoparticles for targeted therapy and water remediation. *Radiat. Phys. Chem.* **2020**, *173*, 108871. [CrossRef]
112. Barcellos-Hoff, M.H.; Park, C.; Wright, E.G. Radiation and the microenvironment–tumorigenesis and therapy. *Nat. Rev. Cancer* **2005**, *5*, 867–875. [CrossRef]
113. D'Arienzo, M.; Mostoni, S.; Crapanzano, R.; Cepek, C.; Di Credico, B.; Fasoli, M.; Polizzi, S.; Vedda, A.; Villa, I.; Scotti, R. Insight into the influence of ZnO defectivity on the catalytic generation of environmentally persistent free radicals in ZnO/SiO_2 systems. *J. Phys. Chem. C* **2019**, *123*, 21651–21661. [CrossRef]
114. Wang, D.; Xie, T.; Li, Y. Nanocrystals: Solution-based synthesis and applications as nanocatalysts. *Nano Res.* **2009**, *2*, 30–46. [CrossRef]
115. Yin, H.; Casey, P.S.; McCall, M.J.; Fenech, M. Effects of surface chemistry on cytotoxicity, genotoxicity, and the generation of reactive oxygen species induced by ZnO nanoparticles. *Langmuir* **2010**, *26*, 15399–15408. [CrossRef]
116. Azizi-Lalabadi, M.; Ehsani, A.; Divband, B.; Alizadeh-Sani, M. Antimicrobial activity of Titanium dioxide and Zinc oxide nanoparticles supported in 4A zeolite and evaluation the morphological characteristic. *Sci. Rep.* **2019**, *9*, 1–10. [CrossRef]
117. Bogdan, J.; Pławińska-Czarnak, J.; Zarzyńska, J. Nanoparticles of titanium and zinc oxides as novel agents in tumor treatment: A review. *Nanoscale Res. Lett.* **2017**, *12*, 1–15. [CrossRef] [PubMed]
118. Yang, B.; Chen, Y.; Shi, J. Reactive oxygen species (ROS)-based nanomedicine. *Chem. Rev.* **2019**, *119*, 4881–4985. [CrossRef] [PubMed]
119. Abrahamse, H.; Hamblin, M.R. New photosensitizers for photodynamic therapy. *Biochem. J.* **2016**, *473*, 347–364. [CrossRef] [PubMed]
120. Zhou, Z.; Song, J.; Nie, L.; Chen, X. Reactive oxygen species generating systems meeting challenges of photodynamic cancer therapy. *Chem. Soc. Rev.* **2016**, *45*, 6597–6626. [CrossRef] [PubMed]
121. Youkhana, E.Q.; Feltis, B.; Blencowe, A.; Geso, M. Titanium dioxide nanoparticles as radiosensitisers: An in vitro and phantom-based study. *Int. J. Med. Sci.* **2017**, *14*, 602. [CrossRef]
122. Higgins, M.C.M.; Clifford, D.M.; Rojas, J.V. Au@ TiO_2 nanocomposites synthesized by X-ray radiolysis as potential radiosensitizers. *Appl. Surf. Sci.* **2018**, *427*, 702–710. [CrossRef]
123. Generalov, R.; Kuan, W.B.; Chen, W.; Kristensen, S.; Juzenas, P. Radiosensitizing effect of zinc oxide and silica nanocomposites on cancer cells. *Colloids Surf. B Biointerfaces* **2015**, *129*, 79–86. [CrossRef]
124. Sharma, H.; Kumar, K.; Choudhary, C.; Mishra, P.K.; Vaidya, B. Development and characterization of metal oxide nanoparticles for the delivery of anticancer drug. *Artif. Cells Nanomed. Biotechnol.* **2016**, *44*, 672–679. [CrossRef]
125. Mahmoudi, M.; Sant, S.; Wang, B.; Laurent, S.; Sen, T. Superparamagnetic iron oxide nanoparticles (SPIONs): Development, surface modification and applications in chemotherapy. *Adv. Drug Deliv. Rev.* **2011**, *63*, 24–46. [CrossRef]
126. Wason, M.S.; Colon, J.; Das, S.; Seal, S.; Turkson, J.; Zhao, J.; Baker, C.H. Sensitization of pancreatic cancer cells to radiation by cerium oxide nanoparticle-induced ROS production. *Nanomed. Nanotechnol. Biol. Med.* **2013**, *9*, 558–569. [CrossRef]
127. Lan, M.; Zhao, S.; Liu, W.; Lee, C.S.; Zhang, W.; Wang, P. Photosensitizers for photodynamic therapy. *Adv. Healthc. Mater.* **2019**, *8*, 1900132. [CrossRef] [PubMed]
128. Mallidi, S.; Anbil, S.; Bulin, A.-L.; Obaid, G.; Ichikawa, M.; Hasan, T. Beyond the barriers of light penetration: Strategies, perspectives and possibilities for photodynamic therapy. *Theranostics* **2016**, *6*, 2458. [CrossRef]
129. Brown, S.B.; Brown, E.A.; Walker, I. The present and future role of photodynamic therapy in cancer treatment. *Lancet Oncol.* **2004**, *5*, 497–508. [CrossRef]
130. Allison, R.R.; Sibata, C.H. Oncologic photodynamic therapy photosensitizers: A clinical review. *Photodiagnosis Photodyn. Ther.* **2010**, *7*, 61–75. [CrossRef]
131. Dolmans, D.E.; Fukumura, D.; Jain, R.K. Photodynamic therapy for cancer. *Nat. Rev. Cancer* **2003**, *3*, 380–387. [CrossRef]
132. Park, J.; Lee, Y.-K.; Park, I.-K.; Hwang, S.R. Current Limitations and Recent Progress in Nanomedicine for Clinically Available Photodynamic Therapy. *Biomedicines* **2021**, *9*, 85. [CrossRef] [PubMed]

133. Allison, R.R.; Downie, G.H.; Cuenca, R.; Hu, X.-H.; Childs, C.J.; Sibata, C.H. Photosensitizers in clinical PDT. *Photodiagnosis Photodyn. Ther.* **2004**, *1*, 27–42. [CrossRef]
134. Kou, J.; Dou, D.; Yang, L. Porphyrin photosensitizers in photodynamic therapy and its applications. *Oncotarget* **2017**, *8*, 81591. [CrossRef] [PubMed]
135. DeRosa, M.C.; Crutchley, R.J. Photosensitized singlet oxygen and its applications. *Coord. Chem. Rev.* **2002**, *233*, 351–371. [CrossRef]
136. Luksiene, Z.; Kalvelyte, A.; Supino, R. On the combination of photodynamic therapy with ionizing radiation. *J. Photochem. Photobiol. B: Biol.* **1999**, *52*, 35–42. [CrossRef]
137. Schwartz, S.; Absolon, K.; Vermund, H. Some relationships of porphyrins, X-rays and tumors. *Univ. Minn. Med. Bull* **1955**, *27*, 1–37.
138. Larue, L.; Mihoub, A.B.; Youssef, Z.; Colombeau, L.; Acherar, S.; André, J.-C.; Arnoux, P.; Baros, F.; Vermandel, M.; Frochot, C. Using X-rays in photodynamic therapy: An overview. *Photochem. Photobiol. Sci.* **2018**, *17*, 1612–1650. [CrossRef] [PubMed]
139. Vasil'ev, A.N. Microtheory of scintillation in crystalline materials. In Proceedings of the International Conference on Engineering of Scintillation Materials and Radiation Technologies, Minsk, Belarus, 26–30 January 2016; pp. 3–34.
140. Dujardin, C.; Auffray, E.; Bourret-Courchesne, E.; Dorenbos, P.; Lecoq, P.; Nikl, M.; Vasil'ev, A.N.; Yoshikawa, A.; Zhu, R. Needs, Trends, and Advances in Inorganic Scintillators. *IEEE Trans. Nucl. Sci.* **2018**, *65*, 1977–1997. [CrossRef]
141. Villa, I.; Moretti, F.; Fasoli, M.; Rossi, A.; Hattendorf, B.; Dujardin, C.; Niederberger, M.; Vedda, A.; Lauria, A. The Bright X-Ray Stimulated Luminescence of HfO2 Nanocrystals Activated by Ti Ions. *Adv. Opt. Mater.* **2020**, *8*, 1901348. [CrossRef]
142. Bulin, A.-L.; Truillet, C.; Chouikrat, R.; Lux, F.o.; Frochot, C.l.; Amans, D.; Ledoux, G.; Tillement, O.; Perriat, P.; Barberi-Heyob, M. X-ray-induced singlet oxygen activation with nanoscintillator-coupled porphyrins. *J. Phys. Chem. C* **2013**, *117*, 21583–21589. [CrossRef]
143. Procházková, L.; Pelikánová, I.T.; Mihóková, E.; Dědic, R.; Čuba, V. Novel scintillating nanocomposite for X-ray induced photodynamic therapy. *Radiat. Meas.* **2019**, *121*, 13–17. [CrossRef]
144. Liu, Y.; Chen, W.; Wang, S.; Joly, A.G. Investigation of water-soluble x-ray luminescence nanoparticles for photodynamic activation. *Appl. Phys. Lett.* **2008**, *92*, 043901. [CrossRef]
145. Rossi, F.; Bedogni, E.; Bigi, F.; Rimoldi, T.; Cristofolini, L.; Pinelli, S.; Alinovi, R.; Negri, M.; Dhanabalan, S.C.; Attolini, G.; et al. Porphyrin conjugated SiC/SiOx nanowires for X-ray-excited photodynamic therapy. *Sci. Rep.* **2015**, *5*, 7606. [CrossRef] [PubMed]
146. Yang, W.; Read, P.W.; Mi, J.; Baisden, J.M.; Reardon, K.A.; Larner, J.M.; Helmke, B.P.; Sheng, K. Semiconductor nanoparticles as energy mediators for photosensitizer-enhanced radiotherapy. *Int. J. Radiat. Oncol. Biol. Phys.* **2008**, *72*, 633–635. [CrossRef] [PubMed]
147. Ren, X.-D.; Hao, X.-Y.; Li, H.-C.; Ke, M.-R.; Zheng, B.-Y.; Huang, J.-D. Progress in the development of nanosensitizers for X-ray-induced photodynamic therapy. *Drug Discov. Today* **2018**, *23*, 1791–1800. [CrossRef]
148. Sun, W.; Zhou, Z.; Pratx, G.; Chen, X.; Chen, H. Nanoscintillator-mediated X-ray induced photodynamic therapy for deep-seated tumors: From concept to biomedical applications. *Theranostics* **2020**, *10*, 1296. [CrossRef] [PubMed]
149. Villa, I.; Villa, C.; Crapanzano, R.; Secchi, V.; Tawfilas, M.; Trombetta, E.; Porretti, L.; Brambilla, A.; Campione, M.; Torrente, Y. Functionalized Scintillating Nanotubes for Simultaneous Radio-and Photodynamic Therapy of Cancer. *ACS Appl. Mater. Interfaces* **2021**, *13*, 12997–13008. [CrossRef]
150. Perego, J.; Villa, I.; Pedrini, A.; Padovani, E.; Crapanzano, R.; Vedda, A.; Dujardin, C.; Bezuidenhout, C.X.; Bracco, S.; Sozzani, P. Composite fast scintillators based on high-Z fluorescent metal–organic framework nanocrystals. *Nat. Photonics* **2021**, *15*, 393–400. [CrossRef]
151. Zhang, X.; Wasson, M.C.; Shayan, M.; Berdichevsky, E.K.; Ricardo-Noordberg, J.; Singh, Z.; Papazyan, E.K.; Castro, A.J.; Marino, P.; Ajoyan, Z. A historical perspective on porphyrin-based metal–organic frameworks and their applications. *Coord. Chem. Rev.* **2020**, *429*, 213615. [CrossRef]
152. Lu, K.; He, C.; Guo, N.; Chan, C.; Ni, K.; Lan, G.; Tang, H.; Pelizzari, C.; Fu, Y.-X.; Spiotto, M.T. Low-dose X-ray radiotherapy–radiodynamic therapy via nanoscale metal–organic frameworks enhances checkpoint blockade immunotherapy. *Nat. Biomed. Eng.* **2018**, *2*, 600–610. [CrossRef] [PubMed]
153. Morgan, N.Y.; Kramer-Marek, G.; Smith, P.D.; Camphausen, K.; Capala, J. Nanoscintillator conjugates as photodynamic therapy-based radiosensitizers: Calculation of required physical parameters. *Radiat. Res.* **2009**, *171*, 236–244. [CrossRef]
154. McMahon, S.J.; Hyland, W.B.; Muir, M.F.; Coulter, J.A.; Jain, S.; Butterworth, K.T.; Schettino, G.; Dickson, G.R.; Hounsell, A.R.; O'sullivan, J.M. Biological consequences of nanoscale energy deposition near irradiated heavy atom nanoparticles. *Sci. Rep.* **2011**, *1*, 1–10. [CrossRef]
155. Banaee, N. Enhanced dose measurement of zinc oxide nanoparticles by radiochromic polymer dosimeter and Monte Carlo simulation. *Rep. Pract. Oncol. Radiother.* **2020**, *25*, 515–520. [CrossRef]
156. Khoshgard, K.; Hashemi, B.; Arbabi, A.; Rasaee, M.J.; Soleimani, M. Radiosensitization effect of folate-conjugated gold nanoparticles on HeLa cancer cells under orthovoltage superficial radiotherapy techniques. *Phys. Med. Biol.* **2014**, *59*, 2249–2263. [CrossRef] [PubMed]
157. Bulin, A.L.; Broekgaarden, M.; Chaput, F.; Baisamy, V.; Garrevoet, J.; Busser, B.; Brueckner, D.; Youssef, A.; Ravanat, J.L.; Dujardin, C. Radiation Dose-Enhancement Is a Potent Radiotherapeutic Effect of Rare-Earth Composite Nanoscintillators in Preclinical Models of Glioblastoma. *Adv. Sci.* **2020**, *7*, 2001675. [CrossRef]

158. Incerti, S.; Douglass, M.; Penfold, S.; Guatelli, S.; Bezak, E. Review of Geant4-DNA applications for micro and nanoscale simulations. *Phys. Med.* **2016**, *32*, 1187–1200. [CrossRef] [PubMed]
159. Sakata, D.; Kyriakou, I.; Okada, S.; Tran, H.N.; Lampe, N.; Guatelli, S.; Bordage, M.C.; Ivanchenko, V.; Murakami, K.; Sasaki, T. Geant4-DNA track-structure simulations for gold nanoparticles: The importance of electron discrete models in nanometer volumes. *Med. Phys.* **2018**, *45*, 2230–2242. [CrossRef]
160. Boudou, C.; Balosso, J.; Estève, F.; Elleaume, H. Monte Carlo dosimetry for synchrotron stereotactic radiotherapy of brain tumours. *Phys. Med. Biol.* **2005**, *50*, 4841. [CrossRef] [PubMed]
161. Edouard, M.; Broggio, D.; Prezado, Y.; Estève, F.; Elleaume, H.; Adam, J.-F. Treatment plans optimization for contrast-enhanced synchrotron stereotactic radiotherapy. *Med. Phys.* **2010**, *37*, 2445–2456. [CrossRef] [PubMed]
162. Bulin, A.-L.; Vasil'Ev, A.; Belsky, A.; Amans, D.; Ledoux, G.; Dujardin, C. Modelling energy deposition in nanoscintillators to predict the efficiency of the X-ray-induced photodynamic effect. *Nanoscale* **2015**, *7*, 5744–5751. [CrossRef]
163. De Jong, W.H.; Hagens, W.I.; Krystek, P.; Burger, M.C.; Sips, A.J.; Geertsma, R.E. Particle size-dependent organ distribution of gold nanoparticles after intravenous administration. *Biomaterials* **2008**, *29*, 1912–1919. [CrossRef]
164. Sykes, E.A.; Chen, J.; Zheng, G.; Chan, W.C. Investigating the impact of nanoparticle size on active and passive tumor targeting efficiency. *ACS Nano* **2014**, *8*, 5696–5706. [CrossRef] [PubMed]
165. Her, S.; Jaffray, D.A.; Allen, C. Gold nanoparticles for applications in cancer radiotherapy: Mechanisms and recent advancements. *Adv. Drug Deliv. Rev.* **2017**, *109*, 84–101. [CrossRef] [PubMed]
166. Wolfram, J.; Zhu, M.; Yang, Y.; Shen, J.; Gentile, E.; Paolino, D.; Fresta, M.; Nie, G.; Chen, C.; Shen, H. Safety of nanoparticles in medicine. *Curr. Drug Targets* **2015**, *16*, 1671–1681. [CrossRef] [PubMed]
167. Sah, B.; Antosh, M.P. Effect of size on gold nanoparticles in radiation therapy: Uptake and survival effects. *J. Nano Med.* **2019**, *2*, 1013.
168. Shi, Y.; Van der Meel, R.; Chen, X.; Lammers, T. The EPR effect and beyond: Strategies to improve tumor targeting and cancer nanomedicine treatment efficacy. *Theranostics* **2020**, *10*, 7921. [CrossRef] [PubMed]
169. Martinelli, C.; Pucci, C.; Ciofani, G. Nanostructured carriers as innovative tools for cancer diagnosis and therapy. *APL Bioeng.* **2019**, *3*, 011502. [CrossRef] [PubMed]
170. Alasvand, N.; Urbanska, A.; Rahmati, M.; Saeidifar, M.; Gungor-Ozkerim, P.; Sefat, F. Therapeutic nanoparticles for targeted delivery of anticancer drugs. In *Multifunctional Systems for Combined Delivery, Biosensing and Diagnostics*; Elsevier: Amsterdam, The Netherlands, 2017; pp. 245–259.
171. Montaseri, H.; Kruger, C.A.; Abrahamse, H. Organic nanoparticle based active targeting for photodynamic therapy treatment of breast cancer cells. *Oncotarget* **2020**, *11*, 2120. [CrossRef]
172. Mills, J.K.; Needham, D. Targeted drug delivery. *Expert Opin. Ther. Pat.* **1999**, *9*, 1499–1513. [CrossRef]
173. Piktel, E.; Niemirowicz, K.; Wątek, M.; Wollny, T.; Deptuła, P.; Bucki, R. Recent insights in nanotechnology-based drugs and formulations designed for effective anti-cancer therapy. *J. Nanobiotechnology* **2016**, *14*, 1–23. [CrossRef]
174. Larson, S.M.; Carrasquillo, J.A.; Cheung, N.-K.V.; Press, O.W. Radioimmunotherapy of human tumours. *Nat. Rev. Cancer* **2015**, *15*, 347–360. [CrossRef] [PubMed]
175. Bernard-Marty, C.; Lebrun, F.; Awada, A.; Piccart, M.J. Monoclonal antibody-based targeted therapy in breast cancer. *Drugs* **2006**, *66*, 1577–1591. [CrossRef]
176. Sutton, D.; Nasongkla, N.; Blanco, E.; Gao, J. Functionalized micellar systems for cancer targeted drug delivery. *Pharm. Res.* **2007**, *24*, 1029–1046. [CrossRef]
177. Iqbal, N.; Iqbal, N. Human epidermal growth factor receptor 2 (HER2) in cancers: Overexpression and therapeutic implications. *Mol. Biol. Int.* **2014**, *2014*. [CrossRef] [PubMed]
178. Zheng, J.; Ren, W.; Chen, T.; Jin, Y.; Li, A.; Yan, K.; Wu, Y.; Wu, A. Recent advances in superparamagnetic iron oxide based nanoprobes as multifunctional theranostic agents for breast cancer imaging and therapy. *Curr. Med. Chem.* **2018**, *25*, 3001–3016. [CrossRef] [PubMed]
179. Samani, R.K.; Tavakoli, M.B.; Maghsoudinia, F.; Motaghi, H.; Hejazi, S.H.; Mehrgardi, M.A. Trastuzumab and folic acid functionalized gold nanoclusters as a dual-targeted radiosensitizer for megavoltage radiation therapy of human breast cancer. *Eur. J. Pharm. Sci.* **2020**, *153*, 105487. [CrossRef]
180. Peer, D.; Karp, J.M.; Hong, S.; Farokhzad, O.C.; Margalit, R.; Langer, R. Nanocarriers as an emerging platform for cancer therapy. *Nano-Enabled Med. Appl.* **2020**, *2*, 751–760.
181. Zhang, X.; Peng, L.; Liang, Z.; Kou, Z.; Chen, Y.; Shi, G.; Li, X.; Liang, Y.; Wang, F.; Shi, Y. Effects of aptamer to U87-EGFRvIII cells on the proliferation, radiosensitivity, and radiotherapy of glioblastoma cells. *Mol. Ther. Nucleic Acids* **2018**, *10*, 438–449. [CrossRef]
182. Delač, M.; Motaln, H.; Ulrich, H.; Lah, T.T. Aptamer for imaging and therapeutic targeting of brain tumor glioblastoma. *Cytom. Part A* **2015**, *87*, 806–816. [CrossRef] [PubMed]
183. Zhao, Y.; Wang, J.; Cai, X.; Ding, P.; Lv, H.; Pei, R. Metal–Organic Frameworks with Enhanced Photodynamic Therapy: Synthesis, Erythrocyte Membrane Camouflage, and Aptamer-Targeted Aggregation. *ACS Appl. Mater. Interfaces* **2020**, *12*, 23697–23706. [CrossRef]
184. Han, Z.; Wang, X.; Heng, C.; Han, Q.; Cai, S.; Li, J.; Qi, C.; Liang, W.; Yang, R.; Wang, C. Synergistically enhanced photocatalytic and chemotherapeutic effects of aptamer-functionalized ZnO nanoparticles towards cancer cells. *Phys. Chem. Chem. Phys.* **2015**, *17*, 21576–21582. [CrossRef]

185. Maiti, S.; Sen, K.K. Introductory chapter: Drug delivery concepts. In *Advanced Technology for Delivering Therapeutics*; Books on Demand: Norderstedt, Germany, 2017; pp. 1–12.
186. Boateng, F.; Ngwa, W. Delivery of nanoparticle-based radiosensitizers for radiotherapy applications. *Int. J. Mol. Sci.* **2020**, *21*, 273. [CrossRef]
187. Boateng, F.; Ngwa, W. Novel bioerodable eluting-spacers for radiotherapy applications with in situ dose painting. *Br. J. Radiol.* **2019**, *92*, 20180745. [CrossRef] [PubMed]
188. Sinha, N.; Cifter, G.; Sajo, E.; Kumar, R.; Sridhar, S.; Nguyen, P.L.; Cormack, R.A.; Makrigiorgos, G.M.; Ngwa, W. Brachytherapy application with in situ dose painting administered by gold nanoparticle eluters. *Int. J. Radiat. Oncol. Biol. Phys.* **2015**, *91*, 385–392. [CrossRef] [PubMed]
189. Zhang, J.; Tang, H.; Liu, Z.; Chen, B. Effects of major parameters of nanoparticles on their physical and chemical properties and recent application of nanodrug delivery system in targeted chemotherapy. *Int. J. Nanomed.* **2017**, *12*, 8483. [CrossRef] [PubMed]
190. DuRoss, A.N.; Neufeld, M.J.; Rana, S.; Thomas, C.R., Jr.; Sun, C. Integrating nanomedicine into clinical radiotherapy regimens. *Adv. Drug Deliv. Rev.* **2019**, *144*, 35–56. [CrossRef] [PubMed]

applied sciences

MDPI

Article

The Impact of Radiation to Epicardial Adipose Tissue on Prognosis of Esophageal Squamous Cell Carcinoma Receiving Neoadjuvant Chemoradiotherapy and Esophagectomy

Hung-Chi Tai [1,2], Jie Lee [1,3], Wen-Chien Huang [3,4], Hung-Chang Liu [4], Chao-Hung Chen [4], Yu-Chuen Huang [5,6], Chi-Jung Lee [1], Chun-Ho Yun [7,*], Shih-Ming Hsu [2,*] and Yu-Jen Chen [1,3,5,8,*]

1 Department of Radiation Oncology, MacKay Memorial Hospital, Taipei 10449, Taiwan; will@mmh.org.tw (H.-C.T.); sinus.5706@mmh.org.tw (J.L.); chijung1979@gmail.com (C.-J.L.)
2 Department of Biomedical Imaging and Radiological Sciences, National Yang Ming Chiao Tung University, Taipei 11221, Taiwan
3 Department of Medicine, MacKay Medical College, New Taipei City 25245, Taiwan; wjhuang0@yahoo.com.tw
4 Division of Thoracic Surgery, Department of Surgery, MacKay Memorial Hospital, Taipei 10449, Taiwan; oncoteam@yahoo.com (H.-C.L.); chchen@ms1.mmh.org.tw (C.-H.C.)
5 Department of Medical Research, China Medical University Hospital, Taichung 404332, Taiwan; yuchuen@mail.cmu.edu.tw
6 School of Chinese Medicine, College of Chinese Medicine, China Medical University, Taichung 406040, Taiwan
7 Department of Radiology, MacKay Memorial Hospital, Taipei 10449, Taiwan
8 Department of Nursing, MacKay Junior College of Medicine, Nursing and Management, Taipei 11260, Taiwan
* Correspondence: med202657@gmail.com (C.-H.Y.); smhsu@ym.edu.tw (S.-M.H.); chenmdphd@gmail.com (Y.-J.C.); Tel.: +886-2-2809-4661-2301 (Y.-J.C.); Fax: +886-2-2809-6180 (Y.-J.C.)

Citation: Tai, H.-C.; Lee, J.; Huang, W.-C.; Liu, H.-C.; Chen, C.-H.; Huang, Y.-C.; Lee, C.-J.; Yun, C.-H.; Hsu, S.-M.; Chen, Y.-J. The Impact of Radiation to Epicardial Adipose Tissue on Prognosis of Esophageal Squamous Cell Carcinoma Receiving Neoadjuvant Chemoradiotherapy and Esophagectomy. *Appl. Sci.* **2021**, *11*, 4023. https://doi.org/10.3390/app11094023

Academic Editor: Salvatore Gallo

Received: 15 March 2021
Accepted: 26 April 2021
Published: 28 April 2021

Abstract: The epicardial adipose tissue (EAT), mainly composed of brown adipose tissue, is a metabolically active tissue releasing various bioactive factors with a critical role in metabolic diseases. The EAT is often irradiated during radiotherapy in patients with esophageal cancer due to its proximity to the target region. We aimed to evaluate the effect of radiation to the EAT on survival outcomes in patients with esophageal cancer receiving neoadjuvant chemoradiotherapy followed by esophagectomy. We analyzed data on 36 patients with esophageal cancer treated with trimodal therapy between 2012 and 2017. The median follow-up period was 22.0 months. The 3-year overall survival and progression-free survival rates were 39.7% and 32.5%, respectively. Multivariate analysis revealed that higher EAT-REI was independently associated with worse overall survival (hazard ratio: 1.002, $p = 0.028$) and progression-free survival (hazard ratio: 1.002, $p = 0.03$). The cutoff value with the highest accuracy for avoiding mortality was EAT-REI = 68.8 cGy/mL (area under the curve, 0.78, $p = 0.006$). The 3-year overall survival rate in patients with EAT-REI $\geq$68.8 and <68.8 was 21.7% and 71.9%, respectively ($p = 0.003$). The EAT should be considered an organ at risk during radiotherapy in patients with esophageal cancer. EAT-REI might serve as a biomarker of survival outcomes in these patients.

Keywords: esophageal cancer; neoadjuvant chemoradiation; squamous cell carcinoma; epicardial adipose tissue

1. Introduction

Esophageal cancer ranks as the seventh most common type of cancer and the sixth leading cause of cancer-related mortality worldwide [1]. Neoadjuvant chemoradiation therapy (NACRT) followed by surgery has become the standard of treatment for advanced esophageal cancer, with an improvement in survival compared with surgery alone [2–5].

The modern radiotherapy technique can deliver a focused dose to targets while minimizing the doses to normal organs. Many thoracic organs are located near the esophagus, and these normal organs could also be irradiated during esophageal cancer radiotherapy.

Previous studies have reported that the radiation dose-volume to the lung is associated with worse survival outcomes in these patients; hence, minimizing the lung radiation dose-volume was one of the treatment goals during the radiotherapy planning process. In order to optimize the lung radiation dose-volume, the heart, trachea/bronchus, great vessels, spinal cord, muscles, adipose tissue, and other soft tissues may receive a higher radiation dose. A higher RT dose delivered to the lung and heart has been reported to impair the survival of lung and breast cancer patients [6–8]. However, the impact of adipose tissues in the thorax, such as the left main coronary artery fat tissue, peri-thoracic adipose tissue (TAT), subcutaneous adipose tissue (SAT), and visceral adipose tissue (VAT), still needs to be determined.

Epicardial adipose tissue (EAT) is a unique thoracic adipose tissue located between the myocardium and the visceral layer of the pericardium. EAT is a metabolically active tissue releasing various bioactive factors that can affect the prognosis of patients with metabolic diseases [9,10]. It is characterized by a highly active fatty acid metabolism and high expression of thermogenic genes. EAT is considered to function in a manner similar to brown adipose tissue with the expression of uncoupling protein-1 (UCP-1), brown adipocyte differentiation transcription factor PR-domain-missing 16 (PRDM16), and peroxisome-proliferator-activated receptor γ co-activator-1α (PGC-1α) [11]. Hence, the radiation dose on EAT may have an impact on the survival outcomes of patients with esophageal cancer undergoing NACRT. As EAT is commonly irradiated during esophageal cancer radiotherapy, the associations between radiation on EAT and survival need to be determined.

We hypothesized that the EAT dose-volume could impact the survival outcomes of patients with esophageal squamous cell carcinoma (ESCC) undergoing NACRT. This study aimed to evaluate the EAT dose-volume and their associations with survival outcomes in patients with ESCC undergoing NACRT.

2. Materials and Methods

2.1. Patients

For analysis of thoracic adipose tissues including EAT, the main criteria for enrolment of patients were ESCC located at the middle to lower-third esophagus, in stage IIA to stage IIIC, and with radiation fields covering these tissues. A total of 36 patients who had been treated with NACRT between July 2012 and December 2017 in a single institute were included in this study. The exclusion criteria included distant metastasis and incomplete CCRT course. This study is retrospective research.

2.2. Neoadjuvant Chemoradiotherapy and Surgery

The NACRT comprised concurrent RT and chemotherapy. The prescribed radiation dose delivered to gross tumors and enlarged lymph nodes was 40–48 Gy, while that delivered to elective regional lymphatics was 36.0–43.2 Gy, delivered in 20–24 fractions with simultaneously integrated boost planning technique using intensity-modulated radiation therapy (Figure 1A). IMRT was performed once daily, 5 days a week. The target volume included the primary tumor (2 Gy per fraction) and lymphadenopathy plus a 1 cm circumferential margin and a 3 to 4 cm longitudinal margin. Elective nodal (1.8 Gy per fraction) irradiation was also included in the target volume as per the physician's discretion [12]. The normal tissue constraints were as follows: a maximal dose of 45 Gy to the spinal cord, the lung volume received 20 Gy or a radiation dose (V20) of $\leq$30%, and a mean heart dose of $\leq$30 Gy. A dose-volume histogram (DVH) parameter of V_x was defined as the percentage of the total organ volume receiving a radiation dose of x (Gy) or more. All patients underwent concurrent chemotherapy during the RT course with weekly cisplatin (30 mg/m^2).

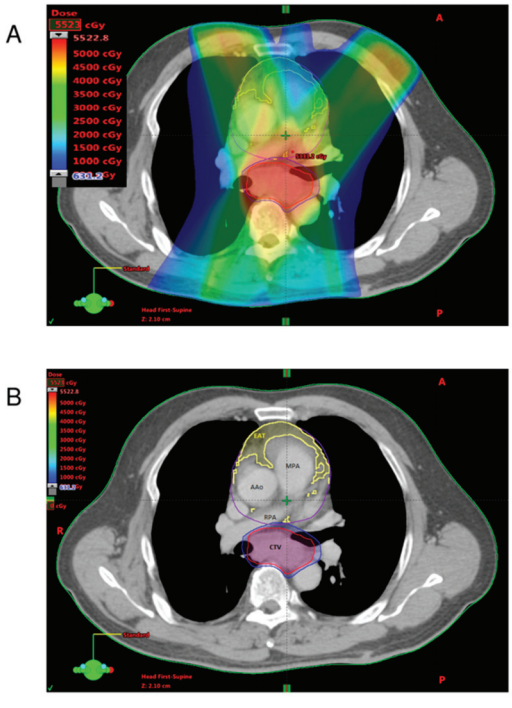

Figure 1. (**A**) The dose distribution was in color wash with IMRT treatment planning; (**B**) the epicardial adipose tissue (*yellow*) was contoured based on the anatomical boundary of heart, ranging from −195 to −45 HU. Abbreviations: EAT, epicardial adipose tissue; MPA, main pulmonary artery; AAo, ascending aorta; RPA, right pulmonary artery; CTV, clinical target volume.

2.3. Quantification of Adipose Tissues

Computed tomography (CT) is a standard imaging modality for simulation and is used in the RT planning system prior to NACRT. Using anatomy to delineate the region of interest (ROI) and the Hounsfield unit (HU) to measure the radiodensity of structures such as tumor and adipose tissue, data on both context and structure volume could be obtained. Images were obtained using a CT scanner (Big-Bore CT simulator, Philips, Amsterdam, Netherlands) equipped for simulation with the following specifications: scanning with 16 × 0.75 mm collimation, rotation time of 420 msec, and tube voltage of 120 kV. The EAT was contoured based on the anatomical boundary between the outer wall of the myocardium and the visceral layer of pericardium from the level of the left main coronary artery to the cardiac base, ranging from −195 to −45 HU (Figure 1B) [13–15]. The left main coronary artery for fat thickness, peri-thoracic adipose tissue (TAT) for peri-thoracic aortic fat volume, and subcutaneous adipose tissue (SAT) and visceral adipose tissue (VAT) of the thorax for fat areas were delineated according to the methods shown in our previous publications [13,16–18]. For example, the TAT tissue was defined as the adipose tissue surrounding the thoracic aorta, extending 67.5 mm caudally from the level of the bifurcation of pulmonary arteries.

2.4. Definition of EAT-REI

The radiation dosimetric parameters included radiation exposure intensity (REI). EAT-REI was defined as the mean radiation dose divided by volume of EAT (cGy/mL). The calculation equation for EAT-REI was listed below

$$\text{EAT-REI} = \text{mean dose of EAT/volume of EAT (cGy/mL)}$$

Quantification of the adipose tissues was performed by reconstruction of delineated images, and calculation was performed using Varian Eclipse 11.3 (Varian Medical Systems, Palo Alto, CA, USA).

2.5. Nutrition Status Evaluation

The patient characteristics with nutrition status, metabolic disease, and cardiac diseases of this cohort and their association with the outcomes were analyzed. As demonstrated in Table 1, the metabolic and cardiac diseases, as well as nutrition status, in terms of pre-treatment BMI, albumin level, lymphocyte count, triglyceride, and total cholesterol were listed.

Table 1. Patient and tumor characteristics.

Characteristics	Overall (n = 36)
Age (years)	58.8 ± 8.6
Sex	
Man	34 (94.4%)
Woman	2 (5.6%)
BMI (kg/m^2)	22.1 ± 4.3
Albumin (g/dL)	4.0 ± 0.5
Hb (g/dL)	12.0 ± 1.4
Lymphocyte (%)	21.8 ± 9.0
Cholesterol (mg/dL)	181.5 ± 40.0
Triglycerides (mg/dL)	116.2 ± 57.2
Metabolic diseases	6 (16.7%)
Cardiac diseases	9 (25.0%)
Clinical T stage	
cT1-2	9 (25.0%)
cT3-4	27 (75.0%)
Clinical N stage	
cN0-1	19 (52.8%)
cN2-3	17 (47.2%)
cTNM stage	
II	10 (27.8%)
III	26 (72.2%)
Target volume (mL)	688.8 ± 271.2
Heart volume (mL)	621.4 ± 117.1
Heart mean dose (Gy)	25.9 ± 6.9
Dose-volume of EAT	
Volume (mL)	19.2 (8.4–29.4)
Mean dose (Gy)	21.5 (16.2–26.4)
V5 *	16.5 (8.2–26.6)
V10	14.0 (6.8–21.9)
V20	10.2 (3.5–16.5)
V30	4.6 (1.5–11.4)
V40	1.1 (0.5–3.5)
SAT volume (mL)	1239.8 (682.8–1795.5)
SAT mean dose (Gy)	6.7 (5.4–7.8)
VAT volume (mL)	124.2 (76.3–251.3)
VAT mean dose (Gy)	22.5 (17.7–26.6)

* Vx = volume (mL) of EAT receiving X Gy or more; data are mean ± standard deviation, median (interquartile range), or n (%). Abbreviations: EAT, epicardial adipose tissue; SAT, subcutaneous adipose tissue; VAT, visceral adipose tissue.

2.6. Surveillance and Recurrence Evaluation

The patients were followed up monthly for 3–6 months, then every 3 months for the first year, and then every 6 months thereafter. The follow-up evaluation included clinical examination, blood tests, chest/abdominal CT, and upper gastrointestinal panendoscopy with biopsies. Further imaging studies were performed if there was clinical suspicion of recurrence. Recurrence was diagnosed on the basis of the results of physical or radiographic examinations or pathological confirmation [19].

2.7. Statistical Analysis

Quantitative data were expressed as means ± standard deviation (SD) and categorical data as frequencies and proportions. Comparisons between the participants were performed using the independent *t*-test and chi-square test, as appropriate. Cox proportional hazards regression analysis was performed to assess the prognostic factors for overall survival (OS) and progression-free survival (PFS). A logistic regression model was used to determine the significance of covariate-adjusted associations between variables and OS and PFS. All statistical analyses were carried out using Statistical Package for the Social Sciences for Windows, SPSS® software V. 22.0 (IBM Corp., New York, NY, USA; formerly SPSS Inc., Chicago, IL, USA), and $p < 0.05$ was considered significant.

3. Results

3.1. Patients and Clinical Outcome

All 36 patients underwent esophagectomy after NACRT (Table 1), with a median follow-up of 22.0 (interquartile range: 11.3–36.3) months, and showed a pCR rate of 33.3%. The 3-year PFS and OS values were 32.5% and 39.7%, respectively.

3.2. Analysis of ROC Curve

ROC analysis provides tools to select possibly optimal models and to independently discard suboptimal ones. ROC analysis is related in a direct and natural way to cost/benefit analysis of diagnostic decision making. In our study, the area under the curve (AUC) for PFS and OS for patient was 0.715 and 0.779 (Figure 2), indicating that REI improved the discrimination ability for OS.

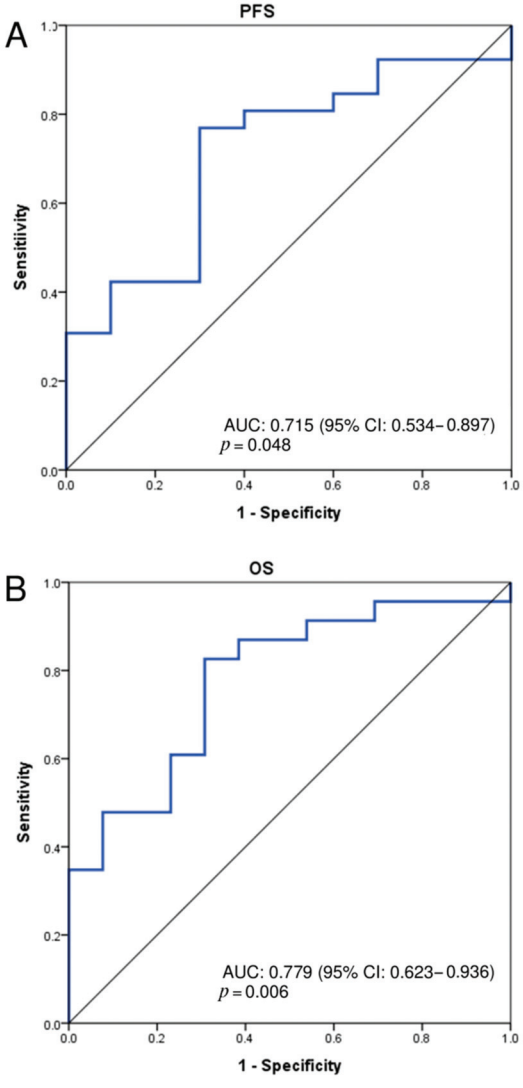

Figure 2. Receiver-operating characteristic curves for (**A**) progression-free survival AUC = 0.715 and (**B**) overall survival AUC = 0.779. AUC, area under the curve; CI, confidence interval.

3.3. Analysis of Radiotherapy Dosimetric Parameters

For OS, the significant univariate prognostic factors were TAT, EAT (V10), and EAT-REI. The results of multivariate Cox regression for OS showed that only EAT-REI (HR: 1.002; 95% CI: 1.000–1.004; p = 0.028) (Table 2) was significant. Patients with a smaller EAT-REI had better OS than those with a higher EAT-REI ($p < 0.05$). Univariate analysis for PFS revealed that TAT, SAT, EAT (V5, V10, and V20), and EAT-REI were significant, but only EAT-REI was significant, as shown in the multivariate analysis (HR: 1.002; 95% CI: 1.000–1.004; p = 0.03) (Table 3). The receiver-operating characteristics analysis showed that the area under curve (AUC) values of EAT-REI for OS/PFS were 0.779 (95% CI: 0.623–0.936, p = 0.006) / 0.715 (95% CI: 0.534–0.897, p = 0.048) and the cut-off value of REI was 68.8 cGy/mL, while the sensitivity and 1-specificity (false positive) was 0.826

and 0.308, respectively. Indicating an informative predictor for Kaplan–Meier curves for 36-month survival according to EAT-REI cut-off value (68.8 cGy/mL) were significant for PFS Kaplan–Meier curves (65.9% and 13.0%, $p = 0.001$) and OS Kaplan–Meier curves (71.9% and 21.7%, $p = 0.003$) (Figure 3). With regard to the radiotherapy parameters evaluated by DVH, the quantities of high-dose and low-dose planning target volumes had no significant impact on clinical outcome.

Table 2. Univariate and multivariate Cox proportional hazards model for overall survival.

	Univariate		Multivariate	
Characteristics	**HR (95% CI)**	***p* Value**	**HR (95% CI)**	***p* Value**
Age	1.005 (0.953–1.060)	0.859		
BMI (kg/m^2)	0.999 (0.907–1.099)	0.979		
Albumin (g/dL)	0.772 (0.351–1.702)	0.522		
Hb (g/dL)	0.986 (0.733–1.326)	0.926		
Lymphocyte (%)	0.976 (0.929–1.025)	0.325		
Cholesterol (mg/dL)	1.002 (0.987–1.017)	0.785		
Triglycerides (mg/dL)	1.000 (0.991–1.008)	0.931		
Metabolic diseases	1.392 (0.470–4.123)	0.550		
Cardiac diseases	0.558 (0.188–1.655)	0.293		
Clinical T (T1–2 vs. T3–4)	0.658 (0.303–1.432)	0.292		
Clinical N (N0–1 vs. N2–3)	1.235 (0.534–2.854)	0.621		
cTNM stage (II vs. III)	0.790 (0.321–1.943)	0.608		
Pathological response (non-pCR vs. pCR)	0.561 (0.218–1.445)	0.231		
Target volume	1.001 (1.000–1.003)	0.125		
Heart mean dose	1.000 (1.000–1.001)	0.639		
Dose-volume of EAT *				
Volume (mL)	0.981 (0.957–1.007)	0.149		
Mean dose (Gy)	1.000 (1.000–1.001)	0.702		
V5	0.971 (0.943–1.000)	0.051		
V10	0.967 (0.935–1.000)	0.049	0.988 (0.952–1.026)	0.529
V20	0.960 (0.917–1.005)	0.081		
V30	0.964 (0.904–1.029)	0.269		
V40	0.887 (0.746–1.055)	0.177		
REI of EAT (EAT-REI)	1.002 (1.001–1.004)	0.002	1.002 (1.000–1.004)	0.028
TAT volume (mL)	0.999 (0.999–1.003)	0.049	1.000 (0.999–1.000)	0.322
TAT mean dose (Gy)	1.001 (0.999–1.000)	0.294		
SAT volume (mL)	0.999 (0.999–1.000)	0.062		
SAT mean dose (Gy)	1.001 (0.998–1.003)	0.501		
VAT volume (mL)	0.995 (0.991–1.000)	0.054		
VAT mean dose (Gy)	1.000 (1.000–1.001)	0.472		

* Vx = volume (mL) of EAT receiving X Gy or more; REI(EAT-REI) was defined as the EAT mean dose divided by volume (cGy/mL). Abbreviations: CI, confidence interval; DVH, dose-volume histogram; REI, radiation exposure intensity; HR, hazard ratio; TAT, total adipose tissue.

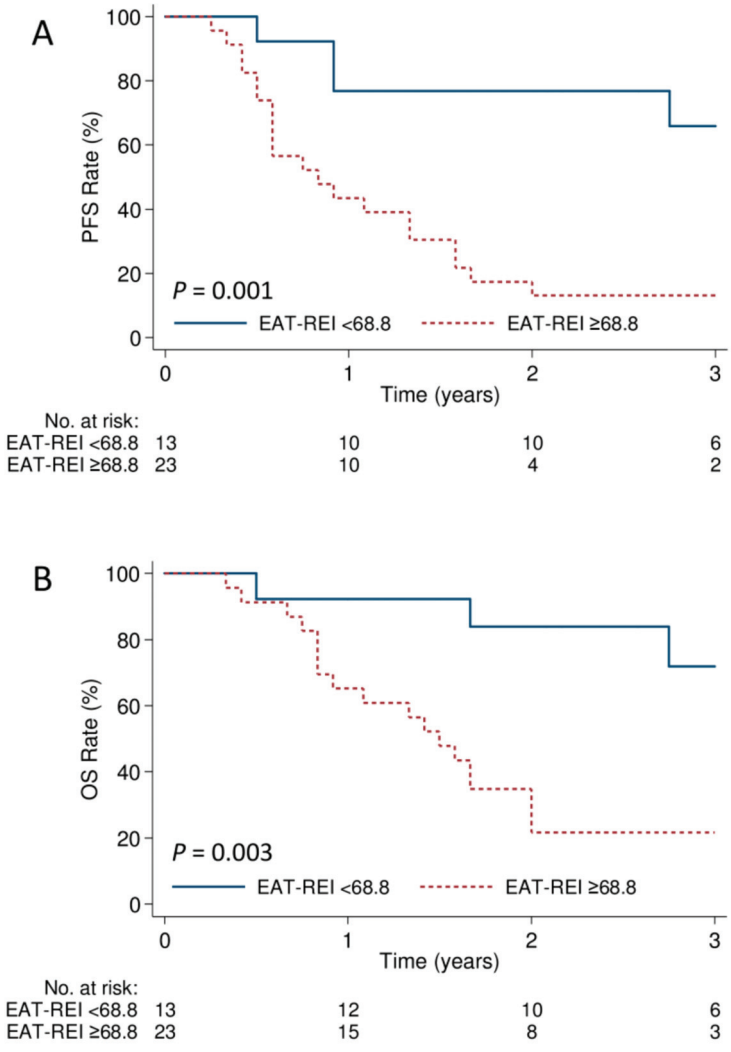

Figure 3. Kaplan–Meier estimates of the 3-year (**A**) progression-free survival $p = 0.001$ and (**B**) overall survival $p = 0.003$ according to EAT-REI cut-off value (68.8 cGy/mL).

Table 3. Univariate and multivariate Cox proportional hazards model for progression-free survival.

	Univariate		Multivariate	
Characteristics	**HR (95% CI)**	***p* Value**	**HR (95% CI)**	***p* Value**
Age	1.014 (0.965–1.066)	0.572		
BMI (kg/m^2)	0.974 (0.873–1.087)	0.637		
Albumin (g/dL)	0.694 (0.277–1.738)	0.435		
Hb (g/dL)	0.998 (0.719–1.385)	0.989		
Lymphocyte (%)	0.958 (0.904–1.015)	0.149		
Cholesterol (mg/dL)	0.992 (0.973–1.011)	0.429		
Triglycerides (mg/dL)	0.996 (0.986–1.007)	0.510		

Table 3. *Cont.*

	Univariate		Multivariate	
Characteristics	**HR (95% CI)**	***p* Value**	**HR (95% CI)**	***p* Value**
Metabolic diseases	0.040 (0.000–20.334)	0.311		
Cardiac diseases	0.344 (0.078–1.522)	0.160		
Clinical T (T1–2 vs. T3–4)	0.904 (0.444–1.839)	0.780		
Clinical N (N0–1 vs. N2–3)	1.524 (0.689–3.375)	0.299		
cTNM stage (II vs. III)	0.828 (0.342–2.004)	0.675		
Pathological response (non-pCR vs. pCR)	0.694 (0.288–1.669)	0.414		
Target Volume	1.001 (1.000–1.002)	0.164		
Heart mean dose	1.000 (0.999–1.000)	0.663		
Dose-volume of EAT *				
Volume (mL)	0.982 (0.959–1.005)	0.114		
Mean dose (Gy)	1.000 (0.999–1.000)	0.751		
V5	0.969 (0.943–0.996)	0.026	1.131 (0.933–1.369)	0.209
V10	0.965 (0.935–0.996)	0.049	0.796 (0.608–1.041)	0.095
V20	0.958 (0.918–1.000)	0.049	1.116 (0.943–1.321)	0.200
V30	0.959 (0.902–1.029)	0.182		
V40	0.871 (0.735–1.032)	0.111		
REI of EAT (EAT-REI)	1.003 (1.001–1.004)	0.002	1.002 (1.000–1.004)	0.030
TAT volume (mL)	0.999 (0.999–1.000)	0.014	0.970 (0.998–1.000)	0.060
TAT mean dose (Gy)	1.000 (0.998–1.002)	0.896		
SAT volume (mL)	0.999 (0.999–1.000)	0.018		
SAT mean dose (Gy)	1.000 (0.998–1.002)	0.855		
VAT volume (mL)	0.995 (0.991–1.000)	0.035	1.003 (0.995–1.010)	0.458
VAT mean dose (Gy)	1.000 (0.999–1.001)	0.739		

* Vx = volume (mL) of EAT receiving X Gy or more. Abbreviations: CI, confidence interval; DVH, dose-volume histogram; REI, radiation exposure intensity; HR, hazard ratio; TAT, total adipose tissue.

Further analysis of EAT-REI was performed to clarify its clinical significance. The EAT-REI was defined as the mean dose divided by the volume of EAT. The mean doses of EAT had no significant impact on OS and PFS ($p > 0.05$). However, the patients with a larger volume of EAT had a trend of less progression without statistical significance ($p > 0.05$). Thus, the lower EAT-REI mainly, but not completely, resulted from the larger volume of EAT.

3.4. Analysis of EAT-REI Ratio High and Low Group

The comparison of high and low EAT-REI groups shows no significant difference among the age, sex, BMI, CRP level, albumin level, lymphocyte count, triglyceride, and total cholesterol. In clinical T stage ($p = 0.69$), clinical N stage ($p = 0.92$), and cTNM stage ($p = 0.72$) also showed no significant difference (Table 4).

Table 4. Compare EAT-REI ratio with high and low patient groups.

Characteristics	EAT-REI $\geq$ 68.8 (n = 23)	EAT-REI < 68.8 (n = 13)	p Value
Age (years),	57.3 ± 7.9	61.6 ± 9.4	0.15
Sex			0.60
Man	22 (95.7%)	12 (92.3%)	
Woman	1 (4.3%)	1 (7.7%)	
BMI (kg/m^2)	21.2 ± 4.4	23.6 ± 3.7	0.11
CRP (mg/dL)	7.0 ± 6.2	6.2 ± 5.5	0.66
Albumin (g/dL)	3.9 ± 0.5	4.0 ± 0.6	0.71
Hb (g/dL)	11.9 ± 1.4	12.3 ± 1.5	0.38
Lymphocyte (number/uL)	1414.4 ± 770.5	1744.2 ± 631.4	0.20
Cholesterol (mg/dL)	178.6 ± 48.6	186.4 ± 18.8	0.60
Triglycerides (mg/dL)	115.8 ± 52.9	116.8 ± 66.1	0.77
Metabolic diseases	4 (17.4%)	2 (15.4%)	1.00
Cardiac diseases	4 (17.4%)	5 (38.5%)	0.24

Table 4. *Cont.*

Characteristics	EAT-REI ≥ 68.8 (n = 23)	EAT-REI < 68.8 (n = 13)	p Value
Clinical T stage			0.69
cT1–2	5 (21.7%)	4 (30.8%)	
cT3–4	18 (78.3%)	9 (69.2%)	
Clinical N stage			0.92
cN0–1	12 (52.2%)	7 (53.8%)	
cN2–3	11 (47.8%)	6 (46.2%)	
cTNM stage			0.72
II	7 (30.4%)	3 (23.1%)	
III	16 (69.6%)	10 (76.9%)	

3.5. Analysis of Nutrition Parameters

The distribution of metabolic disease and cardiac diseases has no significant correlation to OS and PFS. Among the nutrition parameters, no significant survival impact was noted by BMI, albumin level, lymphocyte count, triglyceride, and total cholesterol. As for correlation between nutrition parameters and EAT or EAT-REI, only BMI has a significant correlation to EAT volume.

4. Discussion

EAT is mainly composed of brown adipose tissue [11] and has an impact on the clinical outcomes of patients with metabolic diseases such as coronary artery disease [20] and diabetes mellitus [21]. EAT is a metabolically active tissue releasing various bioactive factors that can affect the prognosis of metabolic diseases [9]. Local expression of chemokine (monocyte chemotactic protein (MCP)-1) and inflammatory cytokines (interleukin (IL)-1β, IL-6, and tumor necrosis factor (TNF)-α) was observed in CAD patients. Significant changes in IL-1β, IL-6, MCP-1, and TNF-α mRNA and protein were observed in the epicardial adipose stores [9,22]. Ionizing radiation is known to induce inflammatory reactions and lipid remodeling of adipose tissues [23–25], but its role in brown adipose tissue or EAT remains unclear. Our investigations indicate that lower radiation exposure intensity may have a correlation with better survival. Whether this correlation resulted from radiation-induced inflammatory reactions or radiation-modulated metabolic changes still needs to be clarified.

The EAT-REI defined as mean radiation dose divided by volume of EAT is a unique biomarker for radiobiological effect derived from conventional physic dosimetric parameters. The radiation effects from exposure dose and irradiated volume may simultaneously contribute to this radiobiological marker. Growing evidence demonstrated that local radiation may have a systemic effect due to the release of soluble mediators within the radiation field. To determine whether EAT-REI has a role in this effect, which is compatible with the simultaneously irradiated dose and volume concerned, further in vivo studies using experimental animals are warranted.

In the era of dose painting RT, the use of CT scan images for simulation and RT planning software is a routine process. Analysis of the volume of EAT and the radiation dose distribution to EAT using these imaging data, therefore, is feasible and applicable. After analyzing the correlation between radiation dosimetric parameters and clinical outcomes, we found that EAT-REI might be a novel imaging biomarker from the radiobiological aspect. This implies that EAT-REI may have the potential to be adopted as a constraint when planning for RT. To the best of our knowledge, this is the first study to report EAT-REI as a constraint to RT planning.

The limitations of this study were mainly due to the retrospective analysis of both clinical factors and radiotherapy parameters. To ensure the estimated radiotherapy parameters were retrieved from the same RT planning algorithm and system, and the sample size of eligible patients was relatively small (N = 36). Another limitation of this retrospective

analysis was the lack of measurement of additional biochemical parameters related to EAT-REI. These study limitations could be overcome by further prospective investigations.

5. Conclusions

The radiation exposure intensity of epicardial adipose tissue might be an important factor, with an impact on overall survival of ESCC patients receiving NACRT and esophagectomy. However, the biological meaning of EAT-REI still needs to be clarified.

Author Contributions: Y.-J.C., S.-M.H. and C.-H.Y. designed the study. H.-C.T. performed the study and drafted the manuscript with the help of J.L. and C.-H.Y. provided assistance in CT measurement. W.-C.H., H.-C.L. and C.-H.C. contributed to the collection and analysis of surgical patients' data. Y.-C.H. analyzed the data. C.-J.L. helped in the collection of patient and measurement data. Y.-J.C. and S.-M.H. critically reviewed the data and content and provided the final approval of the version to be submitted. All authors have read and agreed to the published version of the manuscript.

Funding: This research was supported by MacKay Memorial Hospital (Grant number: MMH-E-109-13 and MMH-E-110-13).

Institutional Review Board Statement: The study protocol was granted institutional review board approval (serial number: 18MMHIS194e, MacKay Memorial Hospital, Taipei, Taiwan).

Informed Consent Statement: Patient consent was waived due to retrospective analysis and it was approved by IRB in MacKay Memorial Hospital.

Data Availability Statement: The datasets presented in this study are available from corresponding author on reasonable request.

Conflicts of Interest: The authors declare no conflict of interest in this work.

References

1. Bray, F.; Ferlay, J.; Soerjomataram, I.; Siegel, R.L.; Torre, L.A.; Jemal, A. Global cancer statistics 2018: GLOBOCAN estimates of incidence and mortality worldwide for 36 cancers in 185 countries. *CA Cancer J. Clin.* **2018**, *68*, 394–424. [CrossRef] [PubMed]
2. Shapiro, J.; van Lanschot, J.J.B.; Hulshof, M.; van Hagen, P.; van Berge Henegouwen, M.I.; Wijnhoven, B.P.L.; van Laarhoven, H.W.M.; Nieuwenhuijzen, G.A.P.; Hospers, G.A.P.; Bonenkamp, J.J.; et al. Neoadjuvant chemoradiotherapy plus surgery versus surgery alone for oesophageal or junctional cancer (CROSS): Long-term results of a randomised controlled trial. *Lancet Oncol.* **2015**, *16*, 1090–1098. [CrossRef]
3. Sjoquist, K.M.; Burmeister, B.H.; Smithers, B.M.; Zalcberg, J.R.; Simes, R.J.; Barbour, A.; Gebski, V. Survival after neoadjuvant chemotherapy or chemoradiotherapy for resectable oesophageal carcinoma: An updated meta-analysis. *Lancet Oncol.* **2011**, *12*, 681–692. [CrossRef]
4. Tepper, J.; Krasna, M.J.; Niedzwiecki, D.; Hollis, D.; Reed, C.E.; Goldberg, R.; Kiel, K.; Willett, C.; Sugarbaker, D.; Mayer, R. Phase III trial of trimodality therapy with cisplatin, fluorouracil, radiotherapy, and surgery compared with surgery alone for esophageal cancer: CALGB 9781. *J. Clin. Oncol. Off. J. Am. Soc. Clin. Oncol.* **2008**, *26*, 1086–1092. [CrossRef] [PubMed]
5. Muro, K.; Lordick, F.; Tsushima, T.; Pentheroudakis, G.; Baba, E.; Lu, Z.; Cho, B.C.; Nor, I.M.; Ng, M.; Chen, L.T.; et al. Pan-Asian adapted ESMO Clinical Practice Guidelines for the management of patients with metastatic oesophageal cancer: A JSMO-ESMO initiative endorsed by CSCO, KSMO, MOS, SSO and TOS. *Ann. Oncol. Off. J. Eur. Soc. Med. Oncol.* **2019**, *30*, 34–43. [CrossRef] [PubMed]
6. Bradley, J.D.; Paulus, R.; Komaki, R.; Masters, G.; Blumenschein, G.; Schild, S.; Bogart, J.; Hu, C.; Forster, K.; Magliocco, A.; et al. Standard-dose versus high-dose conformal radiotherapy with concurrent and consolidation carboplatin plus paclitaxel with or without cetuximab for patients with stage IIIA or IIIB non-small-cell lung cancer (RTOG 0617): A randomised, two-by-two factorial phase 3 study. *Lancet Oncol.* **2015**, *16*, 187–199. [CrossRef] [PubMed]
7. Darby, S.C.; Ewertz, M.; McGale, P.; Bennet, A.M.; Blom-Goldman, U.; Bronnum, D.; Correa, C.; Cutter, D.; Gagliardi, G.; Gigante, B.; et al. Risk of ischemic heart disease in women after radiotherapy for breast cancer. *N. Engl. J. Med.* **2013**, *368*, 987–998. [CrossRef]
8. Lee, J.; Lin, J.B.; Sun, F.J.; Lu, K.W.; Lee, C.H.; Chen, Y.J.; Huang, W.C.; Liu, H.C.; Wu, M.H. Dosimetric predictors of acute haematological toxicity in oesophageal cancer patients treated with neoadjuvant chemoradiotherapy. *Br. J. Radiol.* **2016**, *89*, 20160350. [CrossRef] [PubMed]
9. Mazurek, T.; Zhang, L.; Zalewski, A.; Mannion, J.D.; Diehl, J.T.; Arafat, H.; Sarov-Blat, L.; O'Brien, S.; Keiper, E.A.; Johnson, A.G.; et al. Human epicardial adipose tissue is a source of inflammatory mediators. *Circulation* **2003**, *108*, 2460–2466. [CrossRef]
10. Demir, E.; Harmankaya, N.O.; Kirac Utku, I.; Aciksari, G.; Uygun, T.; Ozkan, H.; Demir, B. The Relationship between Epicardial Adipose Tissue Thickness and Serum Interleukin-17a Level in Patients with Isolated Metabolic Syndrome. *Biomolecules* **2019**, *9*, 97. [CrossRef] [PubMed]

11. Sacks, H.S.; Fain, J.N.; Holman, B.; Cheema, P.; Chary, A.; Parks, F.; Karas, J.; Optican, R.; Bahouth, S.W.; Garrett, E.; et al. Uncoupling protein-1 and related messenger ribonucleic acids in human epicardial and other adipose tissues: Epicardial fat functioning as brown fat. *J. Clin. Endocrinol. Metab.* **2009**, *94*, 3611–3615. [CrossRef] [PubMed]
12. Hou, T.C.; Dai, K.Y.; Wu, M.C.; Hua, K.L.; Tai, H.C.; Huang, W.C.; Chen, Y.J. Bio-physic constraint model using spatial registration of delta 18F-fluorodeoxyglucose positron emission tomography/computed tomography images for predicting radiation pneumonitis in esophageal squamous cell carcinoma patients receiving neoadjuvant chemoradiation. *OncoTargets Ther.* **2019**, *12*, 6439–6451. [CrossRef]
13. Yun, C.H.; Lin, T.Y.; Wu, Y.J.; Liu, C.C.; Kuo, J.Y.; Yeh, H.I.; Yang, F.S.; Chen, S.C.; Hou, C.J.; Bezerra, H.G.; et al. Pericardial and thoracic peri-aortic adipose tissues contribute to systemic inflammation and calcified coronary atherosclerosis independent of body fat composition, anthropometric measures and traditional cardiovascular risks. *Eur. J. Radiol.* **2012**, *81*, 749–756. [CrossRef] [PubMed]
14. Mahabadi, A.A.; Massaro, J.M.; Rosito, G.A.; Levy, D.; Murabito, J.M.; Wolf, P.A.; O'Donnell, C.J.; Fox, C.S.; Hoffmann, U. Association of pericardial fat, intrathoracic fat, and visceral abdominal fat with cardiovascular disease burden: The Framingham Heart Study. *Eur. Heart J.* **2009**, *30*, 850–856. [CrossRef]
15. Lehman, S.J.; Massaro, J.M.; Schlett, C.L.; O'Donnell, C.J.; Hoffmann, U.; Fox, C.S. Peri-aortic fat, cardiovascular disease risk factors, and aortic calcification: The Framingham Heart Study. *Atherosclerosis* **2010**, *210*, 656–661. [CrossRef] [PubMed]
16. Yun, C.H.; Bezerra, H.G.; Wu, T.H.; Yang, F.S.; Liu, C.C.; Wu, Y.J.; Kuo, J.Y.; Hung, C.L.; Lee, J.J.; Hou, C.J.; et al. The normal limits, subclinical significance, related metabolic derangements and distinct biological effects of body site-specific adiposity in relatively healthy population. *PLoS ONE* **2013**, *8*, e61997. [CrossRef] [PubMed]
17. Lai, Y.H.; Yun, C.H.; Yang, F.S.; Liu, C.C.; Wu, Y.J.; Kuo, J.Y.; Yeh, H.I.; Lin, T.Y.; Bezerra, H.G.; Shih, S.C.; et al. Epicardial adipose tissue relating to anthropometrics, metabolic derangements and fatty liver disease independently contributes to serum high-sensitivity C-reactive protein beyond body fat composition: A study validated with computed tomography. *J. Am. Soc. Echocardiogr. Off. Publ. Am. Soc. Echocardiogr.* **2012**, *25*, 234–241. [CrossRef] [PubMed]
18. Lai, Y.H.; Hou, C.J.; Yun, C.H.; Sung, K.T.; Su, C.H.; Wu, T.H.; Yang, F.S.; Hung, T.C.; Hung, C.L.; Bezerra, H.G.; et al. The association among MDCT-derived three-dimensional visceral adiposities on cardiac diastology and dyssynchrony in asymptomatic population. *BMC Cardiovasc. Disord.* **2015**, *15*, 142. [CrossRef]
19. Lin, J.B.; Hung, L.C.; Cheng, C.Y.; Chien, Y.A.; Lee, C.H.; Huang, C.C.; Chou, T.W.; Ko, M.H.; Lai, Y.C.; Liu, M.T.; et al. Prognostic significance of lung radiation dose in patients with esophageal cancer treated with neoadjuvant chemoradiotherapy. *Radiat. Oncol.* **2019**, *14*, 85. [CrossRef]
20. Wu, F.Z.; Chou, K.J.; Huang, Y.L.; Wu, M.T. The relation of location-specific epicardial adipose tissue thickness and obstructive coronary artery disease: Systemic review and meta-analysis of observational studies. *BMC Cardiovasc. Disord.* **2014**, *14*, 62. [CrossRef]
21. Wang, C.P.; Hsu, H.L.; Hung, W.C.; Yu, T.H.; Chen, Y.H.; Chiu, C.A.; Lu, L.F.; Chung, F.M.; Shin, S.J.; Lee, Y.J. Increased epicardial adipose tissue (EAT) volume in type 2 diabetes mellitus and association with metabolic syndrome and severity of coronary atherosclerosis. *Clin. Endocrinol.* **2009**, *70*, 876–882. [CrossRef] [PubMed]
22. Parisi, V.; Rengo, G.; Pagano, G.; D'Esposito, V.; Passaretti, F.; Caruso, A.; Grimaldi, M.G.; Lonobile, T.; Baldascino, F.; De Bellis, A.; et al. Epicardial adipose tissue has an increased thickness and is a source of inflammatory mediators in patients with calcific aortic stenosis. *Int. J. Cardiol.* **2015**, *186*, 167–169. [CrossRef] [PubMed]
23. Poglio, S.; Galvani, S.; Bour, S.; André, M.; Prunet-Marcassus, B.; Pénicaud, L.; Casteilla, L.; Cousin, B. Adipose tissue sensitivity to radiation exposure. *Am. J. Pathol.* **2009**, *174*, 44–53. [CrossRef] [PubMed]
24. Xiao, Y.; Mo, W.; Jia, H.; Yu, D.; Qiu, Y.; Jiao, Y.; Zhu, W.; Koide, H.; Cao, J.; Zhang, S. Ionizing radiation induces cutaneous lipid remolding and skin adipocytes confer protection against radiation-induced skin injury. *J. Dermatol. Sci.* **2020**, *97*, 152–160. [CrossRef]
25. Lee, J.; Lin, J.B.; Wu, M.H.; Jan, Y.T.; Chang, C.L.; Huang, C.Y.; Sun, F.J.; Chen, Y.J. Muscle radiodensity loss during cancer therapy is predictive for poor survival in advanced endometrial cancer. *J. Cachexia Sarcopenia Muscle* **2019**, *10*, 814–826. [CrossRef]

applied sciences

MDPI

Article

Feasibility Study of Robust Optimization to Reduce Dose Delivery Uncertainty by Potential Applicator Displacements for a Cervix Brachytherapy

Byungdu Jo [1], Kyeongyun Park [2], Dongho Shin [2], Young Kyung Lim [2], Jong Hwi Jeong [2], Se Byeong Lee [2], Hee-Joung Kim [3,*] and Haksoo Kim [2,*]

[1] Departments of Radiation Oncology, Kyung Hee University Hospital, Seoul 20447, Korea; misonara.GGam@gmail.com
[2] Proton Therapy Center, National Cancer Center, Goyang 10408, Korea; kypark@ncc.re.kr (K.P.); dongho@ncc.re.kr (D.S.); yklim@ncc.re.kr (Y.K.L.); jonghwijeong@gmail.com (J.H.J.); sblee@ncc.re.kr (S.B.L.)
[3] Department of Radiological Science, College of Health Science, Yonsei University, Wonju 26493, Korea
* Correspondence: hjk1@yonsei.ac.kr (H.-J.K.); haksoo.kim@ncc.re.kr (H.K.)

Featured Application: This study developed a robust optimization algorithm to minimize dose delivery uncertainties by potential applicator-positional errors for MRI or CT-based planning in the Cervix Brachytherapy. It is important to improve clinical outcomes to minimize the dose to the organ at risk (OAR) when covering the target.

Abstract: Brachytherapy is an important technique to increase the overall survival of cervical cancer patients. However, a possible shift of the applicators in relation to the target and organs at risk may occur between imaging and treatment. Without daily adaptive brachytherapy planning, these applicator displacements can lead to a significant change in dose distribution. In order to resolve it, a robust optimization method had been developed using a genetic algorithm combined with a median absolute deviation as a robustness evaluation function. The resulting robustness plans from our strategy might be worth considering according to the GEC-ESTRO guidelines. From the point of view of dose delivery uncertainty from applicator displacement, the robust optimization may be considered with caution in a single-plan approach for High Dose Rate brachytherapy treatment planning and should be confirmed by a more thorough investigation.

Keywords: robust optimization; cervical cancer; high dose rate brachytherapy; single plan approach; median absolute deviation

Citation: Jo, B.; Park, K.; Shin, D.; Lim, Y.K.; Jeong, J.H.; Lee, S.B.; Kim, H.-J.; Kim, H. Feasibility Study of Robust Optimization to Reduce Dose Delivery Uncertainty by Potential Applicator Displacements for a Cervix Brachytherapy. *Appl. Sci.* **2021**, *11*, 2592. https://doi.org/10.3390/app11062592

Academic Editor: Salvatore Gallo

Received: 22 February 2021
Accepted: 9 March 2021
Published: 14 March 2021

1. Introduction

Cervical cancer is the fourth most frequent cancer among women worldwide and ranked second for both incidence and mortality in the lower Human Development Index (HDI) [1,2]. According to previous reports, cervical cancer patients with initial stages (stages IB—IIA) who undergo appropriate treatment will develop a recurrence with a risk factor of 10–15% [3,4]. Therefore, early diagnosis and treatment are crucial for reducing the mortality rate.

One of the most common treatment strategies for cervical cancer, when high dose radiation is required to be curative, is a combination of external beam radiotherapy (EBRT), chemotherapy and brachytherapy, such as EBRT alone, EBRT plus brachytherapy, or combined EBRT plus brachytherapy with concurrent chemotherapy [5]. Several studies have verified that the combination of EBRT, chemotherapy, and brachytherapy improves treatment outcomes [6–8]. It is well known that the brachytherapy boost improves overall survival by 5 years due to its superiority of rapid dose fall-off with distance from the source and limited dose exposure to surrounding tissues in accordance with the inverse square law [9]. Moreover, a remote after-loading platform, including radioactive sources, allows

for a more precise configuration of the dose to the target and the optimization of dwell times [10].

Excellent results were achieved with brachytherapy in combination with EBRT although this approach is not without limitations. The dose distribution in brachytherapy has a sharp dose gradient that is inherent to the radioactive source, and it is more sensitive to uncertainties of patient setup and applicator position [11]. Uncertainties in brachytherapy for cervical cancer are mainly related to source calibration, dose and dose–volume–histogram (DVH) calculation, reconstruction of applicators, contouring, intra- and inter-fraction uncertainties and dose delivery [12–22]. For the definition of the size and location of the cervical cancer, magnetic resonance imaging (MRI)/computed tomography (CT)-guided High Dose Rate (HDR) brachytherapy is currently defined by Groupe Européen de Curiethérapie and the European Society for Radiotherapy and Oncology (GEC–ESTRO) as MR imaging prior to the first fraction of irradiation with the applicator in place and subsequent treatment planning of each fraction [23]. However, an MRI is not routinely available in radiotherapy departments and this optimal approach requires a large amount of personnel, time and equipment infrastructure. An alternative to using CT or radiographs for subsequent fractions is the use of one implantation for several fractions of irradiation with a standardized constant bladder filling [24,25]. In the view from above, the dosimetric impacts of uncertainty should be considered to minimize therapy delivery variations and to improve patient outcomes: Grigsby et al. [26] investigated the interfractional tandem displacement between multiple insertions, and found a displacement of about 1.2 cm in the caudal–cranial direction when a point A based-plan was generated on orthogonal X-rays, and Hellebust et al. [27] applied one brachytherapy plan for several fractions and demonstrated that the average relative standard deviation for 13 series of 3 to 6 fractions were 15 and 17.5% for the rectum and bladder, respectively. Kiristis et al. [25] compared individual MRI-based 3D treatment planning for each of four fractions with the use of only one MRI treatment plan for 14 patients. They found significant mean differences the brachytherapy dose of 9–28% variations.

Applicator displacements especially occurred randomly during interfraction treatments so that the change-of-dose distribution could not be determined mathematically. For that reason, a robust optimization method may be considered to address uncertain conditions. There were many ways to deal with this uncertainty [28–30]; however, there is no direct literature minimizing dose delivery uncertainty by applicator displacements. The most relative and straightforward approach was to predict the worst-case objective value from all scenarios and minimize their dose delivery uncertainty similar to robust optimization strategies in intensity-modulated radiation therapy and proton therapy [31–35]. Consideration of the worst-case scenario for dose delivery uncertainties in cervical brachytherapy is useful for assessing resilience and robustness. In practice, the band of DVHs for a given structure represents the range of possible dose variations. The evaluation of the band width on the DVH can be used as a quantitative measure of robustness. The median absolute deviation (MAD) is used as one of the well-known robustness estimators. It is not only often used as an initial value for computing more efficient robust estimators but also as a good robust estimator in regression problems [36]. To cope with the measurements of bandwidth at the defined dose-volume points on the DVH, a MAD robust estimator was applied to design a robust optimization algorithm in this study.

In real-world optimization problems, objectives can conflict, so there cannot be a single solution [37]. Accordingly, the optimization of dwell times and dwell positions using an inverse optimization technique needed to be carefully considered to improve the target dose coverage and reduce the dose delivered to the organ at risk (OAR). The objective function for determining the dwell times at each of dwell position for the desired dose distributions is a multi-objective optimization problem requiring complex computation [38,39]. Classical optimization techniques are efficient at finding local minimum points; however, they may not yield the global minimum point. To solve this problem, we should search for the set of all optimal compromises. The so-called Pareto set, containing

all Pareto-optimal points based on objective function, has more than one local minimum. As previously mentioned, the feasible solution to a multi-objective problem in real-world optimization is to find a set of solutions. Therefore, the genetic algorithm is well-suited to solving multi-objective optimization problems due to the population-based search approach. Given the above, a preferred efficient genetic algorithm that can search global minimum points as a multi-objective optimizer was selected to overcome the complexity of global searches [39–42]. The focus of this research study was to assess the feasibility of minimizing dose delivery uncertainty by potential applicator displacements of cervical brachytherapy treatment using a MAD-constrained robust optimization method with a multi-objective genetic algorithm.

2. Materials and Methods

2.1. Treatment Plans Data Set

Planning data from five patients who had previously been treated with EBRT followed by cervical HDR brachytherapy with a Tandem-and-Ring (TR) applicator set was used as a representative sample in this retrospective study. Each patient who underwent brachytherapy procedures was placed in a supine position with a CT/MRI applicator clamp attached to a base plate, immobilized and transported during imaging and treatment. All patients received the EBRT dose of 50.40 Gray (Gy) in 28 fractions with a consecutive brachytherapy boost dose of 25 to 30 Gy in 5–6 fractions. For the first fraction of a brachytherapy patient's treatment, an MRI- or CT-based treatment plan was generated and delivered, and then for subsequent fractions (2–5 or 2–6). The mobile C-arm X-ray imaging unit (WHA-50N, Shimadzu, Japan) was used only for registration and applicator position verification prior to each fraction of treatment. It should be noted that the initial brachytherapy plan (made from the first fraction) was reused for subsequent fractions of treatment. This manually optimized "nominal plan" (also called "initial plan") was generated from the first fraction image and compared with that of a robust optimized treatment plan taking into account applicator displacement assumptions. To incorporate dose delivery uncertainty by potential applicator displacements, the translation of the applicator displacement set up 1 mm steps in the upper and lower bound of 5 mm in the x, y and z directions based on assumptions in the pre-study reports: the MRI-based 3D treatment plan for each fraction using only one MRI treatment, interfractional tandem displacement between multiple insertions [26], interapplication variation of doses and spatial location of the OAR [27] and several reports by other groups [20–22]. Then, we applied our robust optimization method to anatomical structures and applicator models delineated from the first fraction image to generate robust treatment plans for all treatment fractions.

2.2. Optimization System Modelling

A In this study, Elekta microSelectronTM (Nucletron, Elekta AB, Stockholm, Sweden) HDR after-loader unit with 192 Ir source was used. OncentraTM (Oncentra, version 3.5, Elekta AB, Stockholm, Sweden) treatment planning system (TPS) was used for making brachytherapy plans. The voxel sizes of the T2 MRI data used for dose calculations as before were $0.5 \times 0.5 \times 4.0$ mm^3. Here, MR-compatible TR applicator sets (MR ring applicator, Elekta AB, Stockholm, Sweden) of two differently sized (small and large) rings were used, each with a 30-degree angle, 2.5 mm source position separation, and with a distance from the first source to the applicator tip defined as 7 mm. Traditionally, an optimization algorithm needs specific input data such as digitized positions, relevant anatomical structures and an applicator path to calculate a dose distribution matrix. Regions of interest (ROIs) including the high-risk clinical target volume (HRCTV), intermediate-risk clinical target volume (IRCTV), bladder, rectum, bowel, and sigmoid were manually contoured on each first-fraction image by oncologists and delineation was based on MRI findings. The contour-point lists for each structure were extracted in sequence from the Digital Imaging and Communications in Medicine–Radiation Therapy (DICOM–RT) structure files using C++ program language. Also, applicator paths were reconstructed and ex-

tracted as radiation source positions in the treatment-planning system. The source dwell positions provided in the applicator coordinate system were pre-defined according to the applicator ring structure. Overall, volume delineation and dose constraints were made in accordance with GEC–ESTRO recommendations and EMBRACE protocol guidelines for both the nominal and robust plan [18,43,44]. Given the above facts, we only used positional information of anatomical structures and source positions from the first fraction image to make the optimization model; then, after determining the positional characteristics of the source relative to the dose, calculations were completed with care in all robust optimization processes (Figure 1).

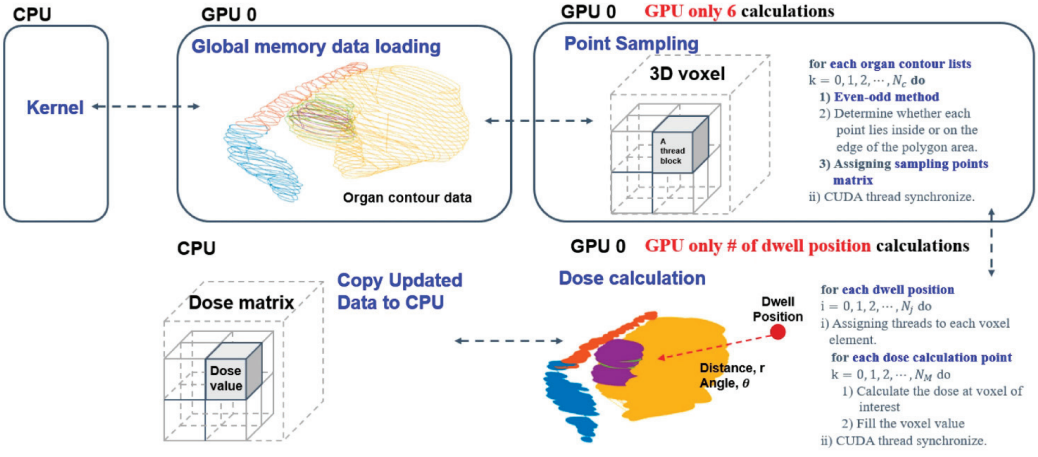

Figure 1. Detailed dose matrix calculation process from the delineation dataset.

2.3. Robust Treatment Plan Optimization

The robust optimization quality evaluation of the treatment plan is defined by the relation of each objective function to an anatomical structure and source position. Thus, the robust optimization is based on minimizing the sum of objective functions, $f_1, \ldots, f_n$. During an optimization iteration, plan quality was optimized by adjusting dwell times at each dwell position, x, and $\chi \subseteq \mathbb{R}^n$ (the certain feasible set). The dose rate to a given dose point i from dwell position j (d_{ij}) was calculated using TG-43 formalism [45–47]. The dose rate coefficient matrix under that dose delivery uncertainty scenario s is denoted by $D(x;s)$. Let $\mathcal{S}$ represent the set of all dose delivery uncertainties under consideration; then for all scenarios, let $s \in \mathcal{S}$, and all possible dose distributions be D_i [32]. In addition, the constraint functions $c(x;s)$ are scalar, so this constrained optimization approach is bounded and feasible [35] and can be formulated as

$$\begin{aligned} \underset{x\in\chi}{\text{minimize}} \quad & \sum_{k=1}^{n} \max_{s\in\mathcal{S}} f_k(D(x;s)) \\ \text{subject to} \quad & D_i = \sum_j d_{ij}x_j \qquad \forall_s \in \mathcal{S}(x) \\ & x_j \geq 0 \\ & c(x;s) \geq D_b \end{aligned} \tag{1}$$

The voxel dose was calculated as $D_i = \sum_j d_{ij}x_j$ (dose rate to a given dose point i from a dwell position j in each structure) and k, and D_b are bounds on the values of the constraint functions and given in the unit Gy. In this formula, the trade-offs related to robustness against uncertainty across a variety of scenarios was important for maximizing plan quality and minimizing uncertainty during optimization. If the set of uncertainty were empty for all decision variables x, then optimization could be a nominal problem. Therefore,

we set up the manual plan, generated by the oncologist and medical physics staff, as a nominal scenario, and it was considered a treatment plan without the shifting position of the applicator (i.e., uncertainty is zero, $s = 0$). Additionally, we used the applicator displacement assumption mentioned in Section 2.1 to create a worst-case scenario.

2.4. Plan Robustness

In this study, the DVH of the target volumes and OARs for each dose distribution were calculated to encompass all applicator displacement scenarios and assess a large number of scenarios for statistical interpretation [48–50]. For the statistical approach, we considered the band width at critical dose-volume points on the DVH under uncertainties used as a quantitative measure of robustness. Thus, the MAD of the bandwidth at the critical dose-volume points on the DVH was calculated for how spread out a set of data is. The worst-case value, determined from a random dataset in a bounded range, may not reflect a normal distribution, so MAD was used as a robust estimator instead of the standard deviation. Using the MAD function as a selection criterion served to protect against potentially large noise in data uncertainties [36]. Therefore, we used the MAD function to minimize the overshot and undershot dose-delivery uncertainty to the target volume in this work. The median and MAD functions are

$$\widetilde{\lambda} = median\{DVH_s\},\ \forall_s \in \mathcal{S}(x),\ \forall_i\ \in \mathcal{V} \tag{2}$$

$$MAD = b \times median\left\{\left|DVH_s - \widetilde{\lambda}\right|\right\},\ \ \forall_s \in \mathcal{S}(x),\ \forall_i\ \in \mathcal{V} \tag{3}$$

where $\widetilde{\lambda}$ is the median value of the DVH curve in a given region of interest (ROI) under uncertainties (DVH_s) and b is a constant scale factor: $b = 1$ was the unscaled default and $b = 1.4826$ was used for the scaled version to maintain consistency with Gaussian distribution.

2.5. Robust Optimization with a Genetic Algorithm Optimizer

In this study, given an n-dimensional decision variable vector of dwell times $x = \{x_1, \ldots, x_n\}$ in the solution space $\mathcal{X}$, the decision variable vector x was called a chromosome. Normally, the first generation of a chromosome is created randomly and called the initial population [51–53]. Randomly generated initial values were used when solving the problem in this work. To find a vector x^* that maximized or minimized a given set of k objectives functions $F(x^*) = \{f_1(x^*), \ldots, f_k(x^*)\}$, we generated fitness functions to minimize the given objective functions and constraints for our purpose.

$$\begin{aligned}\underset{x\in\mathcal{X}}{\text{minimize}}\ \tfrac{1}{N_{TARGET}} \sum_{i\ \in\mathcal{V}} (D_i - D_{TARGET})^2 + \tfrac{1}{N_{OAR}} \sum_{i\ \in\mathcal{V}} H(D_i - D_{OAR})(D_i - D_{OAR})^2\ + \ldots \\ b \times median\left\{\left|DVH_s - \widetilde{\lambda}\right|\right\}\end{aligned} \tag{4}$$

where $(1/N_{TARGET})\sum_{i\ \in\mathcal{V}}(D_i - D_{TARGET})^2$ and $(1/N_{OAR})\sum_{i\ \in\mathcal{V}} H(D_i - D_{OAR})(D_i - D_{OAR})^2$ were objective functions for all contoured organs and $\mathcal{V}$ was the set of all voxels inside each contoured structure. The D_{TARGET} and D_{OAR} were the prescription dose of the target volume and the dose constraints of OARs, and $b \times median\left\{\left|DVH_s - \widetilde{\lambda}\right|\right\}$ was a robustness function of the bandwidth at the critical dose-volume points on the DVH of the target volume and OAR under uncertainty. The constant b was a scalar factor linked to the assumption of normality of the data and the disregard of abnormality induced by out-

liers. Then, we needed to set $b = 1.4826$, as previously mentioned above. The following constraints of the problem were given.

$$\begin{gathered} \text{subject to } D_i = \sum_{j \in \mathcal{T}} d_{ij} x_j \qquad \forall_s \in \mathcal{S}(x) \\ x_j \geq 0 \\ \mathrm{H}(D_i - D_{OAR}) = \begin{cases} 1, & D_i > D_{OAR} \\ 0, & D_i \leq D_{OAR} \end{cases} \\ DVH_{TARGET}(x) \geq D_{TARGET} \\ DVH_{OAR}(x) \leq D_{OAR} \\ \widetilde{\lambda} = median\{DVH_s(D_i)\} \; \forall_s \in \mathcal{S}(x) \end{gathered} \tag{5}$$

where $\mathrm{H}(D_i - D_{OAR})$ was the step function defined as $\mathrm{H}(D_i - D_{OAR}) = 1$ if $D_i > D_{OAR}$; otherwise, $\mathrm{H}(D_i - P_{OAR}) = 0$ if $D_i \leq D_{OAR}$. $\mathcal{T}$ was the set of all dwell positions. The DVH of the target volume and OAR were controlled by each organ's prescription dose in accordance with the EMBRACE protocol guidelines as dose constraints, respectively.

The overall objective functions were optimized by the genetic algorithm in a multi-criteria optimization setting. This robust optimization was performed by calculating the delivered dose to the target and OAR in all worst-case scenarios and searching for the best alternative (a given fitness function) through chromosome evolution in each generation (Figure 2). We performed the multicriteria robust optimization problem with dose delivery uncertainty to maximize the fraction of the target volume receiving at least the prescribed dose and to minimize the maximum dose to the OAR [48].

MAD-constrained robust optimization method with multi-objective genetic algorithm pseudocode

Robust optimization based on genetic algorithm (x, *Fitness*, P_C, P_m)
- x: population size
- *Fitness*: determines the quality of solutions
- P_C: crossover rate
- P_m: mutation rate

1: *Initialise population*: $\mathcal{X} \leftarrow$ *Generate x individuals (candidate solutions) at random*
2: *Evaluate*: for each k **in** $\mathcal{X}$, calculate *Fitness(k),* check *constraints violation*
- · *MAD function*: $b \times median\{|DVH_s - \tilde{\lambda}|\}$
- · *EMBRACE protocol guidelines functions*

3: Realize the non-dominated population sorting
4: **while** termination criterion is not met (*stopping criteria*)
5: $\mathcal{X}_g \leftarrow$ *Create new population for generation* g
- (a) *Sorting*: sort the solutions in the in ascending order
- (b) *Assign*: crowding distance
- (c) *Select*: tournament selection, individuals for the next generation
  - · Perform *crossover* between a pair of selected of individuals according to P_c
  - · Perform *mutation* on a selected individual according to P_m

6: *Update*: $\mathcal{X} \leftarrow \mathcal{X}_g$
7: *Evaluate*: **for each** k **in** $\mathcal{X}$, calculate *Fitness(k)*
- · *MAD function, EMBRACE protocol guidelines functions*

8: **end while**
9: **Return** the individual with the highest fitness from $\mathcal{X}$

Figure 2. Detailed algorithmic process of the robust optimization scheme.

3. Results

We demonstrated what occurs on the curve of the DVH when applicator displacements occurs and then validated the performance of the robust algorithm with random scenario sets of applicator displacements in any direction (x, y, and z). Lastly, we compared treatment

plans between nominal and robust methods. Five patients' MRI cases were analyzed with the cervical brachytherapy of 5 Gy × 5–6 fraction prescription after receiving the EBRT of 1.8 Gy × 28 fractions. All patients received the EBRT dose of 50.40 Gray (Gy) in 28 fractions and consecutive brachytherapy boost doses of 25–30 Gy in 5–6 fractions.

3.1. DVH Variation under Uncertainty

We investigated how DVH curves were changed to the targets and OARs by applicator displacements according to data uncertainty. With the assumption that the applicator moves randomly in any direction in accordance with pre-reported data [20–27], the dose-distribution variation from applicator positional errors for each target and organ was plotted (Figure 3, grey curve). We only considered a total of 79 error scenarios chosen randomly under certain assumptions and a nominal (manual) scenario generated by the oncologist and medical physics staff (Figure 3, blue curve).

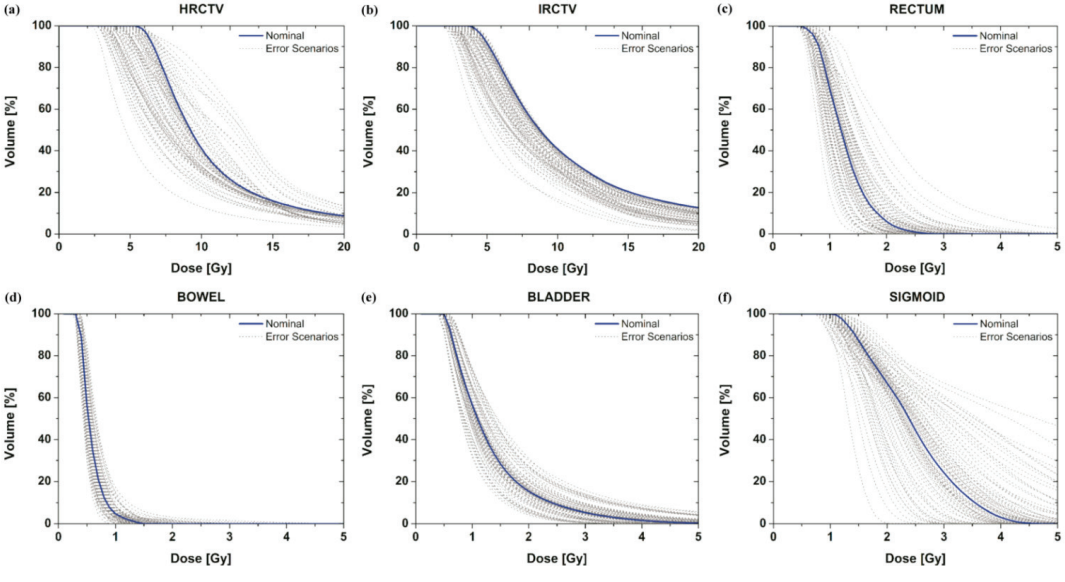

Figure 3. DVH curve variation of the targets (**a**,**b**) and OAR (**c**–**f**) under applicator positional errors with the assumption of shift scenarios. The DVH for the nominal plan setting that does not contain uncertainties is the blue curve; the DVHs for 79 error scenarios containing dose uncertainties are the grey curves.

3.2. Performance of the Robust Optimization Algorithm

3.2.1. DVH Curves

The effect of the proposed robust optimization is demonstrated in Figures 4 and 5. Figure 4 illustrates the DVH curves from the nominal and robust planning for cervical brachytherapy, including inverse planning without considering the applicator displacement parameter. The target received a sufficient dose in all plans with improved rectal and sigmoid dose sparing. We found no severe violation of EMBRACE protocol guidance in any DVH curves of the target volume or OAR using the robust planning.

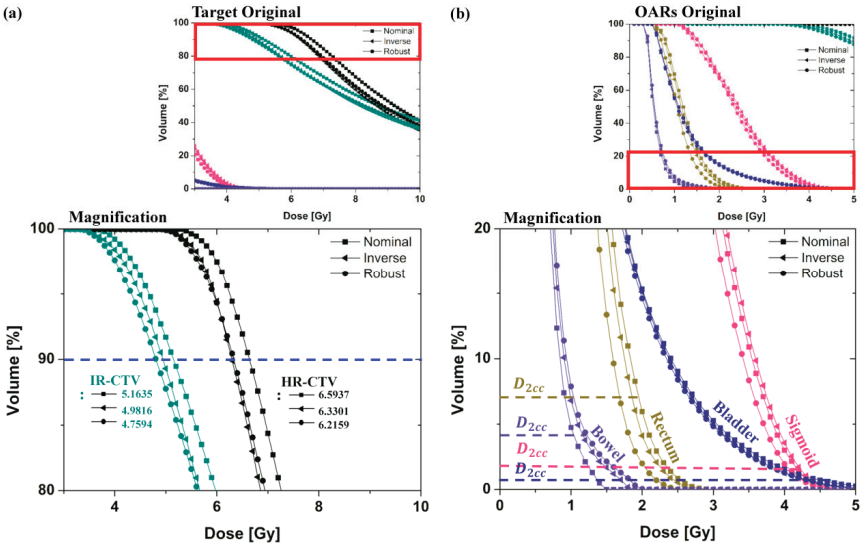

Figure 4. DVH curves for the nominal (manual) plan, inverse plan, and robust plan in EBRT brachytherapy boost treatment of cervical cancer were plotted using colors indicating HRCTV (Black), IRCTV (Teal), Rectum (Dark Yellow), Sigmoid (Pink), Bladder (Royal) and Bowel (Violet). Graphs (**a**,**b**) are the magnification of the DVH curves of the target and OAR.

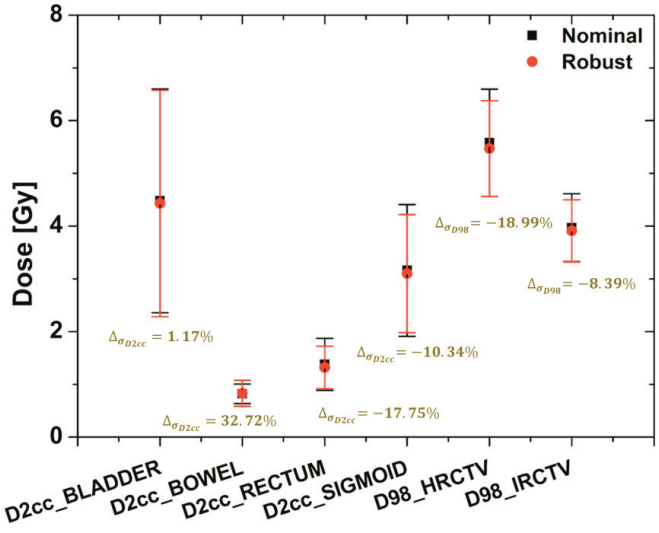

Figure 5. The bandwidth variation at the critical dose-volume points on the DVH of the targets (HRCTV and IRCTV) and OAR (BLADDER, BOWEL, RECTUM, and SIGMOID) under uncertainty with the applicator-shift scenario assumptions. The dose to 98% for target and dose to 2 cc for OAR were shown using a black square (nominal plan) and a red circle (robust plan) with a standard deviation of dose variation based on error scenarios.

In order to show the difference of dose variations between nominal and robust plans, in this case the dose to 98% for target and dose to 2 cc for OAR (with dose variations under applicator-displacement uncertainty) were plotted using colors. The standard deviations

of robust planning were less than the others in most of the target and OARs. They ranged in standard deviation from 32.72 to −18.99%.

Moreover, although both plans satisfied the requirements for the dose coverage of the target and the OAR, the band width of the DVH curves under the uncertainty of the robust plan in all organs was much narrower than its nominal plan.

3.2.2. Isodose Lines

Figures 6 and 7 illustrate the comparison of isodose lines calculated in the Oncentra Brachytherapy TPS of the nominal (manual) plan, inverse plan and robust plan for a cervical cancer patient. In all treatment plans, dwell times at each position for the desired target coverage were successfully encompassed based on EMBRACE protocol guidance. As shown in Figure 6, the bladder contour is encompassed by a minimum of percent isodose line in the robust planning while maintaining target-dose coverage and OAR sparing, rather than both coverage and sparing in the nominal and inverse planning.

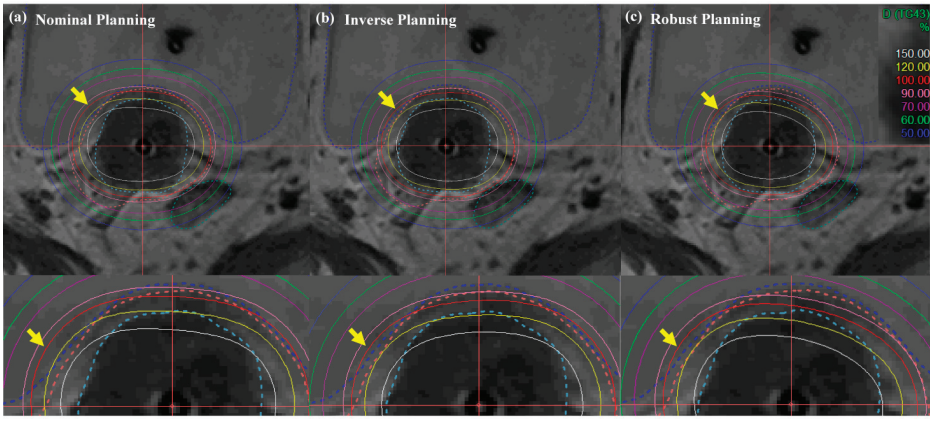

Figure 6. Isodose-line comparison of (**a**) nominal (manual) planning, (**b**) inverse planning, and (**c**) robust planning standard planning in EBRT brachytherapy boost treatment of cervical cancer: axial view. An EBRT total dose of 50.40 Gy was delivered in 28 fractions, and an ICR total dose of 30 Gy was delivered in 6 fractions using a TR applicator.

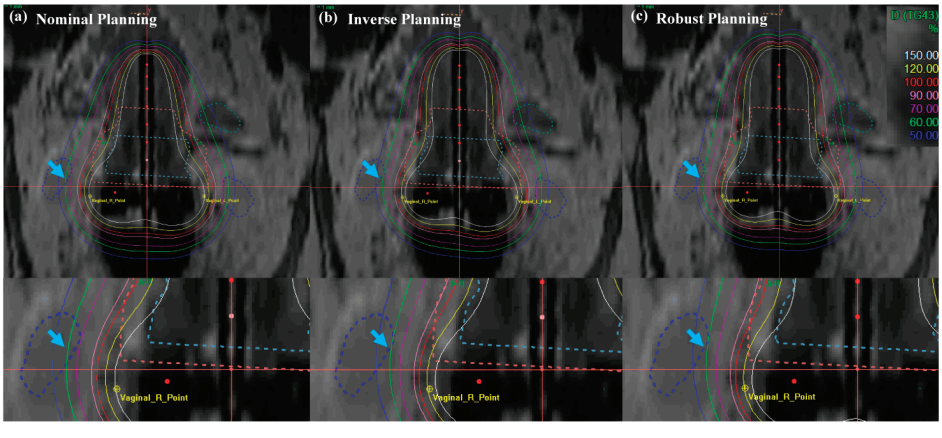

Figure 7. Isodose-line comparison of (**a**) nominal (manual) planning, (**b**) inverse planning and (**c**) robust planning. Standard planning in EBRT brachytherapy boost treatment of cervical cancer: axial view. An EBRT total dose of 50.40 Gy was delivered in 28 fractions, and an ICR total dose of 30 Gy was delivered in 6 fractions using a TR applicator.

In Figure 7, the cervical brachytherapy plan showed the isodose line from a coronal view. Figure 7 demonstrated a reduced dose to the international commission on radiation units (ICRU) vaginal right (R), left (L) point, and sigmoid than nominal and inverse plans (blue arrow with a single arrowhead). Furthermore, the robust plan not only minimized the dose delivery of the ICRU vaginal R and L point, but it also minimized doses to the OAR, while maintaining coverage of uneven HR- and IR-CTV contours. The most distinct difference between the methods in the results for the target and OAR is that the robust optimization method improved the dose distribution and decreased the dose delivery uncertainty. Table 1 displays the numerical results corresponding to Figures 6 and 7.

Table 1. The dose constraints in accordance with EMBRACE recommendation and the total EQD2 (EBRT + BT) of each target and OAR for nominal, inverse and robust plan strategy.

EQD2 and Standard Deviation of Dose Distributions				
Target/OAR	**EMBRACE Recommendation** *	**Nominal Plan EQD2 (Gy)(σ_{BT})**	**Inverse Plan EQD2 (Gy) (σ_{BT})**	**Robust Plan EQD2 (Gy) (σ_{BT})**
	$\alpha/\beta = 10$ Gy	-	-	-
HRCTV	D98 > 75 *	88.59 (±1.0177)	86.71 (±0.9393)	84.84 (±0.9085)
-	D90 > 90 *	92.15 (±1.8840)	92.63 (±0.10983)	91.56 (±1.0341)
IRCTV	D98 > 60 *	74.96 (±0.6424)	73.29 (±0.6063)	72.24 (±0.5883)
-	D90 > 66 *	82.18 (±0.7418)	80.66 (±0.6927)	78.83 (±0.6737)
	$\alpha/\beta = 3$ Gy	-	-	-
Rectum	D_{2cc} < 75 *	55.29 (±0.4927)	54.94 (±0.4620)	54.09 (±0.4052)
Sigmoid	D_{2cc} < 75 *	68.20 (±1.2491)	69.13 (±1.2718)	67.25 (±1.1199)
Bladder	D_{2cc} < 90 *	84.98 (±2.1211)	81.25 (±1.9764)	81.35 (±2.1459)
Bowel	D_{2cc} < 60 *	51.06 (±0.1864)	51.41 (±0.2270)	51.58 (±0.2474)

* Hard constraints which can be used in the treatment plan optimization.

The quantitative results in Table 1 indicate the EQD2 and the standard deviation of each nominal, inverse and robust plan strategy. For cervical cancer treatment, a prescription dose of 50.40 Gy to the target was delivered by EBRT as previously mentioned. Then, the total EQD2 (EBRT + BT) of HRCTV D98 for all plans (nominal, inverse, and robust plans) was estimated at 88.59 Gy_{EQD2}, 86.71 Gy_{EQD2}, and 84.84 Gy_{EQD2}, respectively, and the standard deviation for each plan was ±1.0177, ±0.9393, and ±0.9085, respectively. Also, EQD2 and the standard deviation of the rectum $D_{2cc} < 75^*$ for all plans were also estimated at 55.29 Gy_{EQD2} (±0.4927), 54.94 Gy_{EQD2} (±0.4620) and 54.09 Gy_{EQD2} (±0.4052), respectively.

3.3. Evaluation of Robust Optimization Algorithm with Various Cases

Further validation of our robust strategy compared plan robustness in the nominal and robust plans. Four case-sets of applicator displacements can be divided into two categories. Two cases were a challenge to fit with the EMBRACE protocol guidance, but the other two were easier because of the shape of targets. There was not an enormous difference in total time between the two nominal and robust plans, whereas the dose-delivered results of EQD2 of all cases were affected differently as shown in Figure 8.

It shows the comparison of the EQD2 and the standard deviation values of each target and OAR using both strategies. Regarding quantitative results, this proposed robust optimization could reduce the standard deviation of the target and OAR compared to the nominal plan in most of the cases, whereas the standard deviation of a few organs was not promising. In addition, the proposed robust optimization also reduced EQD2 in most of the cases. Although the standard deviation in a few organs was not sufficiently minimized, the resulting robustness plans from our strategy might be worth considering according to EMBRACE protocol guidance.

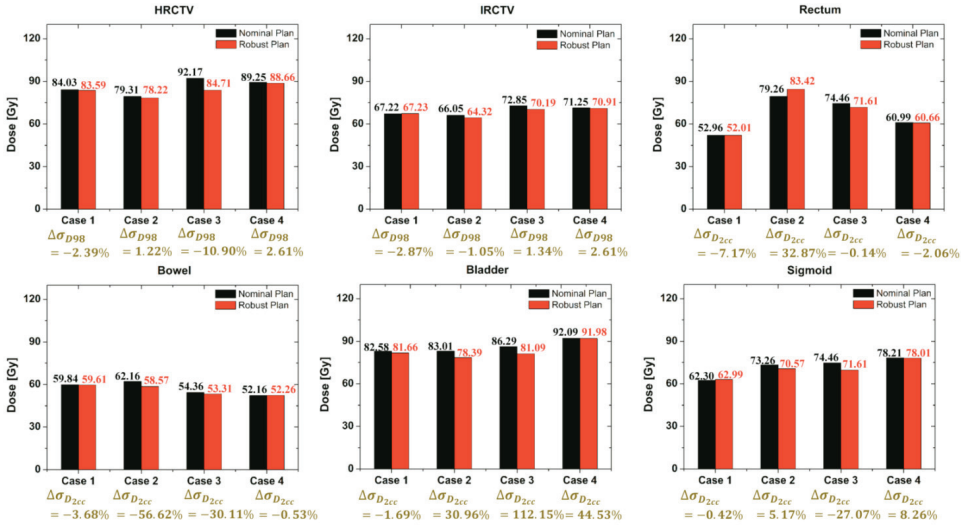

Figure 8. Comparison of the total EQD2 (EBRT + BT) of each target and OAR for both the nominal and robust plan for all cases.

For the evaluation of the effects of irregularly shaped targets on robust optimization outcomes, the degree of asymmetry for HRCTV was measured. The measurements of asymmetric ratios were obtained from the distance difference between the maximum and minimum distances from the activated dwell positions inside the HRCTV to the surface of the HRCTV.

Figure 9 gives a comparison of the measured asymmetric ratios along the given dwell positions inside the HRCTV. When the asymmetric ratio is close to the value of 1, the target shape has symmetry. The results of cases that have lower asymmetric ratio variations along the given dwell positions had a greater standard deviation reduction than the results from the cases of the higher asymmetric ratio as compared with the optimized results as shown in Figure 8.

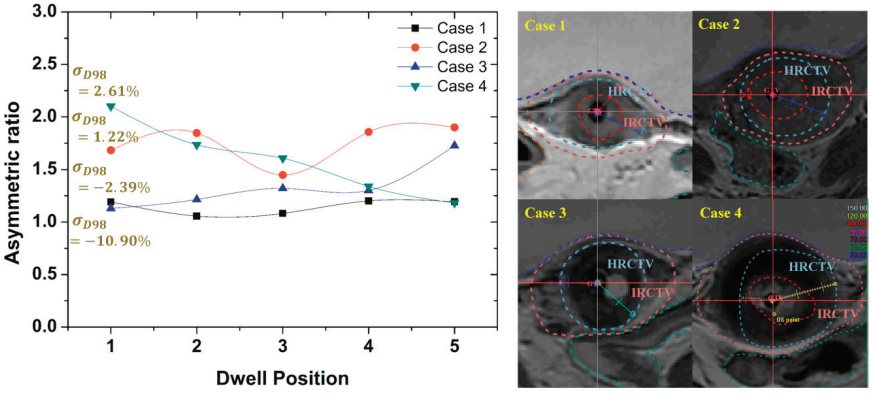

Figure 9. The asymmetric ratio variations along the given dwell positions located inside the HRCTV in all cases.

4. Discussion

We would like to emphasize that the applicator displacements during brachytherapy treatment for cervical cancer led to radical changes in dose distribution [54]. With the advent of MRI-guided brachytherapy, the opportunity to improve outcomes by increasing the target dose while minimizing the dose to the OAR is essential for the management of locally advanced cervical cancer. Hence, the dose-delivery uncertainty by applicator displacements is of significant relevance within the dose distribution. Many studies have demonstrated that applicator displacement is a problem of critical importance.

Joshua et al. [22] quantified the dosimetric impact of applicator displacements and applicator reconstruction uncertainties through simulated planning studies of virtual applicator shifts. In addition, Tanderup et al. [21] reported 2 mm errors in applicator reconstruction. However, the reconstruction approach was rather limited due to the finite slice thickness, resulting in several sources of uncertainty. Junyi et al. [29] developed a real-time applicator position monitoring system with a 1 mm accuracy during long wait times between imaging and treatment. Nevertheless, the real-time monitoring system still depends on the accuracy of distance computability between the camera and marker. Furthermore, the applicator shift and intra- and inter-fractional organ movement are inevitable, and this leads to errors in fractional dose delivery. De Leeuw et al. [16] found geometrical shifts as large as 6 ± 7 mm in the posterior direction during PDR delivery. Several studies have previously reported such movements relative to target and organs [16–18,28]. While these efforts may reduce required dose-delivery errors, there will always remain residual uncertainties.

As mentioned in the above sections, the variations of the DVH parameter due to the applicator displacements could have occurred (Figure 3). The incorporation of applicator displacement worst-case scenarios into the robust optimization with the use of a MAD function may enable the robust optimization approach to minimize the dose delivery uncertainty in a single plan approach for HDR brachytherapy treatment planning. Meerschaert et al. [55] found the importance of adaptive planning method for cervical cancer HDR brachytherapy; however, a simulation device is not routinely available in some institution. Hence, a robust optimization method with a multi-objective genetic algorithm in a single plan approach for minimizing dose delivery uncertainty by potential applicator displacements was proposed. In our study, the robustness of the treatment plan was quantified using the MAD function and could have found the optimal solution of the area of DVH bands defined by worst-case scenarios. We demonstrated the feasibility of using our robust optimization strategy to minimize the dose-delivery uncertainty by potential applicator positional displacements. The dwell positions and times were determined in a way that optimally improved the plan quality according to GEC–ESTRO Gyn Working Group recommendations. Compared to manual plan approaches, our robust optimization method resulted in a reduced standard deviation on DVH parameters while maintaining the target-dose coverage and sparing the OAR, as well as reducing EQD2 in most of the cases. Similarly, the EQD2 and the standard deviation of DVH parameters of robust optimized plan in the Table 1 showed their values to be lower compared to those of the inverse plan without considering applicator displacement assumption. The resulting robustness plans from our strategy might be worth considering according to EMBRACE protocol guidance. Evaluation of the effects of irregularly shaped targets on robust optimization outcomes shows that it was difficult to find an optimized plan for the target with a higher asymmetric ratio because the dose distribution of brachytherapy sources was symmetrically isotropic. As a result of irregularly shaped targets, the OAR (bladder) received a slightly higher radiation dose in some robust optimization process. This difficulty is unavoidable: optimization may not improve on, or reduce, variation under specific circumstances. We should consider the asymmetric ratio of the target to deal with exceptional cases such as overshot and undershot of the target and OAR. Furthermore, applicator displacement relative to important anatomical structures can occur during treatment delivery due to organ mobility [56]. To minimize the intrafractional dose variations, EM tracking [57] and real-time applicator position monitoring system using

an infrared camera and reflective markers may also be considered [29]. Lastly, the quality assurance (QA) could eventually decrease the source of uncertainties whether technical (source/equipment related) or clinical [58].

On another issue, optimized dwell times at certain dwell positions may have been very high compared to adjacent dwell positions, and there may have been almost no dwell times in adjacent source positions. This may carry a very high risk if a small volume of OARs is close to certain source positions. In the manual planning, the planner makes the safer plan by smoothing out dwell times manually over adjacent positions. To resolve this problem in the robust optimization, the algorithm can make the constraint of the difference between dwell times at adjacent source positions in the iteration step.

Nonetheless, one advantage of the proposed method is its applicability to an intensity-modulated brachytherapy (IMBT) system with modifications on the dose matrix and robust measure function. The IMBT, which is a promising method for cervix brachytherapy, is capable of increasing the dose to the target by 36.3% while decreasing the dose to the OAR by 4.7% to 22.4% compared with conventional HDR brachytherapy [59]. However, there are still a number of uncertainties related to the dose delivery in the IMBT system that include (a) uncertainty in the orientation of the shields, (b) uncertainty in source positioning and (c) uncertainty in patient/applicator relative movement [60]. These uncertainties occurring during treatment can decrease target coverage and increase the dose to organs at risk. There is a rising question about minimizing the dose-delivery uncertainty in the IMBT system. For that reason, the implementation of the proposed algorithm into the IMBT system will be investigated in a future study.

5. Conclusions

Here, our results with proposed algorithm show the feasibility of robust planning to reduce dose-delivery uncertainty by potential applicator displacements and EQD2 dose distribution compared to conventional brachytherapy plans. The fundamental assumption is that only random displacements of applicators were used for objective functions. Subsequently, a mathematical robust optimization algorithm was used to minimize the objective function value for meeting the best planning goals. Indeed, although this work concentrated only on a limited number of cases, the implication, at least from the point of view of dose-delivery uncertainty by applicator displacement, is that the robust optimization may be cautiously considered in a brachytherapy plan. Furthermore, our proposed algorithm in treatment planning systems could additionally be updated to incorporate both dwell position rotation and shield angle as degrees of freedom for minimizing the dose-delivery uncertainty in the promising IMBT system. Reducing the dose delivery uncertainty by applicator displacement should be confirmed by a more thorough investigation using different geometries and clinical cases. Additionally, the results mentioned earlier are only used for research reporting and not real treatment planning, including dose constraints.

Author Contributions: B.J. and H.K. conceived and coordinated the study, designed, performed, and analyzed the experiments, and wrote the manuscript. B.J., K.P., H.-J.K., D.S., Y.K.L., J.H.J., S.B.L. and H.K. revised the manuscript. All authors have read and agreed to the published version of the manuscript.

Funding: This research was supported by the National Research Foundation of Korea (NRF-2017R1D1A1B03035002) and the Korean National Cancer Center Fund (1810272-3).

Data Availability Statement: All data generated or analyzed during this study are included in this manuscript.

Conflicts of Interest: The authors declare no conflict of interest.

References

1. Bray, F.; Ferlay, J.; Soerjomataram, I.; Siegel, R.L.; Torre, L.A.; Jemal, A. Global cancer statistics 2018: GLOBOCAN estimates of incidence and mortality worldwide for 36 cancers in 185 countries. *CA Cancer J. Clin.* **2018**, *68*, 394–424. [CrossRef] [PubMed]
2. Kamangar, F.; Dores, G.M.; Anderson, W.F. Patterns of cancer incidence, mortality, and prevalence across five continents: Defining priorities to reduce cancer disparities in different geographic regions of the world. *J. Clin. Oncol.* **2006**, *24*, 2137–2150. [CrossRef] [PubMed]
3. Liu, Y.M.; Ni, L.Q.; Wang, S.S.; Lv, Q.L.; Chen, W.J.; Ying, S.P. Outcome and prognostic factors in cervical cancer patients treated with surgery and concurrent chemoradiotherapy: A retrospective study. *World J. Surg. Oncol.* **2018**, *16*, 1–7. [CrossRef] [PubMed]
4. Yamashita, H.; Nakagawa, K.; Tago, M.; Shiraishi, K.; Nakamura, N.; Ohtomo, K.; Taketani, Y. Comparison between conventional surgery and radiotherapy for FIGO stage I-II cervical carcinoma: A retrospective Japanese study. *Gynecol. Oncol.* **2005**, *97*, 834–839. [CrossRef] [PubMed]
5. Banerjee, R.; Kamrava, M. Brachytherapy in the treatment of cervical cancer: A review. *Int. J. Women's Health* **2014**, *6*, 555–564.
6. Al Feghali, K.A.; Elshaikh, M.A. Why brachytherapy boost is the treatment of choice for most women with locally advanced cervical carcinoma? *Brachytherapy* **2016**, *15*, 191–199. [CrossRef] [PubMed]
7. Mahmoud, O.; Kilic, S.; Khan, A.J.; Beriwal, S.; Small Jr, W. External beam techniques to boost cervical cancer when brachytherapy is not an option—theories and applications. *Ann. Transl. Med.* **2017**, *5*, 207. [CrossRef]
8. Korenaga, T.R.K.; Pierson, W.; Swanson, M.; Chapman, J.S. Better late than never: Brachytherapy is more important than timeframe in cervical cancer outcomes [Abstracts]. *Gynecol. Oncol.* **2019**, *154*, 7. [CrossRef]
9. Nikoofar, A.; Hoseinpour, Z.; Mahdavi, S.R.; Hasanzadeh, H.; Tavirani, M.R. High-Dose-Rate 192Ir Brachytherapy Dose Verification: A Phantom Study. *Iran. J. Cancer Prev.* **2015**, *8*, e2330. [CrossRef] [PubMed]
10. Henschke, U.K. "Afterloading" applicator for radiation therapy of carcinoma of the uterus. *Radiology* **1960**, *74*, 834. [CrossRef] [PubMed]
11. Shwetha, B.; Ravikumar, M.; Palled, S.R.; Supe, S.S.; Sathiyan, S. Dosimetric comparison of high dose rate brachytherapy and intensity-modulated radiation therapy for cervical carcinoma. *J. Med. Phys.* **2011**, *36*, 111–116.
12. DeWerd, L.A.; Ibbott, G.S.; Meigooni, A.S.; Mitch, M.G.; Rivard, M.J.; Stump, K.E.; Venselaar, J.L. A dosimetric uncertainty analysis for photon-emitting brachytherapy sources: Report of AAPM Task Group No. 138 and GEC-ESTRO. *Med. Phys.* **2011**, *38*, 782–801. [CrossRef]
13. Berger, D.; Dimopoulos, J.; Georg, P.; Georg, D.; Pötter, R.; Kirisits, C. Uncertainties in assessment of the vaginal dose for intracavitary brachytherapy of cervical cancer using a tandem-ring applicator. *Int. J. Radiat. Oncol. Biol. Phys.* **2007**, *67*, 1451–1459. [CrossRef]
14. Swamidas, J.; Mahantshetty, U.; Tanderup, K.; Malvankar, D.; Sharma, S.; Engineer, R.; Deshpande, D.D. Inter-application variation of dose and spatial location of D_2cm^3 volumes of OARs during MR image based cervix brachytherapy. *Radiother. Oncol.* **2013**, *107*, 58–62.
15. Vargo, J.A.; Beriwal, S. Image-based brachytherapy for cervical cancer. *World J. Clin. Oncol.* **2014**, *5*, 921–930. [CrossRef] [PubMed]
16. De Leeuw, A.A.; Moerland, M.A.; Nomden, C.; Tersteeg, R.H.; Roesink, J.M.; Jürgenliemk-Schulz, I.M. Applicator reconstruction and applicator shifts in 3D MR-based PDR brachytherapy of cervical cancer. *Radiother. Oncol.* **2009**, *93*, 341–346. [CrossRef] [PubMed]
17. Hellebust, T.P.; Tanderup, K.; Bergstrand, E.S.; Knutsen, B.H.; Røislien, J.; Olsen, D.R. Reconstruction of a ring applicator using CT imaging: Impact of the reconstruction method and applicator orientation. *Phys. Med. Biol.* **2007**, *52*, 4893–4904. [CrossRef] [PubMed]
18. Hellebust, T.P.; Kirisits, C.; Berger, D.; Perez-Caltayud, J.; De Brabandere, M.; De Leeuw, A.; Tanderup, K. Recommendations from Gynaecological (GYN) GEC-ESTRO Working Group (III): Considerations and pitfalls in commissioning and applicator reconstruction in 3D image-based treatment planning of cervix cancer brachytherapy. *Radiother. Oncol.* **2010**, *96*, 153–160. [CrossRef] [PubMed]
19. Andersen, S.E.; Noe, K.Ø.; Sørensen, T.S.; Nielsen, S.K.; Fokdal, L.; Paludan, M.; Tanderup, K. Simple DVH parameter addition as compared to deformable registration for bladder dose accumulation in cervix cancer brachytherapy. *Radiother. Oncol.* **2013**, *107*, 52–57. [CrossRef] [PubMed]
20. Lang, S.; Nesvacil, N.; Kirisits, C.; Georg, P.; Dimopoulos, J.C.; Fedrico, M.; Potter, R. Uncertainty analysis for 3D image-based cervix cancer brachytherapy by repetitive MR imaging: Assessment of DVH variations between two HDR fractions within one applicator insertion and their clinical relevance. *Radiother. Oncol.* **2013**, *107*, 26–31. [CrossRef] [PubMed]
21. Tanderup, K.; Hellebust, T.P.; Lang, S.; Granfeldt, J.; Potter, R.; Lindegaard, J.C.; Kirisits, C. Consequences of random and systematic reconstruction uncertainties in 3D image based brachytherapy in cervical cancer. *Radiother. Oncol.* **2008**, *89*, 156–163. [CrossRef]
22. Schindel, J.; Zhang, W.; Bhatia, S.K.; Sun, W.; Kim, Y. Dosimetric impacts of applicator displacements and applicator reconstruction uncertainties on 3D image-guided brachytherapy for cervical cancer. *J. Contemp. Brachythet.* **2013**, *5*, 250–257. [CrossRef]
23. Haie-Meder, C.; Potter, R.; Van Limbergen, E.; Briot, E.; De Brabandere, M.; Dimopoulos, J.; Wachter-Gerstner, N. Recommendations from Gynaecological (GYN) GEC-ESTRO Working Group* (I): Concepts and terms in 3D image based 3D treatment planning in cervix cancer brachytherapy with emphasis on MRI assessment of GTV and CTV. *Radiother. Oncol.* **2005**, *74*, 235–245. [CrossRef]

24. Lang, S.; Georg, P.; Kirists, C.; Dimopoulos, J.; Kuzucan, A.; Georg, D.; Potter, R. Uncertainty analysis for 3D image based cervix cancer brachytherapy by repeated MRI examinations: DVH-variations between two HDR fractions within one applicator insertion. *Radiother. Oncol.* **2006**, *81* (Suppl. 1), S79.
25. Kirisits, C.; Lang, S.; Dimopoulos, J.; Oechs, K.; Georg, D.; Potter, R. Uncertainties when using only one MRI-based treatment plan for subsequent high-dose-rate tandem and ring applications in brachytherapy of cervix cancer. *Radiother. Oncol.* **2006**, *81*, 269–275. [CrossRef] [PubMed]
26. Grigsby, P.W.; Georgiou, A.; Jeffrey, F.; Ferez, C.A. Anatomic variation of gynecologic brachytherapy prescription points. *Int. J. Radiat. Oncol. Biol. Phys.* **1993**, *27*, 725–729. [CrossRef]
27. Hellebust, T.P.; Dale, E.; Skjonsberg, A.; Olsen, D.R. Inter fraction variations in rectum and bladder volumes and dose distributions during high dose rate brachytherapy treatment of the uterine cervix investigated by repetitive CT examinations. *Radiother. Oncol.* **2001**, *60*, 273–280. [CrossRef]
28. Oku, Y.; Arimura, H.; Nguyen, T.T.T.; Hiraki, Y.; Toyota, M.; Saigo, Y.; Hirata, H. Investigation of whether in-room CT-based adaptive intracavitary brachytherapy for uterine cervical cancer is robust against interfractional location variations of organs and/or applicators. *J. Radiat. Res.* **2016**, *57*, 677–683. [CrossRef] [PubMed]
29. Xia, J.; Waldron, T.; Kim, Y. A real-time applicator position monitoring system for gynecologic intracavitary brachytherapy. *Med. Phys.* **2014**, *41*, 011703. [CrossRef] [PubMed]
30. Webster, M.J.; Devic, S.; Vuong, T.; Han, D.Y.; Scanderbeg, D.; Choi, D.; Song, W.Y. HDR brachytherapy of rectal cancer using a novel grooved-shielding applicator design. *Med. Phys.* **2013**, *40*, 091704. [CrossRef] [PubMed]
31. Fredriksson, A.; Bokrantz, R. A critical evaluation of worst case optimization methods for robust intensity-modulated proton therapy planning. *Med. Phys.* **2014**, *41*, 081701. [CrossRef]
32. Fredriksson, A. A characterization of robust radiation therapy treatment planning methods—From expected value to worst case optimization. *Med. Phys.* **2012**, *39*, 5169–5181. [CrossRef] [PubMed]
33. Chu, M.; Zinchenko, Y.; Henderson, S.G.; Sharpe, M.B. Robust optimization for intensity modulated radiation therapy treatment planning under uncertainty. *Phys. Med. Biol.* **2005**, *50*, 5463–5477. [CrossRef] [PubMed]
34. Tilly, D.; Holm, A.; Grusell, E.; Ahnesjö, A. Probabilistic optimization of dose coverage in radiotherapy. *Phys. Imag. Radiat. Oncol.* **2019**, *10*, 1–6. [CrossRef]
35. Chen, W.; Unkelbach, J.; Trofimov, A.; Madden, T.; Kooy, H.; Bortfeld, T.; Craft, D. Including robustness in multi-criteria optimization for intensity-modulated proton therapy. *Phys. Med. Biol.* **2012**, *57*, 591–608. [CrossRef] [PubMed]
36. Rousseeuw, P.J.; Croux, C. Alternatives to the Median Absolute Deviation. *J. Am. Stat. Assoc.* **1993**, *88*, 1273–1283. [CrossRef]
37. Hu, S.; Wu, X.; Liu, H.; Wang, Y.; Li, R.; Yin, M. Multi-Objective Neighborhood Search Algorithm Based on Decomposition for Multi-Objective Minimum Weighted Vertex Cover Problem. *Sustainability* **2019**, *11*, 3634. [CrossRef]
38. Chiandussi, G.; Codegone, M.; Ferrero, S.; Varesio, F.E. Comparison of multi-objective optimization methodologies for engineering applications. *Comput. Math. Appl.* **2012**, *63*, 912–942. [CrossRef]
39. Deist, T.M.; Gorissen, B.L. High-dose-rate prostate brachytherapy inverse planning on dose-volume criteria by simulated annealing. *Phys. Med. Biol.* **2016**, *61*, 1155–1170. [CrossRef]
40. Morén, B.; Larsson, T.; Tedgren, A.C. Mathematical optimization of high dose-rate brachytherapy derivation of a linear penalty model from a dose-volume model. *Phys. Med. Biol.* **2018**, *63*, 065011. [CrossRef]
41. Ghaheri, A.; Shoar, S.; Naderan, M.; Hoseini, S.S. The Applications of Genetic Algorithms in Medicine. *Oman Med. J.* **2015**, *30*, 406–416. [CrossRef] [PubMed]
42. Ahmad, S.U.; Bergen, S.W. A genetic algorithm approach to the inverse problem of treatment planning for intensity-modulated radiotherapy. *Biomed. Signal Process. Control* **2010**, *5*, 189–195. [CrossRef]
43. Pötter, R.; Tanderup, K.; Kirisits, C.; De Leeuw, A.; Krichheiner, K.; Nout, R.; Jurgenliemk-Schulz, I. The EMBRACE II study: The outcome and prospect of two decades of evolution within the GEC-ESTRO GYN working group and the EMBRACE studies. *Clin. Transl. Radiat. Oncol.* **2018**, *9*, 48–60. [CrossRef] [PubMed]
44. Sturdza, A.; Pötter, R.; Fokdal, L.U.; Haie-Meder, C.; Tan, L.T.; Mazeron, R.; Lindegaard, J.C. Image guided brachytherapy in locally advanced cervical cancer: Improved pelvic control and survival in RetroEMBRACE, a multicenter cohort study. *Radiother. Oncol.* **2016**, *120*, 428–433. [CrossRef]
45. Nath, R.; Anderson, L.L.; Luxton, G.; Weaver, K.A.; Williamson, J.F.; Meigooni, A.S. Dosimetry of interstitial brachytherapy sources: Recommendations of the AAPM Radiation Therapy Committee Task Group No. 43. American Association of Physicists in Medicine. *Med. Phys.* **1995**, *22*, 209–234. [CrossRef] [PubMed]
46. Rivard, M.J.; Coursey, B.M.; DeWerd, L.A.; Hanson, W.F.; Saiful Huq, M.; Ibbott, G.S.; Williamson, J.F. Update of AAPM Task Group No. 43 Report: A revised AAPM protocol for brachytherapy dose calculations. *Med. Phys.* **2004**, *31*, 633–674. [CrossRef] [PubMed]
47. Rivard, M.J.; Ballester, F.; Butler, W.M.; DeWerd, L.A.; Ibbott, G.S.; Meigooni, A.S.; Williamson, J.F. Supplement to the 2004 update of the AAPM Task Group No. 43 Report. *Med. Phys.* **2017**, *34*, 2187–2205. [CrossRef]
48. Kirisits, C.; Rivard, M.J.; Baltas, D.; Ballester, F.; De Brabandere, M.; Van der Laarse, R.; Siebert, F.A. Review of clinical brachytherapy uncertainties: Analysis guidelines of GEC-ESTRO and the AAPM. *Radiother. Oncol.* **2014**, *110*, 199–212. [CrossRef]
49. Park, P.C.; Cheung, J.P.; Zhu, X.R.; Lee, A.K.; Sahoo, N.; Tucker, S.L.; Dong, L. Statistical Assessment of Proton Treatment Plans Under Setup and Range Uncertainties. *Int. J. Radiat. Oncol. Biol. Phys.* **2013**, *86*, 1007–1013. [CrossRef] [PubMed]

50. Trofimov, A.; Unkelbach, J.; DeLaney, T.F.; Bortfeld, T. Visualization of a variety of possible dosimetric outcomes in radiation therapy using dose volume histogram bands. *Pract. Radiat. Oncol.* **2012**, *2*, 164–171. [CrossRef] [PubMed]
51. Deb, K.; Pratap, A.; Agarwal, S.; Mayarivan, T.A.M.T. A Fast and Elitist Multiobjective Genetic Algorithm: NSGA-II. *IEEE Trans. Evol. Comput.* **2002**, *6*, 182–197. [CrossRef]
52. Konaka, A.; Coit, D.W.; Smith, A.E. Multi-objective optimization using genetic algorithms: A tutorial. *Reliab. Eng. Syst. Saf.* **2006**, *91*, 992–1007. [CrossRef]
53. Hajela, P.; Lin, C.Y. Genetic search strategies in multicriterion optimal design. *Struct. Optim.* **1992**, *4*, 99–107. [CrossRef]
54. Tanderup, K.; Eifel, P.J.; Yashar, C.M.; Pötter, R.; Grigsby, P.W. Curative radiation therapy for locally advanced cervical cancer: Brachytherapy is NOT optional. *Int. J. Radiat. Oncol. Biol. Phys.* **2014**, *88*, 537–539. [CrossRef] [PubMed]
55. Meerschaert, R.; Nalichowski, A.; Burmeister, J.; Paul, A.; Miller, S.; Hu, Z.; Zhuang, L. A comprehensive evaluation of adaptive daily planning for cervical cancer HDR brachytherapy. *J. Appl. Clin. Med. Phys.* **2016**, *17*, 323–333. [CrossRef] [PubMed]
56. Nesvail, N.; Tanderup, K.; Hellebust, T.P.; De Leeuw, A.; Lang, S.; Mohamed, S.; Kirisits, C. A multicenter comparison of the dosimetric impack of inter- and intra-fractional anatomical variations in fractionated cervix cancer brachytherapy. *Radiother. Oncol.* **2013**, *107*, 20–25. [CrossRef] [PubMed]
57. Damato, A.L.; Biswanathan, A.N.; Don, S.M.; Hansen, J.L.; Cormack, R.A. A system to use electromagnetic tracking for the quality assureance of brachytherapy catheter digitization. *Med. Phys.* **2014**, *41*, 101702. [CrossRef]
58. Soror, T.; Siebert, F.A.; Lanellotta, V.; Placidi, E.; Fionda, B.; Taliafei, L.; Kovacs, G. Quality Assurance in Modern Gynecological HDR-Brachytherapy (Interventional Radiotherapy): Clinical Considerations and Comments. *Cancers* **2021**, *13*, 912. [CrossRef]
59. Callaghan, C.M.; Adams, Q.; Flynn, R.T.; Wu, X.; Xu, W.; Kim, Y. Systematic review of intensity-modulated brachytherapy (IMBT): Static and dynamic techniques. *Int. J. Radiat. Oncol. Biol. Phys.* **2019**, *105*, 206–221. [CrossRef]
60. Famulari, G.; Duclos, M.; Enger, S.A. A novel 169Yb-based dynamic-shield intensity modulated brachytherapy delivery system for prostate cancer. *Med. Phys.* **2020**, *47*, 859–868. [CrossRef]

applied sciences

MDPI

Article

Radiobiological Outcomes, Microdosimetric Evaluations and Monte Carlo Predictions in Eye Proton Therapy

Giada Petringa [1,2,†], Marco Calvaruso [1,3,*], Valeria Conte [4], Pavel Bláha [5], Valentina Bravatà [1,3], Francesco Paolo Cammarata [1,3], Giacomo Cuttone [1,6], Giusi Irma Forte [1,3], Otilija Keta [7], Lorenzo Manti [5,8], Luigi Minafra [1,3], Vladana Petković [7], Ivan Petrović [7], Selene Richiusa [1,3], Aleksandra Ristić Fira [7], Giorgio Russo [1,3] and Giuseppe Antonio Pablo Cirrone [1,6,9,†]

1 Istituto Nazionale di Fisica Nucleare-Laboratori Nazionali del Sud, 95125 Catania, Italy; giada.petringa@lns.infn.it (G.P.); valentina.bravata@ibfm.cnr.it (V.B.); francesco.cammarata@ibfm.cnr.it (F.P.C.); cuttone@lns.infn.it (G.C.); giusi.forte@ibfm.cnr.it (G.I.F.); luigi.minafra@ibfm.cnr.it (L.M.); selly_93r@hotmail.it (S.R.); giorgio.russo@ibfm.cnr.it (G.R.); pablo.cirrone@infn.it (G.A.P.C.)
2 Extreme Light Infrastructure (ELI)-Beamlines Center, Institute of Physics (FZU), Czech Academy of Sciences, 117 20 Prague, Czech Republic
3 Istituto di Bioimmagini e Fisiologia Molecolare-Consiglio Nazionale delle Ricerche (IBFM-CNR), 90015 Cefalù, Italy
4 Istituto Nazionale di Fisica Nucleare-Laboratori Nazionali di Legnaro, INFN, 35020 Legnaro, Italy; valeria.conte@lnl.infn.it
5 Istituto Nazionale di Fisica Nucleare, Sezione di Napoli, 80126 Napoli, Italy; pavel.blahax@gmail.com (P.B.); lorenzo.manti@na.infn.it (L.M.)
6 Dipartimento di Fisica ed Astronomia "E.Majorana", Catania University, 95124 Catania, Italy
7 Vinča Institute of Nuclear Sciences, University of Belgrade, 11000 Belgrade, Serbia; otilijak@vin.bg.ac.rs (O.K.); vladana@vin.bg.ac.rs (V.P.); ipetrov@vin.bg.ac.rs (I.P.); aristic@vin.bg.ac.rs (A.R.F.)
8 Dipartimento di Fisica "E. Pancini", Radiation Biophysics Laboratory, Università Federico II di Napoli, 80126 Napoli, Italy
9 Centro Siciliano di Fisica Nucleare e Struttura della Materia, 95123 Catania, Italy
* Correspondence: marco.calvaruso@ibfm.cnr.it
† These authors contributed equally to this work.

Citation: Petringa, G.; Calvaruso, M.; Conte, V.; Bláha, P.; Bravatà, V.; Cammarata, F.P.; Cuttone, G.; Forte, G.I.; Keta, O.; Manti, L.; et al. Radiobiological Outcomes, Microdosimetric Evaluations and Monte Carlo Predictions in Eye Proton Therapy. *Appl. Sci.* **2021**, *11*, 8822. https://doi.org/10.3390/app11198822

Academic Editors: Ivan Veronese and Salvatore Gallo

Received: 14 July 2021
Accepted: 18 September 2021
Published: 23 September 2021

Abstract: CATANA (Centro di AdroTerapia ed Applicazioni Nucleari Avanzate) was the first Italian protontherapy facility dedicated to the treatment of ocular neoplastic pathologies. It is in operation at the LNS Laboratories of the Italian Institute for Nuclear Physics (INFN-LNS) and to date, 500 patients have been successfully treated. Even though proton therapy has demonstrated success in clinical settings, there is still a need for more accurate models because they are crucial for the estimation of clinically relevant RBE values. Since RBE can vary depending on several physical and biological parameters, there is a clear need for more experimental data to generate predictions. Establishing a database of cell survival experiments is therefore useful to accurately predict the effects of irradiations on both cancerous and normal tissue. The main aim of this work was to compare RBE values obtained from in-vitro experimental data with predictions made by the LEM II (Local Effect Model), Monte Carlo approaches, and semi-empirical models based on LET experimental measurements. For this purpose, the 92.1 uveal melanoma and ARPE-19 cells derived from normal retinal pigmented epithelium were selected and irradiated in the middle of clinical SOBP of the CATANA proton therapy facility. The remarkable results show the potentiality of using microdosimetric spectrum, Monte Carlo simulations and LEM model to predict not only the RBE but also the survival curves.

Keywords: protontherapy; proton; RBE; radiobiology; microdosimetry; Geant4

1. Introduction

Proton beam therapy is becoming increasingly available due to its potential to deliver maximal doses on tumour while minimizing irradiation of surrounding healthy

tissues/organs at risk. In fact, its ballistic precision has always been regarded as the main physical pillars of such a treatment modality [1]. However, in recent years, with growing numbers of patients treated and longer follow-up periods, concerns about the potential side effects of protontherapy have arisen [2,3]. The potential of a given particle irradiation to induce a greater level of specific biological effects compared to photon irradiation, used as a reference, is expressed in terms of its Relative Biological Effectiveness (RBE) [2]. Nowadays, in the proton-therapy clinical practice, a fixed RBE of 1.1 is assumed [3–5]. This reflects the known relationship between RBE and Linear Energy Transfer (LET), as in the tumour volume low-LET protons can be generally found. Despite this, data emerging from various radiobiological studies indicate that RBE of protons exceed the accepted value, at least in the distal part of the clinical spread out dose distribution, where high-LET slowing-down protons become predominant. Hence, a variable RBE should be used to more precisely describe the radiobiological effects on the tissues and organs involved in the treatment [6–10].

Successful treatment planning largely depends on the accuracy of biophysical models. To assure their precision they need to be validated against data from in vitro studies. Therefore, development of the database with experimental results obtained on various cell lines is useful for RBE model validation as well as for comparing different models [11].

While a vast literature exists reporting on the clinical results of eye proton therapy [12–16], no in vitro data evaluating the cellular radioresponse of uveal cancer cells along a clinical proton SOBP are available. There is only scarce data regarding the response of human melanoma cell lines along with the proton spread-out Bragg peak. According to these data, at the distal end of a 65 MeV proton SOBP, an RBE of 1.27 and even higher for the more resistant melanoma cell lines were recorded [17–19].More recently, work carried out on uveal melanoma Mel270 cells at the mid-SOBP position of a clinical high-energy proton beam showed an increased anti-migratory effect compared to photon irradiation [20]. Currently, many commercial Treatment Planning Systems (TPSs) for proton therapy incorporate the capability of calculating LET distributions and RBE estimations, but there remain challenges on how to deal with uncertainties resulting from potential RBE variations. Future TPS that would potentially be able to take into account RBE variability, could reduce the toxicity and the incidence of later-occurring induced morbidities, thus making it possible to exploit the full potential of proton therapy [2]. The main aim of this work was to study the RBE values at the clinical SOBP of the CATANA proton therapy facility. Radiation-induced biological effects measured in terms of clonogenic cell death (see below) were predicted by the LEM II (Local Effect Model) [21], Monte Carlo approaches [22], and semi-empirical models based on LET experimental measurements [23]. All adopted methods were then compared with in-vitro experimental results. These were evaluated using the human 92.1 uveal melanoma cell line, a well-known model to investigate the aggressive behaviour of such types of neoplasia. In order to compare the effects induced by proton therapy in a non-tumorigenic cell line the human normal retinal pigment epithelial ARPE-19 cell line was also irradiated. The normal cells can easily recover from damage induced by ionizing radiation due to a more efficient damage response machinery with respect to the cancer cells. Moreover, choosing the normal retinal pigment epithelial ARPE-19 cell line allows obtaining insights into the magnitude of biological effects induced by an erroneous dose distribution during a proton therapy treatment plan. The retina is the organ at risk in uveal melanoma treatment and despite the usually excellent precision granted by protontherapy, the anatomical structure of the eye, with dimensions in the order of the millimeter is such that lack of a rigorous dose contouring is possible in actual clinical scenarios, leading to unwanted dose deposition. Such information is therefore of paramount importance to provide an estimate of the possible adverse effects deriving by beam forward straggling.
Microdosimetry experimental spectra acquired to estimate the proton LET in different positions along the SOBP, were measured in the same experimental conditions of the biological sample irradiation. Two different detectors were used to this scope: a mini-TEPC [24,25], developed at the Legnaro National Laboratories of the National Institute

for Nuclear Physics (LNL-INFN) and a Silicon On Insulator (SOI) microdosimeter with 3D Sensitive Volumes (MicroPlus-Bridge) [26,27]. The Loncol's weighting function was then applied to assess the microdosimetric RBE and compare it with the experimental one. The biological damage was estimated also adopting a computational method which couples Geant4 with the LEM-II model as well as the pure LEM-II model. In such a way, it was possible to compare the well-established LEM with a Monte Carlo method and a semi-empirical one and to establish an approach that best reproduces the biological data at a depth of 24 mm, the mid-position of the spread-out Bragg peak.

2. Material and Methods

2.1. CATANA Proton Therapy Facility

The CATANA protontherapy facility [28], built thanks to a collaboration between INFN-LNS and University of Catania Hospital "AOU-Vittorio Emanuele" in Catania (I), has been active since 2002 and successfully treated more than 500 patients. CATANA is dedicated to the radiation treatment of ocular melanomas with the 62 MeV proton beams accelerated by the INFN-LNS superconducting cyclotron. The most frequent neoplasia treated with proton beams is the uveal melanoma, followed by other eye diseases like choroidal metastases, conjunctival tumours, and eyelid tumours. The CATANA facility is based on a passive transport system. The proton maximal range, at the irradiation point, is about 30 mm, ideal for the treatment of eye tumours. The necessary maximum range and energy modulation are achieved by means of a set of polymethyl-methacrylate (or PMMA) absorbers, variable in thickness, and modulator wheels.

2.2. Experimental Set-Up

The clinical SOBP beam configuration was used for the radiobiological and microdosimetric measures. The SOBP penetration range, measured as the depth corresponding to the 80% of the SOBP maximum and measured in the distal part, was 29.5 mm in water. The measured dose distribution as well as the LET and dose simulated by using the Geant4 *Hadrontherapy* advanced example that reproduce the entire beamline [28], is reported in Figure 1). The algorithms adopted to compute the LET take into account both primary and secondary particles interacting in a voxel, more details are reported in [27].

Absolute absorbed dose was measured in water, by means of a plane-parallel PTW 34045 advanced-type Markus ionisation chamber, according to the International Atomic Energy Agency Technical Report Series 398 Code of practice [29]. The absorbed dose in water per monitor unit (cGy/M.U.) for the specific SOBP adopted in cell irradiations, was measured at the isocenter at 24 mm depth in water, corresponding to the middle of the SOBP. A reference 25-mm diameter circular collimator was used to determine the beam spot size at the irradiation point. The absolute dose dosimetry was performed just before each irradiation session; the variation of beam calibration on the various experiments amounted to a total of 3%. The overall uncertainty in absolute dose measurement was kept within 1.5%. Details on the irradiation beamlines, dosimetric procedures and related uncertainties for irradiation conditions can be found elsewhere [28]. As regards cell line irradiation, the experimental procedure was described previously [30]. Briefly, cells were seeded in T25 tissue culture flasks with a density of 3–5 $\times 10^5$ cells per flask 24 h before irradiation. T25 were irradiated in the upright position in front of the proton beam exit and hit with separate shots to ensure a complete dose distribution on the flask area. An automatic system for sample positioning and movement was used to move the flasks after each shot in order to cover its entire surface. Cell sample irradiations were carried out positioning each flask at 24 mm, the mid-position of the spread-out Bragg peak, to mimic a clinical condition, with dose values ranging from 1 to 4 Gy and a dose rate of 6 Gy min^{-1}. Finally, the microdosimetric spectra were acquired positioning the mini-TEPC and MicroPlus-Bridge detectors at the entrance and mid position along the same SOBP, while the depths were varied by placing a stack of calibrated PMMA layers between the detectors and the beam collimator [27]. The mini-TEPC is a miniaturized, tissue-equivalent, proportional

counter developed at the Legnaro National Laboratories of the Italian National Institute for Nuclear Physics (INFN-LNL) to work in a sealed mode, without gas flow [25]. The sensitive volume (SV) is a cylinder with both diameter and height of 0.9 mm; the cathode is made of a 0.35 mm-thick A-150 wall, surrounded by a 0.35 mm-thick Rexolite insulator and a 0.2 mm-thick titanium sleeve; the total external diameter is 2.7 mm. The anode is a 10-µm gold plated tungsten wire. The detector was filled with propane gas, at the pressure of 45.4 kPa at 21.8 °C; these conditions simulate a water volume of 1 µm in diameter.

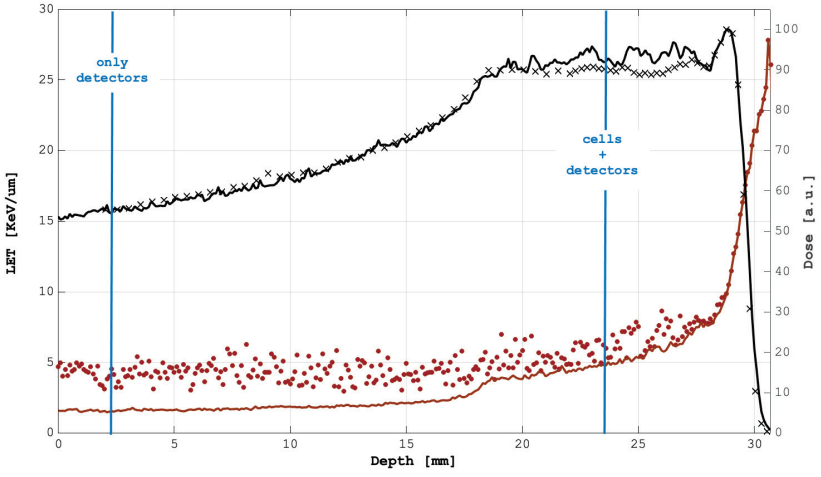

Figure 1. The relative dose measured with the Markus chamber (black crosses), simulated dose distribution (black line), primary LET-dose computed for only primary protons (red line) and LET-Total-dose considering also the contribution of generated secondary particles (red circles) are reported.The vertical blue lines show the positions at which measurements were performed. Simulated and measured values for the absorbed dose are in good agreement when a 2% uncertainty is considered in both sets of data.

The silicon detector adopted was the MicroPlus-Bridge, designed by the Centre for Medical Radiation Physics (CMRP), University of Wollongong, Australia. It consists of an array of 3D right parallelepiped (RPP) shape SVs with an area of 30 µm × 30 µm each and a thickness of 10 µm, constructed on a silicon-on-insulator wafer. The water equivalent thickness of this microdosimeter is 17.24 µm. Additional details and microdosimetric results on the MicroPlus-Bridge microdosimeter technology can be found elsewhere [26]. It has already been shown that the dose mean lineal energy measured with these two detectors reproduces the variation with depth of the dose-averaged LET [23].

2.3. Cell Culture and Clonogenic Assay

The ARPE19 human retinal pigment epithelial cell line was purchased from American Type Culture Collections (ATCC, Manassas, VA, USA) and cultured according to the manufacturer's instructions. Cell culture maintenance was performed with the same methods previously described [31]. The 92.1 human uveal melanoma cell lines were kindly provided by Prof. CD Anfuso and cultured according to the procedure described in the work by Anfuso et collaborators [32]. A clonogenic survival assay was adopted to evaluate cell survival after proton and gamma-ray irradiation. After irradiation, cells were seeded in 6-well plates in triplicate and at an increasing density, depending on the dose delivered; they were incubated for 12–14 days to allow for colony formation. Colonies were stained with 0.05% crystal violet, diluted in 20% ethanol for 30 min at room temperature. Colony-forming ability was determined, both for unirradiated (controls) and irradiated samples, by dividing the counted colony number by the number of cells plated after irradiation

in order to obtain the plating efficiency (PE) and survival fraction (SF) of the samples respectively. For each dose, the SF was then derived by normalizing the above-mentioned results by the PE. For each experimental session, the effect due to the different doses was evaluated on three cell samples. Each point of the survival curves represent the average of three independent experiments. The survival curve was fitted by the linear-quadratic (LQ) equation [33]:

$$S = e^{-\alpha D - \beta D^2} \tag{1}$$

The fit was performed by using the MATLAB-R2019b software, where D is the physical dose deposited by protons and photons, S the surviving fraction, and α and β the radiosensitivity parameters. The fit provided the linear and quadratic parameters with their standad error and the R^2 value. These parameters was used to calculate the enhancement ratios at 10% survival.

Irradiations with γ-rays issued by ^{60}Co source (CIRUS-Cis Biointernational, Gif-sur-Yvette, France) were performed at the Vinca Institute of Nuclear Sciences, Belgrade, Serbia. Cells were irradiated with doses ranging from 1 to 6 Gy at the rate of $\simeq$1 Gy/min, in the air at room temperature, following the same experimental procedures as defined for irradiations with protons.

2.4. Micorodosimetric Spectra

The acquired microdosimetric spectra were represented as the distributions of the lineal energy y, the stochastic variable defined as the energy deposited by a single event in a specific volume, divided by the mean chord length [34]. Frequency $f(y)$ and dose $d(y)$ distributions of the lineal energy obey the usual normalization rules of probability distributions:

$$\int_0^\infty f(y)dy = 1 \tag{2}$$

and

$$\int_0^\infty d(y)dy = 1 \tag{3}$$

with

$$d(y) = \frac{yf(y)}{\int_0^\infty yf(y)} \tag{4}$$

The frequency and dose-mean lineal energy values, y_F and y_D, are calculated as:

$$y_F = \int_0^\infty yf(y)dy \tag{5}$$

and

$$y_D = \int_0^\infty yd(y)dy \tag{6}$$

The microdosimetric lineal energy distribution was used to estimate RBE, following the approach of the biological weighting function [35]. A weighting function $r(y)$ was applied to the measured dose distribution in lineal energy $d(y)$ in order to determine a single parameter, RBE_μ, that estimates the biological effectiveness:

$$RBE_\mu = \int_0^\infty r(y)d(y)dy \tag{7}$$

In this work, the Loncol's function $r(y)$ [36] was adopted to weight the lineal energy. The Loncol's function was numerically determined by an unfolding procedure on empirical and statistical bases. The results of a RBE-microdosimetry intercomparison study between experimental measurements (performed with a TEPC simulating 2 µm) and in-vivo experimental data of intestinal tolerance assessment by crypt cells regeneration was adopted. The unfolding procedure allowed to determine $r(y)$ by minimizing the differences between biological RBE and RBE_μ calculated applying the Equation (7). Despite the function $r(y)$

was derived for a specific biological end-point in vivo (early intestinal tolerance in mice), previous works have already shown that the same function allows to reproduce the trend of the RBE_{10} as a function of depth for a variety of cell lines [22,23]. In this work the RBE_{μ} was here calculated at positions P0 (entrance) and P1 (mid-SOBP). These two results were afterwards multiplied by a constant factor so that RBE_{μ} at position P0 (entrance) equal the clinical value of 1.1:

$$RBE_{\mu}(P_i) = \int_0^{\infty} r(y)d(y, P_i)dy \times [1.1 \div \int_0^{\infty} r(y)d(y, P_0)dy] \quad (8)$$

Applying the LQ model, the estimated RBE_{μ} and the α and β derived from cell survival assessments for reference radiation, were used to calculate α_{μ}, starting from the expression for RBE_{μ}:

$$RBE_{\mu} = \frac{\alpha_{\mu} + \sqrt{\alpha_{\mu}^2 - 4\beta_{\mu} ln(0.1)}}{\alpha_{\gamma} + \sqrt{\alpha_{\gamma}^2 - 4\beta_{\gamma} ln(0.1)}} \quad (9)$$

assuming a constant β_{μ}=β_{γ} and using Equation (9), α_{μ} can be calculated as follows:

$$\alpha_{\mu} = \frac{RBE_{\mu}^2 \cdot A_{\gamma}^2 + 4\beta_{\gamma} ln(0.1)}{2RBE_{\mu} \cdot A_{\gamma}} \quad (10)$$

with

$$A_{\gamma} = \alpha_{\gamma} + \sqrt{\alpha_{\gamma}^2 - 4\beta_{\gamma} ln(0.1)} \quad (11)$$

2.5. Monte Carlo Simulations and LEM II Calculations

The RBE values for the two cell lines used in the experimental part of this work were calculated by means of two different approaches. The first was a hybrid procedure, allowing to link the Monte Carlo simulations of the irradiation with a cell-specific look-up table (LUTs) containing the results of the radiation damage calculated with the LEM II model [21]. The LUTs were derived using the software "Survival" [37]. The second approach consisted in the direct use of the Survival code, without including the mixed field contribution, in order to obtain the direct output of the LEM II model. The Monte Carlo simulation of the experimental set-up, including the specific conditions of biological sample irradiation, was carried out using the Geant4 *Hadrontherapy* application [38,39], freely available inside the official Geant4 [40,41] distribution. *Hadrontherapy* simulates the CATANA eye proton therapy beamline with all its beam passive and dynamical transport elements, including the scattering and modulation systems for spatial and energy distribution beam definition, collimators and detectors for the online beamline monitoring. A voxelized detector at the end of the beamline simulates the typical water tank used for the dose curves reconstructions. In order to reproduce the adopted experimental conditions, the tank was divided into slabs perpendicular to the beam propagation direction, along the *z*-axis. Each slab was $4 \times 4 \times 0.1$ mm^3 in dimension. Dose, fluence, dose- and track-averaged LET, survival, RBE and all the related quantities necessary for their estimation were retrieved using the application as described elsewhere [22,27]. Every quantity was stored at the end of each run. A total number of 3.6×10^7 histories were simulated in each simulation; the production cut for secondary protons, gamma and electrons was fixed at 0.1 mm. All calculations were carried out using the 10.07.p01 version of Geant4.

3. Results and Discussion

One of the aims of this work is the comparison of three methods to calculate the RBE in a clinical setting: microdosimetric-based, Monte Carlo and LEM II model. All of the proposed approaches were compared with experimental data. Radiation-induced cell death was measured by clonogenic assay and RBE values were calculated using the Linear-Quadratic model. The clonogenic survival curves of two specific cell lines were

experimentally measured at 24 mm, the mid-position of the 62 MeV clinical proton SOBP. Additionally, at the SOBP entrance, the survival curves were also estimated from the experimental measurements of the microdosimetric spectra. The estimation of the survival curves with these three approaches permitted the estimation of the RBE values in the centre of the SOBP region. The radiobiological effects of protons were experimentally evaluated using the human 92.1 uveal melanoma cell line. In order to evaluate the damage induced by proton therapy in a typical tissue belonging to the same anatomical site, the human normal retinal pigment epithelial ARPE-19 cell line was also irradiated. The assessment of the detrimental effects in healthy tissues due to radiotherapy is pivotal, especially for the treatment of cancers affecting the eye since even slight impairment of the normal ocular tissue would lead to a loss of function of the entire organ [42]. The results of the clonogenic curves with the fitted parameters, for the two cell lines irradiated at the proton mid-SOBP and under a reference gamma beam, are summarised in Table 1. Table also report the corresponding derived values of RBEs.

Table 1. Survival curve parameters measured for proton and gamma irradiation of the 92.1 and ARPE-19 cell line. The statistical parameters of the double exponential fit function and the values of the derived RBEs are reported.

	Irr. Type	$\alpha(\mathrm{Gy}^{-1})$	$\beta(\mathrm{Gy}^{-2})$	α/β	Fit. Std. Err.	RBE_{10}
92.1	γ-rays	0.20 ± 0.03	0.076 ± 0.004	2.68	0.02	1.4
	protons	0.40 ± 0.02	0.095 ± 0.003	4.25	0.007	
ARPE19	γ-rays	0.34 ± 0.14	0.03 ± 0.02	11.33	0.02	1.2
	protons	0.43 ± 0.01	0.041 ± 0.003	10.49	0.04	

Two fundamental radiobiological parameters were contextually obtained, the alpha and beta values, together with their ratio. Within the LQ model context, the alpha and beta coefficients of the clonogenic survival curves represent the single-hit, lethal damage, generally not repairable, and the multiple-hit damage, associated with sub lethal damage, respectively. Sublethal damage is responsible for the shouldered part of the clonogenic curve and can be usually repaired [43]. The α/β ratio is an useful indicator of radiosensitivity, hence, its calculation is of paramount importance to evaluate the cell response to the radiation therapy (RT) treatment [44,45]. The clonogenic endpoint has, in fact, shown a lower radiosensitivity exhibited by the ocular cancer cells with respect to the normal cells as expected. In addition, for both cell lines, an increased RBE with proton beam irradiation was obtained. The capability of the two microdosimeters to describe not only the RBE but also the survival curve at the mid-SOBP was then investigated. Figure 2 shows the acquired microdosimetric spectra from which the RBEs values and the parameters of the corresponding clonogenic curves were derived. Distributions are presented as $yd(y)$ versus y on a logarithmic x-axis to facilitate visual interpretation. In this representation, the area under the curve between two values of y is proportional to the fraction of physical absorbed dose due to the events in that interval.

Specifically, in Figure 2 the two positions (entrance and mid of the SOBP) and the two detectors (mini-TEPC and MicroPlus Bridge) are considered. In the same figures, the Loncol's biological weighting function $r(y)$ and the corresponding weighted-dose curves $yr(y)d(y)$ are also reported. The observed increase of the area under the red curve (i.e., the $yr(y)d(y)$ curve) for the spectra acquired at the cell position (bottom row of Figure 2), reflects an increase in the RBE. It can be observed, in fact, that at the entrance position the biologically weighted distributions overlap almost perfectly with the un-weighted distributions, because for $y < 10$ keV/µm the weighting function $r(y)$ almost equals almost equals 1. Different behaviour can be observed at the mid-SOBP, where the weighting function augments the contribution of events above 10 keV/µm leading to an increase of the RBE_{μ} (Equations (8)–(11)). The RBE calculated at the mid-SOBP with the mini-TEPC, (RBE_{μ}-TECP = 1.18), resulted slightly higher than that calculated with the Microplus

Bridge (RBE_μ-MicroPlus = 1.12). With respect to the entrance position, the RBE_μ-TECP at the mid-SOBP increases by about 17%, and the RBE_μ-MicroPlus increases by about 13%. The reason for this underestimation of the MicroPlus with respect to the TEPC is the larger simulated site size (about 17 µm with respect to 1 µm of the TEPC): low energy protons stop inside the silicon thickness, therefore the largest proton events (proton-edge) are at about 40 keV/µm for the Microplus, while they are at about 140 keV/µm for the mini-TEPC. The RBE_μ values, corrected by a constant factor to have RBE_μ = 1.1 at the entrance position of the SOBP, and the linear parameters α_μ of the linear-quadratic model, calculated using Equation (11), are reported in Table 2. The β_μ was assumed to be equal to β_γ (see Section 2.4).

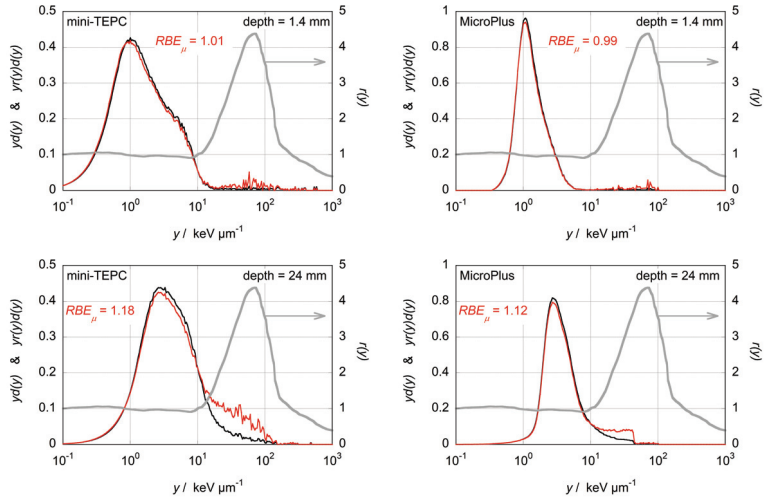

Figure 2. The microdosimetric spectra $yd(y)$ measured at the entrance (**top**) and at cell position (**bottom**) acquired with the mini-TEPC (**left**) and with the MicroPlus Bridge microdosimeter (**right**). The thick grey line represents the biological weighting function $r(y)$ (Loncol, 1994). The red curves are the weighted distributions $yr(y)d(y)$. The black curves are the experimental microdosimetric spectra. See text for more details.

Table 2. RBE_μ calculated from microdosimetric spectra, and corrected by a constant factor to have RBE_μ = 1.1 in entrance. The parameters α_μ TEPC and α_μ MicroPlus were calculated with Equations (8)–(11).

Cell Type	RBE_μ-TEPC	RBE_μ-MicroPlus	α_μ TEPC	α_μ MicroPlus
92.1	1.29	1.24	0.35 ± 0.03	0.31 ± 0.02
ARPE19	1.29	1.24	0.45 ± 0.04	0.41 ± 0.04

Finally, the survival curves relative to the mid-SOBP position and derived from the microdosimetric data, experimentally measured from cell irradiation experiments and calculated with the described Monte Carlo and using the Survival software [37], are reported in Figure 3 (92.1 cell line) and Figure 4 (ARPE-19 cell line). Both figures also show the survival curve measured for the ^{60}Co gamma-ray irradiation. The survival experimental curves were fitted using the double exponential function (Equation (1)) and the α and β derived from it were reported in Table 1. The survival fraction related to the experimental data and applyed approaches for the two investigated curves is reported in the Table 3 (92.1 cell line) and Table 4 ARPE-19 cell line).

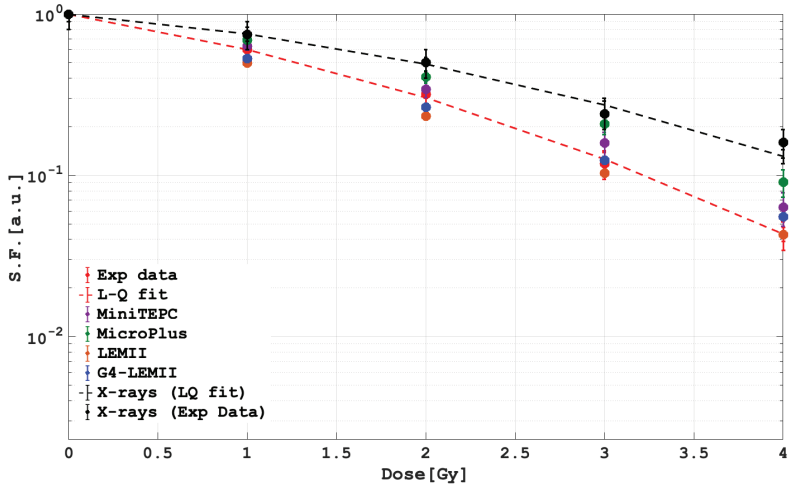

Figure 3. Survival fractions for 92.1. Biological survival data acquired with proton beam irradiations (red symbols) are plotted together with the linear-quadratic best fit (red dashed line). Biological survival data acquired with gamma rays (black symbols) are plotted together with the best fit (black dashed line). The survival fractions predicted from microdosimetric measurements calibrated on gamma-rays cell survival are also plotted. Purple and green points are related to the mini-TEPC and MicroPlus respectively. The blue points were calculated by coupling the Monte Carlo Geant4 with the LEM-II model. Finally, the orange points are obtained with the LEM-II module.

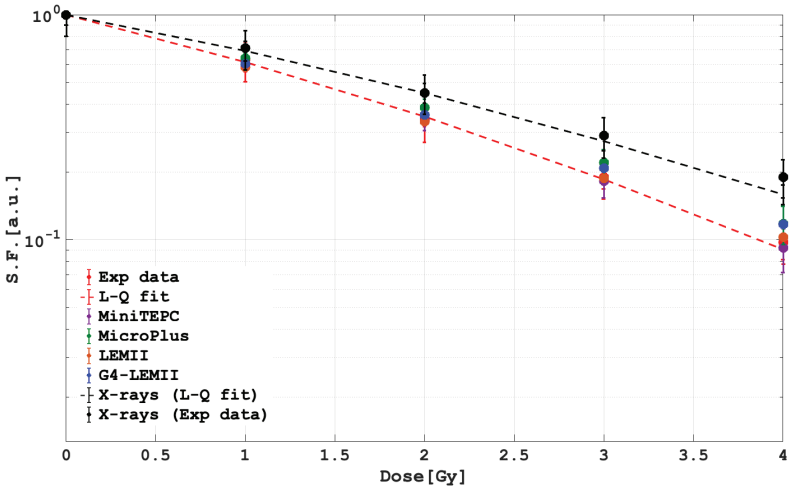

Figure 4. Survival fractions for ARPE19. Biological survival data acquired with proton beam irradiations (red symbols) are plotted together with the linear-quadratic best fit (red dashed line). Biological survival data acquired with gamma rays (black symbols) are plotted together with the best fit (black dashed line). The survival fractions predicted from microdosimetric measurements calibrated on gamma-rays cell survival are also plotted. Purple and green points are related to the mini-TEPC and MicroPlus respectively. The blue points were calculated by coupling the Monte Carlo Geant4 with the LEM-II model. Finally, the orange points are obtained with the LEM-II module.

Table 3. Survival Fraction of the 92.1 cell line obtained applying the three approaches: LEMII, Geant4 coupled with LEMII and Loncol's function applied to the microdosimetric spectra. The first column reports experimental data.

Dose [Gy]	Exp Data	LEMII	G4-LEMII	mini-TEPC	MicroPlus
1	0.606 ± 0.121	0.496 ± 0.009	0.528 ± 0.011	0.62 ± 0.03	0.68 ± 0.02
2	0.304 ± 0.061	0.232 ± 0.004	0.263 ± 0.005	0.34 ± 0.03	0.41 ± 0.02
3	0.126 ± 0.025	0.102 ± 0.002	0.124 ± 0.002	0.15 ± 0.02	0.03 ± 0.20
4	0.043 ± 0.008	0.042 ± 0.001	0.055 ± 0.001	0.06 ± 0.01	0.09 ± 0.01

Table 4. Survival Fraction of the ARPE19 cell line obtained applying the three approaches: LEMII, Geant4 coupled with LEMII and Loncol's function applied to the microdosimetric spectra. The first column reports experimental data.

Dose [Gy]	Exp Data	LEMII	G4-LEMII	mini-TEPC	MicroPlus
1	0.618 ± 0.123	0.584 ± 0.011	0.605 ± 0.012	0.60 ± 0.03	0.64 ± 0.02
2	0.353 ± 0.071	0.334 ± 0.006	0.358 ± 0.007	0.34 ± 0.03	0.38 ± 0.03
3	0.186 ± 0.037	0.187 ± 0.003	0.207 ± 0.004	0.18 ± 0.02	0.22 ± 0.03
4	0.091 ± 0.018	0.102 ± 0.002	0.117 ± 0.002	0.09 ± 0.01	0.11 ± 0.02

The agreement between the three investigated methods, with the experimental radiobiological data, was statistically evaluated by applying the χ^2 test. Results of the test (p-values included) are reported in Tables 5 and 6: the χ^2 values are calculated taking into account the data reported in the Tables 3 and 4.

Table 5. Results of the χ^2 test for the comparison of the experimental survival curves of 92.1 cells against the survival fraction calculated with the LEM II, Geant4 coupled with LEM II and the Loncol's function applied with the microdosimetric spectra obtained with the two detectors. The corresponding χ^2 probabilities are calculated for four degrees of freedom.

	92.1	
	χ^2	p-**Value**
LEM2	3.06	0.38
LEM2-G4	2.70	0.44
MicroPlus	12.87	0.004
MiniTEPC	2.34	0.50

Table 6. Results of the χ^2 test for the comparison of the experimental survival curves of ARPE19 cells against the survival fraction calculated with the LEM II, Geant4 coupled with LEM II and the Loncol's function applied with the microdosimetric spectra obtained with the two detectors. The corresponding χ^2 probabilities are calculated for four degrees of freedom.

	ARPE19	
	χ^2	p-**Value**
LEM2	0.54	0.91
LEM2-G4	2.42	0.49
MicroPlus	1.56	0.67
MiniTEPC	0.04	0.99

In almost all the investigated cases, the resulting p-value is well above 0.25, showing that the models are able to well reproduce the experimental data. The p-value calculated applying the Loncol's function and using the microdosimetric spectra measured with the

MicroPlus probe is lower than 0.05 as shown in Table 5. This disagreement could be related to the higher sensitive volume of the adopted detector with respect to Mini-TEPC.

4. Conclusions and Perspectives

In this study, we showed that the LEM-II model, the Monte Carlo-based LEM model and a semi-empirical method based on microdosimetric spectra, can adequately reproduce experimentally derived survival curves from in vitro cell irradiations performed at the mid-SOBP of the CATANA 62 MeV clinical proton beam.

For both cell lines, an RBE greater than 1.1 was measured and reproduced applying all of the investigated approaches. This points out that the biological damage of both healthy and tumorigenic cells is underestimated if a fixed RBE of 1.1 is assumed. Microdosimetric spectra were measured at the entrance and mid-SOBP position with both a mini-TEPC, simulating a 1 μm water site size, and the MicroPlus microdosimeter (17 μm water equivalent thickness). Despite the markedly different microdosimetric spectra obtained with these two detectors, when the Loncol's weighting function is applied to the dose distributions both lead to an assessment of the RBE10 that is in good agreement with radiobiological data for ARPE-19 cells obtained in the same beamline. The higher discrepancy obtained with the 92.1 cell line and the solid-state detector could be due to a lower detector sensitivity related to the higher SV volume. The remarkable obtained result showed the potentiality of using a microdosimetric spectrum to predict not only the RBE but also the full survival curve, at least at the mid-position of the 62 MeV proton SOBP. Currently, different commercial treatment planning softwares for proton therapy incorporate tools for calculating LET distributions and RBE prediction. However, while the dose prescriptions calculated by the treatment planning are routinely verified with certified ionization chambers, there is no commercial equipment currently available to perform routine verification of LET or RBE distributions calculated by the TPS. The Local Effect Model is the computational radiobiological approach most widely used in hadrontherapy. The LEM model was fully integrated into the analytical treatment planning system TRiP98 and successfully tested for clinical application. In this work, the good agreement between the Monte-Carlo-based LEM model and LEM-II model with the experimental data clearly evidence how a TPS based on an RBE and LET prediction could improve the estimation of the radiobiological response of the treated neoplasia as well as the surrounding healthy tissues. Moreover, the pretty good accordance between the semi-empirical methods based on microdosimetric spectra with the experimental data shows that the LET estimation procedure should be successfully inserted in the clinical routine to optimize the RBE distribution. The current study identifies a clinical and critical aspect of the uveal melanoma protontherapy treatment. The correct evaluation of the damage induced by ionizing radiation during RT treatment, also thanks to Monte Carlo-based simulations, represents a valuable and potent tool to foresees the impact of ionizing radiation on cancer tissues. Moreover, studying both healthy and tumorigenic cells allows obtaining fundamental information about the biological effects induced by an erroneous dose distribution during a proton therapy ocular treatment plan. The biological response is therefore of paramount importance to provide an estimate of the possible adverse effects deriving by beam forward straggling. A correct prediction of the damage is a key point for a more personalized TPS.

Author Contributions: M.C., F.P.C., V.B., L.M. (Luigi Minafra) carried out cell survival measurements at INFN-LNS. A.R.F., I.P., V.P., O.K. performed the cell survival measurements with gamma rays. L.M. (Lorenzo Manti), P.B., S.R., G.R., G.I.F., G.P., G.C., G.A.P.C., V.C. provided overall conceptual contribution. G.A.P.C. and G.P. supervised beam dosimetry at INFN-LNS. V.C., G.P., G.A.P.C. performed microdosimetric measurements. V.C. estimated the biological damage starting from microdosimetric spectra. G.P. performed the Monte Carlo simulations. G.P. conceptualized the study and wrote the first draft of the manuscript. All authors have read and agreed to the published version of the manuscript.

Funding: The authors wish to acknowledge financial support from MAECI PGR No. 00794 Italy-Serbia Project and from the Ministry of Education, Science and Technological Development of Serbia. L.Minafra was supported by the Short Term Mobility (STM) Program (Bando 2018, Consiglio Nazionale delle Ricerche-CNR, Italy). This work was also supported by European Structural and Investment Fund and the Czech Ministry of Education, Youth and Sports (Project International mobility MSCA-IF IV FZU-CZ.02.2.69/0.0/0.0/20-079/0017754).

Institutional Review Board Statement: Each involved institute was informed about the work done.

Informed Consent Statement: Informed consent is not applicable.

Data Availability Statement: Data are not publicly available.

Conflicts of Interest: The authors declare that this device is protected by a national and International patent and that it could be commercialised in the future. At the moment of writing the described device is not commercialised and no conflict of interest is present.

References

1. Liu, H.; Chang, J.Y. Proton therapy in clinical practice. *Chin. J. Cancer* **2011**, *30*, 315–326. [CrossRef] [PubMed]
2. Lühr, A.; von Neubeck, C.; Krause, M.; Troost, E.G.C. Relative biological effectiveness in proton beam therapy—Current knowledge and future challenges. *Clin. Transl. Radiat. Oncol.* **2018**, *9*, 35–41. [CrossRef]
3. Underwood, T.S.; McMahon, S.J. Proton relative biological effectiveness (RBE): A multiscale problem. *Br. J. Radiol.* **2019**, *92*, 20180004. [CrossRef] [PubMed]
4. Giovannini, G.; Böhlen, T.; Cabal, G.; Bauer, J.; Tessonnier, T.; Frey, K.; Debus, J.; Mairani, A.; Parodi, K. Variable RBE in proton therapy: Comparison of different model predictions and their influence on clinical-like scenarios. *Radiat. Oncol.* **2016**, *11*, 2718503. [CrossRef] [PubMed]
5. Paganetti, H. Relating the proton relative biological effectiveness to tumor control and normal tissue complication probabilities assuming interpatient variability in α/β. *Acta Oncol.* **2017**, *56*, 1379–1386. [CrossRef] [PubMed]
6. Chaudhary, P.; Marshall, T.; Manti, L.; Currell, F.J.; McMahon, S.J.; Kavanagh, J.N.; Cirrone, G.A.P.; Romano, F.; Prise, K.M.; Schettino, G. Relative Biological Effectiveness variation along monoenergetic and modulated Bragg peaks of a 62 MeV therapeutic proton beam: A pre-clinical assessment. *Int. J. Radiat. Oncol. Biol. Phys.* **2014**, *90*, 27–35. [CrossRef]
7. Cuaron, J.J.; Chang, C.; Lovelock, M.; Higginson, D.S.; Mah, D.; Cahlon, O.; Powell, S. Exponential Increase in Relative Biological Effectiveness Along Distal Edge of a Proton Bragg Peak as Measured by Deoxyribonucleic Acid Double-Strand Breaks. *Int. J. Radiat. Oncol. Biol. Phys.* **2016**, *95*, 62–69. [CrossRef]
8. Willers, H.; Allen, A.; Grosshans, D.; McMahon, S.J.; von Neubeck, C.; Wiese, C.; Vikram, B. Toward A variable RBE for proton beam therapy. *Radiother. Oncol.* **2018**, *42 128*, 68–75. [CrossRef]
9. Vitti, E.T.; Parsons, J.L. The Radiobiological Effects of Proton Beam Therapy: Impact on DNA Damage and Repair. *Cancers* **2019**, *11*, 946. [CrossRef] [PubMed]
10. Vanderwaeren, L.; Dok, R.; Verstrepen, K.; Nuyts, S. Clinical Progress in Proton Radiotherapy: Biological Unknowns. *Cancers* **2021**, *13*, 604. [CrossRef]
11. Friedrich, T.; Scholz, U.; Elsässer, T.; Durante, M.; Scholz, M. Systematic analysis of RBE and related quantities using a database of cell survival experiments with ion beam irradiation. *J. Radiat. Res.* **2013**, *54*, 494–514. [CrossRef]
12. Keshazare, S.; Masoudi, S.F.; Rasouli, F.S. Effects of defining realistic compositions of the ocular melanoma on proton therapy. *J. Biomed. Phys. Eng.* **2014**, *4*, 141–150. [PubMed]
13. Verma, V.; Mehta, M.P. Clinical Outcomes of Proton Radiotherapy for Uveal Melanoma. *Clin. Oncol. (R. Coll. Radiol.)* **2016**, *28*, e17–e27. [CrossRef] [PubMed]
14. Mishra, K.K.; Daftari, I.K. Proton therapy for the management of uveal melanoma and other ocular tumors. *Chin. Clin. Oncol.* **2016**, *5*, 50 [CrossRef] [PubMed]
15. Spatola, C.; Liardo, R.L.E.; Milazzotto, R.; Raffaele, L.; Salamone, V.; Basile, A.; Foti, P.V.; Palmucci, S.; Cirrone, G.A.P.; Cuttone, G.; et al. Radiotherapy of Conjunctival Melanoma: Role and Challenges of Brachytherapy. *Appl. Sci.* **2020**, *10*, 9071. [CrossRef]
16. Messineo, D.; Barile, G.; Morrone, S.; La Torre, G.; Turchetti, P.; Accetta, L.; Trovato Battagliola, E.; Agostinelli, E.; Pacella, F. Meta-analysis on the utility of radiotherapy for the treatment of Ocular Melanoma. *Clin. Ther.* **2020**, *170*, e89–e98.
17. Courdi, A.; Brassart, N.; Hérault, J.; Chauvel, P. The depth-dependent radiation response of human melanoma cells exposed to 65 MeV protons. *Br. J. Radiol.* **1994**, *67*, 800–804. [CrossRef]
18. Petrović, I.; Ristić-Fira, A.; Todorović, D.; Korićanac, L.; Valastro, L.; Cirrone, P.; Cuttone, G. Response of a radioresistant human melanoma cell line along the proton spread-out Bragg peak. *Int. J. Radiat. Biol.* **2010**, *86*, 742–751. [CrossRef]
19. Petrović, I.M.; Ristić Fira, A.M.; Keta, O.D.; Petković, V.D.; Petringa, G.; Cirrone, P.; Cuttone, G. A radiobiological study of carbon ions of different linear energy transfer in resistant human malignant cell lines. *Int. J. Radiat. Biol.* **2020**, *96*, 1400–1412. [CrossRef]
20. Jasińska-Konior, K.; Pochylczuk, K.; Czajka, E.; Michalik, M.; Romanowska-Dixon, B.; Swakoń, J.; Urbańska, K.; Elas, M. Proton beam irradiation inhibits the migration of melanoma cells. *PLoS ONE* **2017**, *12*, e0186002.

21. Scholz, M.; Kellerer, A.M.; Kraft-Weyrather, W.; Kraft, G. Computation of cell survival in heavy ion beams for therapy. The model and its approximation. *Radiat. Environ. Biophys.* **1997**, *36*, 59–66. [CrossRef] [PubMed]
22. Petringa, G.; Romano, F.; Manti, L.; Pandola, L.; Attili, A.; Cammarata, F.; Cuttone, G.; Forte, G.; Manganaro, L.; Pipek, J.; et al. Radiobiological quantities in proton-therapy: Estimation and validation using Geant4-based Monte Carlo simulations. *Phys. Med.* **2019**, *58*, 72–80. [CrossRef] [PubMed]
23. Conte, V.; Agosteo, S.; Bianchi, A.; Bolst, D.; Bortot, D.; Catalano, R.; Cirrone, G.A.P.; Colautti, P.; Cuttone, G.; Guatelli, S.; et al. Microdosimetry of a therapeutic proton beam with a mini-TEPC and a MicroPlus-Bridge detector for RBE assessment. *Phys. Med. Biol.* **2020**, *65*, 245018. [CrossRef]
24. De Nardo, L.; Cesari, V.; Donà, G.; Magrin, G.; Colautti, P.; Conte, V.; Tornielli, G. Mini-TEPCs for radiation therapy. *Radiat. Prot. Dosim.* **2004**, *108*, 345–352. [CrossRef] [PubMed]
25. Conte, V.; Bianchi, A.; Selva, A.; Petringa, G.; Cirrone, G.A.P.; Parisi, A.; Vanhavere, F.; Colautti, P. Microdosimetry at the CATANA 62 MeV proton beam with a sealed miniaturized TEPC. *Phys. Med.* **2020**, *64*, 114–122. [CrossRef] [PubMed]
26. Rosenfeld, A.B. Novel detectors for silicon based microdosimetry, their concepts and applications. *Nucl. Instrum. Methods Phys. Res. Sect. Accel. Spectrometers Detect. Assoc. Equip.* **2016**, *809*, 156–170. [CrossRef]
27. Petringa, G.; Pandola, L.; Agosteo, S.; Catalano, R.; Colautti, P.; Conte, V.; Cuttone, G.; Fan, K.; Mei, Z.; Rosenfeld, A.B.; et al. Monte Carlo implementation of new algorithms for the averaged-dose and -track linear energy transfer evaluation in 62 MeV clinical proton beams. *Phys. Med. Biol.* **2020**, *65*, 235043. [CrossRef]
28. Cirrone, G.A.; Cuttone, G.; Raffaele, L.; Salamone, V.; Avitabile, T.; Privitera, G.; Spatola, C.; Amico, A.G.; Larosa, G.; Leanza, R.; et al. Clinical and Research Activities at the CATANA Facility of INFN-LNS: From the Conventional Hadrontherapy to the Laser-Driven Approach. *Front. Oncol.* **2017**, *7*, 223. [CrossRef]
29. Development of procedures for in vivo dosimetry in radiotherapy. In *Technical Report Series n. 8*; International Atomic Energy Agency: Wien, Austria, 2013.
30. Bravatà, V.; Cammarata, F.P.; Minafra, L.; Pisciotta, P.; Scazzone, C.; Manti, L.; Savoca, G.; Petringa, G.; Cirrone, G.A.P.; Cuttone, G.; et al. Proton-irradiated breast cells: Molecular points of view. *J. Radiat. Res.* **2019**, *60*, 451–465. [CrossRef]
31. Cammarata, F.P.; Torrisi, F.; Forte, G.I.; Minafra, L.; Bravatà, V.; Pisciotta, P.; Savoca, G.; Calvaruso, M.; Petringa, G.; Cirrone, G.A.P.; et al. Proton Therapy and Src Family Kinase Inhibitor Combined Treatments on U87 Human Glioblastoma Multiforme Cell Line. *Int. J. Mol. Sci.* **2019**, *20*, 4745. [CrossRef]
32. Anfuso, C.D.; Longo, A.; Distefano, A.; Amorini, A.M.; Salmeri, M.; Zanghì, G.; Giallongo, C.; Giurdanella, G.; Lupo, G. Uveal Melanoma Cells Elicit Retinal Pericyte Phenotypical and Biochemical Changes in an in Vitro Model of Coculture. *Int. J. Mol. Sci.* **2020**, *21*, 5557. [CrossRef] [PubMed]
33. Franken, N.; Rodermond, H.; Stap, J.; Haveman, J.; Bree, C. Clonogenic assay of cells in vitro. *Nat. Protocols* **2006**, *1*, 2315–2319. [CrossRef]
34. Menzel, H.G. International Commission on Radiation Units and Measurements. *J. Int. Comm. Radiat. Units Meas.* **2014**, *14*, 1–2.
35. Paganetti, H.; Olko, P.; Kobus, H.; Becker, R. Calculation of relative biological effectiveness for proton beams using biological weighting functions. *Int. J. Radiat. Oncol. Biol. Phys.* **1997**, *37*, 719–729. [CrossRef]
36. Loncol, T.; Cosgrove, V.; Denis, J.M.; Gueulette, J.; Mazal, A.; Menzel, H.G.; Pihet, P.; Sabattier, R. Radiobiological Effectiveness of Radiation Beams with Broad LET Spectra: Microdosimetric Analysis Using Biological Weighting Functions. *Radiat. Prot. Dosim.* **1994**, *52*, 347–352. [CrossRef]
37. Manganaro, L.; Russo, G.; Bourhaleb, F.; Fausti, F.; Giordanengo, S.; Monaco, V.; Sacchi, R.; Vignati, A.; Cirio, R.; Attili, A. Survival': A simulation toolkit introducing a modular approach for radiobiological evaluations in ion beam therapy. *Phys. Med. Biol.* **2018**, *63*, 08NT01. [CrossRef] [PubMed]
38. Cirrone, G.P.; Cuttone, G.; Guatelli, S.; Nigro, S.L.; Mascialino, B.; Pia, M.G.; Raffaele, L.; Russo, G.; Sabini, M.G. Implementation of a new Monte Carlo GEANT4 simulation tool for the development of a proton therapy beam line and verification of the related dose distributions. *IEEE Trans. Nucl. Sci.* **2005**, *52*, 1756–1758. [CrossRef]
39. Cirrone, G.A.P.; Cuttone, G.; Mazzaglia, E.S.; Romano, F.; Sardina, D.; Agodi, C.; Attili, A.; Blancato, A.A.; De Napoli, M.; Di Rosa, F.; et al. Hadrontherapy: A 4-based tool for proton/ion-therapy studies. *Prog. Nucl. Sci. Technol.* **2011**, *2*, 207–212. [CrossRef]
40. Allison, J.; Amako, K.; Apostolakis, J.; Arce, P.; Asai, M.; Aso, T.; Bagli, E.; Bagulya, A.; Banerjee, S.; Barrand, G.J.N.I.; et al. Recent Developments in Geant4. *Nucl. Instrum. Methods* **2016**, *835*, 186–225. [CrossRef]
41. Allison, J.; Amako, K.; Apostolakis, J.E.A.; Araujo, H.A.A.H.; Dubois, P.A.; Asai, M.A.A.M.; Barrand, G.A.B.G.; Capra, R.A.C.R.; Chauvie, S.A.C.S.; Chytracek, R.A.C.R.; et al. Geant4 Developments and Applications. *IEEE Trans. Nucl. Sci.* **2006**, *53*, 270–278. [CrossRef]
42. Calipel, A.; Lux, A.L.; Guérin, S.; Lefaix, J.L.; Laurent, C.; Bernaudin, M.; Mouriaux, F. Geant4 Developments and Applications. *Investig. Ophthalmol. Vis. Sci.* **2015**, *56*, 3085–3094. [CrossRef]
43. McMahon, S.J. The linear quadratic model: Usage, interpretation and challenges. *Phys. Med. Biol.* **2019**, *64*, 01TR01. [CrossRef] [PubMed]

44. Savoca, G.; Calvaruso, M.; Minafra, L.; Bravatà, V.; Cammarata, F.P.; Iacoviello, G.; Abbate, B.; Evangelista, G.; Spada, M.; Forte, G.I.; et al. Local Disease-Free Survival Rate (LSR) Application to Personalize Radiation Therapy Treatments in Breast Cancer Models. *J. Pers. Med.* **2020**, *10*, 177. [CrossRef] [PubMed]
45. Williams, M.V.; Denekamp, J.; Fowler, J.F. A review of alpha/beta ratios for experimental tumors: Implications for clinical studies of altered fractionation. *Int. J. Radiat. Oncol. Biol. Phys.* **1985**, *11*, 87–96. [CrossRef]

applied sciences

MDPI

Article

[99mTc]Tc-Sestamibi Bioaccumulation Can Induce Apoptosis in Breast Cancer Cells: Molecular and Clinical Perspectives

Nicoletta Urbano [1,†], Manuel Scimeca [2,3,4,†], Rita Bonfiglio [5], Alessandro Mauriello [2,5], Elena Bonanno [2,6] and Orazio Schillaci [7,8,*]

1 Nuclear Medicine Unit, Department of Oncohaematology, Policlinico "Tor Vergata", 00133 Rome, Italy; n.urbano@virgilio.it
2 Department of Experimental Medicine, University of Rome "Tor Vergata", Via Montpellier 1, 00133 Rome, Italy; manuel.scimeca@uniroma2.it (M.S.); alessandro.mauriello@uniroma2.it (A.M.); elena.bonanno@uniroma2.it (E.B.)
3 San Raffaele University, Via di Val Cannuta 247, 00166 Rome, Italy
4 Saint Camillus International University of Health Sciences, Via di Sant'Alessandro, 8, 00131 Rome, Italy
5 Tor Vergata Oncoscience Research (TOR), University of Rome "Tor Vergata", 00133 Rome, Italy; rita.bonfiglio@uniroma2.it
6 Diagnostica Medica & 'Villa dei Platani', Neuromed Group, 83100 Avellino, Italy
7 IRCCS Neuromed, Via Atinense, 18, 8607 Pozzilli, Italy
8 Department of Biomedicine and Prevention, University of Rome "Tor Vergata", Via Montpellier 1, 00133 Rome, Italy
* Correspondence: orazio.schillaci@uniroma2.it
† Nicoletta Urbano and Manuel Scimeca equally first author.

Citation: Urbano, N.; Scimeca, M.; Bonfiglio, R.; Mauriello, A.; Bonanno, E.; Schillaci, O. [99mTc]Tc-Sestamibi Bioaccumulation Can Induce Apoptosis in Breast Cancer Cells: Molecular and Clinical Perspectives. *Appl. Sci.* **2021**, *11*, 2733. https://doi.org/10.3390/app11062733

Academic Editor: Salvatore Gallo

Received: 3 March 2021
Accepted: 16 March 2021
Published: 18 March 2021

Abstract: The aim of this study was to investigate the possible role of [99mTc]Tc-Sestamibi in the regulation of cancer cell proliferation and apoptosis. To this end, the in vivo values of [99mTc]Tc-Sestamibi uptake have been associated with the in-situ expression of both Ki67 and caspase-3. For in vitro investigations, BT-474 cells were incubated with three different concentrations of [99mTc]Tc-Sestamibi: 10 μg/mL, 1 μg/mL, and 0.1 μg/mL. Expression of caspase-3 and Ki67, as well as the ultrastructure of cancer cells, was evaluated at T0 and after 24, 48, 72, and 120 h after [99mTc]Tc-Sestamibi incubation. Ex vivo data strengthened the known association between sestamibi uptake and Ki67 expression. Linear regression analysis showed a significant association between sestamibi uptake and the number of apoptotic cells evaluated as caspase-3-positive breast cancer cells. As concerning the in vitro data, a significant decrease of the proliferation index was observed in breast cancer cells incubated with a high concentration of [99mTc]Tc-Sestamibi (10 μg/mL). Amazingly, a significant increase in caspase-3-positive cells in cultures incubated with 10 μg/mL [99mTc]Tc-Sestamibi was observed. This study suggested the possible role of sestamibi in the regulation of pathophysiological processes involved in breast cancer.

Keywords: 99mTc-sestamibi; breast-specific γ imaging; breast cancer; apoptosis; theragnostic

1. Introduction

A recent report by the American College of Radiology released the clinical indications for the use of dedicated breast γ imaging, including breast-specific γ imaging (BSGI), in breast cancer patients not suitable for magnetic resonance imaging (MRI) analysis [1]. Indeed, BSGI with the cationic lipophilic agent [99mTc] (technetium 99-m) labeled sestamibi (99mTc-Sestamibi) is considered a reliable and useful medical device for the early preoperative detection of primary breast cancer [2]. BSGI with [99mTc]Tc-Sestamibi can also be considered complementary to mammography in women showing dense breasts, palpable abnormalities, and mammographically indeterminate breast lesions > 1 cm [3]. For all these reasons, the correct use of BSGI with [99mTc]Tc-Sestamibi in the breast units frequently allows for a reduction in the number of unnecessary biopsies, thus improving

the management of breast cancer patients. Moreover, it established the role of BSGI with [99mTc]Tc-Sestamibi in accurate stereotactic breast biopsy procedures. In fact, Collarino and colleagues [4] described a new clinical method for stereotactic breast biopsy guided by [99mTc]Tc-Sestamibi uptake that allows for the achievement of larger and suitable histopathologic samples, if compared with automated core needle biopsy methods [5,6].

Recently, Urbano et al. demonstrated that BSGI with [99mTc]Tc-Sestamibi can be used to detect breast cancer lesions characterized by the presence of microcalcifications and breast osteoblast-like cells [7]. Indeed, authors showed a significant association between [99mTc]Tc-Sestamibi uptake, the presence of breast microcalcifications made of hydroxyapatite, and the presence of cancer cells associated with the development of bone metastatic lesions breast osteoblast-like cells [8]. Thus, BSGI with [99mTc]Tc-Sestamibi could also be used for the early detection of breast cancer lesions with a high propensity to form bone metastasis [9].

In regard to [99mTc]Tc-Sestamibi uptake, two different biodistribution models based on its chemical-physical characteristics have been proposed [10–12]: (a) binding of [99mTc]-Tc-Sestamibi with 8–10-kDa cytoplasmic proteins, and (b) easy lipid partitioning and membrane translocation mainly reflecting passive transmembrane distribution in accordance with the imposed transmembrane potential. Passive membrane translocation is currently the most supported mechanism [13,14]. Based on this mechanism, the uptake of sestamibi is generally associated with the presence of several mitochondria with a high membrane potential [15].

Despite the important chemical-physical and clinical evidence regarding the use of BSGI with [99mTc]Tc-Sestamibi in the management of breast cancer patients reported above, few studies have been performed on the cellular/molecular modifications of breast cancer tissues induced by the sestamibi uptake. In fact, only indirect data about the association between [99mTc]Tc-Sestamibi uptake and the cellular/molecular characteristics of breast cancer cells, such as their proliferation index, have been investigated. In this context, Erba et al. reported very preliminary data about the role of [99mTc]Tc-Sestamibi uptake as an indicator of chemotherapy induced apoptosis [16]. However, no definitive clinical or in vitro experimental data are currently available.

Starting from these considerations, this study aims to investigate the possible role of [99mTc]Tc-Sestamibi in the regulation of biological processes involved in cancer progression such as proliferation and apoptosis ex vivo and in vitro. To this end, the in vivo values of [99mTc]Tc-Sestamibi uptake have been associated with the in situ expression of both Ki67 (proliferation index) and caspase-3 (apoptosis). In addition, in vitro investigations using a breast cancer cell line (BT474) have been performed to study the possible cellular and molecular modifications of cancer cells following [99mTc]Tc-Sestamibi uptake.

2. Materials and Methods

The Policlinico Tor Vergata ethical committee approved this protocol with the reference number # 129.18, 26 July 2018. Furthermore, all methodologies and experimental procedures described herein were achieved in agreement with the last Helsinki Declaration.

Exclusion criteria were a second cancer and neoadjuvant hormonal or radiation therapy prior to surgery.

According to these criteria, we retrospectively enrolled 40 consecutive breast cancer patients (58.36 $\pm$ 1.99 years; range 42–65 years) who underwent both BSGI with [99mTc]Tc-Sestamibi and breast biopsy procedures.

For each of them, histological diagnosis and immunohistochemical investigations were performed.

2.1. [99mTc]Tc-Sestamibi-High Resolution SPECT

BSGI with [99mTc]Tc-Sestamibi investigations were performed as described in a previous study [17]. Briefly, a BSGI scan was performed in 10–15 min following an intravenous administration of 740 MBq [99mTc]Tc-Sestamibi through an antecubital vein contralateral

to the suspicious breast side to avoid potential false-positive uptake in the axillary lymph nodes. The patients remained seated during the procedure. Craniocaudal and mediolateral oblique (MLO) images were obtained in both breasts using high-resolution BSGI.

All 40 patients had biopsy. BSGI was performed before biopsy in 25 patients and after biopsy in 15 patients. When BSGI was performed after biopsy, the minimum interval between biopsy and imaging was 7 days in an attempt to avoid the effects of post-biopsy inflammation as much as possible.

For the qualitative analysis of the BSGI, two investigators classified positive and negative findings. Lesions with no demonstrable uptake and those with diffuse heterogeneous or minimal patchy uptake were considered negative, whereas lesions with scattered patchy uptake, partially focal uptake, or any other focal uptake were regarded as positive. Irregular-shaped regions of interest (ROIs) were used to encase the lesions. The evaluation of the lesion to nonlesion ratio (L/N) was estimated according to the study of Tan et al. [18]. For patients who underwent BSGI with [99mTc]Tc-Sestamibi before biopsy (n = 25), the BSGI-guided biopsy procedure was performed as previously described [19].

2.2. Histology

Breast biopsy samples were formalin fixed and embedded in paraffin. Serial sections were used for both hematoxylin-eosin (H&E) and immunohistochemistry staining [20].

2.3. Immunohistochemistry

Immunohistochemistry was used to study the expression of an apoptotic in situ biomarker, caspase-3, and the proliferation index by Ki67. Paraffin sections with a thickness of 3 μm were treated with EDTA citrate buffers at a pH of 7.8 for 30 min at 95 °C to antigen retrieval reaction. Afterwards, sections were incubated with the primary antibodies diluted 1:100 for 60 min at room temperature; anti-Ki67 rabbit monoclonal antibody (clone 30-9, Ventana, Tucson, AZ, USA) and anti-caspase-3 mouse monoclonal antibody (31A1067, Novus Biologicals, Centennial, CO, USA). Washing was performed with PBS/Tween 20 with a pH of 7.6 (UCS Diagnostic, Morlupo, RM, Italy).

Digital scanning was used to evaluate the immunohistochemical reactions (Iscan Coreo, Ventana, Tucson, AZ, USA). Specifically, digital images from caspase-3 reactions were evaluated in a semi-quantitative approach by counting the number of positive breast cancer cells (out of a total of 500 in randomly selected regions). Ki67 was calculated in terms of percentage of positive cancer cells. Reactions have been set up by using specific positive and negative control tissues.

2.4. Cell Culture

BT-474 cells obtained from the American Type Culture Collection (ATCC. Manassas, VA, USA) and maintained by the Cell and Tissue Culture Core, Lombardi Cancer Center (Reservoir Rd. NW Washington D.C. 20057, USA). Cells were routinely cultured in DMEM high glucose (Sigma-Aldrich, St. Louis, MO, USA) supplemented with 10% fetal bovine serum (FBS).

In detail, cells from the first or second passage were seeded into a 24-well plate at a density of 30×10^3 cells/well. Successively, BT-474 cells were incubated with: (a) [99mTc]Tc-Sestamibi 10 μg/mL, (b) [99mTc]Tc-Sestamibi 1 μg/mL, and (c) [99mTc]Tc-Sestamibi 0.1 μg/mL. The expression of both Ki67 and caspase-3 were evaluated at T0 and after 24, 48, 72, and 120 h after sestamibi incubation. Cells treated with the vehicle (lyophilisate resuspended) were used as a control (CTRL).

Cell proliferation was investigated both by counting the number of cells for each time point, and by bromodeoxyuridine incorporation assay performed at time 0 and after 72 h. Morphology was studied by both toluidine blue staining.

2.5. Immunocytochemistry

Immunocytochemistry was performed to investigate the expression of caspase-3 and Ki67 on BT-474 cells treated with 99mTc-Sestamibi. Caspase-3 was evaluated by immunoperoxidase analysis, while Ki67 expression was evaluated by immunofluorescence staining in order to reduce the background.

BT-474 Cells were plated on poly-l-lysine coated slides (Sigma-Aldrich cat #P4707) in 24-well cell culture plates and fixed in 4% paraformaldehyde. After pre-treatment with EDTA citrate at 95 °C for 20 min and 0.1% Triton X-100 for 15 min, cells were incubated for 1 h with the anti-Ki67 rabbit monoclonal antibody (clone 30-9, Ventana, Tucson, AZ, USA) and anti-caspase-3 mouse monoclonal antibody (31A1067, Novus Biologicals, Littleton, CO, USA). Washing was performed with PBS/Tween20 with a pH of 7.6. Regarding the study of caspase-3 expression, reactions were revealed by using an horseradish peroxidase-3,3′-Diaminobenzidine detection kit (UCS Diagnostic, Rome, Italy). Conversely, the Ki67 signal was revealed by using a TexasRed conjugate anti-rabbit antibody.

Reactions were evaluated by counting the number of Ki67 or caspase-3-positive cells of 500 in total in randomly selected regions.

2.6. TEM and EDX Analysis of Cell Cultures

Cells were fixed in 4% paraformaldehyde, post-fixed in 2% osmium tetroxide and embedded in EPON resin for morphological studies. After washing with 0.1 M phosphate buffer, the sample was dehydrated by a series of incubations in 30%, 50%, and 70% ethanol. Dehydration was continued by incubation steps in 95% ethanol, absolute ethanol, and hydroxypropyl methacrylate, then samples were embedded in EPON (Agar Scientific, Stansted, Essex, UK).

Eighty μm ultra-thin sections were mounted onto copper grids and observed with a Hitachi 7100FA transmission electron microscope (Hitachi, Schaumburg, IL, USA) to study the mitochondria ultrastructure.

Unstained ultra-thin sections with a thickness of approximately 100 nm were mounted onto copper grids for microanalysis. EDX spectra were acquired with a Hitachi 7100FA transmission electron microscope (Hitachi, Schaumburg, IL, USA) and an EDX detector (Thermo Scientific, Waltham, MA, USA).

2.7. Statistical Analysis

Statistical analysis was performed using GraphPad Prism 5 software (San Diego, CA, USA). Immunohistochemical data were analyzed by the Kruskal-Wallis test ($p < 0.05$) and by Mann-Whitney test ($p < 0.0005$). In vitro data about the number of Ki67-positive cells and caspase-3-positive cells were analyzed by using one-way ANOVA ($p < 0.05$).

3. Results

3.1. 99mTc-Sestamibi-High Resolution SPECT Analysis

BSGI with [99mTc]Tc-Sestamibi showed the uptake of radiopharmaceuticals in all 35 breast cancer patients (L/N max 5.09; min 1.43) (Figure 1A). No significant differences concerning L/N Ratio were observed among breast cancer histotypes.

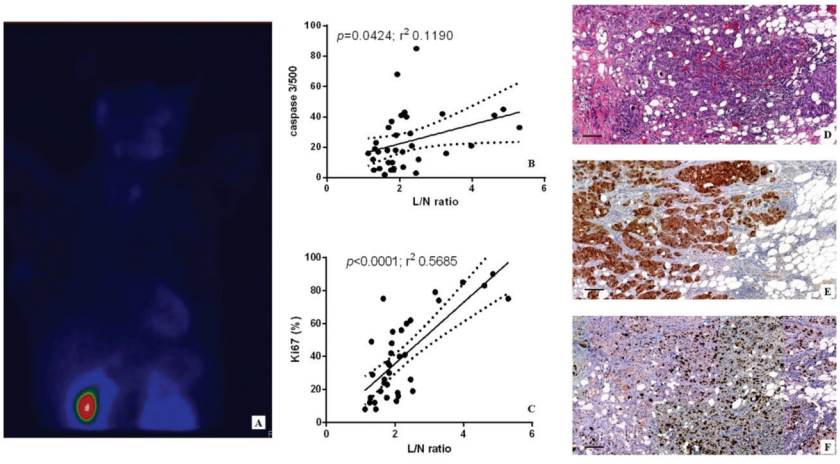

Figure 1. Breast-specific γ imaging with [99mTc]Tc-Sestamibi and both caspase-3 and Ki67 expression. (**A**) Maximum-intensity projection of breast-specific γ imaging with [99mTc]Tc-Sestamibi in a 69-year-old breast cancer patient. (**B**) The graph shows the positive and significant association between the number of caspase-3-positive breast cancer cells and the sestamibi uptake (L/M ratio). (**C**) The graph displays significant association between the number of Ki67-positive breast cancer cells and the sestamibi uptake (L/M ratio). (**D**) T hematoxylin and eosin section shows G3 infiltrating breast carcinomas (scale bar represents 50 μm). (**E**) The image displays numerous caspase-3-positive breast cancer cells (scale bar represents 50 μm). (**F**) High percentage of Ki67-positive breast cancer cells (scale bar represents 50 μm).

3.2. Histology

Breast biopsies were classified according to the Nottingham histological system [21]. In particular, 8/40 G1 infiltrating carcinomas, 14/40 G2 infiltrating carcinomas, and 9/40 G3 infiltrating carcinomas were found.

3.3. [99mTc]Tc-Sestamibi Uptake vs. Apoptosis

To investigate the possible association between sestamibi uptake and the apoptotic phenomenon, linear regression analyses have been performed by comparing the L/N ratio values and the number of caspase-3-positive cells. Linear regression analysis showed a positive association between sestamibi uptake and the number of caspase-3-positive breast cancer cells ($p = 0.0424$; r^2 0.1190) (Figure 1B,D,E), even though the absolute number of apoptotic cells were low, especially if compared with the number of Ki67-positive cells (Figure 1C,D).

3.4. [99mTc]Tc-Sestamibi Uptake vs. Proliferation Index

The percentages of Ki67-positive breast cancer cells, evaluated by immunohistochemistry, have been used as proliferation index values. According to our previous investigation, a positive and significant correlation between sestamibi uptake and the proliferation index was observed ($p < 0.0001$; r^2 0.5685) (Figure 1C,F).

3.5. Effect of Sestamibi on Breast Cancer Cells: In Vitro Study

At the end of each experimental point, BT-474 cells were fixed with 4% paraformaldehyde and used to evaluate the number of both Ki67- and caspase-3-positive cells. One-way ANOVA showed significant data distribution for both the number of caspase-3- ($p < 0.0001$) and Ki67- ($p = 0.0038$) positive cells. Notably, a high concentration of [99mTc]Tc-Sestamibi (10 μg/mL) induced a significant increase in the number of apoptotic cells (caspase-3-positive cells) when compared with all other experimental conditions, including the control

(Figure 2A–I). Specifically, a great increase in the number of caspase-3-positive cells was observed after 48h (Figure 2A,C). This datum suggests that [99mTc]Tc-Sestamibi could be able to induce the apoptotic process by caspase-3 signal only at high concentrations. In other experimental conditions, no significant effects were detected (Figure 2A).

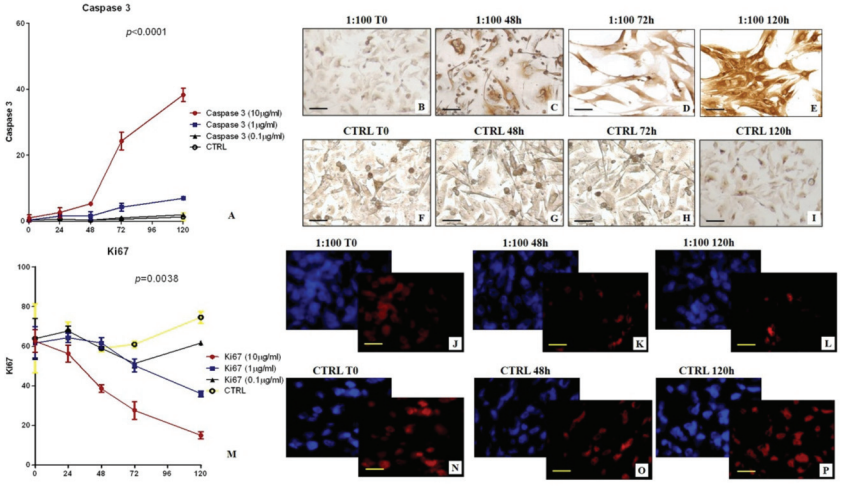

Figure 2. In vitro evaluation of the effect of [99mTc]Tc-Sestamibi on BT474 breast cancer cells. (**A**) The graph shows the number of caspase-3-positive BT474 breast cancer cells after sestamibi treatment. (**B**) No/rare caspase-3-positive cells at T0. (**C**) The image shows caspase-3-positive cells after 48 h of [99mTc]Tc-Sestamibi incubation (10 µg/mL). (**D**) Numerous caspase-3-positive cells after 72 h of [99mTc]Tc-Sestamibi incubation (10 µg/mL). (**E**) High number of caspase-3-positive cells after 120 h of [99mTc]Tc-Sestamibi incubation (10 µg/mL). (**F–I**) No/rare caspase-3-positive cells at each time point in the absence of [99mTc]Tc-Sestamibi incubation. Scale bar represents 50µm for (**B–I**) images. (**J**) Immunofluorescence displays numerous Ki67-positive breast cancer cells (blue DAPI-Texas red Ki67) at T0. (**K**) Some Ki67-positive breast cancer cells (blue DAPI-Texas red Ki67) after 48 h of [99mTc]Tc-Sestamibi incubation (10 µg/mL). (**L**) Rare Ki67-positive breast cancer cells (blue DAPI-Texas red Ki67) after 120 h of 10 µg/mL [99mTc]Tc-Sestamibi incubation. (**M**) The graph shows the number of caspase-3-positive BT474 breast cancer cells after sestamibi treatment. (**N–P**) Numerous Ki67-positive breast cancer cells (blue DAPI-Texas red Ki67) at each time point in the absence of [99mTc]Tc-Sestamibi incubation (10 µg/mL). Scale bar represents 20 µm for (**J–L**,**N–P**) images.

Concerning the cell proliferation (Ki67), a significant decrease in the number of Ki67-positive cells was observed in cell cultures incubated with both 10 µg/mL and 1 µg/mL of [99mTc]Tc-Sestamibi when compared with cells treated with a concentration of 1 µg/mL (Figure 2M–P). Indeed, the data reported here showed that a low concentration of [99mTc]Tc-Sestamibi (1 µg/mL) does not influence the proliferation index (Figure 2M). Cell cultures treated with both 1 µg/mL and 0.1 µg/mL [99mTc]Tc-Sestamibi displayed a proliferation index similar to that observed in the control (Figure 2M). This datum can explain the association observed in vivo between sestamibi uptake and the percentage of Ki67-positive cells. It is important to note that high concentration of [99mTc]Tc-Sestamibi (10 µg/mL) induced a significant reduction in the proliferation index already after 24 h of treatment (Figure 2M–L).

By comparing the value of Ki67 and caspase-3 at every time point it became clear that by only using 10 µg/mL of [99mTc]Tc-Sestamibi concentration, a complete reversion between proliferation and apoptosis was obtained (Figure 3A–C). In particular, after 72h, the number of caspase-3-positive cells was higher than those positive for Ki67, suggesting an imbalance capable of arresting the tumor's proliferation (Figure 3A). Morphological

evaluation confirmed the presence of apoptotic bodies in the cell cultures cultured with a high concentration of [99mTc]Tc-Sestamibi (10 μg/mL) (Figure 3D–G). Transmission electron microscopy investigations showed numerous apoptotic bodies in cell cultures incubated with 10 μg/mL [99mTc]Tc-Sestamibi (Figure 3E–G). The damages were evident after 72 h. EDX microanalysis frequently showed the presence of [99mTc]Technetium in the cytoplasm of apoptotic cells (Figure 3F,G) or in the mitochondria of the cell in the early phases of apoptotic process.

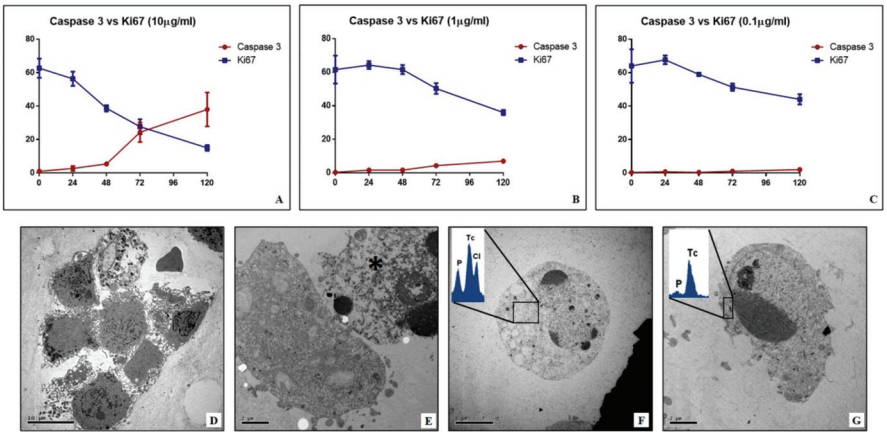

Figure 3. Comparison between apoptosis and proliferation of BT474 breast cancer cells treated with [99mTc]Tc-Sestamibi and ultrastructural analysis. (**A**) Graph shows the number of both caspase-3- and Ki67-positive BT474 breast cancer cells after 24, 48, 72, 96, and 120 h of [99mTc]Tc-Sestamibi incubation (10 μg/mL). (**B**) Graph displays the number of both caspase-3- and Ki67-positive BT474 breast cancer cells after 24, 48, 72, 96, and 120 h of [99mTc]Tc-Sestamibi incubation (10 μg/mL). (**C**) Graph shows the number of both caspase-3- and Ki67-positive BT474 breast cancer cells after 24, 48, 72, 96, and 120 h of [99mTc]Tc-Sestamibi incubation (10 μg/mL). (**D**) Electron micrograph displays ultrastructure of BT474 breast cancer cells (CTRL T0). (**E**) Image shows an apoptotic breast cancer cell (asterisk) close to a non-apoptotic cell (10 μg/mL at 48 h). (**F**,**G**) EDX spectrum revealed the presence of [99mTc]Technetium into the cytoplasm of apoptotic cells (10 μg/mL at 120 h).

4. Discussion

BSGI with [99mTc]Tc-Sestamibi can represent a remarkable opportunity to detect both primary and metastatic lesions characterized by the presence of breast cancer cells with high amounts of mitochondria. In fact, the current data about the chemical-physical characteristics of sestamibi, as well as its pharmacokinetics, seem to indicate its tropism for the accumulation in the cell organelles with a negative membrane potential, such as mitochondria. In support of this, it is known that once in the cytoplasm, sestamibi may translocate into the mitochondria according to its cationic nature [15,16]. The positive charge on sestamibi may drive this molecule into the mitochondria during cell metabolic activities that increase the negative plasma membrane potential. Despite this evidence, few studies have been performed about the possible effect of sestamibi uptake in breast cancer cells. The accumulation of sestamibi in the cell allows it to hypothesize the alteration of normal mitochondria functions and consequently of the cancer cell's homeostasis, mainly at the level of cell proliferation and cell death.

Ex vivo data reported here strengthened the known association between sestamibi uptake and Ki67 expression, thus confirming the capability of BSGI with [99mTc]Tc-Sestamibi to identify breast cancer lesions characterized by high proliferation index [17]. In line with this, Urbano et al. also demonstrated the association between sestamibi uptake and proliferation index in parathyroid lesions [18]. Surprisingly, linear regression analysis also

showed a significant association between the sestamibi uptake and the number of apoptotic cells evaluated as caspase-3-positive cells. Caspase-3 is a protein effector involved in apoptosis [19]. Activated caspase-3, as well as caspase-6 and caspase-7, may cleave multiple structural and regulatory proteins that are critical for cell survival and maintenance [18]. However, caspase-3 is considered the most important executioner caspase and it is involved in both intrinsic and extrinsic apoptotic pathways [20]. Alteration in both mitochondrial function and structure induce the release of mediators such as BCL-2 family proteins that amplify caspase-3 activity, inducing the intrinsic pathway of apoptosis [21]. Thus, the expression of caspase-3 in breast cells can be related to the occurrence of intrinsic apoptosis. Data on both Ki67 and caspase-3, despite being in disagreement, can be related to the same processes involved in breast cancer progression. Indeed, as demonstrated by Ryoo and Bergmann [22], the caspase-3 related apoptotic phenomenon may be related to cancer progression due to the communication between apoptotic cells and surrounding ones. This biological process occurs physiologically during embryogenesis, where proapoptotic proteins—mostly caspases—can induce the proliferation of neighboring surviving cells to replace dying cells. It is demonstrated that the deregulation of this process in cancer tissues could sustain tumor proliferation and progress. Thus, apparently only our in vivo data seem conflicting. The association of sestamibi uptake with both proliferation index and apoptosis could be considered an instrumental/clinical manifestation of pathophysiological mechanisms commonly involved in breast cancer development. However, a molecular characterization of the events associated with the accumulation of sestamibi into the mitochondria could open new clinical perspectives in the management of breast cancer cells. In fact, the regulation of the mitochondria related apoptotic process is currently one of the main targets of anti-cancer therapies.

In this context, the preliminary data of Erba and colleagues suggested that the sestamibi uptake correlated with apoptosis levels in breast cancer tissues following chemotherapy treatment [23].

In this study, the biological link between sestamibi uptake and the apoptotic phenomenon has been investigated in vitro by using BT-474 breast cancer cell lines. In particular, three different concentrations of [99mTc]Tc-Sestamibi (10 μg/mL, 1 μg/mL, 0.1 μg/mL) have been used to investigate the response of breast cancer cells to sestamibi uptake. Concerning the proliferation index, a significant decrease was observed in breast cancer cells incubated with a high concentration of [99mTc]Tc-Sestamibi (10 μg/mL). It is important to note that both in the control and at a lower concentration of [99mTc]Tc-Sestamibi (0.1 μg/mL), no decrease in proliferation index was observed after 120h. Excluding the experiment with a high concentration of [99mTc]Tc-Sestamibi (10 μg/mL), in vitro data confirmed the uptake of sestamibi in breast cancer cells during the proliferation phase. Amazingly, in vitro investigations showed a significant increase in caspase-3-positive cells in cultures incubated with 10 μg/mL of 99mTc-sestamibi. In particular, after 72 h, the presence of sestamibi in the cell medium induced a complete inversion between the proliferation index and apoptosis. In fact, at this time point, the number of caspase-3-positive cells was greater than those positive to the Ki67 markers. From a morphological point of view, these cell cultures showed numerous dead cells characterized by typical apoptotic sign such as pyknosis, or karyopyknosis. In addition, transmission electron microscopy investigations allowed us to evaluate the ultrastructure of breast cancer cells incubated with [99mTc]Tc-Sestamibi, demonstrating a progressive increase in the presence of apoptotic alterations. These damages were associated with both [99mTc]Tc-Sestamibi concentration and incubation time. Remarkably, EDX investigations also showed the presence of [99mTc]Technetium in the cytoplasm of apoptotic cells.

Altogether, the data of this study suggest that, in the early phases, sestamibi uptake occurs mainly in breast cancer cells with a high proliferation index because of the high metabolic cell activity and the subsequent increase in the mitochondrial membrane potential. Then, the accumulation of sestamibi in the breast cancer cell mitochondria can induce an alteration of normal homeostasis, thus triggering the apoptotic event.

5. Conclusions

For the first time, this study reported ex vivo and in vitro data about the correlation between sestamibi uptake and apoptosis, suggesting the possible role of sestamibi in the regulation of the pathophysiological processes involved in breast cancer. The evidence of the accumulation of sestamibi in breast cancer cells and the subsequent mitochondrial damage can open new clinical perspectives on the use of this radiopharmaceutical in both the diagnosis and treatment of breast cancers. If confirmed by further ex vivo and in vitro studies, the capability of sestamibi to induce apoptosis of breast cancer cells can lay down the scientific rationale for considering this molecule as a theragnostic agent. Indeed, different concentrations of [99mTc]Tc-Sestamibi could be used for the detection of cancer lesions with a high proliferation index or to stimulate apoptosis, thus countering cancer growth. Lastly, these investigations further highlight the fundamental cooperation between nuclear medicine and general diagnostic imaging, and the pathology in both research and diagnostic applications [24,25].

Author Contributions: Conceptualization: N.U., M.S., and O.S.; methodology: M.S., R.B., E.B., and A.M.; formal analysis R.B., and E.B.; data curation: A.M., N.U. and O.S.; writing—original draft preparation: N.U., M.S., and O.S.; writing—review and editing: R.B., E.B. and A.M.; supervision, O.S. All authors have read and agreed to the published version of the manuscript.

Funding: This research received no external funding.

Institutional Review Board Statement: The "Policlinico Tor Vergata" ethical committee approved this protocol with the reference number no. 129.18, 26 July 2018. Furthermore, all methodologies and experimental procedures herein described were achieved in agreement with the last Helsinki Declaration.

Informed Consent Statement: Informed consent was obtained from all subjects involved in the study.

Data Availability Statement: The data presented in this study are available on request from the corresponding author. The data are not publicly available due to privacy concerns.

Conflicts of Interest: The authors declare no conflict of interest.

References

1. Narayanan, D.; Berg, W.A. Dedicated Breast Gamma Camera Imaging and Breast PET: Current Status and Future Directions. *PET Clin.* **2018**, *13*, 363–381. [CrossRef]
2. Spanu, A.; Schillaci, O.; Meloni, G.B.; Porcu, A.; Cottu, P.; Nuvoli, S.; Falchi, A.; Chessa, F.; Solinas, M.E.; Madeddu, G. The usefulness of 99mTc-tetrofosmin SPECT scintimammography in the detection of small size primary breast carcinomas. *Int. J. Oncol.* **2002**, *21*, 831–840. [CrossRef]
3. Schillaci, O.; Scopinaro, F.; Danieli, R.; Tavolaro, R.; Picardi, V.; Cannas, P.; Colella, A.C. 99Tcm-sestamibi scintimammography in patients with suspicious breast lesions: Comparison of SPET and planar images in the detection of primary tumours and axillary lymph node involvement. *Nucl. Med. Commun.* **1997**, *18*, 839–845. [CrossRef]
4. Collarino, A.; Olmos, R.A.V.; Neijenhuis, P.A.; den Hartog, W.C.; Smit, F.; de Geus-Oei, L.F.; Arias-Bouda, L.M.P. First Clinical Experience Using Stereotactic Breast Biopsy Guided by 99mTc-Sestamibi. *AJR Am. J. Roentgenol.* **2017**, *209*, 1367–1373. [CrossRef] [PubMed]
5. Liberman, L. Centennial dissertation. Percutaneous imaging-guided core breast biopsy: State of the art at the millennium. *AJR Am. J. Roentgenol.* **2000**, *174*, 1191–1199. [CrossRef] [PubMed]
6. Berg, W.A.; Krebs, T.L.; Campassi, C.; Magder, L.S.; Sun, C.C. Evaluation of 14- and 11-gauge directional, vacuum-assisted biopsy probes and 14-gauge biopsy guns in a breast parenchymal model. *Radiology* **1997**, *205*, 203–208. [CrossRef] [PubMed]
7. Urbano, N.; Scimeca, M.; Di Russo, C.; Bonanno, E.; Schillaci, O. Breast-Specific Gamma Imaging with [99mTc]Tc-Sestamibi: An In Vivo Analysis for Early Identification of Breast Cancer Lesions Expressing Bone Biomarkers. *J. Clin. Med.* **2020**, *9*, 747. [CrossRef] [PubMed]
8. Scimeca, M.; Urbano, N.; Bonfiglio, R.; Schillaci, O.; Bonanno, E. Breast osteoblast-like cells: A new biomarker for the management of breast cancer. *Br. J. Cancer* **2018**, *119*, 1129–1132. [CrossRef] [PubMed]
9. Urbano, N.; Scimeca, M.; Bonanno, E.; Schillaci, O. [99mTc]Tc-Sestamibi SPECT: A possible tool for early detection of breast cancer lesions with high bone metastatic potential. *Future Oncol.* **2019**, *15*, 455–457. [CrossRef]
10. Backus, M.; Piwnica-Worms, D.; Hockett, D.; Kronauge, J.; Lieberman, M.; Ingram, P.; LeFurgey, A. Microprobe analysis of Tc-MIBI in heart cells: Calculation of mitochondrial membrane potential. *Am. J. Physiol.* **1993**, *265 Pt 1*, C178–C187. [CrossRef]

11. Taillefer, R. Clinical applications of [99mTc]Tc-Sestamibi scintimammography. *Semin. Nucl. Med.* **2005**, *35*, 100–115. [CrossRef] [PubMed]
12. Maffioli, L.; Steens, J.; Pauwels, E.; Bombardieri, E. Applications of [99mTc]Tc-Sestamibi in oncology. *Tumori* **1996**, *82*, 12–21. [CrossRef]
13. Piwnica-Worms, D.; Holman, B.L. Noncardiac applications of hexakis(alkylisonitrile) [99mTc]Technetium-99m complexes. *J. Nucl. Med.* **1990**, *31*, 1166–1167. [PubMed]
14. Ghaly, M.; Links, J.M.; Frey, E.C. Optimization and comparison of simultaneous and separate acquisition protocols for dual isotope myocardial perfusion SPECT. *Phys. Med. Biol.* **2015**, *60*, 5083–5101. [CrossRef] [PubMed]
15. Urbano, N.; Scimeca, M.; Tancredi, V.; Bonanno, E.; Schillaci, O. [99mTc]Tc-Sestamibi breast imaging: Current status, new ideas and future perspectives. *Semin. Cancer Biol.* **2020**. [CrossRef]
16. Scimeca, M.; Urbano, N.; Bonfiglio, R.; Duggento, A.; Toschi, N.; Schillaci, O.; Bonanno, E. Novel insights into breast cancer progression and metastasis: A multidisciplinary opportunity to transition from biology to clinical oncology. *Biochim. Biophys. Acta Rev. Cancer* **2019**, *1872*, 138–148. [CrossRef] [PubMed]
17. Schillaci, O.; Danieli, R.; Filippi, L.; Romano, P.; Cossu, E.; Manni, C.; Simonetti, G. Scintimammography with a hybrid SPECT/CT imaging system. *Anticancer Res.* **2007**, *27*, 557–562. [PubMed]
18. Tan, H.; Zhang, H.; Yang, W.; Fu, Y.; Gu, Y.; Du, M.; Cheng, D.; Shi, H. Breast-specific gamma imaging with Tc-99m-sestamibi in the diagnosis of breast cancer and its semiquantitative index correlation with tumor biologic markers, subtypes, and clinicopathologic characteristics. *Nucl. Med. Commun.* **2016**, *37*, 792–799. [CrossRef]
19. Elston, C.W.; Ellis, I.O. Pathological prognostic factors in breast cancer. I. The value of histological grade in breast cancer: Experience from a large study with long-term follow-up. *Histopathology* **1991**, *19*, 403–410. [CrossRef]
20. Urbano, N.; Scimeca, M.; Di Russo, C.; Mauriello, A.; Bonanno, E.; Schillaci, O. [99mTc]Sestamibi SPECT Can Predict Proliferation Index, Angiogenesis, and Vascular Invasion in Parathyroid Patients: A Retrospective Study. *J. Clin. Med.* **2020**, *9*, 2213. [CrossRef]
21. Estaquier, J.; Vallette, F.; Vayssiere, J.L.; Mignotte, B. The mitochondrial pathways of apoptosis. *Adv. Exp. Med. Biol.* **2012**, *942*, 157–183. [PubMed]
22. Ryoo, H.D.; Bergmann, A. The role of apoptosis-induced proliferation for regeneration and cancer. *Cold Spring Harb. Perspect. Biol.* **2012**, *4*, a008797. [CrossRef] [PubMed]
23. Erba, P.A.; Tusi, E.; Manfredi, C.; Locci, M.T.; Sollini, M.; Lazzeri, E.; Massri, K.; Locantore, L.; Mariani, G. 99mTc-Annexin-V and [99mTc]Tc-Sestamibi uptake as indicators of chemotherapy induced apoptosis. *J. Nucl. Med.* **2009**, *50* (Suppl. 2), 1575.
24. Urbano, N.; Scimeca, M.; Bonanno, E.; Schillaci, O. Nuclear medicine and anatomic pathology in personalized medicine: A challenging alliance. *Per. Med.* **2018**, *15*, 457–459. [CrossRef]
25. Scimeca, M.; Urbano, N.; Bonfiglio, R.; Schillaci, O.; Bonanno, E. Management of oncological patients in the digital era: Anatomic pathology and nuclear medicine teamwork. *Future Oncol.* **2018**, *14*, 1013–1015. [CrossRef] [PubMed]

applied sciences

MDPI

Article

Diagnostic Performance and Radiation Dose of the EOS System to Image Enchondromatosis: A Phantom Study

Domenico Albano [1,2], Alessandro Loria [3], Cristiana Fanciullo [4], Alberto Bruno [5], Carmelo Messina [1,6], Antonella del Vecchio [3] and Luca Maria Sconfienza [1,6,*]

1 IRCCS Istituto Ortopedico Galeazzi, 20161 Milano, Italy; albanodomenico@me.com (D.A.); carmelomessina.md@gmail.com (C.M.)
2 Sezione di Scienze Radiologiche, Dipartimento di Biomedicina, Neuroscienze e Diagnostica Avanzata, Università di Palermo, 90127 Palermo, Italy
3 Servizio di Fisica Sanitaria, IRCCS Ospedale San Raffaele, 20132 Milano, Italy; loria.alessandro@hsr.it (A.L.); delvecchio.antonella@hsr.it (A.d.V.)
4 Postgraduate School of Diagnostic and Interventional Radiology, University of Milan, 20122 Milano, Italy; fanciullo.cristiana@gmail.com
5 Centro Salus, 90145 Palermo, Italy; bruno-alberto@hotmail.it
6 Dipartimento di Scienze Biomediche per la Salute, Università degli Studi di Milano, 20133 Milano, Italy
* Correspondence: io@lucasconfienza.it; Tel.: +39-02-66214004

Received: 29 October 2020; Accepted: 9 December 2020; Published: 15 December 2020

Abstract: Background: Radiation doses and capability of EOS, conventional radiography (CR), and computed tomography (CT) to detect and measure enchondromas in a dedicated five-year-old anthropomorphic phantom were compared. Methods: To simulate enchondromas, minced pieces of chicken bone and cartilage were packed in conventional kitchen plastic foil to create ovoidal/rounded masses and randomly hung on the phantom. The phantom was imaged five times with CR, CT, and EOS, each time changing the number and position of inserts. All images were reviewed by a senior radiologist and a radiology resident. Results: EOS and CR detected all inserts in 4/5 cases (80%), while in one case 1/17 inserts was not seen. Excellent agreement of EOS with CR (88% reproducibility; bias = 14 mm; repeatability coefficient (CoR) 2.9; 95% CI from −2.8 to 3.1 mm; $p = 0.5$) and CT (81% reproducibility; bias = 15 mm; CoR 5.2; 95% CI from −5.5 to 5.2 mm; $p = 0.7$) was found. EOS showed 71% interobserver reproducibility (CoR 7.2; bias = 0.6 mm; 95% CI from −6.6 to 7.8 mm; $p = 0.25$). The EOS-Fast radiation dose was also significantly lower than the median radiation dose of CR (644.7 (599.4–651.97) mGy•cm^2, $p = 0.004$). Conclusions: Low-dose EOS has the same capability as CR to detect and measure enchondroma-like inserts on a phantom and may be considered to monitor patients with multiple enchondromas.

Keywords: EOS; conventional radiography; computed tomography; radiation dose; enchondroma; phantom

1. Introduction

Enchondromas are common, benign cartilage tumors that mostly develop in the metaphysis of long bones in close proximity to growth plate cartilage [1–5]. Ollier disease, also known as enchondromatosis, is a nonhereditary disorder defined by the presence of multiple enchondromas, while Maffucci syndrome is that condition in which multiple enchondromatosis is associated with soft tissue hemangiomas [6]. The prevalence of Ollier disease is estimated to be 1/100,000, while there are about 200 reports of Maffucci syndrome. Both conditions usually present during childhood as a possible consequence of a differentiation disorder during endochondral ossification of growth plate tissue [7]. Clinical problems caused by enchondromas depend on the extent of skeletal involvement

and include skeletal deformities associated or not with pathological fracture, limb-length discrepancy, and the potential risk for malignant transformation to chondrosarcoma [3–5]. The diagnosis of Ollier disease is mainly based on clinical and radiological evaluations, which typically show an irregular distribution of multiple, radiolucent, homogenous lesions with an oval or elongated shape and a well-defined, slightly thickened bony margin. Since children affected by Ollier disease will undergo multiple radiographs during childhood for diagnosis and follow-up, the need for accurate assessment of enchondromas has to balance with the risks associated with repeated radiation exposure. Repeated exposure of children to radiation is a major concern, having been reported to be 2 to 5 times more radiosensitive than adults [8] and to have the highest risk of cancer development, as radiologic stochastic damage has a latency of one or even two decades. Thus, in the last few decades, much effort has gone into developing radiologic techniques able to keep radiation doses "as low as reasonably achievable" (ALARA), while not compromising image quality, especially in pediatric imaging [9].

EOS (EOS Imaging, Paris, France) is a relatively novel low-dose imaging system that is capable of producing radiographic images with very low radiation exposure [10]. It exploits a biplanar slot-scanning technology that employs highly sensitive gaseous photon detectors [11–13]. It consists of a cabin in which the patient is positioned standing erect, and the two linear X-ray sources and two gaseous detector arrays allow for the patient to be scanned in two orthogonal planes simultaneously. The X-ray sources move in synchronous fashion so that the beam is always horizontal to the patient, thus avoiding the magnification error (the so-called "parallax effect") of teleradiography. Once acquisition parameters have been set on the basis of three predefined morphotypes, the scan can start. The scan has a variable duration of up to twenty seconds, making this modality sensitive to motion artifacts. However, the acquisition can be shortened, further minimizing the dose with minimal reduction of image quality [14].

In general, the EOS system is excellent in the evaluation of biomechanical alignment of the spine and of the lower limbs, while it is not routinely used in the evaluation of focal bone lesions. Indeed, the diagnostic accuracy of the EOS system to identify and measure bone tumors has not been investigated previously. Moreover, the reduction of dose obtained by the EOS system has been established. Nevertheless, this exam can be acquired with different speeds, which are associated with different radiation doses and image quality, but a comparison of radiation doses of different sets of EOS images and conventional radiography to image the whole skeletal system has not been previously reported. The rationale for conducting this study was the lack of data concerning the potential use of this low-dose imaging examination to follow patients with multifocal bone lesions, namely enchondromatosis, in order to decrease the radiation burden on young patients affected by these conditions but providing images with enough quality to be used for oncologic purposes. Thus, the objective of this study was to compare radiation doses and the capability of the EOS imaging system with those of conventional radiography and computed tomography (CT) to detect and measure enchondromas in a dedicated phantom.

2. Materials and Methods

2.1. Study Design

Institutional review board approval was not needed since no humans were involved in the present study. This report is concerned with the comparison of radiation doses and the capability of the EOS imaging system, a conventional radiographic system, and a CT system to detect and measure enchondromas in a dedicated five-year-old anthropomorphic phantom (ATOM Dosimetry Verification Phantom, Model 705; pediatric 5 years; height = 110 cm; weight = 19 kg; physical density = 1.52 g/cm^3; electron density = 4.801×10^{23}). This phantom is routinely used to perform radiation dose measurements. To simulate enchondromas, minced pieces of chicken bone and cartilage were packed in conventional kitchen plastic foil to create ovoidal/rounded masses. The inserts had a shortest diameter ranging from 1.3 cm to 3.8 cm and a longest diameter ranging from 2 cm to

4.9 cm. They were randomly hung on the phantom anteriorly, posteriorly, and laterally to simulate a real irregular disposition of multiple enchondromas. The phantom was imaged with the use of conventional radiography, CT, and EOS radiographic imaging. Anteroposterior (AP) and laterolateral (LL) conventional radiography and EOS images, as well as CT scans, were performed five times. Each time the number and position of inserts were changed, hanging 3, 6, 9, 16, and 17 inserts on the phantom, respectively. The phantom was configured by a physicist who was then not involved in image analysis.

2.2. Conventional Radiography

Full-length long radiographs of the phantom were made with direct digital acquisition using a Siemens Ysio Max X-ray machine (Siemens AG, Erlangen, Germany) and a Fuji imaging machine (FujiFilm, Stamford, CT) (35.4 × 124.5 cm) behind a standard bucky grid. The phantom was secured to an Octostop immobilizer (Octostop, QC, Canada) with Velcro straps in a vertical orientation and was positioned directly in front of the grid and cassette with the front of the phantom directed anteriorly toward the X-ray source. The X-ray parameters were set automatically by the system.

2.3. Computed Tomography

The phantom was positioned in the center of a 64-slice Siemens CT scanner (Definition AS+, Siemens Healthcare, Forchheim, Germany). The phantom was subjected to a whole-body CT scan from head to feet with the following acquisition parameters: 120 kV; 60 mA; slice thickness 1 mm; pitch 0.8.

2.4. EOS

Different sets of radiographs were made with the EOS scanner. The phantom was fixed with Velcro straps to an Octostop immobilizer and was placed with a vertical orientation in the scanning chamber. The phantom was aligned with laser-light markings to ensure that the anterior side was oriented anteriorly and in the center of the scanning field.

For radiation dose evaluation, three sets of imaging parameters (with 200 mA, 83 kV for AP images and 102 kV for LL images) were used: (1) a slow setting (speed setting 4, 7.6 cm/s), (2) a medium setting (speed setting 3, 11.4 cm/s), and (3) a fast ultralow-dose setting (speed setting 2, 15.2 cm/s). For each configuration of the inserts (i.e., 3, 6, 9, 16, and 17 inserts) and for each set of image parameters, one AP and one LL view were acquired. Thus, a total of 15 AP and 15 LL images of the phantom were acquired, with the phantom being removed and repositioned after each image was made. Only EOS-Fast images were reviewed to detect and to measure the enchondromas-like inserts, while EOS-Medium and EOS-Slow images were used to compare the radiation doses of the different sets of images.

2.5. Image Analysis

All images were downloaded to a picture-archiving and communication system (Andra, Stockholm, Sweden). A radiologist with more than five years of experience in musculoskeletal radiology and research and a radiology resident reviewed the images in a random order and blinded to the number of inserts and type of scan (for EOS images). The number of inserts visible on each image was counted and their size was measured using an electronic caliper.

2.6. Statistical Analysis

The continuous variables are reported as means ± standard deviations. Intermodality and interobserver reproducibility were tested by using the Bland–Altman method [15]. The radiation doses in terms of Kerma-area product (KAP) [16], calculated from both conventional radiography and EOS system examinations, are reported as medians ± interquartile ranges, and differences were analyzed using the Mann–Whitney U test. A p-value less than 0.05 was considered statistically significant,

where appropriate [17]. Statistical analysis was performed using SPSS software (v. 25, IBM, Armonk, NY, USA).

3. Results

3.1. Diagnostic Accuracy

Seventeen different inserts were used for this experiment, whose dimensions ranged from 20 × 14 mm to 49 × 34 mm.

The two different readers measured the longest insert length, with both EOS and conventional radiography obtaining values ranging from 7 mm to 40 mm with the EOS system and from 6 mm to 36 mm with conventional radiography. Both conventional radiography and EOS underestimated the true length of the inserts by an average of 6.6 mm (25.2%) and 6.1 mm (23.9%), respectively, when compared with the true length of a respective insert on its longest axis. The comparison of the mean difference between the measurements for both modalities and the true length is reported in Table 1.

Table 1. Insert length measurements with EOS and CR.

	EOS Imaging System	Conventional Radiography
Difference from true length of phantom inserts (mm) *	−6.1 (from −18 to +1)	−6.6 (from −19 to +1.5)
Relative magnification **	−23.9%	−25.2%

* The values indicate the difference from the true length of the phantom inserts as provided by the manufacturer and are expressed as the mean, with the range in parentheses. ** The relative magnification was derived by dividing the difference between the measured length and the true length by the true length.

Both observers were able to detect the same number of inserts per phantom on EOS and conventional radiography: This was equal to the number of inserts placed on the phantom in 4/5 cases (80%), while in one case, 1 out of 17 inserts was not seen. On CT, both observers always detected the correct number of inserts, as compared to the real number (Table 2).

Table 2. Number of inserts detected per phantom on the three imaging modalities by two different observers who reviewed all images independently.

	Observer 1			Observer 2		
Phantom	**n. Inserts CT**	**n. Inserts EOS**	**n. Inserts CR**	**n. Inserts CT**	**n. Inserts EOS**	**n. Inserts CR**
# 1	16	16	16	16	16	16
# 2	17	16	16	17	16	16
# 3	3	3	3	3	3	3
# 4	6	6	6	6	6	6
# 5	9	9	9	9	9	9
Total	51	50	50	51	50	50

Intermodality reliability, quantified as the mean of the difference between the two modalities' measurements (bias) and the repeatability coefficient (CoR), showed excellent agreement for EOS, conventional radiography, and CT with a bias calculated to be 0.14 mm (88% reproducibility; CoR 2.9; 95% CI from −2.8 to 3.1 mm; $p = 0.5$) and 0.15 mm (81% reproducibility; CoR 5.2; 95% CI from −5.5 to 5.2 mm; $p = 0.7$) when comparing EOS to conventional radiography and CT, respectively. The assessment of interobserver reliability in the EOS modality showed 71% reproducibility between different observers, with a bias as low as 0.6 mm (CoR 7.2; 95% CI from −6.6 to 7.8 mm; $p = 0.25$) (Figure 1).

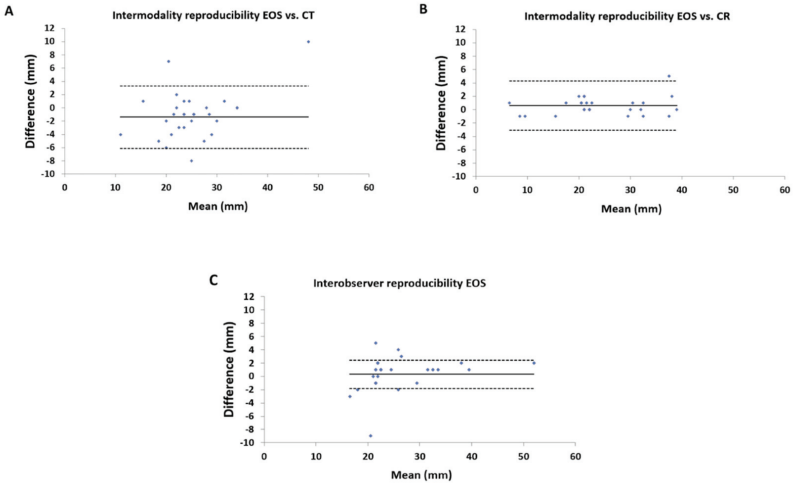

Figure 1. Intermodality and interobserver reliability of insert length measurements among different modalities and among different observers: (**A**) Intermodality reliability between EOS imaging system and computed tomography (CT) scanning. The mean of the measurements obtained with EOS and CT for each insert is reported on the x-axis; the difference between the two measurements is reported on the y-axis. (**B**) Intermodality reliability between the EOS imaging system and conventional X-ray. The mean of the measurements obtained with EOS and X-ray for each insert is reported on the x-axis; the difference between the two measurements is reported on y-axis. (**C**) Interobserver reliability between measurements obtained by two different observers with the EOS imaging system. The mean of the measurements is reported on the x-axis; the difference between them is reported on the y-axis.

3.2. Radiation Dose

By applying different image scanning speeds, the radiation dose delivered was progressively and significantly lower for the EOS-Fast protocol (KAP 258.6 mGy cm^2) compared with the EOS-Medium protocol (KAP 387.89 mGy cm^2, $p < 0.001$), and even more when compared with the EOS-Slow protocol (KAP 517.19 mGy cm^2, $p < 0.001$) (Figure 2). Moreover, the EOS-Fast radiation dose was also significantly lower than the median radiation dose of conventional radiographs (644.7 (599.4–651.97) mGy cm^2, $p = 0.004$) for all phantom configurations (Figure 3). Figure 4 shows a case from this study.

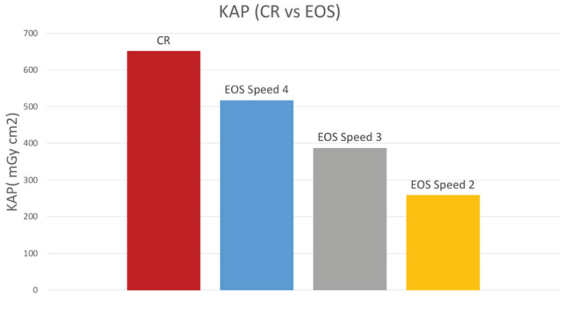

Figure 2. Bar graph illustrating the mean radiation dose by modality. CR = conventional radiographs and EOS = EOS imaging system at three different speed settings (speed 2 = 15.2 cm/s; speed 3 = 11.4 cm/s; speed 4 = 7.6 cm/s).

		KAP (mGy cm²)	
Configuration	EOS Speed	EOS	CR
1	4	517.19	402.2
	3	387.89	
	2	258.6	
2	4	517.19	261.8
	3	387.89	
	2	258.6	
3	4	517.19	599.4
	3	387.89	
	2	258.6	
4	4	517.19	654.4
	3	387.89	
	2	258.6	
5	4	517.19	644.7
	3	387.89	
	2	258.6	

Figure 3. Radiation doses delivered by the EOS-Fast (speed 2), EOS-Medium (speed 3), and EOS-Slow (speed 4) protocols, and CR examinations.

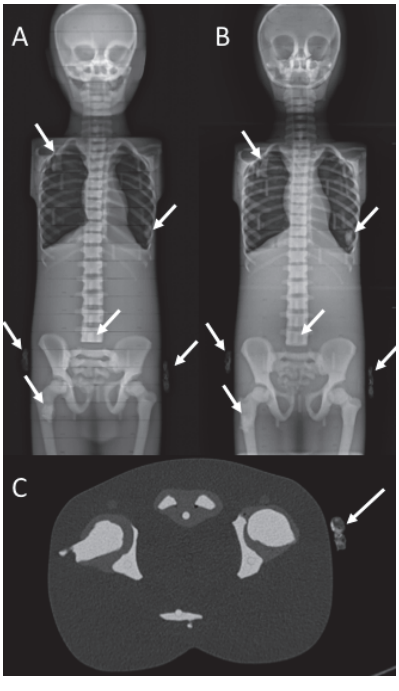

Figure 4. EOS (**A**), CR (**B**), and CT (**C**) images of a phantom with six inserts (arrows).

4. Discussion

The results from this study indicate that EOS performs similarly to conventional radiography in both number detection and length evaluation of enchondroma-like inserts in a standardized phantom setting. The mean difference between insert length assessed with EOS and conventional radiograph, and their true length was in fact as low as 6.1 mm and 6.6 mm, respectively. However, it should be underlined that an underestimation of the insert size was expected, in view of the bidimensional imaging provided by both techniques that does not make a precise identification of the longest diameter

of the inserts possible. Notably, these results were obtained by testing the capability of the reviewers to detect and measure the enchondroma-like inserts on EOS fast-speed images, which should present minimal reduction of image quality when compared with the other sets of EOS images.

The intermodality reliabilities of EOS imaging, conventional radiography, and CT were also excellent, which is essential when dealing with a new diagnostic test not yet used in the clinical routine [18]. Moreover, perfect agreement of measurements performed by different observers with the EOS system was observed, thus demonstrating that EOS is both accurate and reproducible. There was only a single case where the number of inserts was different between conventional radiography and EOS versus CT and the actual number of inserts placed on the phantom. In this case, two inserts were placed very close to one another. Thus, the bidimensional images of conventional radiography and EOS showed them almost superimposed on one another, making the distinction almost impossible.

This study also demonstrates that, since radiation dose is inversely related to scanning speed, you can impact the radiation dose administered by the EOS system by changing the speed of the image-acquisition parameters. Indeed, doubling the speed from EOS-Slow (7.6 cm/s) to EOS-Fast (15.2 cm/s), the radiation dose decreased from 517.19 mGy cm^2 to 258.6 mGy cm^2 without affecting the capability of observers to detect and measure the inserts on the phantom. These data lead us to consider EOS as a potential imaging tool technique for detecting and following enchondromas over time, while minimizing radiation exposure. A drawback of EOS to consider is the increased risk of motion artifacts related to the fact that EOS is performed with the patient in a standing position and the acquisition time at a speed setting of 4 is about 8 s. This should be considered especially in pediatric patients who are particularly prone to movement during a scan. This limitation can be partly overcome, given that image-acquisition time can be decreased to three to four seconds (on the EOS-Fast speed setting of 2) without affecting the capability of observers to detect and measure the inserts on a phantom.

In the future, we may envision a clinical setting where initial evaluation of enchondromas is performed using conventional radiography and follow-up is performed using EOS. In case of a change in the number and size of enchondromas, a standard workup should then be resumed. Clearly, one limitation of this approach is that EOS is not a widely available imaging modality.

A limitation of this work is that the image quality of conventional radiography was not compared with that of EOS at different acquisition speeds. It is known that EOS is very good in assessing spine and limb orientation, but, especially at higher speeds, image quality may also decrease in favor of radiation dose reduction. However, the excellent results of this study were obtained by testing the capability of the reviewers to detect and measure the enchondroma-like inserts on EOS fast-speed images, which should have had reduced image quality when compared with the other sets of EOS images. Also, the enchondroma-like inserts were attached on the external surface (i.e., the "skin") of the phantom, which is not exactly what happens in enchondromatosis. However, this was the best approximation possible, as the anthropomorphic phantom is not empty and lesions cannot be placed inside its body.

In conclusion, low-dose EOS digital radiographic evaluation has the same capability as conventional radiography to detect and measure enchondroma-like inserts on a phantom. Thanks to its lower radiation dose, this method may be considered in the follow-up of patients with multiple enchondromas. However, clinical studies are warranted to confirm these preliminary results on a phantom.

Author Contributions: Conceptualization, D.A., A.d.V., and L.M.S.; methodology, D.A., C.M., A.L, A.d.V., and L.M.S.; formal analysis, D.A., C.F., A.B., C.M., and L.M.S.; investigation, D.A. and A.B.; data curation, D.A., A.L., A.B., C.F., and L.M.S.; writing—original draft preparation, D.A. and C.F.; writing—review and editing, C.M., A.L., A.d.V., and L.M.S.; supervision, L.M.S. All authors have read and agreed to the published version of the manuscript.

Funding: This research received no external funding.

Conflicts of Interest: The authors declare no conflict of interest.

References

1. Albano, D.; Messina, C.; Gitto, S.; Papakonstantinou, O.; Sconfienza, L.M. Differential Diagnosis of Spine Tumors: My Favorite Mistake. *Semin. Musculoskelet. Radiol.* **2019**, *23*, 26–35. [CrossRef] [PubMed]
2. Gitto, S.; Cuocolo, R.; Albano, D.; Chianca, V.; Messina, C.; Gambino, A.; Ugga, L.; Cortese, M.C.; Lazzara, A.; Ricci, D.; et al. MRI radiomics-based machine-learning classification of bone chondrosarcoma. *Eur. J. Radiol.* **2020**, *128*, 109043. [CrossRef] [PubMed]
3. Maroteaux, P.; Le Merrer, M. *Les Maladies Osseuses de L'enfant*; Médecine-Sciences Flammarion: Paris, France, 2002.
4. Unni, K.K. Cartilaginous lesions of bone. *J. Orthop. Sci.* **2001**, *6*, 457–472. [CrossRef] [PubMed]
5. Whyte, M. Acquired disorders of cartilage and bone. *Am. Soc. Bone Miner. Res.* **2003**.
6. Fletcher, C.D.M.; Unni, K.K.; Mertens, F. *Pathology and Genetics of Tumours of Soft Tissue and Bone*; Iarc: Lyon, France, 2002; Volume 4.
7. Hopyan, S.; Gokgoz, N.; Poon, R.; Gensure, R.C.; Yu, C.; Cole, W.G.; Bell, R.S.; Jüppner, H.; Andrulis, I.L.; Wunder, J.S.; et al. A mutant PTH/PTHrP type I receptor in enchondromatosis. *Nat. Genet.* **2002**, *30*, 306–310. [CrossRef] [PubMed]
8. Strauss, K.J.; Kaste, S.C. ALARA in pediatric interventional and fluoroscopic imaging: Striving to keep radiation doses as low as possible during fluoroscopy of pediatric patients—A white paper executive summary. *J. Am. Coll. Radiol.* **2006**, *3*, 686–688. [CrossRef] [PubMed]
9. The 2007 Recommendations of the International Commission on Radiological Protection. ICRP publication 103. *Ann. ICRP* **2007**, *37*, 1–332.
10. Melhem, E.; Assi, A.; El Rachkidi, R.; Ghanem, I. EOS((R)) biplanar X-ray imaging: Concept, developments, benefits, and limitations. *J. Child. Orthop.* **2016**, *10*, 1–14. [CrossRef] [PubMed]
11. Dubousset, J.; Charpak, G.; Dorion, I.; Skalli, W.; Lavaste, F.; Deguise, J.; Kalifa, G.; Ferey, S. A new 2D and 3D imaging approach to musculoskeletal physiology and pathology with low-dose radiation and the standing position: The EOS system. *Bull. Acad. Natl. Med.* **2005**, *189*, 287–300. [PubMed]
12. Dubousset, J.; Charpak, G.; Skalli, W.; Kalifa, G.; Lazennec, J.-Y. EOS stereo-radiography system: Whole-body simultaneous anteroposterior and lateral radiographs with very low radiation dose. *Revue de Chirurgie Orthopedique et Reparatrice de L'appareil Moteur* **2007**, *93*, 141–143. [CrossRef]
13. Albano, D.; Messina, C.; Gambino, A.; Gurgitano, M.; Sciabica, C.; Oliveira Pavan, G.R.; Gitto, S.; Sconfienza, L.M. Segmented lordotic angles to assess lumbosacral transitional vertebra on EOS. *Eur. Spine J.* **2020**, *29*, 2470–2476. [CrossRef] [PubMed]
14. Deschenes, S.; Charron, G.; Beaudoin, G.; Labelle, H.; Dubois, J.; Miron, M.C.; Parent, S. Diagnostic imaging of spinal deformities: Reducing patients radiation dose with a new slot-scanning X-ray imager. *Spine* **2010**, *35*, 989–994. [CrossRef] [PubMed]
15. Bland, J.M.; Altman, D.G. Statistical methods for assessing agreement between two methods of clinical measurement. *Lancet* **1986**, *1*, 307–310. [CrossRef]
16. Huda, W. Kerma-area product in diagnostic radiology. *AJR. Am. J. Roentgenol.* **2014**, *203*, W565–W569. [CrossRef] [PubMed]
17. Di Leo, G.; Sardanelli, F. Statistical significance: P value, 0.05 threshold, and applications to radiomics-reasons for a conservative approach. *Eur. Radiol. Exp.* **2020**, *4*, 18. [CrossRef] [PubMed]
18. Albano, D.; Martinelli, N.; Bianchi, A.; Giacalone, A.; Sconfienza, L.M. Evaluation of reproducibility of the MOCART score in patients with osteochondral lesions of the talus repaired using the autologous matrix-induced chondrogenesis technique. *Radiol. Med.* **2017**, *122*, 909–917. [CrossRef] [PubMed]

applied sciences

MDPI

Article

Evaluation of Organ Dose and Image Quality Metrics of Pediatric CT Chest-Abdomen-Pelvis (CAP) Examination: An Anthropomorphic Phantom Study

Nor Azura Muhammad [1], Zunaide Kayun [1], Hasyma Abu Hassan [2], Jeannie Hsiu Ding Wong [3], Kwan Hoong Ng [3] and Muhammad Khalis Abdul Karim [1,*]

[1] Department of Physics, Faculty of Science, University Putra Malaysia, Serdang 43400, Malaysia; norazura11@gmail.com (N.A.M.); zunaide@moh.gov.my (Z.K.)
[2] Department of Radiology, Faculty of Medicine, University Putra Malaysia, Serdang 43400, Malaysia; hasyma@upm.edu.my
[3] Department of Biomedical Imaging, University Malaya Medical Centre, Petaling Jaya 59100, Kuala Lumpur, Malaysia; jeannie.wong@ummc.edu.my (J.H.D.W.); ngkh@ummc.edu.my (K.H.N.)
* Correspondence: mkhalis@upm.edu.my

Featured Application: We evaluate and propose a method for evaluating optimized CT protocol for pediatric-based figure of merit and image performance metrics.

Abstract: The aim of this study is to investigate the impact of CT acquisition parameter setting on organ dose and its influence on image quality metrics in pediatric phantom during CT examination. The study was performed on 64-slice multidetector CT scanner (MDCT) Siemens Definition AS (Siemens Sector Healthcare, Forchheim, Germany) using various CT CAP protocols (P1–P9). Tube potential for P1, P2, and P3 protocols were fixed at 100 kVp while P4, P5, and P6 were fixed at 80 kVp with used of various reference noise values. P7, P8, and P9 were the modification of P1 with changes on slice collimation, pitch factor, and tube current modulation (TCM), respectively. TLD-100 chips were inserted into the phantom slab number 7, 9, 10, 12, 13, and 14 to represent thyroid, lung, liver, stomach, gonads, and skin, respectively. The image quality metrics, signal to noise ratio (SNR) and contrast to noise ratio (CNR) values were obtained from the CT console. As a result, this study indicates a potential reduction in the absorbed dose up to 20% to 50% along with reducing tube voltage, tube current, and increasing the slice collimation. There is no significant difference ($p > 0.05$) observed between the protocols and image metrics.

Keywords: computed tomography; absorbed dose; signal–noise ratio; contrast–noise ratio; figure of merit

Citation: Muhammad, N.A.; Kayun, Z.; Abu Hassan, H.; Wong, J.H.D.; Ng, K.H.; Karim, M.K.A. Evaluation of Organ Dose and Image Quality Metrics of Pediatric CT Chest-Abdomen-Pelvis (CAP) Examination: An Anthropomorphic Phantom Study. *Appl. Sci.* **2021**, *11*, 2047. https://doi.org/10.3390/app11052047

Academic Editor: Salvatore Gallo

Received: 25 January 2021
Accepted: 11 February 2021
Published: 25 February 2021

1. Introduction

The transformation and sophistication of the computed tomography (CT) system have led to the increased use of CT examinations. The development of CT technology begins from the single detector and now the multidetector CT (MDCT) able to produce high contrast sectional images in short scanning time [1,2]. Recent advances in the technological breakthrough of CT scan performance, such as application of automatic tube current modulation (ATCM) and utilization of iterative reconstruction algorithm technique, have decreased CT radiation exposure while retaining diagnostic image consistency [3–5].

The imaging of pediatric CT examination is still challenging even though the performance and technology of the latest generation of CT scanners have been introduced. Recently, with growing involvement in radiation-induced cancer, this debate is again in the spotlight, as radiation exposure optimization is a particular problem in pediatric patients receiving repeated CT examination [6–8]. Despite the high frequency of CT procedure

usage amongst children, radiation burden from CT examination needs to be considered as children are more sensitive to radiation as compared to adults [9,10]. Since 2007, the American College of Radiology (ACR), the Society for Pediatric Radiology (SPR), the American Association of Physicists in Medicine (AAPM), and the American Society of Radiology Technologists (ASRT) have engaged in the Image Gently campaign in the United States to grow the knowledge of practice by increasing awareness among radiation personnel [11,12].

Generally, the radiation-absorbed dose can be measured by inserting a passive dosimeter inside anthropomorphic phantom as it is the accurate way to measure the radiation absorbed by radiosensitive organs or tissues of patients [13–15]. Likewise, Monte Carlo estimation on computational phantom, such as CT-Expo (Version 2.3.1, Hannover, Germany), is able to estimate an organ-absorbed dose and effective dose based on the subject's age and gender [16–18]. In addition, multiplying organ-absorbed dose with tissue weighting factor as stated in the International Commission on Radiological. Protection (ICRP 103) can also be used to calculate the value of effective dose which is an important radiation metric for the estimation of cancer risk of individual patients [19,20].

CT chest-abdominal pelvis (CAP) examination is generally used to evaluate the anatomy structures and to diagnose the degree of malignancies in lungs, liver, pelvic organ, lymphatic nodules, and bony structures. According to Park et al. [21], CT CAP examination was performed purposely for the cancer staging. The mean effective dose of pediatric CT CAP examination was ranging from 3.4 to 7.5 mSv between one year and five years of age [22,23]. Hence, pediatric patients who require CT CAP scans due to their health problems may have an elevated chance of cancer because children are more vulnerable to radiation effects than adults [24]. CT dose reduction protocols have been developed amongst researchers and a variety of strategies have been established to minimize CT dose without compromising diagnostic image quality [25–27]. These include reducing tube current (mAs) and tube voltage (kVp), automatic attenuation-based tube current selection, decreased pitch factor, increased slice collimation and improper positioning [28,29]. Several researchers have proposed CT dose reduction by increasing the pitch value combined with the iterative reconstruction method to obtain significant dose reduction of the normal chest and abdominal scans while preserving the consistency of the image quality [28,30,31].

The vigorous action by the institution in setting the best optimization protocols, particularly for pediatric patients, is an indispensable part in reducing dose exposure in CT examination. Therefore, the study highlights the current finding in optimizing radiation doses from altering pediatric CT CAP scan parameters in terms of tube voltage, tube current, slice collimation, pitch, and effect of tube current modulation (TCM) application, as well as the effect on image quality indices in regard of image noise, signal to noise ratio (SNR), and contrast to noise ratio (CNR).

2. Materials and Methods

This study utilized 1 y/o anthropomorphic phantom (ATOM, 704 model CIRS, Norfolk, VA, USA). The body weight, height and thorax dimension of the phantom were 10 kg, 75 cm, and 12 × 14 cm, respectively. This phantom was made from tissue equivalent material, which consisted of the lung, soft, and bone tissue. The phantom was made up of 28 slabs with 2.5 cm slice thickness, which cover from head to lower leg and each slab contains a hole about 5.0 mm in diameter for inserting dosimeter, such as TLD, to measure the absorbed dose at the specific area of sensitive organs and for the simulation study of a blood vessel filling with contrast material, as shown in Figure 1.

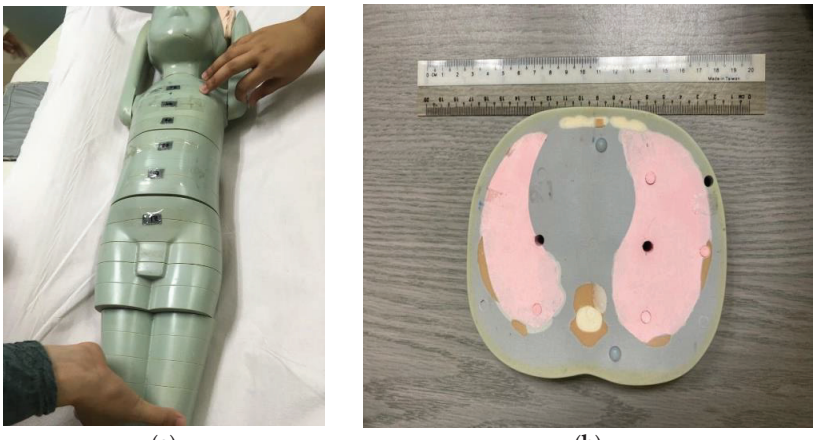

(**a**) (**b**)

Figure 1. (**a**) One-year-old anthropomorphic phantom was set up before the scan. (**b**) The anthropomorphic lung tissue slab comprises a-holes matrix about 5.0 mm in diameter for dosimeter insertion, such as TLD.

The CT CAP examination was performed on 64 slices using a multidetector CT scanner (MDCT) Siemens Definition AS (Siemens Sector Healthcare, Forchheim, Germany) by applying nine different CT protocols (P1 to P9). The tube potential of P1, P2, and P3 were fixed at 100 kVp and P4, P5, and P6 were fixed at 80 kVp with various tube current reference values (ref. mAs: 210, 180, and 150), while in P7, P8, and P9 the modification was made on P1 with changes on slice collimation, pitch factor, and tube current modulation (TCM), respectively. The details of the CT acquisition parameter used in this study were shown in Table 1. The scan range starts from 1 cm above the apex of lungs and ends at 1 cm below symphysis pubis with a total length of 32 cm for all protocols involved. The source to detector (SDD) and source to object distance (SOD) used in this study were 100 cm and 50 cm, respectively.

Table 1. Routine and modified CT CAP acquisition parameters used in this study.

Parameter	Protocols								
	P1	**P2**	**P3**	**P4**	**P5**	**P6**	**P7**	**P8**	**P9**
Slice thickness recon (mm)	3	3	3	3	3	3	3	3	3
Tube potential (kVp)	100	100	100	80	80	80	100	100	100
Effective tube current (mAs)	27	23	19	33	31	26	27	26	-
Ref. mAs	210	180	150	210	180	150	210	210	210
Number of detector	64	64	64	64	64	64	32	64	64
Slice collimation (mm)	0.6	0.6	0.6	0.6	0.6	0.6	1.2	0.6	0.6
Pitch	1.4	1.4	1.4	1.4	1.4	1.4	1.4	1.2	1.4
Dose Modulation	On	On	On	On	On	On	On	On	Off
Table Feed	53.8	53.8	53.8	53.8	53.8	53.8	53.8	56.0	53.8
Exposure time (s)	0.5	0.5	0.5	0.5	0.5	0.5	0.5	0.5	0.5
Kernel filtration	B30f	B30f	B30f	B30f	B30f	B30f	B30f	B30f	B30f
$CTDI_{vol}$ (mGy)	1.8	1.5	1.3	1.0	0.9	0.8	1.7	1.7	6.9
DLP (mGy.cm)	58	48	42	32	29	26	54	54	221
E (DLP x *k* factor)	1.6	1.3	1.2	0.9	0.8	0.7	1.5	1.5	6.2

2.1. CT Radiation Dose

Dose data, such as volume weighted CT Dose Index ($CTDI_{vol}$) and dose length product (DLP), were collected from the CT console. $CTDI_{vol}$ is the most established radiation metric for CT and considered an important value for quality assurance. $CTDI_{vol}$ is defined as:

$$CTDI_{vol} = \frac{CTDI_w}{\text{pitch factor}} \quad (1)$$

where $CTDI_w$ is the weighted average dose across a single slice and pitch is the distance of the table moving in one 360° gantry rotation. DLP is calculated by multiplying the scan range of the patients with the $CTDI_{vol}$, and it represents the overall dose output along the z-axis. Furthermore, the effective dose (E) is estimated by multiplying the DLP with a conversion coefficient factor (CC) [13].

The organ dose of the phantom was measured by using TLD-100 (LiF: Mg, Ti) with dimensions of 3.2 × 3.2 × 0.6 mm. TLD-100 is the common passive dosimeter used in the measurement of radiation dose due to high sensitivity and response to the photon of X-ray. A total of 55 TLD-100 were used in this study and calibrated and compared with standard ionization chamber. The calibration process should be done to obtain a conversion factor (CF) in each TLD-100. Nine TLD-100 were used to measure background radiation. The CF was computed based on the equation:

$$CF = \frac{Q_{rad}}{\left(M - M_{background} - C_{background}\right)} \quad (2)$$

where Q_{rad} is energy photons from X-ray beam, M is the result of the Harshaw TLD reader, $M_{background}$ is the background reading from TLD reader, and $C_{background}$ is the background reading from TLD-100.

All the TLD-100 were read out using a Harshaw 3500 TLD reader (Thermo Scientific, Waltham, MA, USA), combined with an operating software for all Harshaw TLD reader known as WinREMS after 24-h exposure. Before reuse, the TLD-100 chips were annealed using an oven (TLD annealing oven, PTW, Freiburg, Germany) for 1 h at 400 °C and 2 h at 100 °C followed by rapid cooling to make the TLD chips reusable. All the TLD-100 kept inside labeled plastic and sealed before inserting into the hole of the phantom. In this study, four TLD chips were inserted into the phantom slab no 9, 12, and 14 to represent lung, liver, and stomach, three TLD were inserted into slab no 7 and 19 to represent thyroid and gonads, and five TLD was placed on top of the phantom at the area of the thorax (slab number 8 and 11), abdomen (slab number 12 and 13), and pelvis (slab number 18) for the skin dose measurement.

2.2. Image Quality Metrics

The image quality was assessed by using Radiant DICOM Viewer software (Medixant, Poznan, Poland) to extract CT numbers and noise values from each protocol by placing the circular region of interest (ROI) about 0.8 cm^2 in the selected image (Figure 2). The information regarding CT numbers and noise was used to calculate the signal to noise ratio (SNR) and contrast to noise ratio (CNR). The SNR was calculated by dividing the mean (CT number) by the corresponding standard deviation, SD (noise value) as shown in the equation below:

$$SNR = \frac{mean_{ROI}}{SD_{ROI}} \quad (3)$$

Furthermore, the CNR were measured by using the equation below:

$$NR = \frac{|mean_{ROI} - mean_{BG}|}{\frac{SD_{ROI}+SD_{BG}}{2}} \quad (4)$$

where the $mean_{BG}$ and SD_{BG} is CT number value of background and noise value of the background, respectively. We quantify the dose information to correlate with the CT image quality. The figure-of-merit (FOM) was used to characterize the radiation dose trade-off with image quality by considering all the image parameters. In this study, the FOM values represent the efficiency between SNR and $CTDI_{vol}$ with different CT CAP protocols and they can be calculated with the equation below:

$$FOM = \frac{SNR^2}{CTDI_{vol}} \quad (5)$$

Besides SNR, CNR also can be used to calculate the FOM with the $CTDI_{vol}$ parameter. The FOM allows SNR to be evaluated independently of the current tube and the dose of radiation. However, as it is determined for a specific scan mode (helical or axial) and a specific diagnostic task, it should not be used, for example, when comparing head and abdomen imaging, to compare different scanned areas of diagnostic tasks [22].

Data were analyzed using IBM SPSS V25.0 (SPSS, version 25.0 for Windows, Chicago, IL, USA). The data of organ-absorbed dose were presented as mean value with standard deviation (SD). One-way ANOVA with post-hoc Dunnett test was used to analyze the significant value of organ-absorbed dose and image quality between default protocol 1 (P1) with other modified protocols CT CAP. A p-value < 0.05 was considered statistically different.

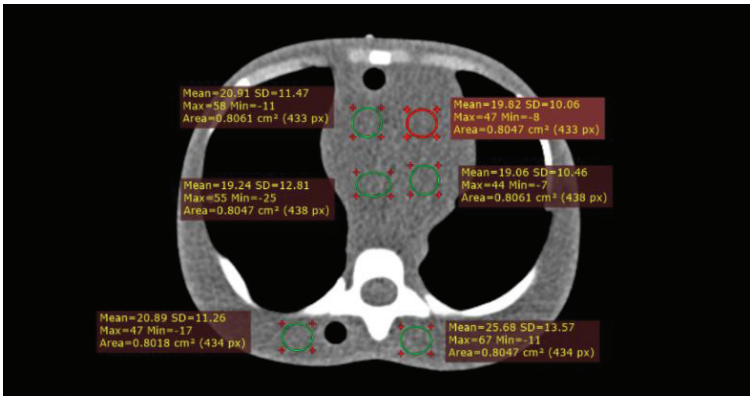

Figure 2. Example of objective image quality analysis of CT number (mean), image noise (SD), SNR, and CNR by putting the region of interest (ROI) in the lungs and soft tissue field.

3. Results

3.1. Organ Equivalent Dose

Table 2 summarized the organ equivalent dose for the selected organs in protocols P1–P6. As observed, the highest organ-absorbed dose was found in the liver and the lowest was presented in the thyroid for 100 kVp with a mean value of 1.22 ± 0.13 mSv (P1) and 0.31 ± 0.07 mSv (P3), respectively. However, for 80 kVp, the highest organ-absorbed dose was found in the stomach compared to the other organs with a mean value of 0.72 ± 0.01 mSv. Figure 3 presents the mean organ equivalent doses of standard pediatric CT CAP examinations with varying tube potential and tube current. As a result, the value of doses reduced as tube voltage and tube current decrease in P2 to P6. In comparison between 100 and 80 kVp, the results of organ-absorbed dose were decreased with the reduction of tube voltage. Overall, this study found that the organ dose measurements in thyroid, lungs, liver, stomach, gonads, and skin were reduced by almost 50% with lessening tube voltage from 100 to 80 kVp.

Table 2. Organ Equivalent Dose from TLD measurement between 100 and 80 kVp with variation ref. mAs.

Selected Organ	Organ Equivalent Dose (mSv)					
	100 kVp			80 kVp		
	P1 (Ref. mAs 210)	P2 (Ref. mAs 180)	P3 (Ref. mAs 150)	P4 (Ref. mAs 210)	P5 (Ref. mAs 180)	P6 (Ref. mAs 150)
Thyroid	0.49 ± 0.03	0.41 ± 0.05	0.31 ± 0.07	0.24 ± 0.16	0.22 ±0.16	0.20 ± 0.17
Lungs	0.88 ± 0.12	0.74 ± 0.06	0.58 ± 0.06	0.51 ± 0.04	0.37 ±0.09	0.35 ± 0.05
Liver	1.22 ± 0.13	0.95 ± 0.06	0.83 ± 0.06	0.53 ± 0.15	0.46 ± 0.12	0.39 ± 0.08
Stomach	1.05 ± 0.03	0.95 ± 0.09	0.82 ± 0.07	0.72 ± 0.01	0.62 ± 0.04	0.56 ± 0.04
Gonads	0.87 ± 0.02	0.75 ± 0.03	0.64 ± 0.06	0.43 ± 0.02	0.40 ± 0.01	0.34 ± 0.02
Skin	1.07 ± 0.14	0.90 ± 0.16	0.68 ± 0.24	0.59 ± 0.14	0.48 ± 0.17	0.32 ± 0.16

Table 2 and Figure 3 present the impact of standard protocol, tube voltage, and tube current on organ equivalent dose during the examination. Table 3 summarizes the influence of increased slice collimation (P7), reduced pitch factor (P8), and disabling the TCM function (P9) on organ dose. The doses were slightly reduced when slice collimation was increased. However, by reducing the pitch value, the organ dose was slightly increased. Furthermore, the organ equivalent dose was increased by more than 50% in P9 after disabling the TCM function. Figure 4 shows the highest organ dose was observed in the liver followed by skin, stomach, lungs, gonads, and thyroid in all protocols. The highest organ dose was detected in P9. Therefore, the application of TCM in pediatric patients offers a big consequence in CT radiation dose due to different in-patient body habitus and thickness.

3.2. Analysis of Image Quality Metrics

The image quality metrics were obtained to compare with the dose information. The mean of image quality indices of CT number, noise, SNR, and CNR were summarized in Table 4. The reduced tube voltage and tube current lead to an increase in image noise. Noting that the highest mean of noise was 13.1 ± 0.6 HU presented in P6. There is no significant difference of CNR in P4 and P6 after reducing the tube voltage from 100 to 80 kVp. However, reducing tube voltage in P4, P5, and P6 resulting in significant differences ($p < 0.05$) of SNR value. The highest mean of SNR and CNR in P9 (disabling TCM) was 6.66 ± 0.5 HU and 1.34 ± 0.2 HU, respectively, and the organ dose in P9 protocol were among the highest. Thus, the highest FOM value was obtained in P9, followed by P7 and P2.

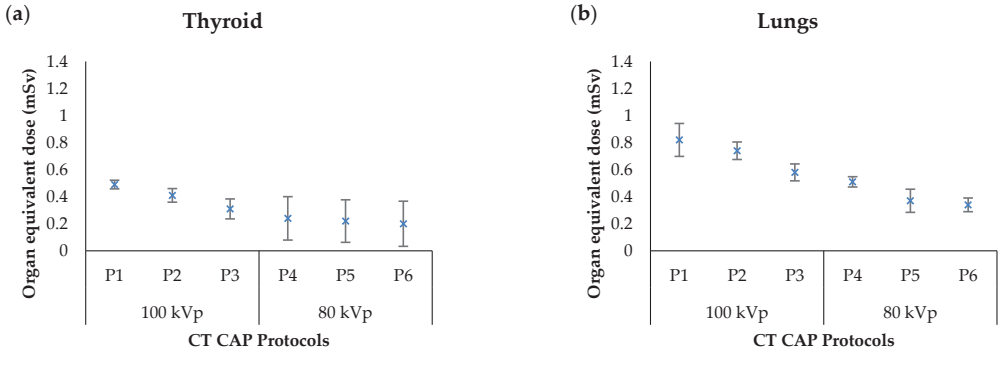

Figure 3. *Cont.*

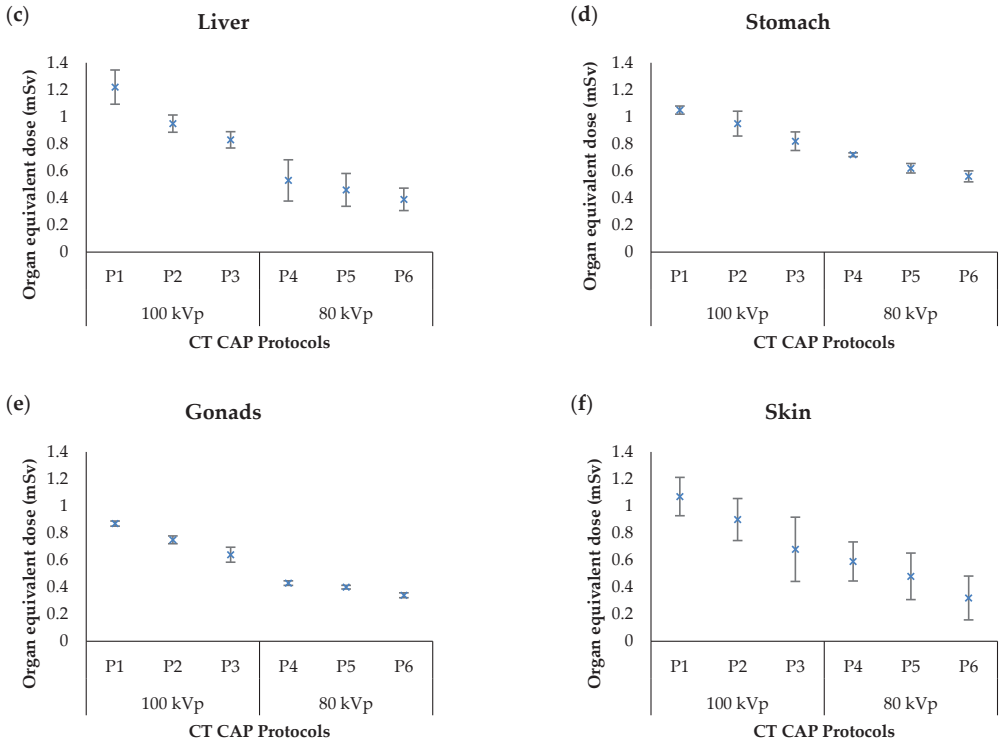

Figure 3. The mean organ-absorbed doses of standard pediatric CT CAP examinations with varying tube potential and tube current in: (**a**) Thyroid, (**b**) lungs, (**c**) liver, (**d**) stomach, (**e**) gonads, and (**f**) skin.

Table 3. Organ Equivalent Dose from TLD measurement from optimization protocols.

Selected Organs	Organ Equivalent Dose (mSv)			
	P1(R)	P7 (S.C = 1.2)	P8 (P = 1.2)	P9 (Off TCM)
Thyroid	0.49 ± 0.03	0.36 ± 0.36	0.58 ± 0.23	4.25 ± 0.27
Lungs	0.88 ± 0.12	0.82 ± 0.14	0.91 ± 0.13	6.2 ± 0.55
Liver	1.22 ± 0.13	1.10 ± 0.07	1.30 ± 0.04	7.10 ± 0.54
Stomach	1.05 ± 0.03	0.97 ± 0.07	1.18 ± 0.11	6.91 ± 0.42
Gonads	0.87 ± 0.02	0.79 ± 0.04	0.90 ± 0.02	6.35 ± 0.10
Skin	1.07 ± 0.14	1.04 ± 0.17	1.15 ± 0.11	6.06 ± 0.74

R = Routine, S.C = Slice Collimation, P = Pitch, TCM = Tube Current Modulation.

Table 4. A comparison of all objective image quality parameter values acquired in different CT CAP protocols.

Image Quality	CT CAP Protocol								
	P1	P2	P3	P4	P5	P6	P7	P8	P9
CT Number (Mean)	22.5 ± 0.9	22.3 ± 0.9	19.9 ± 1.9	19.5 ± 0.8	20.3 ± 1.9	10.1 ± 1.3	22.6 ± 0.5	22.0 ± 0.9	21.4 ± 0.9
Noise (SD)	8.9 ± 1.1	9.3 ± 0.9	10.5 ± 1.6	10.8 ± 2.3	11.5 ± 0.6	13.1 ± 0.6	7.4 ± 1.0	8.8 ± 0.7	3.2 ± 0.2
SNR	2.54 ± 0.4	2.41 ± 0.2	1.93 ± 0.4	1.87±0.4 *	1.77 ± 0.1 *	0.77 ±0.1 *	3.10 ± 0.4	2.51 ± 0.2	6.66 ± 0.5 *
CNR	0.71 ± 0.1	0.69 ± 0.1	0.47 ± 0.1	0.59 ± 0.1	0.45 ± 0.1 *	0.61 ± 0.1	0.54 ± 0.1	0.23 ± 0.1 *	1.34 ± 0.2 *
FOM	3.65	3.90	2.97	3.59	3.54	0.75	5.73	3.73	6.47
Dunnett *t*-tests (*p* value)	Control	1.000	0.058	0.611	0.028	0.779	0.255	0.000	0.000

* *p*-value < 0.05.

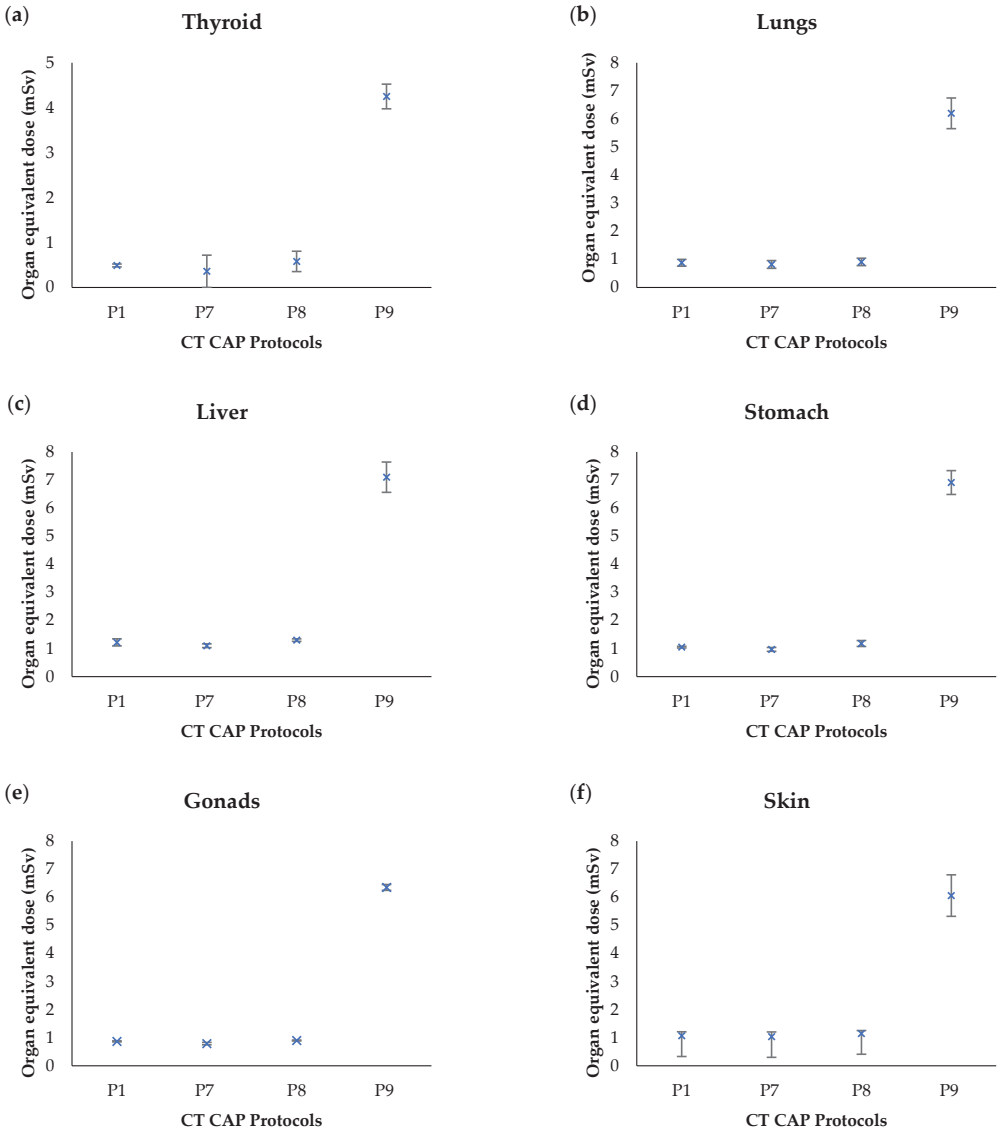

Figure 4. The mean organ-absorbed doses from the modification of standard pediatric CT CAP protocols in: (**a**) Thyroid, (**b**) lungs, (**c**) liver, (**d**) stomach, (**e**) gonads, and (**f**) skin.

4. Discussion

Our aim in this work is to correlate between dose and image quality metrics in pediatric while implementing CT optimization protocols. Among radiation dose metrics, organ equivalent dose is considered one of the best indicators for characterizing patient radiation burden [10,32]. Several researchers have been inspired to reduce the risk by altering the variable of scan parameters, including growing the pitch factor, increasing slice collimation, choosing tube voltage, and utilizing automatic tube current modulation (ATCM) feature [33–35].

In this work, we have measured organ-absorbed dose in pediatric patients by inserting a TL dosimeter into the hole designed at the slab of the one-year-old anthropomorphic phantom to represent specific radiosensitive organ parts. The CT CAP protocol was selected because of the high frequency performed amongst pediatric patients and the rise in repetitive scans due to the standard protocol used for cancer staging. Nevertheless, patients with early detection of malignancy can have multiple follow-up CT scans with elevated combined sensitivity to radiation, contributing to a possibility of radiation-related illness. Consequently, there is the concern as scan length that includes more than one part of the body may lead to the pediatric patient's over-exposure if CT parameter optimization has not been implemented.

The highest organ-absorbed dose was presented in the liver, skin, stomach, and lungs as the site of these organs was situated in the primary beam. As CT CAP is often applied as a routine CT examination in the pediatric population due to its benefit in revealing diseases in the lungs, liver, stomach, and deliberately for cancer staging, this can contribute to a rise in cancer incidence. The modification in CT parameter by lowering the tube voltage and tube current results in substantially different organ equivalent dose. Another research found that small adjustments in tube voltage might significantly reduce the radiation exposure and raise the quantum mottle resulting in increased image noise [36,37].

However, lowering the capacity of the X-ray tube is an acceptable operation to evaluate iodine structures as a consequence of the rise in iodine attenuation energy due to the proximity of the K-edge of iodine and the photoelectric influence. The optimum kilovoltage for a CT analysis should be selected depending on the imaging task and patient habitus [32]. Furthermore, the practice of low tube potential technique with a proper selection of mAs value will improve contrast resolution in a patient with a smaller body thickness. The decrease in tube voltage from 120 to 100 kVp and 80 kVp is the best range tube potential in pediatric CT chest, abdominal and pelvic examination without deteriorating CNR and SNR consistency index.

The alteration of CT scan parameter by reducing the pitch factor from 1.4 to 1.2 slightly increased the organ-absorbed dose without affecting image quality. This was supported by Lambert et al. [38], where the increased pitch factor on selected pediatric CT parameter may decrease the radiation output. As presented in P8, there is no significant difference ($p > 0.05$) in organ-absorbed dose albeit it was slightly increased compared to the routine protocol (P1) and also image diagnostic quality in terms of image noise and SNR value in this study. However, the CNR was found to be varied. Studies have shown that high-pitch CT is not only effective for cardiac imaging, but also for routine chest and abdominal CT analysis by minimizing radiation sensitivity while retaining diagnostic image consistency [33,39]. Moreover, the efficient high pitch value was found along with the iterative reconstruction algorithm for decreased radiation exposure and image noise, while tube current (mAs) stayed unchanged [40,41].

Different size of the detector and slice collimation setting in P7 resulted in declining organ-absorbed dose in pediatric CT CAP analysis by contrasting the organ dose in all protocols. Besides dose reduction, it also indicates that there is no significant difference in image quality. According to the previous study reports, apart from growing pitch factor and reducing tube current and tube voltage in the optimization phase, increasing slice collimation is a technique to minimize radiation dose without sacrificing image quality performance [41,42]. Furthermore, previous research indicates that increased beam collimation resulted in a decrease of around 17% over-ranging in CT study, which may prevent overexposure to patients and decreased dose to radiosensitive organs beyond primary beam [43]. However, a wider detector z-coverage screening applied may increase radiation scattering. Scattered radiation can cause hypodense artefacts, affect the stability of the CT number, and the scatter-induced noise in the images may decrease the CNR [44].

The radiation dose metrics in terms of $CTDI_{vol}$, DLP, E and organ-absorbed dose results were substantially higher in P9. The body habitus of children populations varied in size and weight. In addition to the patient's size, the patient's anatomy has a major effect

on X-ray attenuation and noise. At most children's health centres, CT CAP was applied for further investigation to determine the metastasis of cancer to the patients who were already diagnosed with primary cancer diseases. With the introduction of automatic tube current modulation (ATCM), this technique was used to optimize the radiation dose, particularly amongst pediatric patients. Moreover, with using TCM, 80% of organ-absorbed dose was reduced in pediatric CT CAP examination. This study was similar to the previous study shows by using TCM, 68% of effective dose reduce in CT CAP examination [40]. Therefore, the patient size, the shape, and anatomy of the patient has a significantly effect on TCM in terms of declining radiation dose without sacrificing image quality [4,24].

The adjustments to these scanning parameters were investigated as to how these influences the patient dosage and the performance of CNR, SNR, and image noise. Nevertheless, there is a trade-off between image quality and dosage. The larger dose leading to the higher signal improves contrast resolution, lowering the noise and providing clearer depiction of low-contrast structures. Detection of low contrast information and lesions is restricted primarily by noise, which can be minimized by increasing the radiation exposure. Dose output of CT scanners operating in such modes can be described along with standard-dose indicators by image quality values. Hence, the trade-off between image quality and radiation dose were accessed by FOM based on SNR and $CTDI_{vol}$ in this study. Several studies explored the probability of dose reduction by optimization dependent on FOM approach [14,45,46].

In addition, artificial intelligence has lately been commonly used to optimize radiation-based processes and has several benefits over conventional approaches. The usage of artificial intelligence contributes to refining photon radiation-based applications in both the medical and manufacturing industries [47–49]. Likewise, Machine Learning and Deep Learning a subset of artificial intelligence have been used in a number of applications to evaluate complicated data sets and to identify similarities and associations within those data without being directly configured [50,51].

This research has some limitations to list. First, this analysis just checked the alteration of the pediatric CT CAP protocols on a one-year-old anthropomorphic phantom. Therefore, the age variation in anthropomorphic phantom can be used to present radiation intensity and the dosage received by the organs of children owing to the variation of body size and habitus. Second, this research did not conduct a subjective evaluation of the accuracy of the picture by an expert radiologist. Third, the standard image reconstruction approach, which is Filter Back Projection (FBP) also known as Radon transform, was used for image processing since the CT scanner used in this study did not have an iterative reconstruction algorithm. The degree of image noise filtering is then reduced relative to the use of the iterative reconstruction process. The image quality by leveraging iterative reconstruction information is important to explain the impact on diagnostic quality subjectively as it has enhanced image quality, improve image clarity, and reduce image noise [52].

5. Conclusions

As a conclusion, the impact of the modification of acquisition parameter in pediatric CT CAP, indicates a potential reduction in a dose up to 30% to 80%. Noting that, this study has focused on phantom study by selecting pertinent tube voltage, tube current, pitch value, slice collimation, and comparing ATCM technology. The attenuation-based treatment modifications are more effective than external patient features, such as patient age, weight, BMI, or external measurements. The radiation-induced risk from current CT acquisition parameters is still relatively lower compared to natural background radiation. Even so, the justification for CT scan as well as optimization of the scanning parameters is still paramount for those patients who require multiple CT scans.

Author Contributions: Conceptualization, N.A.M. and M.K.A.K.; methodology, N.A.M.; software, M.K.A.K.; validation, Z.K., M.K.A.K. and J.H.D.W.; formal analysis, N.A.M. and H.A.H.; investigation, N.A.M.; resources, M.K.A.K.; data curation, Z.K. and H.A.H.; original draft preparation, N.A.M.; writing review and editing, M.K.A.K. and K.H.N.; visualization, M.K.A.K.; supervision, M.K.A.K.;

project administration, Z.K.; funding acquisition, M.K.A.K. All authors have read and agreed to the published version of the manuscript.

Funding: This research was funded by Ministry of Higher Education (Malaysia) and Universiti Putra Malaysia with grant number FRGS/1/2020/STG07/UPM/02/3.

Institutional Review Board Statement: Not applicable.

Informed Consent Statement: Not applicable.

Acknowledgments: The authors are grateful to Mohd Kamil bin Mohd Fabell from UMMC for his technical assistance during this work.

Conflicts of Interest: The authors declare no conflict of interest.

References

1. Haleem, A.; Javaid, M. Role of CT and MRI in the design and development of orthopaedic model using additive manufacturing. *J. Clin. Orthop. Trauma* **2018**, *9*, 213–217. [CrossRef]
2. Wang, J.; Fleischmann, D. Improving spatial resolution at CT: Development, benefits, and pitfalls. *Radiology* **2018**, *289*, 261–262. [CrossRef] [PubMed]
3. Kubo, T. Vendor free basics of radiation dose reduction techniques for CT. *Eur. J. Radiol.* **2019**, *110*, 14–21. [CrossRef] [PubMed]
4. Laqmani, A.; Regier, M.; Veldhoen, S.; Backhaus, A.; Wassenberg, F.; Sehner, S.; Groth, M.; Nagel, H.-D.; Adam, G.; Henes, F.O. Improved image quality and low radiation dose with hybrid iterative reconstruction with 80kV CT pulmonary angiography. *Eur. J. Radiol.* **2014**, *83*, 1962–1969. [CrossRef] [PubMed]
5. Papadakis, A.E.; Damilakis, J. Automatic tube current modulation and tube voltage selection in pediatric computed tomography: A phantom study on radiation dose and image quality. *Invest. Radiol.* **2019**, *54*, 265–272. [CrossRef]
6. Aw-Zoretic, J.; Seth, D.; Katzman, G.; Sammet, S. Estimation of effective dose and lifetime attributable risk from multiple head CT scans in ventriculoperitoneal shunted children. *Eur. J. Radiol.* **2014**, *83*, 1920–1924. [CrossRef] [PubMed]
7. Muhammad, N.; Karim, M.; Hassan, H.; Kamarudin, M.; Wong, J.; Ibahim, M. Estimation of effective dose and organ cancer risk from paediatric computed tomography thorax-Abdomen-Pelvis examinations. *Radiat. Phys. Chem.* **2019**, *165*, 108438. [CrossRef]
8. Al-Rammah, T.Y. CT radiation dose awareness among paediatricians. *Ital. J. Pediatr.* **2016**, *42*, 1–6. [CrossRef]
9. Krille, L.; Zeeb, H.; Jahnen, A.; Mildenberger, P.; Seidenbusch, M.; Schneider, K.; Weisser, G.; Hammer, G.; Scholz, P.; Blettner, M. Computed tomographies and cancer risk in children: A literature overview of CT practices, risk estimations and an epidemiologic cohort study proposal. *Radiat. Environ. Biophys.* **2012**, *51*, 103–111. [CrossRef]
10. Perisinakis, K.; Tzedakis, A.; Pouli, S.; Spanakis, K.; Hatzidakis, A.; Damilakis, J. Comparison of patient dose from routine multi-phase and dynamic liver perfusion CT studies taking into account the effect of iodinated contrast administration. *Eur. J. Radiol.* **2019**, *110*, 39–44. [CrossRef] [PubMed]
11. Applegate, K.E.; Frush, D.P. Image gently: A Decade of international collaborations to promote appropriate imaging for children. *J. Am. Coll. Radiol.* **2017**, *14*, 956–957. [CrossRef]
12. Parakh, A.; Kortesniemi, M.; Schindera, S.T. CT radiation dose management. *Radiology* **2016**, *280*, 663–673. [CrossRef]
13. Alqahtani, S.J.M.; Welbourn, R.; Meakin, J.R.; Palfrey, R.M.; Rimes, S.J.; Thomson, K.; Knapp, K.M. Increased radiation dose and projected radiation-related lifetime cancer risk in patients with obesity due to projection radiography. *J. Radiol. Prot.* **2019**, *39*, 38–53. [CrossRef] [PubMed]
14. Racine, D.; Ryckx, N.; Ba, A.; Becce, F.; Viry, A.; Verdun, F.R.; Schmidt, S. Task-based quantification of image quality using a model observer in abdominal CT: A multicentre study. *Eur. Radiol.* **2018**, *28*, 5203–5210. [CrossRef]
15. Hashim, S.; Karim, M.K.A.; Bakar, K.; Sabarudin, A.; Chin, A.; Saripan, M.; Bradley, D. Evaluation of organ doses and specific k effective dose of 64-slice CT thorax examination using an adult anthropomorphic phantom. *Radiat. Phys. Chem.* **2016**, *126*, 14–20. [CrossRef]
16. Gao, Y.; Quinn, B.; Mahmood, U.; Long, D.; Erdi, Y.; St. Germain, J.; Pandit-Taskar, N.; Xu, G.; Bolch, W.; Dauer, L. A comparison of pediatric and adult CT organ dose estimation methods. *BMC Med. Imaging* **2017**, *17*, 28. [CrossRef]
17. Goodman, T.R.; Mustafa, A.; Rowe, E. Pediatric CT radiation exposure: Where we were, and where we are now. *Pediatr. Radiol.* **2019**, *49*, 469–478. [CrossRef]
18. Stamm, G.; Nagel, H.D. CT-expo—A novel program for dose evaluation in CT. *RöFo* **2002**, *174*, 1570–1576. (In German)
19. Hoang, J.K.; Reiman, R.E.; Nguyen, G.B.; Januzis, N.; Chin, B.B.; Lowry, C.; Yoshizumi, T.T. Lifetime attributable risk of cancer from radiation exposure during parathyroid imaging: Comparison of 4D CT and parathyroid scintigraphy. *Am. J. Roentgenol.* **2015**, *204*, W579–W585. [CrossRef] [PubMed]
20. Samei, E.; Tian, X.; Segars, W.P.; Frush, D.P. Radiation risk index for pediatric CT: A patient-derived metric. *Pediatr. Radiol.* **2017**, *47*, 1737–1744. [CrossRef] [PubMed]
21. Park, C.; Gruber-Rouh, T.; Leithner, D.; Zierden, A.; Albrecht, M.H.; Wichmann, J.L.; Bodelle, B.; Elsabaie, M.; Scholtz, J.-E.; Kaup, M.; et al. Single-source chest-abdomen-pelvis cancer staging on a third generation dual-source CT system: Comparison of automated tube potential selection to second generation dual-source CT. *Cancer Imaging* **2016**, *16*, 33. [CrossRef] [PubMed]

22. Gao, Y.; Quinn, B.; Pandit-Taskar, N.; Behr, G.; Mahmood, U.; Long, D.; Xu, G.; St. Germain, J.; Dauer, L. Patient-specific organ and effective dose estimates in pediatric oncology computed tomography. *EJMP* **2018**, *45*, 146–155. [CrossRef]
23. Abdulkadir, M.K.; Mat Rahim, N.A.Y.; Mazlan, N.S.; Daud, N.M.; Shuaib, I.L.; Osman, N.D. Dose optimisation in paediatric CT examination: Assessment on current scanning protocols associated with radiation dose. *Radiat. Phys. Chem.* **2020**, *171*, 108740. [CrossRef]
24. Halid, B.; Karim, M.K.A.; Sabarudin, A.; Bakar, K.A.; Shariff, N.D. Assessment of lifetime attributable risk of stomach and colon cancer during abdominal ct examinations based on Monte Carlo simulation. In *Proceedings of the 8th European Medical and Biological Engineering Conference*; Springer International Publishing: New York, NY, USA, 2017; pp. 455–459.
25. Seeram, E.; Davidson, R.; Bushong, S.; Swan, H. Optimizing the exposure indicator as a dose management strategy in computed radiography. *Radiol. Technol.* **2016**, *87*, 380–391.
26. Tonkopi, E.; Duffy, S.; Abdolell, M.; Manos, D. Diagnostic reference levels and monitoring practice can help reduce patient dose from ct examinations. *Am. J. Roentgenol.* **2017**, *208*, 1073–1081. [CrossRef] [PubMed]
27. Karim, M.K.A.; Hashim, S.; Bradley, D.A.; Bahruddin, N.A.; Ang, W.C.; Salehhon, N. Assessment of knowledge and awareness among radiology personnel regarding current computed tomography technology and radiation dose. *J. Phys. Conf. Ser.* **2016**, *694*, 012031. [CrossRef]
28. Isa, I.; Rahmat, S.; Dom, S.; Kayun, Z.; Karim, M. The effects of mis-centering on radiation dose during CT head examination: A phantom study. *J. X-ray Sci. Technol.* **2019**, *27*, 631–639. [CrossRef]
29. Shaffiq Said Rahmat, S.M.; Abdul Karim, M.K.; Che Isa, I.N.; Abd Rahman, M.A.; Noor, N.M.; Hoong, N.K. Effect of miscentering and low-dose protocols on contrast resolution in computed tomography head examination. *Comput. Biol. Med.* **2020**, *123*, 103840. [CrossRef]
30. Harun, H.; Karim, M.; Abbas, Z.; Sabarudin, A.; Muniandy, S.; Razak, H.; Ng, K. The influence of iterative reconstruction level on image quality and radiation dose in CT pulmonary angiography examinations. *Radiat. Phys. Chem.* **2021**, *178*, 108989. [CrossRef]
31. Harun, H.H.; Karim, M.K.A.; Abbas, Z.; Rahman, M.A.A.; Sabarudin, A.; Ng, K.H. Association of radiation doses and cancer risks from ct pulmonary angiography examinations in relation to body diameter. *Diagnostics* **2020**, *10*, 681. [CrossRef] [PubMed]
32. McCollough, C.; Leng, S. Use of artificial intelligence in computed tomography dose optimisation. *Ann. ICRP* **2020**, *49*, 113–125. [CrossRef]
33. Barrera, C.A.; Otero, H.J.; White, A.M.; Saul, D.; Biko, D.M. Image quality and radiation dose of ECG-triggered High-Pitch Dual-Source cardiac computed tomography angiography in children for the evaluation of central vascular stents. *Int. J. Cardiovasc. Imaging* **2019**, *35*, 367–374. [CrossRef]
34. Cardenas, C.E.; McCarroll, R.E.; Court, L.E.; Elgohari, B.A.; Elhalawani, H.; Fuller, C.D.; Kamal, M.J.; Meheissen, M.A.M.; Mohamed, A.S.R.; Rao, A.; et al. Deep learning algorithm for auto-delineation of high-risk oropharyngeal clinical target volumes with built-in dice similarity coefficient parameter optimization function. *Int. J. Radiat. Oncol. Biol. Phys.* **2018**, *101*, 468–478. [CrossRef]
35. Gomez-Cardona, D.; Hayes, J.W.; Zhang, R.; Li, K.; Cruz-Bastida, J.P.; Chen, G.-H. Low-dose cone-beam CT via raw counts domain low-signal correction schemes: Performance assessment and task-based parameter optimization (Part II. Task-based parameter optimization). *Med. Phys.* **2018**, *45*, 1957–1969. [CrossRef] [PubMed]
36. Berlin, S.C.; Weinert, D.M.; Vasavada, P.S.; Martinez-Rios, C.; Parikh, R.A.; Wien, M.A.; Jordan, D.W.; Novak, R.D. Successful dose reduction using reduced tube voltage with hybrid iterative reconstruction in pediatric abdominal CT. *Am. J. Roentgenol.* **2015**, *205*, 392–399. [CrossRef] [PubMed]
37. Nagayama, Y.; Oda, S.; Nakaura, T.; Tsuji, A.; Urata, J.; Furusawa, M.; Utsunomiya, D.; Funama, Y.; Kidoh, M.; Yamashita, Y. Radiation dose reduction at pediatric CT: Use of low tube voltage and iterative reconstruction. *Radiographics* **2018**, *38*, 1421–1440. [CrossRef] [PubMed]
38. Lambert, J.W.; Phelps, A.S.; Courtier, J.L.; Gould, R.G.; MacKenzie, J.D. Image quality and dose optimisation for infant CT using a paediatric phantom. *Eur. Radiol.* **2015**, *26*, 1387–1395. [CrossRef]
39. Trattner, S.; Chelliah, A.; Prinsen, P.; Ruzal-Shapiro, C.B.; Xu, Y.; Jambawalikar, S.; Amurao, M.; Einstein, A.J. Estimating effective dose of radiation from pediatric cardiac CT angiography using a 64-MDCT scanner: New conversion factors relating dose-length product to effective dose. *Am. J. Roentgenol.* **2017**, *208*, 585–594. [CrossRef]
40. Gariani, J.; Martin, S.P.; Botsikas, D.; Becker, C.D.; Montet, X. Evaluating the effect of increased pitch, iterative reconstruction and dual source CT on dose reduction and image quality. *Br. J. Radiol.* **2018**, *91*. [CrossRef] [PubMed]
41. Booij, R.; Dijkshoorn, M.L.; Van Straten, M. Efficacy of a dynamic collimator for overranging dose reduction in a second- and third-generation dual source CT scanner. *Eur. Radiol.* **2017**, *27*, 3618–3624. [CrossRef]
42. Messerli, M.; Dewes, P.; Scholtz, J.-E.; Arendt, C.; Wildermuth, S.; Vogl, T.J.; Bauer, R.W. Evaluation of an adaptive detector collimation for prospectively ECG-triggered coronary CT angiography with third-generation dual-source CT. *Eur. Radiol.* **2018**, *28*, 2143–2150. [CrossRef] [PubMed]
43. Urikura, A.; Hara, T.; Yoshida, T.; Nishimaru, E.; Hoshino, T.; Nakaya, Y.; Endo, M. Overranging and overbeaming measurement in area detector computed tomography: A method for simultaneous measurement in volume helical acquisition. *J. Appl. Clin. Med. Phys.* **2019**, *20*, 160–165. [CrossRef]
44. Flohr, T. CT Systems. *Curr. Radiol. Rep.* **2013**, *1*, 52–63. [CrossRef]

45. Chang, K.-P.; Hsu, T.-K.; Lin, W.-T.; Hsu, W.-L. Optimization of dose and image quality in adult and pediatric computed tomography scans. *Radiat. Phys. Chem.* **2017**, *140*, 260–265. [CrossRef]
46. Harun, H.H.; Karim, M.K.A.; Muhammad, N.A.; Razak, H.R.A.; Sabarudin, A.; Muniandy, S.C. Effect of iterative reconstruction algorithm associated with low contrast detectability performance from CT pulmonary angiography examinations. *J. Phys. Conf. Ser.* **2020**, 012029. [CrossRef]
47. Meineke, A.; Rubbert, C.; Sawicki, L.M.; Thomas, C.; Klosterkemper, Y.; Appel, E.; Caspers, J.; Bethge, O.T.; Kröpil, P.; Antoch, G.; et al. Potential of a machine-learning model for dose optimization in CT quality assurance. *Eur. Radiol.* **2019**, *29*, 3705–3713. [CrossRef] [PubMed]
48. Roshani, M.; Phan, G.; Faraj, R.H.; Phan, N.-H.; Roshani, G.H.; Nazemi, B.; Corniani, E.; Nazemi, E. Proposing a gamma radiation based intelligent system for simultaneous analyzing and detecting type and amount of petroleum by-products. *Nucl. Eng. Technol.* **2020**. [CrossRef]
49. Roshani, M.; Phan, G.; Roshani, G.H.; Hanus, R.; Nazemi, B.; Corniani, E.; Nazemi, E. Combination of X-ray tube and GMDH neural network as a nondestructive and potential technique for measuring characteristics of gas-oil–water three phase flows. *Measurement* **2021**, *168*, 108427. [CrossRef]
50. Alla Takam, C.; Samba, O.; Tchagna Kouanou, A.; Tchiotsop, D. Spark architecture for deep learning-based dose optimization in medical imaging. *Inform. Med. Unlocked.* **2020**, *19*, 100335. [CrossRef]
51. Singh, R.; Wu, W.; Wang, G.; Kalra, M.K. Artificial intelligence in image reconstruction: The change is here. *Phys. Med.* **2020**, *79*, 113–125. [CrossRef]
52. Verdun, F.R.; Racine, R.D.; Ott, J.G.; Tapiovaara, T.M.; Toroi, P.; Bochud, F.O.; Veldkamp, W.J.H.; Schegerer, A.A.; Bouwman, R.W.; Giron, I.H.; et al. Image quality in CT: From physical measurements to model observers. *Phys. Med.* **2015**, *31*, 823–843. [CrossRef] [PubMed]

applied sciences

MDPI

Article

A Voxel-Based Assessment of Noise Properties in Computed Tomography Imaging with the ASiR-V and ASiR Iterative Reconstruction Algorithms

Patrizio Barca [1,†], Daniela Marfisi [1,†], Chiara Marzi [2], Sabino Cozza [3], Stefano Diciotti [2], Antonio Claudio Traino [1] and Marco Giannelli [1,*]

[1] Unit of Medical Physics, Pisa University Hospital "Azienda Ospedaliero-Universitaria Pisana", 56126 Pisa, Italy; barca.patrizio@gmail.com (P.B.); marfisi.daniela@gmail.com (D.M.); c.traino@ao-pisa.toscana.it (A.C.T.)
[2] Department of Electrical, Electronic and Information Engineering "Guglielmo Marconi", University of Bologna, 47522 Cesena, Italy; chiara.marzi3@unibo.it (C.M.); stefano.diciotti@unibo.it (S.D.)
[3] Department of Radiology, Azienda USL Toscana Nord Ovest, 56025 Pontedera, Italy; sabino.cozza@uslnordovest.toscana.it
* Correspondence: m.giannelli@ao-pisa.toscana.it
† These authors contributed equally to this study.

Abstract: Given the inherent characteristics of nonlinearity and nonstationarity of iterative reconstruction algorithms in computed tomography (CT) imaging, this study aimed to perform, for the first time, a voxel-based characterization of noise properties in CT imaging with the ASiR-V and ASiR algorithms as compared with conventional filtered back projection (FBP). Multiple repeated scans of the Catphan-504 phantom were carried out. CT images were reconstructed using FBP and ASiR/ASiR-V with different blending levels of reconstruction (20%, 40%, 60%, 80%, 100%). Noise maps and their nonuniformity index (*NUI*) were obtained according to the approach proposed by the report of AAPM TG-233. For the homogeneous CTP486 module, ASiR-V/ASiR allowed a noise reduction of up to 63.7%/52.9% relative to FBP. While the noise reduction values of ASiR-V-/ASiR-reconstructed images ranged up to 33.8%/39.9% and 31.2%/35.5% for air and Teflon contrast objects, respectively, these values were approximately 60%/50% for other contrast objects (PMP, LDPE, polystyrene, acrylic, Delrin). Moreover, for all contrast objects but air and Teflon, ASiR-V showed a greater noise reduction potential than ASiR when the blending level was $\geq$40%. While noise maps of the homogenous CTP486 module showed only a slight spatial variation of noise (*NUI* < 5.2%) for all reconstruction algorithms, the *NUI* values of iterative-reconstructed images of the nonhomogeneous CTP404 module increased nonlinearly with blending level and were 19%/15% and 6.7% for pure ASiR-V/ASiR and FBP, respectively. Overall, these results confirm the potential of ASiR-V and ASiR in reducing noise as compared with conventional FBP, suggesting, however, that the use of pure ASiR-V or ASiR might be suboptimal for specific clinical applications.

Keywords: computed tomography; iterative reconstruction algorithms; ASiR; ASiR-V; noise level; noise spatial uniformity

Citation: Barca, P.; Marfisi, D.; Marzi, C.; Cozza, S.; Diciotti, S.; Traino, A.C.; Giannelli, M. A Voxel-Based Assessment of Noise Properties in Computed Tomography Imaging with the ASiR-V and ASiR Iterative Reconstruction Algorithms. *Appl. Sci.* **2021**, *11*, 6561. https://doi.org/10.3390/app11146561

Academic Editors: Ivan Veronese and Salvatore Gallo

Received: 24 May 2021
Accepted: 10 July 2021
Published: 16 July 2021

Publisher's Note: MDPI stays neutral with regard to jurisdictional claims in published maps and institutional affiliations.

1. Introduction

The impact of computed tomography (CT) imaging on patient dose has been a topic of increasing attention in recent years [1–8]. Given that CT examinations are the major source of population exposure to ionizing radiation in industrialized countries [9,10], many strategies have been implemented to keep patient dose as low as reasonably achievable while maintaining a good diagnostic image quality [11]. In this regard, acquisition-related approaches, such as tube current modulation (both in the axial and longitudinal planes), appropriate selection of tube voltage according to patient size, table motion, and gantry rotation speed optimization have been successfully adopted on modern CT scanners [11–13].

The introduction of iterative reconstruction (IR) algorithms in clinical practice represents an important step toward dose optimization [13–18]. Unlike the conventional filtered back-projection (FBP) algorithm, IR algorithms take into account various physical aspects of CT image acquisition and can be based on statistical or model-based approaches [19–22]. While statistical-based IR algorithms usually consider the fluctuations in the projection measurement through a statistical method (e.g., by modeling the photon counting), model-based algorithms include a more complex description of physical and optical aspects in the reconstruction process, resulting in a better representation of the whole imaging process but in a longer reconstruction time [19–22]. When compared with conventional FBP, IR algorithms have proven to significantly decrease noise in CT imaging, allowing CT examinations with reduced patient exposure while providing still acceptable diagnostic images [23–28]. The noise properties of CT images obtained using IR algorithms can be rather different from those of FBP-derived CT images [20,21]. Indeed, IR algorithms can have an impact not only on the noise level but also on the noise texture of CT images [24,29–35]. Therefore, for each specific IR algorithm, a comprehensive characterization of the noise properties and quality of reconstructed CT images is recommended to adequately assess its dose reduction potential and usefulness.

So far, a number of IR algorithms with different characteristics have been implemented on clinical CT scanners [21,22], such as the adaptive statistical iterative reconstruction (ASiR) [36], adaptive statistical iterative reconstruction-V (ASiR-V) [37], and Veo [38] (GE Healthcare, Waukesha, WI, USA). The ASiR algorithm works on sinogram data by modeling the photon statistics and some noise-related properties of the scanned object (e.g., scatter), and can be employed with different FBP–ASiR blending levels [36]. Although ASiR is widely adopted due to its fast reconstruction time, some image quality properties, such as image texture and spatial resolution, depend on the blending level of reconstruction and the dose level, yielding some artificial image texture and degradation of spatial resolution at a higher percentage of blending for low-contrast objects [24,29,33,39,40]. The model-based Veo algorithm allows limiting these drawbacks by modeling the entire imaging system (i.e., X-ray tube output, detector response, radiation scatter properties, geometric features of the beam) [21,22,34,41]. However, due to the complexity of the imaging system model, Veo reconstruction time is greatly increased compared with ASiR, hampering its wide use in clinical practice [31,34,41,42]. The more recent ASiR-V algorithm has been proposed to reduce reconstruction time with respect to Veo while preserving some advantages of the full model-based approach in terms of image quality [22,34,36]. In particular, ASiR-V features more advanced noise and object modeling as compared with ASiR [36] and implements parts of the Veo physics model, but excludes the system optics in the modeling process, enabling reconstruction time almost comparable to that of FBP [36]. Like ASiR, ASiR-V can be blended with FBP at different percentages of reconstruction, from 0% (i.e., FBP) to 100% (i.e., pure ASiR-V) [36].

Several previous studies have characterized the image quality of CT imaging with ASiR [24,28,29,33,39,43,44], finding substantial noise reduction properties as compared with conventional FBP. For instance, Miéville et al. showed that the benefit of ASiR in terms of noise reduction occurs almost independently of dose level ($CTDI_{vol}$ range: 0.2–7.2 mGy) with a noise reduction relative to FBP of approximately 20% and 50% for ASiR 40% and ASiR 100%, respectively [24]. Analogously, Hussain et al. found, for two different radiation exposures (tube loads of 130 and 260 mAs at 120 kVp), a noise reduction relative to FBP of approximately 30% and 50% with ASiR 50% and ASiR 100%, respectively [43]. A study by Barca et al. confirmed that ASiR has the capability of reducing noise by up to 50% relative to FBP while preserving diagnostic information at low radiation exposure [33].

More recently, a number of clinical and phantom studies have evaluated the dose reduction potential and performance of ASiR-V [45–59]. In particular, some studies have assessed the noise properties of CT imaging with ASiR-V in comparison with FBP or other IR algorithms [45,46,49–55,57–59]. For instance, a clinical study by Gatti et al. showed that a relevant noise reduction can be obtained using ASiR-V 40% with respect to ASiR 50% in

the CT imaging of oncologic patients [50]. Goodenberger et al. compared abdomen and phantom CT images reconstructed by adopting FBP, ASiR, Veo, and ASiR-V algorithms [51]. They performed subjective and objective analyses showing that ASiR-V 30% and ASiR-V 60% provided the best combination of qualitative and quantitative performances. In a phantom study, Lim et al. compared the image quality of images reconstructed using FBP, ASiR, and ASiR-V algorithms [52]. They found that ASiR-V can allow an appreciable reduction of CT image noise and an improvement in contrast-to-noise ratio and spatial resolution. Euler et al. evaluated image noise, spatial resolution, lesion detectability, and dose reduction potential of ASiR-V (50% and 100%) in comparison with FBP by performing phantom CT acquisitions [54]. They reported that ASiR-V has the capability of reducing image noise and improving low-contrast lesion detectability when compared with FBP. They suggested that such improvement in detection can allow radiation exposure reduction. De Marco and Origgi [55] assessed the noise level and noise power spectrum properties of CT imaging with ASiR-V, considering phantom images reconstructed with soft, standard, and bone kernels. As compared with FBP, they found a greater noise reduction provided by ASiR-V with respect to ASiR for soft and standard kernels, while less noise reduction was found for the bone kernel.

While these studies [50–52,54,55] have explored in detail some image quality aspects of CT imaging with ASiR-V and possibly ASiR as compared with FBP, noise level has been estimated by computing the standard deviation (SD) of CT numbers within a given region of interest (ROI) [17,60,61]. However, this approach would be conceptually appropriate only for ergodic and stationary imaging systems, which feature uncorrelated noise [17,62]. Actually, due to image reconstruction and processing, CT image noise may present some degrees of correlation [63,64]. Moreover, this approach cannot provide information on the degree of spatial nonuniformity of noise [65]. Therefore, a more rigorous characterization of noise properties should be performed by computing voxelwise noise maps through multiple repeated CT imaging acquisitions [17,41,65]. Notably, these issues might be of particular relevance for IR algorithms given their inherent nonlinearity and nonstationarity properties. Therefore, the purpose of this phantom study was to carry out a voxel-based assessment of noise properties in CT imaging with ASiR-V and ASiR for different blending levels of reconstruction and contrast objects.

2. Materials and Methods

2.1. Scanner and Phantom Acquisitions

A 64-slice CT scanner (Optima CT660, GE Healthcare, Waukesha, WI, USA) was employed to acquire (helical scan mode; pitch, 0.984; rotation time, 1 s; tube load, 100 mAs without modulation; tube voltage, 120 kVp; collimation, 40 mm) images of the Catphan-504 phantom (The Phantom Laboratory, Salem, NY, USA). The entire phantom was scanned 40 times under identical conditions. CT images (slice thickness, 2.5 mm; display field of view, 250 mm $\times$ 250 mm; standard convolution kernel) were reconstructed using conventional FBP and ASiR/ASiR-V algorithms with different blending levels of reconstruction (20%, 40%, 60%, 80%, and 100%).

The Catphan-504 phantom has a cylindrical shape (20 cm outer diameter) and consists of four modules. In particular, the CTP486 and CTP404 modules were employed for noise properties assessment. The CTP486 module is a homogeneous medium, while the CTP404 module includes different contrast objects within a homogeneous background. Nominal CT numbers of the contrast objects are reported in Table 1.

Table 1. Nominal CT numbers of the Catphan-CTP404 contrast objects [66].

Material	CT Numbers (HU)
Air	−1046: −986
PMP [a]	−220: −172
LDPE [b]	−121: −87
Polystyrene	−65: −29
Acrylic	92: 137
Delrin	344: 387
Teflon	941: 1060

[a] Polymethylpentene, [b] low-density polyethylene.

2.2. Noise Maps

In order to assess local noise properties, as suggested by the AAPM Task Group 233 report [65], noise maps of CT images reconstructed by using FBP (N-FBP), ASiR (N-ASiR), and ASiR-V (N-ASiR-V) were obtained on a voxel-by-voxel basis computing the SD of each voxel value across the 40 repeated acquisitions. Then, maps of the percentage difference between noise of FBP-reconstructed images and noise of both ASiR-V-reconstructed (PDN-ASiR-V) and ASiR-reconstructed (PDN-ASiR) images were computed voxelwise. In particular, N-FBP as well as N-ASiR, N-ASiR-V, PDN-ASiR-V, and PDN-ASiR maps with different blending levels of reconstruction were obtained for the slice at the central level of both the CTP486 and CTP404 phantom modules.

For CT imaging of the homogeneous CTP486 module, a summary noise level was estimated as the mean ± SD value of N-FBP, N-ASiR, and N-ASiR-V maps within a central circular ROI of 1 cm diameter. Analogously, a summary percentage noise reduction of ASiR-V and ASiR with respect to FBP was estimated as the mean ± SD value of PDN-ASiR-V and PDN-ASiR maps, respectively, within a central circular ROI of 1 cm diameter.

For CT imaging of the CTP404 module, a summary noise value of each contrast object was estimated as the mean ± SD value of N-FBP, N-ASiR, and N-ASiR-V maps within a circular ROI of 1 cm diameter placed in the center of the contrast object. Analogously, for each contrast object, a summary percentage noise reduction of ASiR-V and ASiR with respect to FBP was estimated as the mean ± SD value of PDN-ASiR-V and PDN-ASiR maps, respectively, within a circular ROI of 1 cm diameter placed in the center of the contrast object.

In order to assess the spatial nonuniformity degree of N-FBP, N-ASiR, and N-ASiR-V maps, the nonuniformity index (*NUI*) [67], as proposed by the AAPM Task Group 233 report [65], was employed. Specifically, for both the CTP486 and CTP404 modules, the entire inner part of the phantom (diameter, 15 cm) was divided into k = 249 ROIs (size, 8 mm × 8 mm). Then, for each map (N-FBP, N-ASiR, and N-ASiR-V), the *NUI* was calculated as:

$$NUI = \frac{100}{< m >} \sqrt{\frac{1}{k-1} \sum_{i=1}^{k} (m_i - < m >)^2} \quad (1)$$

where m_i and <m> are the average of the values of the considered map within the i-th ROI and the average of all m_i values, respectively.

Furthermore, in order to characterize the spatial distribution of noise in CT imaging with ASiR and ASiR-V reconstruction algorithms, the histograms of N-ASiR and N-ASiR-V maps, as well as of N-FBP map, were computed for the entire inner part of the CTP486 module (diameter, 15 cm). Then, the histogram descriptors of median, interquartile range, kurtosis, and skewness were calculated.

Image analysis was performed by using the MATLAB R2018a (MathWorks, Natick, MA, USA) software package.

3. Results

N-FBP and N-ASiR/N-ASiR-V maps (with different blending levels of reconstruction) of the CTP486 homogeneous module and CTP404 module with contrast objects are shown in Figures 1 and 2, respectively.

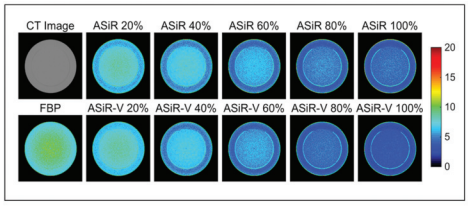

Figure 1. Noise maps (HU) of a CT image of the CTP486 phantom module reconstructed using FBP and ASiR/ASiR-V with different blending levels (20%, 40%, 60%, 80%, and 100%). The corresponding FBP-reconstructed CT image of the phantom is also displayed.

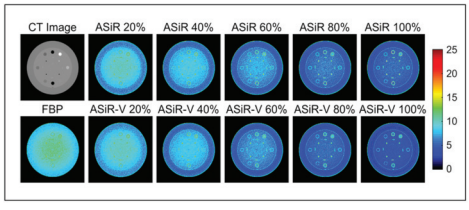

Figure 2. Noise maps (HU) of a CT image of the CTP404 phantom module reconstructed using FBP and ASiR/ASiR-V with different blending levels (20%, 40%, 60%, 80%, and 100%). The corresponding FBP-reconstructed CT image of the phantom is also displayed.

Moreover, PDN-ASiR and PDN-ASiR-V maps (with different blending levels of reconstruction) of the CTP486 homogeneous module and CTP404 module with contrast objects are displayed in Figures 3 and 4, respectively.

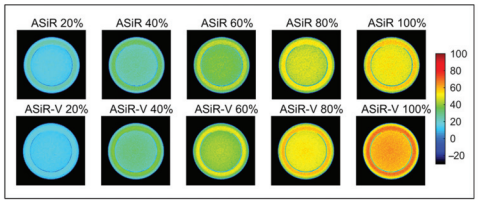

Figure 3. CTP486 phantom module. Maps of the percentage difference (%) between noise of the FBP-reconstructed CT image and noise of both ASiR-V-reconstructed and ASiR-reconstructed CT images with different blending levels (20%, 40%, 60%, 80%, and 100%).

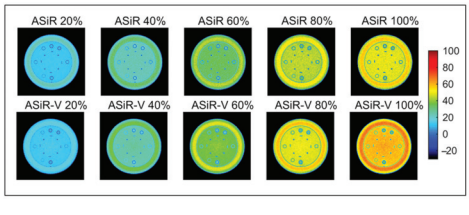

Figure 4. CTP404 phantom module. Maps of the percentage difference (%) between noise of the FBP-reconstructed CT image and noise of both ASiR-V-reconstructed and ASiR-reconstructed CT images with different blending levels (20%, 40%, 60%, 80%, and 100%).

Noise maps of the homogenous CTP486 phantom module (Figure 1) showed only a slight spatial variation of local noise values for the FBP-reconstructed CT image, which seemed less for ASiR-V- and ASiR-reconstructed CT images with higher blending levels. This is corroborated by the *NUI* values reported in detail in Figure 5. In particular, the *NUI* value for the FBP-reconstructed CT image was 5.2%, while the *NUI* values for the ASiR-V- and ASiR-reconstructed CT images with a 100% blending level were 2.7% and 3.4%, respectively. On the other hand, noise maps of the CTP404 phantom module (including various contrast objects) (Figure 2) showed a more appreciable degree of spatial variation of noise, with higher noise values at the boundary between each contrast object and background, especially for ASiR-V- and ASiR-reconstructed CT images. The *NUI* value for the FBP-reconstructed CT image was 6.7%. The *NUI* values for the IR-reconstructed CT images increased nonlinearly with the blending level and were 19% and 15% for pure ASiR-V and ASiR, respectively.

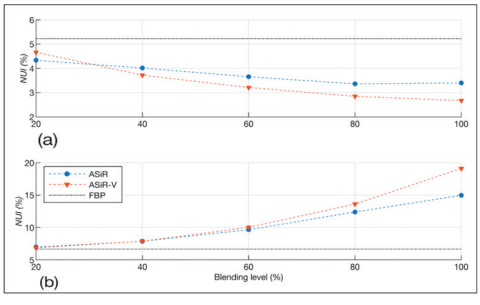

Figure 5. Nonuniformity index (*NUI*) values of noise maps of CT reconstructed images (FBP, ASiR-V, and ASiR) of the CTP486 (**a**) and CTP404 (**b**) phantom modules. For *NUI* estimation, only the inner part of the phantom (diameter, 15 cm) was considered.

As shown by PDN-ASiR-V and PDN-ASiR maps of the homogenous CTP486 module (Figure 3), when compared with conventional FBP, both ASiR and ASiR-V allowed a substantial noise reduction in CT imaging. In this regard, noise values in the CT imaging of the homogenous CTP486 phantom module are reported in Table 2 for FBP, ASiR-V, and ASiR. The percentage difference between noise in the FBP-reconstructed CT image and that in both ASiR-V- and ASiR-reconstructed CT images increased with increasing blending level, up to 64% and 53% for ASiR-V and ASiR, respectively (Figure 6). Except for the lowest blending level of 20%, ASiR-V presented greater noise reduction potential than ASiR (Figure 6).

Table 2. Homogeneous CTP486 module. Noise level estimated as the mean (SD) value of N-FBP, N-ASiR, and N-ASiR-V maps within a central circular ROI of 1 cm diameter.

Blending Level	FBP	ASiR	ASiR-V
0%	9.5 (1.3)		
20%		7.9 (1.1)	8.0 (1.2)
40%		6.9 (1.0)	6.5 (1.0)
60%		5.8 (0.8)	5.4 (0.8)
80%		4.9 (0.7)	4.4 (0.6)
100%		4.5 (0.7)	3.4 (0.5)

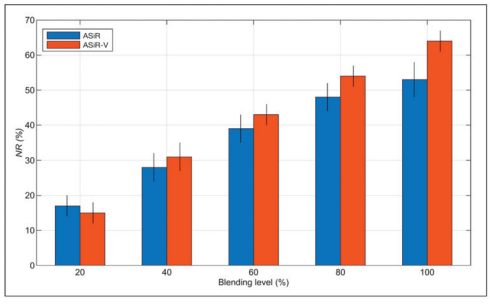

Figure 6. CTP486 homogeneous phantom module. Noise reduction properties of ASiR-V and ASiR reconstruction algorithms with respect to conventional FBP, *NR(%)*, estimated as the mean (SD) value of PDN-ASiR-V and PDN-ASiR-V maps within a central circular ROI of 1 cm diameter.

For different contrast objects (i.e., air, PMP, LDPE, polystyrene, acrylic, Delrin, Teflon) of the CTP404 phantom module, summary noise level values in CT imaging using FBP and ASiR-V/ASiR with different blending levels of reconstruction are reported in detail in Table 3. Figure 7 shows the noise reduction properties of ASiR-V and ASiR reconstruction algorithms with respect to conventional FBP for different contrast objects and blending levels of reconstruction. For all contrast objects, when compared with conventional FBP, both ASiR-V and ASiR allowed a substantial reduction in noise level, which decreased with an increasing blending level of reconstruction (Table 3). The noise reduction properties of both ASiR and ASiR-V depended on the contrast object. In particular, higher contrast objects (i.e., air and Teflon) were characterized by a lower noise reduction degree (Figure 7). Moreover, for all contrast objects but air and Teflon, ASiR-V showed a greater noise reduction potential than ASiR when the blending level was $\geq$40%.

Table 3. CTP404 phantom module with different contrast objects (i.e., air, PMP, LDPE, polystyrene, acrylic, Delrin, Teflon). Summary noise level of each contrast object estimated as the mean (SD) value of N-FBP, N-ASiR, and N-ASiR-V maps within a central circular ROI of 1 cm diameter.

		Air	PMP	LDPE	Polystyrene	Acrylic	Delrin	Teflon
FBP		9.0 (1.0)	9.7 (1.1)	9.8 (1.1)	9.6 (1.0)	9.7 (1.2)	10.4 (1.1)	11.3 (1.3)
ASiR	20%	8.1 (0.9)	8.6 (0.9)	8.6 (0.9)	8.4 (0.9)	8.5 (1.0)	9.2 (0.9)	10.2 (1.2)
	40%	7.3 (0.8)	7.5 (0.8)	7.6 (0.8)	7.4 (0.8)	7.5 (0.9)	8.1 (0.8)	9.4 (1.1)
	60%	6.6 (0.8)	6.5 (0.7)	6.5 (0.7)	6.4 (0.7)	6.4 (0.8)	7.0 (0.7)	8.5 (1.1)
	80%	5.8 (0.7)	5.5 (0.7)	5.6 (0.6)	5.4 (0.6)	5.5 (0.6)	6.0 (0.6)	7.7 (1.0)
	100%	5.4 (0.7)	5.1 (0.7)	5.0 (0.6)	4.9 (0.6)	5.0 (0.7)	5.5 (0.7)	7.3 (1.0)
ASiR-V	20%	8.4 (0.9)	8.5 (0.9)	8.6 (0.9)	8.5 (0.9)	8.5 (1.0)	9.1 (0.9)	10.5 (1.2)
	40%	7.7 (0.9)	7.4 (0.8)	7.4 (0.8)	7.3 (0.8)	7.4 (0.9)	7.9 (0.8)	9.7 (1.2)
	60%	7.1 (0.9)	6.3 (0.7)	6.3 (0.7)	6.2 (0.7)	6.2 (0.7)	6.7 (0.7)	9.0 (1.2)
	80%	6.5 (0.9)	5.3 (0.6)	5.2 (0.6)	5.2 (0.6)	5.1 (0.6)	5.6 (0.6)	8.3 (1.2)
	100%	6.0 (1.0)	4.3 (0.5)	4.2 (0.5)	4.2 (0.5)	4.1 (0.5)	4.6 (0.5)	7.7 (1.3)

Histograms of N-ASiR and N-ASiR-V maps, as well as of the N-FBP map, are shown in Figure 8. Moreover, values of histogram descriptors (median, interquartile range, kurtosis, skewness) are reported in detail in Table 4. While noise map histogram of the FBP-reconstructed CT image approximated a Gaussian distribution (kurtosis and skewness values of 3 and 0.23, respectively), noise map histograms of ASiR- and ASiR-V-reconstructed CT images leaned to deviate from a Gaussian distribution when increasing the blending level of reconstruction, with kurtosis/skewness values for pure ASiR- and ASiR-V-reconstructed CT images of 3.57/0.41 and 3.35/0.24, respectively.

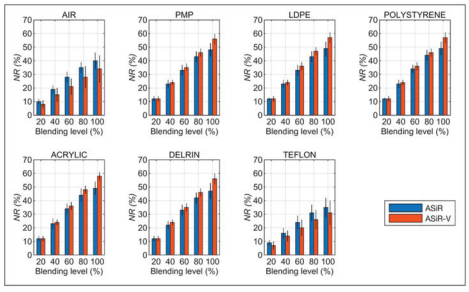

Figure 7. CTP404 phantom module with different contrast objects (i.e., air, PMP, LDPE, polystyrene, acrylic, Delrin, Teflon). Noise reduction properties of ASiR-V and ASiR reconstruction algorithms with respect to conventional FBP, *NR(%)*, estimated as the mean (SD) value of PDN-ASiR-V and PDN-ASiR-V maps within a central circular ROI of 1 cm diameter placed in each contrast object.

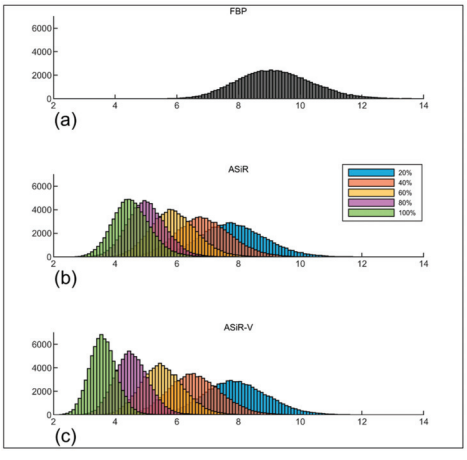

Figure 8. Histograms of noise maps (bin width of 0.1 HU) for FBP- (**a**), ASiR- (**b**), and ASiR-V-reconstructed (**c**) CT images of the homogenous CTP486 module with different blending levels of reconstruction (20%, 40%, 60%, 80%, and 100%).

Table 4. Descriptive metrics of noise map histograms for FBP-, ASiR-, and ASiR-V-reconstructed CT images of the homogenous CTP486 module with different blending levels of reconstruction (20%, 40%, 60%, 80%, and 100%). Median and interquartile range values are expressed as HU; kurtosis and skewness values are unitless.

		Median	Interquartile Range	Kurtosis	Skewness
FBP		9.16	1.62	3.00	0.23
ASiR	20%	7.81	1.39	3.07	0.27
	40%	6.86	1.17	3.10	0.26
	60%	5.88	0.99	3.13	0.25
	80%	5.00	0.83	3.14	0.22
	100%	4.51	0.80	3.57	0.41
ASiR-V	20%	7.91	1.37	3.03	0.24
	40%	6.57	1.15	3.10	0.27
	60%	5.51	0.92	3.11	0.25
	80%	4.52	0.74	3.14	0.23
	100%	3.60	0.57	3.35	0.24

4. Discussion

Given that IR algorithms in CT imaging can be inherently nonlinear and nonstationary, noise properties should be possibly assessed by using a rigorous voxel-based approach exploiting multiple repeated acquisitions. Unlike the widely employed approach of estimating noise as the SD of CT numbers within an ROI, this more complex approach allows for solving potential issues related to nonvalidity of the ergodic theorem for CT imaging with IRs, as well as for assessing the spatial nonuniformity degree of noise. However, so far, only few studies [67–70] have employed such an approach to characterize noise properties in CT imaging with IRs. In particular, Solomon and Samei [68] performed multiple repeated CT acquisitions of a uniform phantom and of two anatomically informed textured phantoms, and used these phantoms to assess noise properties for FBP and the sinogram affirmed iterative reconstruction (SAFIRE, Siemens Healthcare) algorithm. They found that noise was globally nonstationary, and this was mostly relevant for SAFIRE-reconstructed CT images of textured phantoms. In a similar study, Solomon et al. [69] showed that the advanced modeled iterative reconstruction (ADMIRE, Siemens Healthcare) algorithm with different iterative strengths (i.e., 3, 4, and 5) allowed a noise reduction of up to 64% relative to FBP. A study by Funama et al. [70] compared noise in CT images of a porcine liver phantom surrounded by agar gel acquired 100 times, reconstructed using FBP and the iterative model reconstruction (IMR, Philips Healthcare) algorithm with various noise reduction levels (L1, L2, and L3, where L3 offers the greatest noise reduction). They revealed a spatial dependence of noise for IMR-reconstructed CT images. Moreover, for IMR-L3, a noise reduction of 68%–75% relative to FBP was observed. Li et al. [67] acquired 50 repeated acquisitions of a homogeneous phantom in order to assess the spatial nonuniformity of noise maps associated with FBP- and Veo-reconstructed images. Veo-reconstructed CT images were characterized by at least a 50% reduction in *NUI* values relative to FBP-reconstructed CT images.

Some previous clinical or phantom studies have reported a higher noise reduction capability of ASiR-V as compared with ASiR. For instance, Gatti et al. [50] conducted a retrospective case–control study involving oncologic patients who underwent baseline and follow-up CT scans with ASiR 50% and ASiR-V 40%, respectively. Noise was estimated as the SD of CT numbers within three circular ROIs placed in homogeneous regions of three different tissues. Regardless of the anatomical region, noise was found lower in ASiR-V 40%-reconstructed images than in ASiR 50%-reconstructed images, albeit radiation exposure was 38% lower for the ASIR-V examinations than for the ASiR ones. Similarly, Goodenberger et al. carried out a retrospective study on 36 patients who underwent an abdomino-pelvic CT scan [51]. They assessed the noise level within lesions for CT images reconstructed using FBP, ASiR 80%, Veo, and ASiR-V (30%, 60%, and 90%). The highest noise level was revealed on FBP-reconstructed images, followed by ASiR-V 30%-, ASiR 80%-, Veo-, ASiR-V 60%-, and ASiR-V 90%-reconstructed images. Lim et al. [52] compared the noise performances of ASiR-V, ASiR, and FBP on an anthropomorphic phantom using three blending levels of reconstruction (30%, 50%, and 70%) and five different tube currents. By assessing the noise magnitude and noise reduction relative to FBP within a circular ROI in a homogeneous area of the phantom, they found that ASiR-V 30%, ASiR-V 50%, and ASiR-V 70% can allow a noise reduction of 30%–45%, 41%–61%, and 52%–67%, respectively. On the other hand, ASiR with the same blending levels showed a lower noise reduction of 18%–20%, 30%–33%, and 41%–49%, respectively. Euler et al. [54] characterized the noise level of ASiR-V-reconstructed (50% and 100% blending levels of reconstruction) CT images. On average, they found a noise reduction of 37% (ASiR-V 50%) and 72% (ASiR-V 100%) relative to FBP. Another phantom study by De Marco and Origgi [55] compared the noise levels of FBP-, ASiR-V-, and ASiR-reconstructed images (blending levels of 40%, 60%, and 100%) acquired on two different CT scanners (i.e., ASiR-V- and ASiR-reconstructed images were not obtained from the same sinogram data). Specifically, this study assessed the effect of convolution kernel (standard, soft, and bone), slice thickness, and radiation exposure on noise level for all the used reconstruction algorithms. When compared with FBP, ASiR-V

showed a greater noise (estimated as the SD of CT numbers within a square ROI in a homogeneous phantom) reduction than ASiR with noise reduction values of 12%–28%, 18%–41%, and 29%–64% for ASiR-V 40%, 60%, and 100%, respectively. For both ASiR-V and ASiR, noise reduction relative to FBP was almost independent of dose exposure.

To the best of our knowledge, this is the first study that performed, for different blending levels of reconstruction and contrast objects, a voxel-based assessment of noise properties in CT imaging with ASiR-V and ASiR algorithms as compared with conventional FBP. This approach, which can allow a better characterization of noise properties in CT imaging with IR algorithms, is based on spatial noise maps (Figures 1 and 2). In general, we found that, when compared with FBP, ASiR-V presents a greater noise reduction than ASiR for a homogeneous medium, except for the lowest blending level of 20% (Figure 6). In particular, the noise reduction value ranged up to 52.9% and 63.7% for pure ASiR and pure ASiR-V, respectively. This finding has also been confirmed for various contrast objects (i.e., PMP, LDPE, polystyrene, acrylic, Delrin) (Figure 7) with noise reduction values rather independent of contrast objects and ranging up to approximately 50% and 60% for pure ASiR and pure ASiR-V, respectively. On the other hand, for higher contrast objects (i.e., air and Teflon) and all blending levels, ASiR-V showed a lower noise reduction capability than ASiR. In this case, the noise reduction values of ASiR-V-/ASiR-reconstructed images were lower and ranged up to 33.8%/39.9% and 31.2%/35.5% for air and Teflon contrast objects, respectively.

In this work, unlike a few previous studies on the characterization of noise in CT imaging with ASiR-V and ASiR [50–52,54,55], voxelwise noise maps allow an assessment of the spatial uniformity of noise, which might be affected by the nonlinearity and non-stationarity effects of IR algorithms. For the homogeneous medium, FBP-reconstructed images showed a rather low level of the spatial nonuniformity of noise with an *NUI* value of 5.2%. The *NUI* values of ASiR-V- and ASiR-reconstructed CT images were lower than the *NUI* value of FBP-reconstructed images and slightly decreased with an increasing blending level of reconstruction (Figure 5a). This could be partly associated with a shift of noise power spectrum curves toward lower spatial frequencies, which has been observed for CT imaging with ASiR-V and ASiR mostly at higher blending levels of reconstruction [24,29,35,55]. Notably, for the nonhomogeneous medium with contrast objects, both ASiR-V- and ASiR-reconstructed CT images showed *NUI* values greater than the *NUI* value of FBP-reconstructed CT images (approximately 7%), increasing with the blending level of reconstruction (Figure 5b). In particular, the *NUI* values of CT imaging with pure ASiR-V and pure ASiR were approximately three and two times, respectively, that of CT imaging with FBP. This is likely to derive from a noise reduction capability of ASiR-V and ASiR reconstruction algorithms that does not seem so effective at the boundary between different media (Figures 2 and 4). While this effect has been reported for other IR algorithms [68–70], no previous study has observed it for CT imaging with ASiR-V and ASiR. As submitted by Solomon and Samei [68], given that IR algorithms aim at reducing noise while preserving the fidelity of fine details, this necessitates a conservative approach to noise reduction for voxels near edges, and therefore, noise is not reduced as much near edges or structures (i.e., "edge" effect).

The nonuniformity findings of this study suggest that, for CT imaging, a noise evaluation only in homogeneous phantoms could be incomplete and/or partly misleading when IR algorithms are employed. While pure ASiR-V/ASiR offers the maximum noise reduction capability in reconstructed CT images, a blending level of 100% can affect the spatial uniformity of noise mostly at the boundary between different structures. Therefore, for specific clinical applications of CT imaging with ASiR-V and ASiR, the use of a maximum blending level of reconstruction might be not optimal [27,40,43,44,71,72]. In particular, the revealed "edge" effect might partly limit the potential of IR algorithms in studying small structures (such as metastases, vessels, pulmonary nodules, or brain ischemic lesions), especially when they present reduced contrast.

Analysis of noise map histograms (Table 4) showed that, for both ASiR- and ASiR-V-reconstructed CT images, kurtosis and interquartile range/median values monotonically increased and decreased, respectively, with increasing blending level of reconstruction. Moreover, for all the blending levels of reconstruction, noise map histograms of ASiR-reconstructed CT images were characterized by higher or equal kurtosis and interquartile range values compared with that of ASiR-V-reconstructed CT images. Overall, these results might reflect the inherent nonlinear and nonstationary properties of iterative reconstruction algorithms in CT imaging.

5. Conclusions

In this preliminary study, we aimed at characterizing in greater detail noise properties in CT imaging with ASiR-V and ASiR by means of spatial noise maps obtained from multiple repeated acquisitions of a homogeneous phantom and of a phantom with different contrast objects. Our results confirm the potential of ASiR-V and ASiR in reducing noise (up to 60% or more) as compared with conventional FBP. In this regard, while ASiR-V outperforms ASiR in general, this does not necessarily hold true for the CT imaging of structures with high contrast. Both ASiR-V- and ASiR-reconstructed CT images show a higher spatial nonuniformity of noise than FBP-reconstructed images. This effect increases with increasing blending level of reconstruction and reflects a less effective noise reduction potential of ASiR-V and ASiR at the boundary between different structures.

In summary, an exhaustive characterization of noise properties in CT imaging with IR algorithms is needed to actually assess the dose reduction potential of this technique and its possible limitations for specific clinical applications. This study suggests that, when using IR algorithms, the conventional approach of estimating the noise level by computing the SD of CT numbers within a given ROI is inadequate and precludes showing any non-negligible spatial nonuniformity of noise, which may vary with the blending level of reconstruction. Overall, our findings indicate that a voxel-based characterization of noise properties is recommended when dealing with a novel IR algorithm or when comparing the performances of different IR algorithms.

Author Contributions: Conceptualization, P.B. and M.G.; methodology, P.B., D.M. and M.G.; software, D.M.; validation, P.B., D.M., and M.G.; formal analysis, D.M.; investigation, P.B., D.M., and M.G.; resources, A.C.T. and M.G.; data curation, P.B. and D.M.; writing—original draft preparation, P.B., D.M., and M.G.; writing—review and editing, P.B., D.M., C.M., S.C., S.D., A.C.T. and M.G.; visualization, P.B., D.M., C.M., S.C., S.D., A.C.T. and M.G.; supervision, M.G.; project administration, M.G. All authors have read and agreed to the published version of the manuscript.

Funding: This research received no external funding.

Data Availability Statement: The data presented in this study are available on reasonable request from the corresponding author.

Acknowledgments: The authors would like to thank Davide Caramella for a stimulating and constructive discussion.

Conflicts of Interest: The authors declare no conflict of interest.

References

1. Brenner, D.J.; Hall, E.J. Computed Tomography—An Increasing Source of Radiation Exposure. *N. Engl. J. Med.* **2007**, *357*, 2277–2284. [CrossRef] [PubMed]
2. Boone, J.M.; Brink, J.A.; Edyvean, S.; Huda, W.; Leitz, W.; McCollough, C.H.; McNitt-Gray, M.F. Report 87. *J. ICRU* **2012**, *12*. [CrossRef]
3. Thrall, J.H. Radiation Exposure in CT Scanning and Risk: Where Are We? *Radiology* **2012**, *264*, 325–328. [CrossRef] [PubMed]
4. Smith-Bindman, R.; Wang, Y.; Chu, P.; Chung, R.; Einstein, A.J.; Balcombe, J.; Cocker, M.; Das, M.; Delman, B.N.; Flynn, M.; et al. International Variation in Radiation Dose for Computed Tomography Examinations: Prospective Cohort Study. *BMJ* **2019**, k4931. [CrossRef]
5. Lumbreras, B.; Salinas, J.M.; Gonzalez-Alvarez, I. Cumulative Exposure to Ionising Radiation from Diagnostic Imaging Tests: A 12-Year Follow-up Population-Based Analysis in Spain. *BMJ Open* **2019**, *9*, e030905. [CrossRef] [PubMed]

6. Andersson, J.; Pavlicek, W.; Al-Senan, R.; Cody, D.; Dixon, R.; Columbo, P.; Dong, F.; Edyvean, S.; Jansen, J.; Kanal, K.; et al. *Estimating Patient Organ Dose with Computed Tomography: A Review of Present Methodology and Required DICOM Information. A Joint Report of AAPM Task Group 246 and the European Federation of Organizations for Medical Physics (EFOMP)*; AAPM: Alexandria, VA, USA, 2019.
7. Rehani, M.M.; Yang, K.; Melick, E.R.; Heil, J.; Šalát, D.; Sensakovic, W.F.; Liu, B. Patients Undergoing Recurrent CT Scans: Assessing the Magnitude. *Eur. Radiol.* **2020**, *30*, 1828–1836. [CrossRef]
8. De Mattia, C.; Campanaro, F.; Rottoli, F.; Colombo, P.E.; Pola, A.; Vanzulli, A.; Torresin, A. Patient Organ and Effective Dose Estimation in CT: Comparison of Four Software Applications. *Eur. Radiol. Exp.* **2020**, *4*, 14. [CrossRef]
9. European Commission; Directorate-General for Energy. *Medical Radiation Exposure of the European Population*; Radiation Protection; Publications Office of the European Union: Luxembourg, 2015; ISBN 978-92-79-45374-8.
10. National Council on Radiation Protection and Measurements (Ed.) *Medical Radiation Exposure of Patients in the United States: Recommendations of the National Council on Radiation Protection and Measurements*; NCRP Report; National Council on Radiation Protection and Measurements: Bethesda, MD, USA, 2019; ISBN 978-1-944888-16-9.
11. McNitt-Gray, M.F. AAPM/RSNA Physics Tutorial for Residents. Topics in CT: Radiation Dose in CT. *RadioGraphics* **2002**, *22*, 1541–1553. [CrossRef]
12. Gunn, M.L.D.; Kohr, J.R. State of the Art: Technologies for Computed Tomography Dose Reduction. *Emerg. Radiol.* **2010**, *17*, 209–218. [CrossRef]
13. Silva, A.C.; Lawder, H.J.; Hara, A.; Kujak, J.; Pavlicek, W. Innovations in CT Dose Reduction Strategy: Application of the Adaptive Statistical Iterative Reconstruction Algorithm. *Am. J. Roentgenol.* **2010**, *194*, 191–199. [CrossRef] [PubMed]
14. Costello, J.E.; Cecava, N.D.; Tucker, J.E.; Bau, J.L. CT Radiation Dose: Current Controversies and Dose Reduction Strategies. *Am. J. Roentgenol.* **2013**, *201*, 1283–1290. [CrossRef]
15. Hara, A.K.; Paden, R.G.; Silva, A.C.; Kujak, J.L.; Lawder, H.J.; Pavlicek, W. Iterative Reconstruction Technique for Reducing Body Radiation Dose at CT: Feasibility Study. *Am. J. Roentgenol.* **2009**, *193*, 764–771. [CrossRef]
16. Kalra, M.K.; Woisetschläger, M.; Dahlström, N.; Singh, S.; Lindblom, M.; Choy, G.; Quick, P.; Schmidt, B.; Sedlmair, M.; Blake, M.A.; et al. Radiation Dose Reduction with Sinogram Affirmed Iterative Reconstruction Technique for Abdominal Computed Tomography. *J. Comput. Assist. Tomogr.* **2012**, *36*, 339–346. [CrossRef] [PubMed]
17. Vaishnav, J.Y.; Jung, W.C.; Popescu, L.M.; Zeng, R.; Myers, K.J. Objective Assessment of Image Quality and Dose Reduction in CT Iterative Reconstruction: Validating Dose Reduction Claims for CT Iterative Reconstruction. *Med. Phys.* **2014**, *41*, 071904. [CrossRef]
18. Padole, A.; Ali Khawaja, R.D.; Kalra, M.K.; Singh, S. CT Radiation Dose and Iterative Reconstruction Techniques. *Am. J. Roentgenol.* **2015**, *204*, W384–W392. [CrossRef]
19. Beister, M.; Kolditz, D.; Kalender, W.A. Iterative Reconstruction Methods in X-Ray CT. *Phys. Med.* **2012**, *28*, 94–108. [CrossRef]
20. Willemink, M.J.; de Jong, P.A.; Leiner, T.; de Heer, L.M.; Nievelstein, R.A.J.; Budde, R.P.J.; Schilham, A.M.R. Iterative Reconstruction Techniques for Computed Tomography Part 1: Technical Principles. *Eur. Radiol.* **2013**, *23*, 1623–1631. [CrossRef]
21. Geyer, L.L.; Schoepf, U.J.; Meinel, F.G.; Nance, J.W.; Bastarrika, G.; Leipsic, J.A.; Paul, N.S.; Rengo, M.; Laghi, A.; De Cecco, C.N. State of the Art: Iterative CT Reconstruction Techniques. *Radiology* **2015**, *276*, 339–357. [CrossRef]
22. Stiller, W. Basics of Iterative Reconstruction Methods in Computed Tomography: A Vendor-Independent Overview. *Eur. J. Radiol.* **2018**, *109*, 147–154. [CrossRef]
23. Pickhardt, P.J.; Lubner, M.G.; Kim, D.H.; Tang, J.; Ruma, J.A.; del Rio, A.M.; Chen, G.-H. Abdominal CT with Model-Based Iterative Reconstruction (MBIR): Initial Results of a Prospective Trial Comparing Ultralow-Dose with Standard-Dose Imaging. *Am. J. Roentgenol.* **2012**, *199*, 1266–1274. [CrossRef]
24. Miéville, F.A.; Gudinchet, F.; Brunelle, F.; Bochud, F.O.; Verdun, F.R. Iterative Reconstruction Methods in Two Different MDCT Scanners: Physical Metrics and 4-Alternative Forced-Choice Detectability Experiments—A Phantom Approach. *Phys. Med.* **2013**, *29*, 99–110. [CrossRef]
25. Willemink, M.J.; Leiner, T.; de Jong, P.A.; de Heer, L.M.; Nievelstein, R.A.J.; Schilham, A.M.R.; Budde, R.P.J. Iterative Reconstruction Techniques for Computed Tomography Part 2: Initial Results in Dose Reduction and Image Quality. *Eur. Radiol.* **2013**, *23*, 1632–1642. [CrossRef]
26. Chen, J.-H.; Jin, E.-H.; He, W.; Zhao, L.-Q. Combining Automatic Tube Current Modulation with Adaptive Statistical Iterative Reconstruction for Low-Dose Chest CT Screening. *PLoS ONE* **2014**, *9*, e92414. [CrossRef]
27. Smith, E.A.; Dillman, J.R.; Goodsitt, M.M.; Christodoulou, E.G.; Keshavarzi, N.; Strouse, P.J. Model-Based Iterative Reconstruction: Effect on Patient Radiation Dose and Image Quality in Pediatric Body CT. *Radiology* **2014**, *270*, 526–534. [CrossRef] [PubMed]
28. Mangat, J.; Morgan, J.; Benson, E.; Båth, M.; Lewis, M.; Reilly, A. A Study of the Image Quality of Computed Tomography Adaptive Statistical Iterative Reconstructed Brain Images Using Subjective and Objective Methods. *Radiat. Prot. Dosim.* **2016**, *169*, 92–99. [CrossRef] [PubMed]
29. Samei, E.; Richard, S. Assessment of the Dose Reduction Potential of a Model-Based Iterative Reconstruction Algorithm Using a Task-Based Performance Metrology. *Med. Phys.* **2014**, *42*, 314–323. [CrossRef] [PubMed]
30. Dodge, C.T.; Tamm, E.P.; Cody, D.D.; Liu, X.; Jensen, C.T.; Wei, W.; Kundra, V.; Rong, X.J. Performance Evaluation of Iterative Reconstruction Algorithms for Achieving CT Radiation Dose Reduction—A Phantom Study. *J. Appl. Clin. Med. Phys.* **2016**, *17*, 511–531. [CrossRef] [PubMed]

31. Li, G.; Liu, X.; Dodge, C.T.; Jensen, C.T.; Rong, X.J. A Noise Power Spectrum Study of a New Model-Based Iterative Reconstruction System: Veo 3.0. *J. Appl. Clin. Med. Phys.* **2016**, *17*, 428–439. [CrossRef]
32. Andersen, H.K.; Völgyes, D.; Martinsen, A.C.T. Image Quality with Iterative Reconstruction Techniques in CT of the Lungs—A Phantom Study. *Eur. J. Radiol. Open* **2018**, *5*, 35–40. [CrossRef]
33. Barca, P.; Giannelli, M.; Fantacci, M.E.; Caramella, D. Computed Tomography Imaging with the Adaptive Statistical Iterative Reconstruction (ASIR) Algorithm: Dependence of Image Quality on the Blending Level of Reconstruction. *Australas. Phys. Eng. Sci. Med.* **2018**, *41*, 463–473. [CrossRef]
34. Willemink, M.J.; Noël, P.B. The Evolution of Image Reconstruction for CT—From Filtered Back Projection to Artificial Intelligence. *Eur. Radiol.* **2019**, *29*, 2185–2195. [CrossRef]
35. Pan, T.; Hasegawa, A.; Luo, D.; Wu, C.C.; Vikram, R. Technical Note: Impact on Central Frequency and Noise Magnitude Ratios by Advanced CT Image Reconstruction Techniques. *Med. Phys.* **2020**, *47*, 480–487. [CrossRef] [PubMed]
36. Hsieh, J. Adaptive Statistical Iterative Reconstruction. White Papper GE Healthcare; 2008; pp. 1–4.
37. Fan, J.; Yue, M.; Melnyk, R. Benefits of ASiR-V Reconstruction for Reducing Patient Radiation Dose and Preserving Diagnostic Quality in CT Exams. White Papper GE Healthcare; 2014; pp. 1–8.
38. Thibault, J.-B. Veo CT Model-Based Iterative Reconstruction. White Papper GE Healthcare; 2010; pp. 1–12.
39. Richard, S.; Husarik, D.B.; Yadava, G.; Murphy, S.N.; Samei, E. Towards Task-Based Assessment of CT Performance: System and Object MTF across Different Reconstruction Algorithms. *Med. Phys.* **2012**, *39*, 4115–4122. [CrossRef]
40. McCollough, C.H.; Yu, L.; Kofler, J.M.; Leng, S.; Zhang, Y.; Li, Z.; Carter, R.E. Degradation of CT Low-Contrast Spatial Resolution Due to the Use of Iterative Reconstruction and Reduced Dose Levels. *Radiology* **2015**, *276*, 499–506. [CrossRef]
41. Hsieh, J. *Computed Tomography: Principles, Design, Artifacts, and Recent Advances*; SPIE PRESS: Bellingham, WA, USA, 2015; ISBN 978-1-62841-825-5.
42. Thibault, J.-B.; Sauer, K.D.; Bouman, C.A.; Hsieh, J. A Three-Dimensional Statistical Approach to Improved Image Quality for Multislice Helical CT. *Med. Phys.* **2007**, *34*, 4526–4544. [CrossRef]
43. Hussain, F.A.; Mail, N.; Shamy, A.M.; Alghamdi, S.; Saoudi, A. A Qualitative and Quantitative Analysis of Radiation Dose and Image Quality of Computed Tomography Images Using Adaptive Statistical Iterative Reconstruction. *J. Appl. Clin. Med. Phys.* **2016**, *17*, 419–432. [CrossRef]
44. Kim, H.G.; Chung, Y.E.; Lee, Y.H.; Choi, J.-Y.; Park, M.-S.; Kim, M.-J.; Kim, K.W. Quantitative Analysis of the Effect of Iterative Reconstruction Using a Phantom: Determining the Appropriate Blending Percentage. *Yonsei Med. J.* **2015**, *56*, 253. [CrossRef]
45. Kwon, H.; Cho, J.; Oh, J.; Kim, D.; Cho, J.; Kim, S.; Lee, S.; Lee, J. The Adaptive Statistical Iterative Reconstruction-V Technique for Radiation Dose Reduction in Abdominal CT: Comparison with the Adaptive Statistical Iterative Reconstruction Technique. *Br. J. Radiol.* **2015**, *88*, 20150463. [CrossRef]
46. Benz, D.C.; Gräni, C.; Mikulicic, F.; Vontobel, J.; Fuchs, T.A.; Possner, M.; Clerc, O.F.; Stehli, J.; Gaemperli, O.; Pazhenkottil, A.P.; et al. Adaptive Statistical Iterative Reconstruction-V: Impact on Image Quality in Ultralow-Dose Coronary Computed Tomography Angiography. *J. Comput. Assist. Tomogr.* **2016**, *40*, 958–963. [CrossRef]
47. So, A.; Imai, Y.; Nett, B.; Jackson, J.; Nett, L.; Hsieh, J.; Wisenberg, G.; Teefy, P.; Yadegari, A.; Islam, A.; et al. Technical Note: Evaluation of a 160-Mm/256-Row CT Scanner for Whole-Heart Quantitative Myocardial Perfusion Imaging. *Med. Phys.* **2016**, *43*, 4821–4832. [CrossRef]
48. Racine, D.; Ott, J.G.; Ba, A.; Ryckx, N.; Bochud, F.O.; Verdun, F.R. Objective Task-Based Assessment of Low-Contrast Detectability in Iterative Reconstruction. *Radiat. Prot. Dosim.* **2016**, *169*, 73–77. [CrossRef]
49. Kim, H.G.; Lee, H.-J.; Lee, S.-K.; Kim, H.J.; Kim, M.-J. Head CT: Image Quality Improvement with ASIR-V Using a Reduced Radiation Dose Protocol for Children. *Eur. Radiol.* **2017**, *27*, 3609–3617. [CrossRef]
50. Gatti, M.; Marchisio, F.; Fronda, M.; Rampado, O.; Faletti, R.; Bergamasco, L.; Ropolo, R.; Fonio, P. Adaptive Statistical Iterative Reconstruction–V versus Adaptive Statistical Iterative Reconstruction: Impact on Dose Reduction and Image Quality in Body Computed Tomography. *J. Comput. Assist. Tomogr.* **2018**, *42*, 191–196. [CrossRef] [PubMed]
51. Goodenberger, M.H.; Wagner-Bartak, N.A.; Gupta, S.; Liu, X.; Yap, R.Q.; Sun, J.; Tamm, E.P.; Jensen, C.T. Computed Tomography Image Quality Evaluation of a New Iterative Reconstruction Algorithm in the Abdomen (Adaptive Statistical Iterative Reconstruction–V) a Comparison with Model-Based Iterative Reconstruction, Adaptive Statistical Iterative Reconstruction, and Filtered Back Projection Reconstructions. *J. Comput. Assist. Tomogr.* **2018**, *42*, 184–190. [CrossRef]
52. Lim, K.; Kwon, H.; Cho, J.; Oh, J.; Yoon, S.; Kang, M.; Ha, D.; Lee, J.; Kang, E. Initial Phantom Study Comparing Image Quality in Computed Tomography Using Adaptive Statistical Iterative Reconstruction and New Adaptive Statistical Iterative Reconstruction V. *J. Comput. Assist. Tomogr.* **2015**, *39*, 443–448. [CrossRef]
53. Tang, H.; Yu, N.; Jia, Y.; Yu, Y.; Duan, H.; Han, D.; Ma, G.; Ren, C.; He, T. Assessment of Noise Reduction Potential and Image Quality Improvement of a New Generation Adaptive Statistical Iterative Reconstruction (ASIR-V) in Chest CT. *Br. J. Radiol.* **2018**, *91*, 20170521. [CrossRef]
54. Euler, A.; Solomon, J.; Marin, D.; Nelson, R.C.; Samei, E. A Third-Generation Adaptive Statistical Iterative Reconstruction Technique: Phantom Study of Image Noise, Spatial Resolution, Lesion Detectability, and Dose Reduction Potential. *Am. J. Roentgenol.* **2018**, *210*, 1301–1308. [CrossRef]
55. De Marco, P.; Origgi, D. New Adaptive Statistical Iterative Reconstruction ASiR-V: Assessment of Noise Performance in Comparison to ASiR. *J. Appl. Clin. Med. Phys.* **2018**, *19*, 275–286. [CrossRef]

56. Viry, A.; Aberle, C.; Racine, D.; Knebel, J.-F.; Schindera, S.T.; Schmidt, S.; Becce, F.; Verdun, F.R. Effects of Various Generations of Iterative CT Reconstruction Algorithms on Low-Contrast Detectability as a Function of the Effective Abdominal Diameter: A Quantitative Task-Based Phantom Study. *Phys. Med.* **2018**, *48*, 111–118. [CrossRef]
57. Chen, L.; Jin, C.; Li, J.; Wang, G.; Jia, Y.; Duan, H.; Pan, N.; Guo, J. Image Quality Comparison of Two Adaptive Statistical Iterative Reconstruction (ASiR, ASiR-V) Algorithms and Filtered Back Projection in Routine Liver CT. *Br. J. Radiol.* **2018**, *91*, 20170655. [CrossRef]
58. Tang, H.; Liu, Z.; Hu, Z.; He, T.; Li, D.; Yu, N.; Jia, Y.; Shi, H. Clinical Value of a New Generation Adaptive Statistical Iterative Reconstruction (ASIR-V) in the Diagnosis of Pulmonary Nodule in Low-Dose Chest CT. *Br. J. Radiol.* **2019**, *92*, 20180909. [CrossRef]
59. Han, W.K.; Na, J.C.; Park, S.Y. Low-Dose CT Angiography Using ASiR-V for Potential Living Renal Donors: A Prospective Analysis of Image Quality and Diagnostic Accuracy. *Eur. Radiol.* **2020**, *30*, 798–805. [CrossRef]
60. International Atomic Energy Agency. *Quality Assurance Programme for Computed Tomography: Diagnostic and Therapy Applications*; IAEA: Vienna, Austria, 2012; ISBN 978-92-0-128910-0.
61. European Commission. *Criteria for Acceptability of Medical Radiological Equipment Used in Diagnostic Radiology, Nuclear Medicine and Radiotherapy*; Radiation Protection; Publications Office of the European Union: Luxembourg, 2013; ISBN 978-92-79-27747-4.
62. Dance, D.R. (Ed.) *Diagnostic Radiology Physics: A Handbook for Teachers and Students*; STI/PUB; International Atomic Energy Agency: Vienna, Austria, 2014; ISBN 978-92-0-131010-1.
63. Riederer, S.J.; Pelc, N.J.; Chesler, D.A. The Noise Power Spectrum in Computed X-Ray Tomography. *Phys. Med. Biol.* **1978**, *23*, 446–454. [CrossRef]
64. Friedman, S.N.; Fung, G.S.K.; Siewerdsen, J.H.; Tsui, B.M.W. A Simple Approach to Measure Computed Tomography (CT) Modulation Transfer Function (MTF) and Noise-Power Spectrum (NPS) Using the American College of Radiology (ACR) Accreditation Phantom. *Med. Phys.* **2013**, *40*, 051907. [CrossRef]
65. Samei, E.; Bakalyar, D.; Boedeker, K.; Brady, S.; Fan, J.; Leng, S.; Myers, K.; Popescu, L.; Ramirez-Giraldo, J.C.; Ranallo, F.; et al. *Performance Evaluation of Computed Tomography Systems—The Report of AAPM Task Group 233*; AAPM: Alexandria, VA, USA, 2019.
66. The Phantom Laboratory. *Catphan ® 504 Manual*; The Phantom Laboratory: Salem, NY, USA, 2013.
67. Li, K.; Tang, J.; Chen, G.-H. Statistical Model Based Iterative Reconstruction (MBIR) in Clinical CT Systems: Experimental Assessment of Noise Performance. *Med. Phys.* **2014**, *41*, 041906. [CrossRef]
68. Solomon, J.; Samei, E. Quantum Noise Properties of CT Images with Anatomical Textured Backgrounds across Reconstruction Algorithms: FBP and SAFIRE. *Med. Phys.* **2014**, *41*, 091908. [CrossRef]
69. Solomon, J.; Wilson, J.; Samei, E. Characteristic Image Quality of a Third Generation Dual-Source MDCT Scanner: Noise, Resolution, and Detectability. *Med. Phys.* **2015**, *42*, 4941–4953. [CrossRef] [PubMed]
70. Funama, Y.; Taguchi, K.; Utsunomiya, D.; Oda, S.; Katahira, K.; Tokuyasu, S.; Yamashita, Y. Image Quality Assessment of an Iterative Reconstruction Algorithm Applied to Abdominal CT Imaging. *Phys. Med.* **2014**, *30*, 527–534. [CrossRef]
71. Geyer, L.L.; Körner, M.; Harrieder, A.; Mueck, F.G.; Deak, Z.; Wirth, S.; Linsenmaier, U. Dose Reduction in 64-Row Whole-Body CT in Multiple Trauma: An Optimized CT Protocol with Iterative Image Reconstruction on a Gemstone-Based Scintillator. *Br. J. Radiol.* **2016**, *89*, 20160003. [CrossRef]
72. Brady, S.L.; Yee, B.S.; Kaufman, R.A. Characterization of Adaptive Statistical Iterative Reconstruction Algorithm for Dose Reduction in CT: A Pediatric Oncology Perspective. *Med. Phys.* **2012**, *39*, 5520–5531. [CrossRef]

applied sciences

MDPI

Article

The Role of Acquisition Angle in Digital Breast Tomosynthesis: A Texture Analysis Study

Alessandro Savini [1,*], Giacomo Feliciani [1,*], Michele Amadori [2], Stefano Rivetti [3], Marta Cremonesi [4], Francesco Cesarini [5], Tiziana Licciardello [1], Daniela Severi [2], Valentina Ravaglia [6], Alessandro Vagheggini [7], Anna Sarnelli [1] and Fabio Falcini [8]

1 Medical Physics Unit, Istituto Scientifico Romagnolo per lo Studio e la Cura dei Tumori (IRST) IRCCS, 47014 Meldola, Italy; tiziana.licciardello@irst.emr.it (T.L.); anna.sarnelli@irst.emr.it (A.S.)
2 Department of Radiology, Morgagni-Pierantoni Hospital, 47121 Forlì, Italy; michele.amadori@auslromagna.it (M.A.); daniela.severi@irst.emr.it (D.S.)
3 Medical Physics Unit, Sassuolo Hospital, 41049 Sassuolo, Italy; s.rivetti@ospedalesassuolo.it
4 Radiation Research Unit, European Institute of Oncology, 20141 Milano (MI), Italy; marta.cremonesi@ieo.it
5 Post-Graduate School in Medical Physics, University of Bologna, 40126 Bologna, Italy; cfrancescocesarini@gmail.com
6 Medical Physics Unit, Morgagni-Pierantoni Hospital, 47121 Forlì, Italy; valentina.ravaglia@auslromagna.it
7 Unit of Biostatistics and Clinical Trials, Istituto Scientifico Romagnolo per lo Studio e la Cura dei Tumori (IRST) IRCCS, 47014 Meldola, Italy; Alessandro.vagheggini@irst.emr.it
8 Romagna Cancer Registry, Istituto Scientifico Romagnolo per lo Studio e la Cura dei Tumori (IRST) IRCCS, 47014 Meldola, Italy; fabio.falcini@irst.emr.it
* Correspondence: alessandro.savini@irst.emr.it (A.S.); giacomo.feliciani@irst.emr.it (G.F.); Tel.: +39-3274730398 (G.F.)

Received: 24 July 2020; Accepted: 27 August 2020; Published: 31 August 2020

Abstract: Background: Digital breast tomosynthesis (DBT) systems employ a sophisticated set of acquisition parameters to generate an image set, and the DBT acquisition angle is considered to be one of the most important parameters. The aim of this study was to use texture analysis to assess how the DBT acquisition angle might influence DBT images of breast parenchyma. Methods: Thirty-four patients were selected from a clinical study conducted at IRST Institute. Each patient underwent a dual DBT scan performed with Fujifilm Amulet Innovality (Fujifilm Corp, Tokyo, Japan) in standard (ST, angular range = 15°) and high-resolution (HR, angular range = 40°) modalities. Texture analysis was applied on the paired dataset using histogram-based features and gray level co-occurrence matrix (GLCM) features. Wilcoxon-signed rank and Pearson-rank tests were used to assess the statistical differences and correlations between extracted features. Results: The DBT acquisition angle did not affect histogram-based features, whereas there was a significant difference in five GLCM features ($p < 0.05$) between DBT images generated with 15° and 40° acquisition angles. Correlation analysis showed that two GLCM features were not correlated at a $p < 0.05$ significance level. Conclusions: DBT acquisition angle affects the textures extracted from DBT images and this dependence should be considered when establishing baselines for classifiers of malignant tissue. Furthermore, texture analysis could be proposed as a quantitative method for comparing and scoring the contrast of DBT images.

Keywords: medical imaging; radiomics; tomosynthesis; acquisition angle

1. Introduction

Texture analysis is a promising technique for extracting quantitative features from radiographic images to be correlated with clinical or pathological characteristics of a tissue [1,2]. In the 1990s, several authors began applying texture analysis to mammographic images to identify and classify malignant

masses or microcalcifications [3–7]. Other authors correlated texture features with BRCA1/BRCA2 mutations [8] or with breast cancer subtypes [9]. In a recent work by Li et al., texture analysis of digital mammographic images was deemed as an excellent tool for differential diagnosis of benign and malignant tumors, especially if combined with standard visual analysis by radiologists [10]. Digital breast tomosynthesis (DBT) is a relatively new technique compared to digital mammography (DM), and for this reason, studies on texture analysis applied to DBT are less widespread. Kontos et al. studied the correlation between texture features calculated from DBT images and risk factors such as breast percent density or Gail and Claus risk models [11,12]. They concluded that texture features extracted from DBT images are more favorably correlated with risk factors than those extracted from DM. However, the authors also observed that the gray level distribution of DBT images may be affected by several factors such as the image acquisition geometry [13] and the reconstruction algorithm, hence suggesting that further research is needed to analyze the variability of features according to these parameters. At IRST institute, clinical DBTs can be performed with two acquisition geometries that differ in terms of the acquisition angle (15° and 40°) and in-plane image resolution (0.15 and 0.10 mm/pixel). With the final aim of developing a computer-aided diagnosis (CAD) system based on texture features, we first needed to investigate whether different acquisition geometries had an impact on texture values. Several authors have demonstrated that the parameter that most influences DBT images is the DBT acquisition angle. In particular, Li et al. found that an increased acquisition angle positively correlated with improved z-resolution [14]. Goodsitt et al. observed that increasing the DBT acquisition angle improved the contrast-to-noise ratio of disk details, as well as the subjective scoring of image quality by multiple readers [15]. Other authors used a model-observer approach to study the detectability of small signals in simulated DBT datasets, reporting that the acquisition angle had a positive effect on the detectability of each signal size considered [16]. A model-observer approach was also used recently by Lee et al., who studied the signal detectability of simulated DBT patterns by varying several acquisition parameters including angle, reconstruction filter, and slice thickness [17]. However, all these studies were performed on phantoms or simulated DBT datasets. The aim of the present study was to use texture analysis to characterize the impact of the acquisition angle on DBT images. This research was conducted on real DBT images of breast parenchyma originating from a clinical paired dataset (i.e., a single patient underwent dual DBT scan with 15° and 40° acquisition angle). To the best of our knowledge, no similar studies have been published elsewhere.

2. Materials and Methods

We used a Fujifilm Amulet Innovality (Fujifilm Corp, Tokyo, Japan) DBT system, which has 2 imaging modalities, i.e., a "standard" (ST) modality wherein the X-ray tube angular range continuously spans a range of 15°, and a "high-resolution" (HR) modality wherein the angular range is 40°. The number of acquired projections was 15 for both modalities. The in-plane pixel size of DBT reconstructed images was 0.1 mm in the HR modality and 0.15 mm in the ST modality. The slice thickness was 1 mm for both modalities. The automatic exposure control (AEC) of the HR modality was routinely tuned to deliver a higher dose to the breast than that of the ST modality. In order to eliminate this bias, we set up a scanning protocol to equalize the dose for both ST and HR modalities. This was carried out by applying the exposure parameters (i.e., anode/filter, kVp, mAs) for the HR modality, determined by the AEC during the ST acquisition.

This study was conducted as part of a clinical trial called "Digital Breast Tomosynthesis in a screening population—Investigation on angular range and dose level acquisition" currently ongoing at our institute (Protocol Code: IRST174.13). The trial was approved by the IRST Ethics Committee and was conducted in accordance with the ethical standards laid down in the 1964 Declaration of Helsinki. All patients gave written informed consent before being scanned. The trial inclusion criteria were: age between 45 years and 74 years and BI-RADS $\geq$ 3 evaluated with DM from the regional screening program. Exclusion criteria were: pregnancy, participation in another clinical trial, or a clinical diagnosis of breast cancer. Patients satisfying the study criteria were scheduled to undergo

a dual DBT scan in accordance with the above-mentioned scanning protocol. Each DBT scan was accompanied by an ultrasound (US) scan. The present study was conducted on a subset of the enrolled patients. In particular, we selected 34 patients (for a total of 36 image sets) whose DBT and US imaging results were scored as negative by 2 independent radiologists (i.e., BI-RADS = 1 after DBT and US re-evaluation). A follow-up of least two years was available for the selected patients.

We considered the craniocaudal (CC) view for each DBT image set, focusing the analysis on 7 slices at the center of the imaging study (Figure 1). Our choice was guided by Kontos et al., who suggested insulating the fibro-glandular tissue for feature extraction as superficial layers (skin and subcutaneous fat) only act as anatomical noise and are not correlated with breast cancer risk [11]. This choice is particularly relevant for small-sized breasts, as the number of slices in a DBT set is a function of breast thickness. Furthermore, preliminary analysis showed that mean feature values were not influenced by increasing the number of considered slices in large-sized breasts (data not shown). In order to apply a coherent texture analysis and insulate the effect of the acquisition angle, an in-house program developed in MATLAB (MathWorks, Inc., Natick, MA, USA) was used to downsample the in-plane resolution of HR images to the in-plane resolution of ST images, i.e., from 0.1 to 0.15 mm/pixel. The downsampling was performed using nearest-neighbor interpolation to maintain the integrity of original data and avoiding generating fictitious pixel values [18–20]. A region of interest (ROI) of 256×256 pixels was placed behind the nipple (Figure 1). This combination of ROI size and position was previously reported to have the highest discrimination power with regard to texture performance in DM [8,21] and in DBT [12]. Furthermore, the ROI size is a trade-off between different needs. In fact, the ROI size used in the present work is defined to include the limited parenchymal area of small breasts and is assumed standard for all breasts to avoid potential biases in the features' calculation. Feature computation was performed for each ROI in the 2D mode with MaZda software package [22]. We considered first-order features based on the image gray levels histogram and second-order features based on the gray level co-occurrence matrix (GLCM) [1,23] (Table 1). GLCM features were extracted using first-order neighbors and 0°, 45°, 90° and 135° directions. Feature values extracted from each slice were averaged into a single value. The same averaging operation was performed for the feature values obtained along the different GLCM calculation directions (0°, 45°, 90° and 135°). With these averaging operations, a single value for each feature was associated with a single DBT image set. Descriptions and mathematical details of the relevant features for this study can be found in Supplementary Materials.

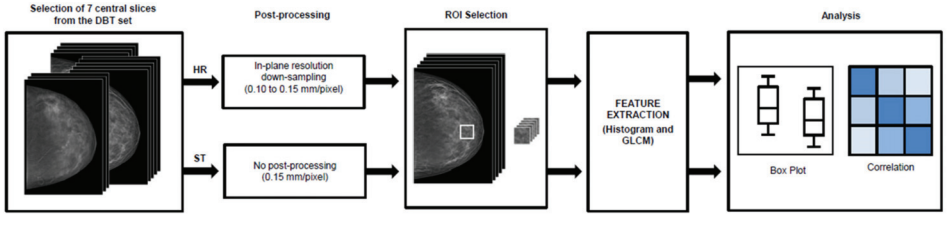

Figure 1. Workflow followed for texture analysis. DBT, digital breast tomosynthesis; ROI, region of interest; GLCM, gray level co-occurrence matrix.

In our DBT system, image gray levels had 14 bits and this resolution was maintained for histogram-based features. However, resampling was needed for GLCM features to avoid the risk of excessively large and sparse matrices that would inhibit a robust statistical analysis [24,25]. We extracted GLCM features after reducing the bits per pixel to 6 bits (MaZda default value), repeating the analysis with 5 bits and 7 bits to confirm the robustness of extracted features in relation to the bits rescaling.

Table 1. Features considered in this study. See [22] and Supplementary Materials for definitions.

First-Order Features (Histogram)	Mean
	Variance
	Skewness
	Kurtosis
Second-Order Features (GLCM)	Angular Second Moment
	Contrast
	Correlation
	Sum of Squares
	Inverse Difference Moment
	Sum Average
	Sum Variance
	Sum Entropy
	Entropy
	Difference Variance
	Difference Entropy

The features reported in Table 1 were extracted from the DBT images obtained with both ST (15° acquisition angle) and HR (40° acquisition angle) scan angles. All statistics comparisons were conducted considering these two paired datasets. Populations were compared with boxplots and the difference was assessed with a Wilcoxon-signed rank test (R-software version 3.5.3 Lucent Technologies, Murray Hill, New Providence, NJ, USA). A p-value < 0.05 was deemed statistically significant. Correlation between features that showed a significant difference between ST and HR images was inferred with Spearman rank correlation test. The datasets generated and/or analyzed during the current study are available from the corresponding authors on reasonable request.

3. Results

For a single DBT image set, feature values deviated within <1% from the value averaged over the slices and over the GLCM direction calculation. This low deviation justified taking the average value for each feature, corresponding to a single DBT image set. A total of 15 features were extracted and five of them (all belonging to the second-order group, i.e., GLCM features) showed significant differences between ST and HR images (see Table 2). The scenario was unchanged when the analysis was repeated after varying the bits' resampling amplitude (i.e., 5-bit, 6-bit and 7-bit). The correlation matrix of the features showing a significant difference between ST and HR images is reported in Figure 2. The Correlation feature was not correlated with any other feature. The Contrast feature was strongly correlated with other features (Spearman-$\rho = \pm 0.99$ with a p-value < 0.001) except the Correlation feature (Spearman-$\rho = 0.31$ with a p-value $= 0.14$). Again, this scenario was unchanged for 5-bit, 6-bit and 7-bit resampling amplitudes. For this reason, further analysis only took into consideration the not correlated GLCM features, Contrast and Correlation. Figure 3 shows boxplots comparing these features in ST and HR images. Figure 4 contains boxplots of Mean and Variance features that showed no significant difference between ST and HR images. Finally, in Figure 5, we show the differences between ST and HR in 2D space employing the two most relevant features.

Table 2. Differences between feature median values calculated from the high-resolution (40° acquisition angle) and standard (15° acquisition angle) DBT images. Only significant differences are reported ($p < 0.05$, Wilcoxon signed-rank test).

		% Difference 40°–15° Acquisition Angle ($p < 0.05$)
First-Order Features (Histogram)		
Second-Order Features (GLCM)	Contrast	+50%
	Correlation	−5%
	Inverse Difference Moment	−14%
	Difference Variance	+45%
	Difference Entropy	+17%

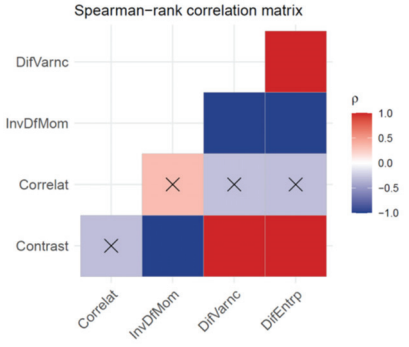

Figure 2. Spearman rank correlation matrix for features showing a significant difference between 15° acquisition angle (standard mode) and 40° acquisition angle (high resolution mode) DBT images. Red and Blue elements indicate a positive and negative correlation, respectively, with a significance: $p < 0.001$. Crossed elements indicate that the correlation is not significant $p > 0.05$.

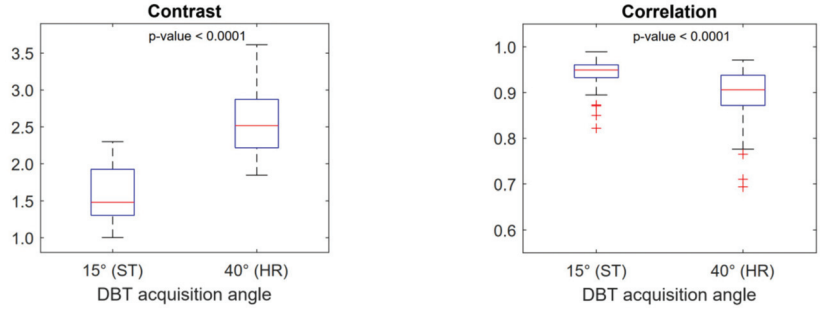

Figure 3. Boxplots of the non-correlated features Contrast (**a**) and Correlation (**b**). These features show a significant difference between 15° acquisition angle (standard mode) and 40° acquisition angle (high resolution mode) DBT images.

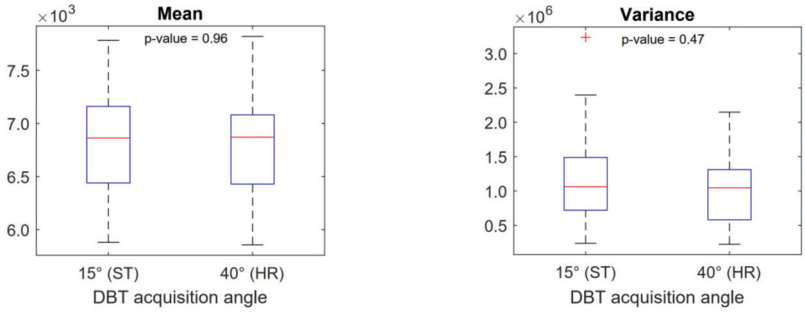

(**a**) (**b**)

Figure 4. Boxplots of Mean (**a**) and Variance (**b**) histogram-based features. These features show no significant difference between 15° acquisition angle (standard mode) and 40° acquisition angle (high resolution mode) DBT images.

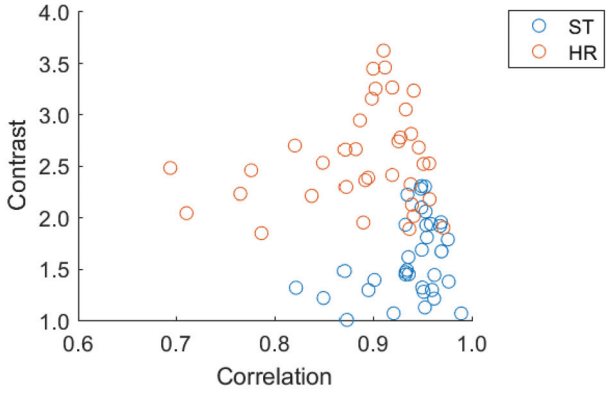

Figure 5. Scatter plot of Correlation vs. Contrast, the two most relevant features, showing the distribution in 2D space of the two imaging modalities.

4. Discussion

In the present work, we investigated the variability in texture features extracted from DBT of breast parenchyma in relation to the DBT acquisition angle. Insulating the effect of the acquisition angle was not a simple task. Different manufacturers use different angles, and comparisons are influenced by numerous confounding variables (e.g., different detector technology, different X-ray quality, different dose levels). The Fujifilm Amulet Innovality offers two acquisition modalities (ST and HR) on the same DBT system, which enabled us to eliminate many of these variables. We succeeded in insulating the DBT acquisition angle effect by designing a specific acquisition and data normalization protocol that equalized the image resolution and the dose of the two modalities. Furthermore, our comparison between feature values was performed on a paired dataset. The DBT acquisition angle influenced second-order features (from GLCM). GLCM features have been widely used in DM to build classifiers of malignant breast tissue [5,7,21,26,27]. Research has also been extended to DBT by other authors using different DBT systems with different acquisition angles [11,12,28]. In the present work, we demonstrated that the DBT acquisition angle significantly influences several GLCM features extracted from healthy breast parenchyma. This must be taken into consideration when developing classifiers for malignant tissue in DBT (i.e., the GLCM feature values for healthy breast tissue may differ simply because of the different DBT acquisition angle) and also when comparing texture values

calculated from different DBT systems, as these may differ on the basis of the acquisition angle. Texture features showing a significant difference may translate to physical considerations in DBT images and in the DBT acquisition process. In particular, the GLCM Contrast feature is a measure of the amount of local variation present in the image [23]. From this viewpoint, our results demonstrate that DBT images show a higher level of local contrast for healthy breast parenchyma (around 50% increase in median value) when DBT reconstruction is performed using projections with a wider acquisition angle (see Table 2). The observed difference can only be attributed to the wider acquisition angle because other variables such as higher dose or higher resolution were ruled out by the chosen acquisition protocol, and the image processing performed before the texture analysis. This result can be considered to be an addition to the existing findings regarding the quantitative comparisons between different DBT acquisition systems [29,30]. Our finding is coherent with findings of other authors regarding the positive effect of wider DBT acquisition angle on several quantitative parameters such as z-resolution, contrast-to-noise ratio of disk details, and subjective scoring of image quality by multiple readers [15,21]. In this context, texture analysis applied to DBT images has the potential to be an additional quantitative method for scoring and comparing DBT images.

Analogous considerations can be made regarding the difference observed for the Correlation feature, which is a measure of gray levels linear dependency in the image [23]. In our study, DBT images, reconstructed using wider acquisition angle projections, showed pixel gray levels which were less correlated.

Histogram-based features were not affected by DBT angular range, which may have been because histogram-based features do not depend on the local distribution of gray levels. Rather, they depend globally on the gray levels which were aggregated in the histogram within the ROI. For this reason, we could argue that local differences induced by different DBT acquisition angles were averaged out when looking globally at the histogram.

Our study had some limitations. We restricted the analysis to the features based on gray levels histogram and GLCM because these are the features most often considered by other authors for developing classifiers in DM [3–7] and DBT [11,12]. However, it might be useful in future studies to extend the analysis to other high-order features (e.g., run length matrix or wavelet features). In this study, we considered a dataset of 34 patients. The sample size was sufficient to reveal with statistical significance (i.e., $p < 0.05$) differences larger than 5% in DBT texture studies due to the different acquisition geometries. This fact needs to be considered when developing feature-based classifiers for healthy/malignant tissues. Statistical significance was obtained for 5 out of 15 considered features. Further studies will be performed with a larger dataset of patients in order to investigate subtler differences between the two imaging modalities.

The added value of our findings is that they were obtained by analyzing real images of breast parenchyma from a paired clinical DBT dataset. Kontos et al. [12] concluded that parenchymal texture features from DBT images have the potential to be used as imaging biomarkers to provide a more comprehensive quantitative characterization of breast parenchyma complexity. The texture analysis methodology applied in this study can be extended to assess the way in which the quantitative texture differences in DBT breast parenchyma might impact the clinical diagnostic performances.

5. Conclusions

In the present study, we found that texture features calculated from DBT images were influenced by the DBT acquisition angle, which is a key geometrical parameter of a DBT scan. This effect was observed for several GLCM-based features. Two main conclusions can be drawn from our results, the first being that the variability in texture values due to different acquisition geometries should be taken into consideration when developing GLCM texture-based classifiers for healthy/malignant tissue. Our second conclusion derives from the physical significance of some GLCM features. In particular, we demonstrated that the Contrast feature, defined from the GLCM, showed a significant increase (+50% in the median value) when a wider DBT acquisition angle was chosen. In this scenario, texture

analysis in DBT has the potential to be an alternative to other quantitative techniques such as model observer methods [16,17] for scoring and comparing DBT images. The approach used in this work could be extended to other clinical parameters and it could have the possibility of reducing the considerable effort of performing clinical studies with real human observers.

Supplementary Materials: The following are available online at http://www.mdpi.com/2076-3417/10/17/6047/s1, Feature mathematical description S1: Short tutorial about relevant features calculations and descriptions.

Author Contributions: Conceptualization, A.S. (Alessandro Savini), A.S. (Anna Sarnelli). and F.F.; methodology, G.F., V.R.; software, G.F., A.S. (Alessandro Savini), F.C.; validation, S.R., A.S. (Anna Sarnelli); formal analysis, G.F., A.S. (Alessandro Savini), A.S. (Anna Sarnelli), E.R.; investigation, M.A., F.C., D.S., F.F.; data curation, A.V.; writing—original draft preparation, A.S. (Alessandro Savini), A.S. (Anna Sarnelli), G.F.; writing—review and editing, A.S. (Alessandro Savini), G.F., A.S. (Anna Sarnelli), S.R., T.L., M.C.; visualization, A.S. (Alessandro Savini), G.F., V.R., T.L.; supervision, M.C., F.F. and A.S. (Anna Sarnelli); project administration, F.F.; All authors have read and agreed to the published version of the manuscript.

Funding: This research received no external funding.

Acknowledgments: The authors thank Gràinne Tierney for language editing.

Conflicts of Interest: The authors declare no conflict of interest.

References

1. Lambin, P.; Rios-Velazquez, E.; Leijenaar, R.; Carvalho, S.; Van Stiphout, R.G.P.M.; Granton, P.; Zegers, C.M.L.; Gillies, R.; Boellard, R.; Dekker, A.; et al. Radiomics: Extracting more information from medical images using advanced feature analysis. *Eur. J. Cancer* **2012**, *48*, 441–446. [CrossRef]
2. Larue, R.T.H.M.; Defraene, G.; De Ruysscher, D.; Lambin, P.; Van Elmpt, W. Quantitative radiomics studies for tissue characterization: A review of technology and methodological procedures. *Br. J. Radiol.* **2017**, *90*, 20160665. [CrossRef]
3. Petrosian, A.; Heang-Ping, C.; Helvie, M.A.; Goodsitt, M.M.; Adler, D.D. Computer-aided diagnosis in mammography: Classification of mass and normal tissue by texture analysis. *Phys. Med. Biol.* **1994**, *39*, 2273–2288. [CrossRef]
4. Chan, H.P.; Sahiner, B.; Petrick, N.; Helvie, M.A.; Lam, K.L.; Adler, D.D.; Goodsitt, M.M. Computerized classification of malignant and benign microcalcifications on mammograms: Texture analysis using an artificial neural network. *Phys. Med. Biol.* **1997**, *42*, 549–567. [CrossRef]
5. Karahaliou, A.N.; Boniatis, I.S.; Skiadopoulos, S.G.; Sakellaropoulos, F.N.; Arikidis, N.S.; Likaki, E.A.; Panayiotakis, G.S.; Costaridou, L.I. Breast cancer diagnosis: Analyzing texture of tissue surrounding microcalcifications. *IEEE Trans. Inf. Technol. Biomed.* **2008**, *12*, 731–738. [CrossRef]
6. Karahaliou, A.; Skiadopoulos, S.; Boniatis, I.; Sakellaropoulos, P.; Likaki, E.; Panayiotakis, G.; Costaridou, L. Texture analysis of tissue surrounding microcalcifications on mammograms for breast cancer diagnosis. *Br. J. Radiol.* **2007**, *80*, 648–656. [CrossRef]
7. Pereira, R.R.; Azevedo Marques, P.M.; Honda, M.O.; Kinoshita, S.K.; Engelmann, R.; Muramatsu, C.; Doi, K. Usefulness of texture analysis for computerized classification of breast lesions on mammograms. *J. Digit. Imaging* **2007**, *20*, 248–255. [CrossRef]
8. Li, H.; Giger, M.L.; Olopade, O.I.; Margolis, A.; Lan, L.; Chinander, M.R. Computerized texture analysis of mammographic parenchymal patterns of digitized mammograms1. *Acad. Radiol.* **2005**, *12*, 863–873. [CrossRef] [PubMed]
9. Ma, W.; Zhao, Y.; Ji, Y.; Guo, X.; Jian, X.; Liu, P.; Wu, S. Breast cancer molecular subtype prediction by mammographic radiomic features. *Acad. Radiol.* **2019**, *26*, 196–201. [CrossRef]
10. Li, Z.; Yu, L.; Wang, X.; Yu, H.; Gao, Y.; Ren, Y.; Wang, G.; Zhou, X. Diagnostic performance of mammographic texture analysis in the differential diagnosis of benign and malignant breast tumors. *Clin. Breast Cancer* **2018**, *18*, e621–e627. [CrossRef]
11. Kontos, D.; Bakic, P.R.; Carton, A.K.; Troxel, A.B.; Conant, E.F.; Maidment, A.D.A. Parenchymal texture analysis in digital breast tomosynthesis for breast cancer risk estimation. A preliminary study. *Acad. Radiol.* **2009**, *16*, 283–298. [CrossRef]

12. Kontos, D.; Ikejimba, L.; Bakic, P. Analysis of parenchymal texture with digital breast tomosynthesis: Comparison with digital mammography and implications for cancer risk assessment. *Radiology* **2011**, *261*, 80–91. [CrossRef]
13. Sechopoulos, I.; Ghetti, C. Optimization of the acquisition geometry in digital tomosynthesis of the breast. *Med. Phys.* **2009**, *36*, 1199–1207. [CrossRef]
14. Li, B.; Avinash, G.B.; Uppaluri, R.; Eberhard, J.W.; Claus, B.E.H. The impact of acquisition angular range on the z-resolution of radiographic tomosynthesis. *Int. Congr. Ser.* **2004**, *1268*, 13–18. [CrossRef]
15. Goodsitt, M.M.; Chan, H.P.; Schmitz, A.; Zelakiewicz, S.; Telang, S.; Hadjiiski, L.; Watcharotone, K.; Helvie, M.A.; Paramagul, C.; Neal, C.; et al. Digital breast tomosynthesis: Studies of the effects of acquisition geometry on contrast-to-noise ratio and observer preference of low-contrast objects in breast phantom images. *Phys. Med. Biol.* **2014**, *59*, 5883–5902. [CrossRef]
16. Reiser, I.; Nishikawa, R.M. Task-based assessment of breast tomosynthesis: Effect of acquisition parameters and quantum noise. *Med. Phys.* **2010**, *37*, 1591–1600. [CrossRef]
17. Lee, C.; Han, M.; Baek, J. Human observer performance on in-plane digital breast tomosynthesis images: Effects of reconstruction filters and data acquisition angles on signal detection. *PLoS ONE* **2020**, *15*, 1–20. [CrossRef]
18. Han, D. Comparison of commonly used image interpolation methods. In Proceedings of the 2nd International Conference on Computer Science and Electronics Engineering, Hangzhou, China, 22–23 March 2013; pp. 1556–1559. [CrossRef]
19. Parker, J.A.; Kenyon, R.V.; Troxel, D.E. Comparison of interpolating methods parker kenyon troxel. *IEEE Trans. Med. Imaging* **1983**, *2*, 31–39. [CrossRef]
20. Larue, R.T.H.M.; van Timmeren, J.E.; de Jong, E.E.C.; Feliciani, G.; Leijenaar, R.T.H.; Schreurs, W.M.J.; Sosef, M.N.; Raat, F.H.P.J.; van der Zande, F.H.R.; Das, M.; et al. Influence of gray level discretization on radiomic feature stability for different CT scanners, tube currents and slice thicknesses: A comprehensive phantom study. *Acta Oncol. (Madr)* **2017**, *56*, 1544–1553. [CrossRef]
21. Li, H.; Giger, M.L.; Huo, Z.; Olopade, O.I.; Lan, L.; Weber, B.L.; Bonta, L. Computerized analysis of mammographic parenchymal patterns for assessing breast cancer risk: Effect of ROI size and location. *Med. Phys.* **2004**, *31*, 549–555. [CrossRef]
22. Szczypiński, P.M.; Strzelecki, M.; Materka, A.; Klepaczko, A. MaZda-A software package for image texture analysis. *Comput. Methods Programs Biomed.* **2009**, *94*, 66–76. [CrossRef]
23. Haralick, R.M.; Shanmugam, K.; Dinstein, I. Textural features for image classification. *IEEE Trans. Syst. Man Cybern.* **1973**, *SMC-3*, 610–621. [CrossRef]
24. Gupta, S.; Markey, M.K. Correspondence in texture features between two mammographic views. *Med. Phys.* **2005**, *32*, 1598–1606. [CrossRef]
25. Rangayyan, R.M.; Nguyen, T.M.; Ayres, F.J.; Nandi, A.K. Effect of pixel resolution on texture features of breast masses in mammograms. *J. Digit. Imaging* **2010**, *23*, 547–553. [CrossRef]
26. Zheng, Y.; Keller, B.M.; Ray, S.; Wang, Y.; Conant, E.F.; Gee, J.C.; Kontos, D. Parenchymal texture analysis in digital mammography: A fully automated pipeline for breast cancer risk assessment. *Med. Phys.* **2015**, *42*, 4149–4160. [CrossRef]
27. Kamra, A.; Jain, V.K.; Singh, S.; Mittal, S. Characterization of architectural distortion in mammograms based on texture analysis using support vector machine classifier with clinical evaluation. *J. Digit. Imaging* **2016**, *29*, 104–114. [CrossRef]
28. Tagliafico, A.S.; Valdora, F.; Mariscotti, G.; Durando, M.; Nori, J.; La Forgia, D.; Rosenberg, I.; Caumo, F.; Gandolfo, N.; Houssami, N.; et al. An exploratory radiomics analysis on digital breast tomosynthesis in women with mammographically negative dense breasts. *Breast* **2018**, *40*, 92–96. [CrossRef]
29. Sechopoulos, I. A review of breast tomosynthesis. Part II. Image reconstruction, processing and analysis, and advanced applications. *Med. Phys.* **2013**, *40*, 014302. [CrossRef]
30. Ortenzia, O.; Rossi, R.; Bertolini, M.; Nitrosi, A.; Ghetti, C. Physical characterisation of four different commercial digital breast tomosynthesis systems. *Radiat. Prot. Dosimetry* **2018**, *181*, 277–289. [CrossRef]

applied sciences

MDPI

Article

Correction for the Partial Volume Effects (PVE) in Nuclear Medicine Imaging: A Post-Reconstruction Analytic Method

Fabio Di Martino [1], Patrizio Barca [2], Eleonora Bortoli [1,*], Alessia Giuliano [3] and Duccio Volterrani [4]

[1] Medical Physics Unit, University Hospital of Santa Chiara, 56126 Pisa, Italy; f.dimartino@ao-pisa.toscana.it
[2] Department of Medical Physics, IRCCS AOUB, 40138 Bologna, Italy; barca.patrizio@gmail.com
[3] Medical Physics Unit, Hospital of San Luca, 55100 Lucca, Italy; alessia.giuliano@uslnordovest.toscana.it
[4] Nuclear Medicine Unit, University Hospital of Santa Chiara, 56126 Pisa, Italy; duccio.volterrani@med.unipi.it
* Correspondence: eleonora.bortoli@gmail.com; Tel.: +39-3408764238

Featured Application: The proposed approach allows recovering the loss of quantification due to Partial Volume Effect. This is an alternative post-processing method to the Recovery Coefficient method, with the same limitations, but with the advantage of deriving theoretically the dependencies of the parameters that describe the effect. With the proposed approach, the need of measuring these parameters every time they change could be overcome.

Abstract: Quantitative analyses in nuclear medicine are increasingly used, both for diagnostic and therapeutic purposes. The Partial Volume Effect (PVE) is the most important factor of loss of quantification in Nuclear Medicine, especially for evaluation in Region of Interest (ROI) smaller than the Full Width at Half Maximum (FWHM) of the PSF. The aim of this work is to present a new approach for the correction of PVE, using a post-reconstruction process starting from a mathematical expression, which only requires the knowledge of the FWHM of the final PSF of the imaging system used. After the presentation of the theoretical derivation, the experimental evaluation of this method is performed using a PET/CT hybrid system and acquiring the IEC NEMA phantom with six spherical "hot" ROIs (with diameters of 10, 13, 17, 22, 28, and 37 mm) and a homogeneous "colder" background. In order to evaluate the recovery of quantitative data, the effect of statistical noise (different acquisition times), tomographic reconstruction algorithm with and without time-of-flight (TOF) and different signal-to-background activity concentration ratio (3:1 and 10:1) was studied. The application of the corrective method allows recovering the loss of quantification due to PVE for all sizes of spheres acquired, with a final accuracy less than 17%, for lesion dimensions larger than two FWHM and for acquisition times equal to or greater than two minutes.

Keywords: partial volume effect; quantitative analysis; point spread function; post-reconstruction-correction-method

Citation: Di Martino, F.; Barca, P.; Bortoli, E.; Giuliano, A.; Volterrani, D. Correction for the Partial Volume Effects (PVE) in Nuclear Medicine Imaging: A Post-Reconstruction Analytic Method. *Appl. Sci.* **2021**, *11*, 6460. https://doi.org/10.3390/app11146460

Academic Editor: Salvatore Gallo

Received: 19 May 2021
Accepted: 4 July 2021
Published: 13 July 2021

1. Introduction

Quantitative positron emission tomography/computed tomography (PET/CT) is currently used as a diagnostic/prognostic tool and for assessing therapy efficacy. Quantification in fluorodeoxyglucose (FDG) PET/CT is mainly performed using standardized uptake value (SUV) [1]. Moreover, there is an increasing interest in deriving other quantitative parameters such as the metabolic tumor volume (MTV) and the total lesion glycolysis (TLG) [2].

It is well known that there are several sources of errors in SUV measurements, which are usually even poorly standardized between institutions with different PET equipment. Image reconstruction variability seems to have a prominent role in the unreliability of quantitative assessment of PET images mainly because of improvements in PET technology, which significantly affect SUV measurement. Thus, it has been reported that PET recon-

structions including PSF compensation can increase SUV_{max} more than 66% in small nodal metastases in breast cancer or for NSCLC [3,4].

Moreover, an international survey reported that 52% of PET centers use alternative protocols with adapted reconstruction parameters. Additional complications arise considering the reconstruction variability between centers running similar systems. In fact, it has been reported that site-specific reconstruction parameters increased the quantitative variability among similar scanners [5,6].

The use of post-processing corrective methods could be a way to reduce this variability in order to achieve a better harmonization of SUV measurements between different PET centers.

In this context, quantitative parameters such as the SUV are strictly related to the system spatial resolution performances.

Spatial resolution depends on the physics of PET imaging (positron range, collinearity, scatter), on the detector design, and on the reconstruction method. All these factors lead to some amount of blurring on the images, limiting the final spatial resolution of the system.

The finite spatial resolution affects the quality of the image and the correct estimation of radioactivity concentration, which consequently causes difficulties in the application of a quantitative approach in the evaluation of PET studies [7].

From a theoretical point of view, spatial resolution is defined as the Full Width Half Maximum (FWHM) of the Point Spread Function (PSF) of the imaging system, which is the description of the image response to a point source [8]. Once the PSF is defined for the imaging system, the final image can be modelled as the real radioactivity distribution convolved by the PSF of the imaging system.

The PSF of the PET system is responsible for the so-called partial volume effect (PVE), which affects images both qualitatively and quantitatively [9].

The direct effect of the PSF on the image is due to the fact that the contribution of each ideal point source of radioactivity is spread over a wider volume, i.e., the content of each voxel is the sum of the contributions of neighboring point sources.

This can result in an overestimation of the object size, but also in an underestimation of the real radioactivity concentration, because part of the signal from the source spills out in the background (spill out effect), hence it is seen outside the actual source, as well as, part of the background surrounding the source spreads into the source (spill in effect). The combined effect depends by the source/background activity concentration ratio and by the size of the source. Moreover, from a quantitative point of view, it becomes particularly important when the target is smaller in comparison to the FWHM of the imaging system [10].

In order to achieve an accurate quantification of the radioactivity concentration, PVE has to be considered and compensated, especially in small structures. To date, several techniques have been proposed to compensate for PVE, which are illustrated in details in many papers and reviews [11–13].

The method proposed in this work can be included in the post-reconstruction correction methods applied at regional level. The method is based on the exact analytical deconvolution of the PSF of the imaging system in the case of an activity distribution, which consist of a single source with homogeneous activity, surrounded by a homogeneous background. The method is experimentally tested by means of an IEC NEMA phantom acquisition, and the results are shown and discussed.

2. Materials and Methods

2.1. Theory

In order to analytically describe how the real counts can be recovered from the image counts, some basic assumptions have been made. Specifically, the method proposed here takes into account only how the system PSF affects the PVE under ideal conditions of uniform radioactive source surrounded by uniform background.

Starting from these assumptions, the post-reconstruction PSF of a 1D PET imaging system can be modeled as a normalized Gaussian function completely described by its standard deviation σ:

$$PSF_{1D} = (x,\ \sigma) = \frac{1}{\sigma\sqrt{2\pi}} e^{-\frac{x^2}{2\sigma^2}} \tag{1}$$

In a 1D case, a source uniformly distributed surrounded by a homogeneous background, can be then described by the following function:

$$S_{1D}(x,l) = \begin{cases} s & \forall\ x\ \in \left[-\frac{l}{2}; \frac{l}{2}\right] \\ b & outside \end{cases} \tag{2}$$

in which "s" is the source counts concentration, "b" the background counts concentration, and "l" the source dimension. In this case, the image of the source (L_{1D}, see Equation (3)) generated by the imaging system characterized by the PSF of Equation (1) is given by the convolution product between the function that describes the source in a uniform background and the PSF, i.e., the convolution between Equations (1) and (2):

$$L_{1D}(x,l,\sigma) = S_{1D}(x,\ l) \times PSF_{1D}(x,\sigma) \tag{3}$$

The $S_{1D}(x,l)$ function that describes the source and the background together can be further split into two factors (Equation(4)), related to the source and background, respectively, $S_{1D}(x,l) = S^s_{1D}(x,l) + S^b_{1D}(x)$, where:

$$S^s_{1D}(x,l) = \begin{cases} (s-b) & \forall x\ \in \left[-\frac{l}{2}; \frac{l}{2}\right] \\ 0 & outside \end{cases} \text{ and } S^b_{1D}(x) = b \forall x \in [-\infty; \infty] \tag{4}$$

By considering the linearity properties of the convolution operator, it follows that:

$$\begin{gathered} L_{1D}(x,l,\sigma) = \left[S^s_{1D}(x,l) + S^b_{1D}(x)\right] \times PSF_{1D}(x,l) = \\ S^s_{1D}(x,l) \times PSF_{1D}(x,\sigma) + S^b_{1D}(x) \times PSF_{1D}(x,\sigma) = \\ (s-b)\frac{1}{\sigma\sqrt{2\pi}} \int_{-\frac{l}{2}}^{\frac{l}{2}} e^{-\frac{(x-x')^2}{2\sigma^2}} dx' + b\frac{1}{\sigma\sqrt{2\pi}} \int_{-\infty}^{+\infty} e^{-\frac{(x-x')^2}{2\sigma^2}} dx' \\ (s-b) I_{1D}(x,l,\sigma) + b \end{gathered} \tag{5}$$

in which the first integral of Equation (5) can be seen as the sum of two error functions (erf) and it is indicated with $I_{1D}(x,l,\sigma)$ (Equation (6)), while the second one results 1. Therefore, the $I_{1D}(x,l,\sigma)$ function can be written as:

$$I_{1D}(x,l,\sigma) = \frac{1}{2}\left[erf\left(\frac{x+\frac{l}{2}}{\sigma\sqrt{2}}\right) - erf\left(\frac{x-\frac{l}{2}}{\sigma\sqrt{2}}\right)\right] \tag{6}$$

The average value of the counts concentration in the image (C_{image}) can then be obtained by integrating Equation (3), within the source bounds [−l/2;+l/2] and dividing by l:

$$\begin{gathered} C_{image} = \frac{1}{l} \int_{\frac{-l}{2}}^{\frac{l}{2}} L_{1D}(x)dx = (s-b)H_{1D}(l,\sigma) + b = \\ sH_{1D}(l,\sigma) + b(1 - H_{1D}(l,\sigma)) \end{gathered} \tag{7}$$

where $H_{1D}(l,\sigma)$ in Equation (7) describes the effect of the PSF on the image counts and can be written as:

$$H_{1D}(l,\sigma) = \frac{1}{l} \int_{\frac{-l}{2}}^{\frac{l}{2}} L_{1D}(x)dx = \frac{\int_{\frac{-l}{2}}^{\frac{l}{2}} I_{1D}(x,\ l,\ \sigma)dx}{\int_{\frac{-l}{2}}^{\frac{l}{2}} I_{1D}(x,\ l,\ \sigma)dx} = \frac{\sigma}{l}\frac{\sqrt{2}}{\sqrt{\pi}}\left(e^{\frac{-l^2}{2\sigma^2}} - 1\right) + erf\left(\frac{\frac{l}{2}}{\sigma\sqrt{2}}\right) \tag{8}$$

From Equation (7) and Equation (8) it is possible to obtain the value of the source counts concentration s (see Equation (9)), as a function of the background counts concentration b, C_{image} and $H_{1D}(l,\sigma)$:

$$s = \frac{1}{H_{1D}(l,\sigma)} C_{image} - b\frac{1 - H_{1D}(l,\sigma)}{H_{1D}(l,\sigma)} \tag{9}$$

Equation (9) shows that it is possible to quantify s from the knowledge of:

(1) the function $H_{1D}(l,\sigma)$, which is an analytic function of measurable parameters: the dimension of the source and the σ of the image system's PSF;
(2) C_{image} directly measurable on the image space;
(3) *b* that, in the practice, can be evaluated considering a background region of interest (ROI) away from the source (i.e., away with respect to the FWHM of the system's PSF) on the image space.

It is important to notice that:

(1) $0 \leq H_{1D}(l,\sigma) \leq 1$;
(2) $\frac{1}{H_{1D}(l,\sigma)}$ is the factor which corrects the effect of loss of counts on the image space inside the ROI (*spill out*);
(3) $\frac{1-H_{1D}(l,\sigma)}{H_{1D}(l,\sigma)}$ is the factor that corrects the effect of increase of counts on the image space inside the ROI due to the background (*spill in*).

The proposed approach can now be generalized in a 3D ideal scenario (Equation (10)), i.e., by considering a 3D source surrounded by a homogeneous background, which can be described as:

$$S_{3D} = (x, l_x; y,\ l_y; z, l_z) = \begin{cases} s & \forall (x,y,z) \in \left[\frac{-l_x}{2}; \frac{l_x}{2}\right];\ \left[\frac{-l_y}{2}; \frac{l_y}{2}\right]; \left[\frac{-l_z}{2}; \frac{l_z}{2}\right] \\ b & outside \end{cases} \tag{10}$$

Since the PSF of the 3-D (three-dimensional) imaging system can be derived as:

$$\begin{gathered} PSF_{3D}(x,\ \sigma_x; y, \sigma_y; z,\ \sigma_z) = \frac{1}{(\sigma_x \sigma_y \sigma_z)\sqrt{8\pi^3}} e^{-\frac{x^2}{\sigma_x^2} - \frac{y^2}{\sigma_y^2} - \frac{z^2}{\sigma_z^2}} = \\ PSF_{1D}(x,\ \sigma_x) PSF_{1D}(x,\ \sigma_y) PSF_{1D}(x,\ \sigma_z) \end{gathered} \tag{11}$$

it is easy to verify that:

$$\begin{gathered} I_{3D}(x, l_x, \sigma_x; y, l_y, \sigma_y; z, l_z, \sigma_z) = \frac{1}{(\sigma_x \sigma_y \sigma_z)\sqrt{8\pi^3}} \int_{\frac{-l_x}{2}}^{\frac{l_x}{2}} \int_{\frac{-l_y}{2}}^{\frac{l_y}{2}} \int_{\frac{-l_z}{2}}^{\frac{l_z}{2}} e^{-\frac{(x-x')^2}{\sigma_x^2} - \frac{(y-y')^2}{\sigma_y^2} - \frac{(z-z')^2}{\sigma_z^2}} dx' dy'\ dz' = \\ I_{1D}(x, l_x, \sigma_x) \times I_{1D}(y, l_y, \sigma_y) \times I_{1D}(z, l_z, \sigma_z) \end{gathered} \tag{12}$$

and

$$\begin{gathered} H_{3D}(x,\ \sigma_x; y,\ \sigma_y; z,\ \sigma_z) = \frac{\int_{\frac{-l_x}{2}}^{\frac{l_x}{2}} \int_{\frac{-l_y}{2}}^{\frac{l_y}{2}} \int_{\frac{-l_z}{2}}^{\frac{l_z}{2}} I_{3D(x,l_x,\ \sigma_x; y, l_y,\ \sigma_y; z, l_z,\ \sigma_z)} dx dy dz}{\int_{-\infty}^{\infty} \int_{-\infty}^{\infty} \int_{-\infty}^{\infty} I_{3D(x,l_x,\ \sigma_x; y, l_y,\ \sigma_y; z, l_z,\ \sigma_z)} dx dy dz} = \\ H_{1D}(l_x, \sigma_x) H_{1D}(l_y, \sigma) H_{1D}(l_z, \sigma_z) \end{gathered} \tag{13}$$

From Equations (12) and (13), it is possible to derive Equation (14), which describes the final 3D generalization of Equation (7) simply as:

$$s = \frac{1}{H_{1D}(l_x,\sigma_x) H_{1D}(l_y,\sigma_y) H_{1D}(l_z,\sigma_z)} C_{image} - b\frac{1 - H_{1D}(l_x,\sigma_x) H_{1D}(l_y,\sigma_y) H_{1D}(l_z,\sigma_z)}{H_{1D}(l_x,\sigma_x) H_{1D}(l_y,\sigma_y) H_{1D}(l_z,\sigma_z)} \tag{14}$$

2.2. Scanner and Phantom

A Discovery 710 PET/TC hybrid system (General Electric Company, Boston, MA, USA) [14] was employed for images acquisition. The PET system collects data in three-dimensional (3D) mode and can reconstruct images with or without time-of-flight technol-

ogy (TOF) [15]. The CT system allows performing data attenuation correction and provides morphological information through automatic image co-registration [16].

A standard NEMA IEC body phantom was adopted in this study [17,18]. The phantom mimics the D-shape of an upper human body; it comprises a cylindrical insert in the center of phantom and 6 fillable spheres of different sizes. The spheres are suspended in the D-shaped cavity with the six centers placed on the same plane and with nominal inner diameters of 10, 13, 17, 22, 28, and 37 mm. The nominal volume of the phantom is 9.7 L (±1%), excluding the volume of the six spheres.

2.3. Experimental Measurements

Two sets of acquisitions were performed in order to apply our correction model. First, point source images were acquired to estimate the point spread function (PSF) of the system [19,20] under different conditions, then, a series of acquisitions of the IEC phantom under the same conditions were performed to test the recovery method.

2.4. Point Source Measurements

An 18 F-FDG point-like source was prepared with an activity of 0.1 mCi. The point-like source was simulated using the needle of a syringe placed in air through a mechanical support.

The system PSF was evaluated under different conditions in order to match the IEC NEMA phantom acquisitions. The measurements were performed by placing the source at the center of the field of view (FOV) and a 5 cm off-center, in order to highlight any anisotropies of the acquisition system.

The acquisitions were corrected for the attenuation, scatter, radionuclide decay, dead time of the detectors, random coincidences, and detector normalization; 47 slices were reconstructed with a matrix size of 256 × 256; the corresponding voxel sizes were 2.73 × 2.73 × 3.27 mm^3. The acquisition and reconstruction parameters were the same as the corresponding IEC phantom measurements described in the following paragraphs.

2.5. IEC Phantom Measurements

The volume of the NEMA phantom and the six spheres were filled with ^{18}F-FDG mixed with pure water using two different signal-to-background (SBR) activity concentration ratio (around 3:1 and 10:1). In order to obtain the concentration on the spheres and background with accuracy, the following procedure was established: first, the initial activity was measured through an activity calibrator (Atomlab 500 Dose Calibrator, Biodex, New York, NY, USA); then, the concentration of the sphere was obtained by mixing the measured activity with pure water and the spheres were filled through a precision syringe; finally, the phantom (background) was filled with the remaining 18 F-FDG solution by adding pure water in order to obtain the 3:1 and 10:1 SBRs. Special care was adopted in order to ensure a proper homogeneity of the radioactive solution.

The final concentrations are reported in Table 1. Once the phantom was set up and an accurate alignment with the FOV center achieved, a series of acquisitions were performed in order to study the effect of different acquisition/reconstruction conditions on the quantitative recovery model.

Table 1. This table reports the two final signal-to-background with the respective concentrations in spheres and in background.

SBR	Spheres (kBq/mL)	Phantom Background (kBq/mL)
3.27	17.27	5.28
10.18	35.94	2.55

The main acquisition and reconstruction parameters are reported in Table 2. All the data were corrected for the attenuation, scatter, radionuclide decay, dead time of the detectors, random coincidences, and detector normalization. The complete details

of the image reconstruction process are reported in Table 3. Both PET and CT images were collected in DICOM (Digital Imaging and Communications in Medicine) format and subsequently analyzed.

Table 2. Acquisition parameters for the phantom acquisitions.

Acquisition Time (min)	Image Matrix Size	Pixel Dimension (mm^2)	Slice Thickness (mm)	Number of Reconstructed Slices
1, 2, 4, 8	256 × 256	2.73 × 2.73	3.27	47

Table 3. Reconstruction parameters of the algorithm.

	Reconstruction Algorithm	Iteration Subs	Gaussian Filter	Reconstruction Enhancement
PET TOF	VUE Point FX	3 iteration 24 subs	5.5 mm	SharpIR
PET noTOF	VUE Point HD	3 iteration 24 subs	5.5 mm	SharpIR

2.6. Data Analysis

Images and data analysis were performed by means of in-house scripts running on Matlab (The MathWorks, Inc., Natick, MA, USA) software package.

2.7. Point Spread Function Assessment

Images of the point source were employed to estimate the PSF of the system, which was characterized by the standard deviation (σ), assuming a Gaussian profile [7]. The three horizontal (x), vertical (y), and axial (z) profiles were extracted from the central region of the image and a Gaussian fit was performed.

2.8. Segmentation Method

In order to study how the PVE quantitatively affects the image, the first step was to determine the number of the counts (C_{image}) inside each of the six spheres of the phantom in the original image. Since the PVE alters the activity distribution making the contours of the volume of interest (VOI) undefined, an ideal segmentation criterion was implemented, using the geometrical information from the CT acquisition.

This criterion consisted of constructing a binary mask of six spherical VOIs with radii R equal to the phantom spheres and centered on the x and y coordinates of their centers, determined from the CT acquisition.

The discretization of the sphere brought to the problem that some voxels on the boundary were partially included in the spherical VOIs. To overcome that, an inclusion criteria has been chosen in such a way that only the voxels which have all the corners with a distance from the coordinates of center less than the radius were considered inside.

These voxel completely included in the VOI have a unitary value, while a value of 0 is assigned to the voxels outside the VOI.

In order to improve the accuracy of the segmentation, the image matrix of PET acquisition were first resampled on a finer grid, i.e., each voxel was divided in smaller voxels. The effect of the resampling on the counts was investigated, starting from the original matrix (256 × 256 × 47) until a 1536 × 1536 × 282 matrix with unitary step.

A voxel by voxel product between the PET image matrix and the binary mask has been calculated in order to select only the counts of the voxels corresponding to the interior of the VOIs.

2.9. Counts Recovery

Once the PSF of the system was characterized and the counts for the original image (C_{image}) in the six spheres of the phantom images obtained, the recovery formula (Equation (14)) was applied in order to obtain the resultant counts ($C_{recover}$) and assess the accuracy of the PVE correction method under different conditions.

The recovery after applying PVE correction, estimated as percentage difference between C_{image} and $C_{recover}$ was estimated for each comparison.

3. Results

With the purpose of evaluating the efficiency in PVE recovery, the method was applied changing one parameter at a time:

1. to investigate the effect of quantum noise both on PVE and on the recovery: fixed SBR and reconstruction algorithm, different acquisition time (1, 2, 4, and 8 min);
2. to investigate the effect of the reconstruction algorithm on the system PSF and PVE: fixed SBR and same acquisition time (4 min), different reconstruction algorithm with TOF (VPFXS) and without TOF (VPHDS) [15];
3. to investigate the effect of different source-to-background concentration ratio on PVE: same acquisition time (4 min) and reconstruction algorithm, different SBRs (3:1 and 10:1).

3.1. PSF

The point-like source was acquired for all the different configurations above, collecting the σ needed for the analysis that follows. The off-center measurements did not show appreciable variations, hence we consider the σ values obtained at the center of the FOV.

Figure 1 reports an example for the 2 min acquisition and reconstruction method with TOF correction. Each of the mono-dimensional data sets were fitted with a Gaussian function, from which the standard deviations were obtained with confidence interval set at the 95% level. The values were respectively 2.54 ± 0.01 mm, 2.76 ± 0.03 mm, and 3.31 ± 0.04 mm.

3.2. Resampling

The effect of resampling on the counts within the spheres is illustrated in Figure 2. The x-axis reports the resampling factor where a factor of 1 represents the original image matrix (256 × 256 × 47), while the maximum resampling resulted in a 1792 × 1792 × 329 matrix with a corresponding factor of 7; the y-axis reports the counts ratio between the counts obtained in the resampled image and the counts associated to the original image.

The accuracy in gain can be appreciated especially in the smallest sphere ("sphere 6" blue dots in Figure 2), where the counts on the resampled image are three times the original ones.

As can be seen in Figure 2, the counts ratio increases with increasing the resampling factor with an asymptotic behavior, which has been verified by fitting the data with the function $f(x) = a - b \times c^x$ and studying the horizontal asymptote (i.e., the *a* parameter). Table 4 reports the asymptotes derived from the fit (with confidence level set at 95%) and the count ratio obtained with a resampling factor of six (i.e., the factor adopted in the following analysis, which corresponds to an image matrix of 1536 × 1536 × 282). The counts ratios associated to a resampling factor of six were very close to the asymptote *a* obtained from the fit. Moreover, a finer matrix of 1536 × 1536 × 282 respect to the original one represents a good compromise between the accuracy in the counts recovery and the increase in computation time. The increment from a resampling factor of six to seven was below the 1.5%, but the computation time became three times higher.

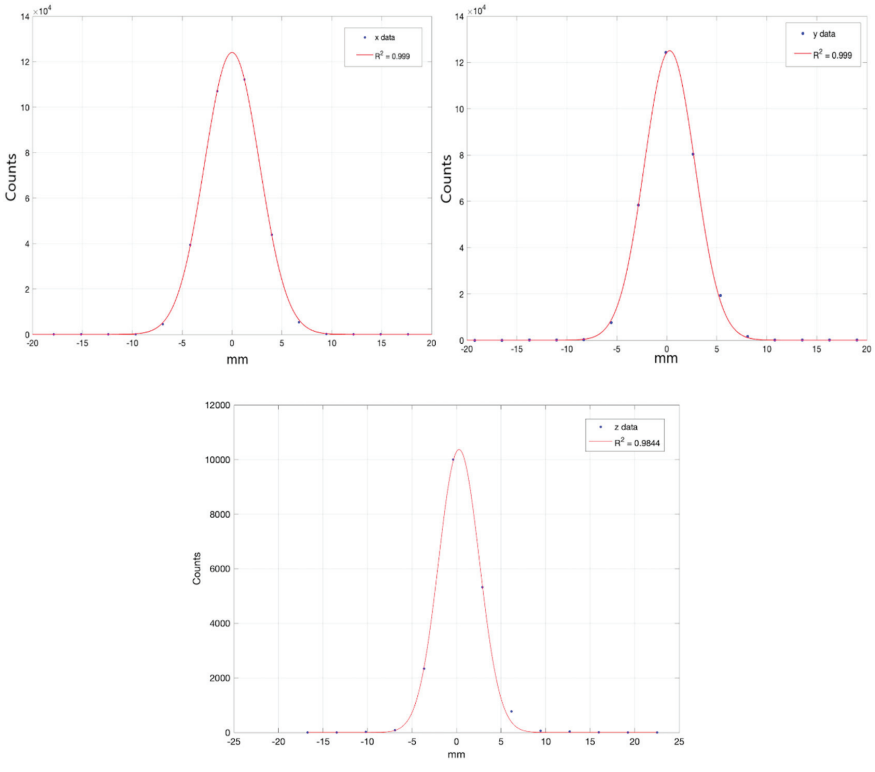

Figure 1. Horizontal (x), vertical (y), and axial (z) profiles extracted from the point-like source fitted with a Gaussian function.

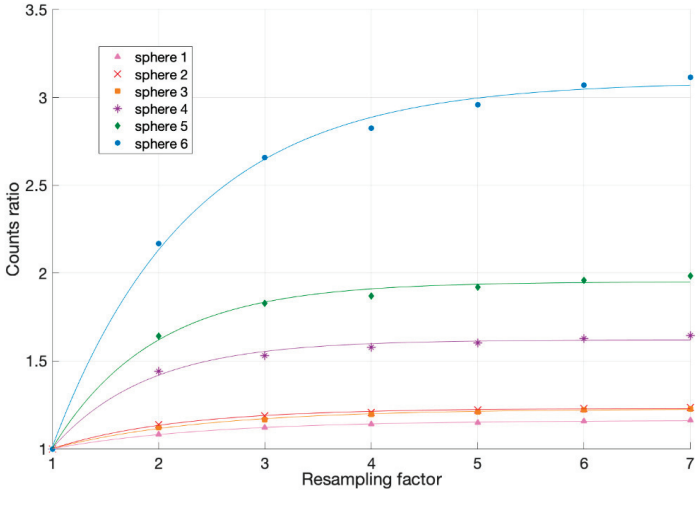

Figure 2. Counts ratio normalized to the original counts at the increasing of the voxel division of the starting matrix (256 × 256 × 47) for each sphere, marked in different color with different markers.

Table 4. Parameters obtained by the fit with the function $f(x) = a - b \times c^x$. The *a* parameter represents the asymptote.

Spheres	1	2	3	4	5	6
a	1.16 ± 0.04	1.23 ± 0.01	1.23 ± 0.01	1.62 ± 0.04	1.95 ± 0.04	3.09 ± 0.09
Counts ratio for a resampling factor of 6	1.16 ± 0.01	1.23 ± 0.01	1.22 ± 0.01	1.63 ± 0.01	1.96 ± 0.01	3.07 ± 0.02
b	0.32 ± 0.03	0.54 ± 0.07	0.45 ± 0.06	1.90 ± 0.70	2.70 ± 0.80	4.50 ± 0.70
c	0.50 ± 0.03	0.42 ± 0.07	0.50 ± 0.07	0.30 ± 0.10	0.30 ± 0.10	0.46 ± 0.07

3.3. Evaluation of PVE Recovery

Figures 3–5 show the sphere-to-background counts concentration ratio as a function of the spheres dimension for the different situations above. However, in order to underline how the relationship between the dimension of lesions and the PSF of the imaging system impacts on PVE, the x-axes are reported as the ratio between the diameter of the six spheres and the σ of the system.

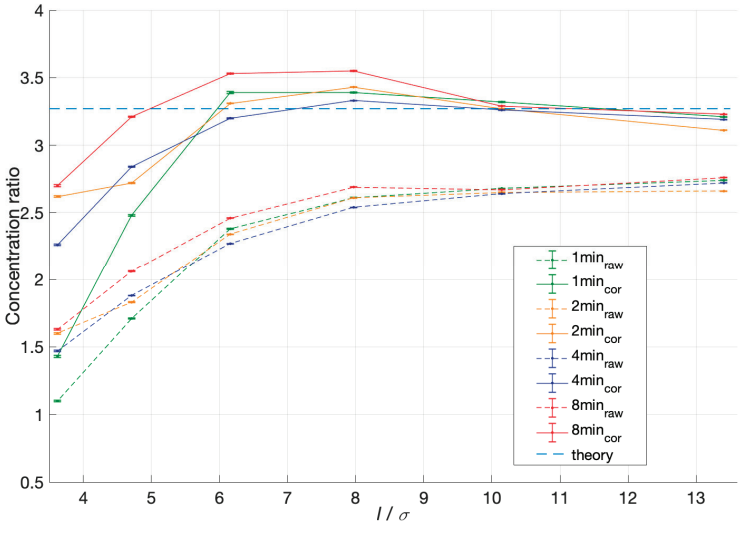

Figure 3. Comparison between the concentration ratio for the raw image (dotted lines) and the PVE corrected image (continuous line) at different acquisition times, shown with different colors.

The sphere-to-background counts concentration ratio was calculated as the ratio between the counts concentration in the spheres and in the background, which were measured as the average over four circular ROIs chosen in areas and slices far from the spheres.

Figure 3 illustrates the comparison in concentration ratio (y-axis) before and after the application of the PVE recovery method at different acquisition times (1, 2, 4, and 8 min).

The SBR and the reconstruction algorithm VPFXS were fixed.

For each acquisition time, reported with the same colors, the smaller the lesion, the greater results the underestimation of the concentration ratio. In particular, the concentration underestimation ranges from a minimum of 16% for largest spheres to a maximum of 66% for the smallest sphere.

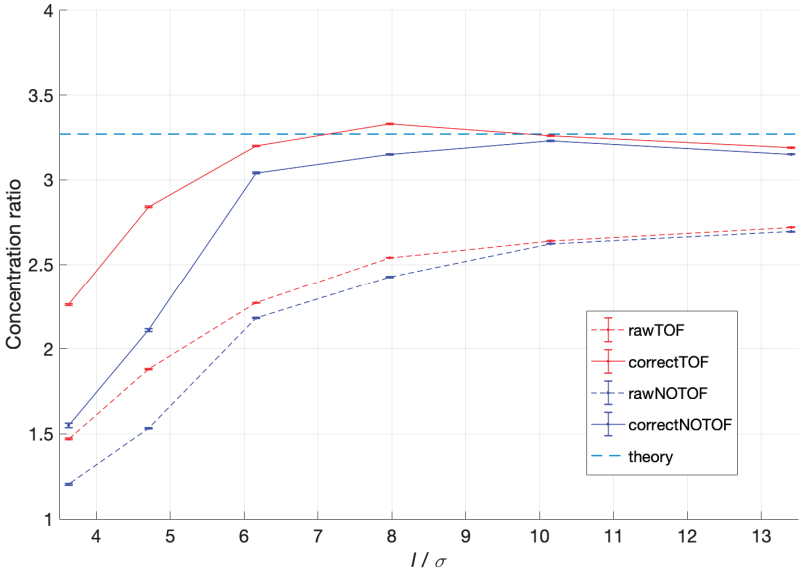

Figure 4. Comparison of the concentration ratio for the same acquisition time (4 min) between the reconstruction with TOF correction, reported in red, and the one without TOF, reported in blue, before (dotted line) and after (continuous line) the application of PVE recovery method.

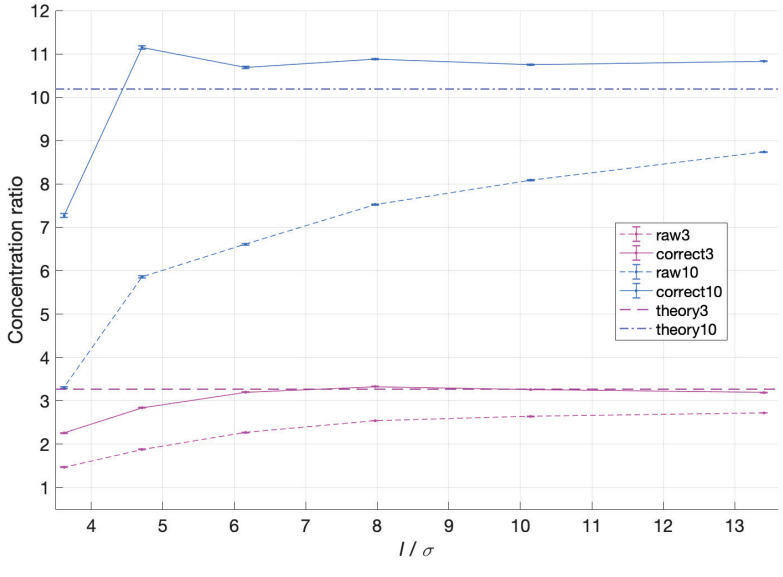

Figure 5. Comparison for concentration ratio for SBR = 10.18 in light blue and SBR = 3.27 in violet. For both acquisitions, acquisition time was fixed at 4 min and the reconstruction algorithm was with TOF correction. The dotted lines represent the raw images, while the continuous ones the PVE corrected images.

Table 5 shows the percentage of recovery for all the spheres of the NEMA phantom for all the acquisition time, highlighting the good PVE recovery for the biggest sphere, which for all the acquisition time results in the range of ±3%.

Table 5. Comparison of percentage of recovery at different acquisition time for the six spheres of NEMA phantom, where the dimensions are expressed as the ratio between the diameter of the six spheres and the PSF of the system.

l/σ	3.6	4.7	6.2	8.0	10.1	13.4
$1\ min_{raw}$	−66 ± 2%	−48 ± 2%	−27 ± 2%	−20 ± 1%	−17.8 ± 0.8%	−16.3 ± 0.5%
$1\ min_{cor}$	−56 ± 2%	−24 ± 2%	+4 ± 2%	+3 ± 1%	+1.4 ± 0.9%	−1.9 ± 0.6%
$2\ min_{raw}$	−51 ± 2%	−44 ± 1%	−28.6 ± 0.9%	−20.3 ± 0.7%	−19.0 ± 0.6%	−17.6 ± 0.5%
$2\ min_{cor}$	−20 ± 2%	−17 ± 1%	+1 ± 1%	+4.9 ± 0.8%	+0.0 ± 0.7%	+3.5 ± 0.5%
$4\ min_{raw}$	−55 ± 2%	−42 ± 1%	−30.5 ± 0.9%	−22.2 ± 0.7%	−19.3 ± 0.6%	−16.7 ± 0.5%
$4\ min_{cor}$	−30 ± 2%	−13 ± 1%	−2 ± 1%	+1.0 ± 0.8%	+0.4 ± 0.7%	−2.5 ± 0.6%
$8\ min_{raw}$	−50 ± 2%	−37 ± 1%	−24.7 ± 0.9%	−17.9 ± 0.7%	−18.4 ± 0.6%	−15.7 ± 0.5%
$8\ min_{cor}$	−17 ± 2%	−1.9 ± 1%	+7% ± 1%	+8.3 ± 0.9%	+0.7 ± 0.7%	−1.2 ± 0.6%

Figure 4 compares the concentration ratio with or without the TOF reconstruction for the 4 min acquisition, showing that every reconstruction underestimates the theoretical SBR, even if the TOF correction tends to have a proximity of 5% more than the NOTOF.

After the recovery method application (continuous line), the PVE compensation is shown in Table 6.

Table 6. Comparison of percentage of recovery for the same acquisition time (4 min) between the reconstruction with TOF correction and the one without TOF.

l/σ	3.6	4.7	6.2	8.0	10.1	13.4
TOF_{raw}	−55 ± 2%	−42 ± 1%	−30.5 ± 0.9%	−22.2 ± 0.7%	−19.3 ± 0.6%	−16.7 ± 0.5%
TOF_{cor}	−30 ± 2%	−13 ± 1%	−2 ± 1%	+1.0 ± 0.8%	+0.4 ± 0.7%	−2.5 ± 0.6%
$NOTOF_{raw}$	−55 ± 2%	−45 ± 1%	−33.3 ± 0.9%	−26.5 ± 0.7%	−21.4 ± 0.6%	−20.1 ± 0.5%
$NOTOF_{cor}$	−31 ± 2%	−19 ± 1%	+7 ± 1%	+4.6 ± 0.8%	+3.3 ± 0.7%	+6.8 ± 0.6%

Finally, Figure 5 illustrates the change in SBRs with the theoretical concentration ratio of 3.27 and 10.19, maintaining unaltered the other parameters (acquisition time = 4 min and TOF reconstruction).

For higher SBR, the underestimation of theoretical ratio concentration results almost always greater, as shown in Table 7.

Table 7. Comparison of percentage of recovery for the different SBR. For both acquisitions, acquisition time was fixed at 4 min and the reconstruction algorithm was with TOF correction.

l/σ	3.6	4.7	6.2	8.0	10.1	13.4
$SBR3_{raw}$	−55 ± 2%	−42 ± 1%	−30.5 ± 0.9%	−22.2 ± 0.7%	−19.3 ± 0.6%	−16.7 ± 0.5%
$SBR3_{cor}$	−30 ± 2%	−13 ± 1%	−2 ± 1%	+1.0 ± 0.2%	+0.4 ± 0.7%	−2.5 ± 0.6%
$SBR10_{raw}$	−67.5 ± 0.6%	−42.5 ± 1%	−35.1 ± 0.2%	−26.1 ± 0.2%	−20.6 ± 0.1%	−14.21 ± 0.07%
$SBR10_{cor}$	−28.7 ± 0.7%	+9.4 ± 1%	+4.9 ± 0.3%	+6.7 ± 0.2%	+5.5 ± 0.1%	+6.27 ± 0.07%

4. Discussion

In this work, we developed a post-reconstruction method for the correction of the PVE in PET images. Quantitative PET images are increasingly required for diagnostic

(SUV) and therapeutic (committed dose in metabolic radiotherapy) purposes and radiomics applications [21]. In general, post-processing corrective methods offer multiple advantages with respect to those integrated into the reconstruction algorithm [19]:

(1) they do not need access to the reconstruction-code, which is practically impossible for the standard user, and they can be easily used;
(2) they allow their application independently of the acquisition machine and, consequently, can be used to standardize data from different sites, for example for multicenter studies.

Our method is based on the theoretical calculation of the PVE effect caused by a uniformly distributed source on a uniform background. The hypotheses on which it is "exactly" valid are:

(1) uniform lesion on a uniform background
(2) ideal segmentation of the ROI (Region Of Interest), or by means of CT imaging

Its application is very simple, as it only needs:

(1) to measure the contribution of the background directly on the image;
(2) to know the PSF (Point Spread Function) of the acquisition system, acquiring a linear or point source or taking the data directly from the NEMA post installation quality assurance;
(3) to implement a simple analytical formula in a spreadsheet.

The limitations and the field of application of the method are identical to those present in the well-known and used RC (Recovery Coefficient) method [22], but, unlike the latter, it has the great advantage that the final formula has been obtained theoretically; therefore, the final formula intrinsically contains the dependencies of the various parameters that influence the PVE: size of the lesion, lesion/background concentration ratio, and FWHM of the PSF of the system. For this reason, it is not necessary, as is the case for the RC method, to measure experimentally these parameters every time they change.

The method was experimentally validated by acquiring an IEC NEMA PHANTOM, which allowed to evaluate the recovery of the quantitative data by varying:

(1) the size of the lesions, filling spheres with a diameter of 10, 13, 17, 22, 28, and 37 mm.
(2) the signal-to-background activity concentration ratio (SBR); in particular we have acquired the values of around 3:1 and 10:1, which covers the standard range of clinical variation in terms of the lesion/background concentration ratio.
(3) the statistical noise, acquiring the same activity for different acquisition times (1, 2, 4, and 8 min)
(4) the tomographic reconstruction algorithm, with and without TOF.

The method guarantees an excellent recovery of the quantitative data in the analyzed conditions. Considering the sigma that characterizes the acquisition system, which is around 2.5 mm (value measured experimentally), the PVE effect determines a loss of counts greater than 50% and the corrective method allows to obtain accuracies of less than 17%, for lesion dimensions equal to or greater than 13 mm in diameter and for acquisition times equal to or greater than 2 min. By increasing the acquisition time, substantial improvements are not appreciated and this is an important and comfortable result, given that an acquisition time of 2 min per bed is the standard clinical PET acquisition time.

Additionally, the application of TOF during the reconstruction algorithm inherently reduces the effect of PVE and the application of the corrective method at this data allows obtaining results that are even more accurate.

Finally, increasing the SBR, in general makes the effect of PVE to be more marked and the accuracy of the corrected data is lower.

5. Conclusions

The proposed approach for the correction of the PVE is an alternative post-processing method to the RC method; it has the same limitations, but the advantage of having

theoretically included the dependencies of the parameters that describe the effect and therefore to overcome the need of measuring these parameters every time they change

It represent a straightforward method to implement and adopt on every PET system. Although its field of application is widespread, its limits are related to the fact that the method is based on an "ideal" segmentation and does not take into account any inhomogeneities within the ROI considered; both of these aspects can be addressed using the same formalism proposed in the theoretical part of Materials and Methods, and are the topics of future works we are working on.

Author Contributions: Conceptualization, F.D.M.; data curation, F.D.M., P.B., E.B., A.G., D.V.; writing—original draft preparation, P.B., E.B., A.G.; writing—review and editing, F.D.M., P.B., E.B., A.G., D.V.; supervision, F.D.M., D.V.; funding acquisition, D.V. All authors have read and agreed to the published version of the manuscript.

Funding: This research received no external funding.

Institutional Review Board Statement: Not applicable.

Informed Consent Statement: Not applicable.

Conflicts of Interest: The authors declare no conflict of interest.

References

1. Diao, W.; Tian, F.; Jia, Z. The prognostic value of SUV_{max} measuring on primary lesion and ALN by 18F-FDG PET or PET/CT in patients with breast cancer. *Eur. J. Radiol.* **2018**, *105*, 1–7. [CrossRef] [PubMed]
2. Ulaner, G.A.; Eaton, A.; Morris, P.G.; Lilienstein, J.; Jhaveri, K.; Patil, S.; Fazio, M.; Larson, S.; Hudis, C.A.; Jochelson, M.S. Prognostic value of quantitative fluorodeoxyglucose measurements in newly diagnosed metastatic breast cancer. *Cancer Med.* **2013**, *2*, 725–733. [CrossRef] [PubMed]
3. Kuhnert, G.; Boellaard, R.; Sterzer, S.; Kahraman, D.; Scheffler, M.; Wolf, J.; Dietlein, M.; Drzezga, A.; Kobe, C. Impact of PET/CT image reconstruction methods and liver uptake normalization strategies on quantitative image analysis. *Eur. J. Nucl. Med. Mol. Imaging* **2016**, *43*, 249–258. [CrossRef] [PubMed]
4. Bellevre, D.; Fournier, C.B.; Switsers, O.; Dugué, A.E.; Levy, C.; Allouache, D.; Desmonts, C.; Crouet, H.; Guilloit, J.M.; Grellard, J.M.; et al. Staging the axilla in breast cancer patients with 18F-FDG PET: How small are the metastases that we can detect with new generation clinical PET systems? *Eur. J. Nucl. Med. Mol. Imaging* **2014**, *41*, 1103–1112. [CrossRef] [PubMed]
5. Beyer, T.; Czernin, J.; Freudenberg, L.S. Variations in clinical PET/CT operations: Results of an international survey of active PET/CT users. *J. Nucl. Med.* **2011**, *52*, 303–310. [CrossRef] [PubMed]
6. Sunderland, J.J.; Christian, P.E. Quantitative PET/CT scanner performance characterization based upon the society of nuclear medicine and molecular imaging clinical trials network oncology clinical simulator phantom. *J. Nucl. Med.* **2015**, *56*, 145–152. [CrossRef] [PubMed]
7. Soret, M.; Bacharach, S.L.; Buvat, I. Partial-Volume Effect in PET Tumor Imaging. *J. Nucl. Med.* **2007**, *48*, 932–945. [CrossRef] [PubMed]
8. Rahmim, A.; Qi, J.; Sossi, V. Resolution modeling in PET imaging: Theory, practice, benefits, and pitfalls. *Med. Phys.* **2013**, *40*, 064301. [CrossRef] [PubMed]
9. Bettinardi, V.; Castiglioni, I.; De Bernardi, E.; Gilardi, M.C. PET quantification: Strategies for partial volume correction. *Clin. Transl. Imaging* **2014**, 199–218. [CrossRef]
10. Boellaard, R.; Krak, N.C.; Hoekstra, O.S.; Lammertsma, A.A. Effects of noise, image resolution, and ROI definition on the accuracy of standard uptake values: A simulation study. *J. Nucl. Med.* **2004**, *9*, 1519–1527.
11. Rousset, O.; Rahmim, A.; Alavi, A.; Zaidi, H. Partial Volume Correction Strategies in PET. *PET Clin.* **2007**, *2*, 235–249. [CrossRef] [PubMed]
12. Hoetjes, N.J.; van Velden, F.H.; Hoekstra, O.S.; Hoekstra, C.J.; Krak, N.C.; Lammertsma, A.A.; Boellaard, R. Partial volume correction strategies for quantitative FDG PET in oncology. *Eur. J. Nucl. Med. Mol. Imaging* **2010**, *37*, 1679–1687. [CrossRef] [PubMed]
13. Munk, O.L.; Tolbod, L.P.; Hansen, S.B.; Bogsrud, T. Point-spread function reconstructed PET images of sub-centimeter lesions are not quantitative. *EJNMMI Phys.* **2017**, *4*, 5. [CrossRef] [PubMed]
14. GE Healthcare Discovery PET/CT 710 System Manufacturer Webpage [Internet]. Available online: http://www3.gehealthcare.com/en/products/categories/pet-ct/pet-ct_scanners/discovery_pet-ct_710 (accessed on 17 September 2020).
15. Grant, A.M.; Deller, T.W.; Khalighi, M.M.; Maramraju, S.H.; Delso, G.; Levin, C.S. NEMA NU 22012 performance studies for the SiPM-based ToF-PET component of the GE SIGNA PET/MR system. *Med. Phys.* **2016**, *43*, 2334–2343. [CrossRef] [PubMed]
16. Townsend, D.W.; Carney, J.P.; Yap, J.T.; Hall, N.C. PET/CT today and tomorrow. *J. Nucl. Med.* **2004**, *45*, 4S–14S. [PubMed]

17. Yester, M.; Al-Senan, R.; White, S. NEMA testing of GE Discovery 710 PET scanner compared to a simplified protocol for routine testing of PET scanners. *J. Nucl. Med.* **2015**, *55*, 2157. [CrossRef]
18. National Electrical Manufactures Association (NEMA). *NEMA NU 2-2007, Performance Measurements of Positron Emission Tomographs*; National Electrical Manufacturers Association: Rosslyn, VA, USA, 2008.
19. Gong, K.; Cherry, S.R.; Qi, J. On the assessment of spatial resolution of PET systems with iterative image reconstruction. *Phys. Med. Biol.* **2016**, *61*, N193–N202. [CrossRef] [PubMed]
20. Anton-Rodriguez, J.M.; Krokos, G.; Kotasidis, F.; Asselin, M.C.; Morris, O.; Julyan, P.; Archer, A.; Matthews, J.C. Experimental validation of estimated spatially variant radioisotope-specific point spread functions using published positron range simulations and fluorine-18 measurements. *Phys. Med. Biol.* **2018**, *63*, 24. [CrossRef] [PubMed]
21. Shiri, I.; Rahmim, A.; Ghaffarian, P.; Geramifar, P.; Abdollahi, H.; Bitarafan-Rajabi, A. The impact of image reconstruction settings on 18F-FDG PET radiomic features: Multi-scanner phantom and patient studies. *Eur. Radiol.* **2017**, *27*, 4498–4509. [CrossRef] [PubMed]
22. Srinivas, S.M.; Dhurairaj, T.; Basu, S.; Bural, G.; Surti, S.; Alavi, A. A recovery coefficient method for partial volume correction of PET images. *Ann. Nucl. Med.* **2009**, *23*, 341–348. [CrossRef] [PubMed]

applied sciences

MDPI

Article

Evaluation of an Early Regression Index (ERI_{TCP}) as Predictor of Pathological Complete Response in Cervical Cancer: A Pilot-Study

Davide Cusumano [1], Francesco Catucci [1], Angela Romano [1], Luca Boldrini [1,*], Antonio Piras [2], Sara Broggi [3], Claudio Votta [1], Lorenzo Placidi [1], Matteo Nardini [1], Giuditta Chiloiro [1], Alessia Nardangeli [1], Viola De Luca [1], Bruno Fionda [1], Maura Campitelli [1], Rosa Autorino [1], Maria Antonietta Gambacorta [1], Luca Indovina [1], Claudio Fiorino [3] and Vincenzo Valentini [1]

[1] Fondazione Policlinico Universitario "Agostino Gemelli" IRCCS, 00168 Rome, Italy; davide.cusumano@policlinicogemelli.it (D.C.); catuccifr@gmail.com (F.C.); angelaromano89@gmail.com (A.R.); claudio.vt@hotmail.it (C.V.); lorenzo.placidi@policlinicogemelli.it (L.P.); matteo.nardini@unicatt.it (M.N.); giuditta.chiloiro@policlinicogemelli.it (G.C.); alessia.nardangeli@policlinicogemelli.it (A.N.); viola.deluca89@gmail.com (V.D.L.); bruno.fionda@policlinicogemelli.it (B.F.); maura.campitelli@policlinicogemelli.it (M.C.); rosa.autorino@policlinicogemelli.it (R.A.); mariaantonietta.gambacorta@policlinicogemelli.it (M.A.G.); luca.indovina@policlinicogemelli.it (L.I.); vincenzo.valentini@policlinicogemelli.it (V.V.)

[2] UO Radioterapia Oncologica, Villa Santa Teresa, 90011 Bagheria, Palermo, Italy; antoniopiras88@gmail.com

[3] Medical Physics, San Raffaele Scientific Institute, 20132 Milano, Italy; broggi.sara@hsr.it (S.B.); fiorino.claudio@hsr.it (C.F.)

* Correspondence: luca.boldrini@policlinicogemelli.it; Tel.: +39-06-3015-5339

Received: 6 October 2020; Accepted: 6 November 2020; Published: 11 November 2020

Featured Application: The paper aim to propose an image-based parameter for response prediction in cervical cancer.

Abstract: Background: Recent studies have highlighted the potentialities of a radiobiological parameter, the early regression index (ERI_{TCP}), in the treatment response prediction for rectal cancer patients treated with chemoradiotherapy followed by surgery. The aim of this study is to evaluate the performance of this parameter in predicting pathological complete response (pCR) in the context of low field MR guided radiotherapy (MRgRT) for cervical cancer (CC). Methods: A total of 16 patients affected by CC were enrolled. All patients underwent a MRgRT treatment, with prescription of 50.6 Gy in 22 fractions. A daily MR acquisition was performed at simulation and on each treatment fraction. Gross tumor volume (GTV) was delineated on the MR images acquired at the following biological effective dose (BED) levels: 14, 28, 42, 54 and 62 Gy. The ERI_{TCP} was calculated at the different BED levels and its predictive performance was quantified in terms of receiver operating characteristic (ROC) curve. Results: pCR was observed in 11/16 cases. The highest discriminative power of ERI_{TCP} was reported when a BED value of 28 Gy is reached, obtaining an area under curve (AUC) of 0.84. Conclusion: This study confirmed ERI_{TCP} as a promising response biomarker also for CC, although further studies with larger cohort of patients are recommended.

Keywords: MR-guided radiotherapy; predictive models; cervical cancer

1. Introduction

Cervical cancer (CC) represents one of the most common and severe female cancers. More than 500,000 new cases per year are diagnosed in the world and despite the significant therapeutic improvements achieved in the recent years, the number of deaths per year ranges from 250,000 to

350,000 [1–3]. The clinical management of CC involves different specialists, with the aim of tailoring the treatment on the basis of the tumor staging [4].

According to the Fédération Internationale de Gynécologie et d'Obstétrique (FIGO) classification, stage IB2-IVA patients are considered as locally advanced cervical cancer (LACC). The standard of care for these patients is represented by neoadjuvant chemoradiotherapy (nCRT) followed by brachytherapy boost, with the primary aim of organ preservation [5].

Despite the good results in terms of overall survival and local control achieved through this approach, alternative approaches have been investigated in the scientific community to further reduce the rate of treatment failure [6,7].

In this context, some experiences have reported the advantage to administer neo-adjuvant external beam radiotherapy with concomitant chemotherapy followed by radical surgery, aiming to remove the residual tumor foci resistant to the previous treatment and reporting favorable rates of local control and disease-free survival, with acceptable acute and long-term toxicity profiles [8–10].

The response to nCRT followed by surgery is quantified on the basis of the histological evaluation of the surgical specimen: Pathological complete response (pCR) is achieved when no residual tumor foci are present.

Clinical experiences reported pCR rates of about 50% for LACC patients undergoing nCRT, also observing that the pCR status is associated with higher rates of long-term and disease-free survival [11–14].

Regardless of the clinical approach adopted, there is growing interest towards the identification of treatment response predictors, to move towards a more personalized clinical approach, avoiding unnecessary surgical procedures in patients with high probability of pCR or modifying the clinical management in the case of poor responders.

Different models have been proposed in literature to predict treatment response in CC, some of them including only clinical data, others combining also image parameters extracted from magnetic resonance (MR) or computed tomography (CT) images acquired at disease staging [15–18].

Magnetic resonance imaging (MRI) is considered the elective imaging modality for diagnosis and staging of CC and the recent development of hybrid MRI-radiotherapy systems, combining a linear accelerator with an on-board MR scanner, may represent a significant step-forward in the clinical management of this disease, as demonstrated by some preliminary experiences [19–21].

The availability of daily MR images leads to the possibility to define image-based predictive models able to study the patient treatment sensitivity by means of the analysis of the MR images acquired during the course of treatment.

In this context, a radiobiological parameter able to predict the treatment response in the locally advanced rectal cancer has been recently proposed and validated, modelling the tumor shrinkage during the first weeks of nCRT treatment through a statistical approach. This parameter, known as early regression index (ERI_{TCP}), combining the tumor volume measured on the MR images acquired at simulation and at mid-therapy, is able to identify the patients who will have complete response with high AUC value on low and high field MR images [22,23].

Aim of this hypothesis generating study is to evaluate the applicability of this parameter in the context of response of nCRT in CC, quantifying its performance in predicting pCR by using MR images acquired using a low field MR-guided radiotherapy unit [24].

2. Materials and Methods

2.1. Patients Selection Criteria and Treatment Workflow

Patients affected by LACC (FIGO IB2-IVA) were enrolled in this study, with the following inclusion criteria: Patients affected by biopsy proven LACC with no evidence of distant metastases at the radiological staging exams; Eastern Cooperative Oncology Group (ECOG) performance status ≤2, no pregnancy or breastfeeding at the moment of nCRT and at least 18 years old at the time of diagnosis.

Informed consent for therapy and image analysis purposes was acquired from all patients. Patients presenting clinical contraindications to MRI (e.g., presence of non MRI-compatible implanted devices, claustrophobia or major psychiatric disorders) or denying specific consent to MR guided radiotherapy (MRgRT) were not included.

The diagnostic workflow consisted in a gynecological exam, a diagnostic 1.5 T MR of the abdominal-pelvic site and a whole-body ^{18}FDG-positron emission tomography (PET)-CT staging scan.

All the patients underwent nCRT, combining weekly 40 mg/m^2 of cisplatin with concurrent MRgRT, administered using a simultaneous integrated boost (SIB) technique delivered in 22 fractions and prescribing a dose value of 50.6 Gy (2.3 Gy/fraction) to clinical target volume (CTV)1 and 39.6 Gy (1.8 Gy/fraction) to CTV2 [20].

All the patients signed a specific informed consent describing in detail the chosen therapeutic approach.

Radiotherapy was delivered using a 0.35 T MRgRT hybrid unit (ViewRay Inc., Mountain View, CA, USA) and therapy volumes were delineated on the 0.35 T TRUFI MR scan acquired during treatment simulation and using co-registered diagnostic 1.5 T staging MR and ^{18}FDG PET-CT images as supporting imaging.

The Gross Tumor Volume (GTV) was identified using the MR and PET-CT supporting images. CTV1 coincided to GTV and CTV2 was delineated as the union of the entire cervix, the uterus, parametria, vagina (entire or upper half, according to presence or absence of disease) and the corresponding drainage nodal.

If the pelvic nodes resulted positive at staging imaging, the common iliac nodes were included in the CTV2 volume, while the para-aortic nodes were included in case that the common nodes were positive [20]. CTV1 and CTV2 were expanded with 5 mm isotropic margin to generate the corresponding planning target volumes, following the institutional MRgRT guidelines [21].

An online adaptive procedure was administered in the treatment fractions where the positioning MR image showed that the GTV was not included in the Planning Target Volume (PTV) margins. GTV, PTV, bladder, bowel bag and rectum were re-contoured in case of online adaptive.

From six to eight weeks after the end of the treatment a restaging was performed, through a gynecological visit and a new MRI and ^{18}FDG PET-CT acquisition. A Querleu–Morrow radical hysterectomy with pelvic lymphadenectomy was performed for each patient within 8 weeks of the end of nCRT [8].

Pathological response to treatment was evaluated on surgical specimens, and three categories of treatment response were identified:

- ✓ Complete response (pR0), as absence of any residual tumor cells at any site;
- ✓ Microscopic response (pR1), as presence of persistent tumor foci not exceeding 3 mm for the maximum dimension;
- ✓ Macroscopic response (pR2), as presence of persistent tumor foci exceeding 3 mm for the maximum dimension

pCR was considered in case of pR0 [25].

2.2. *MRI Imaging Protocol and ERI$_{TCP}$ Definition*

A total of 16 patients were enrolled: All of them underwent a MRI protocol consisting of the acquisition of a T2/T1-weighted MR image each day of therapy (including simulation), acquired using a true fast imaging with steady state precession (TrueFISP) sequence [26].

Images were acquired using the 0.35 T on-board MR scanner integrated into the MRIdian system (ViewRay Inc, Mountain View, CA, USA), with a spatial resolution of 1.5 mm^3 and acquisition time of 175 s.

For the purposes of this study, the GTV was retrospectively delineated by two radiation oncologists with gynecological cancer expertise, blinded with respect the outcome of therapy.

Figure 1 shows a MR image sample with the tumor delineated at the simulation and at 10th day of therapy.

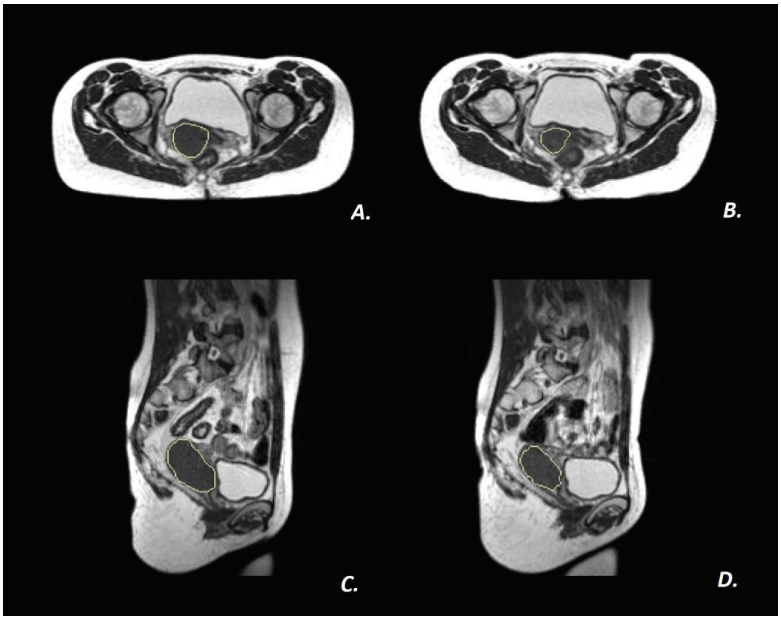

Figure 1. Gross tumor volume (GTV) delineated on simulation imaging and at fraction 10 in axial (**A**) and (**B**) and sagittal plan (**C**) and (**D**).

2.3. ERI_{TCP} Definition and Performance Evaluation

According to the original definition, the early regression index was calculated as follows [23]:

$$ERI_{TCP} = -ln\left[\left(1 - \left(\frac{V_{ther}}{V_{pre}}\right)\right)^{V_{pre}}\right]$$

where V_{pre} is the GTV volume calculated on the MR image acquired during simulation and V_{ther} represents the volume measured on the MR images acquired during the MRgRT treatment.

To identify the optimal time for pCR prediction, GTVs were delineated on MR images acquired at different fractions, and the ERI_{TCP} was calculated at different dose levels. The physical dose values were converted in biologically effective doses (BED) to make generalizable the results, using the following formula:

$$BED = nd\left(1 + \frac{d}{\frac{\alpha}{\beta}}\right)$$

where d is the dose per fraction, n is the number of fractions and α/β is the ratio representative of the tumor radio sensitivity, set equal to 10 Gy [27].

ERI_{TCP} was then calculated at the following BED values: 14, 28, 42, 54 and 62 Gy.

The ERI_{TCP} performance in identifying pCR patients was evaluated calculating the area under curve (AUC) under the receiver operating characteristic (ROC) curve for each dose level, estimating also the 95% exact binomial confidence interval according to the Clopper–Pearson method [28].

For each ERI index calculated, the Youden index (J) was also calculated at different threshold levels, and the one maximizing J was considered as best cut-off level.

The performance of the different ERI_{TCP} indices at the best cut-off level was then quantified considering specificity and sensitivity. The same analysis in terms of ROC curve was performed for the tumor volume calculated at simulation.

The BED value where the ERI_{TCP} reported the higher AUC value was identified as the optimal BED level to predict pCR. The ROC curves calculated at different BED values were then compared using the DeLong's test for correlated ROC curves [29].

Lastly, the robustness of ERI_{TCP} against inter-observer variability in tumor delineation was tested, comparing the volume of the contours independently delineated by the two radiation oncologists using the Mann–Whitney test for paired samples and the intra-class correlation index (ICC) [30,31]. The whole statistical analysis was performed using various software packages implemented in R environment [32,33].

3. Results

The clinical characteristics of the patients enrolled in this study at diagnosis and after surgery are reported in Table 1.

Table 1. Clinical information of the patients enrolled in the study.

Clinical Characteristics	Cases (Percentage)
Histology at the diagnosis	
■ Squamous cell carcinoma	15 (94%)
■ Clear cell adenosquamous carcinoma	1 (6%)
FIGO Stage at the diagnosis	
■ IIA	5 (31.3%)
■ IIB	10 (62.5%)
■ IIIC1	1 (6.2%)
Nodal status	
■ cN0	5 (31.3%)
■ cN1	11 (68.7%)
Pathological Response	
• pR0	11 (68.7%)
• pR1	3 (18.8%)
• pR2	2 (12.5%)

The median age of the patients at the diagnosis was 50.2 years (range 32–84 years), while pCR was achieved in 11/16 patients leading to a pCR rate of 68.7%. Table 2 summarizes the treatment fractions analyzed, with the corresponding physical and biological doses [34].

The median tumor volumes obtained by the two observers with the corresponding ranges and the results of the inter-observer analysis (p-value of Mann–Whitney test and ICC) are summarized in Table 3, to varying of the BED levels in Table 3.

High absolute agreement was observed in the GTV delineations performed by the two observers for all the different investigated time points, reporting no statistically significant differences in terms of Mann–Whitney test and high values in terms of ICC.

Table 2. Analyzed fractions and corresponding physical and biological biologically effective doses (BED) values, considering an α/β equal to 10 Gy for the tumor.

ERI	Fraction	Physical Dose	BED
$ERI_{14\ Gy}$	5	11.5 Gy	14.1 Gy
$ERI_{28\ Gy}$	10	23 Gy	28.3 Gy
$ERI_{42\ Gy}$	15	34.5 Gy	42.9 Gy
$ERI_{54\ Gy}$	19	43.7 Gy	53.8 Gy
$ERI_{62\ Gy}$	22	50.6 Gy	61.7 Gy

Table 3. Results of inter-observer variability to varying of the different BED levels.

BED	Median Tumor Volume (cc)		*p*-Value (Mann–Whitney)	ICC
	Observer 1	Observer 2		
0 Gy (Simulation)	50.5 (7.4–243.6)	45.9 (10.4–259.3)	0.13	0.99
14 Gy	33.7 (6.3–173.4)	33.1 (8.5–155.5)	0.57	0.98
28 Gy	25.8 (4.3–122.3)	21.5 (8.1–108.4)	0.18	0.98
42 Gy	22.2 (4.0–84.5)	20.0 (7.0–72.9)	0.23	0.96
54 Gy	14.7 (3.4–60.8)	33.1 (3.5–59.6.5)	0.53	0.95
62 Gy	11.6 (1.5–50.2)	13.0 (2.6–51.7)	0.32	0.97

The ERI_{TCP} was calculated at the different BED levels considering the contours of both observers and its ability in predicting treatment outcome was quantified by means of the ROC curves, as reported in Figure 2.

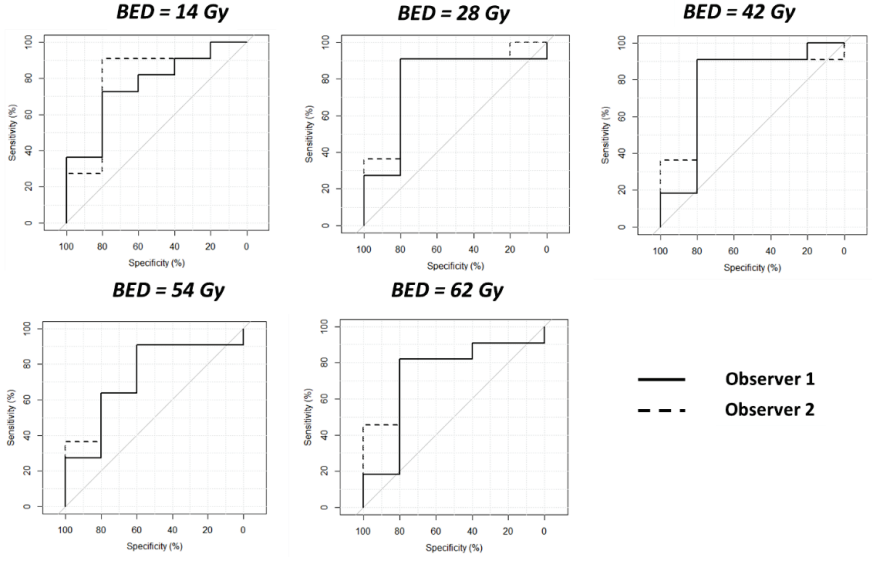

Figure 2. Receiver operating characteristic (ROC) curves calculated at different BED levels considering the two observers.

The ROC curves comparison performed using the DeLong test has reported no significant difference in the predictive performance of ERI_{TCP} to varying of the observer for all the BED levels analyzed. In particular, a p-value of 0.41 was obtained comparing the ROC curves in case of 14 Gy, $p = 0.77$ in case of 28 Gy, $p = 0.74$ in case of BED = 42 Gy, $p = 0.63$ for BED = 54 Gy and $p = 0.42$ for BED = 62 Gy.

The values in terms of predictive performance obtained for ERI_{TCP} to varying of the BED levels are reported in Table 4.

Table 4. Indicators of the predictive performance of the early regression index (ERI_{TCP}) index in the case of cervical cancer at different BED levels.

BED	AUC (95% CI)	Best Cut-Off	Sensitivity	Specificity	Youden Index
14 Gy	0.80 (0.51–1)	149.5	90.9	80	0.71
28 Gy	0.84 (0.58–1)	96.0	90.9	80	0.71
42 Gy	0.80 (0.53–1)	54.0	90.9	80	0.71
54 Gy	0.74 (0.47–1)	31.5	90.9	60	0.50
62 Gy	0.78 (0.53–1)	16.4	81.8	80	0.62

The values of sensitivity and specificity in Table 4 are referred to the discrimination obtained when the best threshold is considered. Figure 3 reports the values of the ERI_{TCP} to the BED values showing the highest predictive performance (BED = 28 Gy) considering the two observers.

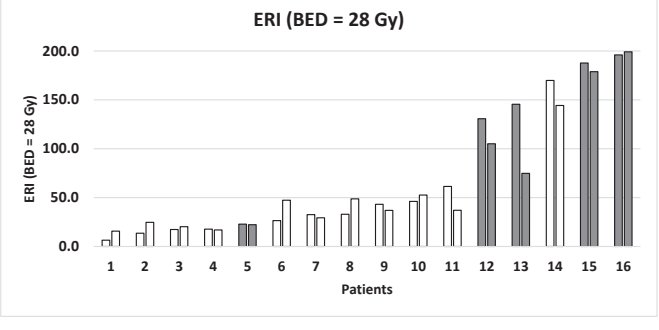

Figure 3. ERI_{TCP} values calculated at the most significant BED level for both observers (one column the highest predictive performance (BED = 28 Gy), no significant difference was observed using the DeLong's test (all *p*-values were >0.05).

As regards the tumor volume at simulation, an AUC value of 0.80 (0.57–1) was obtained, with no significant difference with respect the ROC curve calculated at BED = 28 Gy.

4. Discussion

This study investigated the use of ERI_{TCP} as pCR predictor in CC patients undergoing nCRT, analyzing MR images acquired using a low field MRgRT unit.

Being a morphological parameter, ERI_{TCP} can predict the response to nCRT by modelling the tumor volumetric regression during the treatment, simply using the information due to the volumetric variation of the tumor during the therapy: This makes ERI_{TCP} easy to use and generalizable to MR images acquired using different techniques and imaging parameters, as already demonstrated in the framework of rectal cancer [22,23,35].

One of the peculiarities of this study is represented by the possibility to correlate image-based parameters directly to histopathological data, being quite uncommon in the context of CC, as generally

the patients affected by this disease are addressed to brachytherapy and not to surgery, not allowing comparisons with histopathological ground truth.

The limited dimension of the population analyzed in this hypothesis generating study does not allow to draw definitive conclusions regarding the clinical use of this index, although it is interesting to observe that the predictive performance of this parameter is high and persists between independent observers.

The highest ERI_{TCP} performance in predicting pCR was observed when a BED value of 28 Gy was reached, with an AUC of 0.84, a sensitivity of 0.91 and a specificity of 0.8: The high value of sensitivity reported by this index may allow to successfully identify the patients that will undergo complete response since the second week of nCRT, avoiding unnecessary overtreatments and paving the way towards effective treatment personalization.

Although the DeLong's test did not report statistically significant differences between the ROC curves calculated at different timings (probably due to the reduced number of cases analyzed), it is interesting to observe that the most significant ERI_{TCP} timing identified for CC is the same observed for rectal cancer, regardless the obvious biological and histological differences that make the shrinkage pace not comparable in the two scenarios: This could be one of the reasons why the threshold value identified as best-cut off (96) is very different from the value of 13 observed in the rectal cancer experience [22,23].

A second study including an external cohort of patients is therefore recommended to validate the findings reported in this preliminary experience and confirm the most suitable timing and BED value. Unfortunately, the collection of homogeneous cohorts of patients affected by CC and undergoing nCRT will be particularly challenging, as most of these patients are generally addressed to brachytherapy, according to international guidelines [5].

5. Conclusions

This hypothesis generating study demonstrated that the use of the ERI_{TCP} can be extended to the context of CC, maintaining high levels of discriminative performance.

If validated on larger cohort of patients, the use of this index can represent a valuable tool to personalize the treatment strategy in the context of the CC, moving towards the anatomical and functional preservation of the irradiated tissues.

Author Contributions: Conceptualization: D.C. and C.F.; methodology: D.C., C.F., S.B.; software: L.P.; validation A.R., M.C., F.C., and V.D.L.; formal analysis: D.C., A.N.; investigation: C.V., M.N.; data curation: C.V., B.F., R.A.; writing—original draft preparation, D.C., A.P.; writing—review and editing G.C., L.B., S.B.; supervision: M.A.G., V.V., L.I. All authors have read and agreed to the published version of the manuscript.

Funding: This research received no external funding.

Acknowledgments: In this section you can acknowledge any support given which is not covered by the author contribution or funding sections. This may include administrative and technical support, or donations in kind (e.g., materials used for experiments).

Conflicts of Interest: The authors declare no conflict of interest related to the present work.

References

1. Hillemanns, P.; Soergel, P.; Hertel, H.; Jentschke, M. Epidemiology and Early Detection of Cervical Cancer. *Oncol. Res. Treat* **2016**, *39*, 501–506. [CrossRef] [PubMed]
2. Waggoner, S.E. Cervical cancer. *Lancet* **2003**, *361*, 2217–2225. [CrossRef]
3. Arbyn, M.; Weiderpass, E.; Bruni, L.; Sanjosé, S.; de Saraiya, M.; Ferlay, J.; Bray, F. Estimates of incidence and mortality of cervical cancer in 2018: A worldwide analysis. *Lancet Global Health* **2020**, *8*, e191–e203. [CrossRef]
4. Leath, C.A.; Monk, B.J. Twenty-first century cervical cancer management: A historical perspective of the gynecologic oncology group/NRG oncology over the past twenty years. *Gynecol. Oncol.* **2018**, *150*, 391–397. [CrossRef] [PubMed]

5. Pötter, R.; Tanderup, K.; Kirisits, C.; de Leeuw, A.; Kirchheiner, K.; Nout, R.; Tan, L.T.; Haie-Meder, C.; Mahantshetty, U.; Segedin, B.; et al. The EMBRACE II study: The outcome and prospect of two decades of evolution within the GEC-ESTRO GYN working group and the EMBRACE studies. *Clin. Transl. Radiat. Oncol.* **2018**, *9*, 48–60. [CrossRef] [PubMed]
6. Holschneider, C.H.; Petereit, D.G.; Chu, C.; Hsu, I.-C.; Ioffe, Y.J.; Klopp, A.H.; Pothuri, B.; Chen, L.-M.; Yashar, C. Brachytherapy: A critical component of primary radiation therapy for cervical cancer: From the Society of Gynecologic Oncology (SGO) and the American Brachytherapy Society (ABS). *Brachytherapy* **2019**, *18*, 123–132. [CrossRef]
7. Vordermark, D. Radiotherapy of Cervical Cancer. *Oncol Res. Treat.* **2016**, *39*, 516–520. [CrossRef]
8. Classe, J.M.; Rauch, P.; Rodier, J.F.; Morice, P.; Stoeckle, E.; Lasry, S.; Houvenaeghel, G. Groupe des Chirurgiens de Centre de Lutte Contre le Cancer Surgery after concurrent chemoradiotherapy and brachytherapy for the treatment of advanced cervical cancer: Morbidity and outcome: Results of a multicenter study of the GCCLCC (Groupe des Chirurgiens de Centre de Lutte Contre le Cancer). *Gynecol. Oncol.* **2006**, *102*, 523–529. [CrossRef]
9. Ferrandina, G.; Ercoli, A.; Fagotti, A.; Fanfani, F.; Gallotta, V.; Margariti, A.P.; Salerno, M.G.; Chiantera, V.; Legge, F.; Macchia, G.; et al. Completion surgery after concomitant chemoradiation in locally advanced cervical cancer: A comprehensive analysis of pattern of postoperative complications. *Ann. Surg. Oncol.* **2014**, *21*, 1692–1699. [CrossRef]
10. Gupta, S.; Maheshwari, A.; Parab, P.; Mahantshetty, U.; Hawaldar, R.; Sastri Chopra, S.; Kerkar, R.; Engineer, R.; Tongaonkar, H.; Ghosh, J.; et al. Neoadjuvant Chemotherapy Followed by Radical Surgery Versus Concomitant Chemotherapy and Radiotherapy in Patients with Stage IB2, IIA, or IIB Squamous Cervical Cancer: A Randomized Controlled Trial. *J. Clin. Oncol* **2018**, *36*, 1548–1555. [CrossRef]
11. Cetina, L.; González-Enciso, A.; Cantú, D.; Coronel, J.; Pérez-Montiel, D.; Hinojosa, J.; Serrano, A.; Rivera, L.; Poitevin, A.; Mota, A.; et al. Brachytherapy versus radical hysterectomy after external beam chemoradiation with gemcitabine plus cisplatin: A randomized, phase III study in IB2-IIB cervical cancer patients. *Ann. Oncol.* **2013**, *24*, 2043–2047. [CrossRef] [PubMed]
12. Ferrandina, G.; Palluzzi, E.; Gallotta, V.; Gambacorta, M.A.; Autorino, R.; Turco, L.C.; Macchia, G.; Cosentino, F.; Gui, B.; Mattoli, M.V.; et al. Neo-adjuvant platinum-based chemotherapy followed by chemoradiation and radical surgery in locally advanced cervical cancer (Lacc) patients: A phase II study. *Eur J. Surg Oncol* **2018**, *44*, 1062–1068. [CrossRef] [PubMed]
13. Vizza, E.; Corrado, G.; Zanagnolo, V.; Tomaselli, T.; Cutillo, G.; Mancini, E.; Maggioni, A. Neoadjuvant chemotherapy followed by robotic radical hysterectomy in locally advanced cervical cancer: A multi-institution study. *Gynecol. Oncol.* **2014**, *133*, 180–185. [CrossRef] [PubMed]
14. Ferrandina, G.; Gambacorta, A.; Gallotta, V.; Smaniotto, D.; Fagotti, A.; Tagliaferri, L.; Foti, E.; Fanfani, F.; Autorino, R.; Scambia, G.; et al. Chemoradiation with concomitant boosts followed by radical surgery in locally advanced cervical cancer: Long-term results of the ROMA-2 prospective phase 2 study. *Int. J. Radiat. Oncol. Biol. Phys.* **2014**, *90*, 778–785. [CrossRef]
15. Ai, Y.; Zhu, H.; Xie, C.; Jin, X. Radiomics in cervical cancer: Current applications and future potential. *Crit. Rev. Oncol. Hematol.* **2020**, *152*, 102985. [CrossRef]
16. Liu, Y.; Zhang, Y.; Cheng, R.; Liu, S.; Qu, F.; Yin, X.; Wang, Q.; Xiao, B.; Ye, Z. Radiomics analysis of apparent diffusion coefficient in cervical cancer: A preliminary study on histological grade evaluation. *J. Magn. Reson. Imaging* **2019**, *49*, 280–290. [CrossRef]
17. Lucia, F.; Visvikis, D.; Desseroit, M.-C.; Miranda, O.; Malhaire, J.-P.; Robin, P.; Pradier, O.; Hatt, M.; Schick, U. Prediction of outcome using pretreatment 18F-FDG PET/CT and MRI radiomics in locally advanced cervical cancer treated with chemoradiotherapy. *Eur. J. Nucl. Med. Mol. Imaging* **2018**, *45*, 768–786. [CrossRef]
18. Sun, C.; Tian, X.; Liu, Z.; Li, W.; Li, P.; Chen, J.; Zhang, W.; Fang, Z.; Du, P.; Duan, H.; et al. Radiomic analysis for pretreatment prediction of response to neoadjuvant chemotherapy in locally advanced cervical cancer: A multicentre study. *EBioMedicine* **2019**, *46*, 160–169. [CrossRef]
19. Otero-García, M.M.; Mesa-Álvarez, A.; Nikolic, O.; Blanco-Lobato, P.; Basta-Nikolic, M.; de Llano-Ortega, R.M.; Paredes-Velázquez, L.; Nikolic, N.; Szewczyk-Bieda, M. Role of MRI in staging and follow-up of endometrial and cervical cancer: Pitfalls and mimickers. *Insights Imaging* **2019**, *10*, 19. [CrossRef]

20. Boldrini, L.; Piras, A.; Chiloiro, G.; Autorino, R.; Cellini, F.; Cusumano, D.; Fionda, B.; D'Aviero, A.; Campitelli, M.; Marazzi, F.; et al. Low Tesla magnetic resonance guided radiotherapy for locally advanced cervical cancer: First clinical experience. *Tumori* **2020**, 300891620901752. [CrossRef]
21. Boldrini, L.; Chiloiro, G.; Pesce, A.; Romano, A.; Teodoli, S.; Placidi, L.; Campitelli, M.; Gambacorta, M.A.; Valentini, V. Hybrid MRI guided radiotherapy in locally advanced cervical cancer: Case report of an innovative personalized therapeutic approach. *Clin. Transl. Radiat. Oncol.* **2019**, *20*, 27–29. [CrossRef] [PubMed]
22. Cusumano, D.; Boldrini, L.; Yadav, P.; Yu, G.; Musurunu, B.; Chiloiro, G.; Piras, A.; Lenkowicz, J.; Placidi, L.; Broggi, S.; et al. External validation of an early regression index (ERITCP) as predictor of pathological complete response in rectal cancer using MR-guided Radiotherapy. *Int. J. Radiat. Oncol. Biol. Phys.* **2020**. [CrossRef] [PubMed]
23. Fiorino, C.; Gumina, C.; Passoni, P.; Palmisano, A.; Broggi, S.; Cattaneo, G.M.; Di Chiara, A.; Esposito, A.; Mori, M.; Raso, R.; et al. A TCP-based early regression index predicts the pathological response in neo-adjuvant radio-chemotherapy of rectal cancer. *Radiother. Oncol.* **2018**, *128*, 564–568. [CrossRef]
24. International Commissioning on Radiation Units and Measurements. *Receiver Operating Characteristic (ROC) Analysis in Medical Imaging*; ICRU Report 79; International Commissioning on Radiation Units and Measurements: Bethesda, MD, USA, 2008.
25. Zannoni, G.F.; Vellone, V.G.; Carbone, A. Morphological effects of radiochemotherapy on cervical carcinoma: A morphological study of 50 cases of hysterectomy specimens after neoadjuvant treatment. *Int. J. Gynecol. Pathol.* **2008**, *27*, 274–281. [CrossRef]
26. Chiloiro, G.; Boldrini, L.; Meldolesi, E.; Re, A.; Cellini, F.; Cusumano, D.; Corvari, B.; Mantini, G.; Balducci, M.; Valentini, V.; et al. MR-guided radiotherapy in rectal cancer: First clinical experience of an innovative technology. *Clin. Transl. Radiat. Oncol.* **2019**, *18*, 80–86. [CrossRef] [PubMed]
27. Wang, C.-J.; Huang, E.-Y.; Sun, L.-M.; Chen, H.-C.; Fang, F.-M.; Hsu, H.-C.; Changchien, C.-C.; Leung, S.W. Clinical comparison of two linear-quadratic model-based isoeffect fractionation schemes of high-dose-rate intracavitary brachytherapy for cervical cancer. *Int. J. Radiat. Oncol. Biol. Phys.* **2004**, *59*, 179–189. [CrossRef]
28. Clopper, C.J.; Pearson, E.S. The Use of Confidence or Fiducial Limits Illustrated in the Case of the Binomial. *Biometrika* **1934**, *26*, 404–413. [CrossRef]
29. DeLong, E.R.; DeLong, D.M.; Clarke-Pearson, D.L. Comparing the areas under two or more correlated receiver operating characteristic curves: A nonparametric approach. *Biometrics* **1988**, *44*, 837–845. [CrossRef]
30. Taylor, J. *An Introduction to Error Analysis: The Study of Uncertainties in Physical Measurements; II.*; University Science Books: Sausalito, CA, USA, 1997.
31. Müller, R.; Büttner, P. A critical discussion of intraclass correlation coefficients. *Stat. Med.* **1994**, *13*, 2465–2476. [CrossRef]
32. Gatta, R.; Vallati, M.; Dinapoli, N.; Masciocchi, C.; Lenkowicz, J.; Cusumano, D.; Casá, C.; Farchione, A.; Damiani, A.; van Soest, J.; et al. Towards a modular decision support system for radiomics: A case study on rectal cancer. *Artif. Intell. Med.* **2019**, *96*, 145–153. [CrossRef]
33. Robin, X.; Turck, N.; Hainard, A.; Tiberti, N.; Lisacek, F.; Sanchez, J.-C.; Müller, M. pROC: An open-source package for R and S+ to analyze and compare ROC curves. *BMC Bioinform.* **2011**, *12*, 77. [CrossRef] [PubMed]
34. Passoni, P.; Fiorino, C.; Slim, N.; Ronzoni, M.; Ricci, V.; Di Palo, S.; De Nardi, P.; Orsenigo, E.; Tamburini, A.; De Cobelli, F.; et al. Feasibility of an adaptive strategy in preoperative radiochemotherapy for rectal cancer with image-guided tomotherapy: Boosting the dose to the shrinking tumor. *Int. J. Radiat. Oncol. Biol. Phys.* **2013**, *87*, 67–72. [CrossRef] [PubMed]
35. Fiorino, C.; Passoni, P.; Palmisano, A.; Gumina, C.; Cattaneo, G.M.; Broggi, S.; Di Chiara, A.; Esposito, A.; Mori, M.; Ronzoni, M.; et al. Accurate outcome prediction after neo-adjuvant radio-chemotherapy for rectal cancer based on a TCP-based early regression index. *Clin. Transl. Radiat. Oncol.* **2019**, *19*, 12–16. [CrossRef] [PubMed]

applied sciences

MDPI

Article

An Automatic Approach for Individual HU-Based Characterization of Lungs in COVID-19 Patients

Aldo Mazzilli [1,2], Claudio Fiorino [1], Alessandro Loria [1], Martina Mori [1,3], Pier Giorgio Esposito [1,2], Diego Palumbo [3,4], Francesco de Cobelli [3,4] and Antonella del Vecchio [1,*]

[1] Department of Medical Physics, San Raffaele Scientific Institute, 20132 Milan, Italy; mazzilli.aldo@hsr.it (A.M.); fiorino.claudio@hsr.it (C.F.); loria.alessandro@hsr.it (A.L.); mori.martina@hsr.it (M.M.); esposito.piergiorgio@hsr.it (P.G.E.)
[2] Department of Physics, Università degli Studi di Milano, 20122 Milan, Italy
[3] Department of Medicine, Università Vita-Salute San Raffaele, 20132 Milan, Italy; palumbo.diego@hsr.it (D.P.); decobelli.francesco@hsr.it (F.d.C.)
[4] Department of Radiology, San Raffaele Scientific Institute, 20132 Milan, Italy
* Correspondence: delvecchio.antonella@hsr.it

Abstract: The ongoing COVID-19 pandemic currently involves millions of people worldwide. Radiology plays an important role in the diagnosis and management of patients, and chest computed tomography (CT) is the most widely used imaging modality. An automatic method to characterize the lungs of COVID-19 patients based on individually optimized Hounsfield unit (HU) thresholds was developed and implemented. Lungs were considered as composed of three components—aerated, intermediate, and consolidated. Three methods based on analytic fit (Gaussian) and maximum gradient search (using polynomial and original data fits) were implemented. The methods were applied to a population of 166 patients scanned during the first wave of the pandemic. Preliminarily, the impact of the inter-scanner variability of the HU-density calibration curve was investigated. Results showed that inter-scanner variability was negligible. The median values of individual thresholds th1 (between aerated and intermediate components) were −768, −780, and −798 HU for the three methods, respectively. A significantly lower median value for th2 (between intermediate and consolidated components) was found for the maximum gradient on the data (−34 HU) compared to the other two methods (−114 and −87 HU). The maximum gradient on the data method was applied to quantify the three components in our population—the aerated, intermediate, and consolidation components showed median values of 793 ± 499 cc, 914 ± 291 cc, and 126 ± 111 cc, respectively, while the median value of the first peak was −853 ± 56 HU.

Keywords: Covid-19; chest CT; lungs; HU density

Citation: Mazzilli, A.; Fiorino, C.; Loria, A.; Mori, M.; Esposito, P.G.; Palumbo, D.; de Cobelli, F.; del Vecchio, A. An Automatic Approach for Individual HU-Based Characterization of Lungs in COVID-19 Patients. *Appl. Sci.* **2021**, *11*, 1238. https://doi.org/10.3390/app11031238

Academic Editor: Salvatore Gallo
Received: 20 November 2020
Accepted: 22 January 2021
Published: 29 January 2021

1. Introduction

Severe acute respiratory syndrome coronavirus (SARS-CoV-2), a novel RNA coronavirus from the same family as SARS-CoV and Middle East respiratory syndrome coronavirus (MERS-CoV), was identified in early January 2020 as the cause of a pneumonia epidemic initially striking China, from where it spread very rapidly around the world. The World Health Organization named the syndrome coronavirus disease 2019 (COVID-19) and subsequently declared it a pandemic, given its widespread infectivity and high rate of contagion. To date, many millions of cases have been confirmed worldwide [1]. Human coronaviruses typically cause respiratory and enteric infections. SARS-CoV-2 infection mainly presents flu-like symptoms such as fever, cough, and fatigue, similar to other coronaviruses. In severe cases, the virus can cause severe interstitial pneumonia, acute respiratory distress syndrome (ARDS), and subsequent multi-organ failure, responsible for severe acute respiratory failure and high mortality rates.

Chest CT plays an important role in diagnosing COVID-19 [2]. Recent studies have reported the sensitivity and specificity of CT in COVID-19 pneumonia to be 60–98% and 25–53%, respectively [3,4]. A recent study reported positive and negative predictive values of chest CT in COVID-19 pneumonia of 92% and 42%, respectively [3]. The low negative predictive value suggests that CT may not be suitable as a screening method in COVID-19 pneumonia, at least in the early stages of the disease. CT sensitivity depends on the time elapsed after the onset of symptoms [5], and CT findings vary widely for this disease, depending on clinical severity and the time from symptom onset [6,7]. The disease most commonly affects the lower and peripheral areas of both lungs, with a prevalent multifocal pattern [8]. The posterior areas are affected in about 80% of cases, and the disease is generally quite extensive, with all five lobes affected in a large proportion of patients [9]. Although irregular multifocal distribution is more common than diffuse disease [8], both unilateral and unifocal involvement may occur.

Ground glass opacity (GGO) is defined as a hyper-attenuated area of the lung without darkening of the underlying vessels, and is typically caused by partial filling of the air spaces or interstitial thickening [10]. GGO appears to be the most common CT finding, observed in up to 98% of patients, and is usually the first manifestation [11,12]. It may or may not be accompanied by other findings, in particular consolidation and reticulation [9]. Consolidation is defined as a hyper-attenuated area with darkening of the underlying vessels, caused by the complete filling of the alveolar air spaces [10]. Consolidations are generally irregular, while round-shaped lesions have been reported in 11–54% of patients [13], and are considered to be relatively more specific for this disease [14]. Consolidation usually appears later than GGO and peaks in days 10 to 12 after the onset of the disease [6]. Reticulation is defined as thickened interlobular septa and intralobular lines that appear as linear opacities on CT [10], and was the third most common CT feature, after GGO and consolidation, with a rate of 48.5–59% [8]. Crazy paving pattern (CPP) is defined as thickened interlobular septa or intralobular lines superimposed on GGO, resembling paving stones [12]. This finding may refer to alveolar edema and acute interstitial inflammation, also present in severe acute respiratory syndrome (SARS). It has been reported in 5–36% of patients with COVID-19 pneumonia [12].

Several recent works have evaluated the correlation between quantitative features extracted from CT and the clinical outcome of patients with COVID-19 pneumonia. Few articles have dealt with the prediction of disease severity and short-term disease progression [15–17]. Other authors have developed predictive models of diagnosis and prognosis [18–22]. Artificial-intelligence-based approaches have been shown to significantly improve sensitivity and specificity in diagnosing COVID-19 pneumonia; machine learning approaches using convolutional network models have found promising results in distinguishing COVID-19 from other types of pneumonia [23–25]. This volumetric calculation reflects disease extension, and can be used in predicting disease severity, progression, and response to treatment [26–28].

Within this context, the reliability and repeatability of lung sub-volumes according to their density is a significant issue. The need for operator-independent approaches, possibly defining sub-regions with a clear link to functional meaning, is urgent. Thus, the principles aims of our study were:

1. To develop an automated, operator-independent quantitative method to identify the different lung regions for COVID-19 patients, based on individually optimized Hounsfield unit (HU) thresholds; the proposed method is based on an intuitive, interpretable phenomenological characterization of lungs, with clear functional meaning;
2. To achieve a feasible implementation of the proposed method in such a way as to be potentially usable by other institutions;
3. To demonstrate the robustness of the method with respect to inter-scanner variability within a single institute;

4. To report inter-patient distribution of the HU-based parameters extracted by our approach over a large single-center population of 166 patients during the first wave of the pandemic.

2. Materials and Methods

2.1. Patient Database

The data used in this work are part of an internal database of the San Raffaele Scientific Institute (Milan, Italy). The database consists of more than 250 COVID-19 patients who underwent chest CT scan between 28 February 2020 and 21 May 2020. CTs were performed at maximum inspiration. Demographic data (age, sex) and clinical data (e.g., comorbidities) are available for each patient. Patients who presented an acquisition made with parenchyma reconstruction in non-contrast mode were selected from the database. The database thus obtained consisted of 166 COVID-19 patients. The number was in fact limited by the availability of observers in contouring lungs, which is a quite cumbersome procedure. The significant, temporary reduction of radiotherapy clinical activities during the first phase of the lockdown afforded more time to planners for this activity. Patients were randomly chosen from the largest available set. After a return to full activity, the time available was greatly reduced, and it was thus decided to stop the contouring phase, resulting in a more than sufficient number of patients to test our approach and from whom to derive reliable population data. The equipment used for chest CT scans was as follows:

- Lightspeed VCT (64sl), General Electric Medical System(Boston, MA, USA);
- Brilliance (64sl), Philips (Amsterdam, Netherlands);
- Incisive (64sl), Philips (Amsterdam, Netherlands).

88% percent of the exams were performed with Lightspeed, 7% with Brilliance and 5% with Incisive. All scans were performed with an X-ray tube voltage of 120 kV and automatic current modulation of 149 to 549 mA, slice thickness 1 to 1.25 mm, and matrix 512×512. CT images were retrieved from the hospital picture archiving and communication system (PACS).

2.2. Assessing Inter-Scanner Variations of HU-Density Calibration Curves

Accurate and reproducible assessment of Hounsfield unit (HU) [29] distribution within the lungs is of paramount importance. The values of the HU of the CT images depends on the calibration curve internal to each equipment (HU as a function of the attenuation coefficient of the materials). For verification, we investigated the impact of the HU-density calibration curves obtained with the parameters used in the image acquisition phase of the CT equipment utilized. To assess the impact of the calibration curves, the acquisition parameters of COVID-19 patients we analyzed, and the specific protocol calibration curves reconstructed for all CT scanners used. For the study description, tube voltage and X-ray current were collected from the header DICOM (Digital Imaging and COmmunications in Medicine) of the CT image in the available database. Tube voltage was set at 120 kV for all CT scans, while the X-ray current was modulated according to patient size. The data were divided for each piece of equipment—the median values of the X-ray current for each device were calculated; regarding GE LightSpeed (used for 88% of patients), the values of the minimum, the maximum, and the first and the third quartile were also calculated, as shown in Table 1.

These parameters were used to perform acquisitions with the calibrated CT image quality phantom, Catphan 600—The Phantom Laboratory, Battenville, NY, USA, in the entire HU range (−1000 to +1000). A tube voltage of 120 kV and the median value of X-ray current for each piece of equipment was used for the exposition of the Catphan phantom. Moreover, for the General Electric equipment, the first and third quartiles were also used as exposure parameters. The Catphan consists of an inner layer containing several inserts of different materials corresponding to different attenuation coefficients. Knowing the attenuation coefficients of these materials, and measuring the average HU values inside

each insert, it was possible to obtain the characteristic linearity curve of the equipment at the exposure parameters selected in the acquisition phase.

Table 1. Schematic of the CT chest present in the database based on the equipment used, the number of patients, and the voltage and current range.

Equipment	Number of Patients	Voltage (kV)	Current (mA)			
			Range	Median	1st Quartile	3rd Quartile
Lightspeed	146	120	149–549	352.5	219.5	451.5
Brilliance	12	120	240–500	458.5	-	-
Incisive	8	120	189–368	334	-	-

Five repeated measurements were carried out for each scanner, and each X-ray current value considered. The average HU value was used to calculate the linearity curve for each insert.

Consequently, for Philips Brilliance and Philips Incisive, a single calibration curve was obtained, relative to the median value of the current used for the patient scans carried out on each. For the GE LightSpeed, five calibration curves were obtained, corresponding to the minimum, maximum, 25th quartile, 50th quartile (median), and 75th quartile values. A region of interest (ROI) was selected within each Catphan insert. Using the ImageJ image processing software, the mean value and standard deviation of the HU values within the ROI were evaluated. The variation in the average HU values within each ROI was then calculated between the various acquisitions taken.

2.3. HU-Density Histograms

The first step in the implementation of a method for lung characterization in COVID patients is the accurate identification of the entire lung area. CT acquisitions of the 166 COVID-19 patients considered were initially analyzed, and the 332 lungs were manually segmented by a team of planners from the San Raffaele Scientific Institute (Milan, Italy) skilled in the manual segmentation of CT images for radiotherapy planning purposes. The contouring tool of the Eclipse software (Varian Medical System, Inc. Palo Alto, CA, USA) was used for the manual segmentation of the lungs. Both the aerated component and the component affected by COVID pneumonia were included within the contours thus identified. Right and left lungs were delineated separately for each patient. Since the original dimensions of CT voxels vary depending on the equipment used, CT images were resampled with an isotropic $1.5 \times 1.5 \times 1.5$ mm^3 voxel size, in order to reduce the impact of the different CT voxel dimension used during the acquisition. The original lung contours were overlaid on the resampled images, without any significative differences. The consistency of the contours was checked on a sample of patients by two skilled radiologists. On the other hand, "little" inter-observer variations in lung contouring are not expected to significantly influence our approach, as the threshold values were well away from the inferior and superior HU limits and identifying internal volumes. All procedures regarding the resampling at cubic voxel and the analysis of the resampled images to extract lung HU-density histograms were performed with a specific workflow designed with the MIM software [30]. Each HU-density unit was associated with the number of voxels having that HU-density value; this was performed for each individual lung.

2.4. Threshold Definition Methods

Considering the typical HU-distribution, lungs may be divided into three regions: the aerated component, the consolidated component and an intermediate component. The HU density of the lungs of COVID-19 patients is generally characterized by the presence of two peaks with a shape similar to that of a Gaussian curve, as shown in Figure 1, one next to the air HU (−1000 HU) which defines the aerated, and therefore "properly" functioning, lung; and one next to the water HU (0 HU) [29] corresponding to the lung component with

consolidated disease. Between these two peaks there is a quite evident and pronounced region with highly variable patterns from patient to patient. This region corresponds to the component of the lung affected by the disease, but not yet scarred, and mostly includes ground glass opacities (GGO) and crazy-paving regions. The corresponding region in the HU distribution plot often has a plateau-like trend, while in most cases it is characterized by a bell shape. Taking into account the shape of the HU-density distributions, different strategies were followed to individually define the best threshold values for distinguishing the different lung components.

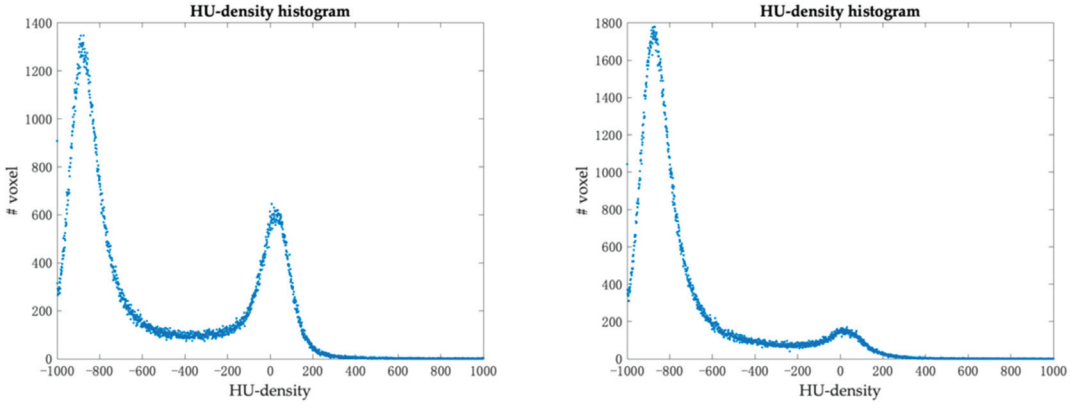

Figure 1. Examples of Hounsfield unit (HU)-density histograms. The histograms shown correspond to the lungs of the same patient; in particular, (**a**) is the histogram relating to the right lung and (**b**) is the histogram relating to the left lung.

The first method consisted of parameterizing the distribution of the HU densities of the individual lungs with a curve given by the linear combination of three Gaussian curves, and considering the half-width half-maximum of the curves to assess the thresholds. This method was named the "Gaussian method". The three Gaussians used in the fit corresponded to the three lung components (see Figure 2). The resulting function used for the fit was as follows:

$$fit(x) = a1 \times \exp\left(-\left(\frac{x-b1}{c1}\right)^2\right) + a2 \times \exp\left(-\left(\frac{x-b2}{c2}\right)^2\right) + a3 \times \exp\left(-\left(\frac{x-b3}{c3}\right)^2\right)$$

where:

- x are the values of the densities HU;
- $a1$, $a2$, and $a3$ are the multiplicative coefficients of the Gaussians;
- $b1$, $b2$, and $b3$ represent the mean values of the Gaussians;
- $c1$, $c2$, and $c3$ are related to the standard deviation from the relation $c^2 = 2\sigma^{2;}$
- Subscript 1 refers to the Gaussian related to the aerated component;
- Subscript 2 refers to the Gaussian related to the intermediate component;
- Subscript 3 to the Gaussian related to the consolidated component.

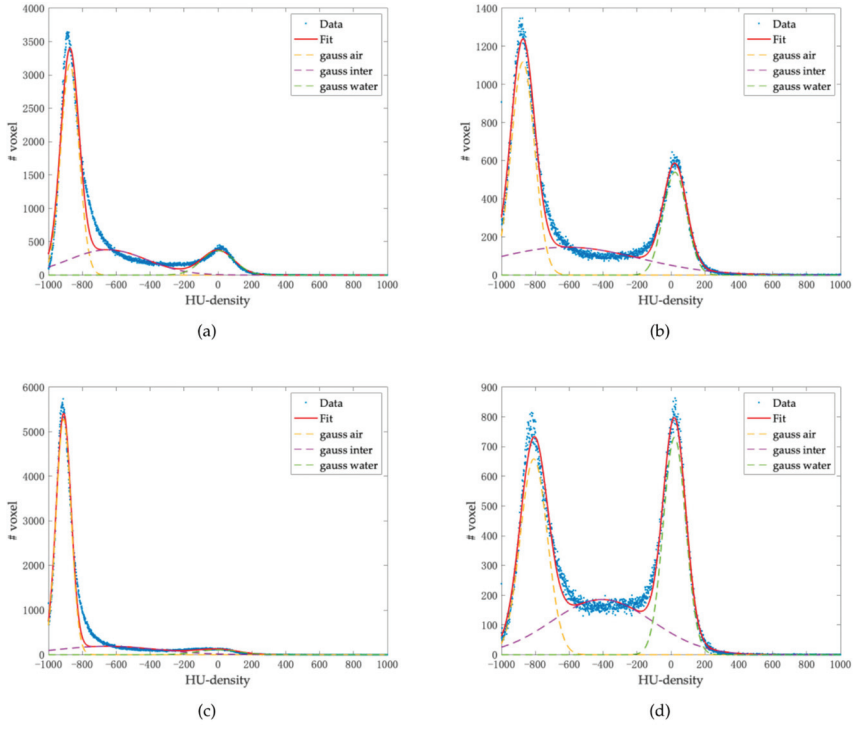

Figure 2. (**a**–**d**) Examples of HU-density histogram fit. Each plot shows the overall fit and the three Gaussians that compose it.

Concerning the fit, it was imposed that the search for peaks corresponding to the aerated and consolidated components would start from the HU-density values typical of air (−1000 HU) and water (0 HU), respectively. The standard deviation σ of the individual Gaussians was obtained from the fit and used to determine the thresholds. The thresholds were given by the following relations:

$$\text{th1} = b1 + \sigma 1$$

$$\text{th2} = b3 - \sigma 3$$

where:

- th1 is the value of HU that separates the aerated component from the intermediate one;
- th2 is the value of HU that separates the intermediate component from the consolidated one;
- $b1$ and $b3$ are the mean values of the Gaussians and $\sigma 1$ and $\sigma 3$ are the relative standard deviations.

All fits were realized with a Matlab script using the cftool for the curve fitting. The fitting method used was the non-linear least squares with the least absolute residual method.

The second method was the maximum gradient "on the fit". With this approach the proper inflection points of the curve were found by looking at the points where the second derivative of the curves was 0.

The third method used was similar to the previous one, without considering the Gaussian fit but directly using the original data. This method was identified as maximum gradient "on the data". The frequency values of the individual HU densities were jagged, and thus had many inflection points. Therefore, in order to apply the maximum gradient

method, it was necessary to post-process the distributions of the HU densities. First, a rebinning of the data to 25 HU was performed; the values obtained were then interpolated, and a smooth function applied (see Figure 3). At this point it was possible to apply the maximum gradient method, as in the case of the fit function, and find the threshold values.

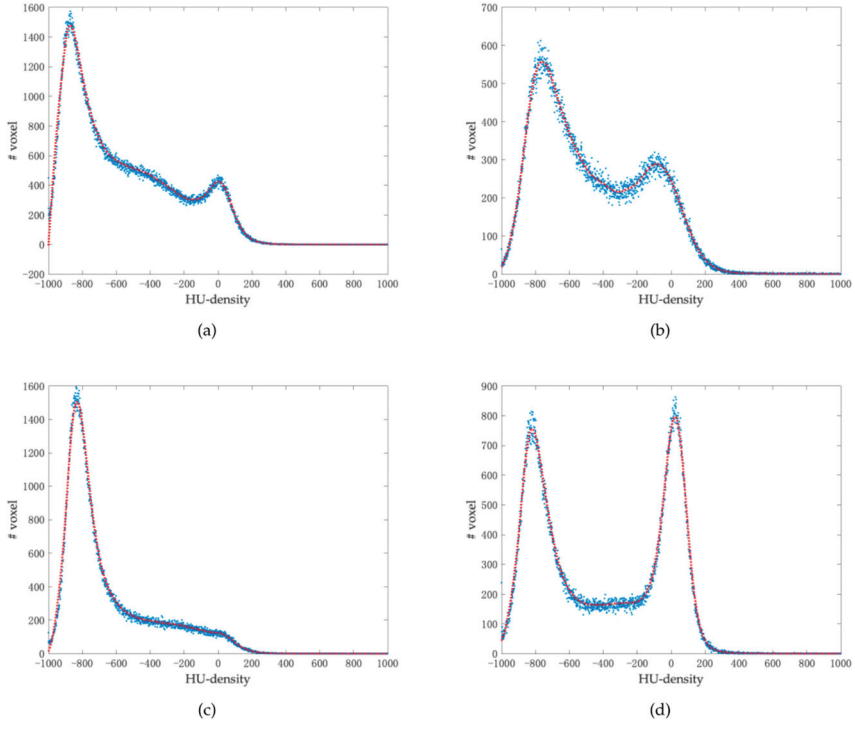

Figure 3. (**a**–**d**) Examples of post-processed HU-density histograms.

For each of the three methods, the individual thresholds for each lung and the median values over the whole population were extracted.

The threshold values individually obtained with the three methods were then compared by means of Kuskall–Wallis tests. Summary statistics of the different lung components and their relative ratios were also reported focusing on the third method, which was found to be the most stable in defining th2 (including visual inspection by two expert radiologists of 30 sample patients).

3. Results

3.1. Impact of the HU-Density Calibration Curve

The variation of the HU values among the different acquisitions (range 0 to 4 HU) was much smaller than the standard deviation of the HU values within each ROI for the single acquisition (range 38 to 69 HU). For this reason, a single HU calibration curve can be considered given by the average of all the measurements made at the different currents also for GE LightSpeed. The values of the calibration curves for the different types of equipment were then compared. It was found that the standard deviation of the HU values of the inserts was considerably smaller than the average of the standard deviations (SD) relating to the measurement on the inserts. Results are shown in detail in Table 2 and Figure 4.

Table 2. Average CT values for the three types of equipment.

Insert	Attenuation Coefficient @70 keV (1/cm)	Light Speed		Brilliance		Incisive	
		N. CT ROI	SD	N. CT ROI	SD	N. CT ROI	SD
Air	0	−981.23	38.35	−972.12	42.43	−972.57	49.64
PMP	0.157	−181.55	48.03	−175.48	54.13	−181.07	66.68
LDPE	0.174	−90.60	46.14	−85.43	53.53	−90.17	67.73
Polystyrene	0.188	−35.30	46.56	−30.19	52.44	−34.59	69.33
Acrylic	0.215	126.99	47.75	125.71	57.40	121.08	66.92
Delrin	0.245	350.22	52.85	347.33	56.96	341.85	70.77
Teflon	0.363	960.24	68.70	940.18	59.92	940.09	74.29

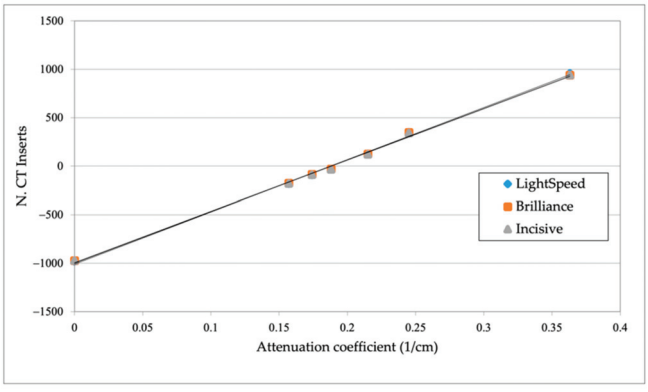

Figure 4. Plot of the number of CT inserts as a function of the attenuation coefficient for the equipment used. The trend line for each of the data sets is also represented.

In summary, we can assume that inter-scanner variability did not significantly affect the HU values of the CT images, regardless of the current used during scanning. The resulting HU-density histograms can therefore be considered reasonably consistent.

3.2. HU-Density Histogram Parameters—Extraction and Analysis of 166 COVID-19 Patients

Through the script created in the Matlab environment, all the histograms were successfully fitted; for each of them, the values of the HU thresholds between the aerated and intermediate components (th1) and between the intermediate and consolidated (th2) were calculated for each of the individual lungs using the methods described:

1. Gaussian;
2. Maximum gradient on the fit;
3. Maximum gradient on the data.

Examples of several histograms of representative lungs are shown in Figure 5 as results of the application of the three methods. Overall (see Table 3), the th1 threshold values using the Gaussian method were in the range of −870 to −386 HU, with a median and standard deviation of −768 and 73 HU, respectively; values obtained with the th2 threshold were between−232 and 32 HU with median and standard deviation of −114 and 41 HU, respectively. Using the method of the maximum gradient on the fit, the HU range was −927 to −322 HU with median and standard deviation of −780 and 77 HU for the threshold th1, and −706 to 10 HU with median and standard deviation of −87 and 61 HU, respectively, for the th2 threshold. Lastly, the values obtained with the maximum gradient method on the data were, for the threshold th1, a range of −900 to −430 HU and median and standard deviation of −798 and 71 HU, and a range of −271 to 64 HU with -34 ± 41 HU for the median and standard deviation of the th2 threshold.

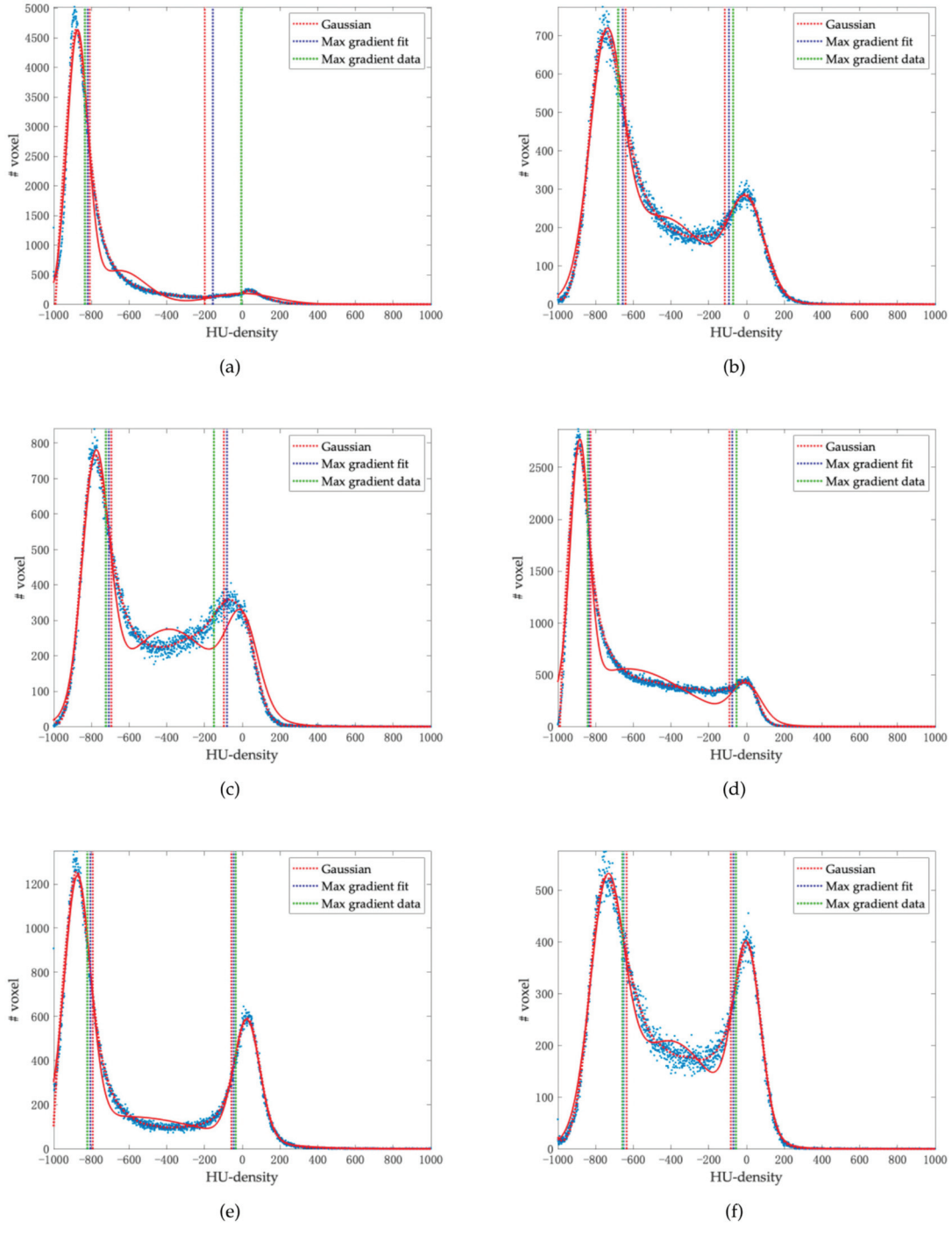

Figure 5. (**a**–**f**) Examples of graphical representation of the threshold values found by analyzing the HU-density histograms with the methods described.

Table 3. Summary table of the threshold values found with the methods used.

Method	Threshold	Minimun	Maximum	Median	Standard Deviation
Gaussian	Th1	−870	−386	−768	73
	Th2	−232	32	−114	41
Maximum gradient fit	Th1	−927	−322	−780	77
	Th2	−706	10	−87	61
Maximum gradient data	Th1	−900	−430	−798	71
	Th2	−271	64	−34	41

The Kruskal–Wallis non-parametric statistical significance test demonstrates that the distributions of the values of the thresholds *th*1 and *th*2 calculated with the three methods described were statistically different, with a significance level p-value <0.001 for both thresholds. While inter-patient variability was low for the th2 threshold, th1 threshold values were far more variable, as they concerned the fibrotic component of the consolidated lung.

This is likely because the aerated component of the lung obtained from CT images, taken in conditions of maximum inspirium, is an extremely patient-dependent measure of lung function.

As can be seen from the boxplots in Figure 6, the method with the least dispersion was the maximum gradient on the data. Also from the qualitative point of view, it was clear that the method that visually best identified the separation of the components of the lungs of COVID-19 patients was that of maximum gradient on the data. Of note, the approach of using a plot that follows the trend of real data, rather than a fit made on these data, removes the intrinsic uncertainty linked to the fit, obtaining values that better represent the true condition of the lungs. Consequently, in the remaining part of this work, sub-segmentation will always refer to this method.

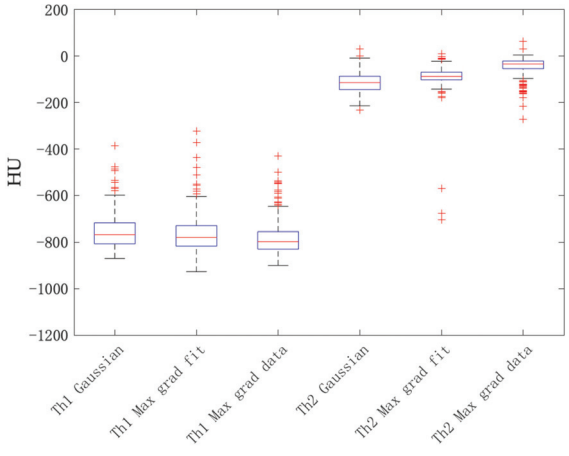

Figure 6. Boxplot of the distributions of threshold values Th1 and Th2 according to method used: Gaussian, maximum gradient on the fit (Max grad fit) and maximum gradient on the data (Max grad data).

After identifying the threshold values that separate the components of the lungs in COVID-19 patients, information characterizing each of the regions of the lungs was extracted from the histograms. The first relevant parameter extracted was the volume (in cc) of the aerated, intermediate, and consolidation regions. To calculate the volume in cc starting from the CT images, the area under the curve of the HU-density histograms was considered. Each voxel had a known size of $1.5 \times 1.5 \times 1.5$ mm^3; thus the area under the

curve was linked to the volume of the lung considered with a normalization factor taking voxel size into account.

Figure 7 shows the histogram of the volume distributions of the lung components within the entire patient population. The bin size used was 150 cc. It can be seen that the consolidated component had the smallest volume, with a median value of 126 cc $\pm$ 111 cc. The intermediate component had a median volume of 914 cc with a standard deviation of 291 cc, while the aerated component had a median volume of 793 $\pm$ 499 cc. In addition to the volumes of the lung regions, their ratio was also calculated. The absolute measurement of volumes, in fact, may not provide full information on the residual functionality of the lung. The values found for the consolidated over aerated component ratio and the ratio between intermediate and aerated components are shown in Figure 8 and were 0.16 $\pm$ 0.89 and 1.09 $\pm$ 2.56, respectively. Other extracted features that characterized the HU-density histogram were:

1. HU value corresponding to the peak of the curve for the aerated regions;
2. Shift with respect to -1000 HU, a characteristic value of the aerated component under normal conditions;
3. Width in HU of the intermediate region.

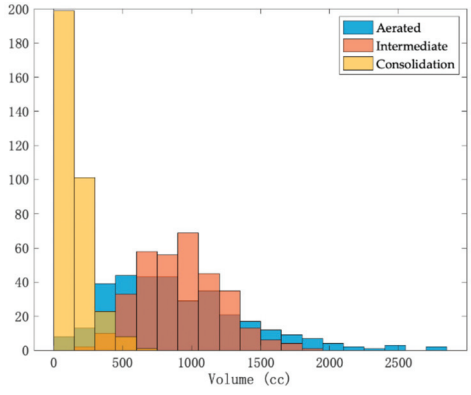

Figure 7. Histogram of the volume distributions of the aerated, intermediate, and consolidated components. The bin size used was 150 cc. The number on the y-axis represents the number of patients per bin.

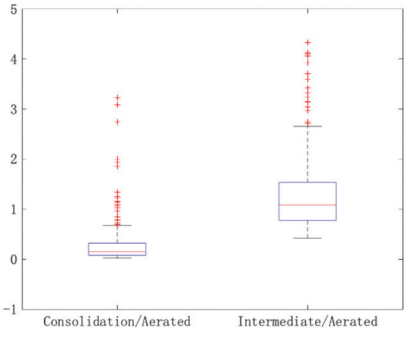

Figure 8. Boxplot of the volume ratios of the consolidated component compared to the aerated component and of the intermediate component compared to the aerated one.

The median of the values of the peak position of the aerated region curve was -853 ± 56 HU in a range of -1000 to -583 HU. Consequently, the median value of the

peak shift of the aerated region with respect to −1000 HU was 147 HU. The width of the intermediate region was calculated as the difference between the th2-th1 threshold values. The width values found were in the range of 282 to 878 HU, with a median and standard deviation of 754 and 88 HU, respectively. As shown in Figure 9, the inter-patient distribution of these values was very large and did not follow a Gaussian shape.

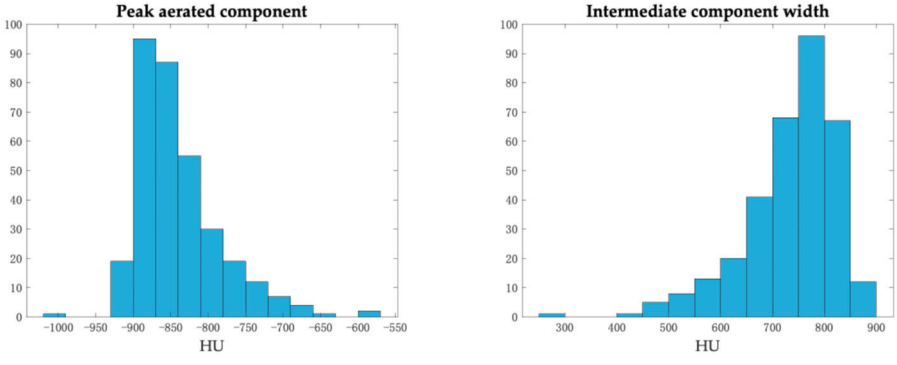

Figure 9. Histograms of the distributions of (**a**) position of the peak of the aerated component and (**b**) width of the intermediate component.

4. Discussion

The proposed method was based on the robust, operator-independent identification of threshold HU values that identified three regions here referred to as aerated, intermediate and consolidated, with intuitively clear functional meaning. It follows a phenomenological approach starting from the manual segmentation of the lung and then analyzing the shape of the HU histogram. Contrary to other approaches, the thresholds that define and differentiate the lung components were identified on the basis of the shape of the HU histograms, rather than second-order features and classifiers or radiologist preferences, thus maintaining a solid link with the residual lung functionality and eliminating, a priori, any operator dependence.

Prior to the quantitative analysis of the images, it was verified that the image database was consistent against inter-scanner variability, although 88% of patients were scanned on one (of the three) scanner. For this purpose, calibrated CT image quality phantom acquisitions at different X-ray currents were performed on each scanner. Importantly, inter-scanner variability was not found to significantly influence the HU value of CT images, and the database can thus be considered consistent.

The lung contours were initially segmented manually. Subsequently, through the implementation of an automatic procedure implemented in a workflow on the MIM software, histograms of the HU values inside the contours were extracted. The histograms obtained were analyzed by means of three different analytical methods.

The maximum gradient on the data method, likely to fit better with visual consistency in lung component separation, was applied in order to quantify the three components in our population. The consolidated component was found to have the smallest volume (126 ± 111 cc) and the intermediate and aerated components showed a volume of 914 ± 291 cc and 793 ± 499 cc, respectively. A number of parameters were also extracted:

1. Ratio between the consolidated component and the aerated component (0.16 ± 0.89);
2. Ratio between the intermediate component and the aerated component (1.09 ± 2.56);
3. HU value corresponding to the peak of the curve for the aerated regions (−853 ± 56 HU);
4. Width in HU of the intermediate region (754 ± 88 HU).

Some considerations may be made when comparing the findings of the current work with other reported results. Colombi et al. [18], for instance, reported a median value of 2900 cc for the aerated component of both lungs in a large population of patients hospitalized in a center in a neighboring city in the same period as our study; this value was significantly higher than ours (considering paired lungs, by about 1600 cc). This difference could be explained by the different segmentation methods used; in fact, Colombi et al. used fixed threshold values of −950 to −700 HU, while we adopted individual thresholds optimized for the distinction between the aerated component and the intermediate component, with a far lower th1 value compared to those found by our individually assessed method. Leonardi et al. [16] reported that the percentage of the lung involved in the disease varied from 6%, for non-critically ill patients, to 38%, for critically ill patients. Their definition of the lung component involved in the disease, manually segmented, seemed to include parts of what we identified as an intermediate component, and this could explain the higher mean values relative to our consolidation estimates (by about 6.4%). Matos et al. [17] reported a median volume of disease of 295 cc on the two lungs, quite consistent with our results. Their method of segmentation of the consolidated component was semi-automatic; the radiologist identified areas of the disease and a region-growing algorithm was then applied, likely resulting in the identification of individual thresholds based on maximum contrast with the tissue surrounding the consolidated component. Liu et al. [15], by applying thresholds to CT values, extracted three quantitative features corresponding to the percentage of GGO volume, semi-consolidation volume and consolidation volume. The percentages of GGO and semi-consolidation volumes were part of what we defined as intermediate component, and were therefore not directly comparable. The consolidation volume percentage obtained in this study was 5.8%, comparable to our estimate (6.4%). Lyu et al. [28] found a volume percentage for the aerated component, using fixed threshold values of −950 to −800 HU, of 43% of the entire segmented lung. This value was in line with that found with our segmentation method, as could be expected, as their fixed threshold value was similar to the median value of our population.

More generally, concerning the choice of threshold to define the aerated component, our findings suggest that for COVID-19 patients the quantity of air inflated during a deep inspiration before the CT scan is highly variable among patients, reflecting the variable residual functionality of the aerated lung. Thus, the individual choice of a "best threshold " seems to be a more reasonable option, able to adapt the "aerated lung" definition to each individual patient/lung. In addition, the relatively large variability of the peak position of the aerated component is also a clear measurement of the change of lung perfusion compared to healthy patients, typically presenting their peak at much lower values.

In conclusion, this work allowed the development of a semi-automatic, operator independent segmentation method identifying the main lung components of COVID-19 patients with respiratory syndrome. Our approach intrinsically gives clear functional meaning to the different sub-volumes identified and overcame the approximation due to the choice of fixed thresholds, taking individual lung functionality carefully into account; this is especially true for th1. Very importantly, due to its simplicity and to the clear, reproducible and interpretable features that can be extracted, the suggested approach can easily be transferred from our institute.

Work is currently underway to make the segmentation method fully automatic; as a matter of fact, manual segmentation is cumbersome and this is a limit of our current approach. An atlas, based on CT images of COVID-19 patients, has been developed to automate the initial identification of the lungs, and is currently being validated. Combining this atlas with the method suggested here should allow an automatic sub-segmentation of the lung components to be obtained in no more than a few minutes. In addition, the quantitative analysis carried out on the HU histograms is being applied to develop predictive models of early clinical outcome. On the other hand, atlas-based approaches for automatic segmentation of the whole lungs do not represent the only way to solve the issue; further research regarding AI/deep learning approaches may be warranted.

Author Contributions: Conceptualization, A.M., C.F. and A.d.V.; Data curation, A.M., A.L., M.M. and D.P.; Formal analysis, A.M., A.L., M.M. and P.G.E.; Investigation, C.F. and A.d.V.; Methodology, A.M., C.F., A.L. and M.M.; Software, A.M. and P.G.E.; Supervision, C.F., F.d.C. and A.d.V.; Writing—original draft, A.M.; Writing—review & editing, C.F., A.L., M.M., P.G.E., D.P., F.d.C. and A.d.V. All authors have read and agreed to the published version of the manuscript. All authors have read and agreed to the published version of the manuscript.

Funding: M. Mori is funded by an AIRC grant (IG 23015).

Institutional Review Board Statement: This study was conducted within the COVID-19 Institutional study (COVID-BioB, Clinical trials govNCT04318366), San Raffaele Scientific Institute, Milano, Italy.

Informed Consent Statement: Informed consent was obtained from all subjects involved in the study.

Data Availability Statement: Due to the study property design, data are not publicly available.

Acknowledgments: The authors thank Davide Raspanti (TEMA Sinergie) for his valued support in the development and implementation of MIM workflows.

Conflicts of Interest: The authors declare no conflict of interest.

References

1. Coronavirus Disease (COVID-19) n.d. Available online: https://www.who.int/emergencies/diseases/novel-coronavirus-2019 (accessed on 9 November 2020).
2. Agricola, E.; Beneduce, A.; Esposito, A.; Ingallina, G.; Palumbo, D.; Palmisano, A.; Ancona, F.; Baldetti, L.; Pagnesi, M.; Melisurgo, G.; et al. Heart and Lung Multimodality Imaging in COVID-19. *JACC: Cardiovasc. Imaging* **2020**, *13*, 1792–1808. [CrossRef]
3. Wen, Z.; Chi, Y.; Zhang, L.; Liu, H.; Du, K.; Li, Z.; Chen, J.; Cheng, L.; Wang, D. Coronavirus Disease 2019: Initial Detection on Chest CT in a Retrospective Multicenter Study of 103 Chinese Patients. *Radiol. Cardiothorac. Imaging* **2020**, *2*, e200092. [CrossRef]
4. Ai, T.; Yang, Z.; Hou, H.; Zhan, C.; Chen, C.; Lv, W.; Tao, Q.; Sun, Z.; Xia, L. Correlation of Chest CT and RT-PCR Testing for Coronavirus Disease 2019 (COVID-19) in China: A Report of 1014 Cases. *Radiology* **2020**, *296*, E32–E40. [CrossRef]
5. Bernheim, A.; Mei, X.; Huang, M.; Yang, Y.; Fayad, Z.A.; Zhang, N.; Diao, K.; Lin, B.; Zhu, X.; Li, K.; et al. Chest CT findings in coronavirus disease 2019 (COVID-19): Relationship to duration of infection. *Radiology* **2020**, *295*, 685–691. [CrossRef]
6. Pan, F.; Ye, T.; Sun, P.; Gui, S.; Liang, B.; Li, L.; Zheng, D.; Wang, J.; Hesketh, R.L.; Yang, L.; et al. Time course of lung changes at chest CT during recovery from coronavirus disease 2019 (COVID-19). *Radiology* **2020**, *295*, 715–721. [CrossRef] [PubMed]
7. Shi, H.; Han, X.; Jiang, N.; Cao, Y.; Alwalid, O.; Gu, J.; Fan, Y.; Zheng, C. Radiological findings from 81 patients with COVID-19 pneumonia in Wuhan, China: A descriptive study. *Lancet Infect. Dis.* **2020**, *20*, 425–434. [CrossRef]
8. Zhao, W.; Zhong, Z.; Xie, X.; Yu, Q.; Liu, J. Relation between chest CT findings and clinical conditions of coronavirus disease (COVID-19) pneumonia: A multicenter study. *Am. J. Roentgenol.* **2020**, *214*, 1072–1077. [CrossRef] [PubMed]
9. Song, F.; Shi, N.; Shan, F.; Zhang, Z.; Shen, J.; Lu, H.; Ling, Y.; Jiang, Y.; Shi, Y. Emerging 2019 novel coronavirus (2019-NCoV) pneumonia. *Radiology* **2020**, *295*, 210–217. [CrossRef]
10. Hansell, D.M.; Bankier, A.A.; MacMahon, H.; McLoud, T.C.; Müller, N.L.; Remy, J. Fleischner Society: Glossary of terms for thoracic imaging. *Radiology* **2008**, *246*, 697–722. [CrossRef]
11. Hamer, O.W.; Salzberger, B.; Gebauer, J.; Stroszczynski, C.; Pfeifer, M. CT morphology of COVID-19: Case report and review of literature. *RöFo* **2020**, *192*, 386–392. [CrossRef]
12. Li, K.; Wu, J.; Wu, F.; Guo, D.; Chen, L.; Fang, Z.; Li, C. The Clinical and Chest CT Features Associated with Severe and Critical COVID-19 Pneumonia. *Investig. Radiol.* **2020**, *55*, 327–331. [CrossRef] [PubMed]
13. Han, R.; Huang, L.; Jiang, H.; Dong, J.; Peng, H.; Zhang, D. Early Clinical and CT Manifestations of Coronavirus Disease 2019 (COVID-19) Pneumonia. *Am. J. Roentgenol.* **2020**, *215*, 338–343. [CrossRef] [PubMed]
14. Simpson, S.; Kay, F.U.; Abbara, S.; Bhalla, S.; Chung, J.H.; Chung, M.; Henry, T.S.; Kanne, J.P.; Kligerman, S.; Ko, J.P.; et al. Radiological Society of North America Expert Consensus Statement on Reporting Chest CT Findings Related to COVID-Endorsed by the Society of Thoracic Radiology, the American College of Radiology, and RSNA—Secondary Publication. *J. Thorac. Imaging* **2020**, *35*, 219–227. [CrossRef] [PubMed]
15. Liu, F.; Zhang, Q.; Huang, C.; Shi, C.; Wang, L.; Shi, N.; Fang, C.; Shan, F.; Mei, X.; Shi, J.; et al. CT quantification of pneumonia lesions in early days predicts progression to severe illness in a cohort of COVID-19 patients. *Theranostics* **2020**, *10*, 5613–5622. [CrossRef] [PubMed]
16. Leonardi, A.; Scipione, R.; Alfieri, G.; Petrillo, R.; Dolciami, M.; Ciccarelli, F.; Perotti, S.; Cartocci, G.; Scala, A.; Imperiale, C.; et al. Role of computed tomography in predicting critical disease in patients with covid-19 pneumonia: A retrospective study using a semiautomatic quantitative method. *Eur. J. Radiol.* **2020**, *130*, 109202. [CrossRef] [PubMed]
17. Matos, J.; Paparo, F.; Mussetto, I.; Bacigalupo, L.; Veneziano, A.; Bernardi, S.P.; Biscaldi, E.; Melani, E.; Antonucci, G.; Cremonesi, P.; et al. Evaluation of novel coronavirus disease (COVID-19) using quantitative lung CT and clinical data: Prediction of short-term outcome. *Eur. Radiol. Exp.* **2020**, *4*, 1–10. [CrossRef]

18. Colombi, D.; Bodini, F.C.; Petrini, M.; Maffi, G.; Morelli, N.; Milanese, G.; Silva, M.; Sverzellati, N.; Michieletti, E. Well-aerated Lung on Admitting Chest CT to Predict Adverse Outcome in COVID-19 Pneumonia. *Radiology* **2020**, *296*, E86–E96. [CrossRef]
19. Sperrin, M.; Grant, S.W.; Peek, N. Prediction models for diagnosis and prognosis in Covid-19. *BMJ* **2020**, *369*, m1464. [CrossRef]
20. Wynants, L.; Van Calster, B.; Collins, G.S.; Riley, R.D.; Heinze, G.; Schuit, E.; Bonten, M.J.M.; Dahly, D.L.; Damen, J.A.A.G.; Debray, T.P.; et al. Prediction models for diagnosis and prognosis of covid-19: Systematic review and critical appraisal. *BMJ* **2020**, *369*, m1328. [CrossRef]
21. Zheng, Y.; Xiao, A.; Yu, X.; Zhao, Y.; Lu, Y.; Li, X.; Mei, N.; She, D.; Wang, D.; Geng, D.; et al. Development and validation of a prognostic nomogram based on clinical and CT features for adverse outcome prediction in patients with COVID-19. *Korean J. Radiol.* **2020**, *21*, 1007–1017. [CrossRef]
22. Li, Y.; Yang, Z.; Ai, T.; Wu, S.; Xia, L. Association of "initial CT" findings with mortality in older patients with coronavirus disease 2019 (COVID-19). *Eur. Radiol.* **2020**, *30*, 6186–6193. [CrossRef] [PubMed]
23. Li, L.; Qin, L.; Xu, Z.; Yin, Y.; Wang, X.; Kong, B.; Bai, J.; Lu, Y.; Fang, Z.; Song, Q.; et al. Using Artificial Intelligence to Detect COVID-19 and Community-acquired Pneumonia Based on Pulmonary CT: Evaluation of the Diagnostic Accuracy. *Radiology* **2020**, *296*, E65–E71. [CrossRef] [PubMed]
24. Fang, M.; He, B.; Li, L.; Dong, D.; Yang, X.; Li, C.; Meng, L.; Zhong, L.; Li, H.; Li, H.; et al. CT radiomics can help screen the Coronavirus disease 2019 (COVID-19): A preliminary study. *Sci. China Inf. Sci.* **2020**, *63*, 1–8. [CrossRef]
25. Harmon, S.A.; Sanford, T.H.; Xu, S.; Turkbey, E.B.; Roth, H.; Xu, Z.; Yang, D.; Myronenko, A.; Anderson, V.; Amalou, A.; et al. Artificial intelligence for the detection of COVID-19 pneumonia on chest CT using multinational datasets. *Nat. Commun.* **2020**, *11*, 1–7. [CrossRef] [PubMed]
26. Long, J.B.; Ehrenfeld, J.M. The Role of Augmented Intelligence (AI) in Detecting and Preventing the Spread of Novel Coronavirus. *J. Med Syst.* **2020**, *44*, 1–2. [CrossRef] [PubMed]
27. Lessmann, N.; Sánchez, C.I.; Beenen, L.; Boulogne, L.H.; Brink, M.; Calli, E.; Charbonnier, J.-P.; Dofferhoff, T.; Van Everdingen, W.M.; Gerke, P.K.; et al. Automated Assessment of COVID-19 Reporting and Data System and Chest CT Severity Scores in Patients Suspected of Having COVID-19 Using Artificial Intelligence. *Radiology* **2021**, *298*, E18–E28. [CrossRef] [PubMed]
28. Lyu, P.; Liu, X.; Zhang, R.; Shi, L.; Gao, J. The performance of chest CT in evaluating the clinical severity of COVID-19 pneumonia. *Investig. Radiol.* **2020**, *55*, 412–421. [CrossRef]
29. Kramme, R.; Hoffmann, K.-P.; Pozos, R. *Springer Handbook of Medical Technology*; Springer: Berlin/Heidelberg, Germany, 2011.
30. *MIM Maestro®, 6.9*; MIM Software Inc: Cleveland, OH, USA, 2019.

applied sciences

MDPI

Article

Classification Performance for COVID Patient Prognosis from Automatic AI Segmentation—A Single-Center Study

Riccardo Biondi [1,†], Nico Curti [1,†], Francesca Coppola [2,3,*], Enrico Giampieri [1,*], Giulio Vara [2], Michele Bartoletti [4], Arrigo Cattabriga [2], Maria Adriana Cocozza [2], Federica Ciccarese [2], Caterina De Benedittis [2], Laura Cercenelli [1], Barbara Bortolani [1], Emanuela Marcelli [1], Luisa Pierotti [5], Lidia Strigari [5], Pierluigi Viale [4], Rita Golfieri [2] and Gastone Castellani [6]

[1] eDIMESLab, Department of Experimental, Diagnostic and Specialty Medicine, University of Bologna, 40138 Bologna, Italy; riccardo.biondi7@unibo.it (R.B.); nico.curti2@unibo.it (N.C.); laura.cercenelli@unibo.it (L.C.); barbara.bortolani@unibo.it (B.B.); emanuela.marcelli@unibo.it (E.M.)
[2] Department of Radiology, IRCCS Azienda Ospedaliero-Universitaria di Bologna, Via Albertoni 15, 40138 Bologna, Italy; giulio.vara@studio.unibo.it (G.V.); arrigo.cattabriga@studio.unibo.it (A.C.); mariaadriana.cocozza@studio.unibo.it (M.A.C.); federica.ciccarese@aosp.bo.it (F.C.); caterina.de@unibo.it (C.D.B.); rita.golfieri@unibo.it (R.G.)
[3] SIRM Foundation, Italian Society of Medical and Interventional Radiology, Via della Signora 2, 20122 Milan, Italy
[4] Infectious Diseases Unit, IRCCS Sant' Orsola-Malpighi Teaching Hospital, 40138 Bologna, Italy; m.bartoletti@unibo.it (M.B.); pierluigi.viale@unibo.it (P.V.)
[5] Department of Medical Physics, IRCCS Azienda Ospedaliero-Universitaria di Bologna, Via Massarenti 9, S. Orsola-Malpighi Hospital, 40138 Bologna, Italy; luisa.pierotti@aosp.bo.it (L.P.); lidia.strigari@aosp.bo.it (L.S.)
[6] Department of Experimental, Diagnostic and Specialty Medicine, University of Bologna, 40138 Bologna, Italy; gastone.castellani@unibo.it
* Correspondence: francesca.coppola@aosp.bo.it (F.C.); enrico.giampieri@unibo.it (E.G.)
† These authors contributed equally to this work.

Citation: Biondi, R.; Curti, N.; Coppola, F.; Giampieri, E.; Vara, G.; Bartoletti, M.; Cattabriga, A.; Cocozza, M.A.; Ciccarese, F.; De Benedittis, C.; et al. Classification Performance for COVID Patient Prognosis from Automatic AI Segmentation—A Single-Center Study. *Appl. Sci.* **2021**, *11*, 5438. https://doi.org/10.3390/app11125438

Academic Editors: Salvatore Gallo and Ivan Veronese

Received: 28 April 2021
Accepted: 4 June 2021
Published: 11 June 2021

Abstract: Background: COVID assessment can be performed using the recently developed individual risk score (prediction of severe respiratory failure in hospitalized patients with SARS-COV2 infection, PREDI-CO score) based on High Resolution Computed Tomography. In this study, we evaluated the possibility of automatizing this estimation using semi-supervised AI-based Radiomics, leveraging the possibility of performing non-supervised segmentation of ground-glass areas. Methods: We collected 92 from patients treated in the IRCCS Sant'Orsola-Malpighi Policlinic and public databases; each lung was segmented using a pre-trained AI method; ground-glass opacity was identified using a novel, non-supervised approach; radiomic measurements were collected and used to predict clinically relevant scores, with particular focus on mortality and the PREDI-CO score. We compared the prediction obtained through different machine learning approaches. Results: All the methods obtained a well-balanced accuracy (70%) on the PREDI-CO score but did not obtain satisfying results on other clinical characteristics due to unbalance between the classes. Conclusions: Semi-supervised segmentation, implemented using a combination of non-supervised segmentation and feature extraction, seems to be a viable approach for patient stratification and could be leveraged to train more complex models. This would be useful in a high-demand situation similar to the current pandemic to support gold-standard segmentation for AI training.

Keywords: radiomics; artificial intelligence; machine and deep learning; medical imaging

1. Introduction

Since the beginning of last year, the world has been facing a health emergency, the pandemic caused by the novel Coronavirus, Sars-CoV2. Even up to the present date, many aspects of the physiopathology of the COVID-19 infection are yet to be fully understood. The diagnostic gold standards for Sars-CoV2 are the reverse transcription-polymerase chain

reaction (rt-PCR) and the gene sequencing of sputum, throat swab and lower respiratory tract secretion [1,2]. These tests have several limitations: a limited testing capacity related to insufficient kits or laboratory supplies; a long reporting time, varying from 6 to 48 h; a great variability in sensitivity, ranging from 37% to 71%. To circumvent these limitations, imaging has emerged as an important tool to guide diagnosis, especially in cases of clinical-laboratory discordances.

Imaging protocols directive from public health authorities are heterogeneous: chest radiography is widely used, although it is not accurate in mild or early COVID-19 infection; there is an improving interest in bedside lung ultrasound, but limited experiences are reported in the literature [3]. Among imaging modalities, Computed Tomography (CT) is the most sensitive (60–98%) acquisition technique, but it has low specificity in the early stage of the disease [4]. For this reason, World Health Organization (WHO) and most radiologic societies do not recommend performing screening CT (WHO characterizes COVID-19 as a pandemic—11 March 2020). High-Resolution Computed Tomography (HRCT) proved nonetheless to be a valuable aid to the clinical and epidemiological management of affected patients, especially during shortages of the necessary reagents, long reporting time, and the high operator-dependency [5–7].

There have been controversial publications about the role of chest CT imaging analysis in the diagnosis and management of COVID-19 [8]. The identification of healthy lung chest CTs from pneumonia cases has been deeply investigated in literature [9,10], but the COVID-19 pandemic has posed the non-trivial problem of classifying different pulmonary diseases. Patchy shadows or ground-glass opacities (GGOs) and consolidations (CSs) are not exclusive of COVID-19 but might be also caused by pulmonary edema, bacterial infection, other viral infection, or alveolar hemorrhage [11].

An initial prospective made by Huang et al. [12] on chest CT scans of patients affected by COVID-19 has shown that the examined subjects have a bilateral GGO and CS. The same medical results were also confirmed by other authors [13,14], who posed the basis for the next quantification studies allowing a better characterization of the COVID-19 features. The classification between early-stage patients and progressive phases has been thoroughly investigated [15–18], and all of them lead to the same conclusion: the main COVID-19 features can be difficult to detect in early stages of the disease, and their correct identification is strongly dependent on the radiologist's expertise.

The role of HRCT in COVID-19 infection management is also controversial due to the radiation exposure problem. Initially, the American College of Radiology (ACR) and the Italian Society of Medical and Interventional radiology (SIRM) guidelines did not recommend HRCT in the diagnostic workup, the former referring to 2018 guidelines for acute respiratory illnesses [19–21]. With the increase of available evidence resulting from clinical trials, a prognostic role of HRCT is now emerging, increasing its value beyond the diagnosis [3,22]. Moreover, a study from Ria et al. evaluated the risk-benefit ratio of radiation exposure in COVID-19 patients, stating that HRCT is justified in patients older than 30 years [23].

The application of automated methods to support the clinicians in the analysis of a large amount of data aims to remove the subjectivity of the measurement and improve the time required for the diagnosis formulation [21,24,25]. Machine learning and deep learning models applied in the medical research field are becoming more popular as the basis for clinical decision support systems. Medical image segmentation plays a pivotal role in the automation of these applications since a correct segmentation of anatomical structures is a crucial step to improve the accuracy of the algorithms and to minimize possible confounders.

In 2015, Mansoor et al. [26] proposed a classification of classical image processing segmentation algorithms, where they divided them into four classes: (1) thresholding-based methods [27]; (2) region-based methods [28,29]; (3) shape-based methods [30]; (4) neighboring anatomy [31]. Deep learning models are outperforming all these techniques [32,33].

Deep learning applications have achieved the most significant results also in the COVID-19 literature [24,27,34–36], with extremely high classification performances and low execution time. The drawback of these methods is the demand for labeled data: the training of a deep learning model requires a vast amount of manual (or semi-automatic) labelled data. This is problematic because data annotation is a very time-consuming operation, dependent on the operator experience.

To overcome this issue, many authors, such as Wang et al. [34], proposed a different approach, combining deep learning features with standard machine learning one, proving the efficiency of this synergy. This approach could also increase the ability to explain the model, potentially leading to an improvement in the understanding of the main features of the COVID-19 disease. Wang et al. highlighted the irregularity and heterogeneous intensities of the lung lesion textures as COVID-19 significant features. Concurrently, in non-COVID-19 patients, Wang et al. found stronger uniformity of Hounsfield values in the chest CT within the lesions. Both these features can be automatically quantified by a machine learning algorithm, allowing stratification of the patients' severity and removing possible false positives. Other identified useful characteristics concern the geometry and shape of the lesions [8,37].

For a more detailed stratification of patients, the Radiological Society of North America (RSNA) released a consensus statement, endorsed by the Society of Thoracic Radiology and the American College of Radiology (ACR), that classifies the CT appearance of COVID-19 pneumonia into four categories: "typical," "atypical," "undetermined," and "negative" [38]. The "typical" pattern is characterized by the presence of round-shaped Ground-Glass Opacities (GGO), usually bilateral with a sub-pleural location on the dorsal basal segments. The GGO can be associated with "Crazy Paving" areas or other signs of organizing pneumonia. The "undetermined" pattern is characterized by the absence of the "typical" pattern findings, with diffuse GGO areas with a perihilar or unilateral distribution, with or without consolidated areas. The "atypical" pattern is characterized by either the absence of the "typical" or "undetermined" signs and the presence of lobar consolidations, "tree in bud," smooth thickening of the septa and pleural effusion; in this presentation, no GGO are detectable. The "negative" pattern is characterized by the absence of pathological findings. The "typical" and "negative" patterns have proven to be very accurate in identifying the disease in patients with suspected COVID-19 infection [3].

Many authors have already proved an occasional discordance between HRCT and rt-PCR. There have been observations of patients with a high clinical suspect of COVID-19 supported by epidemiological criteria and imaging, but with negative rt-PCR [39,40]. On the other hand, there was evidence of patients with a positive rt-PCR and suggestive clinical findings, that did not present pathological findings on HRCT [41]. The clinico-radiological dissociation in asymptomatic individuals requires reconsidering the role of radiological findings in the clinical management of these patients [42].

To improve the reliability of radiological examination, several authors presented Texture Analysis of the CT scans as a valuable tool to aid the diagnosis [43–45] and to identify clinically severe patients [46]. Texture Analysis can identify putative features that are not part of the RSNA criteria, such as enlargement of pulmonary vessels [47–51], and that could be overlooked during the human visual inspection, such as fine characteristics of the GGO areas [52]. Currently, only a few methods exist to automatically process HRCT scans and quantify the extent of the pulmonary involvement [32,53]. From the clinical point of view, the disease can be assessed with the newly developed PREDI-CO (prediction of severe respiratory failure in hospitalized patients with SARS-COV2 infection), which considers clinical parameters predictive of severe respiratory failure in hospitalized patients, and is defined as the sum of the following conditions:

- age $\geq$ 70 years
- obesity BMI $\geq$ 30 kg/m^2
- fever at hospitalization $\geq$ 38 °C
- respiratory rate $\geq$ 22 breaths/minute

- lymphocyte count $\leq$ 900 cells/mm^3
- creatinine $\geq$ 1 mg/dl
- C-reactive protein $\geq$ 10 mg/dl
- lactate dehydrogenase $\geq$ 350 IU/l.

This score outperforms in the stratification of patients the well-established qSOFA, SOFA, CURB-65, and MEWS scores; this is due to the fact that the PREDI-CO score was designed and validated ad-hoc for this purpose [54].

In the current work, we aim to automatize the evaluation of the PREDI-CO score and several radiomic features using a novel, non-supervised image processing pipeline.

2. Materials and Methods

2.1. Patients Selection

This study involves 92 CT scans of patients affected by COVID-19. 10 of these scans come from the public dataset "COVID-19 CT Lung and Infection Segmentation Dataset" published on Zenodo [55]. Left lung, right lung, and infections are labeled by two radiologists and verified by an expert radiologist (with more than 10 years of experience). These scans were used to validate the segmentation performances of the implemented pipeline.

Department of Diagnostic and Preventive Medicine of the IRCCS Policlinic Sant'Orsola-Malpighi provided the remaining 82 scans. The selected patients are composed for the 66.3% by male, the age distribution (min/median/max) is 35/60/89. For each patient, experts ascertained the presence of ground-glass opacities (100%), consolidation (10%), crazy paving (53%), multifocal GGO (multiple locations affected by GGO, 32%), peripheral GGO (presence of GGO areas exclusively far away from the trachea, 23%), and roundish GGO (GGO characterized by round regular shapes, 12%). Moreover, each patient was assigned the PREDI-CO score value estimated by two radiologists.

In IRCCS Policlinic Sant'Orsola-Malpighi, HRCT exams were performed with the following parameters: two different Multi-Slices CT (64 slices, GE VCT or PHILIPS Ingenuity), with keV range 100–120, tube current modulation with a low Quality Index to optimize patient dose, slice thickness range 1–2 mm; images were reconstructed with high-resolution kernel. The CT parameters used in the Zenodo dataset are not available.

2.2. Pipeline Overview

The workflow developed in this work as show in Figure 1 can be split into 3 steps: (1) the segmentation of the lungs; (2) segmentation of the GGO areas; (3) estimation of the radiomic features.

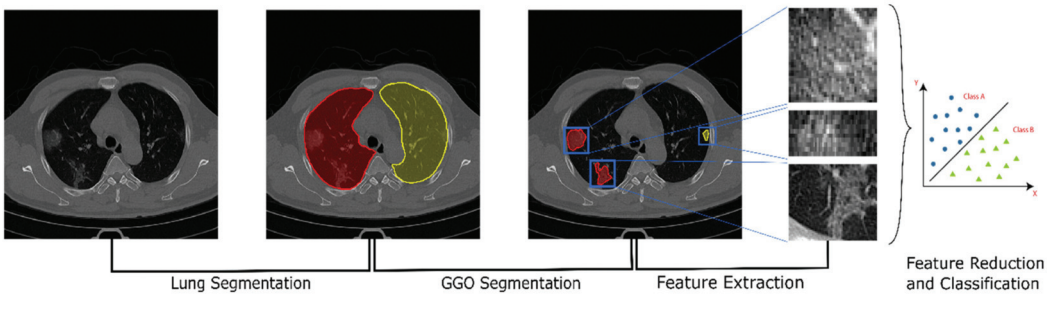

Figure 1. A schematic representation of the proposed pipeline. From the left: raw CT scan; segmentation of the two lungs using a pre-trained U-Net model; segmentation of the GGO areas using k-means clustering; extraction of radiomic and Haralick features; classification and prediction of the clinical characteristics and outcomes.

2.3. Lung Segmentation

Lung segmentation is a pivotal pre-processing step in many image analyses, such as identification and classification of pathologies. Rule-based approach, like thresholding, region growing, etc., usually fails for CT scans of patients with severe Interstitial Lung Disease (ILD) [33]. For this reason, we used a pre-trained publicly available https://github.com/JoHof/lungmaskv0.24 (accessed on 24 March 2021) U-Net model [33] for lung segmentation.

2.4. GGO Segmentation

In the second step, a novel automated pipeline for the segmentation of GGO areas was developed, combining 2 different techniques: vessel artifacts exclusion and k-means clustering. Both these methods are unsupervised learning techniques and have been chosen due to the limited number of available samples. The decision to avoid supervised methods such as Convolutional Neural Networks (CNNs) is based on the likelihood of including strong biases, even including possible data augmentation strategies.

The intensity of pulmonary vessels is very similar to solid components of GGO; therefore, it affects the segmentation, introducing potential false positives [56]. To remove these vessels, we used the vesselness measure, i.e., the presence of multiscale tubular structures. Multiscale Vessel Enhancement Filtering (MVEF) [57] is defined as the likelihood of an image region to contain vessels, and it is estimated using the Frangi filter [58]. The areas with high values of MVEF were identified as vessels and therefore removed from the lung region obtained in the previous step.

After the removal of the vessels, we identified the GGO as areas with a common color texture. To identify these regions, we used k-means clustering, grouping voxels by color and texture similarity, and identifying the tissue corresponding to each cluster [59].

Since GGO involves extended areas, it is informative to include neighborhood voxel information. The color contrast between GGO and healthy areas may change between patients; it is, therefore, useful to consider different gamma corrections of the image. We applied a series of image processing filters to obtain a high-dimensional feature space, including all these features for each individual voxel. For each voxel, we estimated a vector of features obtained by the application of the following filters:

- Gamma corrected image ($\gamma = 1.5$);
- Adaptive Histogram Equalized image, in a radius of 3 voxels;
- Median blurred image with a kernel of radius 3 voxels;
- Standard deviation filtered image with a kernel of radius 1 voxels.

We used the Adaptive Histogram Equalization algorithm for the image standardization: for each slice, the histogram was equalized considering a volume of 3 voxels. The gamma correction is a non-linear operation used to decode the luminance and enhance the low contrast regions. The median blurring allows considering the information about the neighborhood voxels, reducing the effect of outlier voxels. The last feature is the application of a local standard deviation filter; this filter replaces each voxel value with the standard deviation of its neighborhood. This feature is useful as GGO is characterized by highly heterogeneous gray level regions, allowing to filter out bronchial structures and motion artifacts not removed during the lung segmentation.

The k-means clustering is "isotropic" in all directions of space and therefore tends to produce round (rather than elongated) clusters. In this situation, leaving variances unequal is equivalent to put more weight on variables with smaller variance. To avoid this, the features were standardized according to the mean and standard deviation estimated on the training dataset.

We selected 10 scans and applied the k-means clustering for the estimation of the centroids using the Euclidean metric. The k-means clustering is sensitive to the class balance in the training phase (it might give more prominence to more common present structures). Therefore, for the training phase, we considered only a subset of scans with a reasonable amount of GGO areas, excluding in all the cases the (overrepresented) image

background. The k-means cardinality was estimated based on lung anatomy considerations. The resulting clusters were:

- Healthy lung;
- Edges;
- Remaining vessels;
- Noise;
- GGO.

We implemented the whole pipeline using Python, and the source code is publicly available on GitHub (https://github.com/RiccardoBiondi/segmentation, accessed on 24 March 2021). We used SimpleITK [60,61] for the implementation and management of image filters and the OpenCV [62] library for the implementation of the k-means clustering.

We estimated the performances of our segmentation algorithm according to the following scores:

- Sensitivity

$$TPR = \frac{TP}{TP + FN}$$

- Specificity

$$TNR = \frac{TN}{TN + FP}$$

- Precision

$$PPV = \frac{TP}{TP + FP}$$

- F_1 score

$$F_1 = \frac{2TP}{2TP + FP + FN}$$

where *TP, TN, FP*, and *FN* are the True Positives, True Negative, False Positive, and False Negative scores, respectively.

2.5. Feature Extraction

We applied the proposed pipeline on the 82 patients provided by the Department of Diagnostic and Preventive Medicine of the IRCCS Policlinic Sant'Orsola-Malpighi of Bologna. The radiomic features extraction was performed on the identified GGO areas. The extracted features include morphological and texture-based scores:

- Texture;
- Gray Level Distribution;
- GGO Shape;
- Bilaterality (distribution of GGO between left and right lung);
- Peripherality;
- GGO volume

For the scores classification, we included the patient's age as informative features.

We measured the texture properties by computing the Haralick features (Energy, Inertia, Entropy, Inverse Difference Moment, Cluster Shade and Cluster Prominence) from the Gray Level Co-occurrence Matrix (GLCM), computed on the whole identified area [63]. For each identified GGO area, we computed its elongation and roundness [64], obtaining the corresponding distribution for each patient. We computed the distribution of the distances between the lesion and lung centroids, normalized to the semiaxis of the equivalent ellipsoid as a measure of the GGO peripherality. Each distribution was characterized by the minimum, maximum, median, interquartile range (25–75), skewness,

and kurtosis. We estimated the bilaterality distribution using the Matthews coefficient (MCC) defined as follows:

$$MCC = \frac{LGV \cdot LLV - RGV \cdot RLV}{(LGV + RGV)(RLV + LGV)(LLV + RGV)(LLV + RLV)}$$

being RGV = Volume of GGO in the right lung, LGV = Volume of GGO in the left lung, LLV = Left Lung Volume, and RGV = Right Lung Volume. The volume of GGO was normalized according to the total lung volume to overcome possible issues related to anatomical differences between patients.

2.6. Classification

We used the whole set of extracted radiomic features to predict the following GGO characteristics estimated by the expert radiologists:

- Multifocal GGO;
- Presence of Crazy Paving;
- Presence of Consolidation;
- Roundish GGO;
- Peripheral GGO;

Additionally, the two clinical outcomes:

- PREDI-CO score;
- Patient survival.

Not all the above scores were available for all the patients. The GGO characteristics were reported for only 78/82 patients, while the clinical outcomes for only 72 of them. We restricted the score classification on these two subsets of data.

The considered scores are all binary values (True/False), representing the presence/absence of the corresponding characteristic. The only exception is given by the PREDI-CO score, which, by definition, allows an incremental set of values: PREDI-CO score values range from 0 (minimal risk) to 9 (maximal risk). The 47% of patients report a PREDI-CO score of 0 or 1, leading to an overrepresentation of these 2 labels. We grouped multiple labels into the same class to overcome this issue: we applied the cutoff of 1 to dichotomize the PREDI-CO score values into two classes.

We applied a feature selection procedure to filter out redundant and non-informative values for each classification. This step is required to improve the classification performances (remotion of possible confounders) and to make the obtained results more interpretable from a clinical point of view. The selection was performed using a Fisher Exact and a χ^2 tests selecting the 3 features with the highest significance (lower p-values). Both the tests require categorical data, so we dichotomized the features according to their medians.

We used the set of filtered features as input to 4 different classification algorithms to predict the various GGO characteristics and clinical outcomes:

- Logistic Classifier (L1 penalty);
- (Logistic) Ridge Classifier (L2 penalty);
- K-Nearest Neighbors;
- Random Forest Classifier.

The performances of these 4 methods give us an insight into the structure of the data: KNN methods are strongly local, Random Forest relies on the separability of the samples but does not include co-linearities between variables, and linear models (Logistic classifier and Ridge classifier) strongly rely on linear dependencies between the observed values and the predictions.

The classification performances were estimated according to the following metrics:

- Precision
- Sensitivity

- F_1 score
- Balanced accuracy

$$BA = \frac{Sensitity + Specificity}{2}$$

using a leave-one-out cross-validation strategy.

The numerosity of the labels of each characteristic is strongly unbalanced (e.g., only 10% of patients show the presence of consolidations) for every characteristic, except for Crazy Paving and PREDI-CO score (after the dichotomization). To compensate for this, we weighted the classification performances of each algorithm according to the inverse of the class frequency.

We used the scikit-learn [65] Python package for the implementation of all the analyses.

3. Results

3.1. GGO Segmentation

We applied the proposed segmentation pipeline on each patient under analysis. For samples, we collected also a manual segmentation performed by an expert radiologist, which was used as the gold standard.

The collected results were evaluated using the previously introduced metric scores and their distribution analyzed as show in Table 1, details in Table S1.

Table 1. A comparison between the score results for the gold standard segmentation in the included databases. For each score, the average value (and corresponding standard deviation at 1 σ) is reported. For each column the maximum value was indicated with bold font.

Cases	Specificity	Sensitivity	Precision	F_1 Score
CORONACASES OVERALL	0.9992 ± 0.0005	0.62 ± 0.13	$\mathbf{0.79 \pm 0.12}$	$\mathbf{0.67 \pm 0.07}$
GOLD STD OVERALL	$\mathbf{0.9993 \pm 0.0003}$	$\mathbf{0.74 \pm 0.14}$	0.67 ± 0.28	0.65 ± 0.18
OVERALL	0.9992 ± 0.0005	0.66 ± 0.15	0.75 ± 0.20	0.67 ± 0.12

We show in Figure 2 the distribution of the individual scores (Sensitivity, Specificity, Precision, and F_1 score). The scores were obtained by the average of the whole 15 scans (overall) on the 10 corona cases (CORONACASES OVERALL) and on the five gold standard (GOLD STD OVERALL). In Figures 3 and 4, we show a visual comparison between the achieved segmentation and the ground truth labels (both for corona cases and the gold standard).

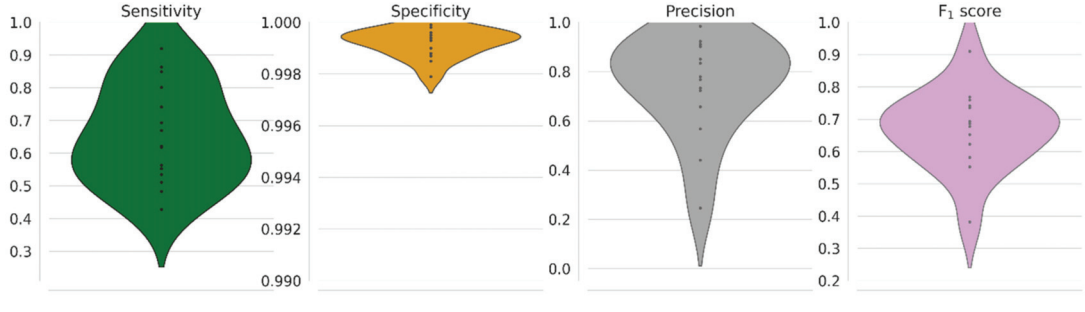

Figure 2. The distribution of segmentation scores obtained by the proposed pipeline. From the left: distribution of Sensitivity, i.e., True Positive rate, Specificity, i.e., True negative rate, Precision, i.e., Positive Predictive Value, and F_1 score, i.e., the harmonic mean of precision and sensitivity.

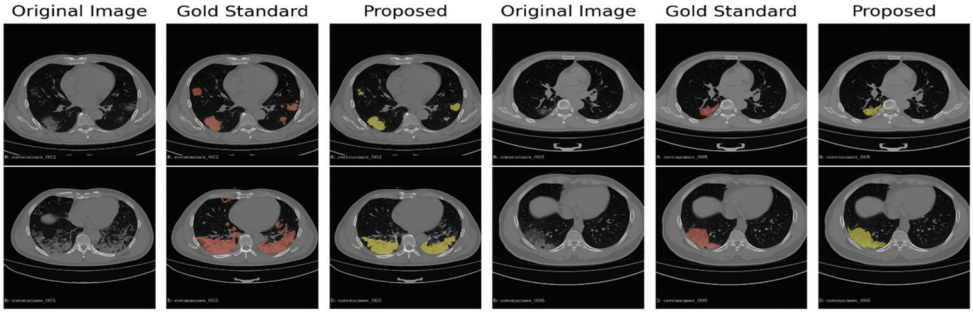

Figure 3. A comparison between the ground truth and the results obtained by the proposed pipeline for the corona cases segmentation. In green are highlighted the GGO areas identified by the experts, and in red, those identified by our segmentation pipeline, respectively.

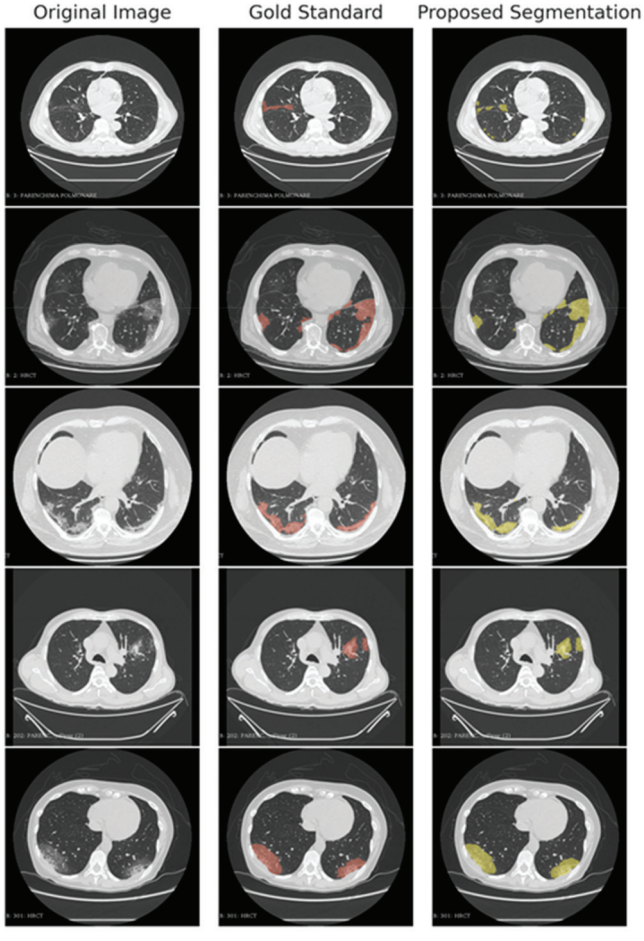

Figure 4. A comparison between the proposed automated segmentation pipeline and a gold standard segmentation manually performed by an expert radiologist.

In Table 2 we report the results of other published pipelines in comparison with our method (details of the employed methods in Table S2). Notice that Jun2020 is a benchmark database for COVID-19 annotation methods and CT scans segmentation (https://gitee.com/junma11/COVID-19-CT-Seg-Benchmark, accessed on 24 March 2020). The evaluation set for both Jun2020 and Muller2020 is COVID-19-CT-Seg, which is the database containing both corona case studies (the one used for annotation) and radiopedia ones (removed because rescaled on 8-bit GL images, which is not compatible with the implemented pipeline). For each technique on each database, only the best results presented in the literature are reported.

Table 2. A comparison between the results of various segmentation techniques applied on the same datasets. For each column the maximum value was indicated with bold font.

Study	Technique	F_1 Score	Sensitivity	Specificity	Precision
Fan2020 [66]	InfNet	0.579	0.870	0.974	0.500
Fan2020 [66]	SemiInfNet	0.597	0.865	0.977	**0.915**
Muller2020 [49]	U-Net	0.761	0.739	**0.999**	-
Jun2020 [52]	3D U-Net	67.3 ± 22.3	-	-	-
Jun2020 [52]	2D U-Net	60.9 ± 24.5	-	-	-
Qingsen2020 [65]	U-Net	**0.726**	**0.751**	-	0.726

3.2. Feature Extraction

We applied the feature extraction step on the GGO areas identified by our segmentation algorithm. In Figure 5 we show the Pearson's correlation matrix between each pair of observed features. The cluster plot highlights the existence of multiple groups of strongly correlated features. The first set of clusters are given by the features related to the roundness, elongation, and distance features. The most prominent cluster is composed of the Haralick features: energy, entropy, inertia, and cluster prominence.

In Figure 6 we show the relation between feature distributions and labels. Using the median of the feature distributions as a threshold, we estimated the percentage of the patients associated with each label who are above this threshold. A result of 0.5 (white-like cells) indicates non-specificity of the variable for that individual label, i.e., a uniform distribution of the feature. A result greater than 0.5 (red-like cells) or smaller than 0.5 (blue-like cells) indicates a high/low percentage of patients for whom the feature values are greater/smaller than the median of the distribution, respectively. This representation allows a visual analysis for the identification and selection of the most informative features related to each label.

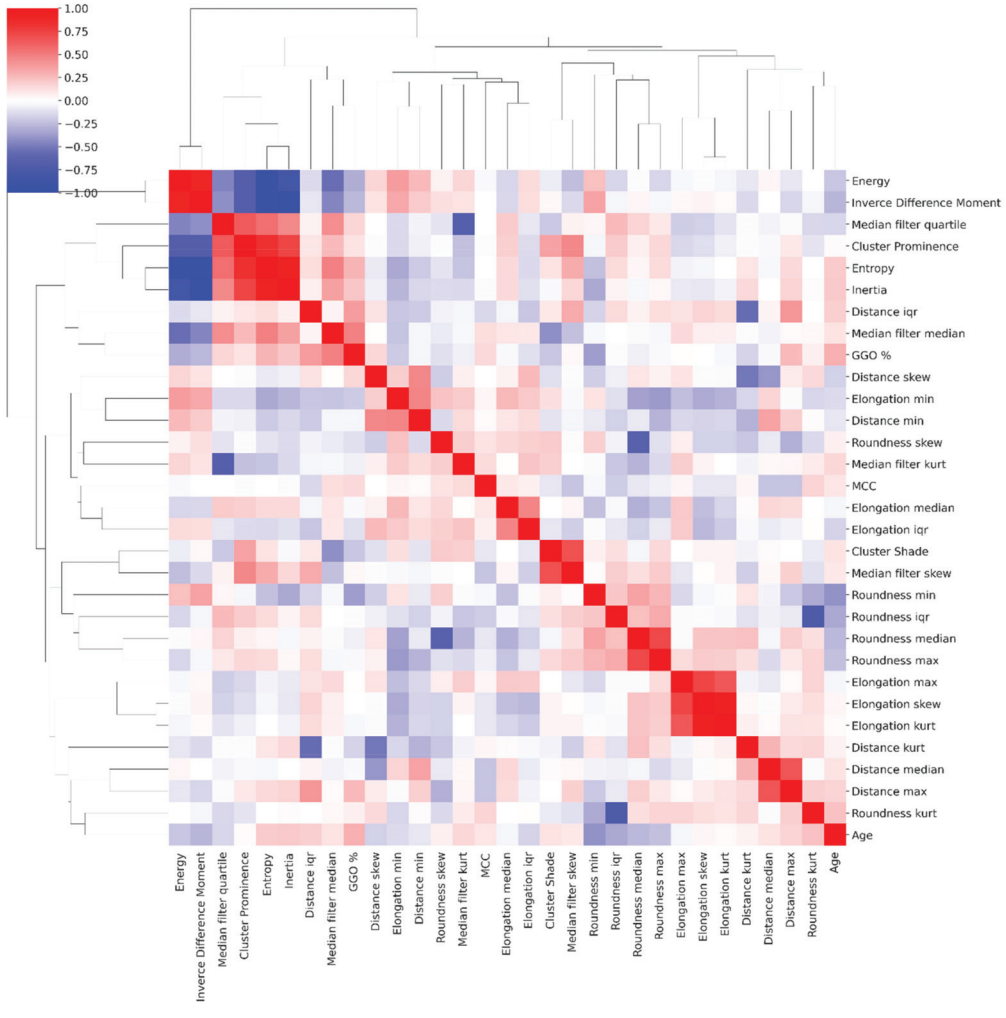

Figure 5. The Correlation Matrix between the estimated features. We report for each pair of features the Pearson's correlation coefficient. In red are highlighted the positive correlations, while in blue the negative ones. White-like colors identify the features with low correlation.

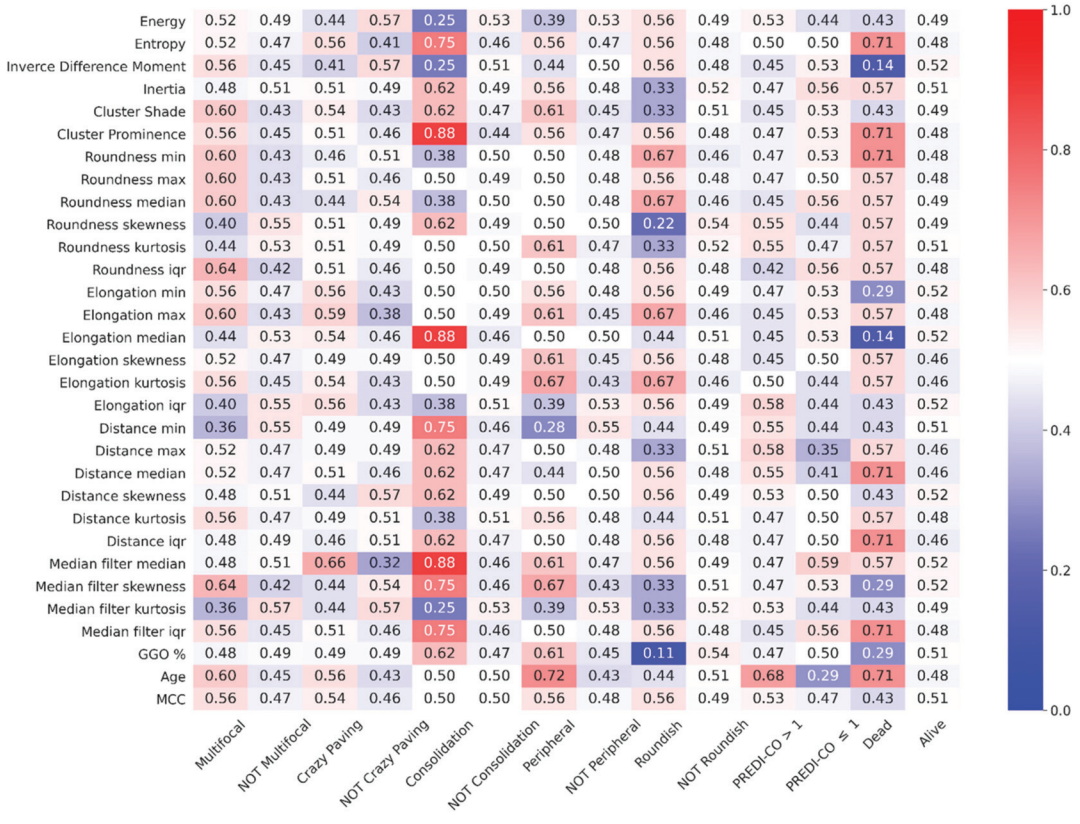

Figure 6. The relationship between individual features and labels. The values range from 0 (all the feature values are lower than the median of the sample distribution) to 1 (all the values are greater than the median of the sample distribution). A value of 0.5 indicates the non-specificity of the variable for the individual label (uniform distribution of the values).

3.3. Individual Features Analysis

For each classification algorithm, we considered the full set of radiomic features extracted and the three best features identified by the feature selection methods (Fisher and χ^2 tests). For each feature selection criteria, we report the list of the three best features ordered according to their informative power.

3.3.1. Multifocal GGO

A Multifocal GGO label equal to 1 (32% of the patients) identifies the patients with the presence of a multifocal lesion, while a label equal to 0 (68% of the patients) identifies its absence.

The three best features selected by the Fisher criterion are (with the type of feature indicated in parenthesis):

- Skewness of the gray level distribution (Radiomics);
- Interquartile (25–75) of the roundness distribution (Radiomics);
- Kurtosis of the gray level distribution (Radiomics).

The three best features selected by the χ^2 criterion are (with type of feature indicated in parenthesis):

- Kurtosis of the gray level distribution (Radiomics);
- Minimum of the distance distribution (Radiomics);
- Skewness of the gray level distribution (Radiomics).

We show in Table 3 the results obtained in terms of global adjusted accuracy and in Table 4 the precision, sensitivity and F_1 score of the same prediction.

Table 3. Global adjusted accuracy of the models to predict multifocal GGO presence using different feature selection strategies. From the left: adjusted accuracy score obtained using only the 3 best features identified by the Fisher Exact test; the 3 best features identified by the $\chi 2$ test; all the radiomic features extracted. For each column the maximum value was indicated with bold font.

	Fisher	χ^2	**All**
Logistic	0.56	0.52	0.42
Ridge	**0.62**	**0.58**	0.45
KNN	0.44	0.44	**0.48**
R. Forest	0.49	0.43	0.47

Table 4. Precision, Sensitivity, and F_1 score for each model and each feature selection strategy to predict multifocal GGO presence. From the left: dichotomized score value, Precision obtained using the 3 best features identified by the Fisher test, Precision obtained using the 3 best features identified by the χ^2 test; Sensitivity obtained using the 3 best features identified by the Fisher test, Sensitivity obtained using the 3 best features identified by the χ^2 test; F_1 score obtained using the 3 best features identified by the Fisher test; F_1 score obtained using the 3 best features identified by the χ^2 test. For each column the maximum value was indicated with bold font.

	Multifocal 1 = Presence 0 = Absence	**Fisher PPV**	χ^2 **PPV**	**Fisher TPR**	χ^2 **TPR**	**Fisher** F_1	χ^2 F_1
Logistic	0	0.72	0.69	0.64	0.64	0.68	0.67
	1	0.39	0.34	0.48	0.40	0.43	0.37
Ridge	0	**0.77**	**0.74**	0.64	0.64	0.70	0.69
	1	0.44	0.41	0.60	0.52	0.51	0.46
KNN	0	0.65	0.65	**0.83**	**0.83**	**0.73**	**0.73**
	1	0.10	0.10	0.04	0.04	0.06	0.06
R. Forest	0	0.67	0.64	0.77	0.77	0.72	0.70
	1	0.29	0.14	0.20	0.08	0.24	0.10

3.3.2. Presence of Crazy Paving

A Crazy Paving label equal to 1 (52% of the patients) identifies the patients with the presence of a crazy-paving pattern, while a label equal to 0 (48% of the patients) identifies its absence.

The three best features selected by the Fisher criterion are (with type of feature indicated in parenthesis):

- Median of the gray level distribution (Radiomics);
- Maximum of the Elongation distribution (Radiomics);
- Entropy (Haralick).

The three best features selected by the χ^2 criterion are (with type of feature indicated in parenthesis):

- Median of the gray level distribution (Radiomics);
- Inverse Difference Moment (Haralick);
- Skewness of the gray level distribution (Radiomics).

We show in Table 5 the results obtained in terms of global adjusted accuracy and in Table 6 the precision, sensitivity and F_1 score of the same prediction.

Table 5. Global adjusted accuracy of the models to predict the presence of crazy paving using different feature selection strategies. From the left: dichotomized score value, Precision obtained using the 3 best features identified by the Fisher test, Precision obtained using the 3 best features identified by the χ^2 test; Sensitivity obtained using the 3 best features identified by the Fisher test, Sensitivity obtained using the 3 best features identified by the χ^2 test; F_1 score obtained using the 3 best features identified by the Fisher test; F_1 score obtained using the 3 best features identified by the χ^2 test. For each column the maximum value was indicated with bold font.

	Fisher	**χ^2**	**All**
Logistic	**0.57**	**0.61**	0.47
Ridge	0.51	0.56	0.45
KNN	0.46	0.50	**0.57**
R. Forest	0.50	0.51	0.51

Table 6. Precision, Sensitivity, and F1 Score for each model and each feature selection strat-egy to predict the presence of crazy paving. From the left: dichotomized score value, Pre-cision obtained using the 3 best features identified by the Fisher test, Precision obtained using the 3 best features identified by the χ2 test; Sensitivity obtained using the 3 best fea-tures identified by the Fisher test, Sensitivity obtained using the 3 best features identified by the χ2 test; F1 score obtained using the 3 best features identified by the Fisher test; F1 score obtained using the 3 best features identified by the χ2 test. For each column the max-imum value was indicated with bold font.

	Crazy Paving 1 = Presence 0 = Absence	**Fisher PPV**	**χ^2 PPV**	**Fisher TPR**	**χ^2 TPR**	**Fisher F_1**	**χ^2 F_1**
Logistic	0	0.56	0.60	0.49	0.57	0.52	0.58
	1	**0.59**	**0.63**	**0.66**	0.66	**0.62**	**0.64**
Ridge	0	0.48	0.55	0.41	0.46	0.44	0.50
	1	0.53	0.57	0.61	0.66	0.57	0.61
KNN	0	0.43	0.47	0.43	0.51	0.43	0.49
	1	0.49	0.43	0.49	0.49	0.49	0.51
R. Forest	0	0.48	0.50	0.35	0.35	0.41	0.41
	1	0.53	0.54	**0.66**	**0.68**	0.59	0.60

3.3.3. Presence of Consolidation

A consolidation label equal to 1 (10% of the patients) identifies the patients with the presence of consolidation, while a label equal to 0 (90% of the patients) identifies its absence.

The three best features selected by the Fisher criterion are (with type of feature indicated in parenthesis):

- Cluster Prominence (Haralick);
- Median of the gray level distribution (Radiomics);
- Median of the elongation distribution (Radiomics).

The three best features selected by the χ^2 criterion are (with type of feature indicated in parenthesis):

- Median of the gray level distribution (Radiomics);
- Median of the elongation distribution (Radiomics);
- Cluster Prominence (Haralick).

We show in Table 7 the results obtained in term of global adjusted accuracy and in Table 8 the precision, sensitivity, and F_1 score of the same prediction.

Table 7. Global adjusted accuracy of the models to predict the presence of consolidations using different feature selection strategies. From the left: dichotomized score value, Precision obtained using the 3 best features identified by the Fisher test, Precision obtained using the 3 best features identified by the χ^2 test; Sensitivity obtained using the 3 best features identified by the Fisher test, Sensitivity obtained using the 3 best features identified by the χ^2 test; F_1 score obtained using the 3 best features identified by the Fisher test; F_1 score obtained using the 3 best features identified by the χ^2 test. For each column the max-imum value was indicated with bold font.

	Fisher	**χ^2**	**All**
Logistic	**0.54**	**0.54**	**0.70**
Ridge	**0.54**	**0.54**	0.69
KNN	0.51	0.51	0.50
R. Forest	0.50	0.50	0.49

Table 8. Precision, Sensitivity, and F_1 Score for each model and each feature selection strategy to predict the presence of consolidations. From the left: dichotomized score value, Precision obtained using the 3 best features identified by the Fisher test, Precision obtained using the 3 best features identified by the χ^2 test; Sensitivity obtained using the 3 best features identified by the Fisher test, Sensitivity obtained using the 3 best features identified by the χ^2 test; F_1 score obtained using the 3 best features identified by the Fisher test; F_1 score obtained using the 3 best features identified by the χ^2 test. For each column the max-imum value was indicated with bold font.

	Consolidation 1 = Presence 0 = Absence	**Fisher PPV**	**χ^2 PPV**	**Fisher TPR**	**χ^2 TPR**	**Fisher F_1**	**χ^2 F_1**
Logistic	0	**0.91**	**0.91**	0.59	0.59	0.71	0.71
	1	0.12	0.12	0.50	0.50	0.20	0.20
Ridge	0	**0.91**	**0.91**	0.59	0.59	0.71	0.71
	1	0.12	0.12	0.50	0.50	0.20	0.20
KNN	0	0.90	0.90	**0.90**	0.90	0.90	0.90
	1	0.12	0.12	0.12	0.12	0.12	0.12
R. Forest	0	0.90	0.90	**0.90**	**1.00**	**0.95**	**0.95**
	1	0.00	0.00	0.00	0.00	0.00	0.00

3.3.4. Roundish GGO

A roundish GGO label equal to 1 (12% of the patients) identifies the patients with the presence of a roundish GGO lesion, while a label equal to 0 (88% of the patients) identifies its absence.

The three best features selected by the Fisher criterion are (with type of feature indicated in parenthesis):

- GGO volume percentage (Radiomics);
- Skewness of the roundness distribution (Radiomics);
- Median of the roundness distribution (Radiomics).

The three best features selected by the χ^2 criterion are (with type of feature indicated in parenthesis):

- GGO volume percentage (Radiomics);
- Skewness of the roundness distribution (Radiomics);
- Median of the roundness distribution (Radiomics).

We show in Table 9 the results obtained in term of global adjusted accuracy and in Table 10 the precision, sensitivity and F_1 score of the same prediction.

Table 9. Global adjusted accuracy of the models to predict the presence of roundish GGO using different feature selection strategies. From the left: dichotomized score value, Precision obtained using the 3 best features identified by the Fisher test, Precision obtained using the 3 best features identified by the χ^2 test; Sensitivity obtained using the 3 best features identified by the Fisher test, Sensitivity obtained using the 3 best features identified by the χ^2 test; F_1 score obtained using the 3 best features identified by the Fisher test; F_1 score obtained using the 3 best features identified by the χ^2 test. For each column the max-imum value was indicated with bold font.

	Fisher	**χ^2**	**All**
Logistic	**0.60**	**0.60**	**0.59**
Ridge	0.58	**0.60**	0.56
KNN	0.43	0.43	0.50
R. Forest	0.45	0.45	0.50

Table 10. Precision, Sensitivity, and F_1 Score for each model and each feature selection strategy to predict the presence of roundish GGO lesions. From the left: dichotomized score value, Precision obtained using the 3 best features identified by the Fisher test, Precision obtained using the 3 best features identified by the χ^2 test; Sensitivity obtained using the 3 best features identified by the Fisher test, Sensitivity obtained using the 3 best features identified by the χ^2 test; F_1 score obtained using the 3 best features identified by the Fisher test; F_1 score obtained using the 3 best features identified by the χ^2 test. For each column the max-imum value was indicated with bold font.

	Roundish 1 = Presence 0 = Absence	**Fisher PPV**	**χ^2 PPV**	**Fisher TPR**	**χ^2 TPR**	**Fisher F_1**	**χ^2 F_1**
Logistic	0	**0.92**	**0.92**	0.64	0.64	0.75	0.75
	1	0.17	0.17	0.56	0.56	0.26	0.26
Ridge	0	0.91	**0.92**	0.61	0.64	0.73	0.75
	1	0.16	0.17	0.56	0.56	0.24	0.26
KNN	0	0.87	0.87	**0.86**	**0.87**	0.86	0.87
	1	0.00	0.00	0.00	0.00	0.00	0.00
R. Forest	0	0.87	0.87	0.90	0.90	**0.94**	**0.89**
	1	0.00	0.00	0.00	0.00	0.00	0.00

3.3.5. Peripheral GGO

A peripheral GGO label equal to 1 (23% of the patients) identifies the patients with the presence of a peripheral GGO lesion, while a label equal to 0 (77% of the patients) identifies its absence.

The three best features selected by the Fisher criterion are (with the type of feature indicated in parenthesis):

- Patient age (Clinical);
- Minimum of the distance distribution (Radiomics);
- Skewness of the gray level distribution (Radiomics).

The three best features selected by the χ^2 criterion are (with type of feature indicated in parenthesis):

- Minimum of the distance distribution (Radiomics);
- Patient age (Clinical);
- Skewness of the elongation distribution (Radiomics).

We show in Table 11 the results obtained in terms of global adjusted accuracy and in Table 12 the precision, sensitivity, and F_1 score of the same prediction.

Table 11. Global adjusted accuracy of the models to predict the presence of peripheral GGO using different feature selection strategies. From the left: dichotomized score value, Precision obtained using the 3 best features identified by the Fisher test, Precision obtained using the 3 best features identified by the χ^2 test; Sensitivity obtained using the 3 best features identified by the Fisher test, Sensitivity obtained using the 3 best features identified by the χ^2 test; F_1 score obtained using the 3 best features identified by the Fisher test; F_1 score obtained using the 3 best features identified by the χ^2 test. For each column the max-imum value was indicated with bold font.

	Fisher	**χ^2**	**All**
Logistic	0.47	0.47	**0.62**
Ridge	**0.52**	**0.52**	0.61
KNN	**0.52**	**0.52**	0.51
R. Forest	0.42	0.42	0.53

Table 12. Precision, Sensitivity, and F_1 Score for each model and each feature selection strategy to predict the presence of peripheral GGO lesions. From the left: dichotomized score value, Precision obtained using the 3 best features identified by the Fisher test, Precision obtained using the 3 best features identified by the χ^2 test; Sensitivity obtained using the 3 best features identified by the Fisher test, Sensitivity obtained using the 3 best features identified by the χ^2 test; F_1 score obtained using the 3 best features identified by the Fisher test; F_1 score obtained using the 3 best features identified by the χ^2 test. For each column the max-imum value was indicated with bold font.

	Peripheral 1 = Presence 0 = Absence	**Fisher PPV**	**χ^2 PPV**	**Fisher TPR**	**χ^2 TPR**	**Fisher F_1**	**χ^2 F_1**
Logistic	0	0.74	0.74	0.43	0.43	0.55	0.55
	1	0.21	0.21	0.50	0.50	0.30	0.30
Ridge	0	**0.79**	**0.79**	0.43	0.43	0.56	0.56
	1	0.24	0.24	0.61	0.61	0.35	0.35
KNN	0	0.78	0.78	**0.87**	**0.87**	**0.82**	**0.82**
	1	0.27	0.27	0.17	0.17	0.21	0.21
R. Forest	0	0.74	0.74	0.83	0.83	0.78	0.78
	1	0.00	0.00	0.00	0.00	0.00	0.00

3.4. Primary Outcomes

3.4.1. PREDI-CO Score

The prediction of the PREDI-CO score was performed considering the dichotomized values obtained by thresholding the labels according to the cutoff of 1: values $\leq$1 (47% of the patients) were labelled as 0 and values > 1 (53% of the patients) were labelled as 1. The considered dataset includes only two patients with a PREDI-CO score $\geq$6 proving the strong unbalancing of the classes and highlighting the prominence of non-severe patients.

The three best features selected by the Fisher criterion are (with type of feature indicated in parenthesis):

- Patient age (Clinical);
- Median of the distance distribution (Radiomics);
- Interquartile (25–75) of the roundness distribution (Radiomics).

The three best features selected by the χ^2 criterion are (with type of feature indicated in parenthesis):

- Patient age (Clinical);
- Interquartile (25–75) of the elongation distribution (Radiomics);
- Maximum of the distance distribution (Radiomics).

We show in Table 13 the results obtained in terms of global adjusted accuracy and in Table 14 the precision, sensitivity and F_1 score of the same prediction.

Table 13. Global adjusted accuracy of the models to predict the dichotomized PREDI-CO score using different feature selection strategies. From the left: dichotomized score value, Precision obtained using the 3 best features identified by the Fisher test, Precision obtained using the 3 best features identified by the χ^2 test; Sensitivity obtained using the 3 best features identified by the Fisher test, Sensitivity obtained using the 3 best features identified by the χ^2 test; F_1 score obtained using the 3 best features identified by the Fisher test; F_1 score obtained using the 3 best features identified by the χ^2 test. For each column the max-imum value was indicated with bold font.

	Fisher	**χ^2**	**All**
Logistic	**0.70**	**0.70**	**0.59**
Ridge	**0.70**	**0.70**	0.52
KNN	0.62	0.60	0.50
R. Forest	0.61	0.61	**0.59**

Table 14. Precision, Sensitivity, and F_1 Score for each model and each feature selection strategy to predict the dichotomized PREDI-CO score. From the left: dichotomized score value, Precision obtained using the 3 best features identified by the Fisher test, Precision obtained using the 3 best features identified by the χ^2 test; Sensitivity obtained using the 3 best features identified by the Fisher test, Sensitivity obtained using the 3 best features identified by the χ^2 test; F_1 score obtained using the 3 best features identified by the Fisher test; F_1 score obtained using the 3 best features identified by the χ^2 test. For each column the max-imum value was indicated with bold font.

	PREDI-CO 1 = PREDI-CO > 1 0 = PREDI-CO $\leq$ 1	**Fisher PPV**	**χ^2 PPV**	**Fisher TPR**	**χ^2 TPR**	**Fisher F_1**	**χ^2 F_1**
Logistic	0	0.67	0.67	0.71	0.71	0.69	0.69
	1	0.72	**0.72**	0.68	0.68	**0.70**	**0.70**
Ridge	0	0.67	0.67	0.71	0.71	0.69	0.69
	1	0.72	**0.72**	0.68	0.68	**0.70**	**0.70**
KNN	0	0.56	0.54	**0.85**	0.85	0.67	0.66
	1	**0.75**	0.72	0.39	0.34	0.52	0.46
R. Forest	0	0.60	0.60	0.53	0.53	0.56	0.56
	1	0.62	0.62	0.68	0.68	0.65	0.65

3.4.2. Patient Survival

A survival label equal to 1 (10% of the patients) identifies the patients survived to the COVID-19, while a label equal to 0 (90% of the patients) identifies death patients.

The three best features selected by the Fisher criterion are (with type of feature indicated in parenthesis):

- Inverse difference moment (Haralick);
- Median of the elongation distribution (Radiomics);
- Median of the distance distribution (Radiomics).

The three best features selected by the χ^2 criterion are (with type of feature indicated in parenthesis):

- Inverse difference moment (Haralick);
- Median of the elongation distribution (Radiomics);
- Skewness of the elongation distribution (Radiomics).

We show in Table 15 the results obtained in terms of global adjusted accuracy and in Table 16 the precision, sensitivity and F_1 score of the same prediction.

Table 15. Global adjusted accuracy of the models to predict mortality using different feature selection strategies. From the left: dichotomized score value, Precision obtained using the 3 best features identified by the Fisher test, Precision obtained using the 3 best features identified by the χ^2 test; Sensitivity obtained using the 3 best features identified by the Fisher test, Sensitivity obtained using the 3 best features identified by the χ^2 test; F_1 score obtained using the 3 best features identified by the Fisher test; F_1 score obtained using the 3 best features identified by the χ^2 test. For each column the maximum value was indicated with bold font.

	Fisher	**χ^2**	**All**
Logistic	0.41	0.48	0.43
Ridge	**0.62**	**0.70**	0.41
KNN	0.41	0.42	**0.50**
R. Forest	0.46	0.48	**0.50**

Table 16. Precision, Sensitivity, and F_1 Score for each model and each feature selection strategy to predict patient survival. From the left: dichotomized score value, Precision obtained using the 3 best features identified by the Fisher test, Precision obtained using the 3 best features identified by the χ^2 test; Sensitivity obtained using the 3 best features identified by the Fisher test, Sensitivity obtained using the 3 best features identified by the χ^2 test; F_1 score obtained using the 3 best features identified by the Fisher test; F_1 score obtained using the 3 best features identified by the χ^2 test. For each column the maximum value was indicated with bold font.

	Survival 1 = Dead 0 = Alive	**Fisher PPV**	**χ^2 PPV**	**Fisher TPR**	**χ^2 TPR**	**Fisher F_1**	**χ^2 F_1**
Logistic	0	0.88	0.90	0.82	0.82	0.85	0.85
	1	0.00	0.08	0.00	0.14	0.00	0.10
Ridge	0	**0.93**	**0.95**	0.82	0.82	0.87	0.88
	1	0.20	0.25	0.43	0.57	0.27	0.35
KNN	0	0.89	0.89	0.83	0.85	0.86	0.87
	1	0.00	0.00	0.00	0.00	0.00	0.00
R. Forest	0	0.90	0.90	**0.94**	**0.95**	**0.92**	**0.93**
	1	0.00	0.00	0.00	0.00	0.00	0.00

4. Discussion

4.1. GGO Segmentation

The examples reported in Figures 3 and 4 show how the non-supervised segmentation method proposed in this paper is able to approximate the gold standard results with satisfactory results.

This result has two strong implications for the Radiomics of the COVID-19 patients. First, given that the amount of information required for the k-means method training is considerably lower than CNN methods, while still retaining good results, this segmentation can be implemented with in-patient training. Secondly, this method can be used with success as a first segmentation method to be used as training for other, more specific methods. We remark that all the proposed techniques are voxel-based algorithms: this kind of method requires the whole patient's scan as input, drastically reducing the dimensionality of the dataset. As a reference, a 3D U-Net-based method [66] required two order of magnitude training samples to achieve comparable results.

It is worth noting that the various segmentation scores are dependent on the class balance, and therefore tend to penalize this kind of segmentation where one class (the GGO class in our case) is substantially under-represented. This can be confirmed by confronting the results of the proposed segmentation with published methods such as those reported in Table 1.

4.2. Individual Features Analysis

We noticed an evident improvement in the prediction converting the clinical outcomes to dichotomized classes. A second improvement in the quality of the prediction was obtained by the application of the feature reduction techniques, which allow a stabilization of the results. Most of the predictive power for each feature can be synthesized in 3 to 4 features per variable. Of all the variables, particular prominence was observed for the Radiomic features. These features were the most important ones in most of the predictions. Of all the predicted characteristics and outcomes, only the peripherality of GGO and PREDI-CO score requires the inclusion of the age value. For the PREDI-CO score, this is not unexpected as it is one of the components of this score. As for the peripherality of GGO lesions, this is an interesting result as they are an important predictor of clinical outcomes and not intuitively associated with patients' age.

If one considers the results for the different predictors (linear penalized, KNN, Random Forest), one can observe that in general, KNN and Random Forests achieve similar performances, while the penalized linear methods consistently perform better. This can be interpreted as the effect of a progressive non-dichotomic behavior in the system. These linear models were also the ones that gained the least from the pre-selection of the features. This can be explained as the L1 and L2 penalization already reducing the effect of the numerosity of the provided features. Methods such as KNN, based on features metrics, are particularly affected by the features numerosity and thus are the ones that have the greatest improvement by feature selection. Linear penalized methods, on the other end, include an implicit feature selection internally and could be even penalized by a reduction in the number of considered features.

Most of these features have a strong class unbalance (down to around 10% of samples in one group, such as in the Consolidation and Roundish GGO), and therefore, the prediction score tends to be strongly unbalanced, with a strong penalization for the prediction of the least represented class. When this unbalance is not present, such as in the case of the prediction of the PREDI-CO score, one can observe good, balanced prediction scores.

The prediction scores for the PREDI-CO are also higher than for similarly balanced classes (such as Crazy Paving). This indicates that the extracted features, albeit not optimal for predicting individuals' components of the score, are indeed able to predict the score as a global value. It is interesting to notice that the variables considered as the most important in the prediction (both for the Fisher and χ^2 method) alongside the age (a well-known risk factor) are (1) the distance between the GGO area and the trachea and (2) the irregularity of the GGO lesion shape. This follows the clinical hypothesis that the spreading of the damaged area toward the peripheral area of the lungs leads to the worst prognosis for the patient.

The results obtained in this work cannot overcome the performances of the already published artificial intelligence techniques. The main limitation of this work is related to the number of available samples: semi-supervised learning algorithms are designed to work with small datasets but require better labeling of them compared to supervised methods.

A second criticality is given by the preliminary choice of the number of clusters for the k-means algorithm: in our work, we identified only five putative clusters for the tissue segmentation. This degree of freedom determines the quality of the areas used for the radiomic feature extraction, and therefore, it could affect the efficiency of the prediction models. In contrast, the manipulation of this single degree of freedom could help to achieve better results on in-patient segmentations.

The clinical characteristics and outcomes considered in this work are scores estimated by the expert radiologists for the description of the state of the patient, but they do not consider the real severity of him. This intrinsic limit does not allow a prediction of the real outcome of the patient, allowing only an undirected evaluation.

5. Conclusions

In the present work, we highlighted the possibility of obtaining a reliable automated segmentation using non-supervised approaches and using this segmentation in a prediction pipeline for patient prognosis.

Artificial Intelligence for diagnostic uses, such as a clinical decision support system, is recognized as an approach rich of potential outcomes but is limited by the requirement of human-driven data curation. With this work, we aimed to prove that semi-supervised approaches to segmentation are promising, as they would combine the best effort of highly trained physicians to develop true gold standard segmentation and the expertise of data analysts to augment that segmentation in full-blown models.

The current COVID-19 pandemic highlights the criticality of relying on high specialized clinicians for time-demanding tasks, as the same experts that can generate gold-standard segmentation for AI training are also the ones responsible for patient diagnosis and care. Improving methods for semi-supervised learning in Radiomics would allow for more effective use of the time and energy of these experts while capitalizing on AI training to support them in patient's diagnosis and treatment.

While the results presented in this work are not yet at the accuracy level necessary for assisted diagnostic use, we surmise that this approach would be helpful in developing a solid triage system, which would help to prioritize the resources available and direct them were most effective.

Supplementary Materials: The following are available online at https://www.mdpi.com/article/10.3390/app11125438/s1, Table S1: Comparison between the score results for the gold standard segmentation in the included databases with details for each sample. For each score, the average value (and corresponding standard deviation at 1 σ) is reported, Table S2 Details of the various state-of-art methods referenced in the paper.

Author Contributions: M.B., A.C., F.C. (Francesca Coppola), A.C., F.C. (Federica Ciccarese), L.P., G.V., B.B., and L.C.: Investigation and Data Curation; R.B., N.C., E.G., and B.B.: Software, Methodology, Data Analysis; P.V., L.S., R.G., F.C. (Francesca Coppola), E.M., and G.C.: Conceptualization and Supervision; C.D.B., R.B., N.C., G.V., and E.G.: Original draft preparation. All authors contributed to reviewing and editing of the manuscript. All authors have read and agreed to the published version of the manuscript.

Funding: This research received no external funding.

Institutional Review Board Statement: The study was conducted according to the guidelines of the Declaration of Helsinki and approved by the Institutional Review Board (or Ethics Committee) of IRCCS Azienda Ospedaliero-Universitaria di Bologna (protocol code no. EM949-2020_507/2020/Oss/AOUBo, approved on date: 16 September 2020).

Informed Consent Statement: This study is an observational, retrospective single-center study and was approved by our local institution review board. Informed consent was waived by the institutional review board owing to the retrospective nature of the study.

Data Availability Statement: The work is based on a mix of public data and data collected in loco. Public data can be found at [52]. Data collected in loco is available on request due to restrictions on privacy (European GDPR).

Conflicts of Interest: The authors declare no conflict of interest.

References

1. Loeffelholz, M.J.; Tang, Y.W. Laboratory diagnosis of emerging human coronavirus infections—The state of the art. *Emerg. Microbes Infect.* **2020**, *9*, 747–756. [CrossRef]
2. Fu, Z.; Tang, N.; Chen, Y.; Ma, L.; Wei, Y.; Lu, Y.; Ye, K.; Liu, H.; Tang, F.; Huang, G.; et al. CT features of COVID-19 patients with two consecutive negative RT-PCR tests after treatment. *Sci. Rep.* **2020**, *10*, 11548. [CrossRef]
3. Ciccarese, F.; Coppola, F.; Spinelli, D.; Galletta, G.L.; Lucidi, V.; Paccapelo, A.; De Benedittis, C.; Balacchi, C.; Golfieri, R. Diagnostic accuracy of north america expert consensus statement on reporting CT findings in patients suspected of having COVID-19 infection: An italian single-center experience. *Radiol. Cardiothorac. Imag.* **2020**, *2*, e200312. [CrossRef]

4. Byrne, D.; Neill, S.B.O.; Müller, N.L.; Müller, C.I.S.; Walsh, J.P.; Jalal, S.; Parker, W.; Bilawich, A.M.; Nicolaou, S. RSNA Expert Consensus Statement on Reporting Chest CT Findings Related to COVID-19: Interobserver Agreement Between Chest Radiologists. *Can. Assoc. Radiol. J.* **2021**, *72*, 159–166. [CrossRef] [PubMed]
5. Esbin, M.N.; Whitney, O.N.; Chong, S.; Maurer, A.; Darzacq, X.; Tjian, R. Overcoming the bottleneck to widespread testing: A rapid review of nucleic acid testing approaches for COVID-19 detection. *RNA* **2020**, *26*, 771–783. [CrossRef]
6. Basso, D.; Aita, A.; Navaglia, F.; Franchin, E.; Fioretto, P.; Moz, S.; Bozzato, D.; Zambon, C.F.; Martin, B.; Dal Prà, C.; et al. SARS-CoV-2 RNA identification in nasopharyngeal swabs: Issues in pre-analytics. *Clin. Chem. Lab. Med.* **2020**, *58*, 1579–1586. [CrossRef] [PubMed]
7. Rubin, G.D.; Ryerson, C.J.; Haramati, L.B.; Sverzellati, N.; Kanne, J.P.; Raoof, S.; Schluger, N.W.; Volpi, A.; Yim, J.J.; Martin, I.B.K.; et al. The Role of Chest Imaging in Patient Management During the COVID-19 Pandemic: A Multinational Consensus Statement from the Fleischner Society. *Chest* **2020**, *158*, 106–116. [CrossRef] [PubMed]
8. Ai, T.; Yang, Z.; Hou, H.; Zhan, C.; Chen, C.; Lv, W.; Tao, Q.; Sun, Z.; Xia, L. Correlation of chest CT and RT-PCR testing for coronavirus disease 2019 (COVID-19) in China: A report of 1014 cases. *Radiology* **2020**, *296*, E32–E40. [CrossRef]
9. Akbari, Y.; Hassen, H.; Al-ma'adeed, S.; Zughaier, S. COVID-19 Lesion Segmentation Using Lung CT Scan Images: Comparative Study Based on Active Contour Models. *Res. Square* **2020**. [CrossRef]
10. Fusco, R.; Granata, V.; Mazzei, M.A.; Meglio, N.D.; Roscio, D.D.; Moroni, C.; Monti, R.; Cappabianca, C.; Picone, C.; Neri, E.; et al. Quantitative imaging decision support (QIDSTM) tool consistency evaluation and radiomic analysis by means of 594 metrics in lung carcinoma on chest CT scan. *Cancer Control* **2021**, *28*, 1073274820985786. [CrossRef]
11. Collins, J.; Stern, E. Ground-glass opacity at CT: The ABCs. *Am. J. Roentgenol.* **1997**, *169*, 355–367. [CrossRef]
12. Huang, C.; Wang, Y.; Li, X.; Ren, L.; Zhao, J.; Hu, Y.; Zhang, L.; Fan, G.; Xu, J.; Gu, X.; et al. Clinical features of patients infected with 2019 novel coronavirus in Wuhan, China. *Lancet* **2020**, *395*, 497–506. [CrossRef]
13. Wang, C.; Shi, B.; Wei, C.; Ding, H.; Gu, J.; Dong, J. Initial CT features and dynamic evolution of early-stage patients with COVID-19. *Radiol. Infect. Dis.* **2020**, *7*, 195–203. [CrossRef] [PubMed]
14. Zhang, C.; Yang, G.; Cai, C.; Xu, Z.; Wu, H.; Guo, Y.; Xie, Z.; Shi, H.; Cheng, G.; Wang, J. Development of a quantitative segmentation model to assess the effect of comorbidity on patients with COVID-19. *Eur. J. Med. Res.* **2020**, *25*, 49. [CrossRef] [PubMed]
15. Adair, L.B.; Ledermann, E.J. Chest CT findings of early and progressive phase COVID-19 infection from a US patient. *Radiol. Case Rep.* **2020**, *15*, 819–824. [CrossRef] [PubMed]
16. Yang, S.; Shi, Y.; Lu, H.; Xu, J.; Li, F.; Qian, Z.; Jiang, Y.; Hua, X.; Ding, X.; Song, F.; et al. Clinical and CT features of early stage patients with COVID-19: A retrospective analysis of imported cases in Shanghai, China. *Eur. Respir. J.* **2020**, *55*, 2000407. [CrossRef] [PubMed]
17. Xu, M.; Qi, S.; Yue, Y.; Teng, Y.; Xu, L.; Yao, Y.; Qian, W. Segmentation of lung parenchyma in CT images using CNN trained with the clustering algorithm generated dataset. *Biomed. Eng. Online* **2019**, *18*, 239. [CrossRef] [PubMed]
18. Neri, E.; Coppola, F.; Larici, A.R.; Sverzellati, N.; Mazzei, M.A.; Sacco, P.; Dalpiaz, G.; Feragalli, B.; Miele, V.; Grassi, R. Structured reporting of chest CT in COVID-19 pneumonia: A consensus proposal. *Insights Imag.* **2020**, *11*, 92. [CrossRef] [PubMed]
19. ACR Website. Position Statement Section. Available online: https://www.acr.org/Advocacy-and-Economics/ACR-Position-Statements/Recommendations-for-Chest-Radiography-and-CT-for-Suspected-COVID19-Infection (accessed on 3 June 2021).
20. Kirsch, J.; Ramirez, J.; Mohammed, T.L.; Amorosa, J.K.; Brown, K.; Dyer, D.S.; Ginsburg, M.E.; Heitkamp, D.E.; Jeudy, J.; Macmahon, H.; et al. ACR Appropriateness Criteria® acute respiratory illness in immunocompetent patients. *J. Thorac. Imaging* **2011**, *15*, W42–W44. [CrossRef]
21. Neri, E.; Miele, V.; Coppola, F.; Grassi, R. Use of CT and artificial intelligence in suspected or COVID-19 positive patients: Statement of the Italian Society of Medical and Interventional Radiology. *Radiol. Med.* **2020**, *125*, 505–508. [CrossRef]
22. Zhang, B.; Ni-Jia-Ti, M.Y.; Yan, R.; An, N.; Chen, L.; Liu, S.; Chen, L.; Chen, Q.; Li, M.; Chen, Z.; et al. CT-based radiomics for predicting the rapid progression of coronavirus disease 2019 (COVID-19) pneumonia lesions. *Br. J. Radiol.* **2021**, *94*, 20201007. [CrossRef]
23. Ria, F.; Fu, W.; Chalian, H.; Abadi, E.; Segars, P.W.; Fricks, R.; Khoshpouri, P.; Samei, E. A comparison of COVID-19 and imaging radiation risk in clinical patient populations. *J. Radiol. Prot.* **2020**, *40*, 1336. [CrossRef]
24. Jin, S.; Wang, B.; Xu, H.; Luo, C.; Wei, L.; Zhao, W.; Hou, X.; Ma, W.; Xu, Z.; Zheng, Z.; et al. AI-assisted CT imaging analysis for COVID-19 screening: Building and deploying a medical AI system in four weeks. *medRxiv* **2020**, *98*, 106897.
25. Cattabriga, A.; Cocozza, M.A.; Vara, G.; Coppola, F.; Golfieri, R. Lung CT Segmentation to Identify Consolidations and Ground Glass Areas for Quantitative Assesment of SARS-CoV Pneumonia. *J. Vis. Exp.* **2020**, 166. [CrossRef]
26. Mansoor, A.; Foster, B.; Xu, Z.; Papadakis, G.; Folio, L.; Udupa, J.; Mollura, D. Segmentation and image analysis of abnormal lungs at CT: Current approaches, challenges, and future trends. *Radiogr. Rev. Publ. Radiol. Soc. N. Am. Inc.* **2015**, *35*, 1056–1076. [CrossRef] [PubMed]
27. Oulefki, A.; Agaian, S.; Trongtirakul, T.; Laouar, A.K. Automatic COVID-19 lung infected region segmentation and measurement using CT-scans images. *Pattern Recognit.* **2020**, *114*, 107747. [CrossRef] [PubMed]
28. Nakagomi, K.; Shimizu, A.; Kobatake, H.; Yakami, M.; Fujimoto, K.; Togashi, K. Multi-shape graph cuts with neighbor prior constraints and its application to lung segmentation from a chest CT volume. *Med. Image Anal.* **2013**, *17*, 62–77. [CrossRef]

29. Dai, S.; Lu, K.; Dong, J.; Zhang, Y.; Chen, Y. A novel approach of lung segmentation on chest CT images using graph cuts. *Neurocomputing* **2015**. [CrossRef]
30. Li, B.; Christensen, G.; Mclennan, G.; Hoffman, E.; Reinhardt, J. Establishing a normative atlas of the human lung: Inter-subject warping and registration of volumetric CT. *Acad. Radiol.* **2003**, *10*, 255–265. [CrossRef]
31. Dey, N.; Rajinikanth, V.; Fong, S.J.; Kaiser, M.S.; Mahmud, M. Social-group-optimization assisted Kapur's entropy and morphological segmentation for automated detection of COVID-19 infection from computed tomography images. *Cogn. Comput.* **2020**, *12*, 1–13. [CrossRef]
32. Abdel-Basset, M.; Chang, V.; Hawash, H.; Chakrabortty, R.K.; Ryan, M. FSS-2019-nCov: A deep learning architecture for semi-supervised few-shot segmentation of COVID-19 infection. *Knowl. Based Syst.* **2021**, *212*, 106647. [CrossRef] [PubMed]
33. Hofmanninger, J.; Prayer, F.; Pan, J.; Röhrich, S.; Prosch, H.; Langs, G. Automatic lung segmentation in routine imaging is primarily a data diversity problem, not a methodology problem. *Eur. Radiol. Exp.* **2020**, *4*, 50. [CrossRef]
34. Wang, H.; Wang, L.; Lee, E.H.; Zheng, J.; Zhang, W.; Halabi, S.; Liu, C.; Deng, K.; Song, J.; Yeom, K.W. Decoding COVID-19 pneumonia: Comparison of deep learning and radiomics CT image signatures. *Eur. J. Nucl. Med. Mol. Imaging* **2020**, *48*, 1–9. [CrossRef]
35. Gozes, O.; Frid-Adar, M.; Greenspan, H.; Browning, P.D.; Zhang, H.; Ji, W.; Bernheim, A.; Siegel, E. Rapid AI development cycle for the coronavirus (COVID-19) pandemic: Initial results for automated detection & patient monitoring using deep learning CT image analysis. *arXiv* **2020**, arXiv:2003.05037.
36. Müller, D.; Rey, I.S.; Kramer, F. Automated chest CT image segmentation of COVID-19 lung infection based on 3D u-net. *arXiv* **2020**, arXiv:2007.04774.
37. Bernheim, A.; Mei, X.; Huang, M.; Yang, Y.; Fayad, Z.A.; Zhang, N.; Diao, K.; Lin, B.; Zhu, X.; Li, K.; et al. Chest CT findings in coronavirus disease-19 (COVID-19): Relationship to duration of infection. *Radiology* **2020**, *295*, 200463. [CrossRef]
38. Simpson, S.; Kay, F.U.; Abbara, S.; Bhalla, S.; Chung, J.H.; Chung, M.; Henry, T.S.; Kanne, J.P.; Kligerman, S.; Ko, J.P.; et al. Radiological Society of North America Expert Consensus Statement on Reporting Chest CT Findings Related to COVID-19. Endorsed by the Society of Thoracic Radiology, the American College of Radiology, and RSNA—Secondary Publication. *J. Thorac. Imaging* **2020**, *35*, 219–227. [CrossRef] [PubMed]
39. Xie, X.; Zhong, Z.; Zhao, W.; Zheng, C.; Wang, F.; Liu, J. Chest CT for Typical Coronavirus Disease 2019 (COVID-19) Pneumonia: Relationship to Negative RT-PCR Testing. *Radiology* **2020**, *296*, E41–E45. [CrossRef]
40. Huang, P.; Liu, T.; Huang, L.; Liu, H.; Lei, M.; Xu, W.; Hu, X.; Chen, J.; Liu, B. Use of Chest CT in Combination with Negative RT-PCR Assay for the 2019 Novel Coronavirus but High Clinical Suspicion. *Radiology* **2020**, *295*, 22–23. [CrossRef] [PubMed]
41. Fang, Y.; Zhang, H.; Xie, J.; Lin, M.; Ying, L.; Pang, P.; Ji, W. Sensitivity of Chest CT for COVID-19: Comparison to RT-PCR. *Radiology* **2020**, *296*, E115–E117. [CrossRef]
42. Inui, S.; Fujikawa, A.; Jitsu, M.; Kunishima, N.; Watanabe, S.; Suzuki, Y.; Umeda, S.; Uwabe, Y. Chest CT findings in cases from the cruise ship diamond princess with coronavirus disease (COVID-19). *Radiol. Cardiothorac. Imag.* **2020**, *2*, e200110. [CrossRef]
43. Belkhatir, Z.; Estépar, R.S.J.; Tannenbaum, A.R. Supervised Image Classification Algorithm Using Representative Spatial Texture Features: Application to COVID-19 Diagnosis Using CT Images. *medRxiv* **2020**. [CrossRef]
44. Liu, C.; Wang, X.; Liu, C.; Sun, Q.; Peng, W. Differentiating novel coronavirus pneumonia from general pneumonia based on machine learning. *Biomed. Eng. Online* **2020**, *19*, 66. [CrossRef]
45. Zeng, Q.Q.; Zheng, K.I.; Chen, J.; Jiang, Z.H.; Tian, T.; Wang, X.B.; Ma, H.L.; Pan, K.H.; Yang, Y.J.; Chen, Y.P.; et al. Radiomics-based model for accurately distinguishing between severe acute respiratory syndrome associated coronavirus 2 (SARS-CoV-2) and influenza A infected pneumonia. *MedComm* **2020**. [CrossRef] [PubMed]
46. Wei, W.; Hu, X.W.; Cheng, Q.; Zhao, Y.M.; Ge, Y.Q. Identification of common and severe COVID-19: The value of CT texture analysis and correlation with clinical characteristics. *Eur. Radiol.* **2020**, *30*, 6788–6796. [CrossRef] [PubMed]
47. Caruso, D.; Zerunian, M.; Polici, M.; Pucciarelli, F.; Polidori, T.; Rucci, C.; Guido, G.; Bracci, B.; De Dominicis, C.; Laghi, A. Chest CT Features of COVID-19 in Rome, Italy. *Radiology* **2020**, *296*, E79–E85. [CrossRef] [PubMed]
48. Ye, Z.; Zhang, Y.; Wang, Y.; Huang, Z.; Song, B. Chest CT manifestations of new coronavirus disease 2019 (COVID-19): A pictorial review. *Eur. Radiol.* **2020**, *30*, 4381–4389. [CrossRef] [PubMed]
49. Albarello, F.; Pianura, E.; Di Stefano, F.; Cristofaro, M.; Petrone, A.; Marchioni, L.; Palazzolo, C.; Schininà, V.; Nicastri, E.; Petrosillo, N.; et al. 2019-novel Coronavirus severe adult respiratory distress syndrome in two cases in Italy: An uncommon radiological presentation. *Int. J. Infect. Dis.* **2020**, *93*, 192–197. [CrossRef]
50. Varga, Z.; Flammer, A.J.; Steiger, P.; Haberecker, M.; Andermatt, R.; Zinkernagel, A.S.; Mehra, M.R.; Schuepbach, R.A.; Ruschitzka, F.; Moch, H. Endothelial cell infection and endotheliitis in COVID-19. *Lancet* **2020**, *395*, 1417–1418. [CrossRef]
51. Zhang, H.; Hung, C.L.; Min, G.; Guo, J.P.; Liu, M.; Hu, X. GPU-Accelerated GLRLM Algorithm for Feature Extraction of MRI. *Sci. Rep.* **2019**, *9*, 10883. [CrossRef]
52. Hu, X.; Ye, W.; Li, Z.; Chen, C.; Cheng, S.; Lv, X.; Weng, W.; Li, J.; Weng, Q.; Pang, P.; et al. Non-invasive evaluation for benign and malignant subcentimeter pulmonary ground-glass nodules ($\leq$1 cm) based on CT texture analysis. *Br. J. Radiol.* **2020**, *93*, 20190762. [CrossRef] [PubMed]
53. Fang, X.; Kruger, U.; Homayounieh, F.; Chao, H.; Zhang, J.; Digumarthy, S.R.; Arru, C.D.; Kalra, M.K.; Yan, P. Association of AI quantified COVID-19 chest CT and patient outcome. *Int. J. Comput. Assist. Radiol. Surg.* **2021**, *16*, 435–44524. [CrossRef] [PubMed]

54. Bartoletti, M.; Giannella, M.; Scudeller, L.; Tedeschi, S.; Rinaldi, M.; Bussini, L.; Fornaro, G.; Pascale, R.; Pancaldi, L.; Pasquini, Z.; et al. Development and validation of a prediction model for severe respiratory failure in hospitalized patients with SARS-CoV-2 infection: A multicentre cohort study (PREDI-CO study). *Clin. Microbiol. Infect.* **2020**, *26*, 1545–1553. [CrossRef] [PubMed]
55. Jun, M.; Cheng, G.; Yixin, W.; Xingle, A.; Jiantao, G.; Ziqi, Y.; Minqing, Z.; Xin, L.; Xueyuan, D.; Shucheng, C.; et al. *COVID-19 CT Lung and Infection Segmentation Dataset*; CERN: Geneva, Switzerland, 2020. [CrossRef]
56. Yokota, K.; Maeda, S.; Kim, H.; Tan, J.K.; Ishikawa, S.; Tachibana, R.; Hirano, Y.; Kido, S. Automatic detection of GGO regions on CT images in LIDC dataset based on statistical features. In Proceedings of the 2014 Joint 7th International Conference on Soft Computing and Intelligent Systems (SCIS) and 15th International Symposium on Advanced Intelligent Systems (ISIS), Kitakyushu, Japan, 3–6 December 2014; pp. 1374–1377.
57. Frangi, R.; Niessen, W.J.; Vincken, K.; Viergever, M. Multiscale vessel enhancement filtering. *Med. Image Comput. Comput. Assist. Interv.* **2000**. [CrossRef]
58. Sato, Y.; Nakajima, S.; Shiraga, N.; Atsumi, H.; Yoshida, S.; Koller, T.; Gerig, G.; Kikinis, R. Three-dimensional multi-scale line filter for segmentation and visualization of curvilinear structures in medical images. *Med. Image Anal.* **1998**, *2*, 143–168. [CrossRef]
59. Arthur, D.; Vassilvitskii, S. K-means++: The advantages of careful seeding. In Proceedings of the Eighteenth Annual ACM-SIAM Symposium on Discrete Algorithms SODA '07, Society for Industrial, Applied Mathematics, New Orleans, LA, USA, 7–9 January 2007; pp. 1027–1035.
60. Yaniv, Z.; Lowekamp, B.C.; Johnson, H.J.; Beare, R. Simple ITK Image-Analysis Notebooks: A Collaborative Environment for Education and Reproducible Research. *J. Digit. Imaging* **2018**, *31*, 290–303. [CrossRef] [PubMed]
61. Lowekamp, B.C.; Chen, D.T.; Ibáñez, L.; Blezek, D. The Design of SimpleITK. *Front. Neuroinf.* **2013**, *7*, 45. [CrossRef] [PubMed]
62. Bradski, G. The OpenCV Library. *Dr. Dobb J. Softw. Tools* **2000**, *120*, 122–125.
63. Haralick, R.M.; Shanmugam, K.; Dinstein, I. Textural features for image classification. *IEEE Trans. Syst. Man Cybern.* **1973**, *3*, 610–621. [CrossRef]
64. Lehmann, G. La Bel Object Representation and Manipulation with ITK. 2007. Available online: http://hdl.handle.net/1926/584 (accessed on 4 June 2021).
65. Buitinck, L.; Louppe, G.; Blondel, M.; Pedregosa, F.; Mueller, A.; Grisel, O.; Niculae, V.; Prettenhofer, P.; Gramfort, A.; Grobler, J.; et al. API design for machine learning software: Experiences from the scikit-learn project. *arXiv* **2013**, arXiv:1309.0238.
66. Yan, Q.; Wang, B.; Gong, D.; Luo, C.; Zhao, W.; Shen, J.; Shi, Q.; Jin, S.; Zhang, L.; You, Z. COVID-19 Chest CT Image Segmentation—A Deep Convolutional Neural Network Solution. *arXiv* **2020**, arXiv:2004.10987.

applied sciences

MDPI

Review

Artificial Intelligence and the Medical Physicist: Welcome to the Machine

Michele Avanzo [1,*], Annalisa Trianni [2], Francesca Botta [3], Cinzia Talamonti [4], Michele Stasi [5] and Mauro Iori [6]

[1] Medical Physics Department, Centro di Riferimento Oncologico di Aviano (CRO) IRCCS, 33081 Aviano, Italy
[2] Medical Physics Unit, Ospedale Santa Chiara APSS, 38122 Trento, Italy; annalisa.trianni@apss.tn.it
[3] Medical Physics Unit, Istituto Europeo di oncologia IRCCS, 20141 Milan, Italy; francesca.botta@ieo.it
[4] Department Biomedical Experimental and Clinical Science "Mario Serio", University of Florence, 50134 Florence, Italy; cinzia.talamonti@unifi.it
[5] Medical Physics Unit, A.O. Ordine Mauriziano di Torino, 10128 Torino, Italy; michele.stasi@unito.it
[6] Medical Physics Unit, Azienda USL-IRCCS di Reggio Emilia, 42122 Reggio Emilia, Italy; mauro.iori@ausl.re.it
* Correspondence: mavanzo@cro.it

Abstract: Artificial intelligence (AI) is a branch of computer science dedicated to giving machines or computers the ability to perform human-like cognitive functions, such as learning, problem-solving, and decision making. Since it is showing superior performance than well-trained human beings in many areas, such as image classification, object detection, speech recognition, and decision-making, AI is expected to change profoundly every area of science, including healthcare and the clinical application of physics to healthcare, referred to as medical physics. As a result, the Italian Association of Medical Physics (AIFM) has created the "AI for Medical Physics" (AI4MP) group with the aims of coordinating the efforts, facilitating the communication, and sharing of the knowledge on AI of the medical physicists (MPs) in Italy. The purpose of this review is to summarize the main applications of AI in medical physics, describe the skills of the MPs in research and clinical applications of AI, and define the major challenges of AI in healthcare.

Keywords: artificial intelligence; deep learning; medical physicist; machine learning; big data

Citation: Avanzo, M.; Trianni, A.; Botta, F.; Talamonti, C.; Stasi, M.; Iori, M. Artificial Intelligence and the Medical Physicist: Welcome to the Machine. *Appl. Sci.* **2021**, *11*, 1691. https://doi.org/10.3390/app11041691

Academic Editors: Francesco Bianconi and Salvatore Gallo

Received: 15 December 2020
Accepted: 8 February 2021
Published: 13 February 2021

1. Introduction

Artificial intelligence (AI) is a branch of computer science dedicated to giving machines or computers the ability to perform human-like cognitive functions, such as learning, problem-solving, and decision making [1,2]. AI-based systems have shown performance superior to experienced human beings in tasks, such as image classification and analysis, speech recognition, and decision-making [3]. Consequently, AI is expected to change profoundly every area of science, including medical physics, the clinical application of the principles of physics to healthcare [4,5]. The knowledge and skills of the medical physicists (MPs), which include aspects of mathematics, bioinformatics, statistics, safety, and ethics in the use of medical devices, are invaluable in the clinical and research applications of AI in medicine.

Moreover, analytical and computational techniques of physics, in particular those derived from statistical physics of disordered systems, can be extended to large-scale problems, including machine learning, e.g., to analyze the weight space of deep neural networks [6,7].

Given the exponential growth of applications of AI, such as machine learning (ML) and deep learning (DL) in all areas of medicine, which use ionizing radiation, ultrasounds, and magnetic fields for diagnostic and treatment purposes, witnessed over the past few years, the MPs' workflow will be profoundly affected by the advent of AI. The areas affected will include quality controls of equipment, as linear accelerators and imaging devices, and software like diagnostic support systems [4,8] and decision support systems.

The MPs will be more and more involved in the use of the new AI applications in medicine for patient diagnosis and treatment, with the primary scope of guaranteeing the quality of the whole process and environment [9].

The Italian Association of Medical Physics (AIFM) has created the AI for Medical Physics (AI4MP) task-group, with the aims of coordinating the efforts, facilitating the communication, and sharing of the knowledge on AI of the MPs in Italy. The aim of the present review is to summarize the point of view of the coordinators of AI4MP on the role and the involvement of MPs in the new AI world by defining the challenges of AI in healthcare for the MPs and by describing the skills the MPs can offer in this field. This will be done with a question in mind: if AI is welcomed by the MPs or vice versa.

2. Artificial Intelligence in Healthcare

Machine learning (ML) is the discipline that builds mathematical models and computer algorithms to perform specific tasks by learning patterns and inferences directly from data using computers, without being explicitly programmed to conduct these tasks [10]. ML algorithms can be either used for supervised learning, where the machine is provided with output labels to be associated with a set of input variables, or unsupervised learning. A popular supervised ML method is Support Vector Machines (SVM), which, by means of a kernel function, projects the data into a higher-dimensional feature space and determines a hyperplane in this feature space, which separates data points into categories [11]. Ensemble ML (EML) methods, such as Random forests or AdaBoost, are other supervised methods, which aggregate multiple learners, such as Decision Trees, into a single learner [12,13]. Naïve-Bayesian (NB) classifier calculates the probability of each class using the Naive Bayes formula [14,15]. In unsupervised learning, the labels for given sets of input variables are not known, and the algorithm aims at finding correlations, patterns, or structures in the input variable space [16,17]. These include k-means clustering [18], principal component analysis (PCA) [19], Stochastic Neighbor Embedding (SNE) [20], and Laplacian eigenmaps [21].

Deep learning (DL) is a group of methods, which can be employed for supervised or unsupervised learning on any type of data, image, or signal. DL employs models with multiple stacks of neural layers to learn inherent patterns from input data and generate comprehensive representations, in contrast to classical ML methods, which use handcrafted features manually extracted as input [2].

Nowadays, radiological and pathology images are stored, together with their reports, in picture archiving and communication systems (PACS). Besides, with the introduction of electronic health records (EHRs), systematic collections of patient health information have been made available, which include qualitative data, such as documents and records of patient demographics, medical records, and laboratory and diagnostics tests [22].

ML and DL, if applied to this large and often unstructured digital content, can determine information useful for epidemiological, clinical, and research studies [23,24]. Natural language processing (NLP) techniques, a combination of AI and linguistics, aimed at developing a computer's ability to understand human language [25], can be used to extract clinically relevant information from pathology and radiology reports [26], which can be integrated with features extracted from digital radiologic and pathology images stored in PACS [27].

The process used for these analyses is defined as "Data Mining". Data mining is used to find trends, patterns, correlations, anomalies, and features of interest in a database [28] in a data-driven inductive approach, which generates hypotheses from data [29]. Ideally, data mining necessitates the '4 V's' of 'Big Data'—volume, variety, velocity, and veracity of data. Instead of being used for prediction or diagnosis, in this case, ML is used to find clinically similar patients in the unstructured database, using all available multimodal clinical data available, with the aim of discovering important groupings or defining features in the data [28].

Once similar patients are identified, the diagnosis, treatment, and outcome extracted from EHRs and other digital content can be ranked to give recommendations [17], e.g., by

computerized clinical decision support systems (CDSS), which aid in decision-making [30]. In this way, pipelines can be designed to continuously and automatically extract information and improve the accuracy of patient outcome prediction [31].

3. Clinical Applications of Artificial Intelligence

3.1. Imaging

The main purpose of the use of AI and ML applications in imaging is to support the specialist in the diagnosis of diseases. Computer-aided diagnosis (CAD) is among the first applications of these new algorithms in the imaging area [32,33] and incorporates ML classifiers trained to distinguish lesions from normal tissue [34]. In lung computed tomography (CT), ML applied to combinations of CT textural features scored high accuracy in distinguishing malignant lesions [35] or invasive from minimally invasive lesions [36].

In the relatively recent radiomics approach, quantitative analysis of radiological images (mainly CT [37–39], magnetic resonance imaging (MRI) [40–42], and positron emission tomography (PET) [43] images, but also ultrasounds [44], mammograms [45], and radiography) by extraction of a large number of image features (up to a few hundred or thousands) can be combined with ML classifiers to produce prognostic and predictive models [39].

In image elaboration, DL algorithms can learn the structure labeling of each image voxel directly (semantic segmentation) in order to contour lesions or organs [46]. U-net, one of the most popular DL architectures for image segmentation, has proven to be capable of automatically segmenting lung parenchyma [47] and lung tumor using PET-CT hybrid imaging [48].

A cornerstone of optimization of clinical imaging protocols is patients' dose estimation, which allows the dose to be balanced with image quality. Dose to the patient can be automatically calculated by DL in CT [49], single-photon emission computed tomography (SPECT) [50], and PET [51]. In interventional radiology, DL has been proposed for skin dose estimation [52]. In chest CT, ML could be used to predict the volumetric computed tomography dose index (CTDIvol) based on scan patient metrics (scanner, study description, protocol, patient age, sex, and water-equivalent diameter (DW)) and identify exams, which hold potential for dose reduction by tuning the acquisition parameters [53].

Another pillar of patient dose optimization is image quality improvement, as it allows dose reduction for the same image quality. The integration of AI algorithms within the imaging technology allows for improving imaging quality and, consequently, to reduce patient dose. DL methods have been used for improving PET image quality, reducing noise [54], removing streak artifacts from CT [55], and developing novel techniques for tomographic image reconstruction based on a reduced amount of acquired data. Other promising applications are a generation of synthetic images, such as synthetic CT from MRI [56], virtual contrast-enhanced images [57], and rigid/deformable intramodal and multimodal image registration [58], and extraction of the respiratory signal [21] that could be used for breathing motion compensation of images [59].

In interventional radiology, AI can predict tumor response to transarterial chemoembolization based on image texture and patient characteristics [60,61]. In the future, real-time registration DL algorithms could be used to superimpose high-resolution preoperative MR imaging with intra-procedural fluoroscopy, guiding the physicians during the catheter's manipulation [62] for estimating ablation margins and helping minimize damages to structures close to the treated area.

AI can be useful also in longitudinal studies during follow-up of treatments in order to detect subtle changes between images, thus identifying progress or recurrence at an earlier stage [63,64]. Ophthalmic imaging, e.g., fundus digital photography, optical coherence tomography, among other imaging fields, is where artificial intelligence can support the specialist in the diagnosis of ophthalmic disorders, such as diabetic retinopathy, age-related macular degeneration, and others [65]. Other areas include cardiology [66,67] and rheumatology, which have a long history of research in AI applications aimed to detect

and assess also rheumatological manifestations, bone erosions, and cartilage loss [68]. The development of digital pathology, due to the introduction of whole-slide scanners, and the progression of computer vision algorithms have significantly grown the usage of AI to perform tumor diagnosis, subtyping, grading, staging, and prognostic prediction. In the big-data era, the pathological diagnosis of the future could merge proteomics and genomics [69]. Spatial metabolomics is a new field aiming at measuring the distribution of molecules, such as metabolites, lipids, and drugs, within body structures, using imaging, such as mass spectrometry, where each pixel is represented by its mass spectrum [70]. Being characterized by a large amount of high dimensional data, including overlapping and noisy molecular signals, this technique looks promising for the application of AI [71].

Other applications that could become a focus of AI in the near future are computer vision [72], dealing with object detection and feature recognition in digital images, and virtual assistants [73], employing speech recognition in neuroradiology [74], radiology, and beyond. By augmented reality, the operator's perception of an operating room environment could be enhanced with AI-generated information [75].

3.2. Therapy

ML can be useful to carry out many of the activities during the whole workflow of radiotherapy, starting with the choice of the optimal radiation approach, e.g., choice of proton vs. photon [76]. A convolutional neural network (CNN) can automatically segment targets and organs at risk in radiotherapy [77]. ML-based auto-planning [78,79] mimics the iterative plan design, evaluation, and adjustments made by experienced operators with the goal of improving quality and efficiency and reducing inter-user variability [46]. Knowledge-based approaches leverage a large database of prior treatment plans (up to thousands) to develop associations between geometric and dosimetric parameters from a selection of previous plans in order to determine achievable dose constraints or dose distributions that can be used for benchmarking the quality of plans [9,80]. ML-based auto planning was also developed for brachytherapy [81].

The dose distribution from radiation therapy treatment can be predicted by DL in order to speed up the optimization [82] or determine the best achievable dose distribution from the patient image [83]. ML was applied to predict dose in brachytherapy [84] and in vivo measured dose in intraoperative radiotherapy [85].

Recently, dosomics, the application of radiomics or DL to the analysis of the dose distribution, eventually corrected into biologically effective dose to account for diverse fractionation, was investigated for the ability to predict side effects of radiation therapy [86,87]. Radiomics can also be applied to cone-beam CT (CBCTs) acquired for image-guidance of the radiotherapy treatment, making these images useful for data mining [88].

A major concern of radiotherapy is the change in the anatomy of the patient during therapy, which could result in unwanted dose changes. In this case, re-planning of the treatment is warranted. ML can identify significant changes in patient anatomy during radiotherapy [19] and predict patients who would benefit from adaptive radiotherapy (ART) [89]. Eventually, by using information extracted from radiomics voxel-based analyses, sensitive/resistant tumor sub-volumes might be identified, requiring higher (or lower) dose, thus enabling dose painting according to a "radiomic target volume" (RTV) [90].

In nuclear medicine, radiometabolic therapy with unsealed (radiopharmaceuticals) or sealed sources (microspheres, etc.) is of growing importance. The application of AI in this area can improve dosimetry by accounting for patients' anatomy, activity distribution, and tissue density, and planning, in order to administer the highest dose to the target while sparing critical organs, as well as for predicting treatment response [91]. Methodological studies have been performed to investigate the robustness of dosomic approaches [92].

3.3. Quality Assurance (QA)

According to the International Organization for Standardization, QA is a system that ensures quality for a given product, service, process. Quality is the degree to which

the system fulfills requirements (need or expectation that is stated—generally implied or obligatory) [93], thus avoiding mistakes and defects. Quality controls (QC) are the tests performed to describe, measure, analyze, improve, and control a certain product or process. In radiological sciences, QCs are applied to verify and monitor devices and procedures for diagnosis and therapy, as well as the support systems used by clinicians. AI can be used to perform automatically QCs that, if carried out manually, would not be feasible routinely due to a large amount of time required. AI QC systems could be used to learn and improve their accuracy over time and develop new tests over time without human intervention.

Quality assurance of radiotherapy (RT) is a significant part of the MP's work, and it is aimed at preventing radiological incidents and misadministration of radiation dose. A number of ML-based approaches have been explored to predict errors in treatment plans in order to automate chart check of plans. A K-means clustering algorithm was employed to learn from prior plans to perform the detection of errors in prostate plans [18].

Automated quality control of LINACs is another promising application of ML, which can be used for predicting machine performance issues, such as deviation of dose output [94], multileaf collimator (MLC) positions [95], and beam symmetry [96]. A method for automated quality control of LINACs by ML applied to electronic portal imaging device (EPID) was proposed, which could identify sag and deviations in the vertical direction and field shift [97]. Other AI applications aim at predicting results of in-phantom patients' specific QA of intensity modulated RT (IMRT) or volumetric modulated arc therapy (VMAT) [98,99].

4. Challenges and Pitfalls of AI

4.1. Data Size and Quality

ML and DL algorithms require a large amount of training samples, which grows rapidly with the dimensionality of data (the curse of dimensionality). An unappropriated data size will lead to a reduction in the certainty of the prediction, considering that many ML applications will always deliver a result, disregard the size and quality of the data set [100]. Unfortunately, a proper metric to evaluate sample size and power for ML and DL is missing.

Frequently, datasets used for training AI have a small number of samples with respect to the dimensionality of data and of the desired tasks [101], to the point that, frequently, there are more features per subject than subjects in the entire dataset [102]. Under these circumstances, overfitting, a condition where models are more sensitive to noise in the data than to their patterns, and instability occur, making the model poorly reproducible and generalizable, meaning that it will perform poorly on unseen datasets [103].

Feature selection algorithms, such as stepwise feature selection [104], the minimum redundancy maximum relevance (mRMR) [105], and RELIEF (relevance in estimating features) [106,107], can be applied to reduce overfitting by selecting a non-redundant subset of variables best suited to predict the outcome.

To reduce overfitting in DL, data augmentation (e.g., by the affine transformation of the images) during training is commonly implemented [10], and layers in the networks are specialized in reducing overfitting, such as dropout layers [108]. On the other side, DL suffers from other sources of uncertainties (e.g., the presence of many local minima in the loss function and the stochastic nature of training algorithms), so that repeating model training multiple times does not necessarily produce the same model [2]. Besides, the class imbalance problem, in which some classes have a significantly higher number of samples, is detrimental for ML performance, if not properly accounted for [109,110]. For overcoming class imbalance, under-sampling or over-sampling can be applied; the latter has been proven to be more effective [110].

Other biases in the training datasets, e.g., age, gender, and race, or in the diagnostic or therapeutical approach, e.g., technologies use for imaging or radiotherapy, may result in biased models, which may lead to poor performance for minority groups who are

poorly represented in the training dataset. This could potentially aggravate healthcare disparities [103].

Another source of unreliability stems from the constant evolving of the patterns of clinical practice over time due to the introduction of new treatment approaches, technologies, or gradual changes in patient population (e.g., percentage of patients with a given histological subtype). This may result in increased unreliability of the AI system's recommendations or prediction over time [30]. The "half-life" of the relevance of clinical data used for training is thought to be typical of 4 months [111].

4.2. Interpretability

Interpretability is the level of understanding of the information that the model extracts from input data, why it is extracted, and how it arrives at its output [2]. ML models are usually perceived as black boxes by the users and clinicians, meaning that they have a low level of interpretability. This issue is exacerbated for deep neural networks, given the complicated multi-layer structures and numerous numerical operations performed by each layer, and hinders the application of AI in the clinic.

Graph approaches can be of help to improve the interpretability of ML and DL methods. The activation maps extracted by the CNN, overlaid with the image analyzed, can show on which image regions the CNN focuses strongly for prediction [112]. For ML classifiers, interpretation can be facilitated by identification of the most important variables or features for prediction and comparing their values in illustrative cases, e.g., patients with a poor and good prognosis, as done in many radiomics studies, e.g., [86,113,114]. In unsupervised learning, some methods, like t-distributed stochastic embedding (t-SNE), allow visualization of high-dimensional data by giving each data point a location in a two or three-dimensional map [20].

4.3. Legal and Ethical Issues

Key ethical issues associated with AI-systems automatically mining large patient databases include informed consent, privacy and data protection, ownership, objectivity, transparency of the obtained clinical or research model, and quality of training and validation data [115]. Automatizing tasks and decisions with the use of AI-based machines on a large scale could bring increased systemic risks of harm and systematic errors. These errors are categorized into omission when humans do not notice the failure of an AI tool and commission when an action is performed following AI's decision when there is evidence that AI is wrong [115]. The responsibility to prevent these errors by anticipating incorrect performance or misuses of AI before incidents occur falls to humans.

A model should be transparent, meaning that its formulas and code should be available and comprehensible so that it is possible to trace why an algorithm has failed and adverse clinical events [115]. The data "truthfulness" consists of understanding the type of information contained, the completeness and accuracy, their variance and bias, and if they reflect the problem of interest. Because of the "black box" phenomenon, informing the patient clearly could become more difficult for the doctor when a decision is influenced by AI [116].

AI systems' decisions are based on the data used for training, the algorithms that are used, and what they have learned since their creation [117]. If some human biases, such as variability in healthcare because of ethnic, social, environmental, or economic factors, or clinically confounding factors, such as comorbidities, are present in the training data, they could result in biased decisions of the AI systems [28,117]. Since AI does not incorporate ethical concepts like equality, humans who use AI will hold the responsibility for preventing these errors [115]. Finally, before integrating AI into medical practice, it is important to prevent the loss of competence of the human who will not be able to carry out a task he used to do before because it has been transferred to the AI, also defined as "deskilling" [116].

5. Role of MP

5.1. Imaging

As already underlined in this paper, one of the major tasks in which the MP is deeply involved in the imaging field is the optimization process, i.e., finding the balance between dose and image quality.

MP understands the components of an imaging device used and the basic physical mechanisms at the root of signal change and image contrast and comprehends the technical and/or physiological artifacts limiting the performance [4,118]. Moreover, the MP understands the limitations and potential pitfalls of dose measurement, calculation, and prediction [90]. Thus, MP has knowledge and skills that are of value for the development, implementation, and use of AI in imaging.

AI-based systems have been developed to estimate patient dose. MP shall validate and periodically check these systems to avoid possible errors in the estimation. For example, the dose to each voxel in the calculated distribution depends on the dose calculation algorithm used, on the calculation voxel spacing, and on the uncertainty in dose measurement in the dataset used for ML training. In phantom, dose measurements can be planned by the MP to test algorithms' predictions.

MP shall also assess image quality through routine testing [119]. Recently, image quality enhancers, based on DL, have been introduced in clinical practice in order to ameliorate image quality. Consequently, image acquisition protocols could be updated to achieve dose reduction, and the MP will be involved in the optimization to ensure the minimum possible ionizing radiation dose to the patient [119,120].

It is also necessary to verify to what extent the imaging parameters' change influences the quantitative image content and, consequently, the response of AI systems. To this purpose, various physical phantoms have been developed. The Credence Cartridge Radiomics (CCR) phantom for radiomics was created for CT [121] and CBCT [122] images. More recently, anthropomorphic phantoms with heterogeneous objects were designed in order to simulate the texture of lung nodules [123]. PET phantoms with 3D printed inserts simulating heterogeneities in FDG uptake have been proposed [124], as well as MR phantoms simulating relaxation times and texture of pelvic tissue and malignancies [125]. Using these kinds of phantoms, the sensitivity of radiomics-based ML classifications on image acquisition parameters has been investigated. In CT, the classification is affected by the device used [121], method of image reconstruction [126], noise reduction algorithms, slice thicknesses [127,128]. PET features depend on acquisition mode [129,130], reconstruction algorithm, image resolution, and discretization [131,132]. MRI features are sensitive to the field of view, field strength, pulse sequence, reconstruction algorithm, and slice thickness [133].

Physical and digital phantoms could also be used to periodically verify the performances of image-based ML algorithms. Digital phantoms are usually representative scans of patients with known acquisition parameters. A dataset of CTs acquired twice on the same patient 15 min apart allows "test-retest", an assessment of the reproducibility of the radiomics workflow under the same conditions [127].

The accuracy of AI-generated segmentation, image reconstruction, and synthetic images (e.g., MRI) can be assessed using a ground truth digital phantom, for example of brain glioma patients [133] and image simulators, capable of simulating MRI acquired with different pulse sequence or field strength and reconstructed with different methods [133]. Specific tests allow assessing the accuracy of AI-based image registration [134].

In addition, MP can ensure correct extraction and quantitative analysis of imaging data. Thus, before performing quantitative analysis with AI algorithms, the accuracy and precision associated with the quantitative parameters within the images (e.g., tumors) should be assessed [29]. Moreover, MP is responsible for the pre-processing of images necessary for correct AI application. This would include the conversion of PET and SPECT images in standard uptake value (SUV), the standardization of MR images intensity scale [135], as well as assessment and correction of confounding factors of images, such

as artifacts for metal implants in CT, magnetic field non-uniformity in MRI, and partial volume effect (PVE) in nuclear medicine images. Multimodal images should be registered using a proper method for rigid or deformable registration [136], a critical step that may affect the accuracy of AI models analyzing hybrid image datasets voxel by voxel [137] in order to combine metabolic, functional, and morphologic information.

In interventional radiology, MPs are involved in monitoring patients' dose and manage patients' radiation risks by reviewing interventional procedures [138]. The involvement of MPs will also reach safe implementation and QA of other AI systems, such as robotic angiographs and/or neuro-navigators, robots, etc., and platforms (catheter navigation assistants, analyzing relationships between catheter positions, therapeutic effect, and patient outcomes, etc.) for interventional therapies.

In other fields of medical imaging where AI is rapidly emerging, such as pathology imaging, MPs can support the acceptance and validation of AI systems. Recently, [139] pathology Digital Imaging and Communications in Medicine (DICOM) file format has standardized the representation, storage, and communication of pathology images acquired with whole-slide scanners [139]. Common acquisition protocols could reduce the variability in slide preparation and digitization procedures and scanner models among different centers and improve the performance of AI detection systems.

5.2. Data Collection and Curation

Given their skills in numerical analysis and clinical integration, MPs can significantly aid in the management of aggregate data [4], which will include clinical and image data from multiple modalities, such as PET, CT, radiography MRI, ultrasound, daily CBCT, hybrid imaging, such as PET/CT and PET/MRI, 3D/4D and image time series, and 3D/4D dose distribution from RT. MP will be involved in the development of metrics to assess the quality and completeness of data, methods to curate data, and QA programs of data archives [140].

CAD systems and other AI-based decision systems using images as input will need minimum quality specification and acquisition protocols in order to ensure output accuracy. The MP can ensure that the images are acquired according to the protocol required for correct AI use, free from relevant imaging artifacts, and correctly preprocessed [141] and harmonized [142] to reduce variability.

Moreover, MP can ensure that image data, together with their acquisition parameters and the dosimetric data from imaging and therapy, are stored in commonly accepted standards, such as the Digital Imaging and Communication in Medicine (DICOM), or comparable format and can create new standards for raw acquisition data to be stored in the standard format [143]. MP will necessarily oversee storage, security, and integrity of the large, machine-readable data collections needed to build a model [103]. The QA of datasets is a guarantee for the clinician, patient, and patient associations of the ethical and unbiased use of patients' health data by AI systems.

5.3. Commissioning and Validation of AI

Commissioning of AI tools is a series of tests to assess if the system installed in the local site operates correctly and is ready for clinical use. The commissioning tasks, tests, schedule, and tolerances, with the required equipment and human resources, should be planned before installation [30]. The test plan could consist, for example, of applying AI to a set of well-known clinical cases, for which ground truth data are available. Comparison of different ML methods on the same dataset is useful and can show which ML algorithms have the best performance and which are more prone to overfitting data for the task at hand [85,144]. A technique called adversarial ML, where attempts to deceive models are carried out with a number of crafted configurations of data, e.g., by adding noise to images, can be used for quality assessment of many classes of ML and DL algorithms [145,146].

The lack of interpretability of AI systems—or 'black-box' problem—constitutes an obstacle towards their adoption in the clinic [10]. Monitoring AI performance by proper

quality controls that test the models in well-known situations can improve the interpretability of models, as well as assessing architectures of DL models and their output using activation and feature maps.

An initiative led by the US FDA, the Microarray Sequencing Quality Control MAQC/SEQC [147], invites researchers to submit their models, features selected as important, and performance estimates to a specific data analysis plan (DAP), which includes ML and statistical crosscheck, before performing external validation data [100].

Validation, e.g., using the criteria in the TRIPOD statement [148], is required because many of the available AI models are trained using small datasets, and although augmentation and resampling methods are frequently applied, they are affected by overfitting and poor generalizability and reproducibility [112]. Large and possibly multi-institutional datasets, independent from the training datasets with realistic variability and the lowest bias as possible, are needed for validation. These can be achieved by increasing the level of collaboration among institutions [112], and the MP can play a role in checking the compliance with the required standards.

5.4. AI in Radiotherapy

MPs contributed to making radiotherapy into a frontier of personalized precision medicine by developing CT-based dose calculation, treatment planning, and image-guided radiation therapy (IGRT) [90]. Other traditional domains of MPs in radiotherapy include quality assurance and radiation protection [90]. MPs have been also at the forefront in using AI in RT, leading to the implementation of knowledge-based treatment planning, where ML algorithms are trained on the dataset, comprising patient images, contours, clinical information, and treatment plans performed by experienced MPs to automatically develop high-quality plans, allowing to accelerate radiotherapy plan design [46].

As with any other ML-based procedures, auto-planning systems also are as good as their human-generated training data, and their outcome will need to be tested and finally approved. Oftentimes, the proposed plan will need to be customized and modified by clinical MPs because of the unique anatomy of every patient. More importantly, when potential issues are identified for a specific plan, MPs communicate with other team members, such as physicians, therapists, and dosimetrists, to reach a clinically acceptable solution [149].

MPs are involved in validation and quality assurance of dose predicted by DL [90], which can be tested by properly designed in-phantom film/ion chamber measurements according to dosimetry protocols and benchmarking against previously established dose calculation algorithms. Another critical aspect is also investigating how the uncertainties of dose affect prognostic or predictive dosomic models [90].

Given their familiarity with imaging devices and LINACs derived from managing QA programs, MP will have a critical role in the analysis of AI applied to the quality control of LINACs. When an AI tool predicts a machine failure, MPs can help identify the cause of the issue and corrective actions, such as calibrations [149].

5.5. Safety/Risk Management

One of the key activities of the MP is patient safety management that is the evaluation of medical devices and procedures to guarantee the safety of patients. MPs are trained to prevent and analyze accidents [149] by using risk assessment, which consists of the analysis of events potentially involving accidental medical exposures or injury to a patient [150], and failure modes and effects analysis (FMEA) [151].

ML has the potential to reduce imaging radiation exposure, which is a hazard for patients and workers, without penalizing image quality [152].

5.6. Periodical Tests

QA should be applied to AI systems themselves, which, having an impact on patient's health, should be considered as medical devices [153]. Physicists are also responsible for

ensuring that clinically used AI algorithms continue to perform with the desired level of accuracy by conducting an appropriate routine QA test program with clearly established frequency, metrics, tolerance levels, and actions to be performed in case of test failure [103]. The frequency and nature of the series of tests will be in need of frequent updates, given the rapid pace of evolution of AI.

This is especially important for those AI systems that, being constantly learning and updating, will be subject to change in terms of their response and accuracy [94,119]. At the same time, it is critical to assess the effect of the decay of the relevance of the training data due to changes in practices (e.g., changes in prescribed dose and dose per fractions) [94].

5.7. Training of AI Users

According to a white paper, the Canadian Association of Radiologists [154] should provide practitioners with an understanding of the value, the pitfalls, weaknesses, and potential errors that may occur in the use of AI products [154]. The medical physics associations are launching initiatives to provide appropriate training and education programs in the field of AI applied to imaging and therapy [90]. On the other hand, being skilled at communication and divulgation of science, MPs are critical to establishing a common language with other professionals and patients [155]; MPs can take part in education and training in the use of AI of other health care professionals, and be a part of the interdisciplinary team working for the effective, efficient, and safe delivery of AI in the clinic [3].

5.8. Research in AI

MPs are often active researchers and, having expertise also in statistics, mathematics, and informatics, are suitable for research in AI. Extensive research is needed to understand how to successfully introduce AI and define the use and characteristics of AI in clinical practice [119].

Other active areas of research where MPs will be primarily involved include assessing data veracity and validity, developing metrics for completeness, accuracy, correctness, and consistency, and perform data cleaning activities [140]. Physicists should promote the integration of digital information from diagnostic and therapeutic procedures with genotyping and phenotyping data into large data sets acquisition across all areas (clinical, dosimetric, imaging, molecular, pathological, etc.), requiring multi-institutional and multinational collaboration [24,90]. Examples of this are The Cancer Imaging Archive (TCIA) [156] and the Platform for Imaging in Precision Medicine (PRISM) platform [157].

The specific task for MPs in AI research includes the definition of the problem to be solved and determining its category (e.g., classification, regression, pattern recognition) in the lexicon of AI, choosing proper models to be trained, determining a strategy for collecting data from the appropriate dataset, and validating the model [103]. MPs also need to investigate and report the possible pitfalls of the AI-based methods developed and on how to overcome them. Besides, challenging is a personalizing therapy according to AI output, e.g., dose painting in radiotherapy [90].

Privacy, security, secure access to health information, de-identification of sensitive data, and obtaining informed consent, which are also of concern in research areas, become more relevant in the era of big data. The MP involved in these research areas will be required to apply the statements and recommendations released by governmental agencies, scientists, healthcare providers, companies, and other interested parties and will have an active role in formulating these statements [140].

Moreover, if MPs work at developing AI models or fine-tuning them on their data, they have to carefully understand and address the limitations of the data used for training and of the trained models [94]. Exploring multiple approaches, such as different feature selection and ML methods and their combinations, can help in understanding these limitations.

The Findability, Accessibility, Interoperability, and Reusability (FAIR) principles are intended to guide researchers into data management and reporting [158]. The methodology of research studies should be detailed thoroughly, including also deep learning architectures

and optimization parameters, and the datasets used to train models should be clearly described in order to increase reproducibility and facilitate meta-analysis. Moreover, decision, automation, and prediction models relying on AI must be tested in independent and sufficiently large datasets to compare their validity against established methods, including conventional biomarkers (e.g., clinical, radiological, etc.). The codes and data used for training and testing the models should be made publicly available, e.g., by The Cancer Image Archive. More guidelines for improving transparency and reproducibility of models can be found in the TRIPOD [148].

6. Conclusions

AI can extend the expertise area of MPs, extracting even more information to improve patient care, and the MP is ready to welcome the AI revolution. On the other hand, the MPs' knowledge and skills will be required and beneficial for safe and optimal implementation of AI, especially in radiological sciences, and their involvement in the multidisciplinary AI team is crucial.

Author Contributions: Writing—Original Draft preparation: M.A., M.I.; Writing—Review & Editing: M.A., A.T., F.B., C.T., M.S., M.I. All authors have read and agreed to the published version of the manuscript.

Funding: This research was funded by the Associazione Italiana di Fisica Medica e Sanitaria (AIFM).

Institutional Review Board Statement: Not applicable.

Informed Consent Statement: Not applicable.

Data Availability Statement: Not applicable.

Conflicts of Interest: The authors declare no conflict of interest.

References

1. Hashimoto, D.A.; Rosman, G.; Rus, D.; Meireles, O.R. Artificial Intelligence in Surgery: Promises and Perils. *Ann. Surg.* **2018**, *268*, 70–76. [CrossRef]
2. Shen, C.; Nguyen, D.; Zhou, Z.; Jiang, S.B.; Dong, B.; Jia, X. An introduction to deep learning in medical physics: Advantages. potential, and challenges. *Phys. Med. Biol.* **2020**, *65*, 05TR01. [CrossRef]
3. Xing, L.; Krupinski, E.A.; Cai, J. Artificial intelligence will soon change the landscape of medical physics research and practice. *Med. Phys.* **2018**, *45*, 1791–1793. [CrossRef]
4. Samei, E.; Grist, T.M. Why physics in medicine? *Phys. Med.* **2019**, *64*, 319–322. [CrossRef]
5. Samei, E.; Pawlicki, T.; Bourland, D.; Chin, E.; Das, S.; Fox, M.; Freedman, D.J.; Hangiandreou, N.; Jordan, D.; Martin, M.; et al. Redefining and reinvigorating the role of physics in clinical medicine: A Report from the AAPM Medical Physics 3.0 Ad Hoc Committee. *Med. Phys.* **2018**, *45*, e783–e789. [CrossRef] [PubMed]
6. Biehl, M.; Caticha, N.; Opper, M.; Villmann, T. Statistical Physics of Learning and Inference. In Proceedings of the European Symposium on Artificial Neural Networks, Computational Intelligence and Machine Learning, Bruges, Belgium, 24–26 April 2019.
7. Ramezanpour, A.; Beam, A.L.; Chen, J.H.; Mashaghi, A. Statistical Physics for Medical Diagnostics: Learning, Inference, and Optimization Algorithms. *Diagnostics* **2020**, *10*, 972. [CrossRef] [PubMed]
8. Tang, X.; Wang, B.; Rong, Y. Artificial intelligence will reduce the need for clinical medical physicists. *J. Appl. Clin. Med. Phys.* **2018**, *19*, 6–9. [CrossRef] [PubMed]
9. Thompson, R.F.; Valdes, G.; Fuller, C.D.; Carpenter, C.M.; Morin, O.; Aneja, S.; Lindsay, W.D.; Aerts, H.J.W.L.; Agrimson, B.C.; Deville, C., Jr.; et al. Artificial intelligence in radiation oncology: A specialty-wide disruptive transformation? *Radiother. Oncol.* **2018**, *129*, 421–426. [CrossRef]
10. Avanzo, M.; Wei, L.; Stancanello, J.; Vallieres, M.; Rao, A.; Morin, O.; Mattonen, S.A.; El Naqa, I. Machine and deep learning methods for radiomics. *Med. Phys.* **2020**, *47*, e185–e202. [CrossRef]
11. Chen, S.; Zhou, S.; Yin, F.F.; Marks, L.B.; Das, S.K. Investigation of the support vector machine algorithm to predict lung radiation-induced pneumonitis. *Med. Phys.* **2007**, *34*, 3808–3814. [CrossRef]
12. Avanzo, M.; Stancanello, J.; El Naqa, I. Beyond imaging: The promise of radiomics. *Phys. Med.* **2017**, *38*, 122–139. [CrossRef]
13. Galar, M.; Fernandez, A.; Barrenechea, E.; Bustince, H.; Herrera, F. A Review on Ensembles for the Class Imbalance Problem: Bagging-, Boosting-, and Hybrid-Based Approaches. *IEEE Trans. Syst. Man, Cybern. Part C Applications Rev.* **2012**, *42*, 463–484. [CrossRef]
14. Ben-Bassat, M.; Klove, K.L.; Weil, M.H. Sensitivity Analysis in Bayesian Classification Models: Multiplicative Deviations. *IEEE Trans. Pattern Anal. Mach. Intell.* **1980**, *PAMI-2*, 261–266. [CrossRef] [PubMed]

15. Kukar, M.; Kononenko, I.; Silvester, T. Machine learning in prognosis of the femoral neck fracture recovery. *Artif. Intell. Med.* **1996**, *8*, 431–451. [CrossRef]
16. Tseng, H.; Wei, L.; Cui, S.; Luo, Y.; Haken, R.K.T.; El Naqa, I. Machine Learning and Imaging Informatics in Oncology. *Oncology* **2020**, *98*, 344–362. [CrossRef] [PubMed]
17. Syeda-Mahmood, T. Role of Big Data and Machine Learning in Diagnostic Decision Support in Radiology. *J. Am. Coll. Radiol.* **2018**, *15*, 569–576. [CrossRef]
18. Azmandian, F.; Kaeli, D.; Dy, J.G.; Hutchinson, E.; Ancukiewicz, M.; Niemierko, A.; Jiang, S.B. Towards the development of an error checker for radiotherapy treatment plans: A preliminary study. *Phys. Med. Biol.* **2007**, *52*, 6511–6524. [CrossRef]
19. Chetvertkov, M.A.; Siddiqui, F.; Kim, J.; Chetty, I.; Kumarasiri, A.; Liu, C.; Gordon, J.J. Use of regularized principal component analysis to model anatomical changes during head and neck radiation therapy for treatment adaptation and response assessment. *Med Phys.* **2016**, *43*, 5307–5319. [CrossRef]
20. Maaten, L.v.d.; Hinton, G.E. Visualizing Data using t-SNE. *J. Mach. Learn. Res.* **2008**, *9*, 2579–2605.
21. Sanders, J.C.; Ritt, P.; Kuwert, T.; Vija, A.H.; Maier, A.K. Fully Automated Data-Driven Respiratory Signal Extraction From SPECT Images Using Laplacian Eigenmaps. *IEEE Trans. Med Imaging* **2016**, *35*, 2425–2435. [CrossRef] [PubMed]
22. Groenhof, T.K.J.; Koers, L.R.; Blasse, E.; de Groot, M.; Grobbee, D.E.; Bots, M.L.; Asselbergs, F.W.; Lely, A.T.; Haitjema, S.; van Solinge, W.; et al. Data mining information from electronic health records produced high yield and accuracy for current smoking status. *J. Clin. Epidemiol.* **2020**, *118*, 100–106. [CrossRef]
23. Gultepe, E.; Green, J.P.; Nguyen, H.; Adams, J.; Albertson, T.; Tagkopoulos, I. From vital signs to clinical outcomes for patients with sepsis: A machine learning basis for a clinical decision support system. *J. Am. Med Inform. Assoc.* **2014**, *21*, 315–325. [CrossRef]
24. Chamunyonga, C.; Edwards, C.; Caldwell, P.; Rutledge, P.; Burbery, J. The Impact of Artificial Intelligence and Machine Learning in Radiation Therapy: Considerations for Future Curriculum Enhancement. *J. Med Imaging Radiat. Sci.* **2020**, *51*, 214–220. [CrossRef]
25. Pons, E.; Braun, L.M.; Hunink, M.G.; Kors, J.A. Natural Language Processing in Radiology: A Systematic Review. *Radiology* **2016**, *279*, 329–343. [CrossRef] [PubMed]
26. Kreimeyer, K.; Foster, M.; Pandey, A.; Arya, N.; Halford, G.; Jones, S.F.; Forshee, R.; Walderhaug, M.; Botsis, T. Natural language processing systems for capturing and standardizing unstructured clinical information: A systematic review. *J. Biomed. Inform.* **2017**, *73*, 14–29. [CrossRef] [PubMed]
27. Burger, G.; Abu-Hanna, A.; de Keizer, N.; Cornet, R. Natural language processing in pathology: A scoping review. *J. Clin. Pathol.* **2016**, *69*, 949–955. [CrossRef] [PubMed]
28. Benke, K.; Benke, G. Artificial Intelligence and Big Data in Public Health. *Int. J. Environ. Res. Public Health* **2018**, *15*, 2796. [CrossRef]
29. Castiglioni, I.; Gallivanone, F.; Soda, P.; Avanzo, M.; Stancanello, J.; Aiello, M.; Interlenghi, M.; Salvatore, M. AI-based applications in hybrid imaging: How to build smart and truly multi-parametric decision models for radiomics. *Eur. J. Nucl. Med. Mol. Imaging* **2019**, *46*, 2673–2699. [CrossRef] [PubMed]
30. Mahadevaiah, G.; Rv, P.; Bermejo, I.; Jaffray, D.; Dekker, A.; Wee, L. Artificial intelligence-based clinical decision support in modern medical physics: Selection, acceptance, commissioning, and quality assurance. *Med Phys.* **2020**, *47*, e228–e235. [CrossRef]
31. Welch, M.L.; McIntosh, C.; McNiven, A.; Huang, S.H.; Zhang, B.B.; Wee, L.; Traverso, A.; O'Sullivan, B.; Hoebers, F.; Dekker, A.; et al. User-controlled pipelines for feature integration and head and neck radiation therapy outcome predictions. *Phys. Medica* **2020**, *70*, 145–152. [CrossRef]
32. El Naqa, I.; Li, R.; Murphy, M.J. *Machine Learning in Radiation Oncology: Theory and Applications*; Springer: Berlin, Germany, 2015.
33. Giger, M.L.; Karssemeijer, N.; Schnabel, J.A. Breast image analysis for risk assessment, detection, diagnosis, and treatment of cancer. *Annu. Rev. Biomed. Eng.* **2013**, *15*, 327–357. [CrossRef] [PubMed]
34. Elter, M.; Horsch, A. CADx of mammographic masses and clustered microcalcifications: A review. *Med. Phys.* **2009**, *36*, 2052–2068. [CrossRef]
35. Chen, C.H.; Chang, C.K.; Tu, C.Y.; Liao, W.C.; Wu, B.R.; Chou, K.T.; Chiou, Y.R.; Yang, S.N.; Zhang, G.; Huang, T.C. Radiomic features analysis in computed tomography images of lung nodule classification. *PLoS ONE* **2018**, *13*, e0192002. [CrossRef]
36. Weng, Q.; Zhou, L.; Wang, H.; Hui, J.; Chen, M.; Pang, P.; Zheng, L.; Xu, M.; Wang, Z.; Ji, J. A radiomics model for determining the invasiveness of solitary pulmonary nodules that manifest as part-solid nodules. *Clin. Radiol.* **2019**, *74*, 933–943. [CrossRef]
37. Botta, F.; Raimondi, S.; Rinaldi, L.; Bellerba, F.; Corso, F.; Bagnardi, V.; Origgi, D.; Minelli, R.; Pitoni, G.; Petrella, F.; et al. Association of a CT-Based Clinical and Radiomics Score of Non-Small Cell Lung Cancer (NSCLC) with Lymph Node Status and Overall Survival. *Cancers* **2020**, *12*, 1432. [CrossRef] [PubMed]
38. Cong, M.; Feng, H.; Ren, J.L.; Xu, Q.; Cong, L.; Hou, Z.; Wang, Y.Y.; Shi, G. Development of a predictive radiomics model for lymph node metastases in pre-surgical CT-based stage IA non-small cell lung cancer. *Lung Cancer* **2020**, *139*, 73–79. [CrossRef]
39. Avanzo, M.; Stancanello, J.; Pirrone, G.; Sartor, G. Radiomics and deep learning in lung cancer. *Strahlenther. Onkol.* **2020**, *196*, 879–887. [CrossRef]
40. Stanzione, A.; Gambardella, M.; Cuocolo, R.; Ponsiglione, A.; Romeo, V.; Imbriaco, M. Prostate MRI radiomics: A systematic review and radiomic quality score assessment. *Eur. J. Radiol.* **2020**, *129*, 109095. [CrossRef] [PubMed]

41. Algohary, A.; Viswanath, S.; Shiradkar, R.; Ghose, S.; Pahwa, S.; Moses, D.; Jambor, I.; Shnier, R.; Bohm, M.; Haynes, A.M.; et al. Radiomic features on MRI enable risk categorization of prostate cancer patients on active surveillance: Preliminary findings. *J. Magn. Reson. Imaging* **2018**, *48*, 818–828. [CrossRef]
42. Zhang, Z.; Yang, J.; Ho, A.; Jiang, W.; Logan, J.; Wang, X.; Brown, P.D.; McGovern, S.L.; Guha-Thakurta, N.; Ferguson, S.D.; et al. A predictive model for distinguishing radiation necrosis from tumour progression after gamma knife radiosurgery based on radiomic features from MR images. *Eur. Radiol.* **2018**, *28*, 2255–2263. [CrossRef]
43. Hatt, M.; Tixier, F.; Visvikis, D.; Le Rest, C.C. Radiomics in PET/CT: More Than Meets the Eye? *J. Nucl. Med.* **2016**, *58*, 365–366. [CrossRef]
44. Lee, S.E.; Han, K.; Kwak, J.Y.; Lee, E.; Kim, E.K. Radiomics of US texture features in differential diagnosis between triple-negative breast cancer and fibroadenoma. *Sci. Rep.* **2018**, *8*, 1–8. [CrossRef]
45. Sapate, S.G.; Mahajan, A.; Talbar, S.N.; Sable, N.; Desai, S.; Thakur, M. Radiomics based detection and characterization of suspicious lesions on full field digital mammograms. *Comput. Methods Progr. Biomed.* **2018**, *163*, 1–20. [CrossRef]
46. Jarrett, D.; Stride, E.; Vallis, K.; Gooding, M.J. Applications and limitations of machine learning in radiation oncology. *Br. J. Radiol.* **2019**, *92*, 20190001. [CrossRef] [PubMed]
47. Skourt, B.A.; El Hassani, A.; Majda, A. Lung CT Image Segmentation USING Deep Neural Networks. *Procedia Comput. Sci.* **2018**, *127*, 109–113. [CrossRef]
48. Zhong, Z.; Kim, Y.; Zhou, L.; Plichta, K.; Allen, B.; Buatti, J.; Wu, X. 3D fully convolutional networks for co-segmentation of tumors on PET-CT images. In Proceedings of the 2018 IEEE 15th International Symposium on Biomedical Imaging (ISBI 2018), Washington, DC, USA, 4–7 April 2018; pp. 228–231.
49. Peng, Z.; Fang, X.; Yan, P.; Shan, H.; Liu, T.; Pei, X.; Wang, G.; Liu, B.; Kalra, M.K.; Xu, X.G. A method of rapid quantification of patient-specific organ doses for CT using deep-learning-based multi-organ segmentation and GPU-accelerated Monte Carlo dose computing. *Med. Phys.* **2020**, *47*, 2526–2536. [CrossRef]
50. Gotz, T.I.; Schmidkonz, C.; Chen, S.; Al-Baddai, S.; Kuwert, T.; Lang, E.W. A deep learning approach to radiation dose estimation. *Phys. Med. Biol.* **2019**, *65*, 035007. [CrossRef]
51. Kaplan, S.; Zhu, Y.M. Full-Dose PET Image Estimation from Low-Dose PET Image Using Deep Learning: A Pilot Study. *J. Digit. Imaging* **2019**, *32*, 773–778. [CrossRef] [PubMed]
52. Roser, P.; Zhong, X.; Birkhold, A.; Strobel, N.; Kowarschik, M.; Fahrig, R.; Maier, A. Physics-driven learning of x-ray skin dose distribution in interventional procedures. *Med. Phys.* **2019**, *46*, 4654–4665. [CrossRef]
53. Meineke, A.; Rubbert, C.; Sawicki, L.M.; Thomas, C.; Klosterkemper, Y.; Appel, E.; Caspers, J.; Bethge, O.T.; Kropil, P.; Antoch, G.; et al. Potential of a machine-learning model for dose optimization in CT quality assurance. *Eur. Radiol.* **2019**, *29*, 3705–3713. [CrossRef]
54. Gong, K.; Guan, J.; Liu, C.; Qi, J. PET Image Denoising Using a Deep Neural Network Through Fine Tuning. *IEEE Trans. Radiat. Plasma Med. Sci.* **2019**, *3*, 153–161. [CrossRef]
55. Xie, S.; Zheng, X.; Chen, Y.; Xie, L.; Liu, J.; Zhang, Y.; Yan, J.; Zhu, H.; Hu, Y. Artifact Removal using Improved GoogLeNet for Sparse-view CT Reconstruction. *Sci. Rep.* **2018**, *8*, 1–9. [CrossRef]
56. Han, X. MR-based synthetic CT generation using a deep convolutional neural network method. *Med. Phys.* **2017**, *44*, 1408–1419. [CrossRef]
57. Kleesiek, J.; Morshuis, J.N.; Isensee, F.; Deike-Hofmann, K.; Paech, D.; Kickingereder, P.; Köthe, U.; Rother, C.; Forsting, M.; Wick, W.; et al. Can Virtual Contrast Enhancement in Brain MRI Replace Gadolinium: A Feasibility Study. *Investig. Radiol.* **2019**, *54*, 653–660. [CrossRef]
58. Litjens, G.; Kooi, T.; Bejnordi, B.E.; Setio, A.A.A.; Ciompi, F.; Ghafoorian, M.; van der Laak, J.A.W.M.; van Ginneken, B.; Sanchez, C.I. A survey on deep learning in medical image analysis. *Med. Image Anal.* **2017**, *42*, 60–88. [CrossRef] [PubMed]
59. Kesner, A.; Schmidtlein, C.R.; Kuntner, C. Real-time data-driven motion correction in PET. *EJNMMI Phys.* **2019**, *6*, 3. [CrossRef] [PubMed]
60. Li, M.; Fu, S.; Zhu, Y.; Liu, Z.; Chen, S.; Lu, L.; Liang, C. Computed tomography texture analysis to facilitate therapeutic decision making in hepatocellular carcinoma. *Oncotarget* **2016**, *7*, 13248–13259. [CrossRef]
61. Yu, J.Y.; Zhang, H.P.; Tang, Z.Y.; Zhou, J.; He, X.J.; Liu, Y.Y.; Liu, X.J.; Guo, D.J. Value of texture analysis based on enhanced MRI for predicting an early therapeutic response to transcatheter arterial chemoembolisation combined with high-intensity focused ultrasound treatment in hepatocellular carcinoma. *Clin. Radiol.* **2018**, *73*, 758.e9–758.e18. [CrossRef]
62. Iezzi, R.; Goldberg, S.N.; Merlino, B.; Posa, A.; Valentini, V.; Manfredi, R. Artificial Intelligence in Interventional Radiology: A Literature Review and Future Perspectives. *J. Oncol.* **2019**, *2019*, 6153041. [CrossRef] [PubMed]
63. van Timmeren, J.E.; van Elmpt, W.; Leijenaar, R.T.H.; Reymen, B.; Monshouwer, R.; Bussink, J.; Paelinck, L.; Bogaert, E.; de Wagter, C.; Elhaseen, E.; et al. Longitudinal radiomics of cone-beam CT images from non-small cell lung cancer patients: Evaluation of the added prognostic value for overall survival and locoregional recurrence. *Radiother. Oncol.* **2019**, *136*, 78–85. [CrossRef] [PubMed]
64. Rahmim, A.; Huang, P.; Shenkov, N.; Fotouhi, S.; Davoodi-Bojd, E.; Lu, L.; Mari, Z.; Soltanian-Zadeh, H.; Sossi, V. Improved prediction of outcome in Parkinson's disease using radiomics analysis of longitudinal DAT SPECT images. *Neuroimage Clin.* **2017**, *16*, 539–544. [CrossRef] [PubMed]
65. Moraru, A.D.; Costin, D.; Moraru, R.L.; Branisteanu, D.C. Artificial intelligence and deep learning in ophthalmology—Present and future (Review). *Exp. Ther. Med.* **2020**, *20*, 3469–3473. [CrossRef]

66. Ricciardi, C.; Cantoni, V.; Improta, G.; Iuppariello, L.; Latessa, I.; Cesarelli, M.; Triassi, M.; Cuocolo, A. Application of data mining in a cohort of Italian subjects undergoing myocardial perfusion imaging at an academic medical center. *Comput. Methods Progr. Biomed.* **2020**, *189*, 105343. [CrossRef]
67. Moccia, S.; Banali, R.; Martini, C.; Muscogiuri, G.; Pontone, G.; Pepi, M.; Caiani, E.G. Development and testing of a deep learning-based strategy for scar segmentation on CMR-LGE images. *MAGMA Magn. Reson. Mater. Phys. Biol. Med.* **2018**, *32*, 187–195. [CrossRef]
68. Stoel, B. Use of artificial intelligence in imaging in rheumatology—Current status and future perspectives. *RMD Open* **2020**, *6*, e001063. [CrossRef]
69. Bera, K.; Schalper, K.A.; Rimm, D.L.; Velcheti, V.; Madabhushi, A. Artificial intelligence in digital pathology—New tools for diagnosis and precision oncology. *Nat. Rev. Clin. Oncol.* **2019**, *16*, 703–715. [CrossRef] [PubMed]
70. Piehowski, P.D.; Zhu, Y.; Bramer, L.M.; Stratton, K.G.; Zhao, R.; Orton, D.J.; Moore, R.J.; Yuan, J.; Mitchell, H.D.; Gao, Y.; et al. Automated mass spectrometry imaging of over 2000 proteins from tissue sections at 100-µm spatial resolution. *Nat. Commun.* **2020**, *11*, 8. [CrossRef] [PubMed]
71. Alexandrov, T. Spatial Metabolomics and Imaging Mass Spectrometry in the Age of Artificial Intelligence. *Annu. Rev. Biomed. Data Sci.* **2020**, *3*, 61–87. [CrossRef]
72. Voulodimos, A.; Doulamis, N.; Doulamis, A.; Protopapadakis, E. Deep Learning for Computer Vision: A Brief Review. *Comput. Intell. Neurosci.* **2018**, *2018*, 7068349. [CrossRef] [PubMed]
73. Cai, T.; Giannopoulos, A.A.; Yu, S.; Kelil, T.; Ripley, B.; Kumamaru, K.K.; Rybicki, F.J.; Mitsouras, D. Natural Language Processing Technologies in Radiology Research and Clinical Applications. *Radiographics* **2016**, *36*, 176–191. [CrossRef]
74. Zaharchuk, G.; Gong, E.; Wintermark, M.; Rubin, D.; Langlotz, C.P. Deep Learning in Neuroradiology. *Am. J. Neuroradiol.* **2018**, *39*, 1776–1784. [CrossRef]
75. Vávra, P.; Roman, J.; Zonča, P.; Ihnát, P.; Němec, M.; Kumar, J.; Habib, N.; El-Gendi, A. Recent Development of Augmented Reality in Surgery: A Review. *J. Health Eng.* **2017**, *2017*, 4574172. [CrossRef]
76. Cheng, Q.; Roelofs, E.; Ramaekers, B.L.; Eekers, D.; van Soest, J.; Lustberg, T.; Hendriks, T.; Hoebers, F.; van der Laan, H.P.; Korevaar, E.W.; et al. Development and evaluation of an online three-level proton vs photon decision support prototype for head and neck cancer—Comparison of dose, toxicity and cost-effectiveness. *Radiother. Oncol.* **2016**, *118*, 281–285. [CrossRef]
77. Lustberg, T.; van Soest, J.; Gooding, M.; Peressutti, D.; Aljabar, P.; van der Stoep, J.; van Elmpt, W.; Dekker, A. Clinical evaluation of atlas and deep learning based automatic contouring for lung cancer. *Radiother. Oncol.* **2018**, *126*, 312–317. [CrossRef] [PubMed]
78. Cagni, E.; Botti, A.; Micera, R.; Galeandro, M.; Sghedoni, R.; Orlandi, M.; Iotti, C.; Cozzi, L.; Iori, M. Knowledge-based treatment planning: An inter-technique and inter-system feasibility study for prostate cancer. *Phys. Med.* **2017**, *36*, 38–45. [CrossRef]
79. Cagni, E.; Botti, A.; Wang, Y.; Iori, M.; Petit, S.F.; Heijmen, B.J.M. Pareto-optimal plans as ground truth for validation of a commercial system for knowledge-based DVH-prediction. *Phys. Med.* **2018**, *55*, 98–106. [CrossRef] [PubMed]
80. Stanhope, C.; Wu, Q.J.; Yuan, L.; Liu, J.; Hood, R.; Yin, F.F.; Adamson, J. Utilizing knowledge from prior plans in the evaluation of quality assurance. *Phys. Med. Biol.* **2015**, *60*, 4873–4891. [CrossRef]
81. Nicolae, A.; Semple, M.; Lu, L.; Smith, M.; Chung, H.; Loblaw, A.; Morton, G.; Mendez, L.C.; Tseng, C.L.; Davidson, M.; et al. Conventional vs machine learning-based treatment planning in prostate brachytherapy: Results of a Phase I randomized controlled trial. *Brachytherapy* **2020**, *19*, 470–476. [CrossRef] [PubMed]
82. Barragan-Montero, A.M.; Nguyen, D.; Lu, W.; Lin, M.H.; Norouzi-Kandalan, R.; Geets, X.; Sterpin, E.; Jiang, S. Three-dimensional dose prediction for lung IMRT patients with deep neural networks: Robust learning from heterogeneous beam configurations. *Med. Phys.* **2019**, *46*, 3679–3691. [CrossRef] [PubMed]
83. Nguyen, D.; Jia, X.; Sher, D.; Lin, M.; Iqbal, Z.; Liu, H.; Jiang, S. 3D radiotherapy dose prediction on head and neck cancer patients with a hierarchically densely connected U-net deep learning architecture. *Phys. Med. Biol.* **2019**, *64*, 065020. [CrossRef] [PubMed]
84. Mao, X.; Pineau, J.; Keyes, R.; Enger, S.A. RapidBrachyDL: Rapid Radiation Dose Calculations in Brachytherapy via Deep Learning. *Int. J. Radiat. Oncol.* **2020**, *108*, 802–812. [CrossRef]
85. Avanzo, M.; Pirrone, G.; Mileto, M.; Massarut, S.; Stancanello, J.; Baradaran-Ghahfarokhi, M.; Rink, A.; Barresi, L.; Vinante, L.; Piccoli, E.; et al. Prediction of skin dose in low-kV intraoperative radiotherapy using machine learning models trained on results of in vivo dosimetry. *Med. Phys.* **2019**, *46*, 1447–1454. [CrossRef]
86. Avanzo, M.; Pirrone, G.; Vinante, L.; Caroli, A.; Stancanello, J.; Drigo, A.; Massarut, S.; Mileto, M.; Urbani, M.; Trovo, M.; et al. Electron Density and Biologically Effective Dose (BED) Radiomics-Based Machine Learning Models to Predict Late Radiation-Induced Subcutaneous Fibrosis. *Front. Oncol.* **2020**, *10*, 490. [CrossRef]
87. Talamonti, C.; Piffer, S.; Greto, D.; Mangoni, M.; Ciccarone, A.; Dicarolo, P.; Fantacci, M.E.; Fusi, F.; Oliva, P.; Palumbo, L.; et al. Radiomic and Dosiomic Profiling of Paediatric Medulloblastoma Tumours Treated with Intensity Modulated Radiation Therapy. *Commun. Comput. Inf. Sci.* **2019**, 56–64.
88. Shi, L.; Rong, Y.; Daly, M.; Dyer, B.A.; Benedict, S.; Qiu, J.; Yamamoto, T. Cone-beam computed tomography-based delta-radiomics for early response assessment in radiotherapy for locally advanced lung cancer. *Phys. Med. Biol.* **2020**, *65*, 015009. [CrossRef]
89. Guidi, G.; Maffei, N.; Meduri, B.; D'Angelo, E.; Mistretta, G.M.; Ceroni, P.; Ciarmatori, A.; Bernabei, A.; Maggi, S.; Cardinali, M.; et al. A machine learning tool for re-planning and adaptive RT: A multicenter cohort investigation. *Phys. Med.* **2016**, *32*, 1659–1666. [CrossRef] [PubMed]

90. Peeken, J.C.; Bernhofer, M.; Wiestler, B.; Goldberg, T.; Cremers, D.; Rost, B.; Wilkens, J.J.; Combs, S.E.; Nusslin, F. Radiomics in radiooncology—Challenging the medical physicist. *Phys. Med.* **2018**, *48*, 27–36. [CrossRef] [PubMed]
91. Arabi, H.; Zaidi, H. Applications of artificial intelligence and deep learning in molecular imaging and radiotherapy. *Eur. J. Hybrid Imaging* **2020**, *4*, 17. [CrossRef]
92. Placidi, L.; Lenkowicz, J.; Cusumano, D.; Boldrini, L.; Dinapoli, N.; Valentini, V. Stability of dosomics features extraction on grid resolution and algorithm for radiotherapy dose calculation. *Phys. Med.* **2020**, *77*, 30–35. [CrossRef]
93. Delis, H.; Christaki, K.; Healy, B.; Loreti, G.; Poli, G.L.; Toroi, P.; Meghzifene, A. Moving beyond quality control in diagnostic radiology and the role of the clinically qualified medical physicist. *Phys. Med.* **2017**, *41*, 104–108. [CrossRef]
94. Kalet, A.M.; Luk, S.M.H.; Phillips, M.H. Radiation Therapy Quality Assurance Tasks and Tools: The Many Roles of Machine Learning. *Med. Phys.* **2020**, *47*, e168–e177. [CrossRef]
95. Kimura, Y.; Kadoya, N.; Tomori, S.; Oku, Y.; Jingu, K. Error detection using a convolutional neural network with dose difference maps in patient-specific quality assurance for volumetric modulated arc therapy. *Phys. Med.* **2020**, *73*, 57–64. [CrossRef] [PubMed]
96. Li, Q.; Chan, M.F. Predictive time-series modeling using artificial neural networks for Linac beam symmetry: An empirical study. *Ann. N. Y. Acad. Sci.* **2017**, *1387*, 84–94. [CrossRef] [PubMed]
97. El Naqa, I.; Irrer, J.; Ritter, T.A.; DeMarco, J.; Al-Hallaq, H.; Booth, J.; Kim, G.; Alkhatib, A.; Popple, R.; Perez, M.; et al. Machine learning for automated quality assurance in radiotherapy: A proof of principle using EPID data description. *Med Phys.* **2019**, *46*, 1914–1921. [CrossRef]
98. Nyflot, M.J.; Thammasorn, P.; Wootton, L.S.; Ford, E.C.; Chaovalitwongse, W.A. Deep learning for patient-specific quality assurance: Identifying errors in radiotherapy delivery by radiomic analysis of gamma images with convolutional neural networks. *Med. Phys.* **2019**, *46*, 456–464. [CrossRef]
99. Valdes, G.; Chan, M.F.; Lim, S.B.; Scheuermann, R.; Deasy, J.O.; Solberg, T.D. IMRT QA using machine learning: A multi-institutional validation. *J. Appl. Clin. Med. Phys.* **2017**, *18*, 279–284. [CrossRef] [PubMed]
100. Bizzego, A.; Bussola, N.; Chierici, M.; Maggio, V.; Francescatto, M.; Cima, L.; Cristoforetti, M.; Jurman, G.; Furlanello, C. Evaluating reproducibility of AI algorithms in digital pathology with DAPPER. *PLoS Comput. Biol.* **2019**, *15*, e1006269. [CrossRef] [PubMed]
101. Shaikhina, T.; Lowe, D.; Daga, S.; Briggs, D.; Higgins, R.; Khovanova, N. Machine Learning for Predictive Modelling based on Small Data in Biomedical Engineering. *IFAC-PapersOnLine* **2015**, *48*, 469–474. [CrossRef]
102. Chatterjee, A.; Vallières, M.; Dohan, A.; Levesque, I.R.; Ueno, Y.; Bist, V.; Saif, S.; Reinhold, C.; Seuntjens, J. An Empirical Approach for Avoiding False Discoveries When Applying High-Dimensional Radiomics to Small Datasets. *IEEE Trans. Radiat. Plasma Med. Sci.* **2019**, *3*, 201–209. [CrossRef]
103. Cui, S.; Tseng, H.H.; Pakela, J.; Haken, R.K.T.; El Naqa, I. Introduction to machine and deep learning for medical physicists. *Med. Phys.* **2020**, *47*, e127–e147. [CrossRef]
104. Stepwise Regression, F.G.R. *Anonymous Wiley International Encyclopedia of Marketing*; American Cancer Society: Atlanta, GA, USA, 2010.
105. Parmar, C.; Grossmann, P.; Rietveld, D.; Rietbergen, M.M.; Lambin, P.; Aerts, H.J. Radiomic Machine-Learning Classifiers for Prognostic Biomarkers of Head and Neck Cancer. *Front. Oncol.* **2015**, *5*, 272. [CrossRef]
106. Lian, C.; Ruan, S.; Denoeux, T.; Jardin, F.; Vera, P. Selecting radiomic features from FDG-PET images for cancer treatment outcome prediction. *Med. Image Anal.* **2016**, *32*, 257–268. [CrossRef]
107. Wu, W.; Parmar, C.; Grossmann, P.; Quackenbush, J.; Lambin, P.; Bussink, J.; Mak, R.; Aerts, H.J. Exploratory Study to Identify Radiomics Classifiers for Lung Cancer Histology. *Front. Oncol.* **2016**, *6*, 71. [CrossRef]
108. Hinton, G.E.; Srivastava, N.; Krizhevsky, A.; Sutskever, I.; Salakhutdinov, R.R. Improving neural networks by preventing co-adaptation of feature detectors. *arXiv* **2012**, arXiv:1207.0580.
109. Lemaitre, G.; Nogueira, F.; Aridas, C.K. Imbalanced-learn: A Python Toolbox to Tackle the Curse of Imbalanced Datasets in Machine Learning. *arXiv* **2016**, arXiv:1609.06570.
110. Buda, M.; Maki, A.; Mazurowski, M.A. A systematic study of the class imbalance problem in convolutional neural networks. *arXiv* **2017**, arXiv:1710.05381. [CrossRef] [PubMed]
111. Chen, J.H.; Alagappan, M.; Goldstein, M.K.; Asch, S.M.; Altman, R.B. Decaying relevance of clinical data towards future decisions in data-driven inpatient clinical order sets. *Int. J. Med. Inform.* **2017**, *102*, 71–79. [CrossRef] [PubMed]
112. Nensa, F.; Demircioglu, A.; Rischpler, C. Artificial Intelligence in Nuclear Medicine. *J. Nucl. Med.* **2019**, *60*, 29S–37S. [CrossRef]
113. Li, H.; Zhu, Y.; Burnside, E.S.; Drukker, K.; Hoadley, K.A.; Fan, C.; Conzen, S.D.; Whitman, G.J.; Sutton, E.J.; Net, J.M.; et al. MR Imaging Radiomics Signatures for Predicting the Risk of Breast Cancer Recurrence as Given by Research Versions of MammaPrint, Oncotype DX, and PAM50 Gene Assays. *Radiology* **2016**, *281*, 382–391. [CrossRef]
114. Aerts, H.J.; Grossmann, P.; Tan, Y.; Oxnard, G.G.; Rizvi, N.; Schwartz, L.H.; Zhao, B. Defining a Radiomic Response Phenotype: A Pilot Study using targeted therapy in NSCLC. *Sci. Rep.* **2016**, *6*, 33860. [CrossRef]
115. Geis, J.R.; Brady, A.P.; Wu, C.C.; Spencer, J.; Ranschaert, E.; Jaremko, J.L.; Langer, S.G.; Kitts, A.B.; Birch, J.; Shields, W.F. Ethics of Artificial Intelligence in Radiology: Summary of the Joint European and North American Multisociety Statement. *Can. Assoc. Radiol. J.* **2019**, *70*, 329–334. [CrossRef]
116. Lai, M.C.; Brian, M.; Mamzer, M.F. Perceptions of artificial intelligence in healthcare: Findings from a qualitative survey study among actors in France. *J. Transl. Med.* **2020**, *18*, 1–13. [CrossRef]

117. Pesapane, F.; Codari, M.; Sardanelli, F. Artificial intelligence in medical imaging: Threat or opportunity? Radiologists again at the forefront of innovation in medicine. *Eur. Radiol. Exp.* **2018**, *2*, 1–10. [CrossRef]
118. Townsend, D.; Cheng, Z.; Georg, D.; Drexler, W.; Moser, E. Grand challenges in biomedical physics. *Front. Phys.* **2013**, *1*, 1. [CrossRef]
119. Sensakovic, W.F.; Mahesh, M. Role of the Medical Physicist in the Health Care Artificial Intelligence Revolution. *J. Am. Coll. Radiol.* **2019**, *16*, 393–394. [CrossRef] [PubMed]
120. Cody, D.D.; Fisher, T.S.; Gress, D.A.; Layman, R.R., Jr.; McNitt-Gray, M.F.; Pizzutiello, R.J., Jr.; Fairobent, L.A. AAPM medical physics practice guideline 1.a: CT protocol management and review practice guideline. *J. Appl. Clin. Med Phys.* **2013**, *14*, 3–12. [PubMed]
121. Mackin, D.; Fave, X.; Zhang, L.; Fried, D.; Yang, J.; Taylor, B.; Rodriguez-Rivera, E.; Dodge, C.; Jones, A.K.; Court, L. Measuring Computed Tomography Scanner Variability of Radiomics Features. *Investig. Radiol.* **2015**, *50*, 757–765. [CrossRef] [PubMed]
122. Fave, X.; Cook, M.; Frederick, A.; Zhang, L.; Yang, J.; Fried, D.; Stingo, F.; Court, L. Preliminary investigation into sources of uncertainty in quantitative imaging features. *Comput. Med. Imaging Graph.* **2015**, *44*, 54–61. [CrossRef] [PubMed]
123. Samei, E.; Hoye, J.; Zheng, Y.; Solomon, J.B.; Marin, D. Design and fabrication of heterogeneous lung nodule phantoms for assessing the accuracy and variability of measured texture radiomics features in CT. *J. Med. Imaging* **2019**, *6*, 021606. [CrossRef]
124. Pfaehler, E.; Beukinga, R.J.; de Jong, J.R.; Slart, R.H.J.A.; Slump, C.H.; Dierckx, R.A.J.O.; Boellaard, R. Repeatability of (18) F-FDG PET radiomic features: A phantom study to explore sensitivity to image reconstruction settings, noise, and delineation method. *Med. Phys.* **2019**, *46*, 665–678. [CrossRef] [PubMed]
125. Bianchini, L.; Botta, F.; Origgi, D.; Rizzo, S.; Mariani, M.; Summers, P.; García-Polo, P.; Cremonesi, M.; Lascialfari, A. PETER PHAN: An MRI phantom for the optimisation of radiomic studies of the female pelvis. *Phys. Med.* **2020**, *71*, 71–81. [CrossRef] [PubMed]
126. Kim, H.; Park, C.M.; Lee, M.; Park, S.J.; Song, Y.S.; Lee, J.H.; Hwang, E.J.; Goo, J.M. Impact of Reconstruction Algorithms on CT Radiomic Features of Pulmonary Tumors: Analysis of Intra- and Inter-Reader Variability and Inter-Reconstruction Algorithm Variability. *PLoS ONE.* **2016**, *11*, e0164924. [CrossRef] [PubMed]
127. Leijenaar, R.T.; Carvalho, S.; Velazquez, E.R.; van Elmpt, W.J.; Parmar, C.; Hoekstra, O.S.; Hoekstra, C.J.; Boellaard, R.; Dekker, A.L.; Gillies, R.J.; et al. Stability of FDG-PET Radiomics features: An integrated analysis of test-retest and inter-observer variability. *Acta Oncol.* **2013**, *52*, 1391–1397. [CrossRef]
128. Zhao, B.; James, L.P.; Moskowitz, C.S.; Guo, P.; Ginsberg, M.S.; Lefkowitz, R.A.; Qin, Y.; Riely, G.J.; Kris, M.G.; Schwartz, L.H. Evaluating Variability in Tumor Measurements from Same-day Repeat CT Scans of Patients with Nonâ€"Small Cell Lung Cancer. *Radiology* **2009**, *252*, 263–272. [CrossRef] [PubMed]
129. Desseroit, M.C.; Tixier, F.; Weber, W.A.; Siegel, B.A.; le Rest, C.C.; Visvikis, D.; Hatt, M. Reliability of PET/CT shape and heterogeneity features in functional and morphological components of Non-Small Cell Lung Cancer tumors: A repeatability analysis in a prospective multi-center cohort. *J. Nucl. Med.* **2016**, *58*, 406–411. [CrossRef]
130. Galavis, P.E.; Hollensen, C.; Jallow, N.; Paliwal, B.; Jeraj, R. Variability of textural features in FDG PET images due to different acquisition modes and reconstruction parameters. *Acta Oncol.* **2010**, *49*, 1012–1016. [CrossRef] [PubMed]
131. Lu, L.; Lv, W.; Jiang, J.; Ma, J.; Feng, Q.; Rahmim, A.; Chen, W. Robustness of Radiomic Features in [11C]Choline and [18F]FDG PET/CT Imaging of Nasopharyngeal Carcinoma: Impact of Segmentation and Discretization. *Mol. Imaging Biol.* **2016**, *18*, 935–945. [CrossRef] [PubMed]
132. Bailly, C.; Bodet-Milin, C.; Couespel, S.; Necib, H.; Kraeber-Bodéré, F.; Ansquer, C.; Carlier, T. Revisiting the robustness of PET-based textural features in the context of multi-centric trials. *PLoS ONE* **2016**, *11*, e0159984. [CrossRef]
133. Yang, F.; Dogan, N.; Stoyanova, R.; Ford, J.C. Evaluation of radiomic texture feature error due to MRI acquisition and reconstruction: A simulation study utilizing ground truth. *Phys. Med.* **2018**, *50*, 26–36. [CrossRef]
134. Kaus, M.R.; Brock, K.K.; Pekar, V.; Dawson, L.A.; Nichol, A.M.; Jaffray, D.A. Assessment of a model-based deformable image registration approach for radiation therapy planning. *Int. J. Radiat. Oncol.* **2007**, *68*, 572–580. [CrossRef]
135. Isaksson, L.J.; Raimondi, S.; Botta, F.; Pepa, M.; Gugliandolo, S.G.; de Angelis, S.P.; Marvaso, G.; Petralia, G.; de Cobelli, O.; Gandini, S.; et al. Effects of MRI image normalization techniques in prostate cancer radiomics. *Phys. Med.* **2020**, *71*, 7–13. [CrossRef]
136. Brock, K.K. Deformable Registration Accuracy Consortium, Results of a multi-institution deformable registration accuracy study (MIDRAS). *Int. J. Radiat. Oncol.* **2010**, *76*, 583–596. [CrossRef] [PubMed]
137. Avanzo, M.; Barbiero, S.; Trovo, M.; Bissonnette, J.P.; Jena, R.; Stancanello, J.; Pirrone, G.; Matrone, F.; Minatel, E.; Cappelletto, C.; et al. Voxel-by-voxel correlation between radiologically radiation induced lung injury and dose after image-guided, intensity modulated radiotherapy for lung tumors. *Phys. Med.* **2017**, *42*, 150–156. [CrossRef] [PubMed]
138. Mahesh, M. Essential Role of a Medical Physicist in the Radiology Department. *Radiographics* **2018**, *38*, 1665–1671. [CrossRef] [PubMed]
139. Herrmann, M.D.; Clunie, D.A.; Fedorov, A.; Doyle, S.W.; Pieper, S.; Klepeis, V.; Le, L.P.; Mutter, G.L.; Milstone, D.S.; Schultz, T.J.; et al. Implementing the DICOM Standard for Digital Pathology. *J. Pathol. Inform.* **2018**, *9*, 37. [PubMed]
140. Kortesniemi, M.; Tsapaki, V.; Trianni, A.; Russo, P.; Maas, A.; Kallman, H.E.; Brambilla, M.; Damilakis, J. The European Federation of Organisations for Medical Physics (EFOMP) White Paper: Big data and deep learning in medical imaging and in relation to medical physics profession. *Phys. Med.* **2018**, *56*, 90–93. [CrossRef] [PubMed]

141. Zwanenburg, A.; Leger, S.; Vallieres, M.; Lock, S. Image Biomarker Standardisation Initiative for, Image biomarker standardisation initiative. *arXiv* **2016**, arXiv:1612.07003.
142. Mahon, R.N.; Ghita, M.; Hugo, G.D.; Weiss, E. ComBat harmonization for radiomic features in independent phantom and lung cancer patient computed tomography datasets. *Phys. Med. Biol.* **2019**, *65*, 015010. [CrossRef]
143. Kesner, A.; Laforest, R.; Otazo, R.; Jennifer, K.; Pan, T. Medical imaging data in the digital innovation age. *Med. Phys.* **2018**, *45*, e40–e52. [CrossRef]
144. Parmar, C.; Grossmann, P.; Bussink, J.; Lambin, P.; Aerts, H.J. Machine Learning methods for Quantitative Radiomic Biomarkers. *Sci. Rep.* **2015**, *5*, 13087. [CrossRef]
145. Barucci, A. Adversarial radiomics: The rising of potential risks in medical imaging from adversarial learning. *Eur. J. Nucl. Med. Mol. Imaging* **2020**, *47*, 2941–2943. [CrossRef]
146. Li, S.; Chen, Y.; Peng, Y.; Bai, L. Learning More Robust Features with Adversarial Training. *arXiv* **2018**, arXiv:1804.07757.
147. U.S. Food and Drug Administration: MicroArray/Sequencing Quality Control (MAQC/SEQC). 2021. Available online: https://www.fda.gov/science-research/bioinformatics-tools/microarraysequencing-quality-control-maqcseqc (accessed on 12 February 2021).
148. Collins, G.S.; Reitsma, J.B.; Altman, D.G.; Moons, K.G. Transparent reporting of a multivariable prediction model for individual prognosis or diagnosis (TRIPOD): The TRIPOD Statement. *MC Med.* **2015**, *13*, 1–10. [CrossRef] [PubMed]
149. Wang, B.; White, G. The role of clinical medical physicists in the future: Quality, safety, technology implementation, and enhanced direct patient care. *J. Appl. Clin. Med. Phys.* **2019**, *20*, 4–6. [CrossRef] [PubMed]
150. Caruana, C.J.; Tsapaki, V.; Damilakis, J.; Brambilla, M.; Martin, G.M.; Dimov, A.; Bosmans, H.; Egan, G.; Bacher, K.; McClean, B. EFOMP policy statement 16: The role and competences of medical physicists and medical physics experts under 2013/59/EURATOM. *Phys. Med.* **2018**, *48*, 162–168. [CrossRef] [PubMed]
151. Okamoto, H.; Ota, S.; Kawamorita, R.; Sakamoto, M.; Nakamura, S.; Nishioka, S.; Kabuki, S.; Masai, N.; Mizuno, N.; Furuya, T.; et al. Summary of the Report of Task Group 100 of the AAPM: Application of Risk Analysis Methods to Radiation Therapy Quality Management. *Igaku Butsuri* **2020**, *40*, 28–34. [PubMed]
152. Bang, J.Y.; Hough, M.; Hawes, R.H.; Varadarajulu, S. Use of Artificial Intelligence to Reduce Radiation Exposure at Fluoroscopy-Guided Endoscopic Procedures. *Am. J. Gastroenterol.* **2020**, *115*, 555–561. [CrossRef]
153. Liu, Y.; Ma, L.; Zhao, J. Secure Deep Learning Engineering: A Road Towards Quality Assurance of Intelligent Systems. In *Lecture Notes in Computer Science*; Springer: Berlin, Germany, 2019; pp. 3–15.
154. Tang, A.; Tam, R.; Cadrin-Chênevert, A.; Guest, W.; Chong, J.; Barfett, J.; Chepelev, L.; Cairns, R.; Mitchell, J.R.; Cicero, M.D.; et al. Canadian Association of Radiologists White Paper on Artificial Intelligence in Radiology. *Can. Assoc. Radiol. J.* **2018**, *69*, 120–135. [CrossRef] [PubMed]
155. Currie, G.; Hawk, K.E.; Rohren, E.; Vial, A.; Klein, R. Machine Learning and Deep Learning in Medical Imaging: Intelligent Imaging. *J. Med Imaging Radiat. Sci.* **2019**, *50*, 477–487. [CrossRef] [PubMed]
156. Prior, F.W.; Clark, K.; Commean, P.; Freymann, J.; Jaffe, C.; Kirby, J.; Moore, S.; Smith, K.; Tarbox, L.; Vendt, B.; et al. TCIA: An information resource to enable open science. *Conf. Proc. IEEE Eng. Med. Biol. Soc.* **2013**, *2013*, 1282–1285.
157. Sharma, A.; Tarbox, L.; Kurc, T.; Bona, J.; Smith, K.; Kathiravelu, P.; Bremer, E.; Saltz, J.H.; Prior, F. PRISM: A Platform for Imaging in Precision Medicine. *JCO Clin. Cancer Inform.* **2020**, *4*, 491–499. [CrossRef] [PubMed]
158. Wilkinson, M.D.; Dumontier, M.; Aalbersberg, I.J.; Appleton, G.; Axton, M.; Baak, A.; Blomberg, N.; Boiten, J.W.; Santos, L.B.D. The FAIR Guiding Principles for scientific data management and stewardship. *Sci. Data* **2016**, *3*, 160018. [CrossRef] [PubMed]

applied sciences

MDPI

Article

Combined Use of a Transmission Detector and an EPID-Based In Vivo Dose Monitoring System in External Beam Whole Breast Irradiation: A Study with an Anthropomorphic Female Phantom

Chiara Arilli [1], Yannik Wandael [2], Chiara Galeotti [2], Livia Marrazzo [1], Silvia Calusi [3], Mattia Grusio [4], Isacco Desideri [3], Franco Fusi [3], Angelo Piermattei [4] and Stefania Pallotta [1,3] and Cinzia Talamonti [1,3,*]

1 AOU Careggi, Medical Physics Unit, 50134 Florence, Italy; chiara.arilli@unifi.it (C.A.); livia.marrazzo@unifi.it (L.M.); stefania.pallotta@unifi.it (S.P.)
2 AOU Careggi, Radiotherapy Unit, 50134 Florence, Italy; yannickwandael@gmail.com (Y.W.); galeottic@aou-careggi.toscana.it (C.G.)
3 Department of Experimental and Clinical Biomedical Sciences "Mario Serio", University of Florence, 50134 Florence, Italy; silvia.calusi@unifi.it (S.C.); isacco.desideri@unifi.it (I.D.); franco.fusi@unifi.it (F.F.)
4 UOC Fisica Sanitaria, Fondazione Policlinico Universitario Agostino Gemelli, 00168 Rome, Italy; mattiagrusio@gmail.com (M.G.); angelo.piermattei@gmail.com (A.P.)
* Correspondence: Cinzia.Talamonti@unifi.it

Received: 23 September 2020; Accepted: 22 October 2020; Published: 28 October 2020

Abstract: We evaluate the combined usage of two systems, the Integral Quality Monitor (IQM) transmission detector and SoftDiso software, for in vivo dose monitoring by simultaneous detection of delivery and patient setup errors in whole breast irradiation. An Alderson RANDO phantom was adapted with silicon breast prostheses to mimic the female anatomy. Plans with simulated delivery errors were created from a reference left breast plan, and patient setup errors were simulated by moving the phantom. Deviations from reference values recorded by both monitoring systems were measured for all plans and phantom positions. A 2D global gamma analysis was performed in SoftDiso for all phantom displacements. Both IQM signals and SoftDiso R-values are sensitive to small MU variations. However, only IQM is sensitive to jaw position variations. Conversely, IQM is unable to detect patient positioning errors, and the R-value has good sensitivity to phantom displacements. A gamma comparison analysis allows one to determine alert thresholds to detect phantom shifts or relatively large rotations. The combined use of the IQM and SoftDiso allows for fast identification of both delivery and setup errors and substantially reduces the impact of error identification and correction on the treatment workflow.

Keywords: quality assurance; in vivo dosimetry; transmission radiation detectors; whole breast irradiation

1. Introduction

After breast conserving surgery, radiotherapy is the usual therapeutic strategy for breast cancer patients providing, with fewer toxicity effects, equivalent survival outcomes when compared with mastectomy [1,2]. Conventional three-dimensional conformal radiotherapy (3DCRT), with tangential external photon beams, is the standard irradiation modality, which is known to successfully ensure the local control of the disease [2,3]. Moreover, in recent years, advanced techniques like intensity modulated radiation therapy (IMRT), helical tomotherapy (HT) and volumetric modulated arc therapy (VMAT) were investigated and compared in terms of normal tissue toxicities and dosimetric

advantages [4–8]. However, the preferred breast irradiation modality differs between radiotherapy departments. At our institution, breast cancer is the most recurrent pathology treated with radiotherapy, and its high incidence encouraged us to build and share a method to improve the dose delivery accuracy in 3DCRT breast treatments. Often in radiotherapy, patient quality assurance programs (QA) are performed in pre-treatment modality. However, pre-treatment verification presents several drawbacks: (1) the actual patient geometry is never included in pre-treatment measurements, making it difficult to estimate the effect of observed dosimetric deviations on the actual patient; (2) deviations from intended treatment occurring during the dose delivery cannot be detected [9,10]; (3) pre-treatment verification requires additional measurement sessions, taking up valuable linac time and increasing workload. The first issue is usually addressed in commercial systems by reworking observed deviations on the patient anatomy (using the planning CT scan) [11–13]; however, the last two issues cannot be circumvented by using pre-treatment verification. To solve these questions, in vivo dosimetry systems (IVDs) that perform dose measurements during the treatment and compare them to the intended dose are sometimes introduced into the clinical routine. In this work, a study of uncertainties affecting breast irradiation was carried out. Three main error sources were analyzed: delivery errors, setup errors and human errors. Delivery errors are systematic errors affecting delivery parameters which can lead to output variations (e.g., incorrect linac dose calibration or incorrect calibration of the multi-leaf collimator or of the jaws). Inter-fraction setup errors instead are more difficult-to-control errors tightly related to the patient alignment procedure followed by operators, to anatomical modifications and to treatment preparation imaging devices. Regrettably, human mistakes could also occur, e.g., incorrect arrangement of the patient, perhaps due to clothes or objects accidentally located inside the treatment field, or incorrect identification of the patient occurs. The effectiveness of IVDs in detecting systematic and random treatment errors has been investigated in several review papers and reports [9,14–19]. In particular, all authors agreed that standard quality pre-treatment checks are not able to detect a large number of treatment errors, highlighting the need for IVDs. Recently, new international recommendations, following the suggestions indicated in many incident reports [20–23], have encouraged the introduction of IVDs as good practice in radiotherapy [24–29]. For example, article 63 of the European Directive 2013/59/Euratom [24] clearly states that the member countries have to include a risk analysis in their quality management systems for radiotherapy practice. In some European countries, such as Sweden, Denmark, Norway, the Czech Republic, and France, an IVD is mandatory [27–29]. Commercial systems for in vivo dose monitoring are available with different objectives. Several devices measure the patient's dose by using detectors placed on the patient (for example, on the patient's skin) or next to the patient (in a known position), or by processing the radiation transmitted through the patient. Other commercial systems measure the photon fluence at the linac output. Real-time in vivo devices, such as diodes, metal-oxide semiconductor field effect transistors (MOSFETs) and electronic portal imaging devices (EPID) [30,31], belong to the first group. In particular, EPID systems use back projection methods on measured portal images to obtain 2D [32–34] or 3D [35,36] patient dose distributions directly comparable with the planned dose. Transmission radiation detectors (TRDs), consisting usually of an array located on the linac head, belong instead to the second group. However, these devices monitor the delivery but not the patient dose; therefore, they cannot be classified as IVDs [37–42]. Our project aims to implement a new quality assurance (QA) procedure for patients undergoing highly conformal radiotherapy treatments that combines a transmission detector to monitor the fluence entering the patient and in vivo dosimetry with an EPID to measure the dose actually released into the patient during the treatment. An Integral Quality Monitor detector (IQM, iRT Systems GmbH, Koblenz, Germany) and a SoftDiso (Best Medical Srl, Italy) system have been simultaneously operated to evaluate their sensitivity in regard to detecting small delivery and setup errors for 3DCRT breast irradiation of a female phantom.

2. Materials and Methods

2.1. Equipment

In this study, 6MV energy photon beams were delivered with Precise and Synergy BM linacs (Elekta AB, Stockholm, Sweden), both equipped with an iViewGT a-Si panel EPID (Elekta AB, Stockholm, Sweden). Precise and Synergy multi-leaf collimators provide maximum field sizes of 40×40 cm^2 and 16×21 cm^2 respectively, both using two banks of 40 leaves. The Synergy linac is also equipped with an advanced robotic patient positioning platform (HexaPOD evo RT system) enabling sub-millimeter couch movements with six degrees of freedom. A scheme of the experimental setup is shown in Figure 1.

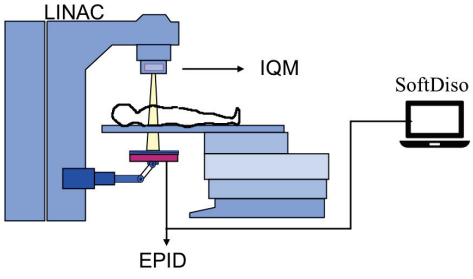

Figure 1. A scheme of measurement setup is displayed.

2.2. Monitoring Devices

The IQM device is an online delivery monitoring system, checking in real time the accuracy of the radiation fluence. The device consists of a large area transmission chamber, designed to be mounted on the linac head. An electric field gradient is generated by the inclined chamber electrode plates, providing a non-uniform charge collection linearly varying in the direction parallel to the multi-leaf collimator's motion. During the irradiation, a spatially sensitive dose-area product is generated and reported in arbitrary units (counts). A picture of an IQM detector mounted on a linac head is shown in Figure 2.

Figure 2. Left. The Integral Quality Monitor detector (IQM) system mounted on the linac head. **Right**. Alderson RANDO phantom with two silicon prostheses to simulate the female anatomy.

The IQM software allows an easy comparison of the acquired measurements with reference data to detect possible deviations from nominal parameters. The system has also an integrated inclinometer to measure collimator and gantry angles. Details of the detector described by several authors can be found in reference [40].

The SoftDiso system is a piece of online monitoring software reconstructing the dose by using the transmission signal measured by an EPID device. The reconstructed dose is compared with the

planned dose through an R-value, defined as the ratio of the measured to calculated doses at the isocenter point (Diso/DTPS) [32,33]. To check the inter-session patient position reproducibility and to identify possible anatomical variations over the whole treatment, a 2D gamma-index analysis tool compares an EPID reference image (usually acquired during the first/second session) with treatment images by using global gamma passing rate (γ_{PR}) and gamma mean value (γ_{mean}) indexes.

2.3. Phantom

A suitable phantom was made to reproduce the real female anatomy. An Alderson RANDO phantom was modified with two silicon breast prostheses placed on the phantom chest. Ultrasound gel was used to reduce the air gap at the prosthesis–chest interface.

A CT scan of the phantom was acquired with a Big Bore Philips scanner (Philips Medical Systems, Fitchburg, WI). Two reference 3DCRT plans of the phantom left breast were created for 50 Gy dose prescription (25 fractions) with Philips Pinnacle3 Professional TPS version 9.10 (Philips Medical Systems, Fitchburg, WI) for Precise and Synergy linacs respectively. Figure 3 shows the dose distribution for the Precise plan. The clinical target volume (CTV), the heart, the ipsilateral and controlateral lungs, the contralateral breast and the spinal cord were defined on the CT phantom.

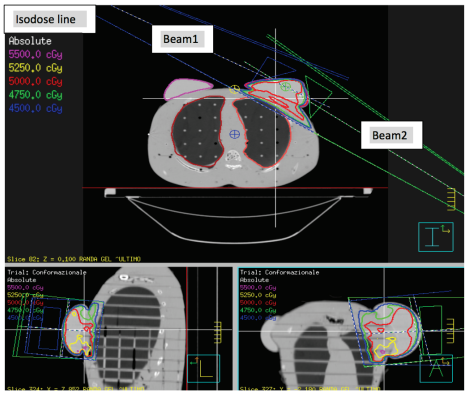

Figure 3. A screenshot of reference treatment plan dose distribution for 50 Gy dose prescription. Isodose lines are displayed in sagittal, coronal and axial views.

Plan parameters are reported in Table 1.

Table 1. Parameters of the two simulated treatment plans used in the study.

Precise	**Beam 1**	**Beam 2**
Gantry angle	120°	295°
Collimator angle	264°	96°
Field size (cm^2)	14×11	14×11
Beam energy (MV)	6	6
MU	177	191
Wedge	yes	yes
Synergy	**Beam 1**	**Beam 2**
Gantry angle	300°	125°
Collimator angle	96°	264°
Equivalent field size (cm^2)	14×11	14×11
Beam energy (MV)	6	6
MU	161	143
Wedge	yes	yes

2.4. Short-Term Reproducibility of Systems

The short-term reproducibility of SoftDiso R-value was checked by repeating the reference Precise plan 20 times and was evaluated by the ratio of the standard deviation to the average value (σ_R / R_{avg}). The short-term reproducibility of IQM signal has already been studied at our department [43].

2.5. Simulated Delivery Errors

To evaluate the sensitivity of the two devices to delivery errors, 12 plans for Precise linac were created by modifying the reference plan parameters. To simulate output errors, derived, for example, for an incorrect dose calibration of linac, MUs were modified by adding 2 MU, 3 MU, 5 MU and 10 MU at nominal collimator positions; to mimic an incorrect calibration of jaws, the jaw located near to the ipsilateral lung was displaced by $\pm$2 mm, $\pm$3 mm, $\pm$5 mm and $\pm$7 mm, at nominal MU. IQM and SofDiso devices were operated simultaneously during the delivery of all 13 plans (the reference and the 12 modified). The average deviations of the IQM signals and R-values from the reference plan values were evaluated in 5 consecutive measurement sessions.

2.6. Simulated Setup Errors

Setup errors were simulated with Synergy couch by displacing the phantom by 2 mm, 3 mm, 5 mm, 7 mm and 10 mm in anterior, lateral and longitudinal directions. The phantom was also rotated around the longitudinal axis by 1° and 2.8° (maximum extent of rotation reachable with HexaPOD system). The average deviations of R-value from reference values were evaluated in five consecutive measurement sessions. The γ_{PR} and the γ_{mean} values were calculated with SoftDiso for all images and compared with the corresponding values obtained with the phantom in the reference position. For all cases, γ_{PR} and γ_{mean} were evaluated with 2%/2 mm global criteria. Alert thresholds to detect shifts of 2 mm were established by using the gamma comparison. With the same thresholds we also studied the sensitivity to rotations.

3. Results

3.1. Short-Term Reproducibility of Systems

The R-value short-term reproducibility ($\sigma_{\mathrm{R/R_{avg}}}$) was found to be 0.6%, while the IQM signal was measured to be reproducible within 0.08%, consistent with our previous study [43].

3.2. Simulated Delivery Errors

The average deviations from reference counts and R-values of simultaneously operated IQM and SoftDiso due to simulated delivery errors obtained from the five measurement runs are reported in Figure 4. Both SoftDiso and IQM detected all MU variations showing excellent linearity and sensitivities of (0.53 ± 0.13)%/MU and (0.53 ± 0.01)%/MU respectively. A remarkable correlation between the outputs of the two devices was also observed. Furthermore, the IQM is also able to detect small jaw position variations, showing again, good sensitivities of (1.17 ± 0.02)%/mm and (1.05 ± 0.02)%/mm in both closing and opening movement directions respectively. The linearity in this case is only approximate, pointing either to an intrinsically non-linear response or to an underestimation of measurement errors. Nevertheless, IQM measurement errors are negligible compared to deviations of signal consequent to delivery errors in clinical routine. On the contrary, the R-value was found to be almost insensitive to the same relatively small jaw position variations, while still showing a reasonable response linearity, with large uncertainty though.

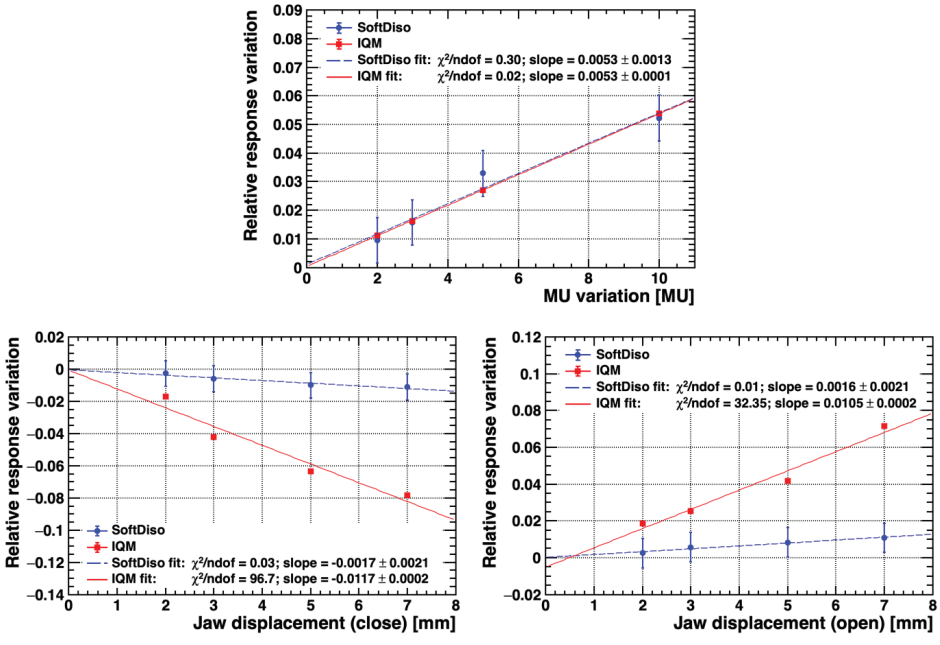

Figure 4. Deviations from reference values of IQM signal and SoftDiso R-values as functions of MU variations (**top**) and of jaw position variation in close (**bottom left**) and open (**bottom right**) directions.

3.3. Simulated Setup Errors

The IQM system is intrinsically insensitive to patient positioning, being placed upstream of the patient along the beam line. The SoftDiso provides, therefore, the only tool available to check for the correct patient positioning. The average R-value deviations (absolute values) for all phantom displacements and rotations with respect to the reference position are shown in Figure 5. Given the characteristics of the beams and the irradiation region considered in this study, the R-value measurements show good linearity and a sensitivity of $(0.74 \pm 0.12\%)$/mm to displacements in the anterior direction, where the strictest control of patient positioning is required. In contrast, as expected, the R-value is insensitive to movements in lateral and longitudinal directions, and to rotations, which are less critical in this specific case.

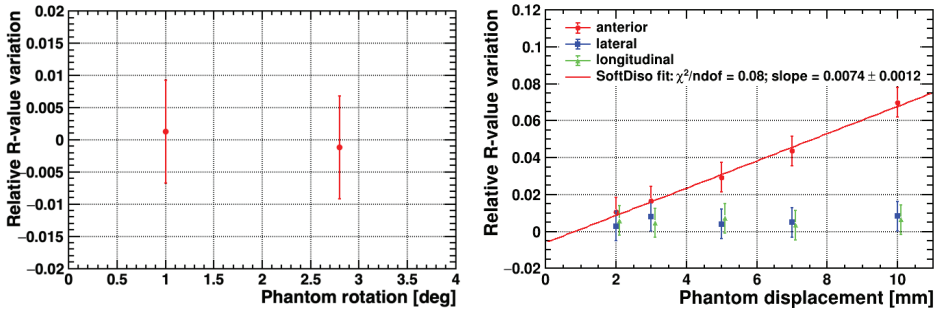

Figure 5. Deviations from reference values of the SoftDiso R-value for phantom rotations (**left**) and translations (**right**).

To further explore the sensitivity of SoftDiso to patient positioning errors, a gamma-index comparison of EPID images with displaced phantom was performed. The results for 2%/2mm global criteria are presented in Figure 6. To reveal phantom shifts $\geq$ 2 mm, alert thresholds of $\gamma_{PR} < 89.7\% \pm 0.4\%$ and $\gamma_{mean} > 0.32 \pm 0.04$ were obtained. The γ_{PR} and γ_{mean} indexes show good linearity with phantom displacements. Results of the comparison for phantom rotations are reported in Table 2.

From the measurements we conclude that the sensitivity to small rotations is difficult to asses, with γ_{PR} remaining within the alert threshold for both rotation angles and γ_{mean} going slightly above-threshold for the maximum simulated rotation of 2.8°.

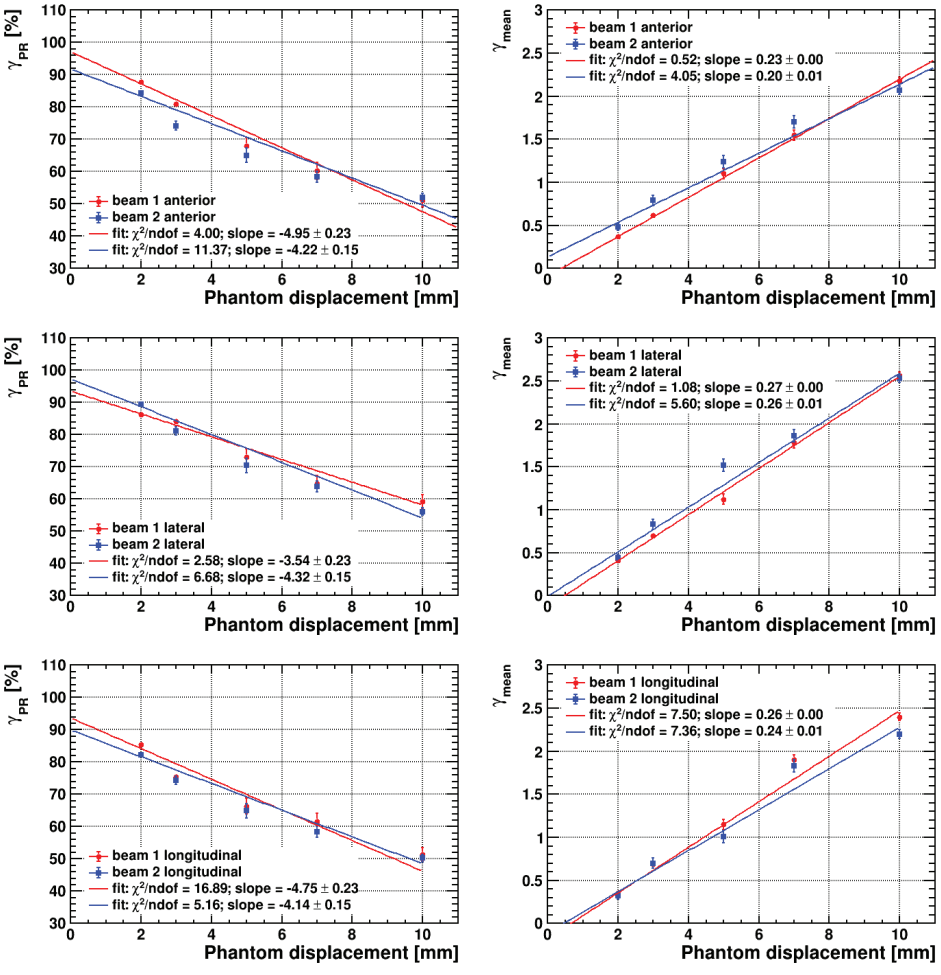

Figure 6. Measured γ_{PR} and γ_{mean} indexes as functions of phantom anterior (**top**); lateral (**middle**) and longitudinal (**bottom**) displacements for both beam 1 and beam 2 used in the simulated treatment plan.

Table 2. Results of the gamma-index comparison for phantom rotations.

Rotation Angle	γ_{PR} Beam 1	γ_{mean} Beam 1	γ_{PR} Beam 2	γ_{mean} Beam 2
1.0°	$(95.0 \pm 0.4)\%$	0.19 ± 0.05	$(95.7 \pm 0.4)\%$	0.18 ± 0.03
2.8°	$(91.0 \pm 0.6)\%$	0.37 ± 0.05	$(91.2 \pm 0.6)\%$	0.33 ± 0.04

4. Discussion

In this study deviations in treatment delivery and in patient setup were simulated. Both types of errors happen in clinical routine. Scenarios can be various: small, but even large deviations can occur during the treatment, for example, when a wrong linac dose calibration is done or when patient is not correctly identified or prepared for the therapy. The strength of the combined use of the two systems in detecting all different kinds of errors, even when very small, has been evidenced in this work. Separate use of IQM or SoftDiso devices has been widely discussed for different irradiation modalities [43–49], but to our knowledge, no study exists of their combined use, in particular for breast irradiation. A clinical study of the SoftDiso-based quality assurance procedure for post-mastectomy IMRT and VMAT radiation therapy is reported in reference [50], where specific thresholds for R-value, γ_{PR} and γ_{mean} indexes were proposed, based on the clinical experience and validated with a phantom chest. The authors confirmed the feasibility and the importance of a QA procedure based on EPID-based IVD to detect inter-fraction setup errors to overcome the weakness of a setup control based only on weekly cone beam CT acquisitions. The high IQM sensitivities to simulated delivery errors have been assessed by several authors [43–46] and confirmed in our work. However, to our knowledge, studies of the application of IQM to breast irradiation have not been reported elsewhere. From our measurements, the IQM device demonstrates high sensitivity to small MU variations and jaw position deviations. The SoftDiso R-value was also found to be able to detect MU variations with a sensitivity slightly smaller than for IQM. However, the R-value is much less sensitive to collimator position variations, as expected given the stability of output factors for small modifications of the field size. The IQM system is obviously insensitive to patient setup errors given its positioning upstream the patient itself. However, in this work we have demonstrated the ability of the EPID-based SoftDiso to detect simulated setup errors. The SoftDiso R-value was shown to have good sensitivity to small displacements in the anterior direction—the error most critical for the particular simulated plan used. To recover full sensitivity to 3D displacements a gamma-index analysis was needed. This analysis, with 2%/2mm criteria, yielded alert thresholds of about 90% for γ_{PR} and 0.4 for γ_{mean}, in agreement with those proposed in the literature [50]. The γ_{mean} threshold was also demonstrated to be able to detect a phantom rotation of 2.8°. It is worth noticing here that the gamma-index analysis, while being fairly sensitive, cannot distinguish between patient positioning errors and beam setup errors. In this study we have therefore shown that the combined and simultaneous use of IQM and an EPID-based system provides a complete monitoring of beam and patient setup errors. Both devices allow one to set alert thresholds, which can be suitably adjusted according to the specific treatment, providing a warning message or sound when the measurement is out of tolerance. The IQM system can generate a real time warning when the delivery is incorrect. On the other hand, the R-values provided by the SoftDiso immediately after the sessions can be saved in a table, showing not only whether the tolerance has been exceeded but also whether a trend over a series of sessions appears, pointing to the need for a setup correction. Finally, the response of gamma analysis comparison is quickly available after a very fast data analysis (few minutes). Consequently, by combining the IQM and the SoftDiso, delivery and/or setup errors are detected quickly during or shortly after the delivery, allowing one to correct the inaccuracies during or immediately following treatment sessions. Both devices can be easily used by the therapist and do not affect the workflow, increase the booking time or involve the physician or physicist except when an alert message is activated. In the latter case, moreover, the combined output of the two devices can help in rapidly identifying the type of error to be corrected. The work presented is a pilot study simulating errors which could occur while delivering a radiotherapy conforming breast

treatment. The clinical implementation and the extension of this quality protocol to other districts is the next step in our project. The combined use of the two detectors is advantageous for IMRT or VMAT treatments too. In these cases, small deviations in positions of the multileaf collimator leaves could toughly affect the output delivery.

5. Conclusions

Although the European Commission clearly identified IVD as a relevant element in radiotherapy QA programs, only a few Institutions use it routinely for different reasons. First of all, many of the commercially available systems, although exhibiting good performances, do not respond in real time, often having very long data processing times. Additionally, many devices require dedicated staff, because of their complicated method to enter the data for processing. Finally, often a single system is not able to discriminate between all treatment errors, as demonstrated in this work. In this study we have presented a pilot study showing a new strategy to perform fast and reliable QA tests with a low impact on the workflow of the institution and patient waiting list. The combined use of IQM and SoftDiso devices was demonstrated to be able to efficiently detect small delivery and setup errors in 3DCRT breast irradiation. We have shown that the two devices provide complementary information to detect in almost real time all types of errors. The method would represent an important step forward in the clinical routine to increase the quality of external breast irradiation. Our study concentrated on breast irradiation, but the method could be easily extended to other anatomical districts or treatment modalities, especially when advanced techniques are used. The method proposed helps to comply with the European Commission requirements [24], and represents a new strategy in QA programs, thereby overcoming the drawbacks of conventional pre-treatment verification, which are very time consuming and ineffective to detect in-treatment errors.

Author Contributions: Methodology, formal analysis and Writing–original draft preparation: C.A.; Funding acquisition: F.F. and S.P.; Investigation: Y.W. and C.G.; Software: M.G. and A.P.; Validation: L.M.; Visualization: S.C. and I.D.; Conceptualization, Supervision, Writing–review and editing: C.T. All authors have read and agreed to the published version of the manuscript.

Funding: This work was supported by Italian MIUR (the Italian Ministry of Education, University and Research) under Grant ex60% to the Department of Experimental and Clinical Biomedical Sciences "Mario Serio", University of Florence.

Conflicts of Interest: The authors declare no conflict of interest.

References

1. Fisher, B.; Jeong, J.H.; Anderson, S.; Bryant, J.; Fisher, E.R.; Wolmark, N. Twenty-Five-Year Follow-up of a Randomized Trial Comparing Radical Mastectomy, Total Mastectomy, and Total Mastectomy Followed by Irradiation. *N. Engl. J. Med.* **2002**, *347*, 567–575. [CrossRef] [PubMed]
2. Fisher, B.; Anderson, S.; Bryant, J.; Margolese, R.G.; Deutsch, M.; Fisher, E.R.; Jeong, J.H.; Wolmark, N. Twenty-Year Follow-up of a Randomized Trial Comparing Total Mastectomy, Lumpectomy, and Lumpectomy plus Irradiation for the Treatment of Invasive Breast Cancer. *N. Engl. J. Med.* **2002**, *347*, 1233–1241. [CrossRef] [PubMed]
3. Veronesi, U.; Cascinelli, N.; Mariani, L.; Greco, M.; Saccozzi, R.; Luini, A.; Aguilar, M.; Marubini, E. Twenty-Year Follow-up of a Randomized Study Comparing Breast-Conserving Surgery with Radical Mastectomy for Early Breast Cancer. *N. Engl. J. Med.* **2002**, *347*, 1227–1232. [CrossRef]
4. Johansen, S.; Cozzi, L.; Olsen, D.R. A planning comparison of dose patterns in organs at risk and predicted risk for radiation induced malignancy in the contralateral breast following radiation therapy of primary breast using conventional, IMRT and Volumetric modulated arc treatment techniques. *Acta Oncol.* **2009**, *48*, 495–503. [CrossRef]
5. Vatanen, T.; Traneus, E.; Lahtinen, T. Comparison of conventional inserts and an add-on electron MLC for chest wall irradiation of left-sided breast cancer. *Acta Oncol.* **2009**, *48*, 446–451. [CrossRef]
6. Cozzi, L.; Fogliata, A.; Nicolini, G.; Bernier, J. Clinical experience in breast irradiation with intensity modulated photon beams. *Acta Oncol.* **2005**, *44*, 467–474. [CrossRef]

7. Fong, A.; Bromley, R.; Beat, M.; Vien, D.; Dineley, J.; Morgan, G. Dosimetric comparison of intensity modulated radiotherapy techniques and standard wedged tangents for whole breast radiotherapy. *J. Med. Imaging Radiat. Oncol.* **2009**, *53*, 92–99. [CrossRef]
8. Haciislamoglu, E.; Colak, F.; Canyilmaz, E.; Dirican, B.; Gurdalli, S.; Yilmaz, A.H.; Yoney, A.; Bahat, Z. Dosimetric comparison of left-sided whole-breast irradiation with 3DCRT, forward-planned IMRT, inverse-planned IMRT, helical tomotherapy, and volumetric arc therapy. *Phys. Med.* **2015**, *31*, 360–367. [CrossRef] [PubMed]
9. Mans, A.; Wendling, M.; McDermott, L.N.; Sonke, J.J.; Tielenburg, R.; Vijlbrief, R.; Mijnheer, B.; van Herk, M.; Stroom, J.C. Catching errors with in vivo EPID dosimetry. *Med. Phys.* **2010**, *37*, 2638–2644. [CrossRef]
10. Ford, E.C.; Terezakis, S.; Souranis, A.; Harris, K.; Gay, H.; Mutic, S. Quality Control Quantification (QCQ): A Tool to Measure the Value of Quality Control Checks in Radiation Oncology. *Int. J. Radiat. Oncol. Biol. Phys.* **2012**, *84*, e263–e269. [CrossRef]
11. Chan, M.F.; Li, J.; Schupak, K.; Burman, C. Using a Novel Dose QA Tool to Quantify the Impact of Systematic Errors Otherwise Undetected by Conventional QA Methods: Clinical Head and Neck Case Studies. *Technol. Cancer Res. Treat.* **2014**, *13*, 57–67. [CrossRef]
12. Nelms, B.E.; Chan, M.F.; Jarry, G.; Lemire, M.; Lowden, J.; Hampton, C.; Feygelman, V. Evaluating IMRT and VMAT dose accuracy: Practical examples of failure to detect systematic errors when applying a commonly used metric and action levels. *Med. Phys.* **2013**, *40*, 111722. [CrossRef]
13. Coleman, L.; Skourou, C. Sensitivity of volumetric modulated arc therapy patient specific QA results to multileaf collimator errors and correlation to dose volume histogram based metrics. *Med. Phys.* **2013**, *40*, 111715. [CrossRef]
14. Essers, M.; Mijnheer, B. In vivo dosimetry during external photon beam radiotherapy. *Int. J. Radiat. Oncol. Biol. Phys.* **1999**, *43*, 245–259. [CrossRef]
15. Fiorino, C.; Corletto, D.; Mangili, P.; Broggi, S.; Bonini, A.; Cattaneo, G.M.; Parisi, R.; Rosso, A.; Signorotto, P.; Villa, E.; Calandrino, R. Quality assurance by systematic in vivo dosimetry: results on a large cohort of patients. *Radiother. Oncol.* **2000**, *56*, 85–95. [CrossRef]
16. Huyskens, D.; Bogaerts, R.; Verstraete, J.; Lööf, M.; Nyström, H.; Fiorino C.; Broggi S.; Jornet N.; Ribas M.; Thwaites D. Practical Guidelines for the Implementation of In Vivo Dosimetry with Diodes in External Radiotherapy with Photon Beams (Entrance Dose). *Eur. Soc. Radiother. Oncol.* **2001**, *1*, 1–168 .
17. AAPM Task Group 62 of the Radiation Therapy Committee. Diode in vivo dosimetry for patients receiving external beam radiation therapy. *AAPM Rep.* **2005**, *1*, 1–84 .
18. World Health Organization. Radiotherapy Risk Profile 2008. WHO/IER/PSP/2008.12. Available online: https://www.who.int/patientsafety/activities/technical/radiotherapy_risk_profile.pdf?ua=1 (accessed on 18 September 2020).
19. *Development of Procedures for In Vivo Dosimetry in Radiotherapy*; Number 8 in Human Health Reports; International Atomic Energy Agency: Vienna, Austria, 2013.
20. Mayles, W. The Glasgow Incident—A Physicist's Reflections. *Clin. Oncol.* **2007**, *19*, 4–7. [CrossRef]
21. Williams, M.V. Radiotherapy Near Misses, Incidents and Errors: Radiotherapy Incident at Glasgow. *Clin. Oncol.* **2007**, *19*, 1–3. [CrossRef]
22. Ortiz-Lopez, P.; Cosset, J.M.; Dunscombe, P.; Holmberg, O.; Rosenwald, J.; Ashton, L.; Llanes, J.; Vatnitsky, S. ICRP publication 112. A report of preventing accidental exposures from new external beam radiation therapy technologies. *Ann. ICRP* **2009**, *39*, 1–86. [CrossRef]
23. Derreumaux, S.; Etard, C.; Huet, C.; Trompier, F.; Clairand, I.; Bottollier-Depois, J.F.; Aubert, B.; Gourmelon, P. Lessons from recent accidents in radiation therapy in France. *Radiat. Prot. Dosim.* **2008**, *131*, 130–135. [CrossRef]
24. Council Directive 2013/59/EURATOM of 5 December 2013. *OJ L* **2014**, *13*, 1–73. Available online: https://eur-lex.europa.eu/LexUriServ/LexUriServ.do?uri=OJ:L:2014:013:0001:0073:EN:PDF (accessed on 18 September 2020).
25. *Radiation Protection and Safety of Radiation Sources: International Basic Safety Standards*; Number GSR Part 3 in General Safety Requirements; International Atomic Energy Agency: Vienna, Austria, 2014.
26. The Royal College of Radiologists, Society and College of Radiographers, Institute of Physics and Engineering in Medicine, British Institute of Radiology. *Implementing In Vivo Dosimetry*; The Royal College of Radiologists: London, UK, 2008.

27. *The Swedish Radiation Protection Institute's Regulations on Radiation Therapy*; Number SSI-FS–2000-4; Swedish Radiation Protection Institute: Stockholm, Sweden, 2000.
28. *Critères D'Agrément Pour la Pratique de la Radiothérapie Externe*; Institut National du Cancer (INCa): Paris, France, 2008.
29. Patient Safety. Paving the Way for Progress. In *Vivo Dosimetry. Newsletters for Radiotherapy Professionals-n.5 2014*; The French Nuclear Safety Authority: Paris, France, 2014.
30. Mijnheer, B.; Beddar, S.; Izewska, J.; Reft, C. In vivo dosimetry in external beam radiotherapy. *Med. Phys.* **2013**, *40*, 070903. [CrossRef]
31. van Elmpt, W.; McDermott, L.; Nijsten, S.; Wendling, M.; Lambin, P.; Mijnheer, B. A literature review of electronic portal imaging for radiotherapy dosimetry. *Radiother. Oncol.* **2008**, *88*, 289–309. [CrossRef]
32. Piermattei, A.; Fidanzio, A.; Stimato, G.; Azario, L.; Grimaldi, L.; D'Onofrio, G.; Cilla, S.; Balducci, M.; Gambacorta, M.A.; Di Napoli, N.; et al. In vivo dosimetry by an aSi-based EPID. *Med. Phys.* **2006**, *33*, 4414–4422. [CrossRef] [PubMed]
33. Piermattei, A.; Fidanzio, A.; Azario, L.; Grimaldi, L.; D'Onofrio, G.; Cilla, S.; Stimato, G.; Gaudino, D.; Ramella, S.; D'Angelillo, R.; et al. Application of a practical method for the isocenter point in vivo dosimetry by a transit signal. *Phys. Med. Biol.* **2007**, *52*, 5101–5117. [CrossRef]
34. Held, M.; Cheung, J.; Andujar, A.P.; Morn, O. Commissioning and Evaluation of an Electronic Portal Imaging Device-Based In-Vivo Dosimetry Software. *Cureus* **2008**, *10*, e2139. [CrossRef] [PubMed]
35. Wendling, M.; McDermott, L.N.; Mans, A.; Sonke, J.J.; van Herk, M.; Mijnheer, B.J. A simple backprojection algorithm for 3D in vivo EPID dosimetry of IMRT treatments. *Med. Phys.* **2009**, *36*, 3310–3321. [CrossRef]
36. Mans, A.; Remeijer, P.; Olaciregui-Ruiz, I.; Wendling, M.; Sonke, J.J.; Mijnheer, B.; van Herk, M.; Stroom, J.C. 3D Dosimetric verification of volumetric-modulated arc therapy by portal dosimetry. *Radiother. Oncol.* **2010**, *94*, 181–187. [CrossRef]
37. Poppe, B.; Thieke, C.; Beyer, D.; Kollhoff, R.; Djouguela, A.; Rühmann, A.; Willborn, K.C.; Harder, D. DAVID—A translucent multi-wire transmission ionization chamber forin vivoverification of IMRT and conformal irradiation techniques. *Phys. Med. Biol.* **2006**, *51*, 1237–1248. [CrossRef]
38. Poppe, B.; Looe, H.K.; Chofor, N.; Rühmann, A.; Harder, D.; Willborn, K.C. Clinical performance of a transmission detector array for the permanent supervision of IMRT deliveries. *Radiother. Oncol.* **2010**, *95*, 158–165. [CrossRef]
39. Venkataraman, S.; Malkoske, K.E.; Jensen, M.; Nakonechny, K.D.; Asuni, G.; McCurdy, B.M.C. The influence of a novel transmission detector on 6 MV x-ray beam characteristics. *Phys. Med. Biol.* **2009**, *54*, 3173–3183. [CrossRef]
40. Islam, M.K.; Norrlinger, B.D.; Smale, J.R.; Heaton, R.K.; Galbraith, D.; Fan, C.; Jaffray, D.A. An integral quality monitoring system for real-time verification of intensity modulated radiation therapy. *Med. Phys.* **2009**, *36*, 5420–5428. [CrossRef] [PubMed]
41. Chang, J.; Heaton, R.K.; Mahon, R.; Norrlinger, B.D.; Jaffray, D.A.; Cho, Y.B.; Islam, M.K. A method for online verification of adapted fields using an independent dose monitor. *Med. Phys.* **2013**, *40*, 072104. [CrossRef] [PubMed]
42. Wong, J.H.D.; Fuduli, I.; Carolan, M.; Petasecca, M.; Lerch, M.L.F.; Perevertaylo, V.L.; Metcalfe, P.; Rosenfeld, A.B. Characterization of a novel two dimensional diode array the "magic plate" as a radiation detector for radiation therapy treatment. *Med. Phys.* **2012**, *39*, 2544–2558. [CrossRef]
43. Marrazzo, L.; Arilli, C.; Pasler, M.; Kusters, M.; Canters, R.; Fedeli, L.; Calusi, S.; Casati, M.; Talamonti, C.; Simontacchi, G.; et al. Real-time beam monitoring for error detection in IMRT plans and impact on dose-volume histograms. *Strahlenther. Onkol.* **2018**, *194*, 243–254. [CrossRef]
44. Casar, B.; Pasler, M.; Wegener, S.; Hoffman, D.; Talamonti, C.; Qian, J.; Mendez, I.; Brojan, D.; Perrin, B.; Kusters, M.; et al. Influence of the Integral Quality Monitor transmission detector on high energy photon beams: A multi-centre study. *Z. Med. Phys.* **2017**, *27*, 232–242. [CrossRef]
45. Razinskas, G.; Wegener, S.; Greber, J.; Sauer, O.A. Sensitivity of the IQM transmission detector to errors of VMAT plans. *Med. Phys.* **2018**, *45*, 5622–5630. [CrossRef]
46. Pasler, M.; Michel, K.; Marrazzo, L.; Obenland, M.; Pallotta, S.; Björnsgard, M.; Lutterbach, J. Error detection capability of a novel transmission detector: a validation study for online VMAT monitoring. *Phys. Med. Biol.* **2017**, *62*, 7440–7450. [CrossRef]

47. Piermattei, A.; Greco, F.; Grusio, M.; Menna, S.; Azario, L.; Stimato, G.; Placidi, E.; Teodoli, S.; Cilla, S.; Porcelli, A.; et al. A validation study of a dedicated software for an automated in vivo dosimetry control in radiotherapy. *Med. Biol. Eng. Comput.* **2018**, *56*, 1939–1947. [CrossRef]
48. Falco, M.; Giancaterino, S.; De Nicola, A.; Adorante, N.; De Lorenzo, R.G.; Di, Tommaso, M.; Vinciguerra, A.; Trignani, M.; Perrotti, F.; Allajbej, A.; et al. A Feasibility Study for in vivo Dosimetry Procedure in Routine Clinical Practice. *Technol. Cancer Res. Treat.* **2018**, *17*, 1533033818779201. [CrossRef]
49. Cilla, S.; Ianiro, A.; Craus, M.; Viola, P.; Deodato, F.; Macchia, G.; Buwenge, M.; Morganti, A.G.; Valentini, V.; Piermattei, A. Epid-based in vivo dose verification for lung stereotactic treatments delivered with multiple breath-hold segmented volumetric modulated arc therapy. *J. Appl. Clin. Med. Phys.* **2019**, *20*, 37–44. [CrossRef]
50. Kang, S.; Li, J.; Ma, J.; Zhang, W.; Liao, X.; Qing, H.; Tan, T.; Xin, X.; Tang, B.; Piermattei, A.; Orlandini, L.C. Evaluation of interfraction setup variations for postmastectomy radiation therapy using EPID-based in vivo dosimetry. *J. Appl. Clin. Med. Phys.* **2019**, *20*, 43–52. [CrossRef] [PubMed]

applied sciences

MDPI

Article

On the Possibility to Use the Charge Imbalance in Patients Undergoing Radiotherapy: A New Online, In Vivo, Noninvasive Dose Monitoring System

G A Pablo Cirrone [1,2,3,*,†], Nino Amato [1], Roberto Catalano [1], Alessandro Di Domenico [4], Giacomo Cuttone [1], Pietro Lojacono [1], Alfio Mazzaglia [1], Fabrizio Pace [5], Giuseppe Pittà [5], Luigi Raffaele [1,4], Vincenzo Salamone [4], Corrado Spatola [4] and Giada Petringa [1,6,†]

1 Istituto Nazionale di Fisica Nucleare, Laboratori Nazionali del Sud, Via S Sofia 62, 95125 Catania, Italy; pablo.cirrone@lns.infn.it (N.A.); roberto.catalano@lns.infn.it (R.C.); cuttone@lns.Infn.it (G.C.); pieroloj73@gmail.com (P.L.); alfiomazzaglia93@gmail.com (A.M.); raffaelepoliclinico@hotmail.com (L.R.); giada.petringa@lns.infn.it (G.P.)
2 Dipartimento di Fisica ed Astronomia "E. Majorana", Catania University, 95100 Catania, Italy
3 Centro Siciliano di Fisica Nucleare e Struttura della Materia (CSFNSM), 95125 Catania, Italy
4 AOU Policlinico of the University of Catania, 95123 Catania, Italy; didomenico@detector-med.com (A.D.D.); vicsal33@gmail.com (V.S.); corrspatola@gmail.com (C.S.)
5 Toret Devices s.r.l., 10153 Torino, Italy; fabrizio.pace@toretdevices.com (F.P.); giuseppe.pitta@detector-med.com (G.P.)
6 Extreme Light Infrastructure (ELI)-Beamlines Center, Institute of Physics (FZU), Czech Academy of Sciences, 18221 Prague, Czech Republic
* Correspondence: pablo.cirrone@infn.it
† These authors contributed equally to this work.

Citation: Cirrone, G.A.P.; Amato, N.; Catalano, R.; Di Domenico, A.; Cuttone, G.; Lojacono, P.; Mazzaglia, A.; Pace, F.; Pittà, G.; Raffaele, L.; et al. On the Possibility to Use the Charge Imbalance in Patients Undergoing Radiotherapy: A New Online, In Vivo, Noninvasive Dose Monitoring System. *Appl. Sci.* **2021**, *11*, 7005. https://doi.org/10.3390/app11157005

Academic Editors: Ivan Veronese and Salvatore Gallo

Received: 9 May 2021
Accepted: 23 July 2021
Published: 29 July 2021

Publisher's Note: MDPI stays neutral with regard to jurisdictional claims in published maps and institutional affiliations.

Abstract: This paper describes a new real-time, in vivo, noninvasive, biasless detector system acting as a beam monitoring and relative dose measurement system. The detector is based on the idea that when a beam current is injected into the body of a patient undergoing a charged particle therapy, the current itself can be collected using a conductive electrode in contact with the patient's skin. This new approach was studied in vitro using an electrically isolated water tank irradiated with monoenergetic proton beams. The conductive electrode was immersed in water and positioned outside the irradiation field. The detection system performance was evaluated by comparing its response against a SEM (Secondary Emission Monitor) detector, used as a reference beam current monitor, and an *Advanced Markus* ionization chamber. Short-, mid- and long-term reproducibility, current monitoring capability, field size dependence, electrode position and environment temperature dependence, linearity with dose, and dose rate dependence were investigated. Few preliminary in vivo tests were also performed that demonstrated the possibility to apply the system in clinical practice. The potential of the proposed method is considerable, representing a simple and economical system for online, in vivo, and noninvasive monitoring of the beam current and relative released dose into the patient during treatment, without perturbing the irradiation field. The system presented in this work is protected with both a National Italian (N. 102017000087851) and an International N. WO 2019/025933 patent.

Keywords: in vivo relative dosimetry; proton; radiotherapy; quality controls; beam monitoring

1. Introduction

In vivo dosimetry (IVD) represents a dosimetric procedure adopted in external beam radiotherapy (EBRT) to detect major errors, assess clinically relevant differences between planned and delivered doses, record doses received by individual patients, and to fulfill the legal requirements needed for a radiotherapy session. IVD is an essential element of modern radiation therapy, providing the ability to catch treatment delivery errors, assist in

treatment adaptation, and record the actual dose delivered to the patient [1,2]. Moreover, IVD is becoming more strategic considering the new flash radiotherapy modalities [3], where potential errors could become even larger and more dangerous than in conventional approaches. It seems, in fact, worthwhile to investigate whether existing IVD detectors can be used for this purpose after determination of their dosimetric characteristics in very-high-dose-rate fields [4,5].

In vivo dosimetry involves several techniques and diversified approaches. All the dosimetric approaches currently adopted, are based on detectors intercepting and, therefore, somehow perturbing the irradiation field. This is of particular relevance in the case of charged particles radiotherapy, where energy losses and scattering effects are not negligible.

Thermoluminescent [6] or Radiochromic detectors [7] (off-line approach), silicon diodes [8–10], diamond detectors [11–13], and MOSFETs (Metal-oxide-semiconductor field-effect transistors) [14,15] (online approach) are conventionally used for in vivo dosimetry [16].

Thermoluminescent dosimeters [6] may be small in size and tissue equivalent but they require a long series of pre- and postirradiation processes and a calibration procedure to be used in the clinical practice. They are not off-line detectors nor usable for real-time dosimetry. Radiochromic films show an excellent spatial resolution; they are tissue equivalent, providing 2D dosimetric information. On the other hand, they are passive detectors, not allowing for real-time measurements. Moreover, their response may be affected by improper handling and scanner performances.

Silicon diodes are standard reference dosimeters for a variety of applications in radiotherapy including quality assurance in stereotactic modalities and in vivo dosimetry. Their major drawback lies in their relatively low radiation resistance, especially when used in charged particle beams.

Diamonds detectors present high sensitivity and spatial resolution comparable to that of silicon diode detectors, low leakage current, and high radiation hardness. On the other hand, some drawbacks limit their use such as high costs and, for the natural diamonds case, long delivery time due to suitable stone selection. Moreover, synthetic diamond detectors present some disadvantages (such as the control of type and amount of incorporated impurities) that seriously limit the production of detector-grade crystals and strongly affect the response stability.

The MOSFETs are able to achieve excellent spatial resolution because of their high sensitivity and small sensitive volume. In particular, the MOSkin, a patented dosimetry based on MOSFET technology and recently introduced by CMRP (Centre for Medical Radiation Physics, University of Wollongong, Australia), is also able to produce a real-time readout and provide a reproducible water equivalent depth of dose measurement of 0.07 mm (suitable for measurements of dose delivered on the patient's skin) [17]. MOSFETs' main disadvantages are finite lifetime (they can collect about 100 Gy as maximum), angular and energy dependence, and sensitivity change with accumulated dose. Moreover, MOSFETs do not provide real-time beam current monitoring. Their information on the dose is accessible only at the end of patient irradiation [18].

All the abovementioned devices can be positioned directly on the patient's skin in order to provide information on the dose deposited but they all intercept and perturb the beam. Moreover, only diodes and diamond detectors are able to follow the beam current trend during the treatment in a real-time modality.

In this work, we will discuss the characteristics of an innovative detection approach for relative dose monitoring, based on the use of a simple and commercial electrode as that used in an electrocardiogram. We will call the name of this detector "Electrode".

A patient undergoing a charged particle radiation treatment absorbs a well-defined quantity of charge and, therefore, is subjected to a net local charge imbalance. The charge disequilibrium generates a potential difference that will produce a current flow through an external, ground-based, floating electrode positioned on the patient's skin, outside the radiation field. The current generated during the potential discharge is directed to a transimpedance, low-pass, and low-noise amplifier, acting as an high-precision picoam-

peremeter. The current is hence integrated. The measured charge corresponds to the net-deposited charge in the patient that can finally be connected to the absorbed dose. The Electrode system was characterized under the 62 MeV clinical monochromatic proton beams, available at the CATANA (Centro di AdroTerapia e Applicazioni Nucleari Avanzate) proton therapy facility of the Laboratori Nazionali del Sud (Istituto Nazionale di Fisica Nucleare) in Catania, Italy [19,20]. Moreover, preliminary tests were performed in vivo on patients undergoing ocular proton-therapy treatments. The tests demonstrated the clinical applicability of the approach as a beam current monitoring system and the possibility to use it for in vivo relative dose monitoring. The described "*Electrode*" technique can be extended to negative-charged beams, such as electrons, thus, covering the entire range of charged radiotherapy beams currently used.

2. Material and Methods

2.1. Low-Noise Acquisition Electronic

Electrode consists of a floating electrode (FIAB, model F2080) connected to a transimpedance, current–voltage converter amplifier, designed and realized by the authors of this paper. The currents collected by the electrode were of the order of nano-Ampere or a fraction of femto-Ampere, and the transimpedance gain was $R = V_{out}/I_{in} = 10^9\ \Omega$. The amplified voltage signals were then sampled by a commercial high speed (1 MS/s) $\pm$ 10 V digital scope (model NI 9223, National Instruments). The acquisition software, able to monitor and register the currents and perform a preliminary analysis of the acquired signals, was also developed by the authors.

The trans-impedance amplifier contains four principal elements:

1. A current–voltage converter (I–V), based on an OPA128 (Texas Instruments) operational amplifier, coupled with a high-resistance feedback resistor (1 GΩ) and a 100-pF capacitor, in parallel to the resistance. This configuration limits the maximum cutting frequency to 1.6 Hz; moreover, it allows the control of the autoinduced oscillations in the converter and avoids overshoot phenomena. The I–V converter response is linear in the output range of $-10\ V \leq V_{out} \leq +10\ V$. The conversion range will hence be $-10\ nA \leq I_{in} \leq +10\ nA$.
2. A low-pass filter made of a Resistive-Capacitance (RC) network, with a cut frequency of 0.9 Hz and an attenuation of -68 dB at 50 Hz. The filter has two main roles: it protects the OPA128 operational amplifier from possible electrostatic discharges (ESD) induced both by patient and/or medical personnel during the pretreatment phases; it also weakens the 50-Hz noise currents, induced in the patient by the environment's electromagnetic fields, by a factor 2.500.
3. A couple of Junction gate Field-Effect Transistors (JFET), which protect the OPA128 whenever the I–V converter reaches saturation. If the I–V converter works inside its operational range, the two JFETs are not operative and the leakage currents they introduce are negligible (order of 100 fA).
4. An active, inverting, second-order, low-pass filter. Its main aim is to cut (with a slope of 40 dB per decade) the residual noise at the output of the I–V converter. The inverting characteristic of this filter was designed to compensate the negative voltage sign at the output of the I–V converter. With this solution, the final output voltage will be positive, i.e., of the same sign as the input current.

2.2. Experimental Set-Up

Irradiations were performed at the INFN-LNS clinical proton therapy facility where a 62 $\pm$ 0.3 MeV proton beam was available. Details on the irradiation beamline, beam characteristics, and dosimetric procedures can be found elsewhere [19–21].

All measurements were performed by positioning the floating electrode inside a $20 \times 20 \times 20\ cm^3$ water tank, on the opposite side of the beam entrance window (see Figure 1) outside the irradiation field. The water tank was electrically isolated to avoid charge leakages. The beam spot size was circular, with a 25-mm diameter (Figure 1).

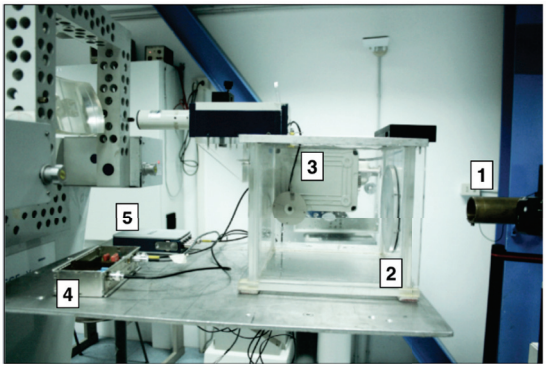

Figure 1. Experimental set-up adopted for the experimental measurements: (1) circular, 25 mm in diameter, brass collimator; (2) the water tank; (3) the electrode, positioned inside its holder and immersed in water outside the proton field; (4) the transimpedance amplifier; (5) the NI 9223 digital scope.

All the experimental measures involved recording the detector signals for five repeated irradiations corresponding with the same released dose. The integrated charge values and the corresponding uncertainties were estimated as the average and standard deviation of the five consecutive measurements, respectively. Figure 2 shows an example of the detector current output in the five irradiations. Each curve corresponds to a dose of 4 Gy, released at the water-tank entrance. The huge variations in the signals are due the proton beam instabilities during the irradiations and could be the cause of the lower observed sensitivity with respect to the calculations.

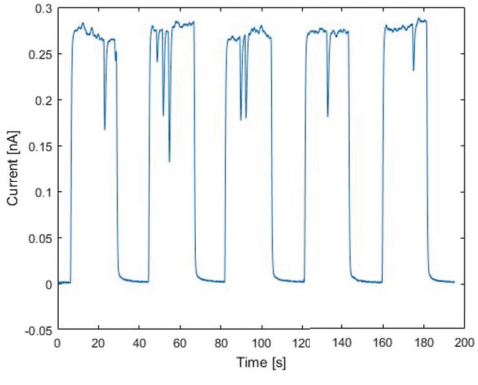

Figure 2. Detector current output for five consecutive proton irradiations. Each positive signal corresponds to a nominal dose of 4 Gy released at the water-tank entrance.

2.3. Set-Up for In Vivo Irradiation

A set of preliminary in vivo tests were also performed on patients undergoing eye melanoma proton-therapy treatments. During the irradiation, the patients were positioned upon an electrically isolated chair and the electrode located on the patient's skin, below the thermoplastic mask, close to the temporal region but outside the proton irradiation field (see Figure 3). The whole electronic chain and acquisition system were identical to those used in the in-phantom measurements.

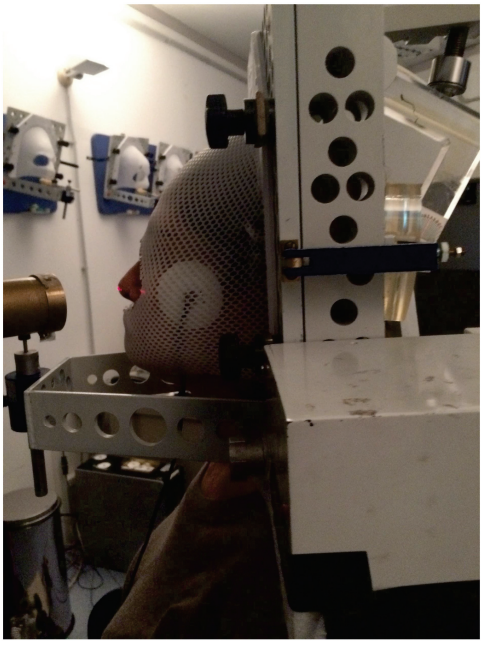

Figure 3. A patient just before the proton therapy session with the electrode system positioned under the thermoplastic mask.

During irradiations, both for the in-phantom and in-patient irradiations, the beam current was also monitored by a SEM (Secondary Emission Monitor) detector. It was positioned in vacuum, just before the beam exit window, at about three meters before the water-tank windows. The SEM is a monitoring system, providing a relative measure of the proton beam fluence. The SEM response is independent from the proton dose-rates [12,21] and was used as a beam reference.

3. Results and Discussion

The electrode dosimetric response was studied to investigate its response with respect to the dose released inside the water-tank and the proton beam dose rate. Short- and long-term stability, response dependence as a function of the proton beam field-size, position in the water-tank, and water temperature were also studied.

3.1. Dose and Dose-Rate Dependence

The detector response, as a function of the total dose released by the 62-MeV monochromatic proton beam, was studied in the 2–20 Gy range. The beam dose rate was kept fixed at 16 Gy/min. Considering that the variance associated to each point is not constant in the whole dose range, a weighted least square regression test was used to linearly fit data points. The fit result is reported in Figure 4. The detector response versus the released dose appears linear with an excellent confidence degree. A sensitivity of 0.3912 nC/Gy was derived from the measured data as the slope of the linear fit. Deviations no larger than $\pm 2\%$ were observed in the whole investigated dose range.

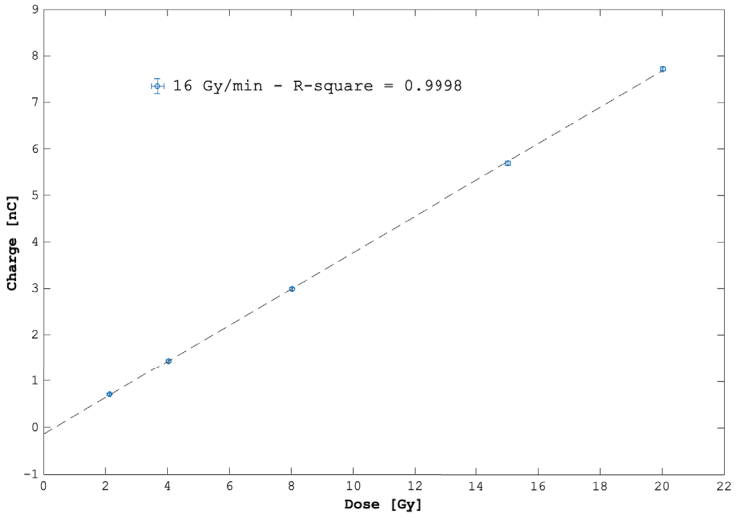

Figure 4. Detector response as a function of the released dose in water. The linear fit shows an excellent confidence degree expressed by the R2 parameter.

The detector sensitivity was also evaluated at six different values of dose-rate, in the range of 10–40 Gy/min. In Figure 5, the percentage discrepancy versus the charge collected at the maximum dose rate (39 Gy/min) is reported. A maximum variation of 3% was found.

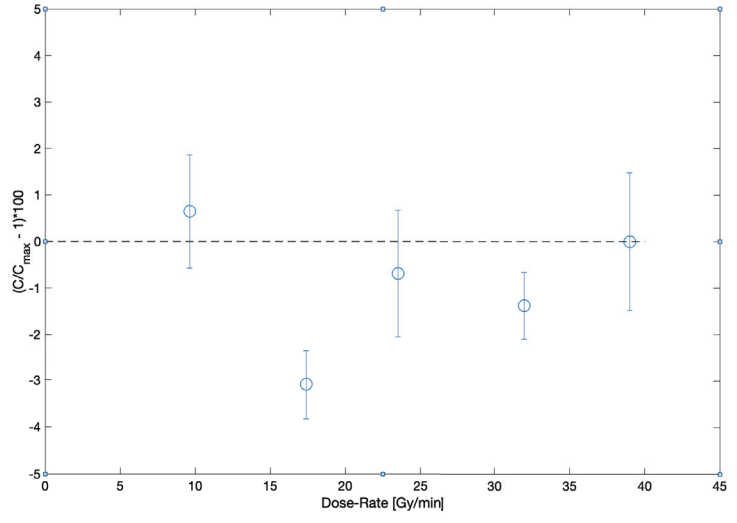

Figure 5. Percentage variations, with respect to the value measured at the maximum dose rate (39 Gy/min) of the collected charge for growing values of beam dose—rate.

3.2. Short-, Mid-, and Long-Term Reproducibility

Short-, mid-, and long-term reproducibility were investigated, and their values are summarized in Table 1. The proton beam dose-rate (16 Gy/min), dose (4 Gy), energy (60 MeV) at the irradiation point (i.e., at the detector position), and a circular beam spot 25 mm in diameter were taken as constants for all the measures.

The short-term reproducibility was investigated, evaluating the detector response in ten repeated irradiations of 4 Gy, then repeated five times within one hour. For each set of the ten measures, the averaged detector sensitivity, expressed in nC/Gy—i.e., as the ratio between measured charge and the corespondent released dose—was calculated. The maximum observed variation in the sensitivity was found to be less than 2% during the whole hour.

Similarly, the mid-term reproducibility was evaluated estimating the detector sensitivity ten times in five consecutive days. The maximum percentage difference observed was about 2.3%. For the long-term reproducibility, the sensitivity was measured ten times within 17 months, using the same irradiation conditions. In this case, the maximum percentage difference was 4.3%.

Table 1. Short-, mid-, and long-term reproducibility expressed as percentage variations of the detector sensitivities for the whole set of measurements.

Short-term reproducibility	≤2%
Mid-term reproducibility	≤2.3%
Long-term reproducibility	≤4.3%

3.3. Current Monitoring Capabilities

Consider again the five current signals reported in Figure 2. Each curve corresponds to a nominal dose D_{nom} of 4 Gy released at the entrance of the water-tank. Integrating the current of each signal, we calculated the charge per dose unit (sensitivity) and measured an average value of $<Q_{exp}/D_{nom}>$ = 0.367 nC/Gy and a standard deviation of 0.005 nC/Gy.

The expected theoretical sensitivity Q_{Th}/D_{nom} was calculated from the expression (1):

$$\frac{Q_{Th}}{D_{nom}} = \frac{N_p \cdot q_e}{D_{nom}} = \frac{S \cdot q_e}{\left(\frac{dE}{dx}\right)_{60\ \mathrm{MeV}}} \quad (1)$$

where S is the beam spot surface at isocenter (S = 5.31 ± 0.21 cm^2); $\frac{dE}{dx}_{60\ \mathrm{MeV}}$ is the 60-MeV (energy at the isocenter point) proton massive stopping power in water (10.78 ± 0.01 MeV·cm^2/g); D_{nom} is the nominal absorbed dose in water at the entrance of the water phantom; N_p is the total number of the incident protons; q_e is the elementary charge unit.

A value of Q_{Th}/D_{nom} = 0.393 ± 0.020 nC/Gy was found, deviating 6.6% from the experimental $<Q_{exp}/D_{nom}>$ result. This demonstrated the ability of the developed system to estimate the total charge received and, hence, of the dose absorbed at the entrance of the water tank. We quantitatively analyzed the SEM and Electrode signals, comparing their main characteristics: signal rise- and fall-time (defined as the time intervals needed to the signal for raising from 10% to 90% and for falling from 90% to 10% of its maximum, respectively), Full Width at Half Maximum (FWHM), and the curve integrals of each signal. Results are summarized in Table 2.

Table 2. Comparisons of the main parameters of the curves reported in Figure 2.

	Rise Time (s)	Fall Time (s)	FWHM (s)	Charge Integral (nC)
SEM	0.43 ± 0.02	0.37 ± 0.02	52.03 ± 0.02	49.32 ± 0.01
ELECTRODE	0.80 ± 0.02	0.65 ± 0.02	52.03 ± 0.02	49.50 ± 0.01
Difference [%]	46	43	0.02	0.36

Despite the rise-time differences, mainly due to the RC time constants of the Electrode front-end read-out circuit (see Section 2.1), the percentage difference between the FWHMs and total integrals was less than 0.02% and 0.4%, respectively.

3.4. Field-Size Dependence

For circular beams with an homogenous lateral distribution, as those used in the current work, a proportionality of the detector signal with the square of the beam radius is expected. In order to verify such a dependence, the collected charge was measured using irradiation fields of different diameters (5 mm, 10 mm, 15 mm, 20 mm, 25 mm, and 36 mm). A second-order polynomial fit was applied and an r^2 value equal to 0.9978 was obtained, confirming the expected behavior of the detector response.

3.5. Position and Temperature Dependence

The Electrode response as a function of its position with respect to the beam entrance and the water temperature was evaluated.

In order to study the position dependence, the detector was irradiated in four different positions, as shown in Figure 6 where a sketch of the water tank (view from the top) and the Electrode positions are presented. In each position, ten consecutive irradiations, corresponding to a released dose of 4 Gy at the entrance position of the water tank, were performed. A maximum percentage difference of 5.3% was found for the detector response in the four positions.

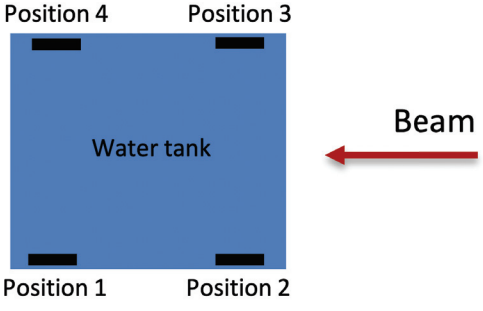

Figure 6. Four different irradiation configurations, each for one electrode position in the water phantom (view from the top).

The detector dependence with respect to the temperature was investigated in the temperature range of 20–40 °C. Differences lower than 3% between the lowest and highest values were observed.

4. Preliminary In Vivo Tests

Some in vivo tests were performed on one patient undergoing eye proton-therapy irradiations at the CATANA facility [19–21].

In each irradiation session (of the four required by the clinical protocols), the patient received a dose of 15-Gy Cobalt-equivalent, released with a clinical Spread Out Bragg Peak obtained from a 62-MeV proton beam and a plastic modulator. The proton beam field was tailored on the tumor shape by means of a brass collimator designed by the treatment planning system [21]. In Table 3, the treatment duration, the collected charge, and the nominal delivered dose in each of the four sessions are reported.

Table 3. Irradiation parameters and results obtained during the patient irradiation session.

Session	Time (s)	Charge (nC)	Nominal Dose (cGy)
1	40	3.32 ± 0.06	1366
2	42	3.14 ± 0.06	1366
3	35	3.19 ± 0.06	1366
4	44	3.35 ± 0.06	1366

The average charge measured in the four sessions was 3.25 ± 0.10 nC; the small percentage error (around 3%) demonstrates the good repeatability of the detector response in the case of patient irradiations.

Figure 7, finally, demonstrates how the system can be successfully used to monitor the beam current during treatment. It shows the detector response corresponding to the treatment session number 3 of Table 3. Around the second 85, the beam (orange dots) suddenly stopped for some technical reasons, restarting around the second 90. At the same time, the detector signal (black dots) dropped off, indicating the beam stop and the missing irradiation.

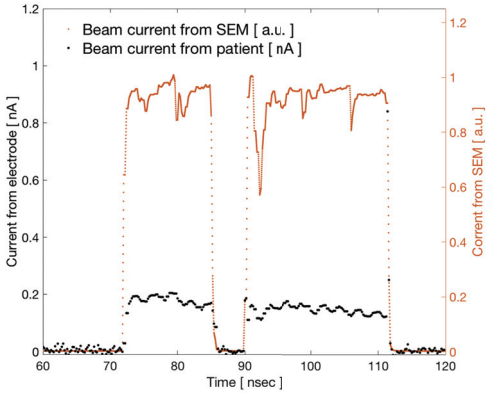

Figure 7. Proton beam signal (orange dots) measured by secondary electron monitoring (SEM) and the corresponding signal acquired by the electrode (black dots) positioned on the patient's skin (see Figure 3). It is interesting to note that the sudden and unexpected beam stop during irradiation (at around second 85) and its next recovery (at around second 90) is perfectly followed by the electrode signal.

5. Conclusions and Perspectives

The suitability of a new online, noninvasive, biasless detector for relative dose monitoring in patients undergoing charged particle radiotherapy treatments was investigated. The device, a floating electrode connected on the patient's skin, collects the charge delivered by the beam and returns a current signal proportional to the total charge deposited by the beam. The system was firstly characterized in vitro, irradiated inside a dosimetric water-tank with a clinical monochromatic 60 MeV proton beam. Short-, mid-, and long-term reproducibilities were studied and their values resulted better than 4.3%. The system resulted was independent from the temperature (5% maximum difference in the 20–40 °C range) and its response was proportional to the irradiation field area with a good confidence degree (R^2 = 0.9978). The characterization evidenced a very good linearity with the dose absorbed in the water tank, in the 2–20 Gy range, with R^2 = 0.9999 and a deviation from linearity of less than 2%.

The device's response was also independent from the proton beam dose rate in the 10–40 Gy/min range, where a maximum percentage difference of 3% was found.

Preliminary in vivo tests highlighted the capability of the device in acting as beam monitoring during a patient proton-therapy treatment and its ability in the verification of the correct dose delivered among the various fractions of the treatment. The set of performed tests, even if preliminary, show the capability of the system in operating as a beam monitoring device. The acquired results appear statistically robust, where no standard deviation bigger of 4.3% was observed in the sets of the repeated measures. On the other way, the system characterization must be completed, including additional tests. For example, the system response with respect to different beams' energies must be studied in order to exclude (or determine) potential dependencies with the proton linear energy

transfer (or LET). Additionally, materials other then water but similar to biological tissue composition must be investigated. The in vivo characterization, that obviously suffers from a lack of sufficient data, must be repeated with several more measures in order to reach a good statistical significance.

Improvement of the *Electrode* read-out circuits are ongoing to minimize the current leakage during in vivo irradiations. Its characterization under electrons and carbon ion beams is under way as well.

6. Patents

The device described in this work is protected by both a National Italian (N. 102017000087851) and an International N. WO 2019/025933 patent.

Author Contributions: The Idea of this device is from G.A.P.C., design and experimental implementation was performed by G.A.P.C. and G.P. (Giada Petringa); the low-noise, front-end electronic was developed by N.A. and A.M.; the clinical implementation was organized and followed by L.R., V.S., C.S. and G.C.; experimental sessions were organized and led by G.A.P.C., G.P. (Giada Petringa), and R.C.; data analysis and data interpretation were performed by G.A.P.C., G.P. (Giada Petringa) and P.L. A.D.D. F.P. and G.P. (Giuseppe Pittà) have realized a research prototype in industrial perspective. All authors have read and agreed to the published version of the manuscript.

Funding: This research was funded by the Tecnology Transfer Committee of the Istituto Nazionale di Fisica Nucleare (INFN) in the framework of the ELECTRODE project (2017–2018). The realization of the device was also supported by the DE.TEC.TOR. Company and by the Committee for the Interdisciplinari Researches of INFN.

Institutional Review Board Statement: This study was conducted irradiating one patient that personally signed an informed consent.

Informed Consent Statement: Informed consent was obtained from all subjects involved in the study.

Data Availability Statement: Data are not publicly available.

Conflicts of Interest: The authors declare that this device is protected by a national and International patent and that it could be commercialized in the future. At the moment of writing the described device is not commercialized and no conflict of interest is present.

References

1. Olaciregui-Ruiz, I.; Beddar, S.; Greer, P.; Jornet, N.; McCurdy, B.; Paiva-Fonseca, G.; Mijnheer, B.; Verhaegen, F. In vivo dosimetry in external beam photon radiotherapy: Requirements and future directions for research, development, and clinical practice. *Phys. Imaging Radiat. Oncol.* **2020**, *15*, 108–116. [CrossRef] [PubMed]
2. Mijnheer, B.; Beddar, B.; Izewska, J.; Reft, C. In vivo dosimetry in external beam radiotherapy. *Med. Phys.* **2013**, *40*, 070903. [CrossRef] [PubMed]
3. Bourhis, J.; Jeanneret Sozzi, W.; Gonçalves Jorge, P.; Gaide, O.; Bailat, C.; Duclos, F.; Patin, D.; Ozsahin, M.; Bochud, F.; Germond, J.; et al. Treatment of a first patient with FLASH-radiotherapy. *Radiother. Oncol.* **2019**, *139*, 18–22. [CrossRef] [PubMed]
4. Gonçalves Jorge, P.; Jaccard, M.; Petersson, K.; Gondré, M.; Durán, M.T.; Desorgher, L.; Germond, J.F.; Liger, P.; Vozenin, M.C.; Bourhis, J.; et al. Dosimetric and preparation procedures for irradiating biological models with pulsed electron beam at ultra-high dose-rate. *Radiother. Oncol.* **2019**, *139*, 34–60. [CrossRef] [PubMed]
5. Schüler, E.; Trovati, S.; King, G.; Lartey, F.; Rafat, M.; Villegas, M.; Maxim, P.G. Experimental platform for ultra-high dose rate FLASH irradiation of small animals using a clinical linear accelerator. *Int. J. Radiat. Oncol. Biol. Phys.* **2017**, *97*, 195–203. [CrossRef]
6. Kortov, V. Materials for thermoluminescent dosimetry: Current status and future trends. *Radiat. Meas.* **2007**, *42*, 576–581. [CrossRef]
7. Niroomand-Rad, A.; Blackwell, C.R.; Coursey, B.M.; Gall, K.P. Radiochromic film dosimetry: Recommendations of AAPM Radiation Therapy Committee Task Group 55. *Med. Phys.* **1998**, *25*, 2093–2115. [CrossRef] [PubMed]
8. Oliveira, F.F.; Amaral, L.L.; Costa, A.M.; Netto, T.G. In vivo dosimetry with silicon diodes in total body irradiation. *Radiat. Phys. Chem.* **2014**, *95*, 230–232. [CrossRef]
9. Dixon, R.L.; Ekstrand, K.E. Silicon diode dosimetry. *Int. J. Appl. Radiat. Isot.* **1982**, *33*, 1171–1176. [CrossRef]
10. *Diode In-Vivo Dosimetry for Patient Receiving External Beam Radiation Therapy*; Report of Task Group 62 of the Radiation Therapy Committee Published for the American Association of Physicists in Medicine by Medical Physics Publishing; AAPM Report No. 87; American Association of Physicists in Medicine: Alexandria, VA, USA, 2005.

11. Ravichandran, R.; Binukumar, J.P.; Al Amri, I. Diamond detector in absorbed dose measurements in high-energy linear accelerator photon and electron beams. *J. Appl. Clin. Med. Phys.* **2016**, *2*, 291–303. [CrossRef] [PubMed]
12. Cirrone, G.A.P.; Cuttone, G.; Rafaele, L.; Sabini, M.G.; De Angelis, C.; Onori, S.; Pacilio, M.; Bucciolini, M.; Bruzzi, M. Natural and CVD type diamond detectors as dosimeters in hadrontherapy applications. *Nucl. Phys. B Proc. Supp.* **2003**, *125*, 179–183. [CrossRef]
13. Bucciolini, M.; Banci Buonamici, F.; Mazzocchi, S.; De Angelis, C.; Onori, S.; Cirrone, G.A.P. Diamond detector versus silicon diode and ion chamber in photon beams of different energy and field size. *Med. Phys.* **2003**, *30*, 2149–2154. [CrossRef] [PubMed]
14. Manigandan, D.; Bharanidharan, G.; Aruna, P.; Devan, K.; Elangovan, D.; Patil, V.; Tamilarasan, R.; Vasanthan, S.; Ganesan, S. Dosimetric characteristics of a MOSFET dosimeter for clinical electron beams. *Phys. Medica* **2009**, *25*, 141–147. [CrossRef] [PubMed]
15. Cirrone, G.A.P.; Cuttone, G.; Lojacono, P.A.; Lo Nigro, S.; Patti, V.I.; Pittera, S.; Raffaele, L.; Sabini, M.G.; Salamone, V.; Valastro, L.M. Preliminary investigation on the use of the MOSFET dosimeter in proton beams. *Physica Medica* **2006**, *22*, 29–32. [CrossRef]
16. *Development of Procedures for In Vivo Dosimetry in Radiotherapy*; Technical Report Series No. 8; International Atomic Energy Agency: Wien, Austria, 2013.
17. Di Venanzio, C.; Marinelli, M.; Milani, E. Characterization of synthetic single crystal diamond Schottky diode for radiotherapy electron beam dosimetry. *Med. Phys.* **2013**, *40*, 021712. [CrossRef] [PubMed]
18. Alnawaf, H.; Butson, M.; Yu, P.K.N. Measurement and effects of MOSKIN detectors on skin dose during high energy radiotherapy treatment. *Australas. Phys. Eng. Sci. Med.* **2012**, *35*, 321–328. [CrossRef] [PubMed]
19. Cirrone, G.A.P.; Cuttone, G.; Lojacono, P.A.; Nigro, S.L.; Mongelli, V.; Patti, I.V.; Privitera, G.; Raffaele, L.; Rifuggiato, D.; Sabini, M.G.; et al. A 62-MeV proton beam for the treatment of ocular melanoma at Laboratori Nazionali del Sud-INFN. *IEEE Trans. Nucl. Sci.* **2004**, *51*, 860–865. [CrossRef]
20. Cuttone, G.; Cirrone, G.A.P.; Di Franco, G.; La Monaca, V.; Lo Nigro, S.; Ott, J.; Pittera, S.; Privitera, G.; Raffaele, L.; Reibaldi, A.; et al. CATANA protontherapy facility: The state of art of clinical and dosimetric experience. *Eur. Phys. J. Plus* **2011**, *126*, 65. [CrossRef]
21. Cirrone, G.A.P.; Cuttone, G.; Raffele, L.; Salamone, V.; Avitabile, T.; Privitera, G.; Corrado, S.; Amico, A.; La Rosa, G.; Leanza, R.; et al. Clinical and Research Activities at the CATANA Facility of INFN-LNS: From the Conventional Hadrontherapy to the Laser-Driven Approach. *Front. Oncol.* **2017**, *7*, 223. [CrossRef] [PubMed]

applied sciences

MDPI

Review

Medical Applications of the GEMPix

Johannes Leidner [1,*], Fabrizio Murtas [1,2] and Marco Silari [1,*]

[1] CERN, 1211 Geneva, Switzerland; fabrizio.murtas@cern.ch
[2] LNF-INFN, 00044 Frascati, Italy
* Correspondence: johannes.leidner@cern.ch (J.L.); marco.silari@cern.ch (M.S.)

Abstract: The GEMPix is a small gaseous detector with a highly pixelated readout, consisting of a drift region, three Gas Electron Multipliers (GEMs) for signal amplification, and four Timepix ASICs with 55 μm pixel pitch and a total of 262,144 pixels. A continuous flow of a gas mixture such as Ar:CO_2:CF_4, Ar:CO_2 or propane-based tissue equivalent gas is supplied externally at a rate of 5 L/h. This article reviews the medical applications of the GEMPix. These include relative dose measurements in conventional photon radiation therapy and in carbon ion beams, by which on-line 2D dose images provided a similar or better performance compared to gafchromic films. Depth scans in a water phantom with ^{12}C ions allowed measuring the 3D energy deposition and reconstructing the Bragg curve of a pencil beam. Microdosimetric measurements performed in neutron and photon fields allowed comparing dose spectra with those from Tissue Equivalent Proportional Counters and, additionally, to obtain particle track images. Some preliminary measurements performed to check the capabilities as the detector in proton tomography are also illustrated. The most important on-going developments are: (1) a new, larger area readout to cover the typical maximum field size in radiation therapy of 20 × 20 cm^2; (2) a sealed and low-pressure version to facilitate measurements and to increase the equivalent spatial resolution for microdosimetry; (3) 3D particle track reconstruction when operating the GEMPix as a Time Projection Chamber.

Keywords: GEMPix; GEMs; Timepix; Medipix; radiation therapy; hadron therapy; microdosimetry; gaseous detectors

Citation: Leidner, J.; Murtas, F.; Silari, M. Medical Applications of the GEMPix. *Appl. Sci.* **2021**, *11*, 440. https://doi.org/10.3390/app11010440

Received: 23 November 2020
Accepted: 16 December 2020
Published: 5 January 2021

Publisher's Note: MDPI stays neutral with regard to jurisdictional claims in published maps and institutional affiliations.

1. Introduction

The GEMPix is an innovative detector developed at CERN a few years ago within a Marie Curie Initial Training Network (ITN) funded by the EU under FP7 between 2012 and 2016. ARDENT (Advanced Radiation Dosimetry European Network Training initiative) [1] was coordinated by CERN and aimed at developing advanced detector technologies for radiation dosimetry. It involved 13 universities, research organisations and industries and recruited 15 Early Stage Researchers (ESR) on 3-year contracts, most of whom obtained a doctorate at the end of the project. The technologies that were part of the program of work were (1) gaseous detectors such as Gas Electron Multipliers (GEM) and tissue equivalent proportional counters (TEPC), (2) solid state detectors such as Medipix and silicon microdosimeters and (3) track detector techniques such as CR-39.

The main objectives of ARDENT targeted radiation dosimetry, microdosimetry and photon/neutron spectrometry. The envisaged applications were the characterization of radiation fields at particle accelerators used in research, industry and medicine, the characterization of radiation fields on-board aircrafts and in space, the assessment of secondary dose to radiation therapy patients and the measurement of the properties of clinical hadron beams used in particle therapy (hadron therapy).

The seed ideas that brought to the development of the GEMPix lie within a workshop held at CNAO, the National Centre for Oncological Hadrontherapy sited in Pavia, Italy [2], soon after the start of ARDENT, in October 2012 [3]. A very fruitful exchange of ideas took

place around current and envisaged Quality Assurance (QA) instrumentation for particle therapy. The discussion focussed on:

(1) commissioning of the Treatment Planning System (TPS). This includes experimental data on integral depth dose distributions of monoenergetic pencil beams using the PTW Peakfinder (Physikalisch-Technische Werkstätten Dr. Pychlau GmbH, Freiburg, Germany, [4]), transversal dose profiles in air measured with External Beam Therapy (EBT3) radiochromic films [5], transversal dose profiles in a water phantom with pin-point Ionisation Chamber (IC) like the PTW 31014 [6], uniformity tests of the scanned beam using EBT3 films;
(2) determination of absorbed dose to water under reference conditions with Farmer-type IC like the PTW 30013 [7], and calibration of beam monitor chambers used to integrate the dose to patient;
(3) determination of procedures and reference values for periodic QA checks. Daily QA checks include spot position accuracy and size checks, and beam energy constancy check, using EBT3 films. Patient-specific pre-treatment QA includes TPS verification plan.

The current commissioning and QA procedures at CNAO are described in [8]. The concept of GEM detectors [9,10], which are mostly used in high-energy physics, was presented, describing the Triple-GEM construction [11] with the standard pad readout made of 128 channels allowing spatial resolution of typically a few mm, the FPGA-based data acquisition system (DAQ) and a specifically designed High Voltage (HV) power supply called HVGEM to supply the required power via seven HV channels. GEMs allow real time track reconstruction, from single particle to high intensity beams. At the same time, the single particle counting pixel detector Timepix [12] was introduced by representatives of the Medipix collaboration [13–15], explaining its particle tracking capabilities and particle discrimination properties by cluster analysis.

The idea to merge these two technologies and combine their advantages to build a gaseous detector with a highly pixelated readout and achieve superior spatial resolution unfolded rapidly, and yielded the design and construction of the first GEMPix prototypes in March 2013. Only a few years later the detector has proven very successful and has been used for several applications. Its use as a tracking detector operated as a highly granular and compact Time Projection Chamber (TPC) has been shown [16]: the device can be operated in a hybrid mode with some pixels measuring deposited charge and others measuring the drift time of the charge in order to obtain a complete 3D reconstruction of the track. It has been introduced as a novel method to detect the very weak (5.9 keV) X-ray emission of ^{55}Fe in radioactive waste produced by the operation of particle accelerators and experimental facilities, to determine its specific activity (Bq/g) in metallic waste characterization [17]. Furthermore, the GEMPix has been used as a soft X-rays diagnostic tool for laser produced plasmas [18,19] and for studies on a dark matter detector with a negative ion TPC read by a GEMPix [20].

The present paper will review the medical applications of the GEMPix. It is mostly a review paper, but the last sections describe on-going work and anticipate the most recent results that will be the subject of two dedicated publications currently under preparation. After illustrating the design and operating principle of the detector (Section 2), Sections 3 and 4 describe its imaging application in photon and electron radiation therapy (that we call 'conventional radiation therapy' in the following) and particle therapy. The results presented in these two sections have been published in [21] and in [22–24], respectively. A proof-of-principle of two GEMPix detectors as TPCs for proton tomography [25] is discussed in Section 5. Section 6 illustrates a very recent version of the detector for microdosimetry called GEMTEQ, whereas Section 7 discusses the latest development for a larger area version of the GEMPix (LaGEMPix) for use in QA in hadrontherapy. Finally, future developments are outlined in Section 8.

2. The GEMPix

The GEMPix couples two CERN technologies, the Gas Electron Multiplier [9,10] as amplifier for electric charges with four highly pixelated Timepix ASICs (the so-called quad or quadboard) as readout [12]. The concept for gas pixel detectors is not new [26]; it was first developed by Bellazzini et al. [27] as an X-ray polarimeter using a custom ASIC [28] for X-ray astronomy [29,30]. Other examples include the GRIDPIX designed for high-energy physics applications [31], but sparks and discharges have proven to be persistent problems with these devices. Thanks to a specially designed High Voltage power supply (HVGEM) [32] and a carefully designed GEM electrode layout, the GEMPix demonstrates good reliability and discharge resistance. Figure 1 shows the GEMPix. It consists of (1) a drift gap of about 1 cm, (2) a triple-GEM setup for charge amplification and (3) an array of 2×2 'naked' Timepix ASICs, i.e., Timepix ASICs without the usual silicon sensor layer. The GEMPix is thoroughly described in [33,34]. Its design and operating principles are recalled here, first illustrating those of its two main components, and then their combination in the GEMPix.

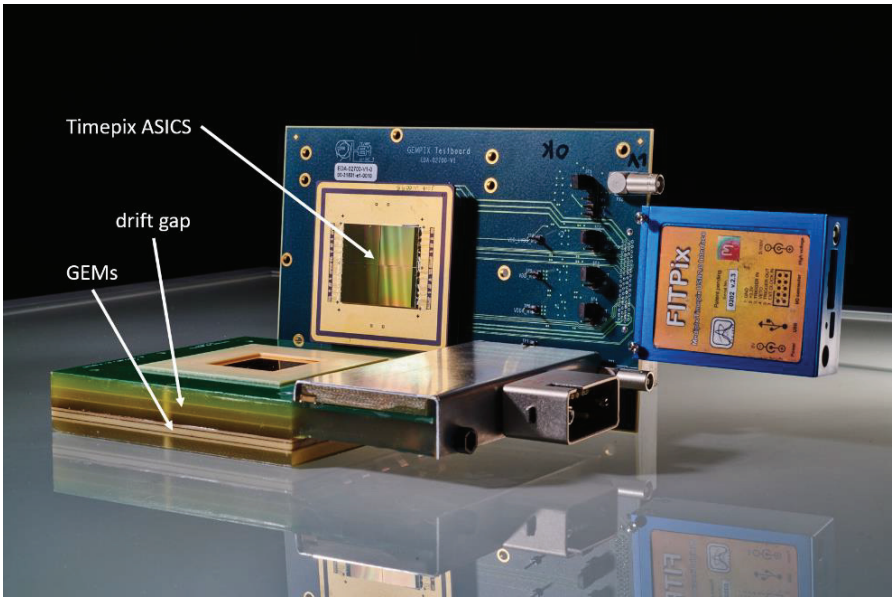

Figure 1. The open GEMPix, showing the four Timepix ASICs and the FITPix readout module. The position of the drift gap and the GEMs is labelled (source: CERN).

The GEM [9] is a thin (50 μm) kapton foil, copper cladded on each side and chemically perforated by a high density of holes having bi-conical structure with an external (internal) diameter of 70 μm (50 μm) and a pitch of 140 μm, as shown in Figure 2. By applying a suitable voltage difference (typically 400 ÷ 500 V) between the two metallic sides, an electric field with a field strength as large as 100 kV/cm is produced inside the holes. The holes act as spatially well-confined electron multiplication channels for the electrons released by ionizing radiation in the drift gap. The maximum gain reachable with a single GEM foil detector is of the order of 10^3. In safe operating conditions, effective gas gains (i.e., the product between the electron multiplication and the transparency, which is the overall efficiency of transporting the electrons through the GEM holes [11]) of up to 10^4–10^5 are reachable by assembling several GEM foils close to each other. The distance between the three GEM foils of the GEMPix is the same as that used by the LHCb muon chambers in order to optimize the time resolution (the first gap is 1 mm) and to reduce the probability of

discharge as much as possible (the second gap is 2 mm, which results in the electron clouds being shared by more holes of the third GEM foil). Typically, the electric field applied between two GEMs to transfer the electrons to the next GEM range between 0.5 and 3 kV/cm depending on the gas and the performance required by the detector application.

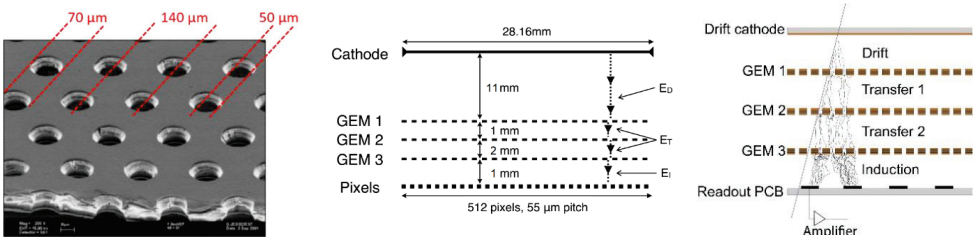

Figure 2. (**Left**) magnified image of a GEM foil. (**Centre**) scheme of a typical triple GEM in the GEMPix detector and the electric transport fields: drift field (ED), transfer fields (ET) and induction field (EI). (**right**) electron multiplication (source: CERN).

Figure 3 shows a scheme of the Timepix chip. The movement of the electric charge produced by the last GEM induces a signal on a group of pads of the chip underlying the charge cluster. The Timepix is able to collect and measure the information of this charge in three different modes, always referring to the time window defined a priori. The first mode ('Medipix mode') allows measuring the number of hits per pixel in the time window. The second mode is the Time-over-Threshold ('ToT'): the Timepix is able to measure with a precision on the order of 10 ns the time spent above the threshold by the analog signal induced on the single pixel; this time is proportional to the collected charge and, therefore, if the detector is calibrated, to the energy deposited by the radiation. This mode is typically used for spectroscopy of X-rays, dosimetry, microdosimetry and for dE/dX measurements. The third mode is the Time-of-Arrival ('ToA'): the Timepix measures the time of arrival of the electron cloud with respect to an external trigger for a maximum of a 2 ms time window. This mode is typically used for 3D reconstruction of a track inside the detector. The readout mode can be chosen for each pixel individually, such that a combined ToT and ToA analysis of a charge cluster becomes possible when using a mixed mode by operating some pixels in ToA mode and the rest of the pixels in ToT mode.

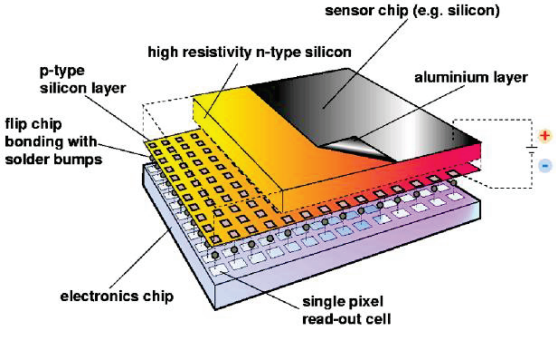

Figure 3. The Timepix chip with the standard silicon sensor on top. The GEMPix uses four 'naked' Timepix ASICs, i.e., without the silicon sensor chip (source: CERN).

The Timepix ASICs are read out by the FITPix, an FPGA based module shown in Figure 1 [35] using the Pixelman software [36]. This software, developed by the University of Prague, is able to save the time and charge information of each pixel within the preset time interval in matrix form, showing the image obtained online and saving the data to a

file. It is also possible to use an online cluster analysis in order to write a file with the list of reconstructed pixel clusters, reporting for each one the main information such as start time of the event, the total number of clusters, and for each of them the total charge, some geometric parameters and the position.

The GEMPix can be assembled with different drift gap sizes according to the type of particle to be detected. In the case of charged particles, a few millimeters are sufficient to produce a dozen electrons distributed along the gap, which are sufficient to generate a detectable signal. There are two possible configurations visible in Figure 4: one in which the particle enters perpendicularly to the GEM foils ("head-on") and one in which the particle enters parallel to them ("side-on"). In the second case, it is possible to expand the drift area up to a few centimeters in order to create a small TPC with the possibility to reconstruct the particle track in three dimensions, as for example used in proton tomography (Section 5). In the case of soft X-rays, a gap of about 1 cm is preferred, both to increase the detection efficiency and to contain all the tracks of the primary electron produced. In addition, metal layers suitably designed for the detection of gamma rays can be inserted in the drift area. Recently, thin layers of B_4C have been used for the detection of thermal neutrons: the lithium ion and alpha particle produced in the $^{10}B(n,\alpha)$ reaction strongly ionize the gas in the drift zone, allowing a good discrimination from the gamma signal.

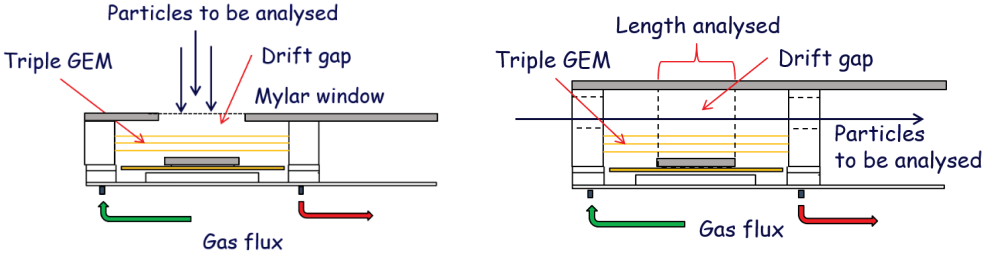

Figure 4. Head-on (**left**) and side-on (**right**) configuration of the GEMPix.

In some applications with high intensity beams or highly ionizing particles, it is possible to reduce the detector configuration to two GEM foils with the advantage of a lower lateral diffusion of the electron cloud and therefore of a better spatial resolution (measurements with only two GEMs turned on are described in Section 3). A detailed study on the gas mixture has been performed in the past [37] showing that a time resolution of better than 5 ns is achieved with CF_4 and iso-C_4H_{10} based gas mixtures, considerably improving the results obtained with the standard Ar/CO_2 (70/30) mixture. Regarding the discharge probability, the use of a small fraction of iso-C_4H_{10} or a large amount of CF_4 results in a very stable detector operation. Therefore, an $Ar/CO_2/CF_4$ (45/15/40) gas mixture is often used with the GEMPix detector.

The HVGEM [32], designed at the Frascati National Laboratories (LNF) of the National Institute of Nuclear Physics (INFN) in Italy, is built with seven floating power supplies with a maximum of 1200 V each, controlled via CANbus and a LabVIEW based software for voltage settings and current monitoring. In this way, each GEM foil has its own power supply allowing a safe operation of the detector, avoiding dangerous discharges versus the front-end electronics. A second shrewdness is the particular electrode path for each GEM foil trying to stave off the High Voltage from the wire bonding of the ASIC readout.

Like all gas detectors, the gain of the GEMPix also depends on the temperature, pressure and humidity of the gas. Therefore, a sensor by yoctopuce [38] reading the thermodynamic variables has been installed inside the detector with the aim of compensating the gain variation by changing the voltages applied to the GEM foils, thus keeping the detector response stable within less than $\pm 5\%$ as shown in Figure 5 (changes of more than 30% were observed without any correction).

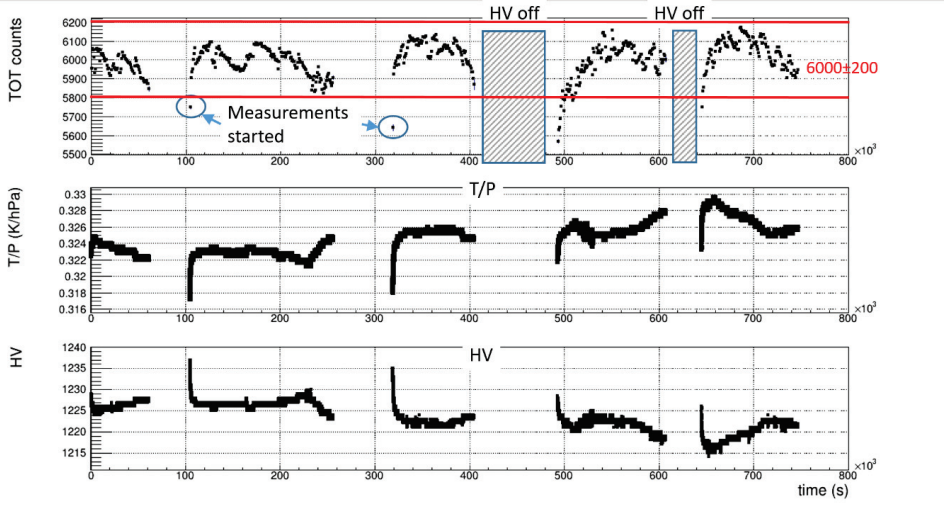

Figure 5. Measurement with an ^{55}Fe source over nine days. The plots show the time evolution of the ToT counts of the 5.9 keV peak from ^{55}Fe (**top plot**), the ratio temperature/pressure (T/P) (**middle plot**), and the High Voltage (HV, **lower plot**). The ToT counts are within 6000 $\pm$ 200 if measurements in the heat-up phase of the detector ('fast rising T') and after the HV was off are discarded.

The GEMPix is able to measure position and charge of the electron clusters produced by the primary ionization of the particles incident on the detector with great precision, thanks to the four Timepix ASICs.

3. Conventional Radiation Therapy

The daily QA and treatment plan verification measurements in radiation therapy facilities are typically performed with gafchromic films or a matrix of small ion chambers [39]. The first method shows very good spatial resolution but needs relatively long time for data analysis, while the second has an online data acquisition but comes with dead space (i.e., non-active detection area) in the treatment area. The GEMPix is a detector that could be used for this application offering advantages on both spatial resolution without dead space and online monitoring capabilities.

Several measurements have been performed with GEM and GEMPix detectors at the Tor Vergata Radiotherapy Centre in Italy (Figure 6) using two electric field configurations [21]: the GEMPix in a standard configuration with all electric fields on, and the triple GEM operated with zero electric drift field and the first GEM foil as a gamma ray converter. In the latter case, the spatial resolution is expected to be better, as the gap between the first and the second GEM now serving as the drift gap is only 1 mm and, therefore, the charge spread is reduced. The conversion efficiency was certainly very low but still reasonably good to obtain a 2D image in 10 times less time as compared with gafchromic films. Moreover, with the GEMPix used in ToT mode, the measured charge is correlated more precisely to the dose released in the gas.

To compare the results obtained with the GEMPix and with gafchromic films quantitatively, the gamma index [40,41] was used, one of the most common quantities for comparison of 2D dose distributions. The gamma index takes into account the dose difference and the distance difference of the two dose distributions to calculate a dimensionless metric for each point. It is commonly accepted that the first must be maximum 3% and the second maximum 3 mm. When the gamma index is less than one, both criteria are satisfied and this condition must be valid for at least 90% of the reference dose points to which a measured dose is compared.

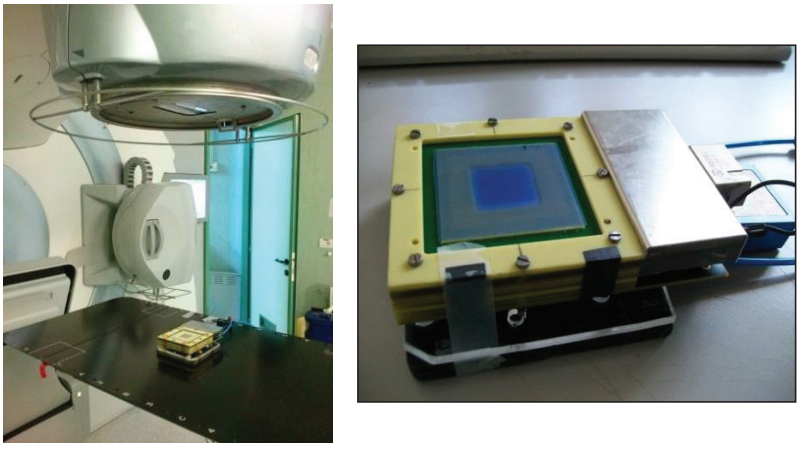

Figure 6. The GEMPix placed in position for irradiation with the Elekta Synergy Linac at the Tor Vergata Radiotherapy Centre (**left**) and the EBT gafchromic film placed on the detector window after irradiation (**right**) [21].

In case of the first, standard GEMPix configuration with three active GEMs, the gamma index shows the best results with the lower energy spectrum (6 MV, gamma index <1 in 96.6% of the points). For higher energy spectra, the percentage of the gamma index decreases (69 and 40% for 10 and 18 MV spectra, respectively). An analogous result is obtained for an Intensity-Modulated Radiation Therapy (IMRT) field. High energy fields are affected by large halos which have no counterpart on the gafchromic films.

A significant optimization of the results has been obtained working in a double-GEM configuration with zero voltage applied to the first GEM foil, i.e., with zero drift field; in this way only two GEMs are used as charge amplifiers. The gamma index percentage improves to better than 90% as shown in Figure 7. Some tests with IMRT fields have shown an excellent agreement, especially when a threshold cut is applied.

The GEMPix presents some advantages with respect to the traditional methods used in radiation therapy:

- It is more sensitive and the gain has been even reduced working with only two GEM foils. The lower limit is represented by the single dose pulse, a limit that gafchromic films cannot reach [5]. The upper limit is the storage bit limit of the read-out register.
- It has an optimal linearity with dose rate and this result is confirmed by the currents measured on the GEM electrodes.
- Compared to gafchromic films, it does not need a scanning process to read the measured doses. This also means no fading and no UV sensitivity problems.
- The spatial resolution obtained with GEM detectors is at least an order of magnitude better than with ion chamber (IC) matrix arrays. With this spatial resolution, no interpolation software is needed to calculate the intermediate dose values as it is the case for IC arrays.
- The pixel pitch of the GEMPix is even better (55 μm) than the one of EBT gafchromic films (340 μm) [5]. The gamma index showed excellent agreement between the GEMPix and gafchromic films.
- The GEMPix is able to perform fast real-time IMRT treatment plan verifications. It has been demonstrated that it is also able to measure single pulses. Then, IMRT fields both in 'step and shoot' and in continuous mode can be reconstructed in time with a very high resolution [21]. No other devices can reach these performances.

The drawback is represented by the active area which is limited to a few cm^2 essentially due to the wire bonding of the chip, while larger fields are used in radiation therapy

(for example, 16 × 21 cm^2 is the maximum field size for the Elekta Synergy Linac used in Tor Vergata). A large area GEMPix is under development, as discussed in Sections 7 and 8.

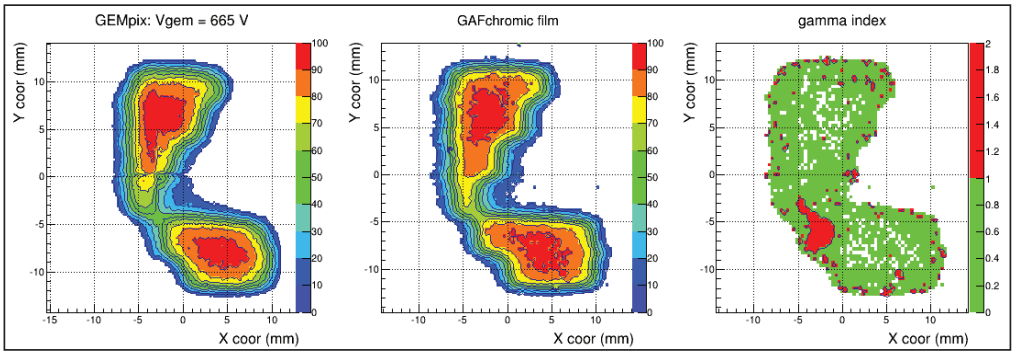

Figure 7. A dose distribution measured with the GEMPix (**left**) is compared to a gafchromic film measurement with a spatial resolution of 160 µm (**centre**) for a 6 MV radiation therapy field: the relative dose is color-coded. The gamma index distribution (**right**) obtained is less than one for 90.5% of the data points [21].

4. Hadron Therapy

Hadron therapy is an advanced radiation modality for cancer treatment. The inherent advantage of hadron therapy is its inverted depth dose curve—the so-called Bragg curve—that allows for highly conformal treatment plans with large dose gradients. The dose is well confined in depth with a moderate lateral spread [42]. Therefore, detectors for beam dosimetry and quality assurance should offer a spatial resolution of the order of 1 mm or better. For patient-specific treatment plan verification, arrays of ionization chambers in a water phantom are often used [43]. However, the spatial resolution is limited to the size of each ionization chamber, which is currently around 5 mm.

The GEMPix potentially offers a much better spatial resolution due to its highly pixelated readout with a pixel pitch of 55 µm. Therefore, it provides new information such as 2D images and 3D data representation. As a first step, a triple-GEM detector coupled to an earlier, coarser readout was irradiated with protons and carbon ions in air [44]. Lateral beam profiles of the GEMPix for one carbon ion beam energy were found in agreement with those obtained by radiochromic EBT3 films. Then, the GEMPix was placed inside a watertight box and mounted on the 3D positioning system of a water phantom used for QA at CNAO in order to measure the 3D dose distribution. Bragg curves were calculated by normalizing the integrated GEMPix response at certain depth positions to the respective delivered dose measured by the Dose Delivery System (DDS) of CNAO [45]. Promising results obtained with this setup [22] led to the development of an integrated system consisting of an IBA Scanditronix Wellhöfer Blue Phantom type 2001 water phantom, a PTW model 34080 reference ionization chamber, the GEMPix, a trigger system and other auxiliary equipment such as the high-voltage supply, and the control and data acquisition software (Figure 8). The system can be set up relatively fast by keeping all equipment on trolleys. It is a stand-alone system as the normalization to the delivered dose is performed with the reference ionization chamber [23,24]. Measurements were performed with carbon ions (C^{6+}) at one of the fixed horizontal beam lines at CNAO, where a synchrotron delivers scanning proton and carbon ion beams to three treatment rooms. The smallest intensity characterized for clinical applications of 2 × 10^6 ions per spill and three beam energies (280, 332 and 380 MeV/u resulting in ranges in water of 150, 200 and 250 mm, respectively) were used. 2D images in the plane perpendicular to the beam axis were acquired at different depths in water. From the 2D images, lateral beam profiles were obtained and compared to radiochromic films showing very good agreement. The Bragg curve was calculated from the 2D images by summing over all pixel values in a

single image, normalizing this value to the corresponding reference ionization chamber measurement, then averaging this normalized sum value over all measurements at the same depth and finally plotting this number versus depth. Bragg curves obtained with the integrated system were compared to a dedicated FLUKA Monte Carlo simulation [46,47] and found to match within ±15% (Figure 9). Figure 10 shows a 3D data representation of the measured dose. The average value per pixel per position is calculated and a linear interpolation between positions is used. The figure shows the lateral beam spreading, the Bragg peak and the fragmentation tail of the carbon ion. This information cannot be acquired with commercially available QA detectors.

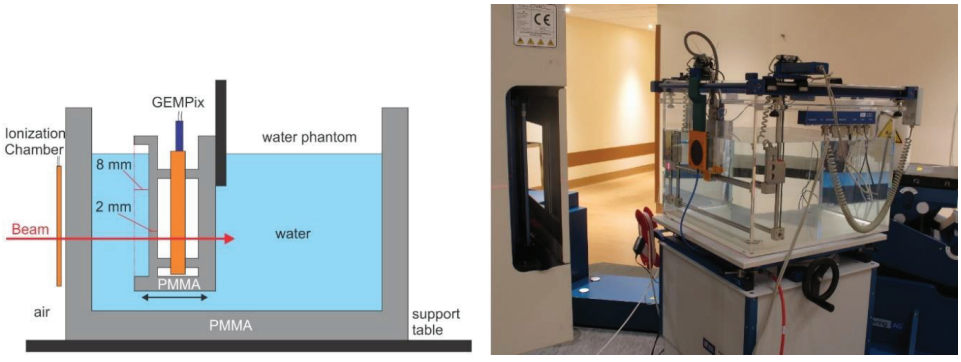

Figure 8. Schematic drawing ((**left**), not to scale) and picture (**right**) of the water phantom setup. The beam enters from the left and passes through the reference ionization chamber before entering the water phantom. The GEMPix is inserted in a watertight box, which is mounted on the positioning system of the phantom. Therefore, depth scans are possible by remotely changing the distance between beam entrance window and GEMPix box.

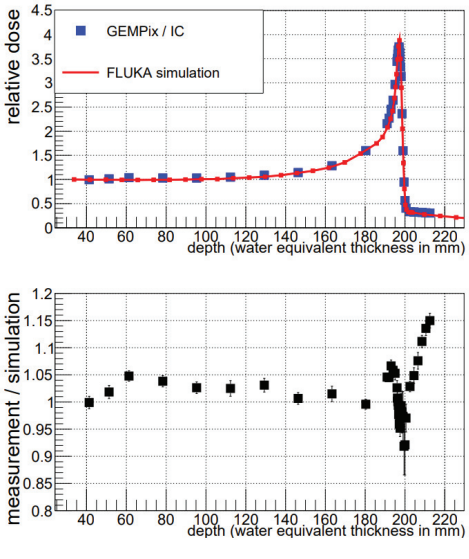

Figure 9. The upper plot shows the Bragg curve for 200 mm range in water, measured by the GEMPix and calculated with FLUKA. The lower plot shows the ratio of the experimental data to the FLUKA curve. The data points match the simulation within ±15%.

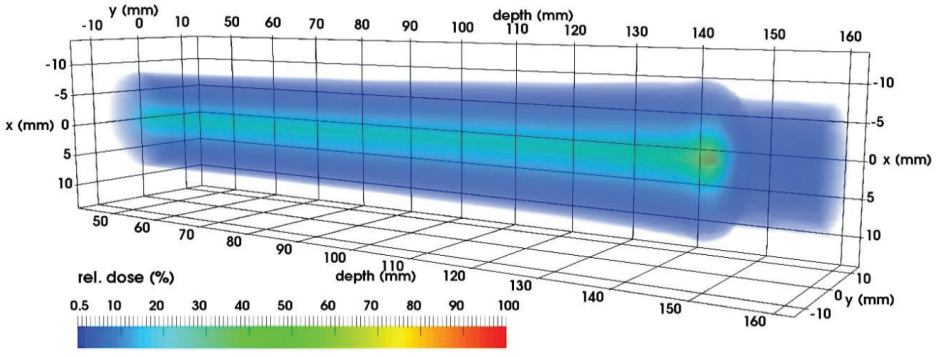

Figure 10. In this 3D representation of the dose, the carbon ion beam enters from the left. Lateral spread out, Bragg peak and fragmentation tail are visible.

5. Proton Tomography

With the increasing number of proton therapy centres there is a renewed interest in proton tomography [48–50]. Preliminary tests with two GEMPix operated as TPCs were performed to measure the position, direction and energy of protons traversing an object in order to reconstruct an image of it. The setup consists of two GEMPix-based TPCs with a Timepix3 (instead of the usual Timepix) quadboard as tracker and a BaF_2 crystal for measurement of the residual proton energy. The results presented in this section are published in [25].

Figure 11 shows the setup. A phantom was placed between the two tracking devices to try and measure the performance and spatial resolution of the system. The phantom and the reconstructed image are shown in Figure 12. Although the sensitive volume of the TPC is $5 \times 5 \times 5$ cm^3 (yielding sufficiently long tracks for measuring the incident angle of the particle) and the improved temporal resolution of the Timepix3 is included (drift coordinate precision), the angular resolution is still not optimal for the phantom image reconstruction. These uncertainties on the track reconstruction are dominated by the clustering effect of the triple-GEM structure and the inhomogeneity of the electric field inside the TPC.

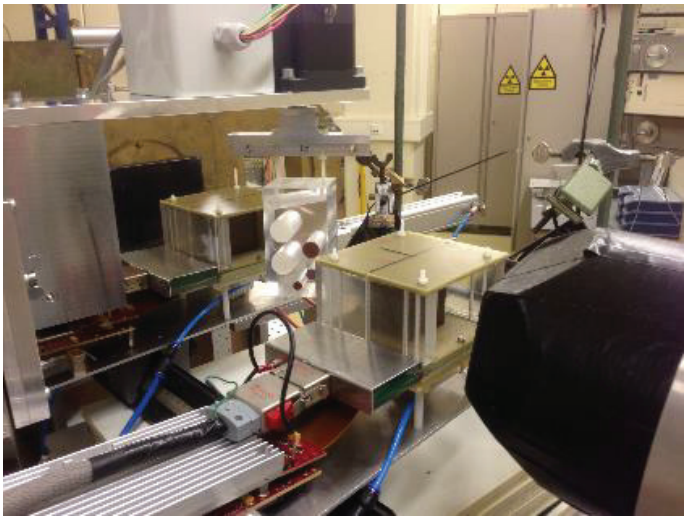

Figure 11. The experimental setup for proton radiography [25].

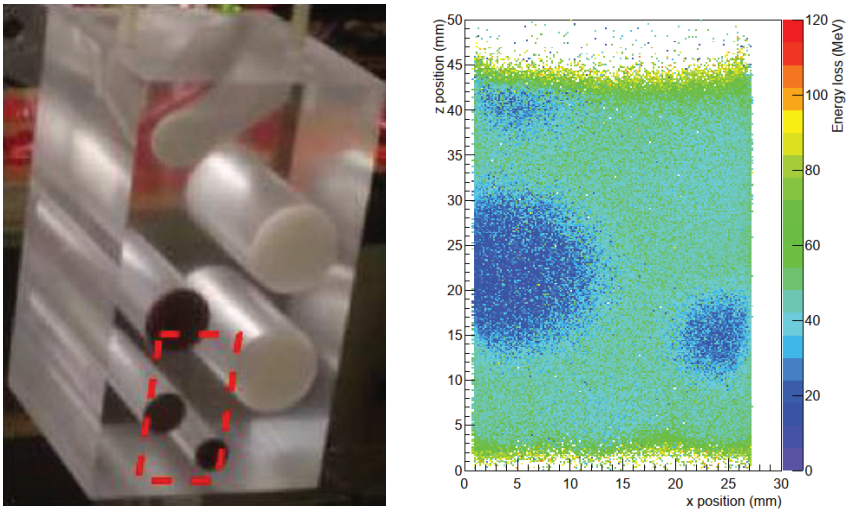

Figure 12. On the left, the portion of the phantom used in the test, on the right the final reconstructed image. The total exposure time was 100 s at a beam intensity of 3 kHz [25].

In order to improve the performance of the system, an algorithm finding the location of the primary ionization would be needed. The track fit using only the location of the primary ionization will be more realistic than using all the hits of the clusters. Another possible improvement could be an optimized triple-GEM configuration and the use of a gas mixture generating less lateral diffusion. The final angular resolution obtained with the current set-up is 30.7 mrad in the xy-plane and 23.4 mrad in the zy-plane. Once the above-mentioned issues are solved and an angular resolution below 1 mrad is reached, a step towards proton-CT can be investigated by irradiating the phantom from different angles. A 3-dimensional energy density map could then be reconstructed to improve future proton therapy treatment plans.

6. Microdosimetry

The most recent application of the GEMPix to medical physics lies in the field of microdosimetry. Microdosimetry is the 'systematic study of the spatial and temporal distributions of absorbed energy in irradiated matter' [51]. The golden standard for detectors in microdosimetry is the Tissue Equivalent Proportional Counter (TEPC). A TEPC is a device consisting of an active volume filled with tissue equivalent (TE) gas, with TE walls and a thin anode wire. The gas pressure is only a few percent of the atmospheric pressure and therefore the ionization of a particle in the active volume is the same as in a small piece of tissue. Both the lineal energy and the absorbed dose to tissue can be measured [52]. It is a well-established technology that can measure the microdosimetric distributions accurately and reliably, but it has important limitations that the GEMPix could in principle overcome. For example, the equivalent mean path length in a TEPC can be selected by adjusting the operational pressure, but it is typically limited to a few micrometres, with a lower limit of operation of 0.3 µm in case of special design [53], which is not enough to obtain details on the particle track structure. Detectors with the best spatial resolutions tend to be complex and bulky [54]. Furthermore, conventional TEPCs feature only a single readout channel in a detection volume of fixed dimensions.

While GEMs had been used before in microdosimetry [55], the combination with a highly pixelated readout is unique to the GEMPix. In case of the GEMPix detector, it is possible to achieve a resolution down to the scale of tens of nanometres because the inherently good spatial resolution (pixel pitch of 55 µm) is scaled down using a gas instead

of a solid material by a factor of approximately 1000. The particle track imaging capability of the GEMPix is completely new to microdosimetry.

The version of GEMPix for use as microdosimeter is called GEMTEQ ('GEMPix detector for microdosimetry with tissue equivalent gas'). For this application, the GEMTEQ is operated with a so-called propane-based TE gas (C_3H_8:CO_2:N_2, 55:39.6:5.4). It was calibrated using an ^{55}Fe source and its performance was tested in various radiation fields (photons from an X-ray generator and from radioactive sources, neutrons from a neutron generator and a mixed photon/neutron field from an AmBe radioactive source). One of the GEMTEQ prototypes is equipped with a tissue equivalent cathode replacing the Mylar foil by an A150 conductive plastic. Figure 13 shows the GEMTEQ detector setup for measurements in a neutron field.

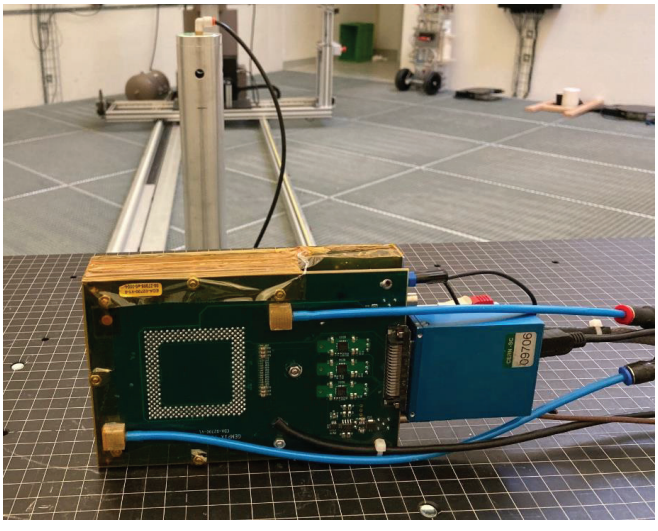

Figure 13. The GEMPix detector (foreground) set up for measurements with an AmBe source (the metal cylinder housing the source is visible in the background).

Standard dose spectra as with a TEPC were obtained. These results were achieved by grouping together several pixels in a 'superpixel': the superpixels can be defined offline to adjust the equivalent mean path length. The energy deposition of all pixels in a superpixel is summed and these values are used to populate a histogram similar to the pulse height histograms obtained in standard microdosimetry. Figure 14 shows the results of measurements with an AmBe source (solid black line). In order to show one of the potential advantages of the pixelated readout of the GEMPix, an analysis to discriminate photons and neutrons in the mixed radiation field provided by the AmBe source was set up: a particle track in the GEMPix often stretches over several superpixels. While for the standard dose distributions, the energy deposition in each superpixel is used to populate the histogram (as shown for the complete data set in Figure 14), the total energy deposition of the entire track is used to discriminate neutrons and photons. The value of the discrimination parameter—the total energy deposition of a particle in the GEMPix—was chosen to be the maximum energy deposition observed in the measurements with an Am-241 source. Any particle track in the AmBe data set with an energy below this limit was assigned as 'photon-like', the remaining tracks were assigned as 'neutron-like'. The dose distributions of the 'photon-like' component of the AmBe data set and the pure Am-241 data set match well. In conclusion, this analysis makes use of the fact that the GEMPix provides multi-channel results (i.e., 2D images of particle tracks), while this is not possible in a TEPC as it features only a single channel.

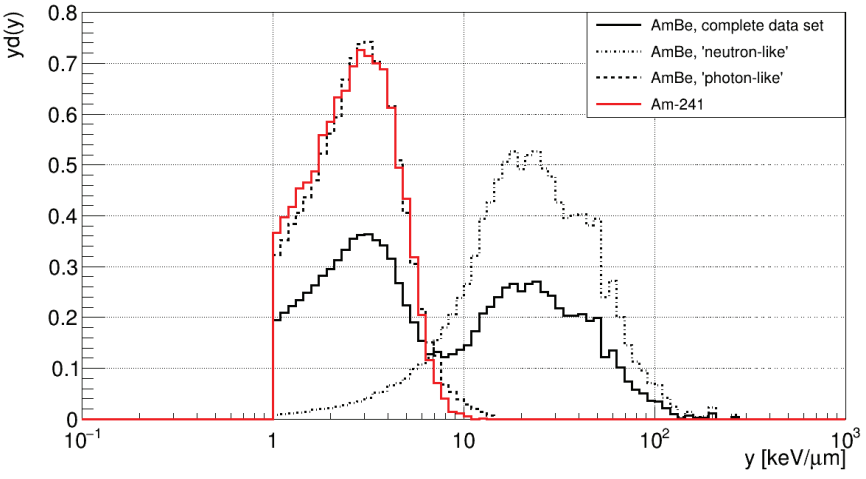

Figure 14. Dose spectra obtained with the GEMPix and an AmBe source (mixed photon/neutron field) in the standard representation for microdosimetry (lineal energy, y, on the *x*-axis and the dose distribution d(y) multiplied by y on the *y*-axis [51]). The complete data set (black line), the 'neutron-like' component (dash-dotted black line) and the 'photon-like' component (dotted black line) are shown. As a comparison, a measurement with the GEMPix and an ^{241}Am source (photons only) is presented (red line).

Two-dimensional particle track images were obtained from the measurements using the same data set as for the dose spectra (Figure 15). This is impossible with conventional TEPCs and opens the door for many new applications in microdosimetry. These include: particle tracks can be studied in detail (track structure microdosimetry), particle identification becomes possible (helping to disentangle contributions from different types of radiation in a mixed field) and effects of the size of sensitive volumes can be studied offline on a single data set. An outline of the results recently obtained can be found in [56], and the full results are given in [57].

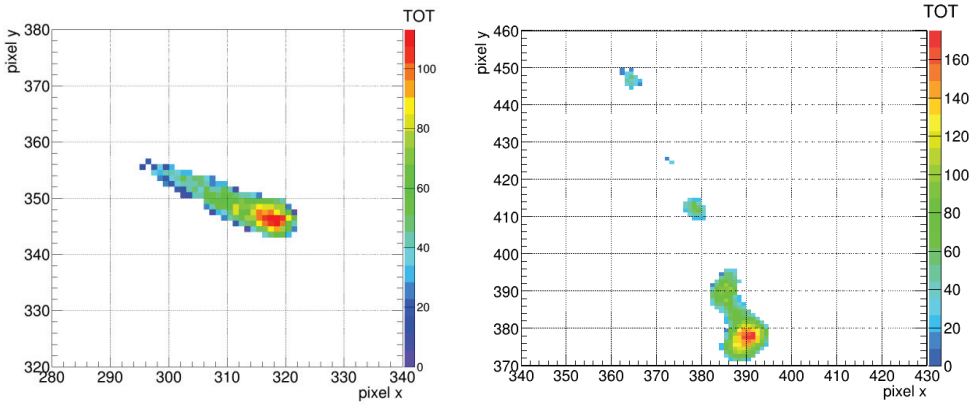

Figure 15. Examples of particle tracks measured with the GEMPix: a proton track (from neutron irradiation) with a visible increase in the energy deposition towards the end of the track (**left**) and an electron track (from ^{137}Cs irradiation, **right**).

7. LaGEMPix, a Large Area GEMPix

The superior imaging and particle discrimination capabilities of the GEMPix have been shown in the previous sections, but the current sensitive area of the detector (2.8 × 2.8 cm) is too small for a practical application as QA tool in hadron therapy. This section focuses on the application in hadron therapy, but a larger area detector is also needed in other fields such as conventional radiation therapy with photon beams. A large area GEMPix (LaGEMPix) with a 20 × 20 cm^2 size (the typical maximum clinical field size with scanned hadron therapy beams) cannot be easily (and economically) achieved by simply scaling up the current design by tiling more Timepix ASICs. First, the current Timepix chip has wire bonds located on one side, so the quad configuration (2 × 2 chips) used in the GEMPix cannot be enlarged to an arbitrary n x n chip configuration. For this, one would need to use the latest Timepix4 version that is about four times larger than the Timepix and in which the connection for data transfer is from below the chip by Through-silicon Via (vertical interconnect access). However, such a solution would be very expensive just for the cost of the Timepix4 ASICs. In addition, the 55 μm pixel size would require complex electronics to handle the large number of signals and each acquisition would generate a huge amount of data, which are actually not needed as spatial resolution of the order of 1 mm is sufficient for application in QA.

We have considered a few alternative readouts for a large area detector. In the present section, we describe the one currently being explored; alternative solutions are briefly illustrated in the next section. The on-going development uses a novel readout based on the detection of the scintillation photons generated in the GEM holes. A first LaGEMPix prototype with a six time larger active area than the GEMPix (6 × 8 cm^2) has been developed in a collaboration between CERN and the Holst Centre/TNO (Eindhoven, The Netherlands) within an EU ATTRACT funded project [58]. The LaGEMPix combines a triple-GEM detector and an optical readout based on three main building blocks: a Thin Film Transistor (TFT) backplane, a light sensitive OPD (optical photo detectors) frontplane and a transparent thin-film encapsulation, serving as a protection against ambient conditions [59]. The triple-GEM detector includes a 20 μm thick Mylar window used as the cathode at 3.5 mm from the first GEM. On the bottom of the third GEM, a 1.1 mm thick ITO (Indium Tin Oxide) coated glass anode is placed at 1.9 mm distance to collect the electrons produced during the amplification process while allowing the optical photons to pass through [60,61].

A LaGEMPix prototype (Figure 16) has been built. A first account of the results obtained are given in [62], the full results can be found in [63]. A number of tests were performed to characterize the detector, placed inside a custom-made black Polymethylmethacrylate (PMMA) box to shield the ambient light and provide a well aligned set-up. A gain scan was performed while exposing the device to photons from a 3 TBq ^{137}Cs source, varying the sum of the GEM voltages from 0 to 1030 V, to define the optimal operating conditions. The spatial resolution was determined with 40 kV X-rays from an X-Ray irradiator employing a 3 mm thick copper plate placed on the inner wall of the box at 7 mm from the Mylar window, with a set of holes of different spacing (from 3 to 20 mm) drilled in it. An image obtained with this copper plate is shown in Figure 17. The FWHM of a single hole of 5 mm diameter is 6.7 ± 0.1 mm. Two holes at a distance of 3 mm (edge to edge) can be resolved in the sense that two peaks with a dip in the intensity between the peaks are visible. The current results are promising but also show that the required sub-millimeter spatial resolution is not yet achieved.

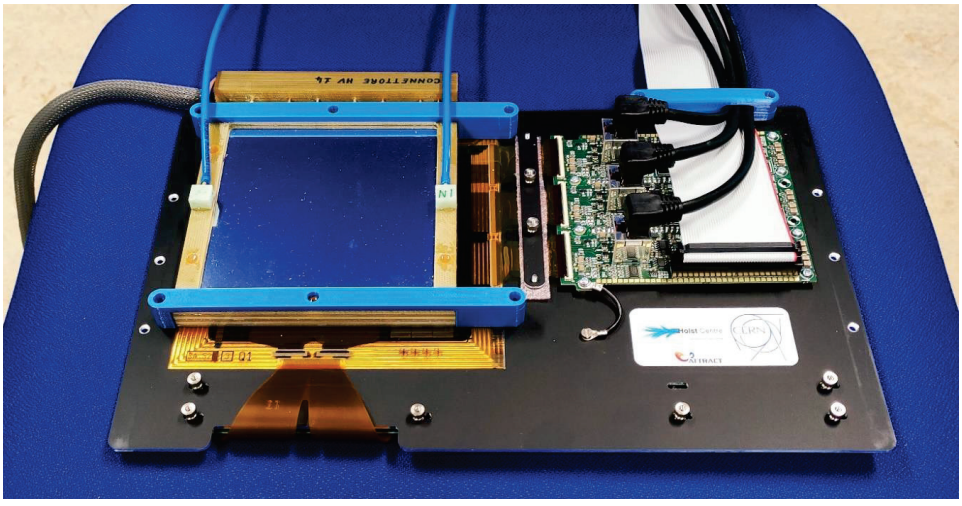

Figure 16. The LaGEMPix prototype. The triple GEM 10 × 10 cm^2 stack coupled to the optical readout matrix is on the left side; on top, there is the thin Mylar window. The readout boards and the cables to connect the detector to the FPGA module are on the right side.

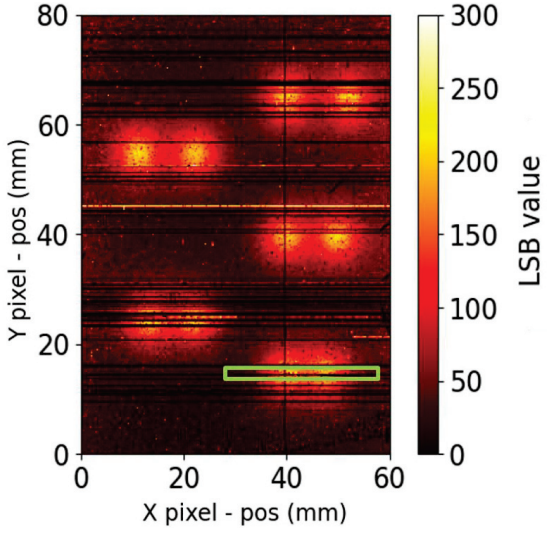

Figure 17. Heat map of the Cu mask for 40 kV X-rays. A Region of Interest (ROI, green lines) was set on the holes in 3 mm distance. The spatial resolution was estimated by fitting the profile in the ROIs by a Gaussian function.

8. On-Going and Future Developments

The developments currently on-going focus on improvements of the GEMTEQ and LaGEMPix versions of the GEMPix. The long-term goal would be to merge the two detectors and integrate them into the motorized water phantom described in Section 4, to achieve an all-in quality assurance tool for treatment planning and dose delivery in particle therapy, driven by a detailed knowledge of the radiobiological effectiveness (RBE) of the radiation.

8.1. GEMTEQ

The GEMTEQ discussed in Section 6 is a version of the GEMPix specifically adapted for microdosimetry. The pixelated readout of the GEMTEQ is a key feature, which unlike the TEPC allows visualizing and analysing the full particle track. TEPCs are sealed detectors operating at low pressure so that the mean path length in the active gas volume is equivalent to typically a few μm in tissue, simulating the cell size. The current version of GEMTEQ works with flushing propane-based TE gas at atmospheric pressure (the way GEMs are usually operated). We are currently designing a sealed version of the GEMTEQ (Figure 18), consisting of a vacuum chamber provided with a thin carbon window housing the detector, connected to a pumping station to adjust the operating pressure. The aim is to be able to run the GEMTEQ in sealed mode, to make it more portable, at pressure below atmospheric to achieve sub-micrometric spatial resolution and head towards microdosimetry at the sub-micron level.

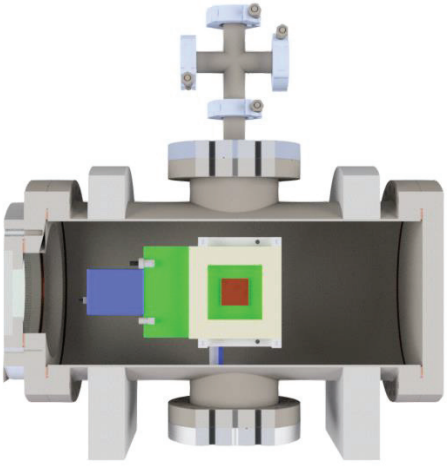

Figure 18. A cross-sectional view of the planned vacuum vessel housing the GEMTEQ for sealed and low-pressure applications. The GEMTEQ is located in the centre of the vacuum vessel and the colors show the different materials and components: the aluminum vessel (gray), the FITPix (blue), the PCB (green), the GEM frames (beige) and the Pixelman ASICs (brown). The GEMs are not included in this drawing.

The spatial information obtained from the pixelated readout will be used to perform data analyses beyond standard microdosimetry, i.e., particle track analysis, and achieve track-structure microdosimetry. Upgrading the readout to the latest generation of Timepix (Timepix3 or Timepix4) will allow for measurements in a data-driven acquisition mode with simultaneous acquisition of charge and time-of-arrival information, for operation as a TPC. In this way, 3D particle tracks will be reconstructed and possibly track lengths and the change of the energy deposition along the track could be measured for each particle.

8.2. LaGEMPix

The final goal of the LaGEMPix development is to achieve a large size detector for monitoring the typical clinical field size used in hadron therapy, up to $20 \times 20\ cm^2$, allowing for a precise evaluation of the dose distribution with scanned ion beams. Two possible modifications of the LaGEMPix described in Section 7 are under consideration and will be explored in the coming months to improve the current spatial resolution. The first implies slightly modifying the present design, by decreasing the distance between the last GEM and the readout plane to reduce the dispersion of the light before reaching the readout. The second focuses on increasing the light detection efficiency by replacing the current OPD

active layer by a different one offering a better match between the emitted light and the OPD's quantum efficiency.

The other options involve changing the readout technology. Excluding the approach of scaling up the current design by tiling more Timepix ASICs (either Timepix3 or Timepix4) for the reasons mentioned in the previous section, there are two alternatives that may be considered. The first alternative to the current readout system is to eliminate the OPD layer leaving a TFT-only electronic readout. With this approach, the readout would directly measure the secondary electrons produced in the electron avalanche. This TFT-only solution could yield a more compact and more efficient device with a higher signal-to-noise ratio, providing a spatial resolution potentially better than 1 mm, as the electrons are guided by the electric field and their diffusion is much smaller than unfocused light. The spatial resolution of the current LaGEMPix has been compared with that of the standard GEMPix with 40 kV X-rays from an X-Ray irradiator, using the "edge response" method [64]. The resolution obtained with the GEMPix is about a factor of 2 better than that of the LaGEMPix, indicating that a better performance can be achieved with the charge readout option.

The other option still exploits the light emitted in the GEM holes, but detecting the optical photons using a CCD/CMOS camera or the TpxCam [65,66]. The TpxCam is a fast optical camera based on a silicon pixel sensor combined with the Timepix chip, providing nanosecond scale time resolution and high quantum efficiency for photons with wavelength between 400 and 1050 nm. In this version, the LaGEMPix would not be as compact as the version using a TFT readout, as it will have to include an optical system consisting of mirror and lenses to focus the light. On the other hand, it would offer the possibility to keep the electronics off the beam.

Another possible future development is to employ air instead of an argon-based gas mixture. This could be an optimal solution to simplify the present device. High photon fluences, like those used in radiation therapy, produce significant ionization in air and the GEMPix is highly sensitive to detect this ionization.

Finally, it is worth mentioning that QA checks are usually performed before patient treatment. Some preliminary attempts have been made to build devices for on-line transit dosimetry: from a measurement of the dose transmitted through the patient during a treatment session, a software would reconstruct the dose released inside the patient. Until now, conventional devices, like matrix array and EPID, have not guaranteed satisfactory and universally accepted results. This is a field where the GEMPix may also bring a contribution.

Author Contributions: Various persons and groups performed the work described in this review article, please see the text and references for more details. M.S. contributed to the manuscript by writing Sections 1, 7 and 8 and by proof reading. F.M. wrote Sections 2, 3 and 5. J.L. wrote Sections 4 and 6, merged the different contributions and performed proof reading. All authors discussed the general idea and structure of the article. All authors have read and agreed to the published version of the manuscript.

Funding: The GEMPix was developed within the ARDENT Marie Curie ITN project funded by the European Commission 7th Framework Programme, Grant Agreement 289198. The GEMTEQ and LaGEMPix projects have received funding from the ATTRACT project funded by the EC under Grant Agreement 777222. Some of the activities described in this paper have been supported by CERN's Budget for Knowledge Transfer to Medical Applications and by the Wolfgang Gentner Programme of the German Federal Ministry of Education and Research (grant no. 05E15CHA).

Acknowledgments: We wish to thank the people with whom we have been or are collaborating for several years and have contributed in various ways to the GEMPix developments: Stuart George (now with NASA, US), Lucía Gallego Manzano (now with CHUV, Lausanne), Natalie Heracleous and Andreia Maia Oliveira (members of the Special Project section of CERN Radiation Protection Group), Michael Campbell (CERN) and colleagues from the Medipix collaboration, G. Corradi and D. Tagnani (INFN, Italy) for the design of the High Voltage and readout boards, J. Alozy (CERN) for the software and hardware support on the Timepix ASIC, R. De Oliveira for the special design of the GEM foils, Albert van Breemen and colleagues from the Holst Centre/TNO (Eindhoven, The Netherlands) for

the development of the LaGEMPix readout, Anthony Waker of the Faculty of Energy Systems and Nuclear Science, Ontario Tech University (Canada) for the GEMTEQ project, Sandro Rossi (CNAO Technical Director), Mario Ciocca (Head of CNAO medical physics) and their colleagues for the measurements performed at CNAO. We also wish to thank Doris Forkel-Wirth and Stefan Roesler, former and current heads of CERN Radiation Protection group, for their continuous support.

Conflicts of Interest: The authors declare no conflict of interest. The funders had no role in the design of the study; in the collection, analyses, or interpretation of data; in the writing of the manuscript, or in the decision to publish the results.

References

1. ARDENT. Available online: www.cern.ch/ardent (accessed on 16 November 2020).
2. CNAO. Available online: https://fondazionecnao.it/en/ (accessed on 16 November 2020).
3. ARDENT Meeting at CNAO. Available online: https://indico.cern.ch/event/209428/contributions/ (accessed on 16 November 2020).
4. PTW Peakfinder. Available online: https://www.ptwdosimetry.com/en/products/peakfinder/ (accessed on 15 October 2020).
5. Gafchromic EBT. Available online: http://www.gafchromic.com/gafchromic-film/radiotherapy-films/EBT/index.asp (accessed on 15 October 2020).
6. PTW PinPoint Ion Chambers. Available online: https://www.ptwdosimetry.com/en/products/pinpoint-ion-chambers-31014-31015/ (accessed on 16 November 2020).
7. PTW Farmer Ionization Chamber 30013 Waterproof. Available online: https://www.ptwdosimetry.com/products/farmer-ionization-chamber-30013-waterproof/?L=0 (accessed on 17 November 2020).
8. Mirandola, A.; Molinelli, S.; Freixas, G.V.; Mairani, A.; Gallio, E.; Panizza, D.; Russo, S.; Ciocca, M.; Donetti, M.; Magro, G.; et al. Dosimetric commissioning and quality assurance of scanned ion beams at the Italian National Center for Oncological Hadrontherapy. *Med. Phys.* **2015**, *42*, 5287–5300. [CrossRef] [PubMed]
9. Sauli, F. GEM: A new concept for electron amplification in gas detectors. *Nucl. Instrum. Methods Phys. Res. Sect. A Accel. Spectrom. Detect. Assoc. Equip.* **1997**, *386*, 531–534. [CrossRef]
10. Sauli, F. The gas electron multiplier (GEM): Operating principles and applications. *Nucl. Instrum. Methods Phys. Res. Sect. A Accel. Spectrom. Detect. Assoc. Equip.* **2016**, *805*, 2–24. [CrossRef]
11. Bencivenni, G.; Felici, G.; Murtas, F.; Valente, P.; Bonivento, W.; Cardini, A.; Lai, A.; Pinci, D.; Saitta, B.; Bosio, C. A triple GEM detector with pad readout for high rate charged particle triggering. *Nucl. Instrum. Methods Phys. Res. Sect. A Accel. Spectrom. Detect. Assoc. Equip.* **2002**, *488*, 493–502. [CrossRef]
12. Llopart, X.; Ballabriga, R.; Campbell, M.; Tlustos, L.; Wong, W. Timepix, a 65k programmable pixel readout chip for arrival time, energy and/or photon counting measurements. *Nucl. Instrum. Methods Phys. Res. Sect. A Accel. Spectrom. Detect. Assoc. Equip.* **2007**, *581*, 485–494. [CrossRef]
13. Medipix. Available online: https://medipix.web.cern.ch/ (accessed on 16 November 2020).
14. Ballabriga, R.; Campbell, M.; Llopart, X. Asic developments for radiation imaging applications: The medipix and timepix family. *Nucl. Instrum. Methods Phys. Res. Sect. A Accel. Spectrom. Detect. Assoc. Equip.* **2018**, *878*, 10–23. [CrossRef]
15. Ballabriga, R.; Campbell, M.; Llopart, X. An introduction to the Medipix family ASICs. *Radiat. Meas.* **2020**, *136*, 106271. [CrossRef]
16. George, S.; Murtas, F.; Alozy, J.; Curioni, A.; Rosenfeld, A.; Silari, M. Particle tracking with a Timepix based triple GEM detector. *J. Instrum.* **2015**, *10*, P11003. [CrossRef]
17. Curioni, A.; Dinar, N.; La Torre, F.; Leidner, J.; Murtas, F.; Puddu, S.; Silari, M. Measurements of 55 Fe activity in activated steel samples with GEMPix. *Nucl. Instrum. Methods Phys. Res. Sect. A Accel. Spectrometers, Detect. Assoc. Equip.* **2017**, *849*, 60–71. [CrossRef]
18. Claps, G.; Pacella, D.; Murtas, F.; Jakubowska, K.; Boutoux, G.; Burgy, F.; Ducret, J.-E.; Batani, D. The GEMpix detector as new soft X-rays diagnostic tool for laser produced plasmas. *Rev. Sci. Instrum.* **2016**, *87*, 103505. [CrossRef]
19. Pacella, D.; Claps, G.; De Angelis, R.; Murtas, F. An hybrid detector GEM-ASIC for 2-D soft X-ray imaging for laser produced plasma and pulsed sources. *J. Instrum.* **2016**, *11*, C03022. [CrossRef]
20. Baracchini, E.; Cavoto, G.; Mazzitelli, G.; Murtas, F.; Renga, F.; Tomassini, S. Negative Ion Time Projection Chamber operation with SF6at nearly atmospheric pressure. *J. Instrum.* **2018**, *13*, P04022. [CrossRef]
21. Claps, G. *A Study of a Triple GEM Detector as Real Time Dosimeter in External Photon Beam Radiotherapy*; University of Tor Vergata: Rome, Italy, 2015.
22. Leidner, J.; Ciocca, M.; George, S.; Mirandola, A.; Murtas, F.; Rimoldi, A.; Silari, M.; Tamborini, A. 3D energy deposition measurements with the GEMPix detector in a water phantom for hadron therapy. *J. Instrum.* **2018**, *13*, P08009. [CrossRef]
23. Leidner, J. *Application of the GEMPix Detector in Radiation Protection and Particle Therapy*; RWTH Aachen University: Aachen, Germany, 2019.
24. Leidner, J.; Ciocca, M.; Mairani, A.; Murtas, F.; Silari, M. A GEMPix-based integrated system for measurements of 3D dose distributions in water for carbon ion scanning beam radiotherapy. *Med. Phys.* **2020**, *47*, 2516–2525. [CrossRef] [PubMed]
25. Radaelli, P. *Proton Radiography with a Timepix3 Based Gaseous Tracking Detector*; Vrije Universiteit Amsterdam: Amsterdam, The Netherlands, 2015.

26. Costa, E.; Soffitta, P.; Bellazzini, R.; Brez, A.; Lumb, N.; Spandre, G. An efficient photoelectric X-ray polarimeter for the study of black holes and neutron stars. *Nat. Cell Biol.* **2001**, *411*, 662–665. [CrossRef]
27. Bellazzini, R.; Angelini, F.; Baldini, L.; Bitti, F.; Brez, A.; Ceccanti, M.; Latronico, L.; Massai, M.; Minuti, M.; Omodei, N.; et al. Reading a GEM with a VLSI pixel ASIC used as a direct charge collecting anode. *Nucl. Instrum. Methods Phys. Res. Sect. A Accel. Spectrom. Detect. Assoc. Equip.* **2004**, *535*, 477–484. [CrossRef]
28. Bellazzini, R.; Spandre, G.; Minuti, M.; Baldini, L.; Brez, A.; Cavalca, F.; Latronico, L.; Omodei, N.; Massai, M.; Sgrò, C.; et al. Direct reading of charge multipliers with a self-triggering CMOS analog chip with 105k pixels at 50μm pitch. *Nucl. Instrum. Methods Phys. Res. Sect. A Accel. Spectrom. Detect. Assoc. Equip.* **2006**, *566*, 552–562. [CrossRef]
29. Bellazzini, R.; Spandre, G.; Minuti, M.; Baldini, L.; Brez, A.; Latronico, L.; Omodei, N.; Razzano, M.; Massai, M.; Pesce-Rollins, M.; et al. A sealed Gas Pixel Detector for X-ray astronomy. *Nucl. Instrum. Methods Phys. Res. Sect. A Accel. Spectrom. Detect. Assoc. Equip.* **2007**, *579*, 853–858. [CrossRef]
30. Fabiani, S.; Da Costa, E.M.; Del Monte, E.; Muleri, F.; Soffitta, P.; Rubini, A.; Bellazzini, R.; Brez, A.; De Ruvo, L.; Minuti, M.; et al. The imaging properties of the gas pixel detector as a focal plane polarimeter. *Astrophys. J. Suppl. Ser.* **2014**, *212*, 25. [CrossRef]
31. Van Der Graaf, H.; Aarnink, T.; Aarts, A.; Van Bakel, N.; Berbee, E.; Berkien, A.; Van Beuzekom, M.; Bosma, M.; Campbell, M.; Chefdeville, M.; et al. The gridpix detector: History and perspective. *Mod. Phys. Lett. A* **2013**, *28*. [CrossRef]
32. Corradi, G.; Murtas, F.; Tagnani, D. A novel High-Voltage System for a triple GEM detector. *Nucl. Instrum. Methods Phys. Res. Sect. A Accel. Spectrom. Detect. Assoc. Equip.* **2007**, *572*, 96–97. [CrossRef]
33. Murtas, F. Applications of triple GEM detectors beyond particle and nuclear physics. *J. Instrum.* **2014**, *9*, C01058. [CrossRef]
34. Murtas, F. The GEMPix detector. *Radiat. Meas.* **2020**, 106421. [CrossRef]
35. Kraus, V.; Holik, M.; Jakubek, J.; Kroupa, M.; Soukup, P.; Vykydal, Z. FITPix—Fast interface for Timepix pixel detectors. *J. Instrum.* **2011**, *6*, C01079. [CrossRef]
36. Turecek, D.; Holy, T.; Jakubek, J.; Pospisil, S.; Vykydal, Z. Pixelman: A multi-platform data acquisition and processing software package for Medipix2, Timepix and Medipix3 detectors. *J. Instrum.* **2011**, *6*, C01046. [CrossRef]
37. Bencivenni, G.; De Simone, P.; Murtas, F.; Lerner, M.; Bonivento, W.; Cardini, A.; Deplano, C.; Pinci, D.; Raspino, D. Advances in triple-GEM detector operation for high-rate particle triggering. *Nucl. Instrum. Methods Phys. Res. Sect. A Accel. Spectrom. Detect. Assoc. Equip.* **2003**, *513*, 264–268. [CrossRef]
38. Yyoctopuce. Available online: http://www.yoctopuce.com/EN/ (accessed on 26 October 2020).
39. Smilowitz, J.B.; Das, I.J.; Feygelman, V.; Fraass, B.A.; Kry, S.F.; Marshall, I.R.; Mihailidis, D.N.; Ouhib, Z.; Ritter, T.; Snyder, M.G.; et al. AAPM Medical Physics Practice Guideline 5.a.: Commissioning and QA of Treatment Planning Dose Calculations—Megavoltage Photon and Electron Beams. *J. Appl. Clin. Med Phys.* **2015**, *16*, 14–34. [CrossRef]
40. Low, D.A.; Harms, W.B.; Mutic, S.; Purdy, J.A. A technique for the quantitative evaluation of dose distributions. *Med. Phys.* **1998**, *25*, 656–661. [CrossRef]
41. Low, D.; Dempsey, J.F. Evaluation of the gamma dose distribution comparison method. *Med. Phys.* **2003**, *30*, 2455–2464. [CrossRef]
42. Dosanjh, M.; Bernier, J. *Advances in Particle Therapy*; CRC Press: Boca Raton, FL, USA, 2018.
43. Giordanengo, S.; Manganaro, L.; Vignati, A. Review of technologies and procedures of clinical dosimetry for scanned ion beam radiotherapy. *Phys. Med.* **2017**, *43*, 79–99. [CrossRef]
44. Aza, E.; Ciocca, M.; Murtas, F.; Puddu, S.; Pullia, M.; Silari, M. Preliminary results of the Gas Electron Multiplier (GEM) as real-time beam monitor in hadron therapy. *Nucl. Instrum. Methods Phys. Res. Sect. A Accel. Spectrom. Detect. Assoc. Equip.* **2017**, *841*, 65–71. [CrossRef]
45. Giordanengo, S.; Garella, M.A.; Marchetto, F.; Bourhaleb, F.; Ciocca, M.; Mirandola, A.; Monaco, V.; Hosseini, M.A.; Peroni, C.; Sacchi, R.; et al. The CNAO dose delivery system for modulated scanning ion beam radiotherapy. *Med. Phys.* **2014**, *42*, 263–275. [CrossRef] [PubMed]
46. Böhlen, T.; Cerutti, F.; Chin, M.; Fasso, A.; Ferrari, A.; Ortega, P.; Mairani, A.; Sala, P.; Smirnov, G.I.; Vlachoudis, V. The FLUKA Code: Developments and Challenges for High Energy and Medical Applications. *Nucl. Data Sheets* **2014**, *120*, 211–214. [CrossRef]
47. Ferrari, A.; Sala, P.R.; Fassò, A.; Ranft, J. *FLUKA: A Multi-Particle Transport Code*; CERN Yellow Reports: Monographs; CERN: Geneva, Switzerland, 2005.
48. Hanson, K.M.; Bradbury, J.N.; Cannon, T.M.; Hutson, R.L.; Laubacher, D.B.; Macek, R.J.; Paciotti, M.A.; Taylor, C.A. Computed tomography using proton energy loss. *Phys. Med. Biol.* **1981**, *26*, 965–983. [CrossRef] [PubMed]
49. Hanson, K.M.; Bradbury, J.N.; Koeppe, R.A.; Macek, R.J.; Machen, D.R.; Morgado, R.; Paciotti, M.A.; Sandford, S.A.; Steward, V.W. Proton computed tomography of human specimens. *Phys. Med. Biol.* **1982**, *27*, 25–36. [CrossRef]
50. Schneider, U.; Pedroni, E. Proton radiography as a tool for quality control in proton therapy. *Med. Phys.* **1995**, *22*, 353–363. [CrossRef]
51. Rossi, H.H.; Zaider, M. *Microdosimetry and Its Applications*; Springer: Berlin/Heidelberg, Germany, 1996.
52. Lindborg, L.; Nen, J.-E.K.; Beck, P.; Bottollier-Depois, J.F.; Gerdung, S.; Grillmaier, R.; Schrewe, U.; Kyllönen, J. The use of TEPC for reference dosimetry. *Radiat. Prot. Dosim.* **1999**, *86*, 285–288. [CrossRef] [PubMed]
53. Bortot, D.; Mazzucconi, D.; Bonfanti, M.; Agosteo, S.; Pola, A.; Pasquato, S.; Fazzi, A.; Colautti, P.; Conte, V. A novel tepc for microdosimetry at nanometric level: Response against different neutron fields. *Radiat. Prot. Dosim.* **2017**, *180*, 172–176. [CrossRef]
54. Bantsar, A.; Colautti, P.; Conte, V.; Hilgers, G.; Pietrzak, M.; Pszona, S.; Rabus, H.; Selva, A. State of The Art of Instrumentation in Experimental Nanodosimetry. *Radiat. Prot. Dosim.* **2017**, *180*, 177–181. [CrossRef]

55. Farahmand, M.; Bos, A.J.J.; De Nardo, L.; Van Eijk, C.W.E. First microdosimetric measurements with a TEPC based on a GEM. *Radiat. Prot. Dosim.* **2004**, *110*, 839–843. [CrossRef]
56. Leidner, J.; Murtas, F.; Silari, M.; Soave, A. GEMTEQ: GEMPix Detector for Microdosimetry with Tissue-Equivalent Gas, ATTRACT Final Conference Article. 2020. Available online: https://attract-eu.com/showroom/project/gempix-detector-for-microdosimetry-with-tissue-equivalent-gas/ (accessed on 18 December 2020).
57. Leidner, J.; Murtas, F.; Silari, M.; Waker, A.J. Microdosimetry with GEMTEQ, a Novel Gas Microdosimeter with a Highly Pixelated Readout. to be submitted for publication.
58. ATTRACT LaGEMPix. Available online: https://attract-eu.com/selected-projects/lagempix-a-large-area-gempix-detector-with-optical-readout-for-hadron-therapy/ (accessed on 16 November 2020).
59. Van De Weijer, P.; Akkerman, H.B. Spotless hybrid thin-film encapsulation stack for organic light-emitting diodes on organic foils. *Org. Electron.* **2019**, *66*, 43–46. [CrossRef]
60. Brunbauer, F. *Applications of Gas Scintillation Properties in Optically Read out GEM-Based Detectors*; TU Wien: Vienna, Austria, 2018.
61. ITO Glass—Conductive Coated Glass Slides & Sheet. Available online: http://www.visionteksystems.co.uk/ito_glass_datasheet.htm (accessed on 16 November 2020).
62. Akkerman, H.B.; van Breemen, A.J.; Manzano, L.G.; Heracleous, N.; Katsouras, I.; Leidner, J.; Oliveira, A.M.; Murtas, F.; Peeters, B.; Silari, M. LaGEMPix: A Large Area GEMPix Detector with Optical Readout for Imaging in Hadron Therapy, ATTRACT Final Conference Article. 2020. Available online: https://attract-eu.com/showroom/project/lagempix-a-large-area-gempix-detector-with-optical-readout-for-hadron-therapy/ (accessed on 18 December 2020).
63. Akkerman, H.B.; van Breemen, A.J.; Manzano, L.G.; Heracleous, N.; Katsouras, I.; Leidner, J.; Oliveira, A.M.; Murtas, F.; Peeters, B.; Silari, M. LaGEMPix: A Large Area GEMPix Detector with Optical Readout for Imaging in Hadron Therapy. to be submitted for publication.
64. Smith, S.W. Special Imaging Techniques. In *Digital Signal Processing*; Elsevier BV: Amsterdam, The Netherlands, 2003; pp. 423–450.
65. TpxCam. Available online: https://www.tpxcam.org/ (accessed on 16 November 2020).
66. Fisher-Levine, M.; Nomerotski, A. TimepixCam: A fast optical imager with time-stamping. *J. Instrum.* **2016**, *11*, C03016. [CrossRef]

applied sciences

MDPI

Article

In Silico Validation of MCID Platform for Monte Carlo-Based Voxel Dosimetry Applied to ^{90}Y-Radioembolization of Liver Malignancies

Alessia Milano [1,*], Alex Vergara Gil [2], Enrico Fabrizi [3], Marta Cremonesi [4], Ivan Veronese [5,6], Salvatore Gallo [5], Nico Lanconelli [7], Riccardo Faccini [8,9] and Massimiliano Pacilio [10]

1 Postgraduate School of Medical Physics, Università Cattolica del Sacro Cuore, 00168 Rome, Italy
2 CRCT, UMR 1037, Inserm, Université Toulouse III Paul Sabatier, 31062 Toulouse, France; alex.vergara-gil@inserm.fr
3 Dipartimento di Scienze di Base ed Applicate per L'ingegneria, Università di Roma "La Sapienza", 00185 Rome, Italy; enricofabrizi@live.it
4 Medical Physics Unit, IEO, European Institute of Oncology IRCCS, 20141 Milan, Italy; marta.cremonesi@ieo.it
5 Department of Physics "Aldo Pontremoli", Università degli Studi di Milano, via Celoria 16, 20133 Milano, Italy; ivan.veronese@unimi.it (I.V.); salvatore.gallo@unimi.it (S.G.)
6 Istituto Nazionale di Fisica Nucleare (INFN) Section of Milan, 20133 Milan, Italy
7 Department of Physics and Astronomy, Università di Bologna, 40126 Bologna, Italy; nico.lanconelli@unibo.it
8 Department of Physics, Università di Roma "La Sapienza", 00185 Rome, Italy; riccardo.faccini@roma1.infn.it
9 INFN Section of Rome, 00185 Rome, Italy
10 Department of Medical Physics, Azienda Ospedaliero-Universitaria Policlinico Umberto I, 00161 Rome, Italy; m.pacilio@policlinicoumberto1.it
* Correspondence: alessia.milano.phys@gmail.com

Citation: Milano, A.; Gil, A.V.; Fabrizi, E.; Cremonesi, M.; Veronese, I.; Gallo, S.; Lanconelli, N.; Faccini, R.; Pacilio, M. In Silico Validation of MCID Platform for Monte Carlo-Based Voxel Dosimetry Applied to ^{90}Y-Radioembolization of Liver Malignancies. *Appl. Sci.* **2021**, *11*, 1939. https://doi.org/10.3390/app11041939

Academic Editor: Chang Ming Charlie Ma

Received: 18 December 2020
Accepted: 20 February 2021
Published: 23 February 2021

Featured Application: Novel treatment planning system performing Monte Carlo-based voxel dosimetry for a tailored radioembolization of liver malignancies.

Abstract: The aim was the validation of a platform for internal dosimetry, named MCID, based on patient-specific images and direct Monte Carlo (MC) simulations, for radioembolization of liver tumors with ^{90}Y-labeled microspheres. CT of real patients were used to create voxelized phantoms with different density and activity maps. SPECT acquisitions were simulated by the SIMIND MC code. Input macros for the GATE/Geant4 code were generated by MCID, loading coregistered morphological and functional images and performing image segmentation. The dosimetric results obtained from the direct MC simulations and from conventional MIRD approach at both organ and voxel level, in condition of homogeneous tissues, were compared, obtaining differences of about 0.3% and within 3%, respectively, whereas differences increased (up to 14%) introducing tissue heterogeneities in phantoms. Mean absorbed dose for spherical regions of different sizes (10 mm $\leq$ r $\leq$ 30 mm) from MC code and from OLINDA/EXM were also compared obtaining differences varying in the range 7–69%, which decreased to 2–9% after correcting for partial volume effects (PVEs) from imaging, confirming that differences were mostly due to PVEs, even though a still high difference for the smallest sphere suggested possible source description mismatching. This study validated the MCID platform, which allows the fast implementation of a patient-specific GATE simulation, avoiding complex and time-consuming manual coding. It also points out the relevance of personalized dosimetry, accounting for inhomogeneities, in order to avoid absorbed dose misestimations.

Keywords: radioembolization; internal dosimetry; Monte Carlo-based dosimetry

1. Introduction

Radioembolization (RE) is a clinical therapy for the treatment of primary or secondary hepatic tumors. The procedure is based on the administration of ^{90}Y-loaded microspheres

through the hepatic artery, which is the major blood supplier for liver malignancies [1]. The vascular targeting makes RE extremely selective: high dose can be delivered to neoplastic areas while preserving nearby healthy tissue. Several approaches, empirical and dosimetric, have been proposed to establish the activity to be administered [2]. Due to their simplicity, empirical models have been applied for several years, but at present they are not considered as adequate for patient-specific treatments. In fact, the clinical benefit evidence of dosimetry-based approaches [3–10] has led the scientific community to recognize the importance of accurate absorbed dose evaluation and to focus on the absorbed dose–biological effectiveness relationship.

Different dosimetric approaches for RE have been applied throughout the years: the MIRD scheme at the organ level [11], the partition model [12], the local energy deposition method (LDM) [13–15], convolution calculations by voxel S-values [16–19], and direct Monte Carlo (MC) simulations [20,21]. Methods based on the MIRD approach at the organ level are mostly widespread due to their ease of use, but they present two main limitations: the regions of interest are considered to have homogeneous density, with uniform activity distributions. These unrealistic hypotheses can be overcome introducing the image-based 3D voxel dosimetry. Predictive patient-specific dosimetry is derived simulating the therapeutical procedure with the injection of ^{99m}Tc-macroaggregated albumin particles (^{99m}Tc-MAA) to mimic the ^{90}Y-microspheres distribution inside the liver. The invasive procedure and the use of nonidentical particles may affect the perfect correspondence of pre vs. post-therapeutical activity distribution, depending on patient specific vascularity, type of disease, experience, and shrewdness. However, many authors [6,9,22,23] have shown the good representativity of ^{99m}Tc-MAA activity distribution for treatment planning, which is verified afterwards by post ^{90}Y-PET or ^{90}Y-SPECT imaging. 3D approaches based on LDM or convolution of S-voxel values allow to account for the nonuniform activity distribution derived from the SPECT images, whereas they still assume a homogeneous density. MC simulation, unlike the previous methods, takes into account both tissue inhomogeneities and nonuniform activity distribution and is considered as the gold standard.

In the last two decades, various Monte Carlo-based internal dosimetry programs or routines have been applied [24–29]. Despite being considered the gold standard, they all differ in complexity and have not been integrated in the clinical practice yet, except in few centers for research purposes only. The main reason is that they usually require very high computer performances and calculation time, which are not compatible with the daily clinical routine. A second reason is often the lack of validation processes.

This work deals with the physical validation of a novel treatment planning system (TPS) named MCID (MC Internal Dosimetry tool) [30,31], performing Monte Carlo-based voxel dosimetry, applied to ^{90}Y-radioembolization of liver malignancies. Patient's CT and SPECT can be imported in MCID software, which creates different macros, i.e., sequences of scripted commands, for the simulation with GATE/Geant4 [32,33]. Each macro contains various settings about a specific aspect of the simulation (e.g., geometry of the system, source type, physics of the simulation etc. [33]). MCID prepares the macros using some settings defined by the user through the platform (e.g., numbers of primaries, type of radionuclide etc.) and some default settings, such as the definition of the physics of the simulation. Most importantly, the activity source of the simulation is defined through the loaded SPECT of the patient, while the geometry of the simulation is defined after the segmentation of the loaded patient CT performed by the user on the platform (i.e., the morphological image is converted into a density map). Default and user-defined settings can be eventually modified, if necessary, manually changing the macros. These features allow the preparation of a personalized simulation, accounting for the specific patient morphology and activity distribution, in a very short time, avoiding manual coding related difficulties. An additional aim of this work was also to investigate the impact of tissue inhomogeneities on the dosimetric evaluation for the RE treatment and the potential improvement of a MC approach in this therapy.

2. Materials and Methods

For the validation workflow voxelized phantoms were defined, starting from real patient images. The choice of using phantoms was expressly made in order to set activity ground truth and to easily define different density/activity combinations by properly modifying the phantom. It is important to remark that the workflow is strictly related to the validation process with computational phantoms; in future clinical applications, real patient images will be directly loaded on MCID.

2.1. Workflow

The workflow developed for the validation and the evaluation of the TPS can be summarized as follows: (i) phantoms creation, (ii) simulation of the SPECT projections, (iii) attenuation map generation and tomographic reconstruction, (iv) creation of the input file for the MC simulation, (v) conversion of the GATE output file in absorbed dose images, (vi) calculation of absorbed dose images by convolution of voxel S-values (the latter calculated independently from the TPS tested here) for comparison and validation purposes. The software packages (and respective references) used for each step are reported in the corresponding subsection.

2.1.1. Phantoms Creation

The voxelized phantoms used in this study were constructed starting from a real patient CT (512 × 512 matrix with a pixel size of 1.367 × 1.367 mm^2 and a spacing between slices of 3.27 mm, high quality full diagnostic scan). CT contouring was performed with ITK-SNAP software [34], using a semiautomatic segmentation technique based on 3D active contours. The contoured volumes of interest (VOIs) were liver, soft tissue, lungs, adipose tissue, cortical bone, trabecular bone, air, breast prosthesis. Activity maps, with the same voxel and matrix size of the CT scan, were also constructed using ITK-SNAP, which allows the definition of the activity concentration ratio among different regions.

2.1.2. SPECT Simulation

^{99m}Tc-SPECT projections were simulated with the SIMIND MC code [35] using the contoured CT and the activity map created with ITK-SNAP as input. The main parameters chosen for the simulation are reported in Table 1.

Table 1. Main parameters set for the SPECT simulation.

Parameter	Value
Crystal material	NaI
Crystal length	39 cm
Crystal thickness	0.9530 cm
Crystal width	53 cm
Energy resolution (at 140 keV)	9.7%
Intrinsic spatial resolution (at 140 keV)	0.32 cm
Final matrix dimension	128 × 128 × 120
Pixel size in the final image	0.41 cm
Photons' histories per projection angle	10^8
Collimator type	Hexagonal parallel holes

These parameters mimic a MEDISO Anyscan gamma camera, which MCID was initially optimized for. The simulated activity was 100 MBq (as suggested in [1]) and an acquisition time for projection angle of 20 s was simulated. Poissonian noise was added to the simulation in order to obtain a more realistic functional image. A resampled CT (128 × 128) was also obtained.

2.1.3. Map of Attenuation and Reconstruction

Attenuation maps and reconstructed projections were obtained from MCID, using the resampled CT and the projections obtained from SIMIND. The reconstruction was performed using the ordered-subset expectation maximization (OSEM) algorithm, with two iterations and 10 subsets. Corrections for the collimator-detector response (CDR), attenuation, and scatter were applied, the latter obtained through the ESSE algorithm [36]. The reconstructed images had cubic voxels of 4.1 mm size and matrix size of 128 × 128.

2.1.4. Input File Elaboration for GATE and Simulation

A new version of the MCID tool, designed for the GATE/Geant4 10.4 code, was used in this study. MCID is a Windows Executable that can also be run on Windows virtual machines. MCID can generate input files for GATE starting from a morphological image (CT) and a coregistered functional image (SPECT or PET). First, the CT image is converted into a density image, assigning to each voxel density and atomic composition. In our case, the CT image was the resampled one, obtained from SIMIND. Tissue segmentation was realized assigning a constant density value for each HU (Hounsfield Units) range we defined on MCID. The materials selected for the segmentation are reported in the description of the simulated scenarios (§ 2.2). The Spectrum source description was set: ^{90}Y β^- spectrum was discretized in steps of 10 keV [37]. 10^8 primaries were also selected for the simulations. All the files generated by MCID, used as input for GATE, are automatically stored in two folders, named *data* and *mac*. Each .mac file contains a group of GATE commands which define the settings of the simulation, such as the geometry and the density of the system, the characteristics of the sources, the physics of the simulation, the features of the output, the level of verbosity, and the visualization settings. Moreover, some .mac files recall specific files stored in the data folder (such as the patient density and activity maps). A list of some .mac files, along with set parameters of most interest, is reported in Table 2.

Table 2. Some .mac files generated by MCID (Monte Carlo Internal Dosimetry tool) and respective main set parameters.

File Name	Function/Set Parameters
_Y90_spectrum.mac	Recalls all the files, # of primaries
actor.mac	Types of output *
geometry.mac	Geometry and density (CT)
physic.mac	Physics list (emstandard_opt3 **)
sourceY90.mac	Source type (SPECT)

* (absorbed dose map, deposited energy map, squared deposited energy map, uncertainty map); ** (standard electromagnetic library, highly accurate for electrons).

The file _Y90_spectrum.mac recalls the other files, therefore the user can start the simulation just running the command gate _Y90_spectrum.mac on the terminal. The simulations were performed on a desktop computer with Intel Core i7 5960X and 3 GHz, 16 GB RAM, and Linux Ubuntu 18.04 LTS.

2.1.5. Conversion of the Output GATE File in Absorbed Dose Images with Requested Units

Gate provides as output absorbed dose maps expressed in Gy units [32,33]. However, to be usable, i.e., quantified coherently, these have to be rescaled considering the effective activity at the injection time, the number of primaries simulated, and the abundancy of emission channels. The user needs to insert a calibration factor to rescale for the original activity at injection time:

$$f = \frac{A_{0,^{90}Y}}{C_{tot} \cdot \lambda_{0,^{90}Y}}, \quad (1)$$

where $A_{0,^{90}Y}$ is the ^{90}Y activity at the injection time, C_{tot} is the total SPECT counts in the whole liver and $\lambda_{0,^{90}Y}$ is the physical decay constant of ^{90}Y, while MCID will automatically rescale for the numbers of primaries and the abundancy of emission channels. The ratio between $A_{0,^{90}Y}$ and C_{tot} consists in a relative calibration factor (converting voxel counts into activity) [1,12], whereas considering microspheres permanently trapped in capillaries (as commonly assumed), biokinetics estimation are not needed, and the physical decay constant of ^{90}Y is used for calculations of number of decays. The ^{90}Y activity at the injection time simulated in this work is 2 GBq.

2.2. Simulated Cases

Voxelized phantoms were designed, simulating three clinical cases with different activity and density maps. The materials selected for the segmentation of the different scenarios are generically reported in Table 3, even though some variations were experienced (according to the scenario) and described in the following. The ICRU atomic composition was always assigned [38].

Table 3. Tissues used for the segmentation of validation scenarios.

Tissue/Material	Density (g/cm^3)
Air	$1.205 \cdot 10^{-3}$
Adipose tissue	0.920
Compact bone	1.850
Lung	0.296
Soft tissue	1.040

2.2.1. Uniform Liver (UL) Case

The Uniform Liver (UL) case has liver with homogeneous density, uniform activity inside the liver and no activity outside of it. Liver homogeneity and uniform activity distribution are the hypotheses of the standard MIRD approach at the organ level, so this scenario was considered in order to compare the average absorbed dose calculated by the MC-based TPS with the average absorbed dose calculated by the classical AAPM (American Association of Physicists in Medicine) formula [1]:

$$D(Gy) = 49.38\ (Gy\ kg/GBq) \cdot \frac{A_0\ (GBq)}{m\ (kg)} \quad (2)$$

where A_0 is the ^{90}Y activity at the injection time and m is the liver mass. The multiplicative factor 49.38 $Gy\ kg/GBq$ accounts for the physical characteristics of ^{90}Y (half-life and average energy emitted per nuclear transition) and has a relative statistical uncertainty of 0.1% [1]. No production of bremsstrahlung and energy completely released inside the mass of interest are also assumed for the calculation of the multiplicative factor.

Examples of slices of the contoured CT, activity map and reconstructed SPECT image for this case are reported in Figure 1.

Liver and breast prosthesis regions were considered as *soft tissue.*

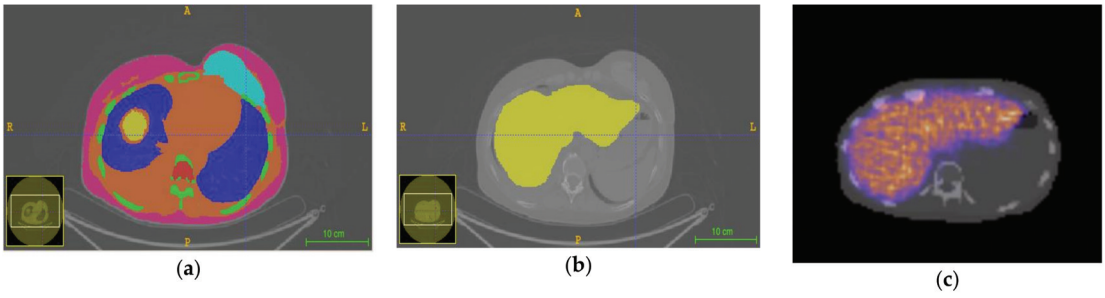

Figure 1. Three transversal slices of different images used in the UL case: (**a**) contoured CT (in this slice all the contoured regions are visible), (**b**) activity map, and (**c**) SPECT superimposed on the coregistered CT.

2.2.2. Spherical Regions (SR) Case

The Spherical Regions (SR) case has homogeneous liver and activity in three spherical regions only. These spheres, placed inside the liver, are named "SS" (Small Sphere), "MS" (Medium Sphere), and "BS" (Big Sphere) and their radii are 10, 20, and 30 mm, respectively. Slices of the contoured CT, activity map and reconstructed SPECT image for this case are reported in Figure 2.

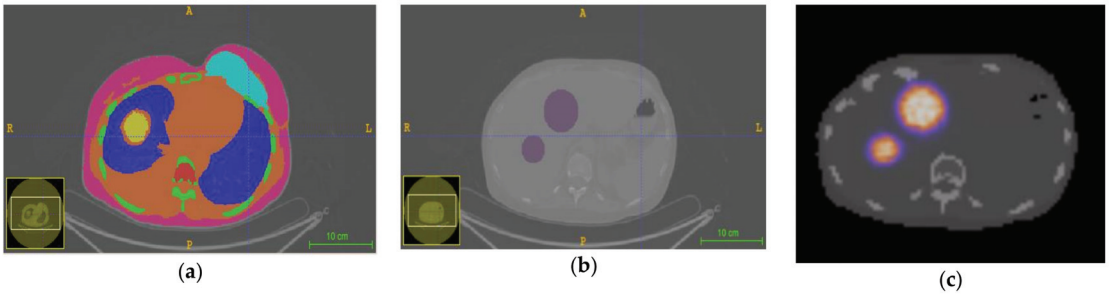

Figure 2. Three transversal slices of different images used in the SR case: (**a**) contoured CT (in this slice all the contoured regions are visible), (**b**) activity map and (**c**) SPECT superimposed on the coregistered CT. Activity is just in the spheres (MS and BS are visible in (**b**,**c**), while SS is located on another transversal plane).

We developed this scenario in order to compare the average absorbed dose for each sphere obtained from the GATE output with that obtained from OLINDA-EXM [39] S-factor for ^{90}Y and spheres of soft tissues with unit density. From the table of S-factors associated to sphere masses included into OLINDA-EXM, the following relationship between S-factor (expressed in $\frac{mGy}{MBq \cdot s}$) and sphere mass m (expressed in g) was obtained and used to derive the corresponding dosimetric factor for a sphere of arbitrary mass:

$$S\left[\frac{mGy}{MBq \cdot s}\right] = 0.12456 \cdot m[g]^{-0.97267} \quad (3)$$

As S-factors are referred to spheres with unit density, the soft tissue density for this scenario was set to 1.00 g/cm^3.

2.2.3. Nonuniform Liver (NUL) Case

The Nonuniform Liver (NUL) case can be divided in two subcases:

- NUL-a, presenting a liver with homogeneous density and activity placed inside both spherical regions and liver with activity concentration ratio of 5:1, respectively;

- NUL-b, presenting a liver with nonhomogeneous density and activity placed inside the spherical regions (possible tumor lesions) and liver with activity concentration ratio of 5:1, respectively (Figure 3). For this scenario, four tissues were added to the segmentation list in Table 3: *tumor* (1.200 g/cm^3), *water* (0.998 g/cm^3), *liver* (1.050 g/cm^3), and *trabecular bone* (1.140 g/cm^3). The spheres were segmented in MCID as *tumor*, with different density as compared to the surrounding liver. The left prosthesis for this subcase was segmented as *water*.

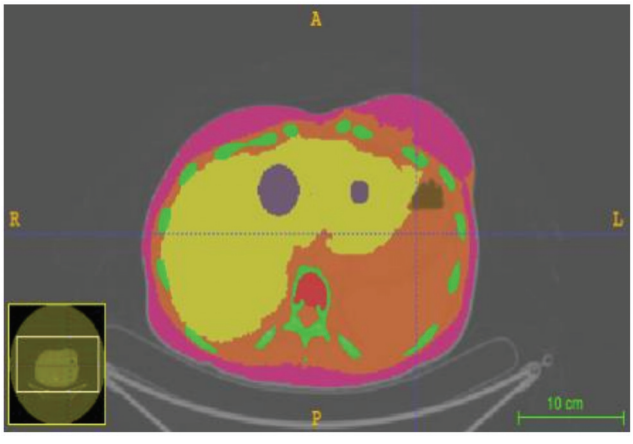

Figure 3. Transversal slice of the NUL-b contoured CT where tumor regions are shown in purple (BS and SS are visible in this slice).

NUL-a case presents a nonuniform activity distribution and was built to evaluate the absorbed dose differences between the S-voxel convolution method and MC (the TPS).

NUL-b is a realistic scenario and was developed in order to quantify the absorbed dose distribution in tumoral regions with different density as compared to the healthy parenchyma, using the S-voxel convolution method and MC (the TPS).

2.3. Convolution with Voxel S-Values Calculated Independently

For validation purposes, absorbed dose images were also obtained applying convolution technique on the reconstructed SPECT images. The voxel S-values used in the convolution were calculated with the EGSnrc code [17], independently from the tested TPS, considering a 4.1 mm voxel size and ICRU soft tissue [38] as medium (density = 1.04 g/cm^3). The S-values calculation was set as described in [17]. The source description was the same as that used for the GATE simulation in the TPS, to increase comparability of dosimetric results. Absorbed dose images obtained by convolution were used to validate and test the TPS. Since the convolution technique is based on the application of MIRD approach at the voxel level, the results obtained with convolution will be labeled as "MIRD" hereinafter.

A schematic representation of the described workflow is reported in Figure 4.

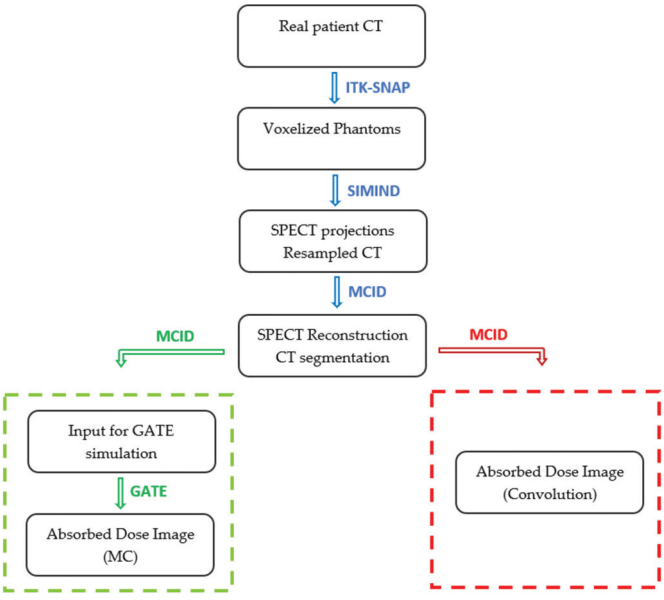

Figure 4. Schematic representation of the workflow and software packages used in this study. The blue steps are specific for the validation with the computational phantoms and they will not be performed (except for the CT segmentation) when dealing with real patient images. The latter should be directly imported into the MCID platform.

2.4. Statistical Uncertainty on the GATE Simulation

A map of relative statistical uncertainties of the absorbed dose in each voxel is obtained as output from each GATE simulation. These values were used for the assessment of the relative statistical uncertainty on the mean absorbed dose in one region of interest (ROI) through the following expression, according to [40]:

$$U_{roi,rel} = \sqrt{\frac{1}{n} \cdot \sum_{k=1}^{n} (u_{k,rel})^2} \quad (4)$$

where $U_{roi,rel}$ is the relative statistical uncertainty on the mean absorbed dose to the ROI, n is the number of the voxels inside the ROI, and $u_{k,rel}$ is the relative statistical uncertainty of the absorbed dose in the voxel k.

3. Results

The computational time for each MC simulation was around 5 h. The relative statistical uncertainty on the absorbed dose value in a single voxel was below 1% for the range 150 Gy–700 Gy, below 2% for the range 50 Gy–150 Gy and below 10% for the range 1 Gy–10 Gy.

3.1. UL Case

The results for the mean absorbed dose calculation with the MIRD approach at the organ level and direct MC simulation are reported in Table 4.

Table 4. Comparison between average absorbed dose values to the liver, calculated from the Gate image (D_{gate}) and from the MIRD approach (D_{mird}) at the organ level. The relative difference (RD) is defined as $= \frac{\overline{D}_{gate} - \overline{D}_{mird}}{\overline{D}_{mird}}$.

D_{gate} (Gy)	D_{mird} (Gy)	RD (%)
36.79	36.69	0.27

The relative statistical uncertainty on D_{gate}, assessed using (4), was 2% while the relative statistical uncertainty on D_{mird}, calculated from the uncertainty on the factor 49.38 $Gy\ kg/GBq$ in (2) (§ 2.2.1), was 0.1%. Therefore, the mean absorbed dose values to the liver obtained from the two methods are compatible.

3.2. SR Case

The comparison between average absorbed dose values for each sphere is reported in Table 5.

Table 5. Mean absorbed dose values for each sphere, calculated from the Gate image (D_{gate}) and from the application of the OLINDA/EXM factors (D_{olinda}). The relative difference (RD) is defined as RD $= \frac{\overline{D}_{gate} - \overline{D}_{olinda}}{\overline{D}_{olinda}}$.

	D_{gate} (Gy)	D_{olinda} (Gy)	RD (%)
BS	666	625	6.57
MS	558	604	−7.62
SS	176	571	−69.20

The relative statistical uncertainties on the mean absorbed dose from GATE simulations for BS, MS and SS are 0.5%, 0.6% and 0.8%, respectively. Statistical uncertainties for OLINDA/EXM S-factors were not available.

In this case, differences are more evident, above all for SS, whose result is probably affected by partial volume effects (PVEs). In order to verify this assumption and reduce these effects, the initial activity map created with ITK-SNAP was used as input for MC simulation, skipping SPECT simulation and reconstruction. The obtained results are reported in Table 6.

Table 6. Mean absorbed dose values for each sphere, calculated from the Gate image (D_{gate}) with a reduced workflow and from the application of the OLINDA/EXM factors (D_{olinda}). The relative difference (RD) is defined as RD $= \frac{\overline{D}_{gate} - \overline{D}_{olinda}}{\overline{D}_{olinda}}$.

	D_{gate} (Gy)	D_{olinda} (Gy)	RD (%)
BS	613	625	−1.92
MS	588	604	−2.65
SS	517	571	−9.46

The relative statistical uncertainties on the mean absorbed dose in the three spheres obtained from the GATE simulations was 1%.

3.3. NUL Case

Several absorbed dose profiles for each subcase were extracted from different transversal slices. One example profile for the NUL-a case, presenting homogeneous liver and activity in three spherical regions and liver in concentration ratio 5:1, respectively, is reported in Figure 5. An image of voxel-by-voxel relative difference (RD) for the same slice from which the profile was selected is also reported in Figure 5.

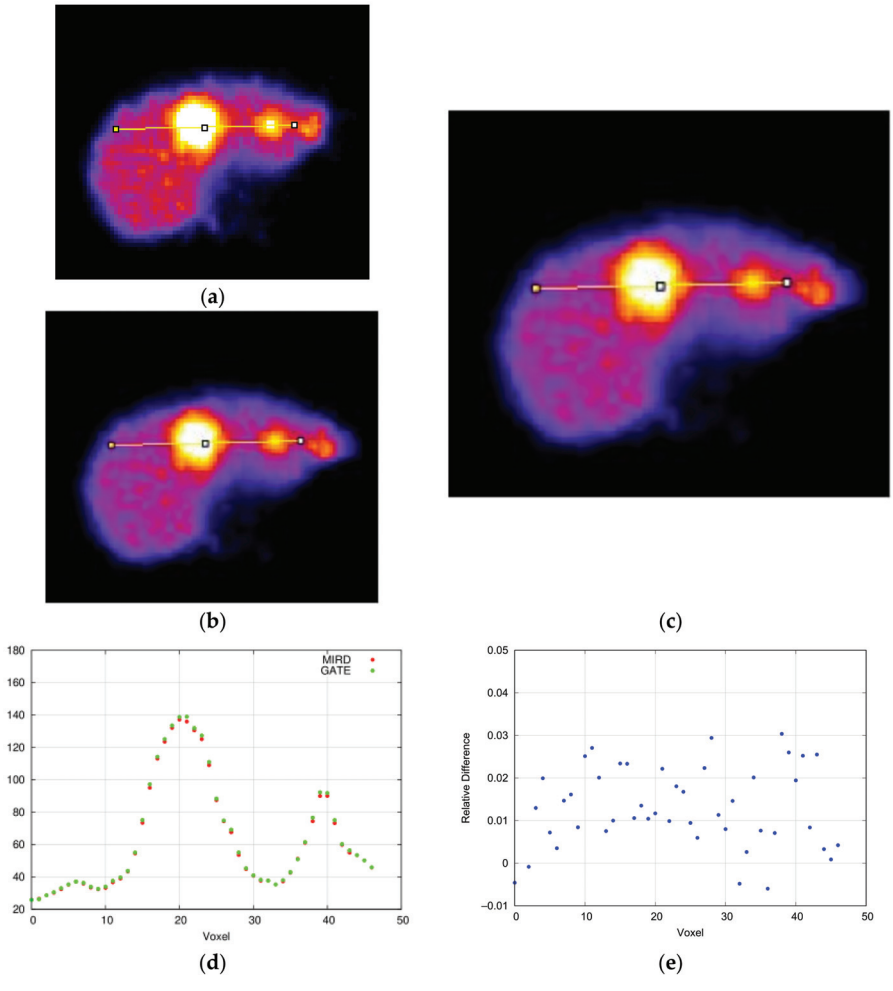

Figure 5. Absorbed dose profile for the NUL-a case and comparison. (**a**) Absorbed dose image obtained with the MIRD scheme and absorbed dose profile selection; (**b**) absorbed dose image obtained with GATE and absorbed dose profile selection; (**c**) relative difference (RD) image for the whole slice; (**d**) comparison between absorbed dose profiles; (**e**) plot of the absorbed dose RDs for each voxel of the profile.

All the profiles selected for the NUL-a case showed a relative difference within 3% between the absorbed dose images calculated by MC simulation and convolution of voxel S-values. Relative differences for the entire liver confirmed that this result is valid for all liver slices, except for some boundary voxels, actually external to the liver and characterized by low dose values (less than few Grays).

Absorbed dose profiles for the NUL-b case, presenting nonhomogeneous liver and nonuniform activity, are reported in Figures 6 and 7.

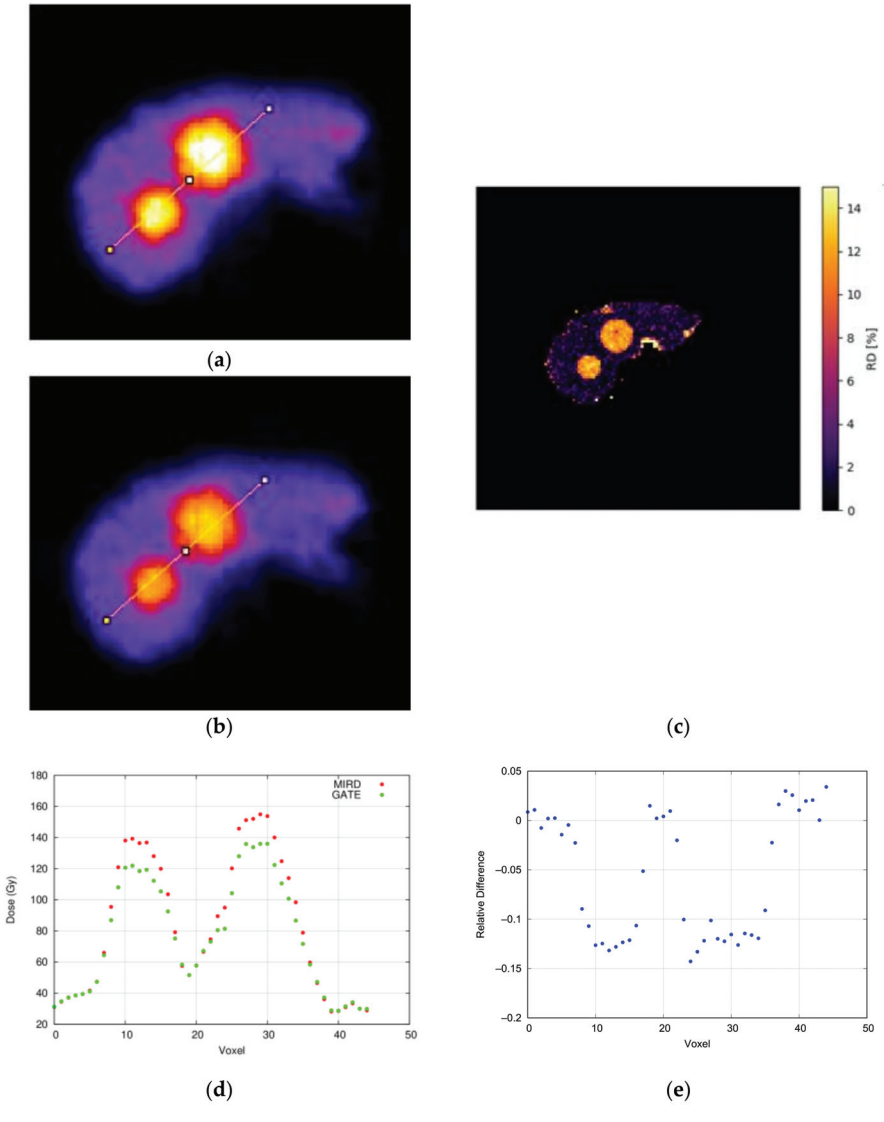

Figure 6. Absorbed dose profile for the NUL-b case and comparison. (**a**) Absorbed dose image obtained with the MIRD schema and absorbed dose profile selection; (**b**) absorbed dose image obtained with GATE and absorbed dose profile selection; (**c**) relative difference (RD) image for the whole slice; (**d**) comparison between absorbed dose profiles; (**e**) plot of the absorbed dose RDs for each voxel of the profile.

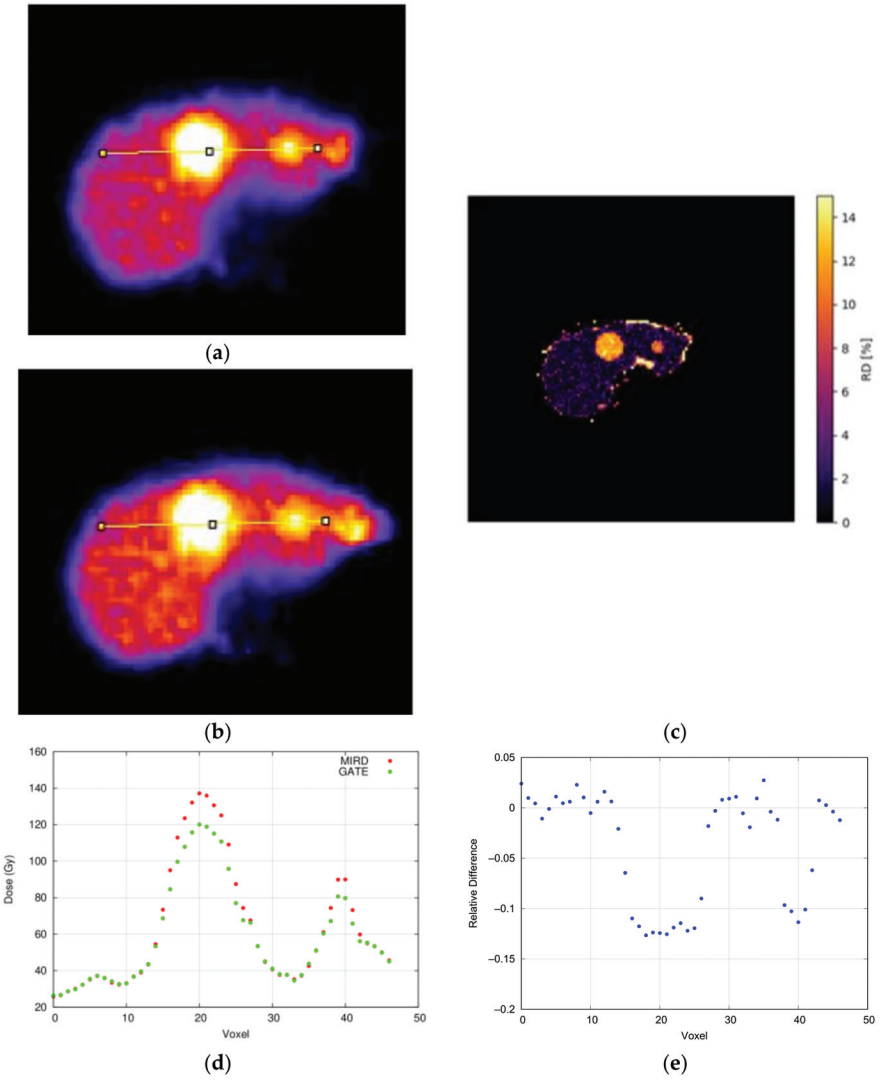

Figure 7. Absorbed dose profile for the NUL-b case and comparison. (**a**) Absorbed dose image obtained with the MIRD schema and absorbed dose profile selection; (**b**) absorbed dose image obtained with GATE and absorbed dose profile selection; (**c**) relative difference (RD) image for the whole slice; (**d**) comparison between absorbed dose profiles; (**e**) plot of the absorbed dose relative differences RD for each voxel of the profile.

The relative differences between the absorbed dose images were up to 14% in the spherical regions, having a different density (1.200 g/cm^3) as compared to the surrounding liver (1.050 g/cm^3).

4. Discussion

The validation of MCID platform is demonstrated at both organ and voxel level. In particular, for the UL scenario, the comparison between mean absorbed doses to liver assessed with the MIRD approach at the organ level and with the MC-based TPS showed a very good agreement (RD = 0.27%). This result highlights the efficiency of the developed

dosimetric routine: under the hypothesis of homogeneous density and uniform activity distribution in each tissue, both methods are equivalent, as expected. It is interesting to point out that D_{mird} is a merely theoretical quantity, while D_{gate} depends on the image quality, e.g., partial volume effects (PVEs), which in this first case appear negligible due to the big size of the observed object (i.e., the whole liver). The effects due to image blurring become relevant instead when dealing with smaller objects, as in the SR case. This scenario allowed a comparison between the average absorbed doses to each sphere. While the BS and the MS present a RD < 8% (absolute value) between the two methods, the SS shows a dramatic RD of −69.2%, caused by the PVEs affecting the SPECT simulation with SIMIND. One contribution to PVEs rises from the matrix resampling (512 × 512 to 128 × 128), an additional contribution derives from the impulsive response of the imaging system, in the SIMIND simulation: spill-out effects affecting voxels cause a change in the activity quantified by imaging, only partially recovered with CDR corrections during the tomographic reconstruction. D_{gate} depends on the activity estimated from the image, while D_{mird} is only related to the theoretical initial activity value. The drastic impact of PVEs is evidenced by the results obtained without the SIMIND simulation: for the BS and the MS, RD reduced to 2% and 3% (absolute values), respectively, while for the SS, RD reduced to 9% (absolute value). Remaining discrepancies could be related to some differences between the MC codes used for calculating the OLINDA-EXM sphere S-factors and the updated code used in this work, and to possible mismatching in source description. Relative differences for the BS and the MS are in agreement with the results shown in [41], where the authors presented an analogous comparison for various sphere diameters: their smallest sphere had a 27 mm diameter, resulting in RD = −5%, so the RD here obtained for SS (20 mm diameter, see Table 6) also appears reasonable and comparable. Dosimetry in lesions with size equal (or less) to the maximum ^{90}Y β^- range (around 12 mm in soft tissue) should be treated carefully, also due to limited resolving power of SPECT imaging. An analysis of dosimetry in small lesions and a correction factor for the MIRD standard equation are proposed in [42].

A validation of the TPS at the voxel level was presented in the NUL-a case. The differences between the two methods (MC simulation and S-voxel convolution) for each absorbed dose profile were always within 3%.

Finally, the NUL-b scenario shows the importance of a personalized dosimetry in heterogeneous tissues, accounting for both activity distribution and density inhomogeneities, which are often overlooked in present internal dosimetry evaluations. The analysis of different absorbed dose profiles reveals that in the tumoral spherical regions absorbed dose values derived from the MC simulation are lower (up to 14% in absolute value) than absorbed dose values calculated with the convolution method, due to a density increase in lesions of about 20% with respect to the surrounding tissue. Therefore, it is necessary to include morphological patient-specific information in the treatment planning system, including careful calibration of the CT and possibly high quality CT systems (to allow HU-based density estimation for each voxel) to avoid inaccuracies based on the assumption of homogeneous tissues. The use of the highest possible quality CT could be of special value to improve the information especially in inhomogeneous tumors or e.g., in bone metastases.

The concept of voxel dosimetry is bright and suitable, but it is a highly complex association between image reconstruction, segmentation, density, PVE, activity recovery, and absorbed dose calculation. All these issues can concur to limitations which still need to be well understood and solved.

The scientific community is investing appreciable efforts to improve and assess the reliability and accuracy of dosimetry at the voxel level in volumes of interest of various scenarios.

Concerning image quantification, relevant studies are ongoing to highlight and compensate imaging and reconstruction deficiencies that may lead to unrealistic absorbed dose distributions for different organ substructures, lesions or voxel dimensions [43].

As regards the potential impact of density and inhomogeneities, the results of this study, although theoretical, based on a MC approach represent a proof of concept and challenge analysis of more complex situations with real patient data of different clinical situations. This is in fact the topic of a current study of some of the authors, and preliminary results will be soon presented.

5. Conclusions

The validated MCID platform allows the fast implementation of a personalized MC dosimetry, based on patient imaging data, avoiding complex and time-consuming manual coding to the user. The system could be easily integrated in the clinical practice, considering the total computational time of the MC simulation (~ 5 h), suitable with clinical routine. For liver with homogenous density, the comparison between absorbed dose assessed from MC simulations and from the MIRD approach at the organ and voxel level showed a very good agreement. For smaller regions, PVEs from imaging deeply influence the final absorbed dose evaluation, therefore a careful analysis and PVEs corrections are required. Finally, patient heterogeneities should be considered in the treatment planning in order to obtain accurate dosimetric estimations.

Author Contributions: Conceptualization, M.P., R.F., A.M.; methodology, M.P., R.F.; software, A.V.G., A.M., E.F., N.L.; validation, E.F., M.P., A.V.G.; formal analysis, A.M., E.F., M.P., R.F., A.V.G.; investigation, A.M., M.P.; resources, M.P., A.V.G., N.L.; data curation, A.M.; writing—original draft preparation, A.M., M.P., M.C.; writing—review and editing, all authors; visualization, all authors; supervision, M.P.; project administration, M.P.; funding acquisition, M.P. All authors have read and agreed to the published version of the manuscript.

Funding: This research was funded by the Union for International Cancer Control, grant number UICC-TF/17/376845.

Institutional Review Board Statement: Not applicable.

Informed Consent Statement: Not applicable.

Data Availability Statement: The data presented in this study are available on request from the corresponding author.

Acknowledgments: The authors would like to thank Edoardo d'Andrea for the useful comments and suggestions on the manuscript.

Conflicts of Interest: The authors declare no conflict of interest.

References

1. Dezarn, W.A.; Cessna, J.T.; DeWerd, L.A.; Feng, W.; Gates, V.L.; Halama, J.; Kennedy, A.S.; Nag, S.; Sarfaraz, M.; Sehgal, V. Recommendations of the American Association of Physicists in Medicine on Dosimetry, Imaging, and Quality Assurance Procedures for 90Y Microsphere Brachytherapy in the Treatment of Hepatic Malignancies. *Med. Phys.* **2011**, *38*, 4824–4845. [CrossRef]
2. Giammarile, F.; Bodei, L.; Chiesa, C.; Flux, G.; Forrer, F.; Kraeber-Bodere, F.; Brans, B.; Lambert, B.; Konijnenberg, M.; Borson-Chazot, F. EANM Procedure Guideline for the Treatment of Liver Cancer and Liver Metastases with Intra-Arterial Radioactive Compounds. *Eur. J. Nucl. Med. Mol. Imaging* **2011**, *38*, 1393. [CrossRef] [PubMed]
3. Strigari, L.; Konijnenberg, M.; Chiesa, C.; Bardies, M.; Du, Y.; Gleisner, K.S.; Lassmann, M.; Flux, G. The Evidence Base for the Use of Internal Dosimetry in the Clinical Practice of Molecular Radiotherapy. *Eur. J. Nucl. Med. Mol. Imaging* **2014**, *41*, 1976–1988. [CrossRef] [PubMed]
4. Hermann, A.-L.; Dieudonné, A.; Ronot, M.; Sanchez, M.; Pereira, H.; Chatellier, G.; Garin, E.; Castera, L.; Lebtahi, R.; Vilgrain, V. Relationship of Tumor Radiation–Absorbed Dose to Survival and Response in Hepatocellular Carcinoma Treated with Transarterial Radioembolization with 90Y in the SARAH Study. *Radiology* **2020**, *296*, 673–684. [CrossRef]
5. Levillain, H.; Derijckere, I.D.; Ameye, L.; Guiot, T.; Braat, A.; Meyer, C.; Vanderlinden, B.; Reynaert, N.; Hendlisz, A.; Lam, M. Personalised Radioembolization Improves Outcomes in Refractory Intra-Hepatic Cholangiocarcinoma: A Multicenter Study. *Eur. J. Nucl. Med. Mol. Imaging* **2019**, *46*, 2270–2279. [CrossRef]
6. Garin, E.; Palard, X.; Rolland, Y. Personalised Dosimetry in Radioembolisation for HCC: Impact on Clinical Outcome and on Trial Design. *Cancers* **2020**, *12*, 1557. [CrossRef]

7. Palard, X.; Edeline, J.; Rolland, Y.; Le Sourd, S.; Pracht, M.; Laffont, S.; Lenoir, L.; Boudjema, K.; Ugen, T.; Brun, V. Dosimetric Parameters Predicting Contralateral Liver Hypertrophy after Unilobar Radioembolization of Hepatocellular Carcinoma. *Eur. J. Nucl. Med. Mol. Imaging* **2018**, *45*, 392–401. [CrossRef]
8. Van den Hoven, A.F.; Rosenbaum, C.E.; Elias, S.G.; de Jong, H.W.; Koopman, M.; Verkooijen, H.M.; Alavi, A.; van den Bosch, M.A.; Lam, M.G. Insights into the Dose–Response Relationship of Radioembolization with Resin 90Y-Microspheres: A Prospective Cohort Study in Patients with Colorectal Cancer Liver Metastases. *J. Nucl. Med.* **2016**, *57*, 1014–1019. [CrossRef] [PubMed]
9. Chiesa, C.; Mira, M.; Bhoori, S.; Bormolini, G.; Maccauro, M.; Spreafico, C.; Cascella, T.; Cavallo, A.; De Nile, M.C.; Mazzaglia, S. Radioembolization of Hepatocarcinoma with 90 Y Glass Microspheres: Treatment Optimization Using the Dose-Toxicity Relationship. *Eur. J. Nucl. Med. Mol. Imaging* **2020**, *47*, 3018–3032. [CrossRef] [PubMed]
10. Willowson, K.P.; Bernard, E.J.; Maher, R.; Clarke, S.J.; Bailey, D.L. Changing Therapeutic Paradigms: Predicting MCRC Lesion Response to Selective Internal Radionuclide Therapy (SIRT) Based on Critical Absorbed Dose Thresholds: A Case Study. *Asia Ocean. J. Nucl. Med. Biol.* **2017**, *5*, 66.
11. Gulec, S.A.; Mesoloras, G.; Stabin, M. Dosimetric Techniques in 90Y-Microsphere Therapy of Liver Cancer: The MIRD Equations for Dose Calculations. *J. Nucl. Med.* **2006**, *47*, 1209–1211.
12. Ho, S.; Lau, W.Y.; Leung, T.W.T.; Chan, M.; Ngar, Y.K.; Johnson, P.J.; Li, A.K.C. Partition Model for Estimating Radiation Doses from Yttrium-90 Microspheres in Treating Hepatic Tumours. *Eur. J. Nucl. Med.* **1996**, *23*, 947–952. [CrossRef]
13. Flamen, P.; Vanderlinden, B.; Delatte, P.; Ghanem, G.; Ameye, L.; Van Den Eynde, M.; Hendlisz, A. Multimodality Imaging Can Predict the Metabolic Response of Unresectable Colorectal Liver Metastases to Radioembolization Therapy with Yttrium-90 Labeled Resin Microspheres. *Phys. Med. Biol.* **2008**, *53*, 6591. [CrossRef] [PubMed]
14. Ljungberg, M.; Sjögreen-Gleisner, K. The Accuracy of Absorbed Dose Estimates in Tumours Determined by Quantitative SPECT: A Monte Carlo Study. *Acta Oncol.* **2011**, *50*, 981–989. [CrossRef] [PubMed]
15. Pasciak, A.S.; Bourgeois, A.C.; Bradley, Y.C. A Comparison of Techniques for 90Y PET/CT Image-Based Dosimetry Following Radioembolization with Resin Microspheres. *Front. Oncol.* **2014**, *4*, 121. [CrossRef]
16. Bolch, W.E.; Bouchet, L.G.; Robertson, J.S.; Wessels, B.W.; Siegel, J.A.; Howell, R.W.; Erdi, A.K.; Aydogan, B.; Costes, S.; Watson, E.E. MIRD Pamphlet No. 17: The Dosimetry of Nonuniform Activity Distributions—Radionuclide S Values at the Voxel Level. *J. Nucl. Med.* **1999**, *40*, 11S–36S. [PubMed]
17. Lanconelli, N.; Pacilio, M.; Meo, S.L.; Botta, F.; Di Dia, A.; Aroche, L.T.; Pérez, M.C.; Cremonesi, M. A Free Database of Radionuclide Voxel S Values for the Dosimetry of Nonuniform Activity Distributions. *Phys. Med. Biol.* **2012**, *57*, 517. [CrossRef]
18. Pacilio, M.; Amato, E.; Lanconelli, N.; Basile, C.; Torres, L.A.; Botta, F.; Ferrari, M.; Diaz, N.C.; Perez, M.C.; Fernández, M.; et al. Differences in 3D Dose Distributions Due to Calculation Method of Voxel S-Values and the Influence of Image Blurring in SPECT. *Phys. Med. Biol.* **2015**, *60*, 1945. [CrossRef] [PubMed]
19. Dieudonné, A.; Garin, E.; Laffont, S.; Rolland, Y.; Lebtahi, R.; Leguludec, D.; Gardin, I. Clinical Feasibility of Fast 3-Dimensional Dosimetry of the Liver for Treatment Planning of Hepatocellular Carcinoma with 90Y-Microspheres. *J. Nucl. Med.* **2011**, *52*, 1930–1937. [CrossRef]
20. Sgouros, G.; Kolbert, K.S. The three-dimensional internal dosimetry software package, 3D-ID. In *Therapeutic Applications of Monte Carlo Calculations in Nuclear Medicine*; CRC Press: Boca Raton, FL, USA, 2002; pp. 249–261.
21. Petitguillaume, A.; Bernardini, M.; De Labriolle-Vaylet, C.; Franck, D.; Desbrée, A. 3D-Personalized Monte Carlo Dosimetry for Treatment Planning Optimization in SIRT. *J. Nucl. Med.* **2014**, *55*, 51.
22. Bastiaannet, R.; Kappadath, S.C.; Kunnen, B.; Braat, A.J.; Lam, M.G.; de Jong, H.W. The Physics of Radioembolization. *EJNMMI Phys.* **2018**, *5*, 1–27. [CrossRef]
23. Kim, S.P.; Cohalan, C.; Kopek, N.; Enger, S.A. A Guide to 90Y Radioembolization and Its Dosimetry. *Phys. Med.* **2019**, *68*, 132–145. [CrossRef]
24. Gardin, I.; Bouchet, L.G.; Assié, K.; Caron, J.; Lisbona, A.; Ferrer, L.; Bolch, W.E.; Vera, P. Voxeldose: A Computer Program for 3-D Dose Calculation in Therapeutic Nuclear Medicine. *Cancer Biother. Radiopharm.* **2003**, *18*, 109–115. [CrossRef]
25. Auditore, L.; Amato, E.; Italiano, A.; Arce, P.; Campennì, A.; Baldari, S. Internal Dosimetry for TARE Therapies by Means of GAMOS Monte Carlo Simulations. *Phys. Med.* **2019**, *64*, 245–251. [CrossRef]
26. Chiavassa, S.; Aubineau-Lanièce, I.; Bitar, A.; Lisbona, A.; Barbet, J.; Franck, D.; Jourdain, J.R.; Bardiès, M. Validation of a Personalized Dosimetric Evaluation Tool (Oedipe) for Targeted Radiotherapy Based on the Monte Carlo MCNPX Code. *Phys. Med. Biol.* **2006**, *51*, 601. [CrossRef]
27. Botta, F.; Mairani, A.; Hobbs, R.F.; Gil, A.V.; Pacilio, M.; Parodi, K.; Cremonesi, M.; Pérez, M.C.; Di Dia, A.; Ferrari, M. Use of the FLUKA Monte Carlo Code for 3D Patient-Specific Dosimetry on PET-CT and SPECT-CT Images. *Phys. Med. Biol.* **2013**, *58*, 8099. [CrossRef] [PubMed]
28. Prideaux, A.R.; Song, H.; Hobbs, R.F.; He, B.; Frey, E.C.; Ladenson, P.W.; Wahl, R.L.; Sgouros, G. Three-Dimensional Radiobiologic Dosimetry: Application of Radiobiologic Modeling to Patient-Specific 3-Dimensional Imaging–Based Internal Dosimetry. *J. Nucl. Med.* **2007**, *48*, 1008–1016. [CrossRef]
29. Marcatili, S.; Pettinato, C.; Daniels, S.; Lewis, G.; Edwards, P.; Fanti, S.; Spezi, E. Development and Validation of RAYDOSE: A Geant4-Based Application for Molecular Radiotherapy. *Phys. Med. Biol.* **2013**, *58*, 2491. [CrossRef] [PubMed]

30. Gil, A.V.; Pérez, M.C.; Aroche, L.T.; Pacilio, M.; Botta, F.; Cremonesi, M. MCID: A Personalized Dosimetric Tool Associating Voxel-Based Models with MCNP5. In Proceedings of the IAEA International Conference on Radiation Protection in Medicine, Setting the Scene for the Next Decade, Bonn, Germany, 3–7 December 2012; pp. 3–7.
31. Gil, A.V.; Perez, M.A.; Aroche, L.A.T.; Pacilio, M. MCID: Personalized Dosimetric Tool to Simulate; MCID: Herramienta Dosimetrica Personalizada Para Simular. In Proceedings of the 9 Regional Congress of IRPA on Radiological and Nuclear Safety, Rio de Janeiro, Brazil, 14–19 April 2013.
32. Jan, S.; Santin, G.; Strul, D.; Staelens, S.; Assie, K.; Autret, D.; Avner, S.; Barbier, R.; Bardies, M.; Bloomfield, P.M. GATE: A Simulation Toolkit for PET and SPECT. *Phys. Med. Biol.* **2004**, *49*, 4543. [CrossRef] [PubMed]
33. OpenGATE Collaboration: Users Guide V8.0. 2017. Available online: http://www.opengatecollaboration.org/sites/default/files/GATE-UsersGuideV8.0.pdf (accessed on 8 November 2020).
34. Yushkevich, P.A.; Piven, J.; Hazlett, H.C.; Smith, R.G.; Ho, S.; Gee, J.C.; Gerig, G. User-Guided 3D Active Contour Segmentation of Anatomical Structures: Significantly Improved Efficiency and Reliability. *Neuroimage* **2006**, *31*, 1116–1128. [CrossRef]
35. Ljungberg, M.; Strand, S.; King, M.A. The SIMIND Monte Carlo Program. In *Monte Carlo Calculations in Nuclear Medicine*; CRC Press: Boca Raton, FL, USA, 2012; pp. 145–163.
36. Frey, E.C.; Tsui, B.M.W. A New Method for Modeling the Spatially-Variant, Object-Dependent Scatter Response Function in SPECT. In Proceedings of the 1996 IEEE Nuclear Science Symposium. Conference Record, Anaheim, CA, USA, 2–9 November 1996; Volume 2, pp. 1082–1086.
37. Eckerman, K.F.; Westfall, R.J.; Ryman, J.C.; Cristy, M. Availability of Nuclear Decay Data in Electronic Form, Including Beta Spectra Not Previously Published. *Health Phys.* **1994**, *67*, 338–345. [CrossRef] [PubMed]
38. White, D.R.; Booz, J.; Griffith, R.V.; Spokas, J.J.; Wilson, I.J. ICRU Report 44: Tissue Substitutes in Radiation Dosimetry and Measurement. *Int. Comm. Radiat. Units Meas.* **1989**, *os23*, NP. [CrossRef]
39. Stabin, M.G.; Sparks, R.B.; Crowe, E. OLINDA/EXM: The Second-Generation Personal Computer Software for Internal Dose Assessment in Nuclear Medicine. *J. Nucl. Med.* **2005**, *46*, 1023–1027.
40. Chetty, I.J.; Rosu, M.; Kessler, M.L.; Fraass, B.A.; Ten Haken, R.K.; McShan, D.L. Reporting and Analyzing Statistical Uncertainties in Monte Carlo–Based Treatment Planning. *Int. J. Radiat. Oncol. Biol. Phys.* **2006**, *65*, 1249–1259. [CrossRef] [PubMed]
41. Kost, S.D.; Dewaraja, Y.K.; Abramson, R.G.; Stabin, M.G. VIDA: A Voxel-Based Dosimetry Method for Targeted Radionuclide Therapy Using Geant4. *Cancer Biother. Radiopharm.* **2015**, *30*, 16–26. [CrossRef]
42. D'Arienzo, M.; Sarnelli, A.; Mezzenga, E.; Chiacchiararelli, L.; Amato, A.; Romanelli, M.; Cianni, R.; Cremonesi, M.; Paganelli, G. Dosimetric Issues Associated with Percutaneous Ablation of Small Liver Lesions with 90Y. *Appl. Sci.* **2020**, *10*, 6605. [CrossRef]
43. Tran-Gia, J.; Salas-Ramirez, M.; Lassmann, M. What You See Is Not What You Get: On the Accuracy of Voxel-Based Dosimetry in Molecular Radiotherapy. *J. Nucl. Med.* **2020**, *61*, 1178–1186. [CrossRef]

applied sciences

MDPI

Article

Dosimetric Issues Associated with Percutaneous Ablation of Small Liver Lesions with ^{90}Y

Marco D'Arienzo [1,2,†], Anna Sarnelli [3,*,†], Emilio Mezzenga [3], Laura Chiacchiararelli [4], Antonino Amato [5], Massimo Romanelli [5], Roberto Cianni [6], Marta Cremonesi [7] and Giovanni Paganelli [8]

1 ENEA, Italian National Institute of Ionizing Radiation Metrology, Via Anguillarese 301, 00123 Rome, Italy; marco.darienzo@enea.it
2 ASL Roma 6, Medical Physics Unit, Borgo Garibaldi, 12, 00041 Albano Laziale, Italy
3 Medical Physics Unit, Istituto Scientifico Romagnolo per lo Studio e la Cura dei Tumori (IRST) IRCCS, Via Piero Maroncelli 40, 47014 Meldola, Italy; emilio.mezzenga@irst.emr.it
4 Medical Physics Unit, Ospedale Sant'Andrea, Via di Grottarossa 1035, 00189 Rome, Italy; laurac@ospedalesantandrea.it
5 BetaGlue Technologies Spa, Lungadige Galtarossa 21, 37133 Verona, Italy; a.amato@betaglue.com (A.A.); m.romanelli@betaglue.com (M.R.)
6 Radiology Unit, San Camillo-Forlanini hospital, Circonvallazione Gianicolense 87, 00152 Rome, Italy; rcianni@scamilloforlanini.rm.it
7 Medical Physics Unit, European Institute of Oncology, Via Ripamonti 435, I-20132 Milano, Italy; marta.cremonesi@ieo.it
8 Nuclear Medicine Unit, Istituto Scientifico Romagnolo per lo Studio e la Cura dei Tumori (IRST) IRCCS, Via Piero Maroncelli 40, 47014 Meldola, Italy; giovanni.paganelli@irst.emr.it
* Correspondence: anna.sarnelli@irst.emr.it
† These authors contributed equally to this work.

Received: 21 August 2020; Accepted: 16 September 2020; Published: 22 September 2020

Abstract: The aim of the present paper is twofold. Firstly, to assess the absorbed dose in small lesions using Monte Carlo calculations in a scenario of intratumoral injection of ^{90}Y (e.g., percutaneous ablation). Secondly, to derive a practical analytical formula for the calculation of the absorbed dose that incorporates the absorbed fractions for ^{90}Y. The absorbed dose per unit administered activity was assessed using Monte Carlo calculations in spheres of different size (diameter 0.5–20 cm). The spheres are representative of tumor regions and are assumed to be uniformly filled with ^{90}Y. Monte Carlo results were compared with the macrodosimetric approach used for dose calculation in liver radioembolization. The results of this analysis indicate that the use of the analytic model provides dose overestimates below 10% for lesions with diameter larger than approximately 2 cm. However, for lesions smaller than 2 cm the analytic model is likely to deviate significantly (>10%) from Monte Carlo results, providing dose overestimations larger than 50% for lesions of 0.5 cm diameter. In this paper an analytical formula derived from MC calculations that incorporates the absorbed fractions for ^{90}Y is proposed. In a scenario of intratumoral injection of microspheres, the proposed equation can be usefully employed in the treatment planning of spherical lesions of small size (down to 0.5 cm diameter) providing dose estimates in close agreement with Monte Carlo calculations (maximum deviation below 0.5%).

Keywords: percutaneous radioablation; monte carlo dosimetry; liver lesions; molecular radiotherapy

1. Introduction

Hepatocellular carcinoma (HCC) is the most common primary liver malignancy and today multiple treatment modalities exist [1]. Due to the lack of effective systemic therapies for HCC, researchers have been investigating the use of locoregional tumor control with ^{90}Y radioembolization since the 1960s. Today radioembolization (or Selective Internal Radio Therapy, SIRT) is an established and effective treatment for liver malignancies based on trans-arterial infusion of ^{90}Y-laden microspheres [2–4]. At present, there are two clinically available microsphere devices in which ^{90}Y is incorporated: one with microspheres made of glass (TheraSphere; MDS Nordion, Ottawa, ON, Canada) and the other with microspheres made of resin (SIR-Spheres; Sirtex Medical, Sydney, Australia). Once administered, the spheres remain in the liver as a permanent implant.

Radiation dose distributions arising from intrahepatic arterial infusion of ^{90}Y microspheres have been investigated by a number of authors in the past. In recent years a number of studies have addressed the problem of dosimetry in therapies based on the use of intratumoral administration of ^{90}Y-conjugates by percutaneous puncture. This technique has been successfully applied to patients treated with ^{90}Y-labeled [DOTA^0-D-Phe^1-Tyr^3]octreotide (^{90}Y-DOTATOC) for malignant gliomas [5–7]. In fact, based on the clinical experience gained in liver radioembolization, it is reasonable to assume that percutaneous ablation of HCC through the intratumoral injection of an appropriate activity of ^{90}Y has the potential to reduce drastically the chances of local recurrence. In this context, there is growing interest in the development of new intratumoral procedures for HCC throughout a localized administration of ^{90}Y in the form of microspheres mixed with biocompatible compounds [8].

As a general rule, intratumoral administration of radionuclides raises questions about the dosimetry of small lesions as this approach allows sub-centimeters tumors to be selectively treated [9,10]. To date, there is no simple way to assess exactly the absorbed dose to tumours and normal liver when ^{90}Y is administered. This is because ^{90}Y only emits pure beta radiation with limited penetration range in tissue. As a consequence, the delivered dose is highly dependent on the distribution of the radionuclide and the tumor mass.

Calculation of the radiation dose to tumors may require consideration of the losses of electron energy. In the traditional macrodosimetric approach, all of the electron energy emitted in a source region is assumed to be absorbed in that region. This is quite reasonable for most situations because the range of most electrons in body tissues is small compared to the size of most source regions. However, when the tumor size is small this assumption is no longer true and the absorbed fraction may be significantly less than unity. Some preliminary work dedicated to the assessment of the absorbed fractions for beta particles in spherical regions of different sizes was carried out in the early 1990s by Siegel [11] and Bardies [12]. In a major advance in 2000 Stabin and Konijnenberg [13] reevaluated and updated absorbed fractions in spherical regions comparing different Monte Carlo codes, while in 2010 Amato and colleagues [14] calculated absorbed fractions for electrons in ellipsoidal volumes. The aim of the present paper is to assess the absorbed dose of ^{90}Y after percutaneous administration in small spherical lesions proposing a practical analytical formula that incorporates the absorbed fractions for ^{90}Y. Of note, in [13] absorbed fractions were assessed for monoenergetic electrons using MCNP version 4B, while in this study absorbed dose fractions were calculated implementing the full ^{90}Y spectrum and using an upgraded version of MCNP (version 4C). Calculations were performed assuming both water and liver density ($\rho = 1.00$ g/cm^3 and $\rho = 1.05$ g/cm^3, respectively) for spheres of different diameter (0.5–20 cm). MC results were then compared with the well enstablished macrodosimetric approach used for the dose assessment in liver radioembolization Equation (4).

2. Materials and Methods

2.1. Percutaneous Ablation with ^{90}Y

Recently, it has been proposed the intralesional injection of ^{90}Y in the form of resin microspheres embedded in a bio-compatible matrix. The injection is performed using a proprietary delivery

system [8]. This procedure is also known as percutaneous radioablation and is a minimally invasive treatment for patients with small (below approximately 3 to 5 cm) liver tumors performed using BAT-90, a combination of the following components: (i) BioGlue® (Cryolife, Atlanta, GA, USA), a FDA-approved mixture of bovine serum albumin (45%) and glutaraldehyde (10%) in a 4:1 ratio, approved for use in soft tissue repair or to seal damaged parenchyma [15] (ii) SIR-Spheres® coated with ^{90}Y (Sirtex Medical, Sydney, Australia) approved for implantation into hepatic tumors via the hepatic artery. BAT-90 is percutaneously injected through the MIPP-Kit® (Svas Biosana, Neaples, Italy) a dedicated coaxial dual-lumen catheter for the direct, imaging-guided intra-tumoral injection.

The two components of BAT-90 are dispensed from a double-barrel syringe and mix within the delivery tip in a predefined ratio. The adhesive begins to polymerize within 20–30 s and reaches maximum bonding strength in 2 min. Once injected into the tumor region, the radiopharmaceutical combination (BAT-90) remains in the lesion delivering the required tumoricidal dose. As a consequence, in order to simulate a scenario of percutaneous ablation, in the present study we assumed that ^{90}Y is homogeneously dispersed into the lesion and that there is no biological removal of the radiopharmaceutical.

2.2. Dosimetry with ^{90}Y

^{90}Y disintegrates by β emission mainly (99.983% [16]) to the stable ^{90}Y ground state level. A weak beta branch occurs to the 1760 keV excited level which decays by a E0 gamma transition [16]. This 0^+-0^+ transition is followed by the emission of two gammas, or an electron-positron pair, or internal conversion. The adopted half life of ^{90}Y ground state is 64.041(31) h or 2.6684(13) days [16].

Among the radionuclides used in clinical practice, ^{90}Y has attractive physical and radiobiologic features that make this radionuclide suitable for a loco-regional therapeutic option. The high-energy β-particles (maximum energy 2278.7(16) keV, average energy 926.7(8) keV [16]) and their penetration depth (maximum particle range in tissue, 11 mm; range in tissue after which 50% of the energy particles is transferred, 4 mm) allows high radiation doses to be selectively delivered to the target area, while sparing surrounding tissues and normal organs. In particular, the penetration depth of the high-energy β-particles is a key element of this radionuclide's success in radioembolization, allowing for high-dose deposition into the tissues between embolized capillars. In the traditional dose calculation formalism (after locoregional administration of ^{90}Y) two important simplifying assumptions are generally made:

- β radiation released from ^{90}Y within a given organ is fully absorbed by that organ. In most cases, this assumption is supported by the average 4 mm ^{90}Y β range in tissue.
- permanence of ^{90}Y in the area where they have been delivered (i.e., no migration of the radiopharmaceutical outside the tumor region).

Combining these two assumptions allows for easy calculation of average absorbed dose to an organ of interest on a macroscopic scale. The calculation, carried out using most up-to-date nuclear data for ^{90}Y [16], is illustrated below and it is generally referred to as the MIRD approach [17]:

$$E_{avg} = \int_0^\infty E\varphi(E)dE = 926.7 \text{ keV} = 1.4847 \times 10^{-13} \text{ J} \quad (1)$$

$$E_{tot} = A_0 E_{avg} \int_0^\infty e^{-\lambda t} dt = \frac{A_0}{\lambda}(1.4847 \times 10^{-13} \text{ J}) = A_0 \cdot k \quad (2)$$

where E_{avg} is the average energy released per decay of ^{90}Y based on the probability density function $\varphi(E)$ for emission, λ is the ^{90}Y decay constant based on the half-life of 64.041(31) hours, and k a constant term. A_0 is the activity present in the organ in GBq and E_{tot} is the total energy released by A_0 from the time that it is infused until it has fully decayed.

Assuming that all of the energy of the β^- decay is absorbed in the volume where the decay occurs, the constant term, k, can be calculated taking the given physical values and their statistical uncertainties:

$$k = \frac{1.4847 \times 10^{-13}\ \text{J}}{\lambda} = \frac{1.4847 \times 10^{-13}\ \text{J} \times 230547\ \text{s}}{0.69315} \times \frac{10^9\ \text{dis/s}}{\text{GBq}} = 49.38(5)\ \text{(J/GBq)} \quad (3)$$

The constant factor 49.38 (J/GBq) is the energy released per unit activity of ^{90}Y. The adopted uncertainties on the nuclear data [16] reported in Equation (4) lead to a relative standard uncertainty of 0.1% on the constant term, i.e., 49.38(5) (J/GBq), in line with [18].

Finally, the absorbed dose D (expressed in Gy) can be obtained by dividing the delivered energy, E_{tot}, by the mass of the target region m (expressed in kg):

$$D_{avg}\ \text{(Gy)} = \frac{A_0\ \text{(GBq)} \times 49.38(5)\ \text{(J/GBq)}}{m\ \text{(kg)}} \quad (4)$$

Of note, the same formula with a slightly different constant term, k, is reported in other publications (e.g., 49.98 [17], 49.67 [19]).

According to the partition model [20–22], Equation (4) can be used to calculate the absorbed dose in the tumor, once the fractional tumor uptake FU_{tumor} (i.e., the fraction of the administered activity accumulated in the tumor) is known:

$$D_{tumor}\ \text{(Gy)} = \frac{A_0\ \text{(GBq)} \times 49.38(5)\ \text{(J/GBq)} \times FU_{tumor}}{m\ \text{(kg)}} \quad (5)$$

It must be reiterated that Equations (4) and (5) are representative of average absorbed dose on a macroscopic scale, i.e., on an organ or a large lesion where the absorbed fraction can be assumed equal to unity. These equations may not hold for very small tumor masses, as the assumption that the energy emitted during decay is totally absorbed by the mass of interest m is no longer true. In particular, when the size of the lesion is very small (especially in the sub-centimeter region), the energy released per unit activity of ^{90}Y may decrease significantly. As a consequence hereafter the constant term k in Equation (3) will be treated as a function of the lesion radius (r) and indicated as $k(r)$.

Monte Carlo Calculations

In the present study the absorbed dose per unit administered activity was assessed using Monte Carlo calculations in a simplified geometry. MC code MCNP4C has been used for this purpose [23]. MCNP is a general-purpose, continuous-energy, generalized-geometry, time-dependent, coupled neutron/photon/electron Monte Carlo transport code. For photon transport, the code takes into account photoelectric absorption, with the possibility of K- and L-shell fluorescent emission or Auger electron, coherent and incoherent scattering and pair production. The photoelectric cross sections are based on Storm and Israel [24] whereas the scattering cross sections are taken from ENDF tabulations [25]. The continuous slowing down approximation energy loss model is used for electron transport.

Spherical lesions of different size (diameter in the range 0.5–20 cm) were simulated for two different densities: $\rho = 1.00\ \text{g/cm}^3$ (water density) and $\rho = 1.05\ \text{g/cm}^3$ (liver density). In both scenarios, spheres were assumed to be immersed in a semi-infinite medium with the same density of the sphere. The spheres are representative of tumor regions and are supposed to be uniformly filled with ^{90}Y, while the surrounding medium is assumed to contain no radioactivity.

Calculations were performed in coupled electron-photon mode [MODE P E] using the el03 electron interaction data library (ELIB = 03E) and the mcnplip2 photon interaction data library (PLIB = 02P). Simulations were carried out taking into account all the available advanced options such as electron

production by photons, Bremsstrahlung effect and knock-on electron production. MCNP simulations were run for an adequate time to get a statistical uncertainty on the absorbed dose below 0.01%.

3. Results

Figure 1 shows the fraction of ^{90}Y absorbed dose into the tumor as a function of the tumor size, obtained from MCNP simulations. The ^{90}Y beta spectrum implemented in the model is also reported in the same figure. Calculations were performed both for water spheres ($\rho = 1.00$ g/cm^3) and for spheres made of liver tissue ($\rho = 1.05$ g/cm^3). In both cases, when the lesion diameter drops below 2 cm, a great amount of the β particle energy is delivered outside the sphere. Consistently, the delivered energy per unit activity, $k(r)$, shows the same trend (Figure 2) confirming that when the tumor size is small such term deviates significantly from the value 49.38 (J/GBq), considered in Equation (4). In order to use information reported in Figure 2 at the clinical level, $k(r)$ data obtained from MC calculations were fitted with the following function:

$$k(r) = k_0 + A \cdot (1 - exp(-\frac{r}{a})) + B \cdot (1 - exp(-\frac{r}{b})) \quad (6)$$

where r is the lesion radius in cm (assuming spherical tumors) and k_0, A, a, B, b are parameters determined by the fit (reported in Table 1 both for water and liver density). An r^2 = 0.999 was obtained form the fit, both for water and liver density. Furthermore, goodness-of-fit was also assessed through the analysis of residuals (Figure 2B), which shows maximum deviations below 0.2 between calculated and fitted data, confirming the accuracy of the fit. Based on the fitting function described in Equation (6), Equation (4) can be rewritten in the following form:

$$D_{avg}(r) = \frac{A_0 \cdot k(r)}{m} \quad (7)$$

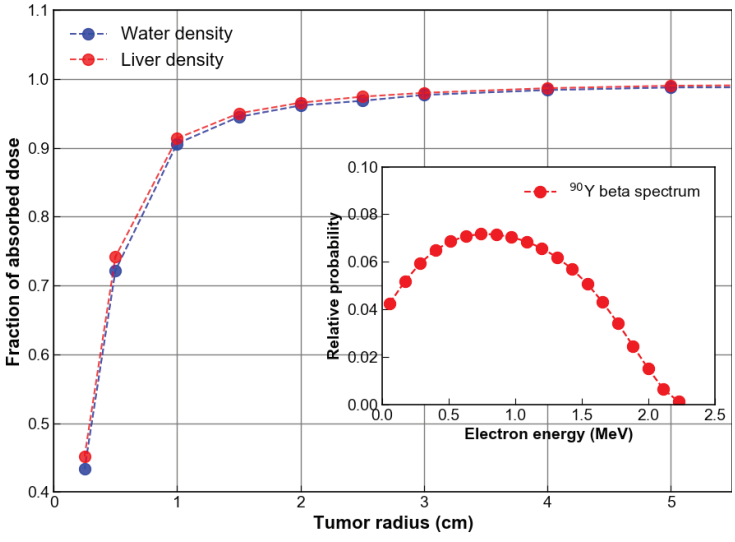

Figure 1. Fraction of ^{90}Y absorbed dose into the tumor as a function of the tumor size. Simulations were performed for $\rho = 1.00$ g/cm^3 (water density) and $\rho = 1.05$ g/cm^3 (liver density). Inset: ^{90}Y beta spectrum implemented in the model.

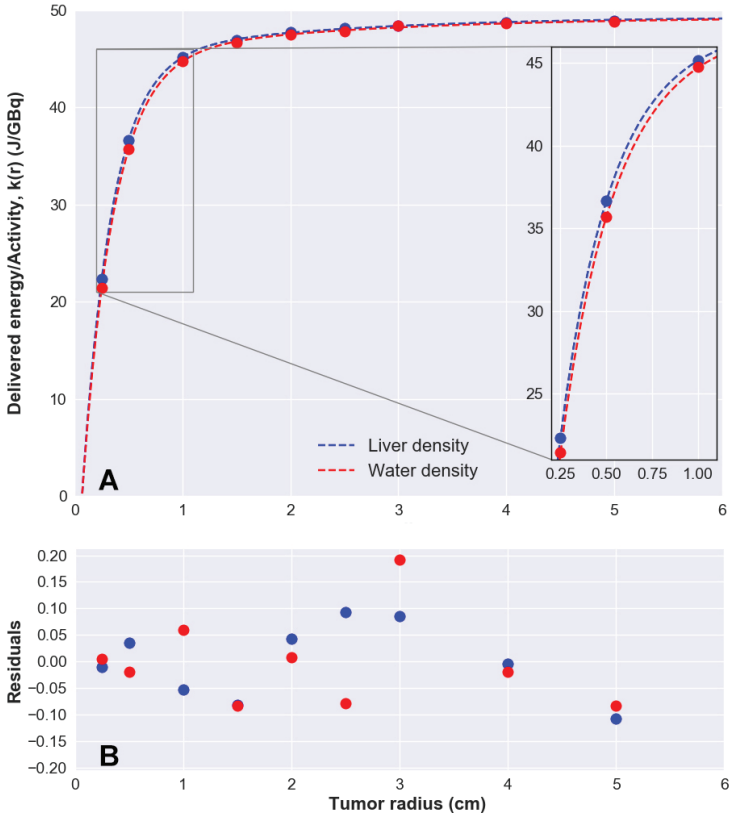

Figure 2. (**A**) Delivered energy per unit activity of ^{90}Y, $k(r)$, calculated with MCNP4c as a function of the tumor diameter. Data were fitted with Equation (6). (**B**) Analysis of residuals.

Table 1. Fitting parameters of Equation (6) with relative standard uncertainties, for water and liver density (denoted with superscripts ^{W} and ^{L}, respectively). $R^2 = 0.999$ in both cases.

Parameter	Value^{W}	$u_{rel}{}^{W/\%}$	Value^{L}	$u_{rel}{}^{L/\%}$
k_0	−11.883	1.10	−12.999	1.00
A	4.416	1.15	4.654	1.10
a	2.190	0.90	1.909	1.00
B	56.820	0.05	57.701	0.05
b	0.290	0.15	0.271	0.10

For a given activity A_0, Equation (7) can be used to accurately calculate the absorbed dose for very small lesions (down to 0.5 cm diameter). The absorbed dose to lesions calculated using Equation (7) provides results in good agreement with MC calculations (maximum deviation below 0.5%). As expected, when ideally $r \to \infty$ Equation (7) reduces to Equation (4). Of note, the energy per unit activity, $k(r)$, obtained from Equation (6) when $x \to \infty$ is 49.35 (J/GBq), against the accepted value of 49.38 (J/GBq) derived from Equation (4) (0.06% deviation).

Figure 3 compares absorbed doses per unit activity (Gy/GBq) calculated with Monte Carlo with those obtained using the analytic approach described by Equation (4), for spherical lesions of different size and for $\rho = 1.05$ g/cm^3. The same results for $\rho = 1.00$ g/cm^3 are shown in Figure 4.

In addition Figure 4 reports absorbed doses calculated using the well established Olinda/EXM code, developed by the RAdiation Dose Assessment Resource (RADAR) Task Group of the Society of Nuclear Medicine [26]. As illustrated in Figure 4, absorbed dose values calculated with MC approach concur well with those obtained using Olinda/EMX. Significant deviations were found between MC calculated dose values and those obtained using the analytic formulation when the lesion diameter drops below 2 cm (Figure 4, inset).

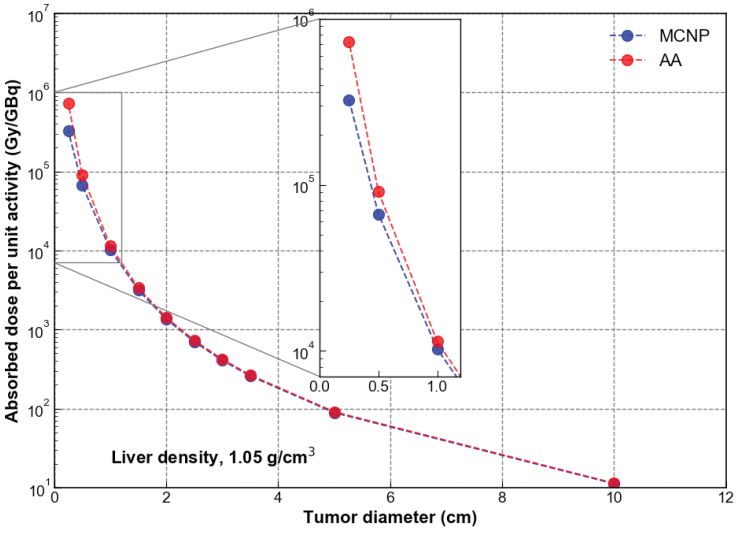

Figure 3. Absorbed dose per unit administered activity (GBq), for $\rho = 1.05$ g/cm^3 (liver density). Comparison between MC approach (MCNP) and the analytical formulation (AA) described by Equation (4). Inset: detail in the range 0 cm–1 cm lesion size.

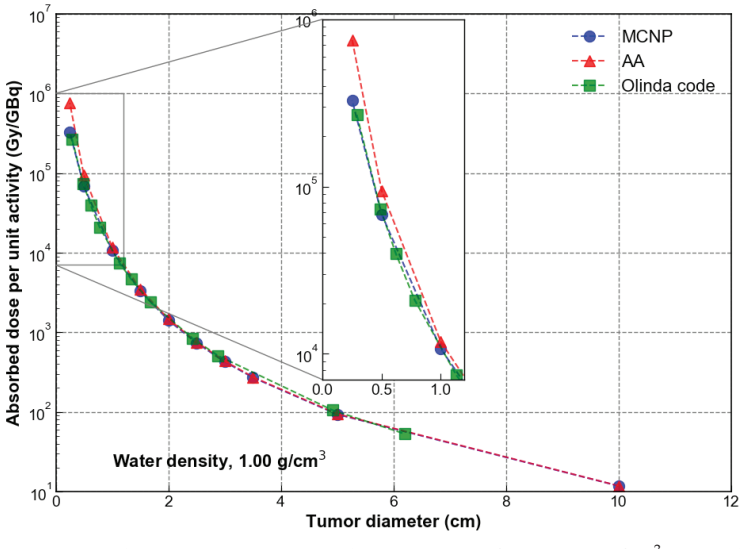

Figure 4. Absorbed dose per unit administered activity (GBq), for $\rho = 1.00$ g/cm^3 (water density). Comparison between MC approach (MCNP) and the analytical formulation (AA) described by Equation (4). Inset: detail in the range 0 cm–1 cm lesion size.

Ultimately, Tables 2 and 3 compare absorbed dose values per GBq of administered activity obtained with MC calculations (D_{MCNP}) and with the analytical approach reported in Equation (4), (D_{AA}). The percentage differences between the two methods (last column of both tables, Δ) is also reported, calculated as $100 \cdot (D_{MCNP} - D_{AA})/D_{AA}$. The difference in absorbed dose values is within ∼10% as long as the diameter of the lesion exceeds 2 cm. The two calculation approaches deviate significantly when the lesion size drops below 2 cm, due to significant energy deposition outside the sphere. This is consistent with the maximum particle range in tissue for ^{90}Y (about 11 mm). In this case, for water (liver) density MC calculations provide absorbed doses −9.3% (−9.6%), −27.8% (−26.7%), −56.7% (−55.4%) lower than those obtained using the analytic formulation described by Equation (4) for tumor diameter of 2 cm, 1 cm and 0.5 cm, respectively (Tables 2 and 3).

Table 2. Dose per unit activity calculated with MCNP4C for spherical lesions of different size uniformly filled with ^{90}Y. The lesions are assumed to have a density of $\rho = 1.05$ g/cm^3 (liver density). The same quantity (dose per unit activity) has been calculated using the analytic approach (AA) described by Equation (4). The last column of the table (Δ) shows the percentage deviation between the two methods, calculated as $100 \cdot (D_{MCNP} - D_{AA})/D_{AA}$.

Lesion Diameter	Mass (kg)	Dose/Particle (Gy/p)	MCNP (Gy/GBq)	AA (Gy/GBq)	Δ
20 cm	4.40	3.38×10^{-14}	1.12×10^{1}	1.14×10^{1}	−1.8%
10 cm	5.50×10^{-1}	2.68×10^{-13}	8.91×10^{1}	9.10×10^{1}	−2.1%
8.0 cm	2.81×10^{-1}	5.21×10^{-13}	1.73×10^{2}	1.78×10^{2}	−2.5%
6.0 cm	1.19×10^{-1}	1.23×10^{-12}	4.08×10^{2}	4.21×10^{2}	−3.1%
5.0 cm	6.87×10^{-2}	2.11×10^{-12}	7.01×10^{2}	7.28×10^{2}	−3.7%
4.0 cm	3.52×10^{-2}	4.08×10^{-12}	1.36×10^{3}	1.42×10^{3}	−4.2%
3.0 cm	1.48×10^{-3}	9.51×10^{-12}	3.16×10^{3}	3.34×10^{3}	−6.2%
2.0 cm	4.40×10^{-3}	3.09×10^{-11}	1.03×10^{4}	1.14×10^{4}	−9.6%
1.0 cm	5.50×10^{-4}	2.01×10^{-10}	6.67×10^{4}	9.10×10^{4}	−26.7%
0.5 cm	6.87×10^{-5}	9.77×10^{-10}	3.25×10^{5}	7.28×10^{5}	−55.4%

Table 3. Dose per unit activity calculated with MCNP for spherical lesions of different size uniformly filled with ^{90}Y. The lesions are assumed to have a density of $\rho = 1$ g/cm^3 (water density). The same quantity (dose per unit activity) has been calculated using the analytic approach (AA) described by Equation (4). The last column of the table (Δ) shows the percentage deviation between the two methods, calculated as $100 \cdot (D_{MCNP} - D_{AA})/D_{AA}$.

Lesion Diameter	Mass (kg)	Dose/Particle (Gy/p)	MCNP (Gy/GBq)	AA (Gy/GBq)	Δ
20 cm	4.19	3.54×10^{-14}	1.18×10^{1}	1.18×10^{1}	0.0%
10 cm	5.23×10^{-1}	2.81×10^{-13}	9.33×10^{1}	9.44×10^{1}	−1.2%
8.0 cm	2.68×10^{-1}	5.47×10^{-13}	1.81×10^{2}	1.84×10^{2}	−1.5%
6.0 cm	1.13×10^{-1}	1.29×10^{-12}	4.27×10^{2}	4.37×10^{2}	−2.3%
5.0 cm	6.54×10^{-2}	2.20×10^{-12}	7.31×10^{2}	7.55×10^{2}	−3.2%
4.0 cm	3.35×10^{-2}	4.27×10^{-12}	1.42×10^{3}	1.47×10^{3}	−3.4%
3.0 cm	1.41×10^{-3}	9.95×10^{-12}	3.30×10^{3}	3.49×10^{3}	−5.4%
2.0 cm	4.19×10^{-3}	3.22×10^{-11}	1.07×10^{4}	1.18×10^{4}	−9.3%
1.0 cm	5.23×10^{-4}	2.05×10^{-10}	6.82×10^{4}	9.44×10^{4}	−27.8%
0.5 cm	6.54×10^{-5}	9.86×10^{-10}	3.27×10^{5}	7.55×10^{5}	−56.7%

4. Discussion

Molecular radiotherapy with ^{90}Y has received much attention in the past two decades and the dosimetry of small lesions remains a key issue. The maximum range of ^{90}Y β-particles is 11 mm in tissue, while its average energy β-particles has a range of about 2.5 mm. It is worth noting that the penetration depth of the high-energy ^{90}Y β-particles is a critical component of this radionuclide's success in liver radioembolization, allowing for high dose delivery into the tissue between embolized capillars. Previous work has been dedicated to the assessment of absorbed fractions for electrons and beta particles in spheres [11–13] and ellipsoidal volumes [14] of various sizes. The present study focused on the assessment of the absorbed dose per unit activity in a scenario of percutaneous ablation of HCC through the intratumoral injection of ^{90}Y in lesions of varying size. A simplified model tumor areas was implemented into MCNP4C MC code with the aim to determine the absorbed dose to the lesion when the tumor mass is uniformly filled with ^{90}Y. Spherical lesions of different size (diameter in the range 0.5–20 cm) were simulated for two different densities: $\rho = 1.00$ g/cm^3 (water density) and $\rho = 1.05$ g/cm^3 (liver density). In both scenarios, lesions were assumed to be immersed in a semi-infinite medium with the same density of the lesion.

The problem of beta dosimetry in small lesions is not new [11–13]. Absorbed fractions calculated in this study are hardly comparable with those assessed in [11,13] as the authors performed calculations assuming monoenergetic electrons, while in this study the full ^{90}Y spectrum was implemented. Furthermore, in [13] the authors used MCNP4B, while in this work MCNP4C was used instead.

The widely used analytic approach described by Equation (4) and MCNP calculations provide results in close agreement (within 10%, no matter the density of the lesion) as long as the lesion diameter exceeds 2 cm. When the lesion diameter drops below 2 cm, significant differences were obtained between MC calculations and the analytic approach (i.e., deviations >10%). As a general rule, the analytic described by Equation (4) tends to overestimate the absorbed dose in small lesions, as the basic assumption of the model is that β radiation is fully absorbed by the tumor or tissue where the decay occurs. When the radius of the tumor is smaller than the maximum range of the β radiation in the medium, a significant amount of the energy is delivered out of the lesion, thus providing smaller absorbed dose values.

Presently, despite the availability of different dose algorithms, the analytic algorithm described by Equation (4) is still widely used to assess the absorbed dose in tumor and in the liver compartment at the clinical level. As a general rule, the size of normal liver is large and Equation (4) provides accurate dose estimates (provided that accurate input parameters are introduced, among which the fractional uptake of the target). However, when this approach is applied to assess the absorbed dose to small tumor masses (i.e., approximately below 2 cm diameter) inaccurate dose estimates can be obtained.

In addition, the analytic algorithm is safely used for treatment planning with glass microspheres. The foundational principle is based on Equation (4), which describes the average dose in a tissue volume as a function of ^{90}Y activity. During treatment planning, this equation can be solved for the treatment activity A_0. The results obtained in the present study raise questions as to whether Equation (4) should be used to assess the prescribed ^{90}Y activity in order to achieve a given tumoricidal endpoint in small liver lesions. This is especially true when intratumoral injection of ^{90}Y is performed. For example, for HCC 120 Gy should be considered to be a reasonable minimum target dose [21,27,28]. Therefore, when treating an HCC patient with ^{90}Y β-particles, one may wish to set D_{tumor} to a minimum of 120 Gy. Equation (5) can be rearranged to derive the prescribed treatment activity: $A(\text{GBq}) = D_{tumor} \cdot m_{tumor}(\text{kg})/49.38\ (\text{J/GBq}) \cdot FU_{tumor}$. Assuming, for example, a tumor mass, m_{tumor}, of 0.52 g (diameter 1 cm), $FU_{tumor} = 1$ and $D_{tumor} = 120$ Gy, Equation (5) would yield a treatment activity of 1.21 MBq (considering $\rho = 1.05$ g/cm^3). On the other hand, if Equation (7) is used instead of Equation (4) a prescribed activity of 1.62 MBq is obtained. As previously outlined, the cause of this difference is a result of a significant energy deposition outside the sphere (about 26% of the β-particles energy is delivered outside the sphere, as reported in Figure 1). As a consequence,

a therapeutic activity of 1.21 MBq would actually correspond to an absorbed dose of about 90 Gy, well below the therapeutic endpoint.

As mentioned, the intratumoral injection of ^{90}Y is likely to pose specific treatment planning issues related to the possibility of treating very small lesions very selectively. In his seminal paper [29], Ariel reported the first interstitial use of ^{90}Y microspheres for the treatment of a rhabdomyosarcoma. A nodule measuring 1.5 cm in diameter was successfully treated with interstitial injection of 185 MBq of microspheres. In another study [30], ^{90}Y-glass microspheres were injected into predetermined tumor sites using an ultrasound-guided procedure. Tumor size ranged from 1.9 to 8.8 cm, with most lesions being less than 5 cm in diameter [30]. More recently, Ferrari and co-workers assessed the absorbed doses to small-volumes brain neocavities and surrounding tissues after local ^{90}Y-DOTATOC injection [5]. A recent review of the literature on the intratumoral treatment with radioactive beta-emitting microparticles can be found in [31].

The evidence from this study suggests that caution must be taken when planning the treatment of very small lesions with ^{90}Y, implementing the standard analytic approach. This is particularly true when intratumoral administration of ^{90}Y is performed, as this approach allows sub-centimeters tumors to be selectively treated. In such a scenario, the use of the analytic approach to calculate the therapeutic activity needed to achieve a given tumoricidal endpoint may result in important dose underestimations. On the other hand, Equation (7) can be usefully employed in the treatment planning of spherical lesions of small size (down to 0.5 cm diameter) providing dose estimates in close agreement with Monte Carlo calculations (maximum deviation below 0.5%).

Finally, two potential limitations need to be considered. The first is that in the present study tumor masses were modelled as perfect spheres. The extent to which it is possible to extend the present results to irregular spheres (e.g., oblate spheroids) should be further investigated. Another limitation is that in this study we considered a uniform distribution of the radionuclide into the spheres. As a consequence, the findings might not be representative of situations where the radionuclide is not homogeneously distributed in the tumor region.

5. Conclusions

In this paper the absorbed dose in small lesions was assessed using Monte Carlo calculations in a scenario of percutaneous ablation using ^{90}Y microspheres embedded into a sealant matrix (BAT-90). Furthermore, an analytical formula derived from MC calculations that incorporates the absorbed fractions for ^{90}Y is proposed. In a scenario of intratumoral injection of microspheres, the proposed equation can be usefully employed in the treatment planning of spherical lesions of small size (down to 0.5 cm diameter) providing dose estimates in close agreement with Monte Carlo calculations (maximum deviation below 0.5%).

Author Contributions: Conceptualization, A.A., M.R., M.D., A.S., G.P.; methodology, A.A., M.D., R.C.; simulations, M.D., A.S., L.C.; formal analysis, M.D., A.S., E.M.; investigation, A.A., M.C., G.P.; writing—original draft preparation, M.D., A.A.; writing—review and editing, all authors; visualization, all authors; supervision, A.A.; project administration, A.A., M.R.; funding acquisition, A.A. All authors have read and agreed to the published version of the manuscript.

Funding: This research was funded in part by BetaGlue Technologies SpA and the APC was funded by Istituto Scientifico Romagnolo per lo Studio e la Cura dei Tumori (IRST) IRCCS, Meldola, Italy.

Conflicts of Interest: A.A is CEO of BetaGlue Technologies SpA, M.R. is head of operations & quality of BetaGlue Technologies SpA. The other authors declare that they have no competing interests.

References

1. Villanueva, A. Hepatocellular Carcinoma. *N. Engl. J. Med.* **2019**, *380*, 1450–1462. [CrossRef] [PubMed]
2. Hsieh, T.; Wu, Y.; Sun, S.; Yen, K.; Kao, C. Treating Hepatocellular Carcinoma with 90Y-Bearing Microspheres: A Review. *BioMedicine* **2016**, *6*, 19. [CrossRef] [PubMed]

3. Wang, E.; Stein, J.; Bellavia, R.; Broadwell, S. Treatment Options for Unresectable HCC with a Focus on SIRT with Yttrium-90 Resin Microspheres. *Int. J. Clin. Pract.* **2017**, *71*, e12972. [CrossRef] [PubMed]
4. Salem, R.; Hunter, R. Yttrium-90 Microspheres for The Treatment of Hepatocellular Carcinoma: A Review. *Int. J. Radiat. Oncol. Biol. Phys.* **2006**, *66*, S83–S88. [CrossRef] [PubMed]
5. Ferrari, M.; Cremonesi, M.; Bartolomei, M.; Bodei, L.; Chinol, M.; Fiorenza, M.; Tosi, G.; Paganelli, G. Dosimetric model for locoregional treatments of brain tumors with ^{90}Y-conjugates: Clinical application with ^{90}Y-DOTATOC. *J. Nucl. Med.* **2006**, *47*, 105–112. [PubMed]
6. Fabbri, C.; Mattone, V.; Casi, M.; De Lauro, F.; Agostini, M.; Bartolini, N.; D'arienzo, M.; Marchi, G.; Bartolomei, M.; Sarti, G. Quantitative evaluation on [90Y] DOTATOC PET and SPECT imaging by phantom acquisitions and clinical applications in locoregional and systemic treatments. *Q. J. Nucl. Med. Mol. Imaging* **2012**, *56*, 522–528. [CrossRef] [PubMed]
7. Fabbri, C.; Mattone, V.; Sarti, G.; Casi, M.; De Lauro, F.; Agostini, M.; Bartolini, N.; Bartolomei, M. ^{90}Y-based PET and SPECT/CT imaging in locoregional brain treatment for high-grade gliomas: Retrospective fusion with MRI. *Eur. J. Nucl. Med. Mol. Imaging* **2012**, *39*, 1822–1823. [PubMed]
8. Beta Glue – A Loco-Regional Radio-Therapy Platform for Tumors. Available online: https://www.betaglue.com/ (accessed on 1 May 2019). [CrossRef] [PubMed]
9. Arazi, L.; Cooks, T.; Schmidt, M.; Keisari, Y.; Kelson, I. Treatment of solid tumors by interstitial release of recoiling short-lived alpha emitters. *Phys. Med. Biol.* **2007**, *52*, 5025–5042. [CrossRef] [PubMed]
10. Bult, W.; Kroeze, S.; Elschot, M.; Seevinck, P.; Beekman, F.; de Jong, H.; Uges, D.; Kosterink, J.; Luijten, P.; Hennink, W.; et al. Intratumoral Administration of Holmium-166 Acetylacetonate Microspheres: Antitumor Efficacy and Feasibility of Multimodality Imaging in Renal Cancer. *PLoS ONE* **2013**, *8*, e52178.
11. Siegel, J.A.; Stabin, M.G. Absorbed fractions for electrons and beta particles in spheres of various sizes. *J. Nucl. Med.* **1994**, *35*, 152–156.
12. Bardies, M.; Chatal, J. Absorbed doses for internal radiotherapy from 22 beta-emitting radionuclides: Beta dosimetry of small spheres. *Phys. Med. Biol.* **1994**, *39*, 961–981 [CrossRef]
13. Stabin, M.G.; Konijnenberg, M.W. Re-evaluation of absorbed fractions for photons and electrons in spheres of various sizes. *J. Nucl. Med.* **2000**, *41*, 149–160. [CrossRef]
14. Amato, E.; Lizio, D.; Baldari, S. Absorbed fractions for photons in ellipsoidal volumes. *Phys. Med. Biol.* **2009**, *56*, 357–365 [CrossRef]
15. Chao, H.; Torchiana, D. BioGlue: Albumin/Glutaraldehyde Sealant in Cardiac Surgery. *J. Card. Surg.* **2003**, *18*, 500–503
16. Bé, M.-M.; Chisté, V.; Dulieu, C.; Browne, E.; Baglin, C.; Chechev, V.; Kuzmenko, N.; Helmer, R.; Kondev, F.; MacMahon, D.; et al. Table of Radionuclides. Monographie BIPM-5, 2006; 3 Bureau International des Poids et Mesures, Pavillon de Breteuil, F-92310 Sèvres, France. Available online: http://www.bipm.org/utils/common/pdf/monographieRI/Monographie_BIPM-5_Tables_Vol3.pdf (acessed on 1 May 2019).
17. McKinney, J.; Pasciak, A.; Bradley, Y. *Handbook of Radioembolization*, 1st ed.; CRC Press-Taylor &Francis Group: Boca Raton, FL, USA, 2017.
18. Dezarn, W.; Cessna, J.; DeWerd, L.; Feng, W.; Gates, V.; Halama, J.; Kennedy, A.; Nag, S.; Sarfaraz, M.; Sehgal, V.; et al. Recommendations of the American Association of Physicists in Medicine on dosimetry, imaging, and quality assurance procedures for ^{90}Y microsphere brachytherapy in the treatment of hepatic malignancies. *Med. Phys.* **2011**, *38*, 4824–4845. [CrossRef]
19. Dieudonné, A.; Hobbs, R.; Sanchez-Garcia, M.; Lebtahi, R. Absorbed-dose calculation for treatment of liver neoplasms with ^{90}Y-microspheres. *Clin. Transl. Imaging* **2016**, *4*, 273–282. [CrossRef]
20. Ho, S.; Lau, W.; Leung, T.; Chan, M.; Ngar, Y.; Johnson, P.; Li, A. Partition model for estimating radiation doses from yttrium-90 microspheres in treating hepatic tumours. *Eur. J. Nucl. Med.* **1996**, *23*, 947–952. [PubMed]
21. Ho, S.; Lau, W.; Leung, T.; Chan, M.; Johnson, P.; Li, A. Clinical evaluation of the partition model for estimating radiation doses from yttrium-90 microspheres in the treatment of hepatic cancer. *Eur. J. Nucl. Med.* **1997**, *24*, 293–298. [CrossRef] [PubMed]
22. Gulec, S.A.; Mesoloras, G.; Stabin, M. Dosimetric techniques in ^{90}Y-microsphere therapy of liver cancer: The MIRD equations for dose calculations. *J. Nucl. Med.* **2006**, *47*, 1209–1211. [CrossRef] [PubMed]
23. Briesmeister, J.F. *MCNP-A General Monte Carlo N-Particle Transport Code Version 4C*; Los Alamos National Laboratory: Los Alamos, NM, USA, 2000. [CrossRef]

24. Storm, L.; Israel, H. Photon Cross Sections From 1 Kev To 100 Mev For Elements Z = 1 To Z = 100. *At. Data Nucl. Data Tables* **1970**, *7*, 565–681. [PubMed]
25. Hubbell, J.; Veigele, W.; Briggs, E.; Brown, R.; Cromer, D.; Howerton, R. Atomic Form Factors, Incoherent Scattering Functions, And Photon Scattering Cross Sections. *J. Phys. Chem. Ref. Data* **1975**, *4*, 471–538. [CrossRef] [PubMed]
26. Stabin, M.G.; Sparks, R.B.; Crowe, E. OLINDA/EXM: The second-generation personal computer software for internal dose assessment in nuclear medicine. *J. Nucl. Med.* **2005**, *46*, 1023–1027.
27. Kennedy, A.; Nutting, C.; Coldwell, D.; Gaiser, J.; Drachenberg, C. Pathologic response and microdosimetry of 90Y microspheres in man: Review of four explanted whole livers. *Int. J. Radiat. Oncol. Biol. Phys.* **2004**, *60*, 1552–1563.
28. Strigari, L.; Sciuto, R.; Rea, S.; Carpanese, L.; Pizzi, G.; Soriani, A.; Iaccarino, G.; Benassi, M.; Ettorre, G.; Maini, C. Efficacy and toxicity related to treatment of hepatocellular carcinoma with ^{90}Y-SIR spheres: Radiobiologic considerations. *J. Nucl. Med.* **2010**, *51*, 1377–1385.
29. Ariel, I. Cure of an embryonal rhabdomyosarcoma of the nose of an infant by interstitial 90Yttrium microspheres: A case report. *Int. J. Nucl. Med. Biol.* **1978**, *5*, 37–41.
30. Tian, J.H.; Xu, B.X.; Zhang, J.M.; Dong, B.W.; Liang, P.; Wang, X.D. Ultrasound-guided internal radiotherapy using yttrium-90-glass microspheres for liver malignancies. *J. Nucl. Med.* **1996**, *37*, 958–963.
31. Bakker, R.; Lam, M.; van Nimwegen, S.; Rosenberg, A.; van Es, R.; Nijsen, J. Intratumoral treatment with radioactive beta-emitting microparticles: A systematic review. *J. Radiat. Oncol.* **2017**, *6*, 323–341.

applied sciences

MDPI

Article

An Attempt to Reduce the Background Free Radicals in Fingernails for Monitoring Accidental Hand Exposure of Medical Workers

Chryzel Angelica B. Gonzales [1], Jolan E. Taño [1,2] and Hiroshi Yasuda [1,*]

[1] Research Institute for Radiation Biology and Medicine, Hiroshima University, Hiroshima 734-8553, Japan; chryzelgonzales@hiroshima-u.ac.jp (C.A.B.G.); jolantano@hiroshima-u.ac.jp (J.E.T.)
[2] Graduate School of Biomedical and Health Sciences, Hiroshima University, Hiroshima 739-8511, Japan
* Correspondence: hyasuda@hiroshima-u.ac.jp; Tel.: +81-82-257-5872

Received: 25 November 2020; Accepted: 14 December 2020; Published: 15 December 2020

Featured Application: The technique presented here could be effectively applied for retrospective assessment of the accidental radiation hand exposure of medical workers.

Abstract: While it is recognized that some medical workers could receive significantly higher radiation doses to their hands than the routinely monitored personal doses, accurate retrospective dosimetry of their hand exposure is still challenging. To solve this issue, a combination of electron spin resonance (ESR) measurement and fingernails is worth to be investigated. However, the application of fingernail ESR dosimetry requires establishing an effective protocol to eliminate the background signal (BKG) which changes due to mechanical stress and other unclear factors, so that the radiation doses would be precisely evaluated from the radiation-induced signals (RIS) only. Thus, the authors investigated possible applications of antioxidants to remove or reduce the BKG in fingernails. In the present study, the effectiveness of chemical treatment using the dithiothreitol (DTT) reducing reagent was examined in irradiated and unirradiated fingernails. Chemically and non-chemically treated fingernails were subsequently exposed to 20 Gy of ^{137}Cs γ-rays and the time changes of the BKG and RIS were confirmed in two different storage conditions: vacuum chamber and freezer. The results show that the non-chemically treated fingernails displayed significant intra-individual variations in the peak-to-peak intensities of both BKG and RIS. RIS from chemically and non-chemically treated samples showed correlations after freezer storage; signals were more stable than the samples stored in the vacuum chamber. Moreover, while the BKG of non-chemically treated samples demonstrated higher levels than those chemically treated, the intra-individual variations were further reduced by the DTT treatment. Our results imply that the use of an antioxidant for hand washing of medical workers prior to starting their work could be effective in reducing the pre-existing free radicals in their fingernails. This also suggests a practical application of hand exposure monitoring using fingernails as a part of radiological emergency preparedness in occupations where radiation or radionuclides are used. Research for finding safer and easier-to-handle antioxidants is to be focused on in future studies.

Keywords: medical worker; radiological accident; emergency response; retrospective dosimetry; ESR; EPR; fingernails; antioxidant

1. Introduction

It is recognized that some medical workers involved in interventional radiology/cardiology, diagnostic/therapeutic nuclear medicine, positron emission tomography, brachytherapy, among others, could receive notably high radiation doses to their extremities. Their hand doses tend to be higher than the personal doses routinely measured with commonly used personal dosimeters; sometimes they may

exceed the skin dose limit (500 mSv per year) even though the values from their personal dosimeters are insignificant [1–3]. In addition, it is still difficult to properly and routinely monitor local hand exposure as dose distributions change to a large extent, depending on the type of handling radiation or radionuclide, and the geometric situation between the hands and radiation source. Recent studies also reported that their fingertip doses could be significantly higher than the average hand dose measured with a ring-type dosimeter [3,4]. We thus need to develop a novel and practical measure to solve this issue.

For this aim, a combination of electron spin resonance (ESR) measurement and fingernails is worth to be investigated. The application of "fingernail ESR dosimetry" has a good potential for quantifying the number of radiation-induced free radicals that could stay long after exposure. For many decades, ESR (or electron paramagnetic resonance, EPR) of biomaterials, such as tooth enamel and bone, has been used successfully for retrospective dosimetry in atomic bomb survivors, radiological accident victims, residents around nuclear testing sites, and radiotherapy patients [5–20]. However, in the case of emergency dosimetry, which requires an urgent assessment of absorbed doses to affected individuals, the number of potential applications using ESR is relatively small and the present guidelines are yet to be developed. Indeed, in both short-term and long-term aftereffects of any radiation accident, a systematic protocol for feasible dose assessment, using the available biomaterials is an utmost need. Additionally, in the search for developing potential tools for retrospective dosimetry, most of the attention has been paid to alternative materials that are carried close to the human body.

Fingernails are no doubt one of the most promising biomaterials in this context. Its potential use as a dosimetry tool was first suggested in the late 1980s [21]. Fingernails are mainly composed of α-keratin, a protein which consists of three long right-handed α-helical peptide chains twisted into a left-handed coil strengthened by disulfide bridges (S-S) formed from adjacent cysteine groups [22]. Its exposure to ionizing radiation could generate stable free radicals that are the main sources of ESR signals. Subsequent studies on the ESR signals from fingernails revealed that the spectra are composed of three main components: radiation-induced signal (RIS), which is assumed to be correlated with absorbed dose; mechanic-induced signal (MIS), which is attributable to α-radicals formed along the shear edge of the nail through the breakage of S-S bonds caused by cutting/clipping and other mechanical stresses [21–23]; pre-existing native signal (PES), whose origin remains unknown [24]. Despite such complexities in the signal processing, the easier sampling of fingernails compared to tooth enamel and bone has attracted some researchers who paved the way for notable developments in fingernail ESR dosimetry techniques in the 21st century [25–40]. Comprehensive reviews about the free radical mechanism and characteristics of fingernail ESR signals can also be found in the literature [41–43].

In those studies, many authors noted that one of the most problematic issues regarding fingernail ESR dosimetry is how to identify and quantify the true component of RIS alone, separated from other background signals (BKG). As demonstrated in some previous studies [36,44–46], the presence of MIS, PES, and other potential confounding factors, such as ultraviolet light and high temperature, contributes to the difficulty in the analyses of fingernail ESR signals. Not surprisingly, numerous attempts have been carried out to circumvent BKG, while RIS remains intact. For example, it was found that water treatment worked effectively in erasing the BKG (e.g., [25,29,30,35,38,47–49]). The application of an antioxidant to freshly cut fingernails was also investigated; it was reported that the 0.1 M dithiothreitol (DTT) reducing reagent with 20 min treatment time reduced both MIS and BKG [26]. It is still unclear, however, if the DTT treatment would be effective for fingernail samples that were stored for a long time.

Long storage in an ambient, humid conditions could cause unstable RIS, as well as changing BKG [29,43]. The difficulty in keeping the stability of RIS and BKG has led some authors to investigate other variants, such as storage in the freezer at low (sub-zero) temperature [31], in a vacuum desiccator with 0% air humidity [35,36,38,49], or in olive oil with low water content [39]. Since research on such

storage mediums started very recently, further comparative studies are desirable to clarify the efficacy for improving the signal stability of RIS and BKG in conjunction with possible chemical treatments.

The present study pursues this direction and tries to contribute to the development of a practical protocol of fingernail ESR dosimetry for routine monitoring of the extremity exposures of medical workers handling radiation sources. Here we investigate the effects of chemical treatment using DTT on the changes of the ESR spectra in irradiated and unirradiated fingernails after a long storage time. The efficacy of DTT in the reduction in intra-individual variations of BKG is also examined through comparative experiments using chemically and non-chemically treated samples stored in two different mediums (i.e., vacuum chamber and freezer).

2. Materials and Methods

2.1. Sample Preparation

Fingernail samples were obtained from one adult volunteer during regular hygienic practice at different collection times (usually every two weeks). In every collection, the samples were immediately placed inside a small tightly sealed plastic bag and stored in darkness inside a vacuum chamber (VE-ALL 1-8-989-01, AS ONE, Osaka, Japan) with silica gel (FUJIFILM Wako Pure Chemical Corporation, Osaka, Japan) at room temperature. A total of 16 sample collections were used in the experiments described below. All the experiments in the present study (except during irradiation) were performed under subdued red lighting conditions to avoid ambient light exposure.

2.2. Experimental Procedures

Two experimental setups were used in the present study, as illustrated in Figure 1. One "with chemical treatment" process involving the application of DTT reducing reagent and the other "without chemical treatment" process without the DTT reducing agent. It should be noted that this study is only limited to fingernail samples collected from one individual to investigate the intra-individual variations along with the two experimental procedures; no additional experiments were performed for the examination of inter-individual variations.

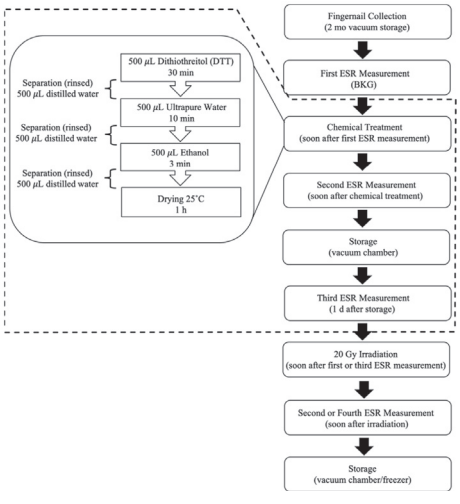

Figure 1. Flowchart of the stages of fingernail sample preparation and electron spin resonance (ESR) measurements. Two experimental setups were employed—one "with chemical treatment" process including application of dithiothreitol (DTT) and the other "without chemical treatment" process without DTT. The part indicated with a dashed line in the above flow chart was omitted in the "without chemical treatment" process.

2.2.1. With Chemical Treatment

This experiment used eight sample collections with two different storage conditions: four for vacuum chamber and four for freezer. A more detailed description of the storage conditions is given in Section 2.4. In each collection, the fingernails from the right/left hands of the volunteer (~90 mg) were pooled and divided into four portions. Each portion contained 5–6 aliquots, totaling 20 mg. It must be noted that the first measurement of BKG from all the samples was performed before the chemical treatment process. Three portions were treated for 30 min with 500 µL aqueous solutions of 0.1 M DTT reducing reagent (FUJIFILM Wako Pure Chemical Corporation, Osaka, Japan), while the remaining portion was not treated or irradiated and kept as the control. In total, each storage condition consisted of 12 portions of treated samples and 4 portions of control samples. Following the treatment, all the samples were rinsed with 500 µL ultrapure water separated through microfiltration, treated with 500 µL of ethanol (FUJIFILM Wako Pure Chemical Corporation, Osaka, Japan) for 3 min and rinsed again with 500 µL ultrapure water separated through microfiltration. The samples were dried inside the dry heat sterilizer (MOV-112 S-PJ, PHC Holdings Co., Ltd., Tokyo, Japan) at 25 °C for 1 h (hereafter we will call them as chemically treated samples.) After drying the chemically treated samples, the second ESR measurement was immediately conducted to examine the efficacy of chemical treatment using DTT to the ESR spectra of fingernails. Additionally, soon after the second ESR measurement, all the samples were stored inside the vacuum chamber (12 portions of chemically treated, 4 portions of control) for 24 h and the third ESR measurement was performed the next day. Shortly after the third ESR measurement, three portions from each collection of the chemically treated samples were irradiated to 20 Gy of ^{137}Cs γ-rays. Further technical details of the irradiation are provided in the next section.

2.2.2. Without Chemical Treatment

Similar to the experiment mentioned above, eight sample collections with two different storage conditions (i.e., 4 sample collections for each storage condition) were also made. In each collection, the fingernails from the right/left hands of the volunteer (~90 mg) were also pooled and divided into four portions (20 mg each). The samples used in this experiment were not given any chemical treatment (hereafter we will call them as non-chemically treated samples). Three portions from each collection of the non-chemically treated samples were irradiated to 20 Gy of ^{137}Cs γ-rays while the other one was left unirradiated and kept as the control. The first measurement of BKG from all the samples was performed before the irradiation process. In total, each storage condition used in this experiment consisted of 12 portions of non-chemically treated samples and 4 portions of control samples. A summary of the experimental work on non-chemically treated samples is also shown in Figure 1. It is important to note that the storage conditions and irradiations utilized in non-chemically treated samples were also similar to the chemically treated samples, as described in the following Sections 2.3 and 2.4.

2.3. Irradiation

Irradiation of the samples was administered using a γ-ray irradiator (Gammacell40 Exactor Low Dose Rate Research Irradiator, Best Theratronics Ltd., Ottawa, Canada) with a dose rate equal to 0.80 Gy min^{-1}. It has dual ^{137}Cs γ-ray sources with a total radiation activity of 178 TBq. All the samples were irradiated to a dose of 20 Gy with consideration of the clinical dose level in radiotherapy (tens of Gy). Though we recognized that this dose level was higher than the reported skin doses (0.5 to 2 Gy) of the hands in recent radiological incidents that occurred in medical facilities (e.g., [50–52]), we envisaged that the local doses to fingertips could be much higher than the average skin dose in such an incident. Thus, we have intended to assess the three-dimensional dose distribution of a hand based on measured fingernail doses.

Three portions of the samples from each collection were positioned at the center of the container (φ 260 × 100 mm) perpendicular to the radiation sources, as shown in Figure 2. The dose uniformity

inside the whole area of the sample container was ±7%. During irradiation, the room lighting inside the facility was turned off to limit the ambient light exposure of the samples. Following exposure of the samples to radiation, ESR measurements were immediately performed.

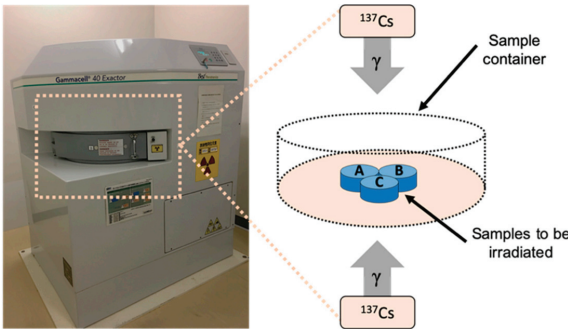

Figure 2. Experimental setup for the irradiation of the fingernail samples with the γ-ray irradiator (**left**) and the geometry of irradiated samples placed in between two ^{137}Cs γ-ray sources (**right**).

2.4. Storage Conditions

In experiments with chemically and non-chemically treated samples, two different storage conditions (vacuum chamber and freezer) were used. The samples were initially placed inside a stainless-steel vacuum fresh box (E-305, Asahi Light Metal Industry Co. Ltd., Osaka, Japan) with silica gel (192-18285, FUJIFILM Wako Pure Chemical Corporation, Osaka, Japan) before storage in the vacuum chamber or freezer. The humidity logger (LR5001, Hioki, Nagano, Japan) with a built-in sensor (LR9504, Hioki, Nagano, Japan) and a communication adapter (LR5091, Hioki, Nagano, Japan) were used to record the air humidity inside the two storage conditions. The recorded air humidity and temperature inside the vacuum chamber were 2% and 20°C, respectively. In the case of freezer storage, the recorded temperature was −20 °C, and approximately a 3% air humidity level was achieved with the use of silica gel.

2.5. Instrumental Settings

ESR measurements were conducted at room temperature on an X-band (~9.4 GHz) spectrometer JES-FA 100 (JEOL Inc., Chiba, Japan) with an ES-UCX2 standard cavity using a 5 mm sample tube. Spectra acquisition parameters were as follows: 1 mW microwave power; 10 mT sweep width; 30 s sweep time; 0.5 mT modulation width; time constant 0.03 s; number of scans 10. During spectra acquisition, the MgO: Mn^{2+} internal reference sample was used for calibration. The ESR signal intensities were measured as the peak-to-peak amplitude (App) of the main "singlet" of the ESR spectra (i.e., BKG-singlet, RIS-singlet), as described by Sholom and McKeever [36]. The ESR spectra were adjusted in linear baseline correction within the analytical software of the spectrometer. The ESR spectra were recorded before and after the chemical treatment and exposure to radiation. ESR measurements were also repeated at different times to test the stability of the signal after radiation exposure.

3. Results and Discussion

Figure 3 shows the evolution of the ESR spectra obtained from (a) non-chemically and (b) chemically treated fingernail samples before and after irradiation with 20 Gy of ^{137}Cs γ-rays following storage in the vacuum chamber. All spectra were recorded soon after the corresponding chemical treatment or irradiation of the samples and continuously monitored for up to 7 days. Each spectrum is an average of 12 spectra from 4 sample collections (3 portions of chemically/non-chemically treated samples per collection). Solid lines correspond to the ESR signals measured after exposure to radiation,

while dotted lines are the background signal before irradiation (referred to as "NT−BKG". Dashed lines show the background signal after chemical treatment of the samples (referred to as "T−BKG").

As can be seen, the ESR signals of both non-chemically and chemically treated samples increased during the first day of storage in the vacuum chamber and continuously increased up to 7 days after γ-ray irradiation. This behavior was very similar to most of the irradiated vacuum-stored samples with water treatment [35,36,38]. It seemed, notwithstanding, that the increase rate in chemically treated samples (30% signal increase over the first 24 h after irradiation) was slower than those in the non-chemically treated samples (39%). Moreover, it was found that the non-zero, quasi-stable background signal substantially reduced its ESR intensity when subjected to DTT, compared to the non-chemically treated background signal (NT−BKG) demonstrated in Figure 3a. It should also be noted that the background signal with chemical treatment (T−BKG) was quite stable: there was no signal growth in its ESR intensity for 1 day after storage in the vacuum chamber at room temperature.

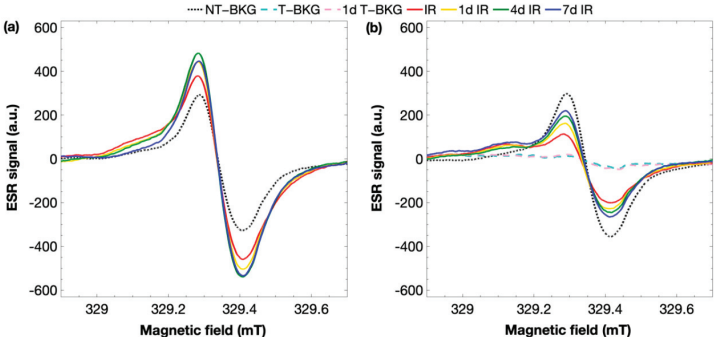

Figure 3. Evolution of the ESR spectra recorded at different times in (**a**) non-chemically and (**b**) chemically treated fingernail samples exposed to 20 Gy of ^{137}Cs γ-rays following storage in the vacuum chamber (2% air humidity level, 20 °C temperature). The notations NT−BKG and T−BKG correspond to the background signal before irradiation for non-chemically treated samples and after chemical treatment for those chemically treated, respectively. IR represents γ-ray irradiation.

Comparative plots on the evolution of ESR spectra observed in the fingernail samples exposed to 20 Gy of ^{137}Cs γ-rays, following storage in the freezer, are shown in Figure 4. Each of the spectra shown here is the mean of 12 spectra obtained from four sample collections (three portions of chemically/non-chemically treated samples per collection). It is worth mentioning that the chemically treated samples presented in Figure 4b were also kept inside the vacuum chamber for 24 h in between chemical treatment and irradiation. All notations used in Figure 4 are the same as those described in Figure 3.

As seen in this figure, the freezer storage resulted in better stability of ESR signals for both chemically and non-chemically treated samples following γ-ray irradiation, in contrast with the vacuum-stored samples. The recorded ESR signals in freezer-stored non-chemically treated samples increased by about 15% after 1 day of exposure and further increased up to 25% after a week (Figure 4a). As with chemically treated samples, there was only about a 9% increase in the ESR intensity after 1 day and 17% after 7 days (Figure 4b). Furthermore, the use of DTT for chemical treatment prior to irradiation was found to have significantly reduced the intensity of the ESR spectra in irradiated fingernail samples (i.e., RIS). These observations are in accordance with previously reported work from Romanyukha et al. [26]. It was confirmed that the background signal from unirradiated freezer-stored samples with chemical treatment (T−BKG) also showed no significant increase within 24 h of storage time inside the vacuum chamber (Figure 4b), as seen with the vacuum-stored samples (Figure 3b).

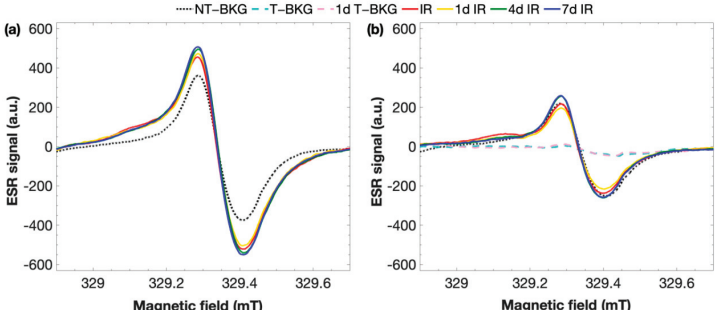

Figure 4. Evolution of the ESR spectra recorded at different times in (**a**) non-chemically and (**b**) chemically treated samples exposed to 20 Gy of ^{137}Cs γ-rays following storage in the freezer. The NT−BKG, T−BKG, and IR have the same notations as in Figure 3.

Results shown in Figure 5 indicate the efficacy of DTT on the stability of RIS in chemically and non-chemically treated samples at two different storage conditions (vacuum chamber and freezer). ESR signals were measured as the peak-to-peak intensity in the magnetic field range from 328.9 mT to 329.7 mT. All experimental data points were normalized to the first ESR signal of the samples measured soon after exposure to 20 Gy (this corresponds to the fourth and second ESR measurement for chemically and non-chemically treated samples, respectively, as illustrated in Figure 1. Measurements of the RIS were also taken up to 7 days in irradiated fingernail samples collected from the same individual. The dotted lines with unfilled and filled box markers correspond to non-chemically treated samples stored in the vacuum chamber and freezer, respectively. Solid lines with unfilled and filled circle markers represent chemically treated samples stored in the vacuum chamber and freezer, respectively.

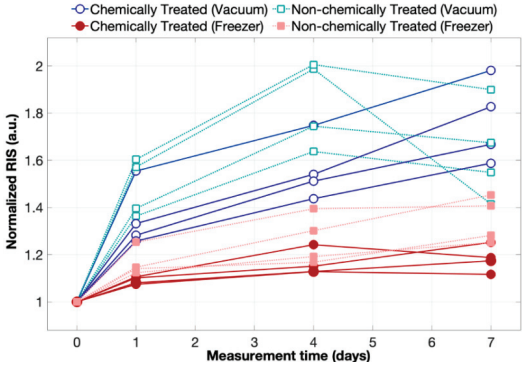

Figure 5. ESR signal peak-to-peak amplitude (App) changes with time in chemically and non-chemically treated samples stored at two different conditions (vacuum chamber and freezer). All experimental points from each experiment were normalized with regard to the first measurement data soon after the exposure to 20 Gy of ^{137}Cs γ-rays.

As shown in Figure 5, it can be argued that the effect of DTT is more pronounced in fingernail samples stored in the freezer than those in the vacuum chamber. It may be observed that the signal intensities in chemically treated samples stored in the freezer increased after 24 h but remained almost unchanged for up to 7 days after irradiation, while the corresponding signals in the vacuum-stored chemically treated samples continued to increase for the same measurement times. Another interesting observation is that the behavior of the signals obtained in non-chemically treated samples correlated well with the measured signals in chemically treated samples for both storage conditions and

hence the freezer-stored samples (with 3% air humidity at −20 °C temperature) were deemed to be significantly more stable than the vacuum-stored samples (with 2% air humidity at 20 °C temperature). This observation broadly supports the finding of Reyes et al. [31], that persistent ESR signals can be achieved if samples are kept at low (sub-zero) temperature, although the air humidity level was not mentioned in their experimental work.

Next, a comparison was made for background signals measured from non-chemically treated unirradiated fingernail (control) samples stored in the vacuum chamber and freezer, as presented in Figure 6. ESR signals were measured as the peak-to-peak amplitude (App) of the main background-singlet of the spectra from the (a) vacuum-stored and (b) freezer-stored samples. Each storage medium in this figure consisted of eight portions of non-chemically treated unirradiated samples and measured in the same way as the irradiated samples, as described in Figure 5. It may be observed that the median intensity of the background signals in both storage conditions were all at the same level, but the data sets between the two mediums showed a very different distribution view. One can also notice from the plots in Figure 6 that the background signals obtained from the freezer-stored samples span much the same range of values and were more variable than in the vacuum-stored samples. Moreover, some individual outlying data points can be seen in the vacuum-stored samples which may be caused by intra-individual variations within the group of samples. Nevertheless, the stability of the background signals observed in storage conditions with either low humidity at room temperature or low humidity at sub-zero temperature can be regarded as good overall, and conclusions regarding the effect of low or lack of oxygen to the signal stability were equivocal and formed the needs of further scrutiny.

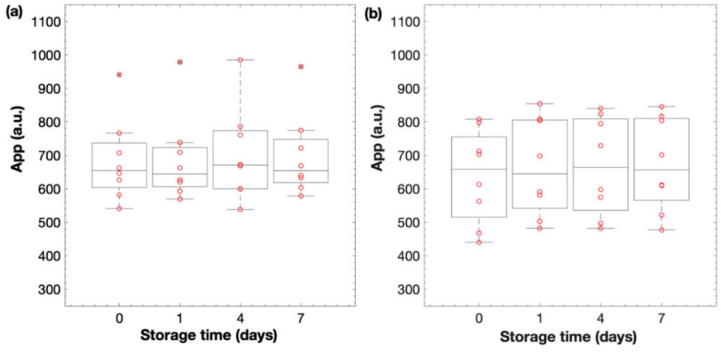

Figure 6. Distribution of the ESR signal peak-to-peak amplitude (App) from non-chemically treated unirradiated fingernail samples stored inside the (**a**) vacuum chamber with 2% air humidity at 20 °C and (**b**) freezer with 3% air humidity at −20 °C recorded at different times.

Figure 7 compares the intra-individual variations of the ESR signal peak-to-peak amplitude (App) measured before and after treatment with DTT in unirradiated fingernail samples stored in the (a) vacuum chamber and (b) freezer. Each storage consisted of four sample collections and the time interval between sample collections was 2 weeks. Each experimental data point shown in this plot is an average of spectral measurements on three portions of unirradiated fingernail samples obtained from a single donor, and the reported errors are the standard deviation. The background signals of the samples were measured as the peak-to-peak intensity from the main singlet of the ESR spectra. Measurements were taken prior to chemical treatment, soon after the corresponding drying conditions in the chemical treatment process, and at 1, 2, 3, and 7 days after chemical treatment.

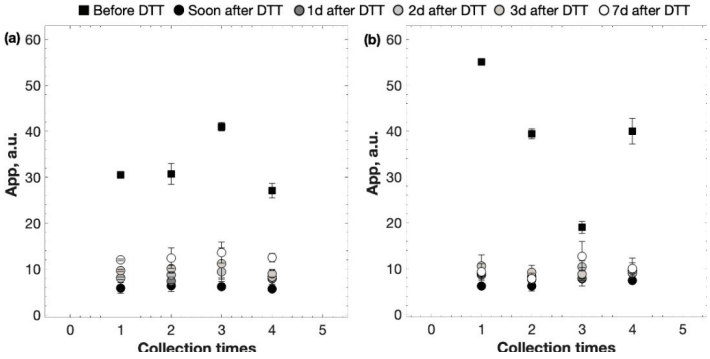

Figure 7. Changes in the background ESR signal (peak-to-peak amplitude, App) in unirradiated fingernail samples stored in the (**a**) vacuum chamber and (**b**) freezer measured before and after (soon, 1, 2, 3, and 7 days) the DTT treatment.

As seen in this figure, there was a significant intra-individual variation in the recorded initial background signals between the samples from the same individual, whereupon no pre-treatment was applied. After application of DTT treatment, however, the background signals were observed to be broadly consistent with each other, giving rise to the opportunity to correct for such uncertainties in the intra-individual variations within the same group of samples. Furthermore, the recorded App of the native background signals have been reduced and are quite stable over the 24 h time delay between chemical treatment and storage of the samples: no substantial gain in the peak-to-peak intensity was encountered in both storage conditions. This finding is interesting and could be useful as many of the previous studies advanced differing views that pre-existing native background signal tends to grow after drying in ambient air conditions and thus cannot be entirely removed in the spectra [42]. Further investigations into this notable observation should be made with applications of other antioxidant materials that could have similar effects.

4. Conclusions

In the present work, we confirmed that the BKG (non-RIS) of fingernails can be significantly reduced by applying the DTT reducing reagent. After the DTT treatment, the fingernail samples provided good signal stability for both background and RIS signals with less intra-individual variations. Additionally, we demonstrated that the freezer storage would be more effective to maintain the stability of RIS after γ-ray irradiation than vacuum storage; it is thus desirable that collected fingernail samples be stored below the freezing point for performing more accurate dosimetry.

These findings are preferably to be applied in the monitoring of hand exposure of medical workers. More concretely, workers who might face high hand dose exposure from radiation sources are proposed to take the following steps to carry out precise dose assessments: (1) dip or wipe one's fingers with a reducing reagent before the relevant work; (2) get a small portion of the fingernail (e.g., from the little finger) as a control sample and store it in a freezer (<0 °C); (3) perform the work; (4) cut the fingernails soon after completing the work in the same way as with the control sample; (5) store the collected samples in the freezer; (6) measure the ESR signals of all the samples, including the control at the same time; (7) evaluate the finger dose by subtracting the MIS measured with the control sample from the ESR signal of the respective sample; (8) assess the three-dimensional dose distribution of the hand.

While the efficacy of DTT for chemical treatment was particularly good for BKG reduction and RIS stabilization in the fingernail ESR dosimetry, this procedure has some weaknesses. One is that the DTT treatment substantially reduced the peak-to-peak intensities of both BKG and RIS. This fact implies that the chemical treatment would reduce the capacity of trapping free radicals, which could induce an unfavorable saturation response at a lower dose level. Further, the samples used in this study were

obtained from the fingernails of only one individual and that possible inter-individual variations have not been identified. It must be critical for practical application of fingernail ESR dosimetry to verify that the findings of the current study can be universally applied through comprehensive analyses of the fingernail samples taken from different individuals. Another technical drawback is the toxicity of DTT, which allows only trained professionals to use hazardous chemicals. Considering these issues, we are currently focusing on research to find a better antioxidant material that is safer and easier to handle for any workers posing occupational risks of hand exposure from radiation sources.

Author Contributions: Conceptualization, H.Y. and C.A.B.G.; validation, C.A.B.G. and J.E.T.; investigation, C.A.B.G., H.Y. and J.E.T.; resources, H.Y.; data curation, C.A.B.G. and J.E.T.; writing—original draft preparation, C.A.B.G.; writing—review and editing, H.Y.; supervision, H.Y.; funding acquisition, H.Y. All authors have read and agreed to the published version of the manuscript.

Funding: This research was partially funded by JSPS KAKENHI Grant Number 18KK0147 and the Program of the Network-type joint Usage/Research Center for Radiation Disaster Medical Science funded by the Ministry of Education, Culture, Sports, Science, and Technology (MEXT) of Japan and Hiroshima University.

Acknowledgments: This study was approved by the Ethics Review Committee of Hiroshima University (Number E-1495).

Conflicts of Interest: The authors declare no conflict of interest.

References

1. Vanhavere, F.; Carinou, E.; Donadille, L.; Ginjaume, M.; Jankowski, J.; Rimpler, A.; Sans Merce, M. An overview on extremity dosimetry in medical applications. *Radiat. Prot. Dosim.* **2008**, *129*, 350–355. [CrossRef]
2. Zargan, S.; Ghafarian, P.; Shabestani Monfared, A.; Sharafi, A.A.; Bakhshayeshkaram, M.; Ay, M.R. Evaluation of radiation exposure to staff and environment dose from [18F]-FDG in PET/CT and cyclotron center using thermoluminescent dosimetry. *J. Biomed. Phys. Eng.* **2007**, *7*, 1–12.
3. Adlienea, D.; Gricieneb, B.; Skovorodko, K.; Laurikaitienea, J.; Puiso, J. Occupational radiation exposure of health professionals and cancer risk assessment for Lithuanian nuclear medicine workers. *Environ. Res.* **2020**, *183*, 109144. [CrossRef]
4. Parikh, J.R.; Geise, R.A.; Bluth, E.I.; Bender, C.E.; Sze, G.; Jones, A.K. Potential radiation-related effects on radiologists. *Amer. J. Roentgenol.* **2017**, *208*, 595–602. [CrossRef] [PubMed]
5. Ikeya, M.; Miyajima, J.; Okajima, S. ESR dosimetry for atomic bomb survivors using shell buttons and tooth enamel. *Jpn. J. Appl. Phys.* **1984**, *23*, 697–699. [CrossRef]
6. Ishii, H.; Ikeya, M.; Okano, M. ESR dosimetry of teeth of residents close to Chernobyl reactor accident. *J. Nucl. Sci. Technol.* **1990**, *27*, 1153–1155. [CrossRef]
7. Skvortzov, V.G.; Ivannikov, A.I.; Eichhoff, U. Assessment of individual accumulated irradiation doses using EPR spectroscopy of tooth enamel. *J. Mol. Struct.* **1995**, *347*, 321–329. [CrossRef]
8. Schauer, D.A.; Desrosiers, M.F.; Kuppusamy, P.; Zweier, J.L. Radiation dosimetry of an accidental overexposure using EPR spectrometry and imaging of human bone. *Appl. Radiat. Isot.* **1996**, *47*, 1345–1350. [CrossRef]
9. Chumak, V.; Sholom, S.; Pasalkaya, L. Application of high precision EPR dosimetry with teeth for reconstruction of doses to Chernobyl populations. *Radiat. Protect. Dosim.* **1999**, *84*, 515–520. [CrossRef]
10. Haskell, E.H.; Hayes, R.B.; Kenner, G.H.; Wieser, A.; Aragno, D.; Fattibene, P.; Onori, S. Achievable precision and accuracy in EPR dosimetry of tooth enamel. *Radiat. Prot. Dosim.* **1999**, *84*, 527–535. [CrossRef]
11. Ivannikov, A.I.; Gaillard-Lecanu, E.; Trompier, F.; Stepanenko, V.F.; Skvortsov, V.G.; Borysheva, N.B.; Tikunov, D.D.; Petin, D.V. Dose reconstruction by EPR spectroscopy of tooth enamel: Application to the population of Zaborie Village exposed to high radioactive contamination after the Chernobyl accident. *Health Phys.* **2004**, *86*, 121–134. [CrossRef] [PubMed]
12. Zhumadilov, K.; Ivannikov, A.; Apsalikov, K.; Zhumadilov, Z.; Toyoda, S.; Zharlyganova, D.; Tieliewuhan, E.; Endo, S.; Tanaka, K.; Miyazawa, C.; et al. Radiation dose estimation by tooth enamel EPR dosimetry for residents of Dolon and Bodene. *J. Radiat. Res.* **2006**, *47*, A47–A53. [CrossRef] [PubMed]
13. Hoshi, M.; Toyoda, S.; Ivannikov, A.; Zhumadilov, K.; Fukumura, A.; Apsalikov, K.; Zhumadilov, Z.; Bayankin, S.; Chumak, V.; Ciesielski, B.; et al. Interlaboratory comparison of tooth enamel dosimetry on Semipalatinsk region: Part 1, general view. *Radiat. Meas.* **2007**, *42*, 1005–1014. [CrossRef]

14. Ciesielski, B.; Karaszewska, A.; Penkowski, M.; Schultka, K.; Junczewska, M.; Nowak, R. Reconstruction of doses absorbed by radiotherapy patients by means of EPR dosimetry in tooth enamel. *Radiat. Meas.* **2007**, *42*, 1021–1024. [CrossRef]
15. Ciesielski, B. EPR biodosimetry—Fundamentals, applications and perspectives. *Curr. Top. Biophys.* **2010**, *33*, 7–8.
16. Fattibene, P.; Callens, F. EPR dosimetry with tooth enamel: A review. *Appl. Radiat. Isot.* **2010**, *68*, 2033–2116. [CrossRef]
17. Ivannikov, A.I.; Skvortsov, V.G.; Stepanenko, V.F.; Tsyb, A.F.; Khamidova, L.G.; Tikunov, D.D. Tooth enamel EPR dosimetry: Sources of errors and their correction. *Appl. Radiat. Isot.* **2010**, *52*, 1291–1296. [CrossRef]
18. Ciesielski, B.; Krefft, K.; Penkowski, M.; Kaminska, J.; Drogoszewska, B. Effects of water treatment and sample granularity on radiation sensitivity and stability of EPR signals in X-ray irradiated bone samples. *Radiat. Protect. Dosim.* **2014**, *159*, 141–148. [CrossRef]
19. He, X.; Gui, J.; Matthews, T.P.; Williams, B.B.; Swarts, S.G.; Grinberg, O.; Sidabras, J.; Wilcox, D.E.; Swartz, H.M. Advances towards using finger/toenail dosimetry to triage a large population after potential exposure to ionizing radiation. *Radiat. Meas.* **2011**, *46*, 882–887. [CrossRef]
20. Krefft, K.; Drogoszewska, B.; Kaminska, J.; Juniewicz, M.; Woakiewicz, G.; Jakacka, I.; Ciesielski, B. Application of EPR dosimetry in bone for ex vivo measurements of doses in radiotherapy patients. *Radiat. Protect. Dosim.* **2014**, *162*, 38–42. [CrossRef]
21. Dalgarno, B.G.; McClymont, J.D. Evaluation of ESR as a radiation accident dosimetry technique. *Appl. Radiat. Isot.* **1989**, *40*, 1013–1020. [CrossRef]
22. Chandra, H.; Symons, M.C. Sulphur radicals formed by cutting alpha-keratin. *Nature* **1987**, *328*, 833–834. [CrossRef] [PubMed]
23. Black, P.J.; Swarts, S.G. Ex vivo analysis of irradiated fingernails: Chemical yields and properties of radiation-induced and mechanically-induced radicals. *Health Phys.* **2010**, *98*, 301–308. [CrossRef]
24. Symons, M.C.; Chandra, H.; Wyatt, J.L. Electron paramagnetic resonance spectra of irradiated fingernails: A possible measure of accidental exposure. *Radiat. Protect. Dosim.* **1995**, *58*, 11–15.
25. Trompier, F.; Kornak, L.; Calas, C.; Romanyukha, A.; LeBlanc, B.; Mitchell, C.A.; Swartz, H.M.; Clairand, I. Protocol for emergency EPR dosimetry in fingernails. *Radiat. Meas.* **2007**, *42*, 1085–1088. [CrossRef] [PubMed]
26. Romanyukha, A.; Trompier, F.; LeBlanc, B.; Calas, C.; Clairand, I.; Mitchell, C.A.; Smirniotopoulos, J.G.; Swartz, H.M. EPR dosimetry in chemically treated fingernails. *Radiat. Meas.* **2007**, *42*, 1110–1113. [CrossRef] [PubMed]
27. Reyes, R.A.; Romanyukha, A.; Trompier, F.; Mitchell, C.A.; Clairand, I.; De, T.; Benevides, L.A.; Swartz, H.M. Electron paramagnetic resonance in human fingernails: The sponge model implication. *Radiat. Environ. Biophys.* **2008**, *47*, 515–526. [CrossRef]
28. Reyes, R.A.; Romanyukha, A.; Olsen, C.; Trompier, F.; Benevides, L.A. Electron para-magnetic resonance in irradiated fingernails: Variability of dose dependence and possibilities of initial dose assessment. *Radiat. Environ. Biophys.* **2009**, *48*, 295–310. [CrossRef]
29. Trompier, F.; Romanyukha, A.; Kornak, L.; Calas, C.; LeBlanc, B.; Mitchell, C.; Swartz, H.; Clairand, I. Electron paramagnetic resonance radiation dosimetry in fingernails. *Radiat. Meas.* **2009**, *44*, 6–10. [CrossRef]
30. Romanyukha, A.; Trompier, F.; Reyes, R.A.; Melanson, M.A. EPR measurements of fingernails in Q-band. *Radiat. Meas.* **2011**, *46*, 888–892. [CrossRef]
31. Reyes, R.A.; Trompier, F.; Romanyukha, A. Study of the stability of signals after irradiation of fingernail samples. *Health Phys.* **2012**, *103*, 175–180. [CrossRef] [PubMed]
32. Trompier, F.; Queinnec, F.; Bey, E.; De Revel, T.; Lataillade, J.J.; Clairand, I.; Benderitter, M.; Bottollier-Depois, J.F. EPR retrospective dosimetry with fingernails: Report on first application cases. *Health Phys.* **2014**, *106*, 798–805. [CrossRef] [PubMed]
33. Romanyukha, A.; Trompier, F.; Reyes, R.A.; Christensen, D.M.; Iddins, C.J.; Sugarman, S.L. Electron paramagnetic resonance radiation dose assessment in fingernails of the victim exposed to high dose as result of an accident. *Radiat. Environ. Biophys.* **2014**, *53*, 755–762. [CrossRef]
34. Trompier, F.; Romanyukha, A.; Swarts, S.; Reyes, R.; Gourier, D. Influence of nails polish in EPR dosimetry with human nails. *Radiat. Meas.* **2015**, *75*, 6–8. [CrossRef]
35. Sholom, S.; McKeever, S.W.S. Emergency EPR dosimetry technique using vacuum-stored dry nails. *Radiat. Meas.* **2016**, *88*, 41–47. [CrossRef]

36. Sholom, S.; McKeever, S.W.S. Stability of X-band EPR signals from fingernails under vacuum storage. *Radiat. Phys. Chem.* **2017**, *141*, 78–87. [CrossRef]
37. Swarts, S.G.; Sidabras, J.W.; Grinberg, O.; Tipikin, D.S.; Kmiec, M.M.; Petryakov, S.V.; Schreiber, W.; Wood, V.A.; Williams, B.B.; Flood, A.B.; et al. Developments in biodosimetry methods for triage with a focus on X-band electron paramagnetic resonance in vivo fingernail dosimetry. *Health Phys.* **2018**, *115*, 140–150. [CrossRef]
38. Gonzales, C.A.B.; Yasuda, H.; Hirota, S.; Miki, K.; Saito, A.; Taño, J.E.; Nagata, Y. Investigation of the applicability of the ESR nail dosimetry for assessment of accidental exposure in medical facilities. *Radiat. Meas.* **2019**, *124*, 91–97. [CrossRef]
39. Sholom, S.; McKeever, S.W.S. An advance in EPR dosimetry with nails. *Radiat. Prot. Dosim.* **2019**, *186*, 60–64. [CrossRef]
40. Lu, C.-C.; Lin, H.-H.; Hsu, C.-H.; Wang, F.-N.; Lin, J.-P.; Lai, L.-H. Potential use of environmental biological samples for retrospective electron paramagnetic resonance dosimetry of radiation accidents. *Appl. Sci.* **2020**, *10*, 6867. [CrossRef]
41. Trompier, F.; Romanyukha, A.; Reyes, R.; Vezin, H.; Queinnec, F.; Gourier, D. State of the art in nail dosimetry: Free radicals identification and reaction mechanisms. *Radiat. Environ. Biophys.* **2014**, *53*, 291–303. [CrossRef] [PubMed]
42. Bailiff, I.K.; Sholom, S.; McKeever, S.W.S. 2016. Retrospective and emergency dosimetry in response to radiological incidents and nuclear mass-casualty events: A review. *Radiat. Meas.* **2016**, *94*, 83–139. [CrossRef]
43. Marciniak, A.; Ciesielski, B. EPR dosimetry in nails—A review. *Appl. Spectrosc. Rev.* **2016**, *51*, 73–92. [CrossRef]
44. Wilcox, D.E.; He, X.; Gui, J.; Ruuge, A.E.; Li, H.; Williams, B.B.; Swartz, H.M. Dosimetry based on EPR spectral analysis of fingernail clippings. *Health. Phys.* **2010**, *98*, 309–317. [CrossRef]
45. Marciniak, A.; Ciesielski, B.; Juniewicz, M.; Prawdzik-Dampc, A.; Sawczak, M. The effect of sunlight and UV lamps on EPR signal in nails. *Radiat. Environ. Biophys.* **2019**, *58*, 287–293. [CrossRef] [PubMed]
46. Gonzales, C.A.B.; Hirota, S.; Taño, J.E.; Yasuda, H. Investigation of the dose-response in multiple irradiated fingernails and the combined effect of drying time-temperature to the ESR signal. *Radiat. Meas.* **2020**, *136*, 106337. [CrossRef]
47. Marciniak, A.; Ciesielski, B.; Prawdzik-Dampc, A. The effect of dose and water treatment on EPR signals in irradiated fingernails. *Radiat. Prot. Dosim.* **2014**, *162*, 6–9. [CrossRef]
48. Zhang, T.; Zhao, Z.; Zhang, H.; Zhai, H.; Ruan, S.; Jiao, L.; Zhang, W. Effects of water on fingernail electron paramagnetic resonance dosimetry. *J. Radiat. Res.* **2016**, *57*, 460–467. [CrossRef]
49. Gonzales, C.A.B.; Yasuda, H.; Hirota, S.; Miki, K.; Saito, A.; Taño, J.E.; Nagata, Y. Fingernail dosimetry using electron spin resonance for radiation disaster response. *J. Phys. Conf. Ser.* **2019**, *1248*, 012072. [CrossRef]
50. Overexposure of a Worker (France, 31 January 2019). Laka: Documentation and Research Center on Nuclear Energy. Available online: https://www.laka.org/docu/ines/event/1144 (accessed on 10 December 2020).
51. Hand Contamination and Overexposure of Workers at a Nuclear Medical Facility (UK, 31 March 2019). Laka: Documentation and Research Center on Nuclear Energy. Available online: https://www.laka.org/docu/ines/event/1155 (accessed on 10 December 2020).
52. Hand Contamination of Radiation Workers (Australia, 21 June 2019). Laka: Documentation and Research Center on Nuclear Energy. Available online: https://www.laka.org/docu/ines/event/1154 (accessed on 10 December 2020).

MDPI
St. Alban-Anlage 66
4052 Basel
Switzerland
Tel. +41 61 683 77 34
Fax +41 61 302 89 18
www.mdpi.com

Applied Sciences Editorial Office
E-mail: applsci@mdpi.com
www.mdpi.com/journal/applsci

MDPI
St. Alban-Anlage 66
4052 Basel
Switzerland

Tel: +41 61 683 77 34
Fax: +41 61 302 89 18

www.mdpi.com

ISBN 978-3-0365-3614-9